Highlights in Theoretical Chemistry 11
Series Editors: Christopher J. Cramer · Donald G. Truhlar

Manuel F. Ruiz-Lopez
Francisco J. Olivares del Valle *Editors*

9th Congress on Electronic Structure: Principles and Applications (ESPA 2014)

A Conference Selection from Theoretical Chemistry Accounts

Springer

Highlights in Theoretical Chemistry

Vol. 11
Series Editors: Christopher J. Cramer • Donald G. Truhlar

More information about this series at http://www.springer.com/series/11166

Manuel F. Ruiz-Lopez • Francisco J. Olivares del Valle
Volume Editors

9th Congress on Electronic Structure: Principles and Applications (ESPA 2014)

A Conference Selection from Theoretical Chemistry Accounts

With contributions from

Diego R. Alcoba • Ibon Alkorta • Xavier Assfeld • Luis Miguel Azofra
V. G. Baonza • Zoila Barandiarán • Gian Luigi Bendazzoli • Oriana Brea
Luigi Cavallo • M. Natália D. S. Cordeiro • Christopher J. Cramer
Hugo Gattuso • Élise Dumont • Stefano Evangelisti • A. V. Evstafev
José L. C. Fajín • Edoardo Fertitta • R. Franco • Juan Frau • Laura Gagliardi
José R. B. Gomes • Leticia González • Ana M. Graña • Raymond Grüber
Francesc Illas • F. Izquierdo-Ruiz • Georgia M. A. Junqueira
Yukio Kawashima • Tsutomu Kawatsu • Muammar El Khatib • Daniel Kinzel
T. Latychevskaia • Paolo Lazzeretti • Luis Lain • Thierry Leininger
Diego López-Carballeira • Marcos Mandado • M. Marqués
Ana África Márquez García • Marilia T. C. Martins-Costa • J. M. Menéndez
Josef Michl • Antonio Monari • A. Morales-García • Ibério de P. R. Moreira
Francisco Muñoz • Rana Obaid • Yudai Ogata • Josep M. Oliva
Francisco J. Olivares del Valle • Ofelia B. Oña • Markus Oppel
E. V. Orlenko • F. E. Orlenko • Joaquín Ortega-Castro • Francisco Partal Ureña
Beate Paulus • Quan Manh Phung • Ignacio Pérez-Juste • Albert Poater
María del Carmen Ramírez Avi • Nicolás Ramos-Berdullas • J. M. Recio
Daniel Reta Mañeru • Manuel F. Ruiz-López • Fernando Sato
Steve Scheiner • Luis Seijo • David Semrouni • Christian Solís-Calero
Masanori Tachikawa • Kaito Takahashi • Filipe Teixeira • Alicia Torre
Sai Vikrama Chaitanya Vummaleti • Sara Watanabe

Springer

Volume Editors
Manuel F. Ruiz-Lopez
Campus Vandoeuvre-lès-Nancy
Université de Lorraine
Nancy, France

Francisco J. Olivares del Valle
Campus Badajoz
Universidad de Extremadura
Badajoz, Spain

Originally published in Theor Chem Acc, Volume 133 (2014), volume 134 (2015),

ISSN 2194-8666 ISSN 2194-8674 (electronic)
Highlights in Theoretical Chemistry
ISBN 978-3-662-48793-8 ISBN 978-3-662-49221-5 (eBook)
DOI 10.1007/978-3-662-49221-5

Library of Congress Control Number: 2016932408

Springer Heidelberg New York Dordrecht London

Printed on acid-free paper

Springer-Verlag GmbH Berlin Heidelberg is part of Springer Science+Business Media (www.springer.com)

Contents

Theor Chem Acc (2015) 134:92
DOI 10.1007/s00214-015-1687-6

PREFACE

Preface to the ESPA-2014 special issue

Manuel F. Ruiz-López[1] · Francisco J. Olivares del Valle[2]

Published online: 11 July 2015

This issue of Theoretical Chemistry Accounts collects a compilation of research works presented at the 9th edition of the *Electronic Structure: Principles and Applications* conference (ESPA-2014) held in Badajoz, Spain, on the July 2–4, 2014.

The ESPA conferences were initiated in 1998, and since then, they have been organized every 2 years. The previous editions were organized in Madrid (1998), San Sebastián (2000), Sevilla (2002), Valladolid (2004), Santiago de Compostela (2006), Palma de Mallorca (2008), Oviedo (2010) and Barcelona (2012). The ESPA conferences were initially intended to bring together the Spanish community in the field of Theoretical and Computational Chemistry. However, ESPA has grown over time in terms of national and international participation, and in the last years, it has become a key scientific event of international reputation.

ESPA-2014 was organized by the Quantum Chemistry and Molecular Modelling (QCAMM) group of the University of Badajoz (see Fig. 1). Four main topics were covered in the conference: "Theory, Methods and Foundations," "Materials Science," "Structure and Chemical Reactivity" and "Environmental Effects and Modelling." They were properly represented by means of nine invited Plenary Talks, twenty-four Oral Communications and about 120 Poster Presentations. The meeting was attended by a total number of 178 participants coming from different universities around the world. The official picture of the meeting is shown in Fig. 2. Most of the participants came from Spain, but delegates from 14 other countries were present, which include (in alphabetic order) Austria, Brazil, Czech Republic, Denmark, France, Germany, Italy, Japan, the Netherlands, Portugal, Russia, Sweden, UK and the USA.

Together with a high-quality scientific program, the organizers tried to provide delegates with the opportunity to experience the Extremadura region as part of the congress. To this aim, an engaging social program was designed starting on the evening of July 2 with a welcome reception at the Archeological Museum of Badajoz. Besides, the delegates enjoyed a mid-conference excursion to the old town of Cáceres, a UNESCO World Heritage Site since 1986. Finally, the congress was closed with a banquet at the Ethnographic Museum gardens of the magnificent city of Olivenza.

As an important satellite event of the ESPA-2014 conference, the *Third Annual Workshop of the Joint Doctorate Program on Theoretical Chemistry and Computational Modelling* (TCCM) took place on July 1 at the Faculty of Sciences of the University of Extremadura. Such a workshop event is regularly organized for Ph.D. students, as a complementary training of the TCCM doctorate program, and offers them the opportunity to present their research work via oral communications at the end of the first year of the doctorate studies.

During the conference, the members of the organizing committee brought to the attention of the delegates the extremely difficult situation that is presently facing the Spanish research system as a consequence of the drastic R + D funding reduction decided by the Spanish government. A document describing this situation, known as the "Badajoz Manifesto," was sent to the media. It stated, in

Published as part of the special collection of articles derived from the 9th Congress on Electronic Structure: Principles and Applications (ESPA 2014).

✉ Manuel F. Ruiz-López
Manuel.Ruiz@univ-lorraine.fr

✉ Francisco J. Olivares del Valle
fjov@unex.es

[1] University of Lorraine, Nancy, France

[2] University of Badajoz, Badajoz, Spain

Fig. 1 The ESPA 2014 Organizing Committee, from *left* to *right*: Dr. José Carlos Corchado Martín-Romo, Glauco Garrido Almeida (guest Ph.D. student), Dr. María de la Luz Sánchez Mendoza, Dr. Aurora Muñoz Losa, Dr. María Elena Martín Navarro (Secretary), Rute Barata Morgado (Ph.D. student), Prof. Francisco J. Olivares del Valle (Chairman) and Dr. Manuel Angel Aguilar Espinosa. Dr. Ignacio Fernández Galván (not in the picture) was also a member of the Organizing Committee

Fig. 2 The ESPA 2014 official picture with the 178 delegates coming from 15 different countries

particular, that such an unprecedented budget reduction has marked a turning point for the Spanish scientific growth, while it is creating a great discouragement of the Spanish young talents, who do not see any perspectives to develop a scientific carrier in their country.

The next ESPA conference will be organized in 2016 in the city of Castellón, Spain, close to the Mediterranean Sea. All our best wishes to the organizers for a successful conference, and we hope to see you there!

Theor Chem Acc (2015) 134:1590
DOI 10.1007/s00214-014-1590-6

REGULAR ARTICLE

AMOEBA force field parameterization of the azabenzenes

David Semrouni · Christopher J. Cramer · Laura Gagliardi

Received: 30 August 2014 / Accepted: 21 October 2014 / Published online: 11 November 2014

Abstract We present an extension of the AMOEBA force field to several common organic heterocycles, namely pyridine, pyrazine, pyrimidine, pyridazine, the three unique triazines, and the two unique tetrazines. Atomic multipoles for newly defined atom types were obtained from quantum chemical calculations on the isolated molecules. Atomic polarizability parameters are maintained at their standard AMOEBA values for corresponding atomic classes while standard van der Waals parameters are rescaled to reproduce CCSD(T) intermolecular interaction energies of selected dimer structures. In order to improve vibrational frequencies that are important both spectroscopically and for flexible dynamics, parameters for covalent terms, i.e., bond-stretching, angle-bending, and stretch-bend terms, were optimized and added to the existing AMOEBA force field. We validate our force field through comparison of molecular structural, vibrational, electrostatic, and energetic properties—including intermolecular interaction energies—to reliable quantum chemical data for the various systems of interest.

Published as part of the special collection of articles derived from the 9th Congress on Electronic Structure: Principles and Applications (ESPA 2014).

Electronic supplementary material The online version of this article (doi:10.1007/s00214-014-1590-6) contains supplementary material, which is available to authorized users.

D. Semrouni · C. J. Cramer (✉) · L. Gagliardi (✉)
Department of Chemistry, Chemical Theory Center, and Supercomputing Institute, University of Minnesota, 207 Pleasant St. SE, Minneapolis, MN 55455, USA
e-mail: cramer@umn.edu

L. Gagliardi
e-mail: gagliard@umn.edu

Keywords Polarizable force field · Intermolecular interactions · Molecular mechanics · Pi stacking

1 Introduction

Assessment of chemical properties can often require a computationally costly sampling of a high-dimensional phase space in order accurately to predict ensemble-averaged values. Molecular mechanics simulations offer an efficient way to sample such ensembles, with the quality of the results depending on the ability of the force field adequately to describe the energetics of the system under the conditions of the simulation. The range of applicability of a particular force field depends both upon its functional form (e.g., the degree to which it employs harmonic terms vs anharmonic, and the degree to which it includes cross-terms (which couple different internal coordinates), high-order electric multipoles, or polarization) and its various parameters. Force fields are usually made more accurate through the proliferation of atom types, i.e., atoms of the same element that, as a consequence of belonging to different chemical functional groups, have interaction energies that are computed using different parameters.

One such force field, AMOEBA, was originally devoted to water and biomolecules, but it now also finds use for more general applications involving organic molecules. We here present an extension of AMOEBA through a complete parameterization of the stable azabenzene series, i.e., six-membered N-heterocyclic rings incorporating varying numbers of N atoms from 1 to 4. Such heterocycles are found widely in various pi-conjugated systems [1] and their derivatives are ubiquitous in biological [2] and pharmaceutical [3] compounds, as well as a number of metal–organic cages [4–6] and frameworks [7–9]. Thus, we focus here on

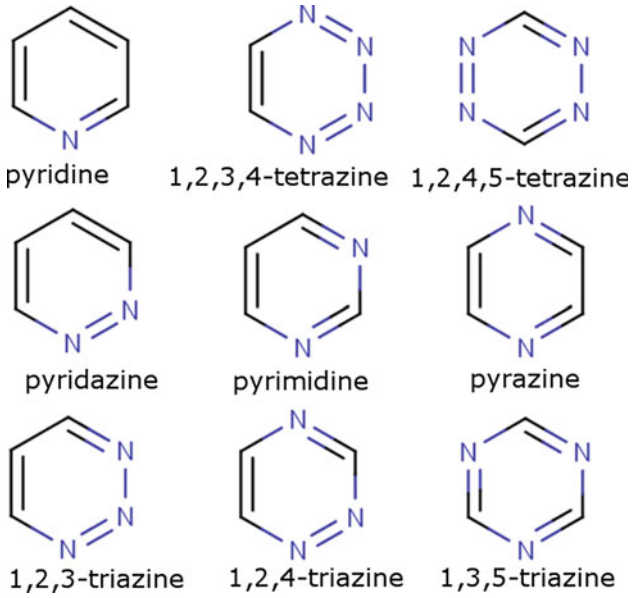

Fig. 1 Six-Membered N-heterocyclic compounds (azabenzenes)

heterocycles having the formula $C_{6-x}H_{6-x}N_x$, $x = 1$–4 (the corresponding compounds for $x = 5$ and 6 are insufficiently stable to be of interest). This series includes pyridine, pyrazine, pyrimidine, pyridazine, 1,2,3-, 1,2,4-, and 1,3,5-triazine, and 1,2,3,4- and 1,2,4,5-tetrazine (Fig. 1).

In Sect. 2, we report the details of quantum and molecular mechanics calculations undertaken in order to optimize parameters for the various isolated molecules. In Sect. 3, we examine dimeric intermolecular interactions and make use of such energies to validate our model, refine the force field's van der Waals parameters, and assess the relative importance of the different terms in the force field for these N-heterocyclic systems. Finally, Sect. 4 offers some conclusions. We anticipate that this extension of AMOEBA will be particularly useful for the study of host–guest (or enzyme–substrate) chemistry involving aromatic N-heterocycles in either or both components of such interacting systems.

2 Computational details

We describe our extension of the AMOEBA force field. Our parameterization of the various azabenzenes relies on quantum chemical reference calculations.

2.1 Quantum calculations

All quantum chemical calculations were performed with the Gaussian 09 suite of electronic structure programs [10]. Density functional theory (DFT) calculations were performed employing an ultrafine grid for the computation of all two-electron integrals and their derivatives. Unless otherwise noted, geometry optimizations and vibrational frequency calculations were performed using the M06-L functional [11] with the cc-pVDZ basis set [12]. This level of theory has been documented to predict energies and structures in good agreement with highly correlated electronic structure theories for many systems relevant to those examined here [13, 14]. Electronic probability densities and electrical moments were also computed at these geometries using M06-L, but for these properties, the cc-pVTZ basis set was employed [12]. Intermolecular interaction energies were calculated using Møller–Plesset second-order perturbation theory [15] (MP2) and coupled cluster theory including single, double, and perturbatively estimated triple excitations (CCSD(T)) [16–18]. In all calculations, basis set superposition error (BSSE) corrections were included through counterpoise correction [19]. For efficiency, we estimate large basis CCSD(T) energies according to [20–23]

$$U_{\text{large}}^{\text{CCSD(T)}} \cong U_{\text{large}}^{\text{MP2}} + \left(U_{\text{small}}^{\text{CCSD(T)}} - U_{\text{small}}^{\text{MP2}}\right) \quad (1)$$

2.2 Force field

Force field energies are typically separable into bonded and non-bonded interactions. Bonded interactions can be treated most simply using harmonic potentials. Additional anharmonic correction terms generally improve the predicted shape of associated potential energy hypersurfaces. Force fields conventionally include bond-stretching, angle-bending, and torsional potentials, as well as out-of-plane bending or improper torsional potentials. In addition, cross-terms can be considered to couple more elementary motions, e.g., stretch-bend terms that couple bond-stretching and angle-bending deformations. Non-bonded non-electrostatic [van der Waals (vdW)] interactions, by contrast, are traditionally modeled using Buckingham or 6–12 Lennard–Jones potentials. Another formalism is the buffered 7–14 potential advanced by Halgren [24], which has been shown to give improved descriptions of intermolecular interactions, especially for rare gas dimers and clusters, where interactions are dominated by vdW dispersion–repulsion interactions.

In this manuscript, we make a distinction between polarization and permanent electrostatic interactions. Therefore, "electrostatic interactions" refers to all Coulomb interactions before the calculation of induced moments. Intermolecular electrostatic interactions, in the simplest case, employ a distribution of atom-centered partial atomic point charges to represent the continuous distribution of charge that characterizes a quantum mechanical molecule. Several models have been proposed to assign atomic point charges based on quantum mechanical

calculations [25–29]. Such point charge models necessarily assume that the local distribution of charge about each nucleus in a molecule is spherically symmetric; however, the anisotropy of the electron density around each nucleus can also be important. This is most evident when considering the density perturbation associated with a lone pair on a heteroatom, or a π cloud in an aromatic, for example. A simple atom-centered point charge model is unable to represent such a charge distribution at such levels of detail [30]. A similar limitation of models based on atom-centered point charges is associated with the description of sigma and pi-holes that have been characterized for halogens, chalcogens, and other atoms; [31, 32] in these cases, the globally negative partial atomic charge of, say, a halogen atom is unable accurately to describe the small electrically positive region of space at the outside of the bond axis that is responsible for the so-called halogen bonding. In all of these various cases, however, the complexity of the charge density can be described in a more accurate way using atomic multipoles [33, 34], and/or by adding point charges to additional, non-atomic sites of the molecular model [35–37]. We note that increased physicality can also be achieved through consideration of charge penetration effects, or by replacing atomic point charge monopoles with atomic Gaussian charge density distributions [38–43]. Lastly, polarization and charge transfer [44, 45] effects can, at least to some extent, be incorporated into otherwise classical force fields. In the case of atomic point induced dipole models [46], a damping factor can be used to smear the charge distribution of an atomic charge model [47]. This smearing approach has been extended to higher-order atomic multipoles [48]. Rasmussen et al. [49] have shown the importance of including both higher-order electrical moments and polarization when accurate conformational energies are desired.

In this study, we work within the framework of the flexible, anharmonic, polarizable, AMOEBA force field, which includes a distribution of atomic electrical multipole moments up through quadrupoles. We extend this force field to include atom types corresponding to the azabenzene series and propose new van der Waals and covalent parameters for the atom classes involved in these aromatic systems.

2.2.1 The AMOEBA formalism

AMOEBA bonded interactions follow the MM3 force field [50, 51]. Thus, the total energy, U_{tot} is defined as a sum of intramolecular covalent terms and both intra- and intermolecular non-covalent terms according to:

$$U_{\text{tot}} = U_{\text{str}} + U_{\text{bnd}} + U_{\text{str-bnd}} + U_{\text{oop}} + U_{\text{torsion}} + U_{\text{vdW}} + U_{\text{elec}} + U_{\text{pol}} \quad (2)$$

where U_{str} and U_{bnd} are, respectively, the bond-stretching and the angle-bending terms, $U_{\text{str–bnd}}$ is a term coupling bond-stretching and angle-bending. U_{oop} describes out-of-plane deformations and U_{torsion} defines the energetic term associated with a dihedral angle. The remaining terms U_{vdW}, U_{elec}, and U_{pol} account for van der Waals, permanent electrostatic, and polarization interactions, respectively.

Considering a bond distance b, its force constant K_{b}, and the equilibrium value b_0 associated with this term, the stretching component of the energy is expressed as a harmonic potential with cubic and quartic contributions to the anharmonicity:

$$U_{\text{str}}(b) = K_{\text{b}}(b-b_0)^2\left[1 - 2.55(b-b_0) + \frac{7}{12}2.55^2(b-b_0)^2\right] \quad (3)$$

The energy to deform a valence angle to a value θ differing from an ideal reference value θ_0 with a force constant K_θ includes anharmonic contributions through a sextic term:

$$U_{\text{bnd}}(\theta) = K_\theta(\theta-\theta_0)^2\left[1 - 0.014(\theta-\theta_0) + 5.6\times10^{-5}(\theta-\theta_0)^2 - 7\times10^{-7}(\theta-\theta_0)^3 + 2.2\times10^{-8}(\theta-\theta_0)^4\right] \quad (4)$$

The coupling between bond-stretching and angle-bending is described by Eq. (5), in which $K_{\text{str–bnd}}$ is a force constant associated with angular deformation (θ–θ_0) and the bond length variations ($b - b_0$) and ($b' - b'_0$) for the two bonds that form the valence angle.

$$U_{\text{str-bnd}}(b,b',\theta) = K_{\text{str-bnd}}\left[(b-b_0)\left(b'-b'_0\right)\right](\theta-\theta_0) \quad (5)$$

For trivalent and "planar" sp^2-hybridized atoms, the energy associated with an out-of-plane deformation, also called an improper torsion, is determined following Wilson, Decius, and Cross [52] as the product of the square of the dihedral χ defined by the four atoms and an associated force constant K_χ.

$$U_{\text{oop}}(\chi) = K_\chi\chi^2 \quad (6)$$

Torsional energies for rotation about the central bond of four consecutively bonded atoms are computed from the first three terms of a Fourier series that depends on the dihedral angle α, and an amplitude A_n and phase angle ϕ_n (taken to be either 0 or 180°) associated with each Fourier term, i.e.,

$$U_{\text{torsion}}(\alpha) = \frac{1}{2}\sum_{n=1}^{3}A_n[1+\cos(n\alpha-\phi_n)] \quad (7)$$

Non-bonded energies in AMOEBA are computed from pairwise van der Waals (vdW) interactions, as well as permanent electrostatic and many-body polarization

interactions. The vdW term is modeled as a buffered 14–7 potential as proposed by Halgren [24]:

$$U_{\mathrm{vdW}}^{ij} = \varepsilon_{ij}\left(\frac{1+\delta}{\frac{R_{ij}}{R_{ij}^0}+\delta}\right)^7\left(\frac{1+\gamma}{\left(\frac{R_{ij}}{R_{ij}^0}\right)^7+\gamma}-2\right) \tag{8}$$

where ε_{ij} is the potential well depth, R_{ij} is the interatomic distance, R_{ij}^0 is the minimum energy distance, and δ and γ are unitless buffering constants set to 0.07 and 0.12, respectively. The mixing rules used by AMOEBA to determine ε_{ij} values from atomic ε_{ii} and ε_{jj} parameters are:

$$\varepsilon_{ij} = \frac{4\varepsilon_{ii}\varepsilon_{jj}}{\left(\varepsilon_{ii}^{1/2}+\varepsilon_{jj}^{1/2}\right)^2} \tag{9}$$

and for the case of R_{ij}^0 values

$$R_{ij}^0 = \frac{\left(R_{ii}^0\right)^3+\left(R_{jj}^0\right)^3}{\left(R_{ii}^0\right)^2+\left(R_{jj}^0\right)^2} \tag{10}$$

In the case of hydrogen atoms, an additional parameter (called the reduction factor) is used to scale the position of the hydrogenic vdW interacting site along the corresponding covalent bond involving that atom. This scaling moves the site closer to the heavy atom to which the hydrogen is attached and is meant to reflect the degree to which hydrogenic electron density is displaced toward the heavy atom when covalent bonding takes place.

2.2.2 *Details of AMOEBA calculations*

All AMOEBA calculations were performed with the Tinker software package [53]. We employed a vdW cutoff radius of 9 Å. A successive over-relaxation algorithm [54] was employed to accelerate the convergence of the self-consistent calculation of the mutually induced atomic point dipoles. Geometry optimizations were performed with a 10^{-6} kcal/mol/Å criterion on the gradient of the energy.

2.3 Parameterization

In a recent study, Ren et al. proposed a method to automate small-molecule parameterization within the AMOEBA force field [55]. We followed a similar approach to theirs in the parameterization of the azabenzenes. In particular, within the context of standard AMOEBA atomic polarizabilities and van der Waals parameters, we first determined the atomic multipoles to be used to describe electrostatic interactions, and we subsequently determined a set of bonded interaction parameters that would reproduce both equilibrium structures and harmonic vibrational frequencies.

AMOEBA is designed to permit a consistent treatment of intra- and intermolecular polarization. For large molecules, intramolecular polarization takes place between defined polarization groups. Given the small size of the six-membered aromatic rings considered here, all atoms in the molecule were taken to be a single polarization group, i.e., there is no internal polarization from intramolecular atomic interactions in any of the heterocycles. As in the original AMOEBA force field, we permit C and H atoms in aromatic rings to have atomic polarizabilities larger than those employed for aliphatic analogs, but the polarizability of nitrogen does not vary from the AMOEBA parameter that is always used for N. For van der Waals interactions, we employed both the atomic radii and well-depth parameters proposed by Ren et al. [55], who derived these as a function of element and associated valence orbitals.

2.4 Atomic multipoles

The importance of the consideration of the molecular quadrupole when computing intermolecular interactions for complexes of benzene, graphene [56], and arenes [57] has been repeatedly emphasized. Quadrupole elements out of the molecular plane can be particularly important for the modeling of electrostatic effects associated with π electron distributions. However, a single-center molecular quadrupole may be insufficient to capture all of the energetically important electrostatic interactions. Atomic multipoles permit a more detailed description of the full molecular charge distribution. As in the original AMOEBA force field, we determine atomic multipoles from quantum chemical calculations using distributed multipole analysis (DMA) [58, 59] as implemented in the GDMA (Gaussian Distributed Multipole Analysis) program; [60] a radius of 0.65 Å is taken for all atoms except hydrogen, for which a radius of 0.31 Å was used (this approach is similar to one used previously by Price and Stone when they examined Hartree–Fock charge distributions in six-member N-heterocyclic aromatics [61, 62]). The DMA fitting was done to the Kohn–Sham electron density obtained from M06-L/cc-pVTZ calculations.

Multipoles determined from GDMA are spherical harmonics that can be projected to a global Cartesian frame. For practical use, however, atomic multipoles must be defined within local coordinate frames. The choice of local frame influences variations in overall molecular electrical moments when flexible molecules sample accessible conformations, so for purposes of stability it is good practice to define the local frame for a given atom using the least flexible framework available within which that atom is found. Thus, for example, a bond vector involving a hydrogen

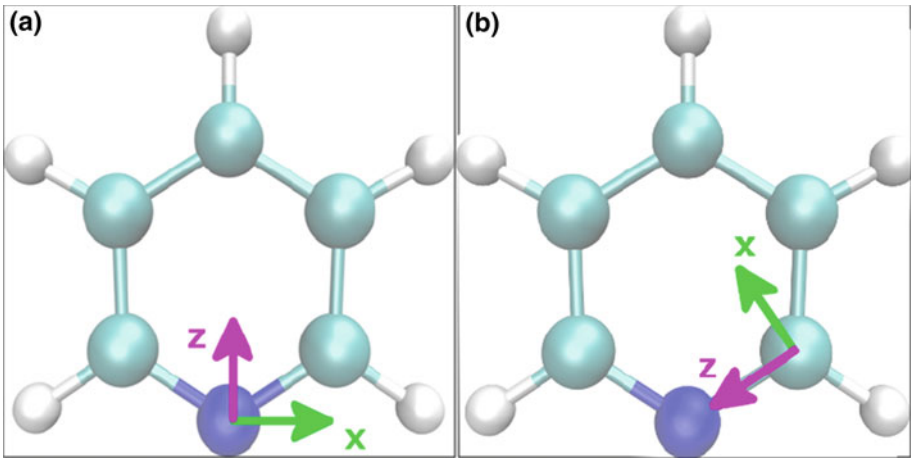

Fig. 2 Local frame *x*- and *z*-axes of pyridine N defined according to the Bisector convention (**a**), and C_α defined according to the *z*-then-*x* convention (**b**)

atom would generally be a poor choice to define the local frame for a heavy atom because the hydrogen atom will sample space more widely around its most probable position than would normally be true for alternative heavy atoms. Thus, it is important to note that choosing a local frame convention is in some sense equivalent to choosing the functional form for an interaction energy—it is a fundamental component of the force field.

We illustrate the bisector and *z*-then-*x* conventions that we employed for the case of pyridine in Fig. 2. The symmetry axis that includes the nitrogen atom permits the definition of its first local frame axis, *z*, to be taken as the C–N–C bisector. The *x*-axis is then taken to be the line orthogonal to *z* within the C–N–C plane. Whenever symmetry permits, we employ this bisector definition of local frames. For atoms not found on a symmetry axis, in order to have local frame axes as insensitive to molecular vibrations as possible, we define the first axis to be the vector to the heaviest neighboring atom. Thus, for the carbon atom at the 2 position in pyridine, the *z*-axis is defined by its bond to nitrogen (Fig. 2). The next axis, *x*, is determined as the line orthogonal to *z* and in the plane defined by the N1–C2–C3 linkage. The remaining axis, *y*, is of course uniquely defined by the constraint that it be orthogonal to both the *x*- and *z*-axes. Local frames for hydrogen atomic multipoles were defined with *z*-axes along the vector to the heavy atom to which they are connected, and with the *x*-axis then defined by one of the subsequent atoms bonded to the heavy atom. We take approaches analogous to that for pyridine for all of the heterocycles examined here.

Parameter files are provided in supporting information. They include atomic multipoles attributed to each site with local frame definitions, and atomic *c*, μ, and *Q* components. While we have chosen to adopt the DMA algorithm of Stone, we note that other methods have also been employed to assign local multipoles from molecular QM calculations [63–66].

3 Force field validation and refinement of vdW parameters

3.1 Bonded interactions, force constants, and vibrational frequencies

For all systems, we have optimized bonded interaction parameters in order to reproduce reference vibrational frequencies computed at the M06-L/cc-pVDZ level of theory. Frequencies corresponding to C–H stretching modes are easily identified and compared. Modes involving in-plane and out-of-plane angular deformations of H atoms are also typically well localized, although they do not depend only on diagonal terms (bond-stretching, angle-bending, and improper torsions), but also on coupling terms. While matching vibrational frequencies for lower frequency modes is not necessarily more difficult, it does become increasingly difficult to assign the various normal modes to specific localized motions and it is correspondingly difficult to obtain good agreement for the composition of internal coordinate displacement vectors between the QM and MM calculations. Nevertheless, in our tuning of parameters, we did undertake such comparisons when assessing the relative quality of alternative parameter choices. Thus, bond-stretching, in-plane angle-bending, out-of-plane angle-bending, and stretching-bending terms were tuned to reproduce as closely as possible the M06-L frequencies of selected vibrational normal modes, paying special attention to modes having harmonic frequencies near 1,500 cm^{-1}, as such modes are associated with internal aromatic ring stretching modes. Vibrational frequencies computed for pyridine with our extension of AMOEBA are presented in Table S1 and compared to M06-L reference values, as well as to frequencies computed using the Universal Force Field [67] (UFF). As a more complete measure of the accuracy of our intramolecular bonded interactions, we also compared the full Cartesian Hessian matrices computed at the

Table 1 Mean unsigned and root-mean-square deviations (kcal/mol/Å^2) of Cartesian Hessian elements from AMOEBA and UFF compared to M06-L values averaged over all and over only diagonal elements

Molecule	AMOEBA				UFF			
	Full		Diag.		Full		Diag.	
	MUD	RMSD	MUD	RMSD	MUD	RMSD	MUD	RMSD
Pyridine	14	38	47	83	32	95	191	300
Pyrazine	34	93	57	93	69	176	324	470
Pyridazine	20	46	58	97	48	153	289	479
Pyrimidine	19	48	59	107	46	136	288	430
1,2,3-Triazine	29	66	76	119	97	249	480	479
1,2,4-Triazine	28	61	83	133	70	200	418	608
1,3,5-Triazine	29	65	108	154	69	181	395	551
1,2,3,4-Tetrazine	44	90	107	158	110	298	595	772
1,2,4,5-Tetrazine	41	82	121	172	101	267	568	772
Average over all	29	66	80	124	71	195	394	570

MM and QM levels. As can be seen in Table 1, errors are similar across the various heterocycles. These errors are, as expected, larger for diagonal elements than for off-diagonal elements. Encouragingly, we see significant improvement for AMOEBA over UFF when compared to the QM reference values, noting, of course, that UFF was not directly parameterized against this figure of merit, as we have done here for our AMOEBA extension.

While vibrational frequencies are a particularly sensitive indicator of the quality of the parameterization, equilibrium structures are obviously also important. Structural RMSD values for optimized azabenzene structures computed with AMOEBA compared to M06-L are on the order of a few hundredths of an Ångstrom (Table S2); the maximum RMSD is 0.08 Å for 1,2,4,5-tetrazine, for which some subtleties of the bonding may conceivably require the use of more than just three atom types, but we consider this RMSD acceptable for most purposes. AMOEBA, and M06-L yield bond lengths that differ in general by less than 0.01 Å (the larger values of RMSD are due to small differences in angles amplifying bonding differences across the entire molecular structure).

3.2 Molecular multipoles and electrostatic potential

We next assess the utility of our force field by comparing the MM and QM electrical moments for the individual molecules at the same geometry, considering dipole and quadrupole moments in all cases. In those molecules having a center of inversion, the dipole moment is zero by symmetry, of course. The traceless quadrupoles, however, which provide a measure of the deviation of the charge distribution from spherical symmetry [68, 69], may be compared in every instance.

As all of the studied molecules are neutral (uncharged), the molecular dipole moment is independent of origin, but this is not true for the quadrupole moment in those molecules having a nonzero dipole moment (only the first nonvanishing moment in an electrical multipole expansion is independent of origin) [70]. We report quadrupole moments that take the center of nuclear charge (the charge barycenter) as the origin for all cases. AMOEBA electrical multipole moment components are compared to those computed at the M06-L level in Table 2. As electric quadrupole tensors are symmetric, we report only their *xx*, *xy*, *yy*, *xz*, *yz,* and *zz* components. In general, M06-L molecular dipole moments are reproduced by the newly parameterized AMOEBA atomic multipoles. For the molecular quadrupoles, AMOEBA agrees satisfactorily with M06-L in terms of anisotropy but absolute tensor components tend to be somewhat overestimated.

3.3 Intermolecular interactions

While comparison of the AMOEBA and QM absolute molecular electrical moments for the various heterocycles is an important part of validation, the primary motivation for our development of atomic multipole parameters is to use them for the computation of physically realistic intermolecular electrostatic interactions. In this context, Zhou et al. [71] extended the AMOEBA force field to benzene following a strategy analogous to that undertaken here. With their parameterization, they optimized structures for the benzene dimer that were found to be close to those computed at the coupled cluster with single, double, and perturbatively estimated triple excitations extrapolated to a complete basis set (CCSD(T)/CBS) level of theory, and the force–field interaction energies were found to have an average absolute deviation of 0.46 kcal/mol from the CCSD(T) energies evaluated over different dimers. We now assess the quality of our extension of AMOEBA to the various N-heterocycles by examining similar collections of homodimers.

Table 2 Molecular electric multipoles from M06-L (QM) and from AMOEBA (FF)

Molecule	μ_{FF}(D)	μ_{QM}(D)	Q_{FF}(B)	Q_{QM}(B)
Pyridine	0.000	0.000	6.861	4.164
	2.158	2.159	−0.011 −2.680	−0.007 −1.867
	0.000	0.000	0.001 0.000 −4.181	0.001 0.000 −2.747
Pyrazine	0.000	0.000	−3.884	−2.589
	0.000	0.000	8.969 5.080	5.980 3.387
	0.000	0.000	0.000 0.000 −1.196	0.000 0.000 −0.797
Pyrimidine	−2.252	−2.252	5.302	3.450
	0.000	0.000	0.000 −3.955	0.000 −2.594
	0.000	0.000	0.000 0.000 −1.347	0.000 0.000 −0.855
Pyridazine	0.000	0.000	6.551	4.497
	4.036	4.036	0.000 −4.660	0.000 −3.366
	0.000	0.000	0.000 0.000 −1.890	0.000 0.000 −1.130
1,2,3-Triazine	4.239	4.241	−0.994	−0.666
	2.199	2.200	−0.922 0.318	−0.612 0.215
	0.000	0.000	0.000 0.000 0.676	0.000 0.000 0.451
1,2,4-Triazine	2.174	2.174	−8.710	−5.863
	−1.274	−1.274	−4.373 7.569	−2.853 5.056
	0.000	0.000	0.000 0.000 1.141	0.000 0.000 0.808
1,3,5-Triazine	0.000	0.000	−0.788	−0.526
	0.000	0.000	0.000 −0.788	0.000 −0.526
	0.000	0.000	0.000 0.000 1.577	0.000 0.000 0.808
1,2,3,4-Tetrazine	2.333	2.277	−3.874	−2.472
	3.689	3.601	4.821 0.700	2.982 0.357
	0.000	0.000	0.000 0.000 3.174	0.000 0.000 2.116
1,2,4,5-Tetrazine	0.000	0.000	−13.141	−8.761
	0.000	0.000	0.000 9.472	0.002 6.315
	0.000	0.000	0.000 0.000 3.669	0.000 0.000 2.446

Dipole moment (μ) and quadrupole tensor (Q) elements are in units of Debye and Buckinghams, respectively, with the former listed as Cartesian components and the latter as lower-triangle tensor components

The accurate prediction of interaction energies between aromatic rings can be challenging for various levels of theory [13, 72–77], in part because the relative contributions of electrostatics, exchange repulsion, and dispersion tend to be of similar magnitude, so poor performance with respect to one of these phenomena can lead to significant errors overall. Having derived atomic partial charges and multipoles from consideration of molecular electrical moments, the final remaining AMOEBA parameters to be modified, in order to optimize computed interaction energies, are the various vdW terms (which up to now have played no role in the validations described above). The computed vdW non-bonded interactions empirically account for exchange repulsion, dispersion, and other quantum effects like charge transfer that are not explicitly taken into account by the force field. To maximize simplicity and transferability, we considered only three atom classes above for bonded parameters, namely H, C, and N. We continue to adopt that restriction in our optimization of vdW parameters adjusted to minimize the mean unsigned error over all dimer interaction energies comparing AMOEBA to extrapolated CCSD(T) values (see Eq. 1).

In the discussion below, AMOEBA0 refers to our AMOEBA extension with respect to electrostatics but employing the otherwise default AMOEBA vdW parameters for H, C, and N. We also present results for AMOEBA1, in which we scale the sets of default ε_{ii} and R_{ii}^0 parameters by values of 1.17 and 0.95, respectively. We additionally present AMOEBA2, in which the same scaling procedure as for AMOEBA1 is adopted with scale factors of 1.19 and 0.94, but in addition, we change the hydrogen reduction factor from its default value of 0.920–0.985. These additional adjustments may be regarded as sequentially increased relaxations of the N-heterocycle parameter set away from values originally optimized against more general training sets, where the value of such further relaxations must be judged by increased accuracy and an assessment of the physicality of the relaxed parameters, which in this instance involves variation from original AMOEBA defaults by only 5–19 %.

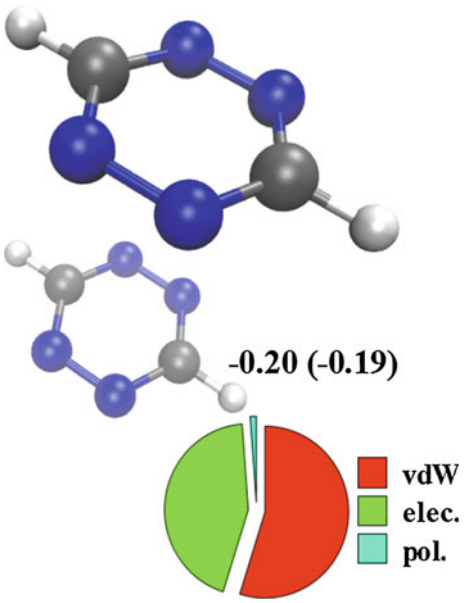

Fig. 3 Sandwich (S) conformation of the 1,2,4,5-tetrazine dimer; CCSD(T) and AMOEBA2 (*parentheses*) intermolecular interaction energies (kcal/mol) and relative contributions of AMOEBA2 terms (*pie chart*) are shown

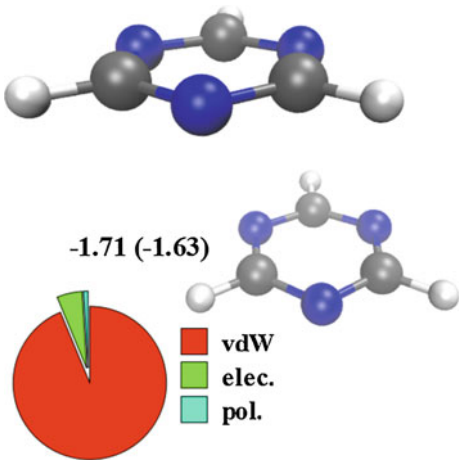

Fig. 4 Parallel-displaced (PD) conformation of the 1,3,5-triazine dimer; CCSD(T) and AMOEBA2 (*parentheses*) intermolecular interaction energies (kcal/mol) and relative contributions of AMOEBA2 terms (*pie chart*) are shown

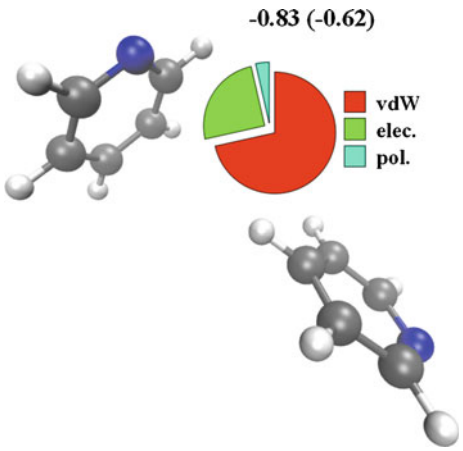

Fig. 5 T-shape (T) conformation of the pyridine dimer; CCSD(T) and AMOEBA2 (*parentheses*) intermolecular interaction energies (kcal/mol) and relative contributions of AMOEBA2 terms (*pie chart*) are shown

While the local functional, M06-L describes well the monomer properties, the use of Hartree–Fock exchange in M06 is expected to improve the description of weak intermolecular interactions. Thus, simply to generate a set of dimer structures for use in further benchmarking, we chose the M06/cc-pVDZ level of theory; the M06 family of functionals has been shown to give reasonable geometries for non-covalently interacting systems [14, 78]. For each heterocycle, we generated a number of dimers having geometries we describe as sandwich (S, stacked face-to-face), parallel displaced (PD, stacked face-to-face but displaced so that the vector between the two ring centers is not orthogonal to the molecular planes), T-shaped (T, the two ring planes are roughly perpendicular to one another and interacting edge-to-face), and in-plane (IP, both rings in essentially the same plane and interacting edge-to-edge). Many of the starting structures did not lead to stationary analogs, but instead relaxed to a different geometry. Ultimately, we obtained 5 S, 8 PD, 3 T, and 9 IP structures, for a total of 25 structures evaluated involving each of the heterocycles in at least one homodimer. Figures 3, 4, 5, and 6 show an example for each of the S, PD, T, and IP types of dimer geometries, respectively.

Our goal here is not to explore these geometries with respect to any meaningful chemical trends, but merely to generate a training set with sufficient diversity to be useful for parameterization, and we consider these final 25 structures to be adequate for that purpose (all structures are provided in Figure S1). For each homodimer, intermolecular interaction energies were computed with the AMOEBA0, AMOEBA1, and AMOEBA2 parameterizations. We also computed these energies with the UFF force field, as well as at a variety of QM levels of theory, including the DFT levels M06-L, M06, and M06-2X, as well as the post-Hartree–Fock levels MP2, CCSD, and CCSD(T). For the various QM levels, we employed the cc-pVTZ basis set. For *reference*, we take extrapolated CCSD(T) energies computed according to Eq. 1, and accounting for BSSE, as our benchmarks. Mean unsigned deviations (MUDs) over the 25 structures are presented in Table 3 for the various levels of theory.

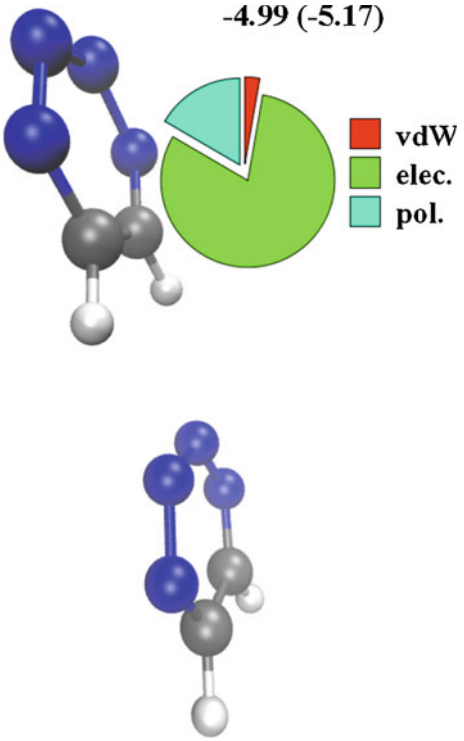

Fig. 6 In-plane (IP) conformation of the 1,2,3,4-tetrazine dimer; CCSD(T) and AMOEBA2 (*parentheses*) intermolecular interaction energies (kcal/mol) and relative contributions of AMOEBA2 terms (*pie chart*) are shown

Considering the MUDs on the intermolecular interaction energies, M06 and M06-L give similar values: 0.87 and 0.83 kcal/mol. As abundantly documented in the literature, M06-2X does well for these predictions, exhibiting a mean unsigned deviation of 0.51 kcal/mol compared to our reference values [78–81]. This is similar to the MUD for the considerably more expensive MP2/cc-pVTZ level. The MP2 and CCSD(T) levels with the smaller cc-pVDZ basis set do poorly, as expected given the sensitivity of correlated wave function theories to incompleteness in the single particle basis set.

In the case of the force field predictions, UFF does very poorly, with a MUE of 3.29 kcal/mol. With AMOEBA0, by contrast, the MUE is 0.68 kcal/mol, which is on the order of 10 % of the considered interaction energies and competitive with results from the M06 family of density functionals. When the various vdW parameters are scaled as described above to create AMOEBA1, the MUE is reduced from 0.68 to 0.18 kcal/mol, which is a considerable improvement. This is a not unexpected result, since adjustment of the electrostatic non-bonding term of a force field without the simultaneous adjustment of its dispersion/exchange repulsion non-bonding term would generally be expected to lead to an imbalance. Scaling while *additionally* adjusting the position of the H-atom displacement as described above to create AMOEBA2 further reduces the MUE to 0.15 kcal/mol, which is a 17 % improvement over AMOEBA1. This is accompanied by a decrease of the maximum error over the data set; in AMOEBA1, the maximum error is 0.73 kcal/mol for 1,2,4-triazine (IP) while in AMOEBA2 the maximum error is 0.57 kcal/mol for 1,2,4,5-tetrazine (IP). While the adjustment of the H-atom displacement offers a less significant improvement than scaling the non-electrostatic non-bonded parameters, permitting it to relax after having adjusted those latter parameters appears logically consistent to us.

In order better to indicate the diversity of force field energy components that contribute to the overall homodimer interaction energies, we also present in Figs. 3, 4, 5 and 6 a decomposition of those energies into vdW, fixed electrostatic, and polarization components of the AMOEBA2 intermolecular interaction energies for the 25 dimers of the 9 azabenzenes. We observe that the vdW component of the energy dominates the other two for S and PD structures, while the electrostatic energy is dominant for the IP structures. Since most of the IP and T structures include H atoms either hydrogen bonded to N lone pairs or directed toward the π electrons of a partner aromatic ring, the greater importance of electrostatics for these cases is not unexpected. As expected, the magnitude of the contribution from polarization correlates directly with the magnitude of the electrostatic term itself. While negligible for many structures, polarization reaches more than 20 % of the total intermolecular interaction energy for some of the in-plane geometries, e.g., those for pyridine, pyrimidine, and pyridazine.

Table 3 Mean unsigned deviations (kcal/mol) for intermolecular interaction energies over 25 homodimers (Figure S1) compared to extrapolated CCSD(T)/aug-cc-pVTZ values[a]

	CCSD(T)[b]	MP2[b]	MP2[c]	MP2	M06-L	M06	M06-2X
MUD	1.57	0.91	0.56	0.66	0.83	0.87	0.51
	UFF	AMOEBA0	AMOEBA1	AMOEBA2			
MUD	3.29	0.68	0.18	0.15			

[a] QM levels use the cc-pVTZ basis set unless otherwise specified

[b] cc-pVDZ basis set

[c] aug-cc-pVTZ basis set

4 Conclusions

Using electron probability distributions computed from the M06-L meta-GGA functional, together with Stone's distributed multipole analysis, we have determined the necessary atomic charges, dipoles, quadrupoles, and adjusted van der Waals parameters needed to extend the AMOEBA force field to pyridine, pyrazine, pyrimidine, pyridazine, the three unique triazines, and the two unique tetrazines. We accurately reproduce reference quantum mechanical molecular electric dipole moments, while we somewhat overestimate molecular electrical quadrupole moments. A minimal parameterization of covalent interactions, considering only one atom class per element, generates a flexible force field that provides Cartesian Hessian matrix elements in good agreement with those computed at the M06-L level. Over 25 azabenzene homodimers, interaction energies computed with this force field extension (AMOEBA0) have a mean unsigned deviation from reference extrapolated CCSD(T)/aug-cc-pVTZ values of 0.68 kcal/mol. This mean unsigned deviation is reduced to 0.18 kcal/mol by a simple scaling of vdW parameters (AMOEBA1) and is further reduced to 0.15 kcal/mol by scaling while simultaneously adjusting the location of the hydrogen atom interaction site (AMOEBA2). We anticipate that this extension of the AMOEBA force field to the azabenzenes will prove useful for condensed-phase simulations in which these heterocycles are present.

5 Supporting information

All the force field parameters are included in the form of ready-to-use Tinker.key parameter files. Structural RMSD for monomer geometries optimized with AMOEBA and M06-L; harmonic vibrational frequencies; detailed homodimer interaction energies at various levels of calculations; Cartesian coordinates in Tinker format are included.

Acknowledgments This work was supported by the U.S. National Science Foundation (CHE-1124244).

Conflict of interest The authors declare no competing financial interest.

References

1. Achelle S, Plé N, Turck A (2011) RSC Adv 1:364–388
2. Lagoja IM (2005) Chem Biodivers 2:1–50
3. Castro M, Rosa E, A-Osuna J, Garcia-Ferreiro T, Loza M, Cadavid M, Fontenla J, F-Masaguer C, Cid J, Raviña E, García-Mera G, Rodriguez J, de Ceballos M (1994) Eur J Med Chem 29:831–839
4. Young NJ, Hay BP (2013) Chem Commun 49:1354–1379
5. Chifotides H, Giles I, Dunbar K (2013) J Am Chem Soc 135:3039–3055
6. Smulders MMJ, Riddell IA, Browne C, Nitschke JR (2013) Chem Soc Rev 42:1728–1754
7. Dincă M, Long JR (2008) Angew Chem Int Ed 47:6766–6779
8. Abrahams BF, Batten SR, Hamit H, Hoskins BF, Robson R (1996) Angew Chem Int Ed Engl 35:1690–1692
9. Inokuma Y, Arai T, Fujita M (2010) Nat Chem 2:780–783
10. Frisch MJ, Trucks GW, Schlegel HB, Scuseria GE, Robb MA, Cheeseman JR, Scalmani G, Barone V, Mennucci B, Petersson GA, Nakatsuji H, Caricato M, Li X, Hratchian H P, Izmaylov AF, Bloino J, Zheng G, Sonnenberg JL, Hada M, Ehara M, Toyota K, Fukuda R, Hasegawa J, Ishida M, Nakajima T, Honda Y, Kitao O, Nakai H, Vreven T, Montgomery JA Jr., Peralta JE, Ogliaro F, Bearpark M, Heyd JJ, Brothers E, Kudin KN, Staroverov VN, Kobayashi R, Normand J, Raghavachari K, Rendell A, Burant JC, Iyengar SS, Tomasi J, Cossi M, Rega N, Millam JM, Klene M, Knox JE, Cross JB, Bakken V, Adamo C, Jaramillo J, Gomperts R, Stratmann RE, Yazyev O, Austin AJ, Cammi R, Pomelli C, Ochterski JW, Martin RL, Morokuma K, Zakrzewski VG, Voth GA, Salvador P, Dannenberg JJ, Dapprich S, Daniels AD, Farkas Ö, Foresman JB, Ortiz JV, Cioslowski J, Fox DJ (2009) Gaussian 09 revision C.01. Gaussian, Inc., Wallingford
11. Zhao Y, Truhlar DG (2006) J Chem Phys 125:194101
12. Balabanov NB, Peterson KA (2005) J Chem Phys 123:064107
13. Remya K, Suresh CH (2013) J Comput Chem 34:1341–1353
14. Fernandez N, Ferro Y, Carissan Y, Marchois J, Allouche A (2014) Phys Chem Chem Phys 16:1957–1966
15. Møller C, Plesset MS (1934) Phys Rev 46:618–622
16. Raghavachari K, Trucks GW, Pople JA, Head-Gordon M (1989) Chem Phys Lett 157:479–483
17. Bartlett RJ, Watts JD, Kucharski SA, Noga J (1990) Chem Phys Lett 165:513–522
18. Crawford TD, Stanton JF (1998) Int J Quantum Chem 70:601–611
19. Boys SF, Bernardi F (1970) Mol Phys 19:553–566
20. Sherrill CD, Takatani T, Hohenstein EG (2009) J Phys Chem A 113:10146–10159
21. DiStasio RA Jr, von Helden G, Steele RP, Head-Gordon M (2007) Chem Phys Lett 437:277–283
22. Janowski T, Pulay P (2007) Chem Phys Lett 447:27–32
23. Vogiatzis KD, Klopper W (2013) Mol Phys 111:2299–2305
24. Halgren TA (1992) J Am Chem Soc 114:7827–7843
25. Mulliken RS (1955) J Chem Phys 23:1833–1840
26. Reed AE, Weinstock RB, Weinhold F (1985) J Chem Phys 83:735–746
27. Hirshfeld FL (1977) Theor Chim Acta 44:129–138
28. Besler B, Merz K, Kollman P (1990) J Comput Chem 11:431–439
29. Marenich AV, Jerome SV, Cramer CJ, Truhlar DG (2012) J Chem Theory Comput 8:527–541
30. Price SL (1996) J Chem Soc Faraday Trans 92:2997–3008
31. Ibrahim MAA (2012) J Mol Model 18:4625–4638
32. Ibrahim MAA (2012) J Phys Chem B 116:3659–3669
33. Mu X, Wang Q, Wang L, Fried SD, Piquemal J, Dalby KN, Ren P (2014) J Phys Chem B 118:6456–6465
34. Kramer C, Gedeck P, Meuwly M (2013) J Chem Theory Comput 9:1499–1511
35. Ibrahim MAA (2011) J Comput Chem 32:2564–2574
36. Jorgensen WL, Schyman P (2012) J Chem Theory Comput 8:3895–3901
37. Kolář M, Hobza P, Bronowska AK (2013) Chem Commun 49:981–983
38. Masia M, Probst M, Rey R (2005) J Chem Phys 123:164505
39. Elking DM, Cisneros GA, Piquemal J, Darden TA, Pedersen LG (2010) J Chem Theory Comput 6:190–202

40. Piquemal J, Cisneros GA, Reinhardt P, Gresh N, Darden TA (2006) J Chem Phys 124:104101
41. Wang B, Truhlar DG (2010) J Chem Theory Comput 6:3330–3342
42. Wang B, Truhlar DG (2012) J Chem Theory Comput 8:1989–1998
43. Cisneros GA (2012) J Chem Theory Comput 8:5072–5080
44. Clavaguéra-Sarrio C, Brenner V, Hoyau S, Marsden CJ, Millié P, Dognon J- (2003) J Phys Chem B 107:3051–3060
45. Engkvist O, Åstrand P, Karlström G (2000) Chem Rev 100:4087–4108
46. Applequist J, Carl JR, Fung K (1972) J Am Chem Soc 94:2952–2960
47. Tholé BT (1981) Chem Phys 59:341–350
48. Ponder JW, Case DA (2003) Adv Protein Chem 66:27–85
49. Rasmussen TD, Ren P, Ponder JW, Jensen F (2007) Int J Quantum Chem 107:1390–1395
50. Allinger NL, Yuh YH, Lii JH (1989) J Am Chem Soc 111:8551–8566
51. Lii JH, Allinger NL (1989) J Am Chem Soc 111:8566–8575
52. Wilson EBJ, Decius JC, Cross PC (1955) Molecular vibrations: the theory of infrared and Raman vibrational spectra. McGraw-Hill, New York
53. Ponder JW (2011) TINKER: software tools for molecular design, version 6.0. Washington University, School of Medecine, Saint Louis
54. Young, D. M. (1971) Iterative solution of large linear systems. Academic Press, reprinted by Dover in 2003, New York
55. Wu JC, Chattree G, Ren P (2012) Theor Chem Acc 131:1138
56. Kocman M, Pykal M, Jurecka P (2013) Phys Chem Chem Phys 16:3144–3152
57. Bauza A, Deya PM, Frontera A, Quinonero D (2014) Phys Chem Chem Phys 16:1322–1326
58. Stone AJ (1981) Chem Phys Lett 83:233–239
59. Stone AJ, Alderton M (2002) Mol Phys 100:221–233. Reprinted from Molecular Physics (1985) 56:1047–1064
60. Stone AJ (2005) J Chem Theory Comput 1:1128–1132
61. Price SL, Stone AJ (1983) Chem Phys Lett 98:419–423
62. Stone AJ (2008) GDMA 2.2.02 program documentation. Cambridge University, Cambridge
63. Gagliardi L, Lindh R, Karlström G (2004) J Chem Phys 121:4494–4500
64. Manz TA, Sholl DS (2010) J Chem Theory Comput 6:2455–2468
65. Ángyán JG, Chipot C, Dehez F, Hättig C, Jansen G, Millot C (2003) J Comput Chem 24:997–1008
66. Sokalski WA, Poirier RA (1983) Chem Phys Lett 98:86–92
67. Rappé AK, Casewit CJ, Colwell KS, Goddard WA III, Skiff WM (1992) J Am Chem Soc 114:10024–10035
68. Buckingham AD (1959) Q Rev Chem Soc 13:183–214
69. Gunning MJ, Raab RE (1997) Mol Phys 91:589–596
70. Böttcher CJF, van Belle OC, Bordewijk P, Rip A (1973) Theory of electric polarization. Elesevier, Amsterdam
71. Zhou Y, Zhang IY, Wu J, Wu A, Xu X (2011) Chin J Chem Phys 24:635–639
72. Riley KE, Hobza P (2011) Wiley Interdiscip. Rev Comput Mol Sci 1:3–17
73. Burns LA, Mayagoitia ÁV, Sumpter BG, Sherrill CD (2011) J Chem Phys 134:084107
74. Riley KE, Pitoňák M, Jurečka P, Hobza P (2010) Chem Rev 110:5023–5063
75. Stepanian SG, Karachevtsev MV, Glamazda AY, Karachevtsev VA, Adamowicz L (2008) Chem Phys Lett 459:153–158
76. Klimeš J, Michaelides A (2012) J Chem Phys 137:120901
77. Cheng C, Zhang M, Sheng LI (2013) J Theor Comput Chem 12:1350012
78. Burns LA, Mayagoitia ÁV, Sumpter BG, Sherrill CD (2011) J Chem Phys 134:084107
79. Hohenstein EG, Chill ST, Sherrill CD (2008) J Chem Theory Comput 4:1996–2000
80. Walker M, Harvey AJA, Sen A, Dessent CEH (2013) J Phys Chem A 117:12590–12600
81. Li Z, Couzijn EPA, Zhang X (2012) Chem Commun 48:9864–9866

Theor Chem Acc (2015) 134:18
DOI 10.1007/s00214-015-1619-5

REGULAR ARTICLE

Triplet–singlet gap in structurally flexible organic diradicals

Daniel Reta Mañeru · Ibério de P. R. Moreira · Francesc Illas

Received: 28 November 2014 / Accepted: 16 January 2015 / Published online: 31 January 2015

Abstract A key factor in the search of high-spin ground state purely organic molecules concerns the effect of the inherent non-rigid structures on the magnetic and optical properties. This structural feature has not been properly addressed in previous theoretical works. Here, based on the experimentally characterized high-spin ground state of dendritic and star-branched polyradicals, we study four alternant hydrocarbon biradicals that intend to model these effects and, at the same time, provide a first step toward understanding more extended experimental structures. A series of density functional theory (DFT) and of wave function-based methods have been used to explore the richness of structural minima in the corresponding potential energy surfaces and to discuss its effect on the triplet–singlet gap of the proposed model systems. For a given model, the DFT-based B3LYP, M06-2X and MN-12SX methods provide a consistent description. Likewise, a multiconfigurational quasi-degenerate perturbation theory approach with the minimal π space as CASSCF reference is found to provide unbiased results. Despite the conformational richness found for these systems, they all can be described by a reduced set of values referred to only two structural parameters, being those the dihedral angles between the phenyl rings. For a given model, there is no significant change in the triplet–singlet gap depending on the chosen local minima.

Published as part of the special collection of articles derived from the 9th Congress on Electronic Structure: Principles and Applications (ESPA 2014).

D. Reta Mañeru · I. P. R. Moreira · F. Illas (✉)
Departament de Química Física & Institut de Química Teòrica i Computacional (IQTCUB), Universitat de Barcelona, C/ Martí i Franquès 1, 08028 Barcelona, Spain
e-mail: francesc.illas@ub.edu

Keywords Diradicals · Triplet–singlet gap · CASSCF · MRQDPT · DFT

1 Introduction

The search of high-spin ground state organic molecules has been inspired and developed by comparison with previous efforts carried out in the field of inorganic chemistry. In this sense, two important landmarks have paved the road to the synthesis of organic magnetic systems. First, the discovery of single-molecule magnets [1] promoted attempts to mimic the behavior displayed by the nd ($n = 3, 4, 5$) orbitals in magnetic transition metal complexes to purely organic systems. This implies an open-shell ground state involving C($2p$) orbitals only. The second landmark comes from the double-exchange model proposed by Zener [2, 3] to explain the giant magnetoresistive effects observed in manganites since it is strongly related to the more recent work of Shultz and Kumar [4] leading to the first example of enhanced ferromagnetic coupling in a mixed-valence bis(semiquinone) biradical anion that lacks an effective π-type ferromagnetic coupler.

From a single-molecule magnet perspective, the initial roadmap to organic molecules displaying high-spin ground state has been facilitated by theoretical predictions carried out in alternant hydrocarbons. In particular, we mention the seminal work of Longuet-Higgins [5], stating how many non-bonding singly occupied orbitals will be present depending on the number of carbon atoms and double bonds, and the valence bond theory-based study of Ovchinnikov [6], predicting the ground state spin quantum number of a given structure. This theoretical evidence leads to the conclusion that organic molecules with high-spin ground state can be synthesized from non-Kekulé alternant hydrocarbons with

non-disjoint singly occupied molecular orbital (MO) systems [7, 8]. The experimental approach often consists on generating one unpaired electron per center, and it was developed mainly by Rajca et al. [9]. In the strategy followed by Rajca [10] for carbon-centered radicals, the species are obtained from the corresponding polyethers precursors that are treated with lithium metal in tetrahydrofurane (THF), yielding the subsequent carbopolyanions which are further oxidized with iodine at 180 K. This treatment leads to the type of polyradicals that are generally studied in frozen THF solutions by SQUID magnetometry and often generates a broad set of systems such as di–tri–tetra radicals, star-branched and dendritic polyradicals. Although most of Rajca's research is based on C-centered radicals, recent work has also focused on N-centered radicals, both in diradical [10] and polyradical [11] compounds. An alternative approach for obtaining persistent triplet ground state molecules has recently emerged from research devoted to synthesizing molecules with singlet biradical ground state [12]. The referred persistent triplet ground state molecule is a heptazethrene isomer [13] and was synthesized following a strategy similar to the one by Rajca [9], i.e., by oxidation of the corresponding dianion. Clearly, all these strategies result in an appealing approach toward the synthesis of the so-called single-molecule organic magnet.

In this work, following the well-established theoretical framework described in detail in the recent book by Datta et al. [14], we focus on a series of Rajca-type extended systems that are based on the repetition of the *m*-xylylene diradical unit, a system investigated in detail in previous work [15]. Previous works have addressed the possibility to obtain polymeric radicals precisely by considering the *m*-xylylene diradical as a building block. However, important structural features derived from the particularities of the radical centers have often been overlooked. In fact, the few works dealing with this type of delocalized systems either assume co-planarity of the phenyl rings [16, 17] or neglect the existence of multiple minima [18]. In this sense, it is worth pointing out the many contributions of Barone et al. on providing an accurate way of predicting magnetic interactions in organic radicals (see for instance Ref. [19] and references therein) and the application to the similar problems as those here investigated [20]. However, it is important to note that the focus of these works is on radicals which exhibit more markedly localized magnetic centers dominated by σ–π-type orbitals. This is not the case of the present work where the magnetic interactions involve two interconnected π systems. It is also important to mention that the work of Barone et al. [21] on nitrogen-based radical centers, also synthesized by Rajca [22], is perhaps better related to the present work although it does not deal with the influence of conformational effects simply because the diradical of interest is structurally rigid. Finally and related to the study of magnetic interactions through space, it is worth noting the work on verdazyl-based compounds [23]. However, here the focus is on the interaction between magnetic moieties rather than on structurally flexible magnetic molecules. Here, we go one step further and address the problems derived from the existence of multiple minima and their effect on the relative energy of the low-lying electronic states. This constitutes a necessary preliminary step before studying periodic structures that resemble the star-branched and dendritic structures proposed by Rajca [9] where planarity will be the exemption rather than the rule. In this sense, the present work complements a recent study by Pal and Datta [24] on calix[4]arene-based radicals with bis(biphenylene)methyl linkers, which are presented as possible precursors of spin glass and superparamagnets. Following this line of reasoning, the model systems here described would eventually permit one exploring the effect of defect introduction as well as the loss of a radical center in the propagation of spin coupling throughout the system.

2 Model systems

In order to investigate the effect of substituents and of conformational freedom in polycyclic aromatic hydrocarbons with branched and dendritic structures such as those suggested by Rajca [9], a series of model systems have been designed. They all share the skeleton depicted in Scheme 1 where the θ_1 and θ_2 dihedral angles in the molecular framework confer a richness of possible structural isomers even including enantiomeric forms. In the simplest system, all substituents are hydrogen atoms so that the resulting compound is the 3-methyldiphenylmethyl-diyl diradical, hereafter referred to as compound **1**.

To investigate the effect of electron donating groups in the electronic structure of the diradical thus formed and also in the potential energy surface corresponding to the θ_1 and θ_2 dihedral angles, a second model is built where all substituents in Scheme 1 are methyl groups. The resulting system is 1-methyl-3-(2-yl-isopropyl)-3′-methyldiphenylmethyl compound **2**. Forcing orthogonality between the two phenyl rings, thus enabling the study of the effect of the extension

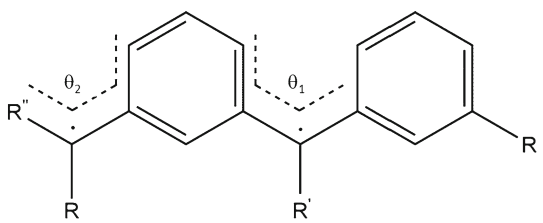

Scheme 1 Schematic representation of studied model systems indicating the relevant dihedral angles, the different *R* substituents are listed in Table 1

Table 1 Models for alternant hydrocarbons used in the present work

System	R	R'	R''	Schematic representation	IUPAC name
1	–H	–H	–H	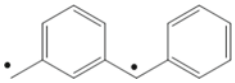	3-Methyldiphenylmethyl-diyl
2	$-CH_3$	$-CH_3$	$-CH_3$	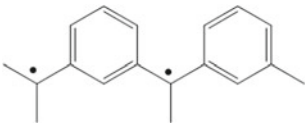	1-Methyl-3-(2-yl-isopropyl)-3′-methyldiphenylmethyl
3	$-CH_3$	*Tert*-butyl	$-CH_3$	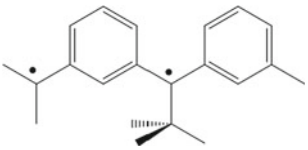	1-(Tertbutyl)-3-(2-yl-isopropyl)-3′-methyldiphenylmethyl
4	–H	–H	Phenyl	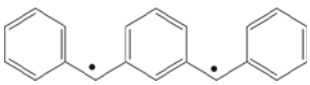	1,1′-(1,3-Phenylene)bis[1-phenylmethyl]

of the π-system throughout the molecule, may be achieved by introducing a bulky group, such as *tert*-butyl in position R'. The resulting system is 1-(tertbutyl)-3-(2-yl-isopropyl)-3′-methyldiphenylmethyl, referred to as compound **3**. Finally, the introduction of a phenyl group in R'' keeping the rest of substituents as hydrogen depicts the continuation toward the linear polymer introducing also the possibility of a larger delocalization over the molecule. The resulting 1,1′-(1,3-phenylene)bis[1-phenylmethyl]diradical will be referred to as compound **4**.

2.1 Computational approach

We start this section by pointing out that the main focus of the present work is to explore the effect of the conformational richness displayed by the proposed models on the electronic structure properties related to the open-shell character rather than providing an exhaustive discussion of the possible effect of the different available electronic structure methodologies on the reported properties. Hence, fine details of the electronic structure such as zero-field splitting (ZFS) and anisotropy can be safely ignored. Consequently, the different sets of calculations are based on previous experience in several systems [14] and, in particular, on recent systematic work on the *m*-xylylene diradical [15].

The molecular and electronic structure of model systems in Table 1 has been studied using density functional theory (DFT) and wave function-based methods. In a first step, geometry optimization of all systems in the triplet and broken symmetry approach to singlet electronic states has been performed at the DFT level by means of three different exchange–correlation potentials, namely the standard B3LYP hybrid functional [25] which overall provides robust results, the M06-2X which was found to provide accurate results for the *m*-xylylene diradical [15] and the MN12-SX, one of the latest functionals of the Minnesota family which significantly improves over previous members of the series [26]. These calculations have been carried out using the standard 6-311G** basis set [27, 28] since, for this kind of systems, it has been proven that the results thus obtained do not vary significantly by increasing the basis set size and quality [15]. Nevertheless, this has been further verified using system **2** as a case for study and the more extended 6-311++G** basis set [29].

Since, for each compound, the three DFT geometry-optimized structures are almost identical, vertical and adiabatic triplet–singlet energy differences have always been obtained from the B3LYP-optimized structures, using the broken symmetry approach [30–32] to estimate the open-shell singlet [33] and with the Yamaguchi correction for spin contamination [34–36]. Here, it is important to note that even if alternative approaches exist to describe open-shell singlet states such as those based on spin-flip time-dependent DFT (TD-DFT) methods [37–40], there is strong evidence that, for a given functional and for systems with two unpaired electrons as it is the case here, broken symmetry and spin-flip TD-DFT approaches provide essentially the same description [41]. Nevertheless, in order to have an appropriate unbiased, albeit approximate reference, triplet–singlet gaps have been also obtained from single-point energy calculations at each DFT geometry using a CAS-SCF wave function using minimal—CAS(2,2)—and full π-valence—CAS(14,14)—active spaces. For the minimal CAS, dynamical correlation effects were estimated from second-order multi-reference Møller–Plesset (MRMP) perturbation theory [42–45] calculations, hereafter referred to as MCQDPT that stands for multiconfigurational

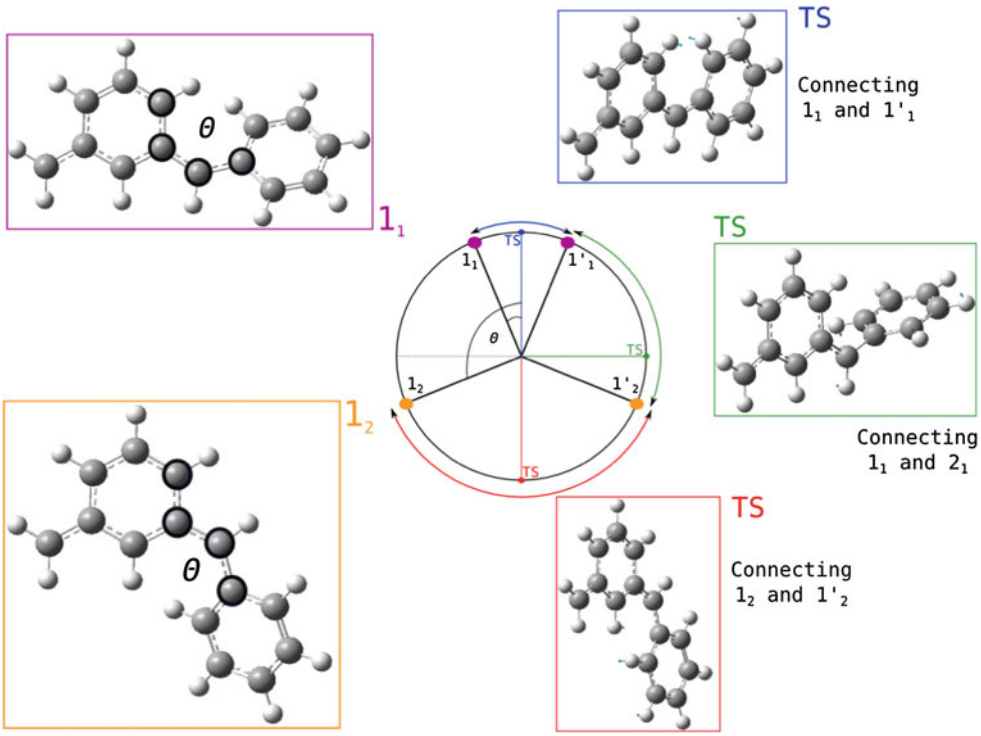

Fig. 1 Structural landscape of compound **1** featuring two structural isomers ($\mathbf{1}_1$ and $\mathbf{1}_2$), each with an enantiomeric counterpart ($\mathbf{1}_1$ and $\mathbf{1}_{1'}$; $\mathbf{1}_2$ and $\mathbf{1}_{2'}$) and the corresponding Newman's projections. The transition-state (TS) structures for interconversion of these isomers are also included. θ stands for θ_1 in Scheme 1 since θ_2 remains close to zero in all structures. The *arrows* in the outermost part of the *circle* indicate the local minima that the corresponding transition state connects

quasi-degenerate perturbation theory. Note, however, that MRMP has some noticeable differences with respect to the broadly used CASPT2 method [46, 47]. These involve essentially the number of states used to span the first-order wave function. In the CASPT2 method, the total energy is obtained from single and double excitations out of the reference wave CASSCF function. However, in MRPT all singly and doubly excited determinants obtained from each of the determinants in the reference wave function are considered. In the language of configuration interaction methods, one would state that CASPT2 uses a contracted reference function, whereas MRPT does not. The use of a contracted/uncontracted reference may be advantageous depending on the particular case although there is not a general rule. The CASSCF and MCQDPT calculations have been carried out using the 6-311G** standard basis set as in most of the DFT calculations except for compound **2** where, because of the rather large size, a 6-31G* basis set was selected.

A brief comment is required when calculating the vertical and adiabatic transitions within the broken symmetry approach. For vertical transitions, one can simply apply the appropriate mapping as illustrated in the review paper by Moreira and Illas [48] or the Yamaguchi formula, which approximately accounts for non-orthogonality of alpha and beta MOs [34–36]. The latter is the choice here because of the larger delocalization of magnetic orbitals in organic radicals [49]. However, for the adiabatic transitions, one should estimate the energy of the decontaminated open-shell singlet at the broken symmetry geometry. This can simply be done by calculating the energy of the triplet state at that geometry as recently shown in the case of *m*-xylylene [15]

$$\Delta_{\mathrm{TS}}^{\mathrm{adia}} \equiv \Delta_{\mathrm{adia}} = E_{\mathrm{S}^i} - E_{\mathrm{T}^j} = \frac{2\left(E_{BS^i} - E_{\mathrm{T}^i}\right)}{\left\langle S_{\mathrm{T}^i}^2 \right\rangle - \left\langle S_{BS^i}^2 \right\rangle} + E_{\mathrm{T}^i} - E_{\mathrm{T}^j} \tag{1}$$

where i and j refer to the molecular geometry of the singlet and triplet, respectively.

3 Results and discussion

3.1 Local minima, isomers and enantiomers

The analysis of the potential energy surface for compounds **1**–**4** either in the triplet ground state or in the open-shell singlet—represented by a broken symmetry solution—reveals a quite rich landscape with multiple minima corresponding to structural isomers and, depending on the case, enantiomers. The search for stable structures has been carried out for the three different density functionals, and the picture obtained is always qualitatively the same. For simplicity, we will next describe the results corresponding to the B3LYP functional. To illustrate the rich structural landscape above-mentioned, let us take the simplest case of compound **1** where R, R' and R'' substituents in Scheme 1 are all hydrogen atoms. The existence of two (structurally

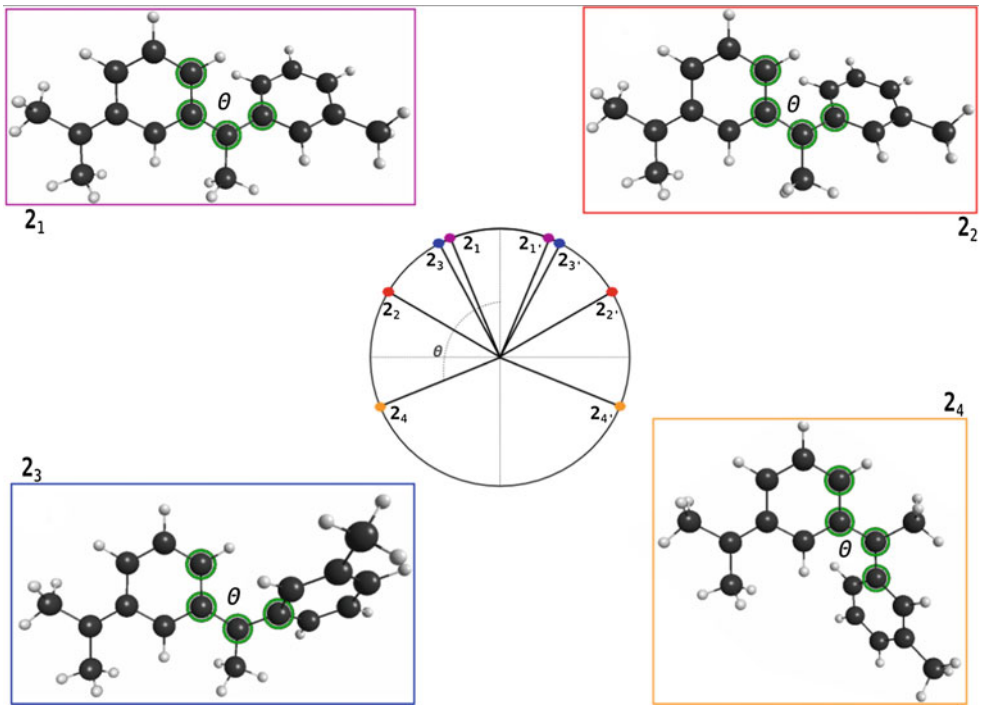

Fig. 2 Structural landscape of compound **2** featuring four structural isomers ($\mathbf{2}_1$, $\mathbf{2}_2$, $\mathbf{2}_3$ and $\mathbf{2}_4$), each with an enantiomeric counterparts ($\mathbf{2}_{1'}$, $\mathbf{2}_{2'}$, $\mathbf{2}_{3'}$ and $\mathbf{2}_{4'}$) and the corresponding Newman's projection through the dihedral angle θ. θ stands for θ_1 in Scheme 1 since θ_2 remains close to zero in all structures

different) phenyl rings separated by a radical center leads to different stable nuclear configurations, which can be easily understood from Fig. 1. A first energy minimum in the triplet potential energy surface is encountered for a situation where the two phenyl rings are separated by an angle of ~17° either through a clockwise or a counter clockwise rotation. The frequency analysis reveals that both structures are minima in the triplet potential energy surface having exactly the same energy and being mirror images, they are enantiomers and will be referred to as $\mathbf{1}_1$ and $\mathbf{1}_{1'}$, respectively. A similar situation is found for the open-shell singlet potential energy surface. The origin of this quite exotic form of enantiomerism—there is no typical asymmetric C—lies in the particular nature of the radical center linking two different rings where the pyramidal sp^3 like hybridization results in three different chemical substituents and one "dangling bond" which effectively acts as the fourth one. The two enantiomers, hereafter referred to as $\mathbf{1}_1$ and $\mathbf{1}_{1'}$, can be interconverted through an appropriate transition-state structure. The search for this stationary saddle point in the potential energy surface led to a structure connecting $\mathbf{1}_1$ and $\mathbf{1}_{1'}$ where the two rings are coplanar and which, in principle [50], corresponds to the appropriate transition state. The energy barrier for interconversion is, however, very small, of a 4.64 kJ mol^{-1} (387 cm^{-1}). The sp^3 pyramidal character of the radical center linking the two rings has another interesting effect, namely the existence of a second type of minimum energy structure in the triplet potential energy surface where the two rings are now separated by 166° (Fig. 1) and accidentally degenerate with the previous one with a calculated B3LYP energy difference of 0.02 kJ mol^{-1} (2 cm^{-1}) only. A slightly larger energy difference of 0.23 kJ mol^{-1} (20 cm^{-1}) is found between the two broken symmetry solutions, at the same B3LYP level. Again, the rotation from a coplanar situation can be clockwise or a counterclockwise meaning that this new structure does also exhibit two enantiomers that will be denoted as $\mathbf{1}_2$ and $\mathbf{1}_{2'}$ and are connected through a transition state where the two rings are also coplanar opposed by a 180° angle. The energy barrier for interconversion is also of 4.63 kJ mol^{-1} as in the case of the $\mathbf{1}_1$ and $\mathbf{1}_{1'}$ enantiomers. The different structural isomers $\mathbf{1}_1$ and $\mathbf{1}_2$ (or $\mathbf{1}_{1'}$ and $\mathbf{1}_{2'}$) can also be interconverted through overcoming an energy barrier of 21.79 kJ mol^{-1} corresponding to a transition-state structure where the two rings are separated by a 90° angle.

The landscape exhaustively described for compound **1** is applicable to the rest of model systems with some variations, which will be now described in some detail. Therefore, the discussion will be limited to the different energy minima without further comments on the energy barriers for interconversion. In compound **2,** the R, R' and R'' substituents in Scheme 1 are all methyl groups. The presence of the methyl groups significantly affects the potential energy surface landscape with the appearance of two new minima which following the notation introduced above are denoted as $\mathbf{2}_1$, $\mathbf{2}_2$, $\mathbf{2}_3$ and $\mathbf{2}_4$, whereas the corresponding enantiomers are denoted as $\mathbf{2}_{1'}$, $\mathbf{2}_{2'}$, $\mathbf{2}_{3'}$ and $\mathbf{2}_{4'}$. The molecular structure of these four energy minima, fully characterized by frequency analysis, involves essentially the relative

Table 2 Vertical and adiabatic triplet–singlet energy differences, Δ_{vert} and Δ_{adia}, respectively, for the minimum energy structures ($\mathbf{1}_1$ and $\mathbf{1}_2$) of compound **1** as predicted by different density functionals and wave function-based methods using the B3LYP-optimized geometries

Structure	Method	Δ_{vert}	Δ_{adia}
$\mathbf{1}_1$	B3LYP	3,350	2,816
	M06-2X	3,182	2,543
	MN12-SX	2,947	2,455
	CAS(2,2)SCF	1,384	751
	MCQDPT	3,169	2,659
	CAS(14,14)SCF	3,841	2,941
$\mathbf{1}_2$	B3LYP	3,304	2,767
	M06-2X	3,167	2,527
	MN12-SX	2,901	2,398
	CAS(2,2)SCF	1,359	734
	MCQDPT	3,108	2,620
	CAS(14,14)SCF	3,812	2,767

All values are in cm^{-1}. Wave function-based results are obtained using the set of orbitals corresponding to each electronic state

orientation of the phenyl rings as schematically illustrated in Fig. 2. Consequently, the energy differences between these structures are relatively small. For the B3LYP triplet potential energy surface, the most stable structure is $\mathbf{2}_3$ followed by $\mathbf{2}_1$, $\mathbf{2}_4$ and $\mathbf{2}_2$ lying at 2, 28 and 102 cm^{-1} above $\mathbf{2}_3$, respectively. In the case of the broken symmetry potential energy surface, the most stable structure is $\mathbf{2}_1$ followed by $\mathbf{2}_4$, $\mathbf{2}_3$ and $\mathbf{2}_2$ with the corresponding broken symmetry solutions lying at 194, 207 and 218 cm^{-1}, respectively, above that of $\mathbf{2}_1$. Compound **3** differs from compound **2** only by substitution of the methyl group of the radical center connecting the two rings by a bulkier *tert*-butyl group. Here, only two energy minima have been located in spite of running several optimization geometry calculations starting from the situations corresponding to energy minimum in **2**. The energy difference between $\mathbf{3}_1$ and $\mathbf{3}_2$ in the triplet state is of 22 cm^{-1} only, which is similar to the situation described for compound **1**. Finally, compound **4** attempts to mimic the initial step of a polyradical generated from **1**. Hence, it contains three phenyl rings and involves up to five different conformers properly characterized from the corresponding frequency calculations separated by at most 153 cm^{-1} in the triplet state, whereas the broken symmetry solution are separated by at most 130 cm^{-1}.

3.2 Triplet–singlet gaps

The existence of multiple minima, as described above, introduces a certain degree of complexity in the energy difference between the lowest triplet and open-shell singlet states. Therefore, we have chosen to analyze these energy differences, previously defined as Δ, for each minimum energy structure. Following previous work, vertical and adiabatic (Δ_{vert} and Δ_{adia}) gaps have been calculated where the geometry optimization has been carried out at the B3LYP level. This is justified from the recent systematic work on the *m*-xylylene diradical where it has been shown that the effect of the geometry is much smaller than the one introduced by the method used to estimate the total energy [15].

Let us now discuss in some detail the situation for compound **1** for which results are summarized in Table 2. Several interesting issues emerge from this table. First, the three density functionals predict Δ values that differ at most by 10 %. Moreover, these values are significantly smaller (~30 %) than those predicted for the *m*-xylylene diradical which indeed were in fair agreement with experiment [15], indicating that increasing the extension of the π system can result in energy difference in the range of those expected for magnetic systems which seems to confirm the hypothesis set out in the introduction. The minimal CAS(2,2)SCF wave function badly fails to predict the proper order of magnitude of the triplet–singlet gap although this is remedied by including dynamical correlation effects through the MCQDPT approach. The results thus found are now similar to those predicted by the different density functionals, in particular with the M06-2X, which seemed to provide the best estimate of the triplet–singlet gap in the *m*-xylylene diradical [15]. Part of the correlation effects missing in the CAS(2,2)SCF description are recovered with the full π valence CAS(14,14)SCF although the Δ values are now significantly overestimated because dynamical correlation out of this space is missing. A graphical comparison between the two singly occupied canonic orbitals for compound $\mathbf{1}_1$, obtained either by a CAS(2,2) SCF or CAS(14,14)SCF description, can be made from inspecting Fig. 3. In line with previous results, the problem of using a minimal CAS(2,2)SCF set of orbitals comes from an inadequate description of the degree of localization of the magnetic orbitals [51, 52]. In these organic diradicals, usually exhibiting a more delocalized π system, the minimal CAS(2,2)SCF description leads to an excessive localization with respect to the full π valence CAS(14,14) SCF description which provides a more accurate reference. This is similar to the case of Cu dinuclear complexes where the minimal CAS(2,2) description also leads to exceedingly localized orbitals [52]. Nevertheless, adding dynamical correlation out of the minimal CAS(2,2)SCF also provides a convenient and less computationally demanding way to recover the appropriate orbitals while including as well the dynamic correlation effects that affect the triplet–singlet energy difference as recently shown for the difficult case of *m*-xylylene [15]. In this sense, MCQDPT calculation on top of the CAS(2,2)SCF seems to be an adequate option

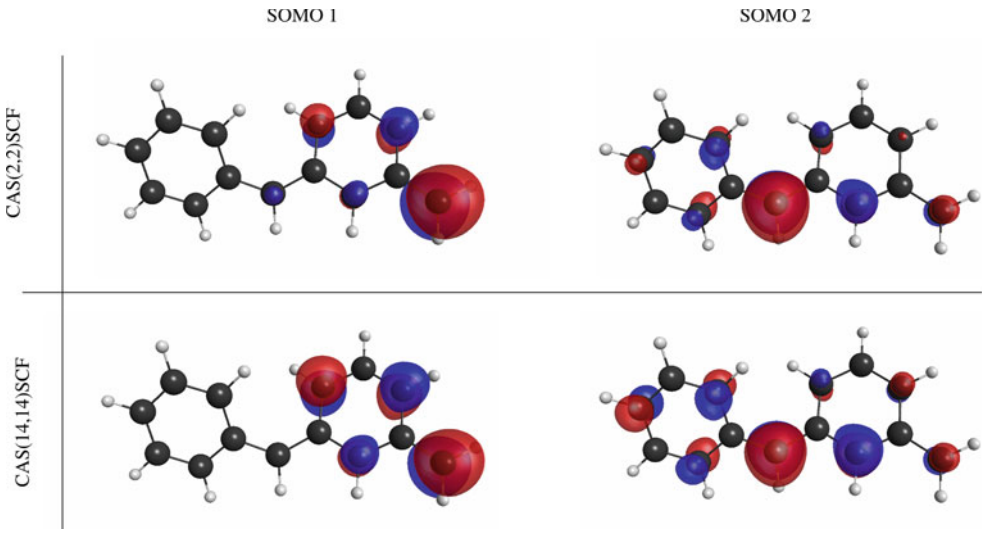

Fig. 3 Graphical representation of the two singly occupied canonic orbitals obtained either by a minimal CAS(2,2)SCF or a full π valence CAS(14,14) SCF calculation for compound $\mathbf{1}_1$. The differential localization between the two sets of orbitals also holds for compound **2**

Table 3 Vertical and adiabatic triplet–singlet energy differences, Δ_{vert} and Δ_{adia}, respectively, for the minimum energy structures ($\mathbf{2}_1$–$\mathbf{2}_4$) of compound **2** as predicted by different density functionals and wave function-based methods using the B3LYP-optimized geometries

Structure	Method	Δ_{vert}	Δ_{adia}
$\mathbf{2}_1$	B3LYP	2,737	2,047
	M06-2X	2,610	1,950
	MN12-SX	2,319	1,778
	CAS(2,2)SCF	1,072	655
	MCQDPT	2,512	1,983
	CAS(14,14)SCF	3,499	2,561
$\mathbf{2}_2$	B3LYP	2,168	1,498
	M06-2X	2,017	1,319
	MN12-SX	1,852	1,299
	CAS(2,2)SCF	832	197
	MCQDPT	1,924	1,422
	CAS(14,14)SCF	2,525	1,815
$\mathbf{2}_3$	B3LYP	2,715	2,053
	M06-2X	2,587	1,968
	MN12-SX	2,300	1,752
	CAS(2,2)SCF	1,061	649
	MCQDPT	2,486	1,982
	CAS(14,14)SCF	3,458	2,486
$\mathbf{2}_4$	B3LYP	2,652	1,934
	M06-2X	2,513	1,879
	MN12-SX	2,246	1,689
	CAS(2,2)SCF	1,051	655
	MCQDPT	2,466	1,943
	CAS(14,14)SCF	3,449	2,414

All values are in cm^{-1}. Wave function-based results are obtained using the set of orbitals corresponding to each electronic state

and is the one employed in the larger **2**, **3** and **4** model systems. It is also important to note that the set of molecular orbitals used (MOs) in the MCQDPT calculations is the canonic orbitals of the CAS(2,2)SCF triplet and singlet, respectively. Finally, it is worth pointing out that the above discussion applies equally to the $\mathbf{1}_1$ and $\mathbf{1}_2$ minimum energy structures (Table 1).

We now focus the discussion on compound **2**, for which results are summarized in Table 3. As in the previous case, the three different exchange–correlation potentials used yield results that are fairly consistent, and the calculated triplet–singlet gap differs by at most 14 %. Once again, the minimal CASSCF description fails to provide a reliable estimate of the triplet–singlet gap, but the introduction of dynamical correlation out of the minimal space by means of MCQDPT provides values lying in the average value predicted by DFT-based methods. Once more, the extension to the full π valence CAS(14,14)SCF space overestimates the Δ values, confirming that the best strategy for a wave function-based description is provided by a MCQDPT calculation using the CAS(2,2) as reference space. Comparing to compound **1**, the Δ values for the DFT-based methods are in average a 19 % smaller for the case of vertical transitions and a 26 % for the adiabatic ones. This trend is maintained for the case of MCQDPT on top of CAS(2,2)SCF calculations. This observation indicates that another way of decreasing the triplet–singlet gap, and thus approaching the range of magnetic transitions in polycyclic aromatic hydrocarbons with C-centered unpaired electrons, would be the introduction of carefully chosen σ-donating groups directly bonded to the radical center. Finally, $\mathbf{2}_1$, $\mathbf{2}_3$ and $\mathbf{2}_4$ conformers present the same trend for the Δ values, being $\mathbf{2}_2$ the

exception with a deviation from the average value for Δ of 20 % in the case of vertical transitions and 25 % for the adiabatic ones.

Table 4 Vertical and adiabatic triplet–singlet energy differences, Δ_{vert} and Δ_{adia}, respectively, for the lowest energy minimum energy structures of compounds **3** and **4** as predicted by different density functionals and wave function-based methods using the B3LYP-optimized geometries

Structure	Method	Δ_{vert}	Δ_{adia}
$\mathbf{3}_1$	B3LYP	3,458	3,084
	M06-2X	3,250	2,720
	MN12-SX	3,000	2,621
	CAS(2,2)SCF	1,221	491
	MCQDPT	3,065	2,755
$\mathbf{4}_1$	B3LYP	2,355	1,994
	M06-2X	2,245	1,841
	MN12-SX	2,065	1,740
	CAS(2,2)SCF	1,090	749
	MCQDPT	2,389	2,067

All values are in cm^{-1}. Wave function-based results are obtained using the set of orbitals corresponding to each electronic state

In view of the trends discussed above for compounds **1** and **2**, we will limit the discussion of the triplet–singlet gap in **3** and **4** to the lowest energy conformer, the differences with respect to the other stable structures being really meaningless. The Δ values for the most stable minima of compounds **3** and **4** are listed in Table 4. They are not reported for the full π valence CAS(14,14)SCF space due to the increasing amount of determinants needed, and because based on the above discussion for compounds **1** and **2**, it is known that these results would overestimate the triplet–singlet gap. Compound **3** presents Δ values similar to the ones of compound **1**, deviating from the decreasing tendency in the triplet–singlet gap in the series of proposed compounds which implies that the substitution of a methyl group in **2** by a of *tert*-butyl group goes in the opposite direction as when introducing the methyl groups in **1** leading to compound **2**. The overall trends are summarized in Fig. 4, displaying the vertical and adiabatic triplet–singlet gaps predicted by the MCQDPT calculations as a function of the dihedral angles θ_1 and θ_2. This figure clearly shows that, in spite of the different nature of the *R*, *R*′ and *R*″ substituents in Scheme 1, the richness of minima showed by the potential energy surfaces can be described by a reduced

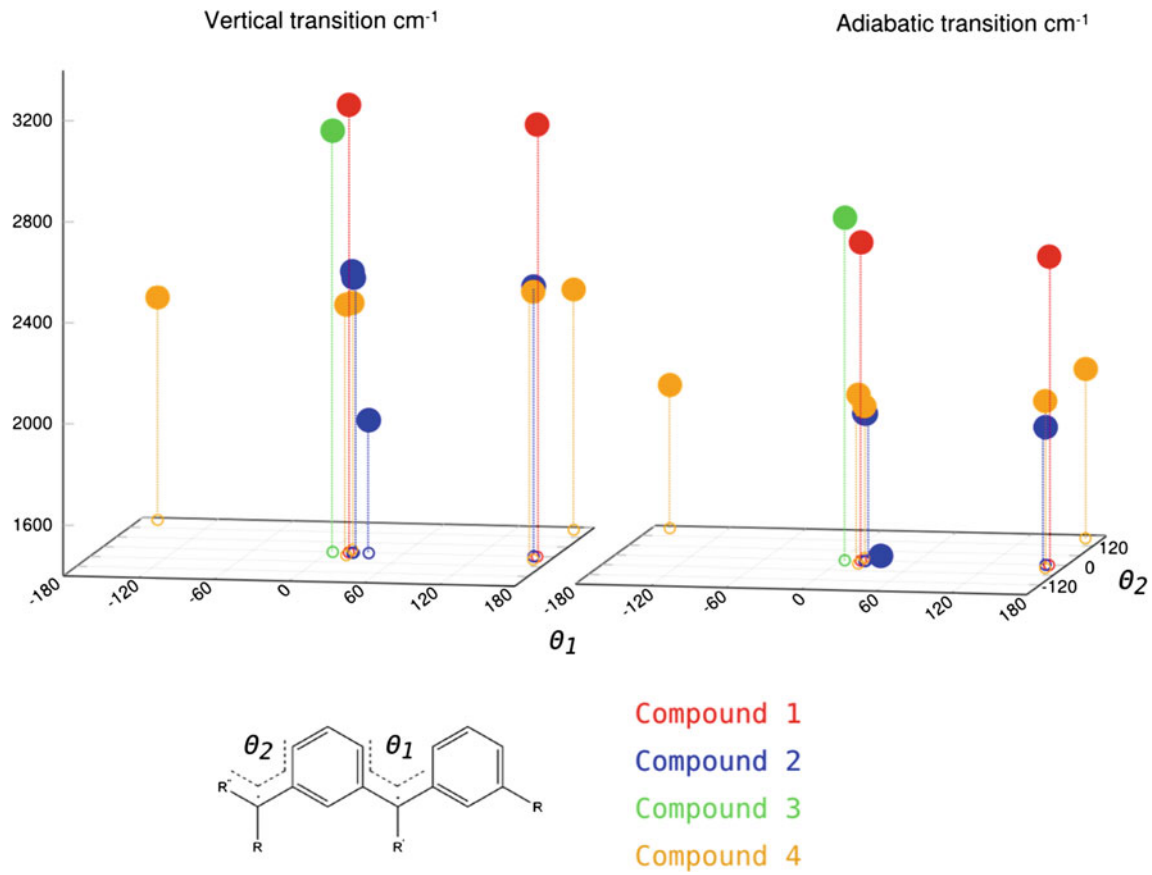

Fig. 4 Schematic representation of the calculated MCQDPT (on top of minimal CAS(2,2)SCF) vertical and adiabatic triplet–singlet gap of compounds **1**–**4** as a function of the dihedral angles θ_1 and θ_2

set of values referred to only two structural parameters, the θ_1 and θ_2 dihedral angles. This represents an important input in a forthcoming study of polymeric radical chains based on these monomers.

Finally it is worth to point out that, as it has already been commented, compound **4** presents the same environment for both of the radical centers, but at the same time introduces a more extended π system. The direct effect is a significant reduction in the triplet–singlet gap, which is evident in Fig. 4. Note also that the trends predicted by DFT and wave function-based methods are similar to those commented for the rest of compounds. Thus, the DFT-based methods yield values that are very similar among each other and to the MCQDPT result on top of the minimal CASSCF calculation. Compound **4** already allows one to imagine the possible conformations that a hypothetic polymer would display, and the importance of the relative position of the phenyl rings in order to predict a linear, helical or any other disposition in the 3D growth of the sought polymer. A study on these issues is currently being carried out in our group.

4 Conclusions

In this work, a series of four compounds chosen to model the star-branched and dendritic structures experimentally characterized by Rajca [9] has been studied by different theoretical methods, the focus being on the richness of structures in their ground state (triplet) potential energy surface and on the triplet–singlet gap. At the DFT level, the B3LYP, M06-2X, MN-12SX functionals were explored, whereas wave function methods include minimal CASSCF followed by second-order MCQDPT. In some cases, the full π valence CASSCF has also been explored. In light of the preceding discussion, several conclusions can be extracted, which are listed below.

- There are no stable planar structures of these compounds, which has implications when considering possible polymeric chains.
- The corresponding potential energy surface of these compounds exhibits many low-lying local minima that can be described by only considering the θ_1 and θ_2 dihedral angles. This represents an important input in a forthcoming study of polymeric radical chains based on these monomers, since it reduces drastically the difficulty of choosing the relative position of the phenyl rings in the growth of the polymer.
- The B3LYP, M06-2X and MN12-SX density functionals predict very similar structures for the proposed models, being all of them able to find the several minima of the potential energy surface for each compound.
- Single-point MCQDPT calculations using a minimal CASSCF reference space at the B3LYP-optimized geometries appear to be the best strategy to estimate the triplet–singlet gap in this kind of compounds with wave function-based methods, which is consistent with previous work on *m*-xylylene [15].
- For a given compound, the magnitude of triplet–singlet gap predicted by both DFT and wave function-based methods does not depend significantly on the minimum energy structure chosen to carry out the calculation.
- The triplet–singlet gap predicted by both DFT and wave function-based methods indicates that it is possible to tune this property by appropriate choice of substituents which opens the possibility to keep decreasing the triplet–singlet gap in these high-spin ground state compounds to the limit of entering magnetic transitions.

Therefore, the conclusions from this work, even if based on a limited set of model systems, provide a basis for subsequent studies aimed at predicting polymers exhibiting high-spin ground state, a project that is now under development in our group.

Acknowledgments The authors are indebted to Prof. Sambhu N. Datta for stimulating discussion. This work has been supported by Indo-Spain Collaborative Program in Science—Nanotechnology (DST Grant INT-Spain-P42-2012 and Spanish Grant PRI-PIBIN-2011-1028) and, in part, by Spanish MICINN through research Grant CTQ2012-30751 and by *Generalitat de Catalunya* through Grants 2014SGR97, XRQTC. FI acknowledges additional financial support through the 2009 ICREA Academia Award for Excellence in University Research.

References

1. Kahn O (1993) Molecular magnetism. VCH, New York
2. Zener C (1951) Phys Rev 81:440
3. Zener C (1951) Phys Rev 82:403
4. Shultz DA, Kumar RK (2001) J Am Chem Soc 123:6431
5. Longuet-Higgins HC (1950) J Chem Phys 18:3
6. Ovchinnikov AA (1978) Theor Chim Acta 47:297
7. Borden WT, Davidson ER (1977) J Am Chem Soc 99:4587
8. Lineberger WC, Borden WT (2011) Phys Chem Chem Phys 13:11792
9. Rajca A (1994) Chem Rev 94:871
10. Rajca A, Olankitwanit A, Rajca SJ (2011) Am Chem Soc 133:4750
11. Rajca A, Olankitwanit A, Wang Y, Boratynski PJ, Pink M, Rajca S (2013) J Am Chem Soc 135:18205
12. Sun Z, Zeng Z, Wu J (2014) Acc Chem Res. doi:10.1021/ar5001692
13. Li Y, Huang KW, Sun Z, Webster RD, Zeng Z, Zeng W, Chi C, Furukawa K, Wu J (2014) Chem Sci 5:1908
14. Datta SN, Trindle CO, Illas F (2014) Theoretical and computational aspects of magnetic organic molecules. Imperial College Press, World Scientific Publishing, London. ISBN 978-1-908977-21-2
15. Mañeru DR, Pal KP, Moreira I de PR, Datta SN, Illas F (2014) J Chem Theory Comput 10:335

16. Li S, Ma J, Jiang Y (1997) J Phys Chem A 101:5567
17. Ma H, Liu C, Zhang C, Jiang Y (2007) J Chem Phys A 111:9471
18. Zhang G, Li S, Jiang Y (2003) Tetrahedron 59:3499
19. Barone V, Cacelli I, Ferreti A, Monti S, Prampolini G (2011) J Chem Theory Comput 7:699
20. Barone V, Boilleau C, Cacelli I, Ferreti A, Prampolini G (2013) J Chem Theory Comput 9:1958
21. Barone V, Boilleau C, Cacelli I, Ferreti A, Monti S, Prampolini G (2013) J Chem Theory Comput 9:300
22. Rajca A, Olankitwanit A, Rajca S (2011) J Am Chem Soc 133:4750
23. Rota J-B, Le Guennic B, Robert V (2010) Inorg Chem 49:2010
24. Pal AK, Datta SN (2014) J Phys Chem C 118:27599
25. Becke AD (1993) J Chem Phys 98:5648
26. Peverati R, Truhlar DG (2012) Phys Chem Chem Phys 14:16187
27. Ditchfield R, Hehre WJ, Pople JA (1971) J Chem Phys 54:724
28. Hehre WJ, Ditchfield R, Pople JA (1972) J Chem Phys 56:2257
29. Clark T, Chandrasekhar J, Spitznagel GW, Schleyer PVR (1983) J Comput Chem 4:294
30. Noodleman L (1981) J Chem Phys 74:5737
31. Noodleman L, Davidson ER (1986) J Chem Phys 109:131
32. Noodleman L, Peng CY, Case DA, Mouesca JM (1995) Coord Chem Rev 144:199
33. Caballol R, Castell O, Illas F, Malrieu JP, Moreira I de PR (1997) J Phys Chem A 101:7860
34. Yamaguchi K, Takahara Y, FuenoT, Nasu K (1987) Jpn J Appl Phys 26:L1362
35. Yamaguchi K, Jensen F, Dorigo A, Houk KN (1988) Chem Phys Lett 149:537
36. Yamaguchi K, Takahara Y, Fueno T, Houk KN (1988) Theor Chim Acta 73:337
37. Shao Y, Head-Gordon M, Krylov AI (2003) J Chem Phys 118:4807
38. Wang F, Ziegler T (2004) J Chem Phys 121:12191
39. Krylov AI (2005) J Phys Chem A 109:10638
40. Levine BG, Ko C, Quenneville J, Martinez TJ (2006) Mol Phys 104:1039
41. Valero R, Illas F, Truhlar DG (2011) J Chem Theory Comput 7:3523
42. Hirao K (1992) Int J Quantum Chem S26:517
43. Hirao K (1992) Chem Phys Lett 196:397
44. Hirao K (1992) Chem Phys Lett 190:374
45. Hirao K (1993) Chem Phys Lett 201:59
46. Andersson K, Malmqvist P-Å, Roos BO, Sadlej AJ, Wolinski K (1990) J Phys Chem 94:5483
47. Andersson K, Malmqvist P-Å, Roos BO (1992) J Chem Phys 96:1218
48. Moreira I de PR, Illas F (2006) Phys Chem Chem Phys 8:1645
49. Datta SN, Pal AK, Hansda S, Illas F (2013) J Phys Chem A 117:1773
50. Bofill JM, Quapp W (2011) J Chem Phys 134:074101
51. Suaud N, Ruamps R, Guihéry N, Malrieu JP (2012) J Chem Theory Comput 8:4127
52. Angeli C, Calzado CJ (2012) J Chem Phys 137:034104

Theor Chem Acc (2015) 134:46
DOI 10.1007/s00214-015-1644-4

REGULAR ARTICLE

Separating nuclear spin isomers using a pump–dump laser scheme

Rana Obaid[1,2] · Daniel Kinzel[1] · Markus Oppel[1] · Leticia González[1]

Received: 30 January 2015 / Accepted: 2 March 2015 / Published online: 29 March 2015

Abstract The concept of nuclear spin isomers was already introduced in the early days of quantum mechanics. Despite its importance, not much work has been done to separate them experimentally by pushing the ratio away from its equilibrium value. We propose to use ultrashort laser pulses in a pump–dump-like experiment to enhance the ratio between different nuclear spin isomers. Exemplary wave packet simulations with optimized femtosecond pump and dump laser pulses are shown on a quinodimethane derivative to illustrate that the ratio between two different groups of nuclear spin isomers is enhanced.

Keywords Pump–probe spectroscopy · Quantum dynamics · Nuclear spin isomers

1 Introduction

Shortly after the experimental discovery of phenomena such as the anomalous specific heat capacity of molecular hydrogen (H_2) in 1912 by Eucken [1] or the intensity alternations in rotational spectra of several diatomic molecules by Mecke [2] in 1925, Heisenberg [3] and Hund [4] introduced independently the concept of nuclear spin isomers. This concept was used in 1929 by Bonhöffer and Harteck [5] to explain the experimental results for the H_2 molecule, leading to the notion of *ortho*- and *para*-hydrogen. Soon after, nuclear spin isomers were also advocated to explain the missing lines in other diatomic molecules, see e.g. Ref. [6] for an overview.

Today, the concept of spin isomerism is well understood from a theoretical point of view, and it is well known that it plays an important role in a number of research fields, with implications in nuclear magnetic resonance (NMR) spectroscopy [7], selective reaction rates [8], boiling and melting points and heats of vaporization [9, 10], to name few examples. Due to its relevance, significant efforts have been made to study and separate nuclear spin isomers. The separation of *ortho*- from *para*-hydrogen is technically feasible for quite some time [11, 12], but the separation of nuclear spin isomers in polyatomic molecules is far from straightforward. Until now, separation or interconversion of nuclear spin isomers has been successfully achieved for CH_3F [13–16], $^{13}C^{12}CH_4$ [17], H_2CO [18], $^{12}C_2H_4$ [19] and H_2O [20–22]. In most of the previous cases, the light-induced drift (LID) technique [23] is the method of choice.

On the theoretical side, one promising avenue to separate nuclear spin isomers is to rely on selective coherent quantum dynamical effects. Upon excitation with moderate to intense ultrashort laser pulses, different nuclear spin isomers exhibit different excited-state properties that can be exploited for its separation, see e.g. Refs. [24–31]. Recently, the implications of molecular symmetry on nuclear spin selective torsional states [26, 31, 32] have been stated, and it has been shown that it is possible to discriminate different nuclear spin isomers based on their different excited-state torsional dynamics [31, 33]. In Ref. [33], we used representative quantum dynamical simulations to discriminate the nuclear spin isomers of a quinodimethane

Published as part of the special collection of articles derived from the 9th Congress on Electronic Structure: Principles and Applications (ESPA 2014).

✉ Leticia González
leticia.gonzalez@univie.ac.at

[1] Institut für Theoretische Chemie, Universität Wien, Währinger Str. 17, 1090 Vienna, Austria

[2] Applied Chemistry Department, Palestine Polytechnic University, Hebron, Palestine

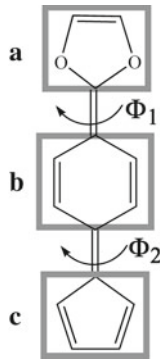

Fig. 1 2-[4-(Cyclopenta-2,4-dien-1-ylidene)cyclohexa-2,5-dien-1-ylidene]-2H-1,3-dioxole, abbreviated CCD in the text. Depicted are the three rings **a**, **b** and **c** together with the two torsional coordinates Φ_1 and Φ_2 which generate the different nuclear spin isomers and are used in the dynamical simulations as the two degrees of freedom

derivative, the 2-[4-(cyclopenta-2,4-dien-1-ylidene)-cyclohexa-2,5-dien-1-ylidene]-2H-1,3-dioxole molecule (abbreviated CCD), which is shown in Fig. 1. In particular, in Ref. [33] the different dynamical behaviour of different groups of nuclear spin isomers is monitored by tracking the dispersion of the position and the angular momentum operators. There, it is proposed that these dynamical differences could be exploited in a pump–probe experiment to separate nuclear spin isomers. In the present work, we present the proof-of-principle numerical experiment which shows that a femtosecond (fs) pump–dump laser sequence can be used to enhance the ratio of one particular nuclear spin isomer of CCD beyond its equilibrium value.

The rest of the paper is organized as follows. Section 2 briefly describes the theoretical methods that were used to simulate the pump–dump experiment. Section 3 describes the results of the wave packet propagations and Sect. 4 concludes.

2 Methods

For simplicity, the wave packet simulations are restricted to four adiabatic potential energy surfaces, the ground and lowest three electronic singlet (S) excited states. Accordingly, the time evolution of the torsional motion of the molecule is described by the time-dependent Schrödinger equation written as,

$$i\frac{\partial}{\partial t}\begin{pmatrix}|\psi_{\mathrm{tor}}^{S_0}(t)\rangle\\ |\psi_{\mathrm{tor}}^{S_1}(t)\rangle\\ |\psi_{\mathrm{tor}}^{S_2}(t)\rangle\\ |\psi_{\mathrm{tor}}^{S_3}(t)\rangle\end{pmatrix} = \begin{pmatrix}\hat{\mathbf{H}}_{00} & \hat{\mathbf{H}}_{01} & \hat{\mathbf{H}}_{02} & \hat{\mathbf{H}}_{03}\\ \hat{\mathbf{H}}_{10} & \hat{\mathbf{H}}_{11} & \hat{\mathbf{H}}_{12} & \hat{\mathbf{H}}_{13}\\ \hat{\mathbf{H}}_{20} & \hat{\mathbf{H}}_{21} & \hat{\mathbf{H}}_{22} & \hat{\mathbf{H}}_{23}\\ \hat{\mathbf{H}}_{30} & \hat{\mathbf{H}}_{31} & \hat{\mathbf{H}}_{32} & \hat{\mathbf{H}}_{33}\end{pmatrix}\begin{pmatrix}|\psi_{\mathrm{tor}}^{S_0}(t)\rangle\\ |\psi_{\mathrm{tor}}^{S_1}(t)\rangle\\ |\psi_{\mathrm{tor}}^{S_2}(t)\rangle\\ |\psi_{\mathrm{tor}}^{S_3}(t)\rangle\end{pmatrix}, \tag{1}$$

where the Hamilton operator $\hat{\mathbf{H}}_{jj}$ for the particular state j can be written as the sum of the kinetic $\hat{\mathbf{T}}$ and potential $\hat{\mathbf{V}}_j$ energy operators,

$$\hat{\mathbf{H}}_{jj} = \hat{\mathbf{T}} + \hat{\mathbf{V}}_j. \tag{2}$$

The expression for the kinetic energy operator $\hat{\mathbf{T}}$ for the CCD molecule is given by

$$\hat{\mathbf{T}} = \frac{\hat{\mathbf{L}}_1^2}{2I_{\mathrm{A,B}}} + \frac{\hat{\mathbf{L}}_2^2}{2I_{\mathrm{B,C}}} + \frac{\hat{\mathbf{L}}_1\hat{\mathbf{L}}_2}{I_{\mathrm{B}}}, \tag{3}$$

where the following definitions for the angular momenta,

$$\hat{\mathbf{L}}_1 = -i\frac{\partial}{\partial\Phi_1}, \tag{4}$$

$$\hat{\mathbf{L}}_2 = -i\frac{\partial}{\partial\Phi_2}, \tag{5}$$

and reduced moments of inertia,

$$I_{\mathrm{A,B}} = \frac{I_{\mathrm{A}}I_{\mathrm{B}}}{(I_{\mathrm{A}} + I_{\mathrm{B}})} \tag{6}$$

$$I_{\mathrm{B,C}} = \frac{I_{\mathrm{B}}I_{\mathrm{C}}}{(I_{\mathrm{B}} + I_{\mathrm{C}})}, \tag{7}$$

are used. The magnitudes $I_{\mathrm{A}}, I_{\mathrm{B}}$ and I_{C} are the moments of inertia of the ring fragments A, B and C, respectively, as depicted in Fig. 1.

The operator $\hat{\mathbf{V}}_j$ contains the potential energy surfaces of CCD, which were calculated along Φ_1 and Φ_2 (see Fig. 1) using the complete active space self-consistent field method [34] averaged over the lowest four singlet states and including 12 electrons in 10 orbitals, i.e. with a SA4-CASSCF(12,10) procedure, as in Refs. [33, 35].

The off-diagonal (coupling) elements $\hat{\mathbf{H}}_{ij}$ in Eq. (1) connect the four electronic states via the transition dipole moment μ_{ij} and the time-dependent electric field of the laser pulse $E(t)$,

$$\hat{\mathbf{H}}_{ij} = -\mu_{ij}E(t). \tag{8}$$

The transition dipole moments μ_{ij} between states i and j were calculated using the same level of *ab initio* theory as the potential energy surfaces. The field of the laser pulse $E(t)$ is formulated as

$$E(t) = E_0 s(t)\cos(\omega_0 t), \tag{9}$$

with ω_0 being the central frequency of the laser pulse, E_0 the maximum amplitude and $s(t)$ the shape function of the pulse assumed to be of $\sin^2$ type, i.e.

$$s(t) = \begin{cases}\sin^2(\pi t/t_p), & \text{if } t_s < t < t_s + t_p\\ 0, & \text{otherwise}\end{cases} \tag{10}$$

starting at time t_s with duration t_p.

Equation (1) is propagated starting from a superposition of localized torsional eigenfunctions in the electronic ground state, which represent different nuclear spin isomers of CCD, as shown elsewhere [33]. The torsional wave functions were obtained using the method of propagation in imaginary time [36]. The propagation is carried out on equidistant temporal and spatial grids with time steps 0.1 fs and grid parameters $\Delta\Phi_1 = \Delta\Phi_2 = 0.7049$ for the regions $-\frac{\pi}{2} < \Phi_1, \Phi_2 < \frac{3\pi}{2}$, using the split operator [37] and fast Fourier transformation techniques [38].

3 Results and discussion

The number of identical protons with spin up or down determines the number of nuclear spin isomers. For instance, the combination of the nuclear spins of the two protons of H_2 leads to four different nuclear spin wave functions, which can be grouped into the well-known o-H_2 and p-H_2. In the case of CCD, ten equivalent protons support $2^{10} = 1024$ spin states, which according to molecular symmetry can be grouped into eight different nuclear spin isomers [35]. Taking the energy difference between the lowest and second lowest torsional eigenfunctions of the electronic ground state, one can calculate the level spacing between these states. The first excited torsional state is 106 cm^{-1} above the ground state. Considering a Boltzmann distribution of the torsional levels, one can estimate that at 50 K—a temperature that can be easily produced as the vibrational temperature within a molecular beam [39]— less than 5 % of the molecules are torsionally excited, a percentage that can be neglected. Therefore, we assume low temperature (50 K or less) so that only the lowest torsional energy level is populated and then only four of the eight nuclear spin isomers exist in CCD [35]. These four relevant nuclear spin isomers will be henceforth labelled Γ_1, Γ_4, Γ_6 and Γ_7, according to the irreducible representations of the Abelian molecular symmetry group they belong to [35].

The electronic ground state potential of CCD shows four equivalent minima along the torsional angles Φ_1 and Φ_2. Accordingly, the corresponding torsional ground state wave functions representing the nuclear spin isomers are linear combinations of wave functions localized within one potential well with a particular sign. The sign pattern of the four different torsional spin wave functions (denoted by Ψ^{Γ_i}, $i = 1, 4, 6, 7$) is shown in Fig. 2. As it can be seen, while Ψ^{Γ_1} is totally symmetric, Ψ^{Γ_7} and Ψ^{Γ_4} have only one nodal plane along Φ_1 and Φ_2, respectively, and Ψ^{Γ_6} has both nodal planes along Φ_1 and Φ_2.

One-dimensional cuts along Φ_1 and Φ_2 of the two-dimensional potential energy surfaces of CCD in the

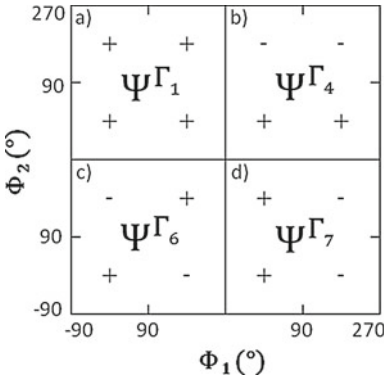

Fig. 2 Sign pattern of the torsional wave functions along Φ_1 and Φ_2 corresponding to the four nuclear spin isomers of CCD, labelled as Γ_1 (a), Γ_4 (b), Γ_6 (c) and Γ_7 (d)

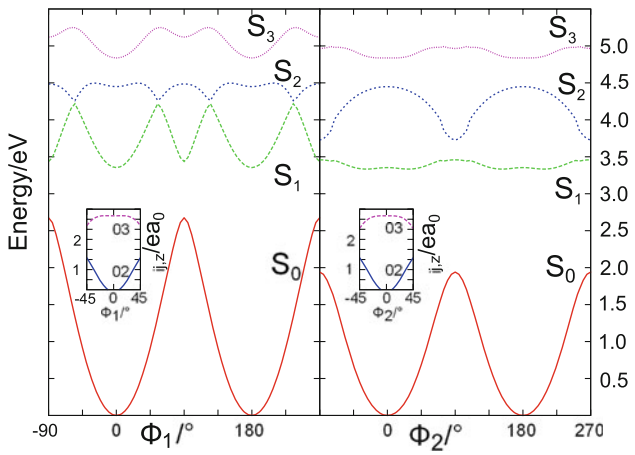

Fig. 3 One-dimensional cuts of the S_0, S_1, S_2 and S_3 potential energy surfaces of CCD along Φ_1 (a) and Φ_2 (b), with $\Phi_2 = 0°$ and $\Phi_1 = 0°$, respectively. The *inset* depicts the transition dipole moments in the z-polarization direction, exemplarily around the Franck–Condon region for the left localized minimum: μ_{02} in *solid line*, μ_{03} in *dash line*

electronic ground (S_0) and excited S_1 to S_3 states are shown in Fig. 3. The potential energy surfaces were calculated varying only the two torsional angles, while the rest of the degrees of freedom were frozen. This approximation is justified, assuming that on the proposed fs time scales, the intramolecular vibrational redistribution to other degrees of freedom will not dramatically change the essential dynamics. Within this two-dimensional model, the S_0 possesses two local minima at $\Phi_1 = 0°$ and 180°, with $\Phi_2 = 0°$, and another two at $\Phi_1 = 0°$ and 180°, with $\Phi_2 = 180°$. The four equivalent minima are separated by a potential barrier amounting to 2.68 and 1.94 eV along the Φ_1 and Φ_2 coordinates. The S_1 and S_3 states also show four local minima at the mentioned geometries. In contrast, the S_2 excited state shows a local minimum along the Φ_1 coordinate for

$\Phi_2 = 0°$ and 180°, while a local maximum can be found along Φ_2 for $\Phi_1 = 0°$ and 180°. It is the topology of the S_2 potential which precisely allows to exploit the concept of quantum interferences to separate nuclear spin isomers. An excitation from S_0 to S_2 of any of the torsional wave functions will lead to a wave function which will immediately start to move along the Φ_2 coordinate because here it is promoted to a local maximum. Shortly afterwards, different parts of the wave packet will meet along this coordinate and start to show interference effects. At some later time, similar interference effects can also be seen along the Φ_1 coordinate, due to the motion along this coordinate, which is somewhat slower due to the shallow local minimum one can find along this coordinate. Accordingly, the S_2 state is suitable to observe different excited-state dynamics for the different nuclear spin isomers.

Given the sign pattern of the four torsional wave functions (recall Fig. 2), it is clear that one can differentiate two groups of nuclear spin isomers according to the different sign combination along the Φ_2 coordinate: Ψ^{Γ_1} and Ψ^{Γ_7}, which will show constructive interferences, and Ψ^{Γ_4} and Ψ^{Γ_6}, which will show destructive interferences along the Φ_2 coordinate. To illustrate the discrimination of nuclear spin isomers by its light-induced torsional dynamics is therefore enough to consider one isomer representative of each of the two groups, for example, of Γ_1 and Γ_6. The hypothesis is that since these two nuclear spin isomers show a different excited-state dynamics due to different interferences (as shown in Ref. [33]), an appropriate pump–dump scheme should be able to detect an enrichment of one of the isomers in the electronic ground state. A pump pulse excites the nuclear spin isomers, triggering different excited-state dynamics, and a properly-timed dump pulse brings different amounts of population of the nuclear spin isomers to the ground state.

In the following, we then propagate according to Eq. (1) the two initial wave functions Ψ^{Γ_i}, $(i = 1, 6)$, representing the two classes of nuclear spin isomers. A sequence of two laser pulses E^p and E^d is used to simulate a pump–dump-like fs experiment using the S_2 state as an intermediate state. Each of the two pulses can be varied by its frequency ω, its intensity E_0 and its pulse duration t_p. Furthermore, the time delay between the two pulses t_d can be used as an additional variable. The total electric field induced by the laser pulses can thus be written as:

$$E^{\text{tot}}(t) = E^p(t) + E^d(t). \tag{11}$$

With a $\sin^2$-shaped envelope function, the individual pulses can be expressed as:

$$E^p(t) = \begin{cases} E_0^p \sin^2\left(\pi t/t_p^p\right)\cos(\omega^p t), & \text{if } t < t_p^p \\ 0, & \text{otherwise} \end{cases} \tag{12}$$

and

$$E^d(t) = \begin{cases} E_0^d \sin^2\left(\pi t/t_p^d\right)\cos(\omega^d t), & \text{if } t_d + t_p^p < t < t_d + t_p^p + t_p^d \\ 0, & \text{otherwise} \end{cases} \tag{13}$$

assuming that the pump pulse E^p starts at $t = 0$.

We therefore have two processes triggered by individual pulses which have to be controlled, the pump and the dump process, which will be discussed in the following.

3.1 Pump process

The pump process brings population from the electronic ground state S_0 to the electronically excited state S_2. This process is exactly the same for any of the two classes of nuclear spin isomers. For convenience and to stay close to typical experimental conditions, the pulse length is fixed at 200 fs, corresponding to a standard 100 fs FWHM (full-width half-maximum) fs second pulse, as it is easily produced by a commercial Ti:Sapphire laser system [40].

The laser frequency was tuned to 4.4493 eV, which corresponds to a resonant $S_0 \rightarrow S_2$ 0–0 transition. In order to get a reasonable population transfer and taking into account that the transition dipole moment between states S_0 and S_2 around the Franck–Condon is rather small (see inset in Fig. 3), an amplitude of 1.5 GV/m was chosen; this should resemble an experimental feasible pulse. Figure 4 shows the time evolution of the population (measured as the norm) of the three electronic states involved, S_0, S_2 and S_3, along the first 300 fs. As the pump pulse is switched on, one can clearly see a decrease of the population of the electronic ground state S_0 and a concomitant raise of the population of the desired target state S_2. At the end of the laser pulse, i.e. at 200 fs, both populations have reached a steady state, and we find an overall population transfer of approximately 2 % from the electronic ground state S_0 to the electronically excited state S_2. Note that how much population is excited is not relevant since absolute populations are not known experimentally.

A closer look at Fig. 4 shows an interesting additional effect. During the duration of the pump laser, there is an intermediate increase of the population of the S_3 state. This is due to the fact that the transition dipole between the ground and the S_3 state, μ_{03}, is very large, in comparison with μ_{02} (see inset in Fig. 3), and thus, the intensity of the laser is enough to populate non-resonantly this state. Note, however, that although the S_3 is populated by almost the same amount as the S_2 while the laser pulse intensity is at its maximum at 100 fs, there is no overall population transfer to this state, since this increase in population is antagonized by a decrease starting at 100 fs until the end of the pump pulse at 200 fs. The μ_{01} is negligible, and therefore, the S_1 state is never populated (not depicted).

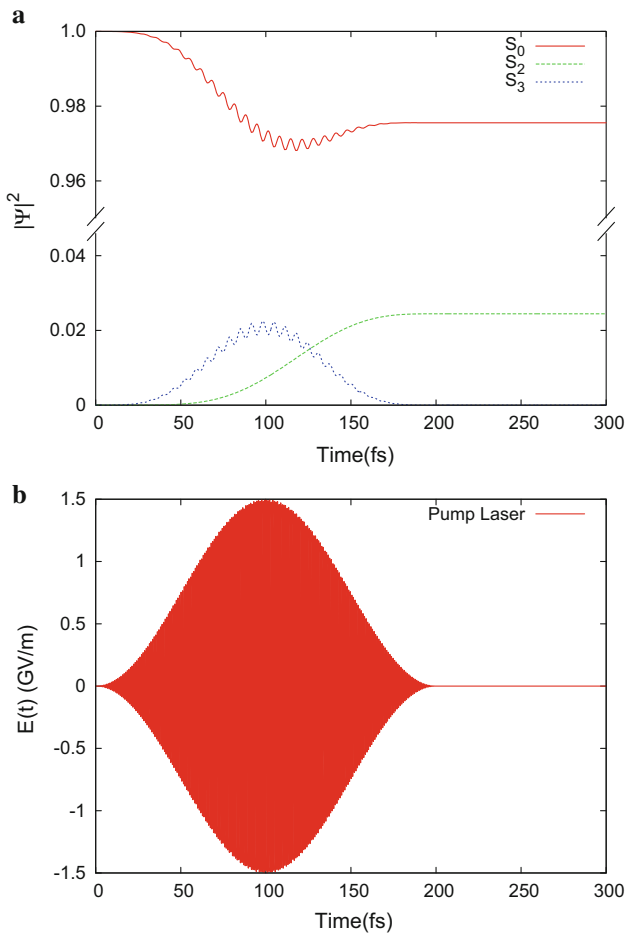

Fig. 4 **a** Time evolution of the norm of S_0, S_2 and S_3 states during the pump process. **b** The pump laser with parameters $E_0^p = 1.5$ GV/m, $\omega^p = 4.4493$ eV and $t_p^p = 200$ fs

Table 1 Scan of the population $|\Psi|^2$ of the two nuclear spin isomers Γ_1 and Γ_6 for the two electronic states S_0 and S_2 as a function of the intensity of the dump laser pulse E_0^d

E_0^d (GV/m)	$\lvert\psi_{S_0}^{\Gamma_1}\rvert^2$	$\lvert\psi_{S_2}^{\Gamma_1}\rvert^2$	$\lvert\psi_{S_0}^{\Gamma_6}\rvert^2$	$\lvert\psi_{S_2}^{\Gamma_6}\rvert^2$
0.8	0.087	0.913	0.077	0.923
0.9	0.106	0.894	0.093	0.906
1.0	0.125	0.8755	0.111	0.889
1.1	0.145	0.855	0.129	0.870
1.2	0.164	0.835	0.147	0.852

3.2 Dump process

In order to find a suitable dump pulse that creates a difference in the population of the nuclear spin isomers, a systematic scan of various laser parameters, such as the intensity and the frequency of the dump pulse as well as the delay time between the pump and the dump pulse, was carried out. We start with a scan of the intensity (for a fixed delay time and laser frequency equal to $t_d = 1800$ fs and $\omega^d = 4.45$ eV), assuming that the S_2 state is 100 % populated, i.e. using a fictions delta pulse excitation. In this way, we can better identify the intensity which gives rise to a noticeable population transfer; in reality, the dump efficiency has to be scaled with the pump efficiency. Starting then from a normalized population of 1 in the excited S_2 state and 0 in the electronic ground state S_0, Table 1 shows the population of the S_0 state versus the intensity of the dump pulse for the two groups of nuclear spin isomers. Note that already at this stage of the simulation, just using an initial guess for the frequency of the dump pulse and the delay time between the pump and the dump pulse, a coarse grain scan of the dump intensity shows a substantial difference in the population transfer between the two groups of nuclear spin isomers. As expected, the stronger the pulse, the more population is dumped to the ground state for both nuclear spin isomers. A dump pulse with intensity of 1.2 GV/m transfers roughly 15 % population back to the electronic ground state S_0. Since higher pulse intensities might become non-physical and we are only interested in qualitative results, we fix the intensity to the value of 1.2 GV/m, in order to optimize the frequency and delay time.

The remaining two parameters, i.e. the frequency ω^d of the dump laser pulse and the time delay t_d between the pump and the dump laser pulse, were optimized by carrying out a two-dimensional scan of the parameter space. The boundaries of the search space are chosen to lie within the interval of 3.05 eV $< \omega^d <$ 4.45 eV and 300 fs $< t_d <$ 2000 fs. The former boundaries are justified by the fact that an energy lower than 3.05 eV would not be sufficient to trigger any electronic excitation within the system, whereas an energy higher than 4.45 eV would trigger unwanted excitations into the S_3 state and thus minimize the efficiency of the process. The range for the time delay is justified by the fact that the two groups of nuclear spin isomer dynamics start to meet and thus to interfere at around 300 fs, and the largest difference in their dynamics can be seen at 1000 fs [33]. Therefore, there is no need to look at simulations with time delay below 300 fs, while after 2200 fs the different patterns in the dynamics should be smeared out by the dissipation of the wave packet along the second degree of freedom.

As a criterion for the efficiency of the dump process, the difference in the population of the electronic ground state S_0 after the action of the dump pulse was used. Figure 5 shows the difference in the population transfer from the S_2 state back to the electronic ground state S_0 as a function of the frequency (energy of the dump pulse) and the time delay. As one can see, noticeable differences in the S_2 population occur only for laser energies larger than ca

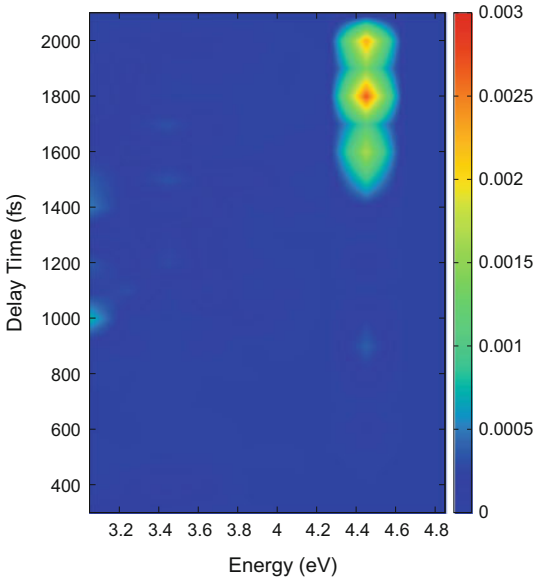

Fig. 5 Scan of the population difference of the ground state wave function of the two nuclear spin isomers at the end of the laser pulse sequence ($t = 2200$ fs) as a function of the time delay t_d between the pump and the dump pulse (*left axis*) and the frequency of the dump laser pulse (*bottom axis*). All simulations were carried out with a fixed laser intensity of $E_0^d = 1.2$ GV/m

Table 2 Optimal parameters for the pump and the dump laser pulses to obtain a maximum difference in the population ratio of the different nuclear spin isomers in the electronic ground state S_0

Parameter	E^{Pump}	E^{Dump}
E_0 (GV/m)	1.5	1.2
t_p (fs)	200	200
ω (eV)	4.4493	4.45
t_d		1800 fs

4 eV and time delays larger than ca 1400 fs, with a peak in the population difference for a time delay of $t_d = 1800$ fs and a laser pulse frequency of $\omega^d = 4.45$ eV. The energy range can be explained by the fact that with lower energies than 4 eV almost no transition from the S_2 to the S_0 takes place. The range of the time delay can be explained recalling that efficient discrimination between the two groups of isomers starts at approximately 700 fs after the initial excitation [33], i.e. at roughly $t_p^p + t_d = 900$ fs. Then, one has to wait for another 500 fs until the effect has evolved so far that one can see a difference after dumping the wave packet back onto the electronic ground state.

According to the results of Fig. 5, the optimal laser parameters given in Table 2 are selected to trigger the maximum difference between the population of the nuclear spin isomers. Now both pulses are applied in a sequence, and Fig. 6 depicts the difference in the population of the

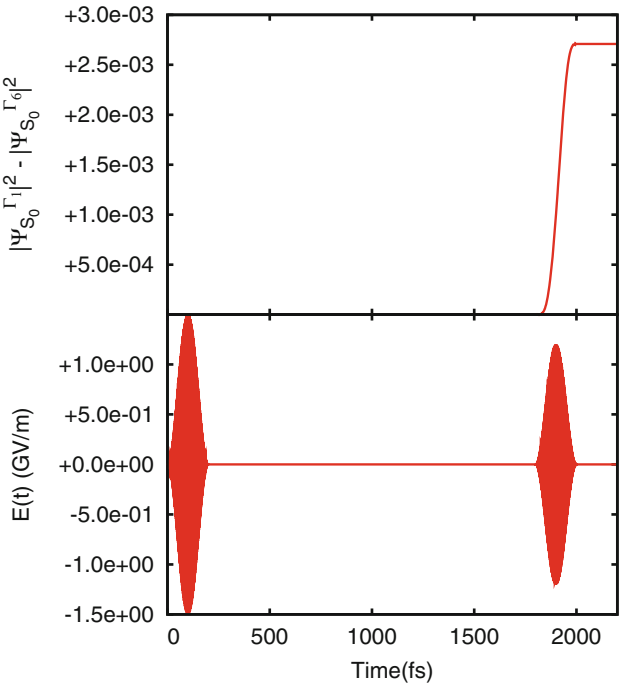

Fig. 6 Difference in population of the S_0 state for the two different nuclear spin isomers Γ_1 and Γ_6. The propagation was carried out with the laser parameters shown in Table 2 and a total propagation time of 2200 fs. One can clearly see the appearance of the population difference with the onset of the dump pulse, starting at $t = t_p^p + t_d = 1800$ fs

electronic ground state S_0 between the two nuclear spin isomers Γ_1 and Γ_6 along the total propagation time. Obviously, there is no difference whatsoever in the population during the pump pulse and the waiting time since for both nuclear spin isomers we have an excitation of some parts of the ground state population onto the excited state, which evolves in time. Only after the onset of the dump laser pulse, when the population transfers back to the ground state from the electronically excited state S_2 there is a difference in the population of the ground electronic state between the two isomers, which is maximal at the end of the dump pulse at $t = t_p^p + t_d + t_p^d = 2200$ fs, demonstrating that the dump process is different for the two different nuclear spin isomers due to its different excited-state dynamics. This is due to the fact that different interference effects (constructive versus destructive) are present in the two nuclear spin isomers in the electronically excited state S_2, leading to a difference in the effect of the dump process and therefore in the amount of population returned to the ground state. This difference in the ground state population between the two nuclear spin isomers implies a ratio of nuclear spin isomers that is shifted away from the thermodynamical equilibrium (with which we started with). In summary, we have achieved an enrichment of one of the nuclear spin isomers in the ground electronic state. In

order to increase this enrichment, it is possible to repeat the pump–dump experiment a number of times, in a distillation fashion.

4 Conclusion

We have shown for 2-[4-(cyclopenta-2,4-dien-1-ylidene) cyclohexa-2,5-dien-1-ylidene]-2H-1,3-dioxole, a quinodimethane derivative, representing a general class of A–B–C molecules with ethylene type bound connecting the rings A, B and C, that one can control the ratio of the different nuclear spin isomers by means of pump–dump spectroscopic methods, exploiting interference effects in the electronic excited state. Our model simulations show an increase of one of the nuclear spin isomers relative to the other, thus shifting the ratio away from its equilibrium value in the electronic ground state.

Acknowledgments We specially would like to thank Jörn Manz for suggesting these calculations but also Monika Leibscher, Thomas Grohmann and Omar Deeb for fruitful discussions. Financial support by the Deutsche Forschungsgemeinschaft via projects GO 1059/7-3 and MA 515/25-3 is gratefully acknowledged.

References

1. Eucken A (1912) Sitzber Preuss Akad Wiss 141
2. Mecke R (1925) Z Physik 31:709
3. Heisenberg W (1927) Z Physik 41:239
4. Hund F (1927) Z Physik 42:93
5. Bonhoeffer K, Harteck P (1929) Naturwissenschaften 17:182
6. Farkas A (1935) Orthohydrogen, parahydrogen and heavy hydrogen. Cambridge University Press, London
7. Buntkowsky G, Limbach HH (2006) Dihydrogen and symmetry: the role of symmetry on the chemistry of dihydrogen transfer in the light of NMR spectroscopy. In: Hynes JT, Klinman J, Limbach HH, Schowen RL (eds) Hydrogen-transfer reactions, vol 2. Wiley-VCH, Weinheim
8. Quack M (1977) Mol Phys 34:477
9. Bunker PR, Jensen P (2009) Spectroscopy and broken symmetry. Elsevier, Amsterdam
10. Chapovsky PL, Hermans LJF (1999) Annu Rev Phys Chem 50:315
11. Sandler YL (1954) J Phys Chem 58:58
12. Cunningham CM, Johnston HL (1958) J Am Chem Soc 80:2382
13. Panfilov V, Strunin V, Chapovsky PL (1983) Sov Phys J Exp Theor Phys 58:510
14. Chapovsky PL, Krasnoperov LN, Panfilov VN, Strunin VP (1985) Chem Phys 97:449
15. Bakarev AE, Chapovsky PL (1986) J Exp Theor Phys Lett 44:4
16. Chapovsky PL (1990) Sov Phys J Exp Theor Phys 70:895
17. Chapovsky P, Cosléou J, Herlemont F, Khelkhal M, Legrand J (2000) Chem Phys Lett 322:424
18. Peters G, Schramm B (1999) Chem Phys Lett 302:181
19. Sun ZD, Takagi K, Matsushima F (2005) Science 310(5756):1938
20. Tikhonov VI, Volkov AA (2002) Science 296(5577):2363
21. Kravchuk T, Reznikov M, Tichonov P, Avidor N, Meir Y, Bekkerman A, Alexandrowicz G (2011) Science 331(6015):319
22. Horke DA, Chang YP, Długołęcki K, Küpper J (2014) Chem Int Ed 53:11965
23. Gel'mukhanov FK, Shalagin AM (1979) J Exp Theor Phys Lett 29:773
24. Al-Jabour S (2011) Molecular symmetry, quantum chemistry and dynamics: simulation of laser driven molecular torsion in the presence of a conical intersection (Dissertation, Freie Universität Berlin)
25. Fujimura Y, González L, Hoki K, Kröner D, Manz J, Ohtsuki Y (1999) Chem Phys Lett 310:578
26. Brackhagen O, Busse H, Giraud-Girard J, Manz J, Oppel M (2000) J Chem Phys 112:8819
27. Evers F, Giraud-Girard J, Grimme S, Manz J, Monte C, Oppel M, Rettig W, Saalfrank P, Zimmermann P (2001) J Phys Chem A 105:2911
28. Hoki K, Kröner D, Manz J (2001) Chem Phys 267:59
29. Manz J, Proppe B, Schmidt B (2002) Phys Chem Chem Phys 4:1876
30. Fujimura Y, González L, Kröner D, Manz J, Mehdaoui I, Schmidt B (2004) Chem Phys Lett 386:248
31. Kröner D, Klaumützer B (2007) Phys Chem Chem Phys 9:5009
32. Obaid R, Leibscher M (2015) J Chem Phys 142(6):064315
33. Obaid R, Kinzel D, Oppel M, González L (2014) J Chem Phys 141:164323
34. Roos BO, Taylor PR, Siegbahn PEM (1980) Chem Phys 48:157
35. Belz S, Deeb O, González L, Grohman T, Kinzel D, Leibscher M, Manz J, Obaid R, Oppel M, Xavier GD, Zilberg S (2013) Z Phys Chem 227:1021
36. Lehtovaara L, Toivanen J, Eloranta J (2007) J Comp Phys 221:148
37. Feit MD, Fleck JA Jr (1983) J Chem Phys 78:301
38. Leforestier C, Bisseling RH, Cerjan C, Feit MD, Friesner R, Guldberg A, Hammerich A, Jolicard G, Karrlein W, Meyer HD, Lipkin N, Roncero O, Kosloff R (1991) J Comput Phys 94:59
39. Levy DH (1981) Science 214:263
40. Rulliere C (2004) Femtosecond laser pulses: principles and experiments. Advanced texts in physics. Springer, Berlin

Theor Chem Acc (2015) 134:29
DOI 10.1007/s00214-015-1625-7

REGULAR ARTICLE

Spin delocalization in hydrogen chains described with the spin-partitioned total position-spread tensor

Muammar El Khatib · Oriana Brea · Edoardo Fertitta · Gian Luigi Bendazzoli · Stefano Evangelisti · Thierry Leininger · Beate Paulus

Received: 18 November 2014 / Accepted: 23 January 2015 / Published online: 13 February 2015

Abstract The formalism of the spin-partitioned total position spread (SP-TPS) tensor is applied to model systems treated at ab initio level. They are hydrogen linear chains having different geometries and showing qualitatively different behaviors. Indeed, the SP-TPS behavior depends in a crucial way on the entanglement properties of the chain wave function. It is shown that the SP-TPS tensor gives a measure of the spin delocalization in the chain. This is very low in the case of isolated fixed-length dimers and maximal for chains of equally spaced atoms. The present formalism could be used to describe, for instance, the spin fluctuation associated with spintronic devices.

Published as part of the special collection of articles derived from the 9th Congress on Electronic Structure: Principles and Applications (ESPA 2014).

Electronic supplementary material The online version of this article (doi:10.1007/s00214-015-1625-7) contains supplementary material, which is available to authorized users.

M. El Khatib · O. Brea · S. Evangelisti (✉) · T. Leininger
Laboratoire de Chimie et Physique Quantiques - LCPQ/IRSAMC, Université de Toulouse (UPS) et CNRS (UMR-5626), 118, Route de Narbonne, 31062 Toulouse Cedex, France
e-mail: Stefano.Evangelisti@irsamc.ups-tlse.fr

O. Brea
Departamento de Química, Facultad de Ciencias, Módulo 13, Universidad Autónoma de Madrid, Cantoblanco, 28049 Madrid, Spain

E. Fertitta · B. Paulus
Institut für Chemie und Biochemie - Freie Universität Berlin, Takustr. 3, 14195 Berlin, Germany

G. L. Bendazzoli
Dipartimento di Chimica Industriale "Toso Montanari", Università di Bologna, Viale Risorgimento 4, 40136 Bologna, Italy

Keywords Hydrogen chains · Total position spread · Full CI · Spintronics · Spin fluctuation

1 Introduction

In the last decades, electronic devices have been reduced in size [1] and now tend to be in the one-dimensional regime. Experimental evidences have shown that the manipulation of individual atoms is possible [2], so that atoms can be used as building blocks for the fabrication of molecular circuits. The simplest quantum chemical model of a one-dimensional arrangement of atoms consists of a hydrogen chain with each hydrogen atom described using a single 1*s* atomic orbital. Dissociation of hydrogen chains is known to be a good model system for the investigation of strong electronic correlation effects. Moreover, they show a metal–insulator transition that can be well described by varying the inter-atomic distance and that strongly depends on the accuracy with which the electron correlation is treated [3, 4].

One possibility to quantify the behavior in the vicinity of the metal–insulator transition is the localization tensor (LT), a quantity introduced in the context of the theory of Kohn [5] to characterize the electrical conductivity properties. Indeed, in his seminal work Kohn realized that the most fundamental picture of electrical conductivity is more related to the delocalization of the wave function than to the simple gap closure. Subsequently, Resta et al. [6–10], with the introduction of the localization tensor, provided an important tool to give a quantitative formulation of this effect. According to their results, one of the key properties of this quantity is that *it diverges in the thermodynamic limit for a conductor, while remaining finite for an insulator* [11, 12]. A remarkable sum rule connecting explicitly

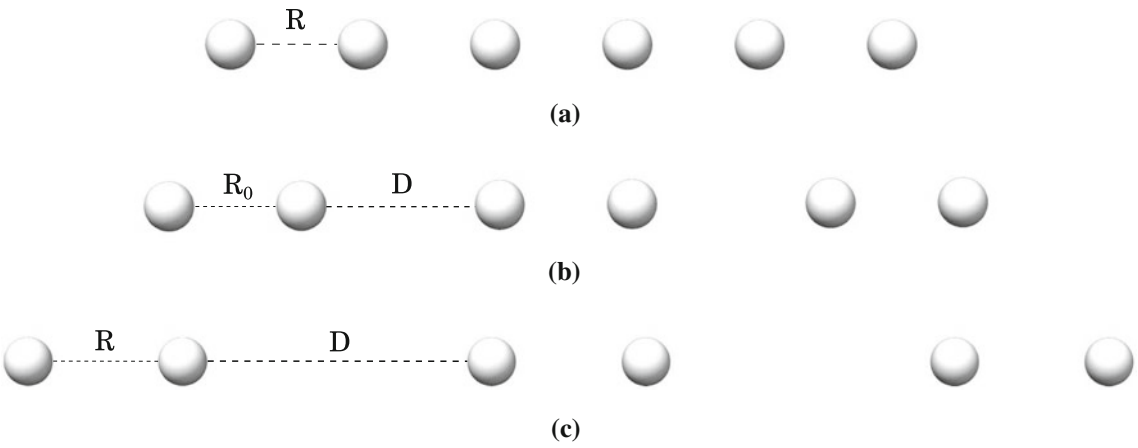

Fig. 1 Schematic representation of the different structural models of the hydrogen chains considered in this investigation. **a** Equally spaced chains. **b** Fixed-bond dimerized chains; $R_0 = 2$ bohr. **c** Homothetic dimerized chains; $D = 2R$

electrical resistivity and the LT was later given by Souza et al. [13].

For finite-size systems like molecules or clusters, since one is interested in the overall behavior of the systems, the total position spread (TPS) tensor is more appropriate than the LT [14–16]. This new quantity is trivially related to the LT given that it is defined as the LT not divided by the number of electrons. Having a rotational invariant trace, and being invariant under the translation of center-of-mass coordinates, the TPS tensor is more suitable to describe molecular issues, such as size consistency. We have found that the TPS is a powerful tool to monitor charge mobility and the nature of the wave functions which are useful indicators when exploring metal–insulator transitions [17–21]. Recently, we have studied the behavior of the TPS tensor in several types of structures (ranging from atoms, molecules to clusters) treated either at ab initio level [20, 22–24], or through the use of *model* [25, 26] Hamiltonians. Moreover, in one of our latest investigations, we realized that the TPS partitioned accordingly to spin variables will be an important quantity to understand spin fluctuation and quantum entanglement [27–29].

In this work, hydrogen chains of different sizes have been considered (see Fig. 1) in order to investigate how Peierls distortions (dimerizations) [30] and Mott transitions [31] (in the case of non-dimerized chains) affect the fluctuation of the electrons from their mean positions. According to Peierls' theorem, *an equally spaced atomic chain with one electron per ion is unstable*, so that equally spaced chains tend to be stabilized by subtle changes in their inter-atomic distances (e.g., dimerizations), and this has an impact on the metallic character of the chains. To monitor the charge and spin fluctuations, we employed the TPS tensor and its spin-partitioned components whose behavior is shown to strongly depend on the dimerization. The determination of the wave function was carried out at full-CI (FCI) level using a minimal 1*s* basis set.

This investigation is divided as follows: In Sect. 2, the general formalism of the spin partition of the TPS tensor is shown; Sect. 3 describes the computational details; in Sect. 4, we present the results and discussions, and finally Sect. 5 contains the conclusions.

2 General formalism: spin partition of TPS tensor

In order to elaborate the formalism of the spin-partitioned TPS (SP-TPS) tensor, let us express the position operator $\hat{\mathbf{r}}$ of an electron as the sum of its components with α-spin and β-spin, by multiplying the position operator with the particle number operator for α-spin $\hat{\mathbf{n}}_\alpha$ and β-spin $\hat{\mathbf{n}}_\beta$:

$$\hat{\mathbf{r}} = \sum_{\sigma=\alpha,\beta} \hat{\mathbf{r}}\,\hat{\mathbf{n}}_\sigma \tag{1}$$

From the one-particle position operator $\hat{\mathbf{r}}$ it is possible to define the total position operator $\hat{\mathbf{R}}$ as sum over all electrons in the molecular system:

$$\hat{\mathbf{R}} = \sum_{i=1}^{n} \sum_{\sigma=\alpha,\beta} \hat{\mathbf{r}}(i)\hat{\mathbf{n}}_\sigma(i) \tag{2}$$

and its corresponding spin-partitioned terms

$$\hat{\mathbf{R}}_\sigma = \sum_{i=1}^{n} \hat{\mathbf{r}}(i)\hat{\mathbf{n}}_\sigma(i) \tag{3}$$

The spin-summed TPS (SS-TPS) tensor is defined as the second moment cumulant [32] of the total position operator:

$$\mathbf{\Lambda} = \langle\Psi|\hat{\mathbf{R}}^2|\Psi\rangle - \langle\Psi|\hat{\mathbf{R}}|\Psi\rangle^2 \tag{4}$$

Large values of the TPS are related to a high delocalization of the wave function. That is the reason why we decided to drop the name *localization* tensor, in favor of *TPS* tensor [14, 15, 33]. The TPS tensor $\mathbf{\Lambda}$, being a second-order cumulant, does not depend on the origin of the coordinate system, which means that it is invariant with respect to center-of-mass translations. Therefore, it can be conveniently computed in the particular coordinate system where $\langle\Psi|\hat{\mathbf{R}}|\Psi\rangle = 0$ so that $\mathbf{\Lambda} = \langle\Psi|\hat{\mathbf{R}}^2|\Psi\rangle$.

Since, according to Eqs. 2 and 3, the operator $\hat{\mathbf{R}}$ can be partitioned as the sum of a $\hat{\mathbf{R}}_\alpha$ and a $\hat{\mathbf{R}}_\beta$ term, the squared operator $\hat{\mathbf{R}}^2$ and, therefore, $\mathbf{\Lambda}$ becomes the sum of four terms, $\alpha\alpha$, $\beta\beta$, $\alpha\beta$ and $\beta\alpha$:

$$\mathbf{\Lambda} = \mathbf{\Lambda}_{\alpha\alpha} + \mathbf{\Lambda}_{\beta\beta} + \mathbf{\Lambda}_{\alpha\beta} + \mathbf{\Lambda}_{\beta\alpha} \tag{5}$$

where the different components of the TPS tensor are:

$$\mathbf{\Lambda}_{\alpha\alpha} = \langle\Psi|\hat{\mathbf{R}}_\alpha^2|\Psi\rangle - \langle\Psi|\hat{\mathbf{R}}_\alpha|\Psi\rangle^2 \tag{6}$$

$$\mathbf{\Lambda}_{\beta\beta} = \langle\Psi|\hat{\mathbf{R}}_\beta^2|\Psi\rangle - \langle\Psi|\hat{\mathbf{R}}_\beta|\Psi\rangle^2 \tag{7}$$

$$\mathbf{\Lambda}_{\alpha\beta} = \langle\Psi|\hat{\mathbf{R}}_\alpha\hat{\mathbf{R}}_\beta|\Psi\rangle - \langle\Psi|\hat{\mathbf{R}}_\alpha|\Psi\rangle\langle\Psi|\hat{\mathbf{R}}_\beta|\Psi\rangle \tag{8}$$

$$\mathbf{\Lambda}_{\beta\alpha} = \langle\Psi|\hat{\mathbf{R}}_\beta\hat{\mathbf{R}}_\alpha|\Psi\rangle - \langle\Psi|\hat{\mathbf{R}}_\beta|\Psi\rangle\langle\Psi|\hat{\mathbf{R}}_\alpha|\Psi\rangle \tag{9}$$

It is worth to remark the fact that $\mathbf{\Lambda}_{\alpha\alpha}$ and $\mathbf{\Lambda}_{\beta\beta}$ are second-order cumulants themselves, of the spin-projected total position operators $\hat{\mathbf{R}}_\alpha$ and $\hat{\mathbf{R}}_\beta$, and satisfy therefore all the corresponding properties. Their sum, however, *is not* a cumulant, because $\mathbf{\Lambda}_{\alpha\beta}$ and $\mathbf{\Lambda}_{\beta\alpha}$ are not cumulants [29]. Also, $\mathbf{\Lambda}_{\alpha\beta}$ and $\mathbf{\Lambda}_{\beta\alpha}$ components are equal, because of the vanishment of the commutator between $\hat{\mathbf{R}}_\alpha$ and $\hat{\mathbf{R}}_\beta$.

Therefore, in this investigation, we will report the global component $2\mathbf{\Lambda}_{\alpha\beta}$ and, in all situations where the S_z spin component is equal to zero, $2\mathbf{\Lambda}_{\alpha\alpha}$, since in this special case $\mathbf{\Lambda}_{\alpha\alpha}$ and $\mathbf{\Lambda}_{\beta\beta}$ are identical. Regarding the translational invariance of the TPS, one can assume a coordinate system with $\langle\Psi|\hat{\mathbf{R}}_\alpha|\Psi\rangle = 0$, and for systems with $S_z = 0$ it holds that also $\langle\Psi|\hat{\mathbf{R}}_\beta|\Psi\rangle = 0$. Therefore, in this case, the spin-summed TPS tensor (SS-TPS) can be written as:

$$\mathbf{\Lambda} = 2\mathbf{\Lambda}_{\alpha\alpha} + 2\mathbf{\Lambda}_{\alpha\beta} = 2\langle\Psi|\hat{\mathbf{R}}_\alpha^2|\Psi\rangle + 2\langle\Psi|\hat{\mathbf{R}}_\alpha\hat{\mathbf{R}}_\beta|\Psi\rangle. \tag{10}$$

3 Computational details

Hydrogen chains, H_n ($n = 2, 4, 6, 8, 10, 12, 14, 16$) have been considered, covering molecular configurations from inter-atomic distances between 1 and 8 bohr. All calculations were performed at the FCI level using our algorithm NEPTUNUS [34–37]. We employed the STO-12G minimal basis set by Tunega and Noga [38], which yields excellent results compared with the exact solution of the hydrogen atom [39].

In FCI calculations, all possible Slater determinants of the proper spatial and spin symmetry are included in the variational treatment, obtaining the best possible approximation to the solution of the nonrelativistic Schrödinger equation, within the accuracy of the basis set. For the case $n = 16$, the size of the FCI space contains up to 82,820,900 configuration state functions (CSF) with total z-spin component equal to zero. NEPTUNUS uses the one- and two-electron molecular integrals computed on the Hartree–Fock atomic orbitals (AO) that are obtained with the DALTON quantum chemistry package [40]. Then, the AO integrals are transformed on the Hartree–Fock molecular orbital (MO) basis set, using a 4-index transformation.

Since both DALTON and our FCI program are not able to treat non-abelian symmetry groups, the calculations for such systems (point group $D_{\infty h}$) are generally performed in the abelian subgroup D_{2h}. However, since we are using only s atomic functions, only molecular orbitals which transform according to the IRREPS Σ_g^+ and Σ_u^+ can be generated. Therefore, the calculation can simply be performed in the C_i subgroup.

Three different types of atomic structures have been explored in the present investigation, covering equally spaced as well as dimerized cases, as illustrated in Fig. 1:

1. Equally spaced hydrogen chains: All nearest-neighbor H–H distances are equal to a variable parameter R (see Fig. 1a).
2. Fixed-bond dimerized hydrogen chains: A dimerization of the chain produces fixed-length short bonds (bond length R_0) and variable-length long bonds (bond length D). In the present investigation, we chose $R_0 = 2$ bohr (see Fig. 1b).
3. Homothetic dimerized hydrogen chains: The short (R) and long (D) bonds of the dimerized chain have proportional lengths, defined by the constant factor $\delta = D/R$. In the present work, we choose $\delta = 2$ (see Fig. 1c). Of course, the limit $\delta = 1$ represents the equally spaced chains.

It has to be noticed that the first and the third structural models correspond to homothetic "explosions" of the chains, although with different ratios between the lengths of two consecutive bonds. Moreover, the reader should notice that in our structural models, the short bonds are always placed at the ends of the chains, regardless of the number of atoms in the chain, in order to avoid huge edge effects induced by isolated or almost-isolated atoms [25]. In fact, a systematic study of this situation goes well beyond the scope of the present work and would deserve a dedicated investigation.

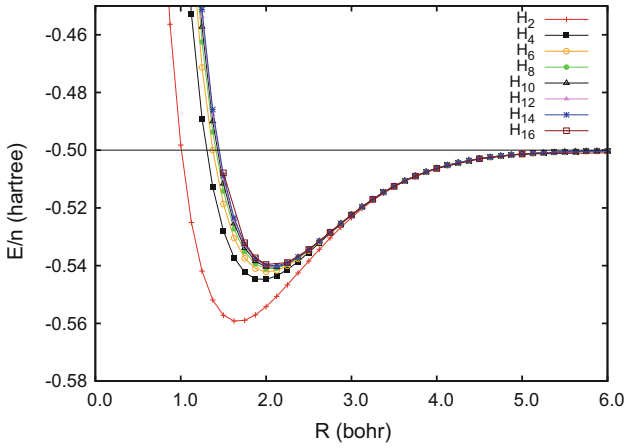

Fig. 2 Energy *per atom* of the equally spaced hydrogen chains as a function of the inter-nuclear distance R (FCI/STO-12G)

4 Results and discussions

We present in this section the results corresponding to the three different structural models of even-numbered hydrogen chains in their singlet ground state. In order to facilitate the comparison among chains having different number of atoms, in this article all energies and TPS tensor values presented are divided by the number of atoms in the chain, n.

4.1 Equally spaced hydrogen chains

In Fig. 2, the *per atom* potential energy curves corresponding to the homothetic expansion of the equally spaced hydrogen chains are shown. There is a minimum in the region of $R = 2$ bohr, and the depth of the curves only weakly depends on the number of atoms of the chains, except for the H_2 molecule whose minimum is significantly deeper than those of longer chains. Only one covalent bond can be formed.

In the case of equally spaced chains, the longitudinal SS-TPS $\Lambda^{\parallel}$ has a nonadditive growth at intermediate inter-nuclear distances, while for $R > 4$ bohr, the isolated atom value of 1 bohr^2 is recovered [39]. This is illustrated in Fig. 3a, where the values of the *per atom* longitudinal component, $\Lambda^{\parallel}/n$, are shown as a function of R for the different values of n. At very short distances, $R < 1$ bohr, $\Lambda^{\parallel}/n$ has a sudden drop (not shown in the figure), due to the missing flexibility of the basis set in this region. For this reason, results in the short-distance regimes cannot be considered as being particularly significative. At intermediate distances, between 1 and 4 bohr, the SS-TPS shows a region with a maximum, which is peaked at about 2 bohr for the longer chains. The height of the maximum significantly depends on the number of atoms in the chain, suggesting a delocalized behavior of the wave function, that seems to diverge in this region for large values of n as it is expected for a metal.

In the spin-partitioned TPS tensor, the longitudinal terms have a very different behavior. In Fig. 3b, the two SP-TPS components, $\Lambda^{\parallel}_{\alpha\alpha}$ and $\Lambda^{\parallel}_{\alpha\beta}$, are reported. Being a second-order cumulant, $\Lambda^{\parallel}_{\alpha\alpha}$ is always positive. The mixed-spin component, $\Lambda^{\parallel}_{\alpha\beta}$, on the other hand, is not a cumulant, and it can be either positive or negative. The only constraint is that the sum $2\Lambda^{\parallel}_{\alpha\alpha} + 2\Lambda^{\parallel}_{\alpha\beta}$ gives the spin-summed TPS tensor $\Lambda^{\parallel}$, which is also positive by definition. Therefore, the *sign* of $\Lambda^{\parallel}_{\alpha\alpha}$ determines the relative size of $\Lambda^{\parallel}$ and $\Lambda^{\parallel}_{\alpha\beta}$, as we discussed for the case of H_2 in Ref. [29]. In the case of "neutral" systems (i.e., systems whose most important configurations are neutral ones in the valence bond language), the $\Lambda^{\parallel}_{\alpha\alpha}$ component of the SP-TPS tensor has a value that is larger than that of the SS-TPS. Accordingly, $\Lambda^{\parallel}_{\alpha\beta}$ mixed component is negative. In fact, the two components have similar absolute values and opposite sign, although the magnitude of $\alpha\beta$ component is obviously slightly lower than the $\alpha\alpha$ one, their sum being positive. Both the $\alpha\alpha$ and $\alpha\beta$ components diverge quadratically for increasing values of R, indicating a delocalization of the spins on different centers of the chain. Moreover, the *per electron* value of both components increases linearly as a function of n. This clearly indicates that, in equally spaced chains, the delocalization effect is a collective phenomenon that concerns all the spins in the chain.

4.2 Dimerized chains

Dimerized chains behave in a qualitatively different way with respect to equally spaced ones. Moreover, it will be shown that the type of dimerization has a strong influence on the TPS behavior, particularly on the SP components. We describe here the behavior of the spreads for the two types of Peierls' distorted chains, illustrated in Fig. 1b and c, the fixed-bond dimers and the homothetic dimers.

4.2.1 Fixed-bond dimerized hydrogen chains

The potential energy curves for the chains corresponding to different values of n, divided by the number of atoms, are virtually superposed because we consider only the large-distance part of the potential energy curve with $R = 2$ bohr as the fixed distance. However, the desired behavior of the TPS tensor is obtained especially in this region.

The *per atom* spin-summed TPS $\Lambda^{\parallel}/n$ is presented in Fig. 3c. All curves show marked maxima in the region of $D = 2$ bohr (this distance corresponds to equal spacing). In the asymptotic limit for large D, the longitudinal component of the spread tensor converges to the value of the isolated dimer at the inter-nuclear distance of 2 bohr, i.e.,

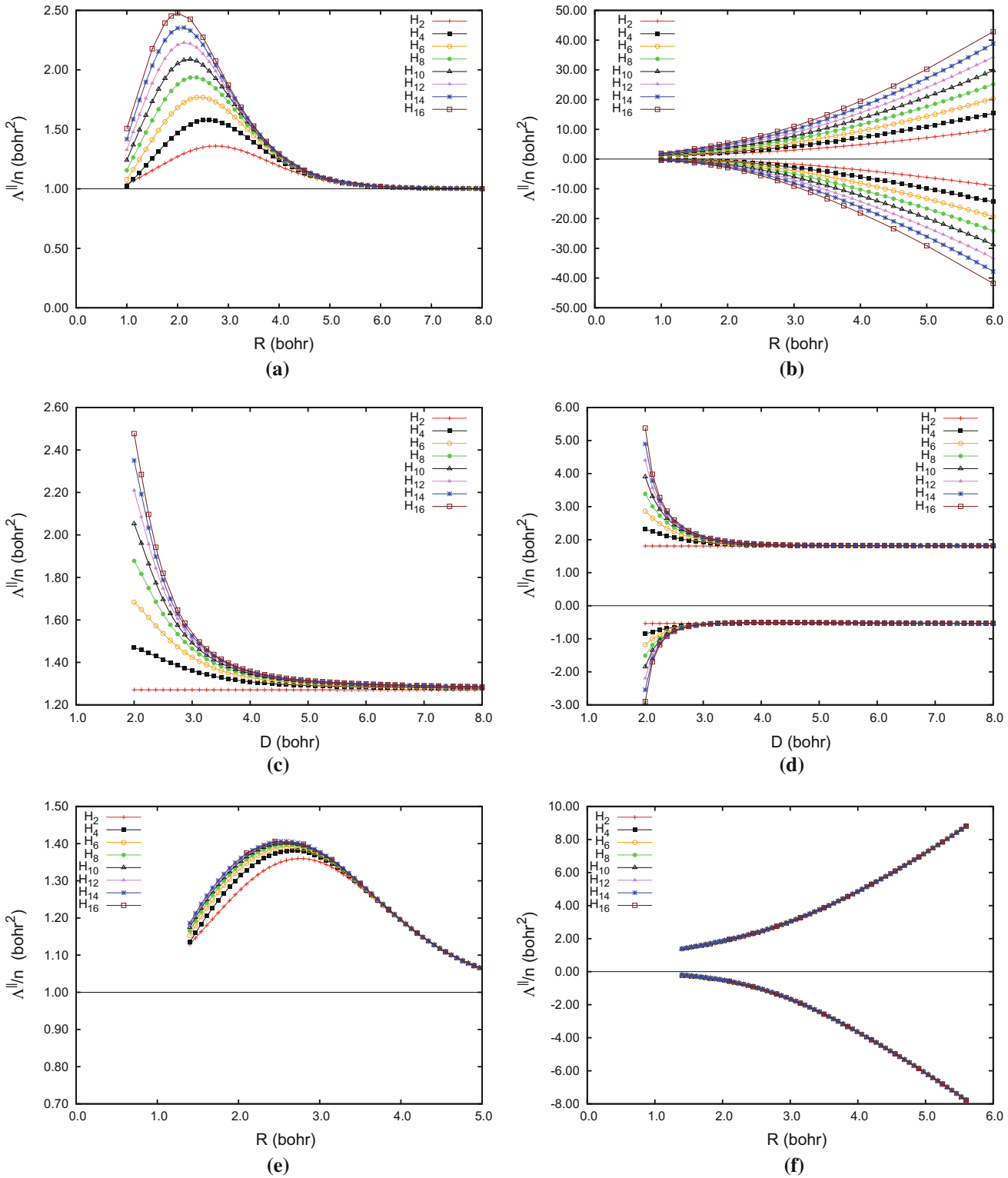

Fig. 3 Spin-summed (SS, *left-side figures*) and spin-partitioned (SP, *right-side figures*) TPS tensors divided by the number of atoms for the different hydrogen chains (FCI/STO-12G). In the SP-TPS figures, *positive values* represent the $\alpha\alpha$ component, and *negative values* the $\alpha\beta$ component of the tensor. **a** SS-TPS, equally spaced chains. **b** SP-TPS, equally spaced chains. **c** SS-TPS, fixed-bond dimerized chains. **d** SP-TPS, fixed-bond dimerized chains. **e** SS-TPS, homothetic dimerized chains. **f** SP-TPS, homothetic dimerized chains

$\Lambda^{\parallel} = 1.27\,\text{bohr}^2$. As one would expect, for large values of D the charge does not fluctuate among the dimers.

In Fig. 3d, the SP-TPS values $2\Lambda^{\parallel}_{\alpha\alpha}$ and $2\Lambda^{\parallel}_{\alpha\beta}$ are reported. As seen for the equally spaced chains, the SP-TPS values are larger than SS-TPS ones, but the behavior of the $2\Lambda^{\parallel}_{\alpha\alpha}$ and $2\Lambda^{\parallel}_{\alpha\beta}$ is very different from the one seen for the equally spaced chains. In the asymptotic limit of large D, there is no divergence of the two components. This means that spin fluctuation is very limited in dimerized chains. Generally speaking, both the spin-summed and spin-partitioned results at large D values are identical to those obtained for the H_2 dimer at an inter-nuclear distance of 2 bohr. In other words, the system is composed of $n/2$ independent dimers with a fixed inter-nuclear distance. The total energies and both types of TPS tensors are additive, being given by $n/2$ times those of an isolated dimer.

4.2.2 *Homothetic dimerized hydrogen chains*

The second type of dimerized chains is now taken into account, where both inter-nuclear distances are increased with the fixed ratio of $\delta = 2$. The energy curves are perfectly superposed for different n, because the systems represent weakly interacting hydrogen dimers with an optimal intra-dimer distance of $R = 1.4$ bohr. At large values of R, all the energies converge to the energy of the isolated hydrogen atom, because in the homothetic model the dimers are dissociated.

The *per atom* longitudinal component of the SS-TPS tensor $\Lambda^{\parallel}/n$ as a function of R is shown in Fig. 3e. All the curves are roughly superposed, indicating the absence of noticeably collective effects. A maximum occurs at $R = 2$ bohr, which roughly corresponds to the distance of the maximum in the isolated H_2 dimer. Indeed, in this regime the nearest-neighbor dimer is at $D = 4$ bohr, and this explains the small differences among curves corresponding to the different n values. At large R values, all systems tend to a collection of isolated hydrogen atoms, and $\Lambda^{\parallel}/n$ converges toward the isolated atomic value.

The behavior of the *per atom* SP-TPS tensor is illustrated in Fig. 3f. It is remarkable that the SP-TPS (particularly at large distances) does not depend on the number of atoms in the chains, but depends strongly on the distance R as in their equally spaced counterparts, Fig. 3b. This is related to the absence of inter-dimer delocalization (entanglement) in the dimerized case, contrary to what happens in the equally spaced systems, where the delocalization of the different structures involves the whole chain. Notice, however, that all these structures are characterized as having a single electron *per atom*, and this explains why the long distance value of both geometrical arrangements are identical. This fact will be discussed in more detail in Sect. 4.3.

It is important to stress that, although the limit for large R values is the same for the homothetic dimerized and the equally spaced chains, the structure of the wave function is completely different in the two cases. For the equally spaced chains, the wave function cannot be factorized as a product of dimers, since *all atoms* are entangled, whereas for homothetic dimerized chains, the wave functions can be asymptotically written as the product of antisymmetrized dimer wave functions, since the entanglement concerns only within *the single dimers*. This fact is reflected by completely different large R behaviors of the SP-TPS tensor in the two cases, while the spin-summed counterparts are strictly identical.

4.3 Asymptotic behavior of the longitudinal position-spread tensors

We discuss in this section the general behavior of the *per atom* longitudinal components of the TPS tensors $\Lambda^{\parallel}(n)/n$ for the different distances and the different types of chains. In particular, to investigate the large n behavior, we fitted each series of values, for any fixed inter-nuclear distance, with a linear function as a function of the number of atoms (*least squared polynomial fit* procedure using Python [41, 42] and NumPy [43]):

$$\Lambda^{\parallel}(R,n)/n = \Lambda^{\parallel}_0(R) + \Lambda^{\parallel}_1(R)\,n \tag{11}$$

In this way, the coefficients obtained with the fitting have condensed information about the considered systems. The constant term $\Lambda^{\parallel}_0$ of this expansion is capable of describing the usual behavior of a weakly interacting system, for which the delocalization grows *additively* with the size of the system (an "insulating" regime). The linear term $\Lambda^{\parallel}_1$, on the other hand, accounts for a *faster than additive* growth of the total mobility, associated with a strong delocalization (a "metallic" regime).

In Figure 1 of the Supplementary Material (SM1), the coefficients for the equally spaced chains are plotted as a function of the distance R. We consider first the spin-summed TPS tensor, whose coefficients present a remarkable behavior. Both terms, $\Lambda^{\parallel}_0(R)$ and $\Lambda^{\parallel}_1(R)$, show a maximum for intermediate values of the distance, whose positions, however, do not coincide, and the shape of the curves is only apparently similar. Indeed, the constant term $\Lambda^{\parallel}_0(R)$ has a shallow maximum at $R \simeq 3$ bohr, and then its value goes down to the isolated atom limit. This curve is very much reminiscent of the one obtained for the hydrogen dimer, Fig. 3a. The linear term, on the other hand, has a high peak close to $R \simeq 2$ bohr, the distance for which the system exhibits a metallic-like behavior. Then, the size of the coefficient goes down, reaching negligible values for $R > 5$ bohr. At this distance, the system has the behavior of an insulator. In other words, these coefficients mark the change from a metallic to an insulating character of the chains.

For the $\alpha\alpha$ component of the SP-TPS tensor (the $\alpha\beta$ component has a similar behavior, but presents a opposite sign), both coefficients diverge as a function of R. This can be seen as the result of the combined effect of delocalization both within the intra- and inter-dimer region, although the concept of dimers in this case is somehow arbitrary.

In Figure SM2, the case of fixed-bond dimerization is shown. Coefficients of the $\alpha\alpha$ component and the spin-summed TPS show very similar responses. This is the signature of very localized systems. For $D = 2$ bohr, the systems coincide with the equally spaced chains. Therefore, at such molecular configurations, $\Lambda_0^{\parallel}$ shows minimum contribution and $\Lambda_1^{\parallel}$ takes their highest values. Then, for $D > 2$ bohr, $\Lambda_0^{\parallel}$ reaches its maximum contribution because of the strong entanglement of the electrons within the intra-dimer region. At the same time, $\Lambda_1^{\parallel}$ drops abruptly to zero because both spin fluctuation and electron mobility are very small between different dimers.

Finally, in the case of the homothetic dimerization (Figure SM3), the SP-TPS, $\Lambda_0^{\parallel}$ diverges while $\Lambda_1^{\parallel}$ tends to 0. This means that the systems present a large spin fluctuation and that it is not directly related to the metallic character. This, combined to the fact that energies *per atom* are degenerated, implies that we are in the presence of an entanglement of the wave functions. Lastly, the SS-TPS tensor shows coefficients whose decay is similar to the case of the fixed-bond dimerized case. This confirms that the system, at long distances, has a low electron mobility in the chains, but a large spin fluctuation *within the dimers*.

5 Conclusions

In this investigation, the formalism of the spin-partitioned position-spread tensor has been applied to hydrogen chains. The results for equally spaced chains showed that the divergence of the SS-TPS is related to charge entanglement and revealed a strong metallic character of the wave function. Furthermore, divergent values of the SP-TPS are associated with spin entanglement. Equally spaced chains showed pronounced maxima of the SS-TPS with peaks in the region of 2 bohr, suggesting that the structure has a metallic character at that distance. At long distances, the SP-TPS component $\Lambda_{\alpha\alpha}^{\parallel}$ diverges, indicating a large spin fluctuation, while the SS-TPS converges to the isolated atom value of 1 bohr^2. Fixed-bond dimerized chains present a different behavior of the TPS tensor. The $\alpha\alpha$ component does not diverge at large values of D, while the SS-TPS recovers the value of the isolated dimer. Therefore, one can conclude that the fixed-bond case depicts insulators, presenting a small spin fluctuation between the dimers. Homothetic dimers, on the other hand, showed a large spin fluctuation within the dimers in the insulating regime (low electron mobility), indicating an entanglement of the wave function.

The long-range behavior of the SP-TPS tensors is related to the presence of entanglement in the wave function. Indeed, the same-spin components are large, mainly because of the one-electron contributions that are obviously positive. The different-spin components (of a two-electron nature by definition) are also large, but of opposite sign, since the two electrons tend to be, in the average, on different sides with respect to the inversion center of symmetry of the system. These behaviors can be related to the two-body reduced density matrices (RDM), whose deviation from a product form is due to the Fermi (same spin) and Coulomb (different spin) correlations. For instance, it appears that in all the three cases examined in this work, there exists a competition between Fermi and Coulomb correlations. A more sophisticated partitioning should take into account the fact that the same-spin contributions are not due to a pure Fermi correlation effect, but probably it does not change the general trend: The Coulomb correlation reduces the magnitude of TPS, and it makes electrons more localized. This relation between TPS and RDM is not surprising, since the SS-TPS is directly related to the two-electron reduced density matrix (and indeed, this is the way we implemented the calculation in the MOLPRO package [33]). In a similar way, the SP-TPS tensors are related to the spin-dependent reduced density matrices. This is a promising direction of investigation, that is, however, well beyond the scope of the present article. A detailed investigation of the connection between TPS and density matrices is planned for future works.

Finally, the asymptotic behavior for long chains of the SS-TPS and SP-TPS tensors was studied by performing a linear fitting of all values for any fixed inter-nuclear distance. In this way, the coefficients obtained from the fitting had condensed information about the systems. Therefore, prediction about the metallic or insulating character of hydrogen chains of a large number of atoms is possible.

Acknowledgments We thank the University of Toulouse and the French CNRS for financial support. MEK and EF acknowledge the ANR-DFG action (ANR-11-INTB-1009 MITLOW PA1360/6-1) for their PhD grant. OB thanks to the Spanish "Ministerio de Educación Cultura y Deporte" for her PhD grant. We acknowledge the support of the Erasmus Mundus programme of the European Union (FPA 2010-0147). This work was supported by the Programme Investissements d'Avenir under the program ANR-11-IDEX-0002-02, reference ANR-10-LABX-0037-NEXT. We thank Prof. R. Cimiraglia of the University of Ferrara for using his 4-index transformation code. Finally, we also thank the HPC resources of CALMIP under the allocation 2011-[p1048].

References

1. Wunderlich T, Akgenc B, Eckern U, Schuster C, Schwingenschlögl U (2013) Modified Li chains as atomic switches. Sci Rep 3:2605

2. Scheer E, Agraït N, Cuevas JC, Yeyati AL, Ludoph B, Martín-Rodero A, Bollinger GR, van Ruitenbeek JM, Urbina C (1998) The signature of chemical valence in the electrical conduction through a single-atom contact. Nature 394:154–157
3. Sinitskiy AV, Greenman L, Mazziotti D (2010) Strong correlation in hydrogen chains and lattices using the variational two-electron reduced density matrix method. J Chem Phys 133:014104
4. Kohanoff J, Hansen JP (1995) Ab initio molecular dynamics of metallic hydrogen at high densities. Phys Rev Lett 74:626–629
5. Kohn W (1964) Theory of the insulating state. Phys Rev 133:A171–A181
6. Resta R, Sorella S (1999) Electron localization in the insulating state. Phys Rev Lett 82:370–373
7. Sgiarovello C, Peressi M, Resta R (2001) Electron localization in the insulating state: application to crystalline semiconductors. Phys Rev B 64:115202
8. Resta R (2002) Why are insulators insulating and metals conducting? J Phys Condens Matter 14:R625–R656
9. Resta R (2005) Electron localization in the quantum hall regime. Phys Rev Lett 95:196805
10. Resta R (2011) The insulating state of matter: a geometrical theory. Eur Phys J B 79:121–137
11. Resta R (2006) Polarization fluctuations in insulators and metals: new and old theories merge. Phys Rev Lett 96:137601
12. Resta R (2006) Kohns theory of the insulating state: a quantum-chemistry viewpoint. J Chem Phys 124:104104
13. Souza I, Wilkens T, Martin R (2000) Polarization and localization in insulators: generating function approach. Phys Rev B 62:1666–1683
14. Brea O, El Khatib M, Angeli C, Bendazzoli GL, Evangelisti S, Leininger T (2013) Behavior of the position–spread tensor in diatomic systems. J Chem Theory Comput 9:5286–5295
15. Ángyán JG (2009) Electron localization and the second moment of the exchange hole. Int J Quantum Chem 109:2340–2347
16. Ángyán J (2011) Linear response and measures of electron delocalization in molecules. Curr Org Chem 15:3609–3618
17. Bendazzoli GL, Evangelisti S, Monari A, Paulus B, Vetere V (2008) Full configuration-interaction study of the metal-insulator transition in model systems. J Phys Conf Ser 117:012005
18. Vetere V, Monari A, Bendazzoli GL, Evangelisti S, Paulus B (2008) Full configuration interaction study of the metal-insulator transition in model systems: LiN linear chains (N = 2, 4, 6, 8). J Chem Phys 128:024701
19. Bendazzoli GL, Evangelisti S, Monari A, Resta R (2010) Kohns localization in the insulating state: one-dimensional lattices, crystalline versus disordered. J Chem Phys 133:064703
20. Bendazzoli GL, Evangelisti S, Monari A (2011) Full-configuration-interaction study of the metal- insulator transition in a model system: Hn linear chains n $= 4, 6, \ldots, 16$. Int J Quantum Chem 111:3416–3423
21. Giner E, Bendazzoli GL, Evangelisti S, Monari A (2013) Full-configuration-interaction study of the metal-insulator transition in model systems: Peierls dimerization in H(n) rings and chains. J Chem Phys 138:074315
22. Vetere V, Monari A, Scemama A, Bendazzoli GL, Evangelisti S (2009) A theoretical study of linear beryllium chains: full configuration interaction. J Chem Phys 130:024301
23. Evangelisti S, Bendazzoli GL, Monari A (2010) Electron localizability and polarizability in tight-binding graphene nanostructures. Theor Chem Acc 126:257–263
24. Bendazzoli GL, El Khatib M, Evangelisti S, Leininger T (2014) The total position spread in mixed-valence compounds: a study on the H4+ model system. J Comput Chem 35:802–808
25. Monari A, Bendazzoli GL, Evangelisti S (2008) The metal-insulator transition in dimerized Hückel chains. J Chem Phys 129:134104
26. Bendazzoli GL, Evangelisti S, Monari A (2012) Asymptotic analysis of the localization spread and polarizability of 1-D noninteracting electrons. Int J Quantum Chem 112:653–664
27. Horodecki R, Horodecki M, Horodecki K (2009) Quantum entanglement. Rev Mod Phys 81:865–942
28. Gühne O, Tóth G (2009) Entanglement detection. Phys Rep 474:1–75
29. El Khatib M, Brea O, Fertitta E, Bendazzoli L, Evangelisti S, Leininger T (2014) The total position–spread tensor : spin partition (submitted to JCP)
30. Peierls RE (1955) Quantum theory of solids. Clarendon Press, Oxford
31. Mott NF (1968) Metal-insulator transition. Rev Mod Phys 40:677–683
32. Kubo R (1962) Generalized cumulant expansion method. J Phys Soc Jpn 17:1100–1120
33. El Khatib M, Leininger T, Bendazzoli GL, Evangelisti S (2014) Computing the position–spread tensor in the CAS-SCF formalism. Chem Phys Lett 591:58–63
34. NEPTUNUS is a FORTRAN code for the calculation of FCI energies and properties written by Bendazzoli GL, Evangelisti S with contributions from Gagliardi L, Giner E, Monari A, Verdicchio M. http://irssv2.ups-tlse.fr/codes/pages/neptunus.html
35. Bendazzoli GL, Evangelisti S (1993) A vector and parallel full configuration interaction algorithm. J Chem Phys 98:3141
36. Bendazzoli GL, Evangelisti S (1993) Computation and analysis of the full configuration interaction wave function of some simple systems. Int J Quantum Chem 48:287–301
37. Gagliardi L, Bendazzoli GL, Evangelisti S (1997) Direct-list algorithm for configuration interaction calculations. J Comput Chem 18:1329–1343
38. Tunega D, Noga J (1998) Static electric properties of LiH: explicitly correlated coupled cluster calculations. Theor Chim Acta 100:78–84
39. Angeli C, Bendazzoli GL, Evangelisti S (2013) The localization tensor for the H2 molecule: closed formulae for the Heitler–London and related wavefunctions and comparison with full configuration interaction. J Chem Phys 138:054314
40. Dalton A Molecular electronic structure program See: http://www.kjemi.uio.no/software/dalton/dalton.html
41. Oliphant TE (2007) Python for scientific computing. Comput Sci Eng 9:10–20
42. Millman KJ, Aivazis M (2011) Python for scientists and engineers. Comput Sci Eng 13:9–12
43. van der Walt S, Colbert SC, Varoquaux G (2011) The NumPy array: a structure for efficient numerical computation. Comput Sci Eng 13:22–30

Theor Chem Acc (2015) 134:54
DOI 10.1007/s00214-015-1646-2

REGULAR ARTICLE

Invariant time-dependent exchange perturbation theory and its application to the particles collision problem

E. V. Orlenko[1] · T. Latychevskaia[2] · A. V. Evstafev[1] · F. E. Orlenko[1]

Received: 5 November 2014 / Accepted: 11 March 2015 / Published online: 11 April 2015

Abstract We present the formalism of time-dependent exchange perturbation theory built to all orders of perturbation, for the arbitrary time dependency of perturbation. The theory takes into account the rearrangement of electrons among centers. We show how the formalism can be reduced to the standard form of invariant perturbation theory by "switching off" the re-arrangement of electrons among centers. The elements of the scattering S-matrix and transitions T-matrix and the formula for the electron scattering differential cross section are derived. The application of the theory to scattering and collision problems is discussed. As an example, we apply the theory to proton scattering on a lithium atom, calculating the differential and total cross sections.

Keywords Perturbation theory · Exchange interaction · Symmetrization · Time dependent · Collisions

1 Introduction

Time-dependent perturbation theory is a well-known approach for finding an approximate solution to various problems in quantum mechanics. However, despite its powerful methods, perturbation theory cannot offer a general solution when addressing the problems of collisions between complex particles, such as molecules and atoms, especially when collision is accompanied by a change in the molecular/atomic structure. For instance, the otherwise very efficient diagram technique [1–4] fails when applied to the collision problem as it requires a wavefunction basis such that the wavefunctions of electrons assigned to different atoms are orthogonal. In turn, obtaining such an orthogonal basis given the random movement of the atomic centers is rather an irresolvable task. Overall, finding a general theoretical approach describing molecular collisions has proven to be a non-trivial problem.

Second quantization methods describing multicenter systems have been reported previously, which are, however, mainly effective when addressing collisions between atoms with a many electron structure. Within the diagram method, an attempt has been made to correct the commutation relations between the creation and annihilation operators by also taking into account permutations of electrons between orthogonal states that belong to different atomic centers. This, however, requires a transformation of the creation and annihilation operators and particle states into the irreducible representations of a mathematically convenient chain of subgroups, which in turn leads to complicated unitary transformations.

As a result, the application of this diagram technique is limited to two-electron systems [4]. Another, more promising method employing second quantization is based on creating a so-called "chemical" Hamiltonian using a biorthogonal basis. In this method, the use of the so-called "mixed" formalism allows compressing the interactions to one- and two-center terms by applying projection operators. However, the employed biorthogonal set of spin

Published as part of the special collection of articles derived from the 9th Congress on Electronic Structure: Principles and Applications (ESPA 2014).

✉ E. V. Orlenko
eorlenko@mail.ru

[1] Theoretical Physics Department, Petersburg State Polytechnic University, Polytechnicheskaya, 29, 195251 St.-Petersburg, Russian Federation

[2] Physics Institute, University of Zurich, Winterthurerstrasse 190, 8057 Zurich, Switzerland

orbitals and the corresponding creation–annihilation operators require related unitary transformation into the "mixed" formalism and a so-called "basis extension". As a consequence, the method is effective when applied to simple systems. This explains why every given problem of a scattering event is solved by applying an ad hoc approach, as for example shown in works [5–8]. In the textbook by Davydov [2], one finds a detailed discussion problem of particles collision summarized by the conclusion that a general theoretical approach to address collision problems is required.

In this work, we attempt to develop a dedicated perturbation theory, named exchange perturbation theory (EPT), which takes into account the indistinguishability of electrons participating in multicenter molecular/atomic collisions to any order of perturbation.

It is worth noting that the development of EPT requires careful study of the wavefunctions associated with electrons assigned to different atomic centers. The overlap of these wavefunctions is responsible for the exchange effects that play a crucial role in both adiabatic and dynamic scattering events. The exchange effects are most pronounced at the so-called intermediate atomic distances, when the molecule is re-arranging itself and its electrons are being redistributed. At these distances, the exchange effects are already larger than van der Waals forces, but at the same time, they are weak when compared to intra-atomic interactions, and thus, they can be considered as a perturbation. We should also mention density functional theory (DFT) and time-dependent DFT (TDDFT) which are very popular methods for obtaining the electronic structure of many body systems [9–12]. However, these theories are based on using approximate exchange–correlation, which is functional and limited to large molecules, such as DNA or molecular clusters, whereas for smaller molecules, only EPT gives accurate results [13, 14]. EPT, in principle, can also be applied to the calculation of large molecules or molecular clusters, but it would require significant computer time and power.

When creating a new perturbation theory formalism, one should remember that a perturbation theory should solve the two fundamental difficulties [15]:

1. The zero-approximation antisymmetrized wavefunctions are non-orthogonal, and therefore, they form an overfilled basis. This problem has been solved in EPT [16–19]; it has been demonstrated that the basis of non-orthogonal, antisymmetrized wavefunctions may constitute a complete set [17–19].
2. A zero-approximation antisymmetrized wavefunction is not an eigenfunction of the Hamiltonian $\widehat{H}_0$ because of the non-invariance of Hamiltonian $\widehat{H}_0$ with respect to the permutations of electrons among atoms [17]. Therefore, EPT must be formulated in such a way that it would give properly symmetrized wavefunction corrections to any order of perturbation.

An overview of several EPT formalisms can be found in [15, 18]. Kaplan in his book [15] classifies EPT formalisms into two groups: (1) formalisms with asymmetric unperturbed Hamiltonian $[\hat{A}, \hat{H}_0] \neq 0$ and asymmetric perturbation $[\hat{A}, \hat{V}] \neq 0$; (2) formalisms with symmetric zero-approximation Hamiltonian $[\hat{A}, \hat{H}_0] = 0$ and symmetric perturbation $[\hat{A}, \hat{V}] = 0$.

The first type of formalism, also named symmetry-adapted EPT formalism, has the advantage of being a simple representation of the perturbation operator, and, therefore, is often favored as a basis for software packages. The drawback of these formalisms is that they require a post-factum antisymmetrization procedure, that is, after the action of the perturbation operator on the non-symmetrized wavefunction of the system: $\hat{A}\hat{V}(\psi^{(0)} + \psi^{(1)} + \cdots)$, the problem which has been previously described in detail in [15] and references therein, and [17–19].

The second type of formalism allows the standard perturbation theory to be applied by constructing a symmetric zero-approximation Hamiltonian $[\hat{A}, \hat{H}_0] = 0$ with antisymmetric eigenfunction functions and a symmetrized perturbation $[\hat{A}, \hat{V}] = 0$ [15]. Both Hamiltonian $\widehat{H}_0$ and the perturbation operator $\hat{V}$ invariant to intercenter permutations can be obtained for the time-independent case [16–20], which allows energy corrections to be obtained using the correct antisymmetric basis of the wavefunctions. Moreover, as has been shown in [18], the energy and wavefunction corrections can be significantly simplified while preserving all the multicenter exchange inputs. Our formalism presented in this work can be assigned to the second type of formalism, for details see [18, 19].

An attempt to build a formalism of time-dependent exchange perturbation theory (TDEPT) that accounts for the exchange of electrons among atomic centers was reported in [21]. The authors obtained series expansion of the transition amplitude up to the second order of perturbation. Examples of the implementation of TDEPT to electron and atomic scattering can be found in works [22, 23].

2 Exchange perturbation theory (EPT), time-dependent perturbation

In zero-order approximation, when neglecting the interaction among particles, the coordinate part of the wavefunction of the system can be simply represented as a product of the wavefunctions of the isolated particles:

$$\Phi(r_1,\ldots,r_N)=\prod_{\alpha}\psi_{\alpha}(r_{n_\alpha},\ldots,r_{N_\alpha}), \tag{1}$$

where α is the atomic center number and $r_{n_\alpha},\ldots,r_{N_\alpha}$ are the coordinates of the electrons assigned to atom α. The spin part of the wavefunction can be expressed as a product of spinors of the same electrons: $X(\xi_1,\ldots,\xi_N)=\prod_i \chi_i(\xi_i)$. The Hamiltonian of the system includes the kinetic energy of all electrons, the potential energy of the interaction between electrons and their atomic centers, and the interaction among electrons that belong to different centers:

$$H^0|\Phi_n)=E_n^0|\Phi_n), \tag{2}$$

where $\{E_n^0\}$ are the eigenvalues of the energy and $|\Phi_n)$ are the eigenfunctions of the system and defined as a product of coordinate and spin parts. Here, the round bracket emphasizes that the eigenfunctions are not symmetrized [24, 25]. We write this zero-approximation wavefunction in Dirac's symbols as vector $\left|\Phi^0\right)$.

The relatively short distances between the atomic centers cause overlap between the wavefunctions of the electrons from different centers. According to the Pauli exclusion principle, the complete wavefunction must be antisymmetric. An antisymmetrized wavefunction of the system can be obtained as a product of the coordinate and spin parts corresponding to conjugate Young diagrams (YD) [18, 26]:

$$\begin{aligned}\Psi_n^0(r_1,\ldots r_N,\xi_1\ldots\xi_N)&=\widehat{A}\Phi_n(r_1,\ldots r_N)\cdot \mathrm{X}(\xi_1\ldots\xi_N)\\&=\frac{1}{\sqrt{R_\lambda}}\sum_r \Phi_{nr}^{[\lambda]}(r_1,\ldots r_N)\mathrm{X}_{\tilde{r}}^{[\tilde{\lambda}]}(\xi_1\ldots\xi_N),\end{aligned} \tag{3}$$

where $\widehat{A}$ is the operator of antisymmetrization, the summation is over all r standard Young tableau (λ) of a given Young diagram λ. The factor $1/\sqrt{R_\lambda}$ is the normalization factor of the Young diagram λ. $\left[\tilde{\lambda}\right]$ denotes transposed Young diagram.

The antisymmetrized vector which includes both coordinate and spin parts is now:

$$\left|\Psi_n^0\right\rangle=\frac{1}{f_n^P}\sum_p^P(-1)^{g_p}\left|\Phi_n^{0p}\right), \tag{4}$$

where p is the permutation's number, $\frac{1}{f_n^P}$ is the normalization factor, g_p is the parity of the permutation, and P is the total number of possible intercenter permutations. The wavevector $\left|\Phi_n^{0p}\right)$ has the form provided in Eq. 3, thus including both coordinate and spin parts, and corresponds to the p-th permutation. We set the condition of normalization in the form $\left(\Phi_n^{0\,p=0}\middle|\Psi_n^0\right\rangle=1$, which gives the normalization factor:

$$f_n^P=\sum_{p=0}^{P}(-1)^{g_p}\left(\Phi_n^{0(p=0)}\middle|\Phi_n^{0(p)}\right) \tag{5}$$

that is different by the factor $\sqrt{P}$ from the normalization factor obtained in the conventional EPT where the normalization condition is $\left\langle\Psi^0\middle|\Psi^0\right\rangle=1$.

To find the wavefunction of the system in the presence of the time-dependent perturbation $\widehat{V}(t)$, we must solve the Schrödinger equation:

$$-\frac{\hbar}{i}\frac{\partial}{\partial t}|\Psi\rangle=\left(\widehat{H}_0+\widehat{V}(t)\right)|\Psi\rangle. \tag{6}$$

for the antisymmetrized vector $|\Psi\rangle$, where the total Hamiltonian of the system $\widehat{H}_0+\widehat{V}(t)$ is invariant. Zero-approximation Hamiltonian $\widehat{H}_0$ and time-independent perturbation operator $\widehat{V}$ were obtained in symmetrized form in works [17–19].

Because electrons which belong to different centers cannot be distinguished, Eq. 2 holds for any intercenter arrangement of the electrons, and we rewrite it as

$$H^{0(p)}\left|\Phi_n^{0(p)}\right)=E_n^0\left|\Phi_n^{0(p)}\right), \tag{7}$$

where $|\Phi_n^{0(p)})$ is the zero-order approximation wavefunction corresponding to the p-th permutation.

It has been shown that a set of eigenfunctions of the unperturbed system $\left\{\left|\Phi_n^{0\,(p)}\right)\right\}$ is orthogonal and complete for any permutation [17–19]:

$$\begin{aligned}&\left(\Phi_m^{0(p)}\middle|\Phi_n^{0(p)}\right)=\delta_{mn};\\&\sum_n\left|\Phi_n^{0(p)}\right)\left(\Phi_n^{0(p)}\right|=\widehat{1};\\&\left(\Phi_m^{0(p)}\middle|\Phi_n^{0(p')}\right)\approx\delta_{mn}S_n^{(p-p')}.\end{aligned} \tag{8}$$

Here, $S_n^{(p-p')}$is the overlap integral of the wavefunctions associated with the relative number of intercenter permutations of electrons $(p-p')$. We use a "truncated" overlap which takes into account only the overlap between similar states assigned to different centers with the following hierarchy rule: $\left(\Phi_m^{0(p)}|\Phi_n^{0(p')}\right)<<\left(\Phi_n^{0(p)}|\Phi_n^{0(p')}\right)\sim\left(\Phi_m^{0(p)}|\Phi_m^{0(p')}\right)$.

As has been shown in [17–19], the basis of antisymmetric functions of the unperturbed system is complete:

$$\sum_n\left|\Psi_n^0\right\rangle\frac{f_n^P}{P}\left(\Phi_n^{0(0)}\right|=\widehat{1}, \tag{9}$$

where antisymmetrized vector $|\Psi_n^0\rangle$ is given by Eq. 4.

To write Hamiltonian and perturbation operators in invariant form, we introduce the projection operator:

$$\Lambda^{(p)}=\sum_n\left|\Phi_n^{0(p)}\right)\frac{f_n^P}{P}\left(\Phi_n^{0(p)}\right|, \tag{10}$$

which when applied to the wavevector $|\Psi_i^0\rangle$ given by Eq. 4 at $n = i$, selects the wavefunction corresponding to p-th permutation: $\Lambda^{(p)}|\Psi_i^0\rangle = (-1)^{g_p}|\Phi_i^{0(p)}\rangle$ [19].

We use operator $\Lambda^{(p)}$ to write the Hamiltonian and perturbation operators in a form invariant under intercenter permutations:

$$\widehat{V}(t) = \sum_{p=0}^{P} V^{(p)}(t)\,\Lambda^{(p)}, \quad \widehat{H}_0 = \sum_{p=0}^{P} H^{0(p)}\Lambda^{(p)} \tag{11}$$

here $H^{0(p)}$ and $V^{(p)}(t)$ are the Hamiltonian and perturbation operators corresponding to the p-th permutation of the electrons between the centers. The antisymmetrized zero-approximation wavevector $|\Psi_i^0\rangle$ is an eigenvector of the invariant Hamiltonian of the unperturbed system: $\widehat{H}_0\big|\Psi_i^0\big\rangle = E_i^0\big|\Psi_i^0\big\rangle$, where energy eigenvalues E_i^0 are real [16, 19, 20]. Note that through the entire text, we use the "hat" symbol for symmetrized operators and do not use the "hat" symbols for operators that are related to p-th permutation.

We search for the wavevector $|\Psi\rangle$ which is the solution to the Schrödinger equation, Eq. 6, by the method of successive approximations, as it is typically solved in conventional perturbation theory.

3 Perturbation theory to the first order

Let $|\Psi^1(t)\rangle$ be the first-order correction to the wavefunction $|\Psi\rangle$, which in the first-order approximation satisfies the following equation

$$-\frac{\hbar}{i}\big|\dot{\Psi}^1(t)\big\rangle = \widehat{H}_0\big|\Psi^1(t)\big\rangle + \widehat{V}(t)\big|\Psi_i^0\big\rangle. \tag{12}$$

We write the solution to this equation in the form of series

$$\big|\Psi^1(t)\big\rangle = \sum_n C_n^{(1)}(t)\exp\left(-\frac{i}{\hbar}E_n t\right)\big|\Psi_n^0\big\rangle, \tag{13}$$

where the expansion coefficients $C_n^{(1)}(t)$ are to be found.

Next, we introduce two skew-projection operators $\widehat{P}_i$ and $\widehat{O}_i$. The skew-projection operator $\widehat{P}_i = |\Psi_i^0\rangle(\Phi_i^{0(0)}|$ projects onto the subspace of the vectors parallel to the vector $|\Psi_i^0\rangle$ giving $\widehat{P}_i\big|\Psi_i^0\big\rangle \equiv \big|\Psi_i^0\big\rangle$. The skew-projection operator $\widehat{O}_i = 1 - \widehat{P}_i$ projects onto the subspace of vectors orthogonal to the vector $|\Psi_i^0\rangle$ giving $\widehat{O}_i\big|\Psi_i^0\big\rangle \equiv 0$.

By substituting Eq. 13 into Eq. 12 and applying operator $\widehat{O}_i$ to both sides of the equation, we obtain the following expression for coefficients $\dot{C}_n^{(1)}(t)$ (see Appendix 1 for details):

$$-\frac{\hbar}{i}\dot{C}_n^{(1)}(t) = \frac{f_0}{P}\exp(-i\omega_{ni}t)\Big(\Phi_n^{0(0)}\big|\widehat{O}_i\widehat{V}\big|\Psi_i^0\Big\rangle, \tag{14}$$

where we used the property of completeness of the antisymmetrized basis given by Eq. 9 and introduced frequencies: $\frac{1}{\hbar}(E_i - E_n) = \omega_{in}$. The solution to Eq. 14 can be written in the form of a definite integral:

$$C_n^{(1)}(t) = \frac{f_0}{i\hbar P}\int_0^t \exp(i\omega_{ni}t')\Big(\Phi_n^{0(0)}\big|\widehat{O}_i\widehat{V}\big|\Psi_i^0\Big\rangle \mathrm{d}t'. \tag{15}$$

Next, we use the following results

$$\widehat{O}_i\big|\Psi_n^0\big\rangle \approx \big|\Psi_n^0\big\rangle, \tag{16}$$

$$(\Phi_n^{0(0)}|\widehat{O}_i = (\Phi_n^{0(0)}| - (\Phi_n^{0(0)}\big|\Psi_i^0\big\rangle(\Phi_i^{0(0)}| \approx (\Phi_n^{0(0)}|,$$

$$(\Phi_i^{0(0)}|\widehat{O}_i = (\Phi_i^{0(0)}| - (\Phi_i^{0(0)}\big|\Psi_i^0\big\rangle(\Phi_i^{0(0)}| \equiv 0$$

which were derived in [17], and we obtain the first-order corrections to the expansion coefficients as

$$C_n^{(1)}(t) = \frac{f_n}{i\hbar P}\int_0^t \exp(i\omega_{ni}t')\Big(\Phi_n^{0(0)}\big|\widehat{V}\big|\Psi_i^0\Big\rangle \mathrm{d}t'. \tag{17}$$

Equation 17 describes the amplitude of the transition between states i and n. By substituting $C_n^{(1)}(t)$ from Eq. 17 into Eq. 13, we find the first-order correction to the wavevector of the system.

The matrix elements of the perturbation operator in Eq. 17 can be rewritten using the perturbation operator expressed through projection operator $\Lambda^{(p)}$ see Eq. 11:

$$\begin{aligned}\Big(\Phi_n^{0(0)}\Big|\widehat{V}\Big|\Psi_i^0\Big\rangle &= \Big(\Phi_n^{0(0)}\Big|\sum_{p=0}^{P} V_p\frac{(-1)^{g_p}}{f_i^P}\Big|\Phi_i^{0(p)}\Big)\\ &= \frac{f_n^P}{f_i^P}\big\langle\Psi_n^0\big|V_{p=0}\Big|\Phi_i^{0(0)}\Big).\end{aligned} \tag{18}$$

By substituting the result of Eq. 18 into Eq. 17, we obtain the final expression for the coefficients:

$$C_n^{(1)}(t) = \frac{\left(f_n^P\right)^2}{i\hbar P}\int_0^t \exp(i\omega_{ni}t')\big\langle\Psi_n^0\big|V_{p=0}\Big|\Phi_i^{0(0)}\Big)\mathrm{d}t'. \tag{19}$$

If we neglect the exchange interaction and replace $\Psi \to \Phi$, Eq. 19 will give the same result as the result obtained in conventional perturbation theory.

4 Perturbation theory to the second and higher orders

The time-dependent Schrödinger equation, Eq. 6, is now written up to the second order. By substituting the wavevector found to the first order and after some

simplifications, we obtain the equation for the second-order correction to the wavefunction:

$$-\frac{\hbar}{i}\left|\dot{\Psi}_i^2\right\rangle = \widehat{H}_0\left|\Psi_i^2\right\rangle + \widehat{V}\left|\Psi_i^1\right\rangle. \tag{20}$$

As above, we seek the solution in the form of series:

$$\left|\Psi_i^2\right\rangle = \sum_n C_n^{(2)}(t)\exp\left(-\frac{i}{\hbar}E_n t\right)\left|\Psi_n^0\right\rangle. \tag{21}$$

where the expansion coefficients $C_n^{(2)}(t)$ are to be found.

The procedure for finding the coefficients is similar to the procedure described above. We obtain:

$$-\frac{\hbar}{i}\sum_n P\dot{C}_n^{(2)}\exp\left(-\frac{i}{\hbar}E_n t\right)\left|\Psi_n^0\right\rangle = \widehat{O}_i\widehat{V}\left|\Psi_i^1\right\rangle. \tag{22}$$

Next, we can use the property of completeness Eq. 9 and rewrite the right part of Eq. 22 as

$$\widehat{O}_i\widehat{V}\left|\Psi_i^1\right\rangle = \sum_n \frac{f_n}{P}\left|\Psi_n^0\right\rangle\left(\Phi_n^{0(0)}\middle|O_i\widehat{V}\middle|\Psi_i^1\right\rangle. \tag{23}$$

Substituting Eq. 23 into Eq. 22, after some re-arrangement of the terms, we obtain:

$$C_n^{(2)}(t) = \frac{f_b}{i\hbar P}\int_0^t \mathrm{d}t'\exp(iE_n t'/h)\left(\Phi_n^{0(0)}\middle|\widehat{O}_i\widehat{V}\middle|\Psi_i^1(t')\right\rangle.$$

Applying the result of Eq. 18 we rewrite the last equation as

$$\begin{aligned} C_{n_2}^{(2)}(t) &= \frac{f_b}{i\hbar P}\int_0^t \mathrm{d}t'\exp(iE_{n_2}t'/\hbar)\left(\Phi_{n_2}^{0(0)}\middle|\widehat{V}\middle|\Psi_i^1(t')\right\rangle \\ &= \left(\frac{f_0^2}{ihP}\right)^2\sum_{n_1}\int_0^t \mathrm{d}t'\exp(i\omega_{n_2n_1}t')\left\langle\Psi_{n_2}^0\middle|V_{p=0}\middle|\Phi_{n_1}^{0(0)}\right\rangle \\ &\quad\times\int_0^{t'}\mathrm{d}t''\left\langle\Psi_{n_1}^0\middle|V_{p=0}\middle|\Phi_i^{0(0)}\right\rangle\exp(i\omega_{n_1i}t''). \end{aligned} \tag{24}$$

This expression is almost the same as that in conventional perturbation theory with the orthogonal basis of eigenfunctions. The difference is that Eq. 24 includes matrix elements enclosing overlap integrals produced by accounting for exchange and superexchange contributions.

The second-order correction to the wavevector in its full form is:

$$\begin{aligned} \left|\Psi_i^2\right\rangle &= \sum_{n_2}\exp\left(-\frac{i}{\hbar}E_{n_2}t\right)\left|\Psi_{n_2}^0\right\rangle \\ &\quad\times\left(\frac{f_0^2}{i\hbar P}\right)^2\sum_{n_1}\int_0^t \mathrm{d}t'\exp(i\omega_{n_2n_1}t') \\ &\quad\times\left\langle\Psi_{n_2}^0\middle|V_{p=0}(t')\middle|\Phi_{n_1}^{0(0)}\right\rangle\int_0^{t'}\mathrm{d}t''\left\langle\Psi_{n_1}^0\middle|V_{p=0}(t'')\middle|\Phi_i^{0(0)}\right\rangle \\ &\quad\times\exp(i\omega_{n_1i}t''). \end{aligned} \tag{25}$$

From the expressions for the first-order and second-order corrections, $|\Psi_i^1\rangle$ and $|\Psi_i^2\rangle$, respectively, we can see the general tendency and derive the following expression for an n-th correction to the wavefunction:

$$\begin{aligned} \left|\Psi_i^n\right\rangle &= \sum_{n_n}\sum_{n_{n-1}}\cdots\sum_{n_1}\left(\frac{f_0^2}{i\hbar P}\right)^n\left|\Psi_{n_n}^0\right\rangle\exp\left(-\frac{i}{\hbar}E_{n_n}t\right) \\ &\quad\times\int_0^t \mathrm{d}t_1\left\langle\Psi_{n_n}^0\middle|V_{p=0}(t_1)\middle|\Phi_{n_{n-1}}^{0(0)}\right\rangle\exp(i(\omega_{n_nn_{n-1}}t_1) \\ &\quad\times\int_0^{t_1}\mathrm{d}t_2\left\langle\Psi_{n_{n-1}}^0\middle|V_{p=0}(t_2)\middle|\Phi_{n_{n-2}}^{0(0)}\right\rangle\exp(i\omega_{n_{n-1}n_{n-2}}t_2)\cdots \\ &\quad\times\int_0^{t_{n-1}}\mathrm{d}t_n\left\langle\Psi_{n_1}^0\middle|V_{p=0}(t_n)\middle|\Phi_i^{0(0)}\right\rangle\times\exp(i\omega_{n_1i}t_n). \end{aligned} \tag{26}$$

A note to this equation: The transition matrix elements related to later times are placed before the transition matrix elements related to earlier times, as it holds:

$t > t_1 > t_2 > \cdots > t_n > 0.$

Equation 26 can be transformed to a more symmetric form by introducing the time ordering operator $\hat{\tau}$:

$$\begin{aligned} \left|\Psi_i^n\right\rangle &= \frac{1}{n!}\left(\frac{f_0^2}{ihP}\right)^n\sum_{n_n}\sum_{n_{n-1}}\cdots\sum_{n_1}\left|\Psi_{n_n}^0\right\rangle\exp\left(-\frac{i}{\hbar}E_{n_n}t\right) \\ &\quad\times\int_0^t\cdots\int_0^t\hat{\tau}\left\{\left\langle\Psi_{n_n}^0\middle|V_{p=0}(t_1)\middle|\Phi_{n_{n-1}}^{0(0)}\right\rangle\exp\right. \\ &\quad\times(i(\omega_{n_nn_{n-1}}t_1)\cdots\left\langle\Psi_{n_1}^0\middle|V_{p=0}(t_n)\middle|\Phi_i^{0(0)}\right\rangle \\ &\quad\left.\times\exp(i\omega_{n_1i}t_n)\right\}dt_1\ldots dt_n. \end{aligned} \tag{27}$$

This expression defines the corrections to the wavefunction of a multicentered system with exchange effects to any order of perturbation. Equation 27 can also be applied to the system where the intercenter exchange is negligible, in which case Eq. 27 transforms into the expression for wavefunction corrections obtained in conventional time-dependent perturbation theory.

The coefficient corresponding to the transition from the initial state $|i\rangle$. to the final state $|f\rangle$ can be written in an invariant form:

$$C_f(t) = \left\langle \Psi_f^0 \middle| \hat{\tau} \exp\left(-\frac{if_0^2}{\hbar P} \int_0^t \widehat{W}(t')\mathrm{d}t' \right) \middle| \Phi_i^{0(0)} \right\rangle, \tag{28}$$

where we introduced operator

$$\widehat{W}(t) = e^{\frac{i}{\hbar}H_0^{p=0}t} V^{p=0}(t) e^{-\frac{i}{\hbar}H_0^{p=0}t}. \tag{29}$$

The probability of transition at the time t is given by $w_{fi}(t) = \left|C_f(t)\right|^2$ when transition occurs between states of a discrete spectrum, and it is given by $dw_{fi}(t) = \left|C_f(t)\right|^2 dv_f$ when the transition occurs in the range dv_f of continuous spectrum.

5 S-scattering and T-matrix elements

We consider two non-interacting subsystems (examples include: an electron and an atom or an alpha particle, an ion and an atom, two atoms, an atom and a molecule, two molecules, etc., also possible are a light wave and a molecule which decomposes into fragments, and similar). Two states $|i\rangle$, $|f\rangle$ and their energies E_i, E_f are the solution to the equation $\widehat{H}_0 \left|\Psi_i^0\right\rangle = E_i^0 \left|\Psi_i^0\right\rangle$ or eigenstates and eigenenergies of the whole system Hamiltonian $\widehat{H}_0$. Perturbation which causes interaction between the two subsystem and a transition between the two states is described by operator $\widehat{V} = \sum_{p=0}^{P} V^{(p)} \Lambda^{(p)}$, which is time independent in the Schrödinger representation.

The time-dependent transition coefficient $C_f(t) \equiv C_{if}(t)$ given by Eq. 28 turns into a scattering S-matrix element when the time variable t ranges from $-\infty$ to $+\infty$:

$$\begin{aligned} C_{if}(\infty) &= \left\langle \Psi_f^0 \middle| S \middle| \Phi_i^{0(0)} \right\rangle \\ &= \left\langle \Psi_f^0 \middle| \hat{\tau} \exp\left(-\frac{i}{\hbar}\frac{f_0^2}{P} \int_{-\infty}^{\infty} \widehat{W}(t)\mathrm{d}t | \Phi_i^{0(0)} \right) \right\rangle \\ &\equiv \left\langle \Psi_f^0 \middle| \left\{ 1 + \frac{1}{i\hbar}\frac{f_0^2}{P} \int_{-\infty}^{\infty} \widehat{W}(t)\mathrm{d}t + \frac{1}{(ih)^2}\left(\frac{f_0^2}{P}\right)^2 \right.\right. \\ &\quad \left.\left. \times \int_{-\infty}^{\infty} \mathrm{d}t_1 \int_{-\infty}^{\infty} \mathrm{d}t_2 \widehat{W}(t_1)\widehat{W}(t_2) + \cdots \right\} \middle| \Phi_i^{0(0)} \right\rangle \\ &= \sum_{\alpha}^{\infty} \left\langle \Psi_f^0 \middle| S^{(\alpha)} \middle| \Phi_i^{0(0)} \right\rangle. \end{aligned} \tag{30}$$

Using this result, we obtain the first-order correction to the S-matrix elements:

$$\begin{aligned} \left\langle \Psi_f^0 \middle| S^{(1)} \middle| \Phi_i^{0(0)} \right\rangle &= -\frac{i}{\hbar}\frac{f_0^2}{P} \left\langle \Psi_f^0 \middle| V_0 \middle| \Phi_i^{0(0)} \right\rangle \int_{-\infty}^{\infty} e^{i(E_f - E_i)\frac{t}{\hbar}} \mathrm{d}t \\ &= -2\pi i \delta(E_f - E_i) \frac{f_0^2}{P} \left\langle \Psi_f^0 \middle| V_0 \middle| \Phi_i^{0(0)} \right\rangle, \end{aligned} \tag{31}$$

where we took into account the formula for the time-dependent transition coefficient given by Eq. 28.

The second-order correction to the S-matrix element equals to [2]:

$$\begin{aligned} \left\langle \Psi_f^0 \middle| S^{(2)} \middle| \Phi_i^{0(0)} \right\rangle &= -2\pi i \delta(E_i - E_f) \left(\frac{f_0^2}{P}\right)^2 \\ &\quad \times \sum_n \frac{\left\langle \Psi_f^0 \middle| V_0 \middle| \Phi_n^{0(0)} \right\rangle \left\langle \Psi_n^0 \middle| V_0 \middle| \Phi_i^{0(0)} \right\rangle}{E_i - E_n + i\eta}. \end{aligned} \tag{32}$$

Other higher-order corrections to the S-matrix elements can be found in a similar manner.

Because the interaction between the atomic centers is much slower than the interaction between their electrons, adiabatic approximation can be applied and interaction between atoms can be considered as a time-independent perturbation. The transitions caused by that perturbation are transitions between an initial state and a different final state, so that $\langle \Psi_f | \Phi_i \rangle \approx 0$ is fulfilled. Thus, we can rewrite matrix elements of the S-matrix in Eq. 30 in the form

$$\left\langle \Psi_f^0 \middle| S \middle| \Phi_i^{0(0)} \right\rangle = -2\pi i \delta(E_f - E_i) \left\langle \Psi_f^0 \middle| \hat{T} \middle| \Phi_i^{0(0)} \right\rangle, \tag{33}$$

where we introduced an operator of transition on the energy surface $\hat{T}$, and the result is expressed through its matrix elements $\left\langle \Psi_f^0 \middle| \hat{T} \middle| \Phi_i^{0(0)} \right\rangle$. We would like to emphasize that matrix elements of operator $\hat{T}$, obtained here, unlike the commonly used matrix elements of operator $\hat{T}$ [2], account for all possible electron permutations between the two subsystem, which was achieved by antisymmetrization of the wavefunction of the whole system.

The matrix elements of operator $\hat{T}$ can be expressed as:

$$\begin{aligned} \left\langle \Psi_f^0 \middle| \hat{T} \middle| \Phi_i^{0(0)} \right\rangle &= \frac{f_0^2}{P} \left\langle \Psi_f^0 \middle| V_0 \middle| \Phi_i^{0(0)} \right\rangle \\ &+ \left(\frac{f_0^2}{P}\right)^2 \sum_n \frac{\left\langle \Psi_f^0 \middle| V_0 \middle| \Phi_n^{0(0)} \right\rangle \left\langle \Psi_n^0 \middle| V_0 \middle| \Phi_i^{0(0)} \right\rangle}{E_i - E_n + i\eta} + \cdots + \left(\frac{f_0^2}{P}\right)^v \\ &\times \sum_{n, n_1 \ldots n_{v-2}} \frac{\left\langle \Psi_f^0 \middle| V_0 \middle| \Phi_n^{0(0)} \right\rangle \cdots \left\langle \Psi_{n_{v-2}}^0 \middle| V_0 \middle| \Phi_i^{0(0)} \right\rangle}{(E_i - E_n + i\eta)(E_i - E_{n_1} + i\eta) \cdots (E_i - E_{n_{v-2}} + i\eta)} \cdots \end{aligned} \tag{34}$$

where ν is the expansion order. The matrix elements of various orders contained in Eq. 34 can be displayed

graphically using Feynman diagrams, as has been demonstrated in previous works [19, 20].

Because the functions $\Phi_n^{0(0)}$ are the eigenfunctions of the non-symmetrical Hamiltonian $H^0_{(p=0)}$, the second term on the right side of Eq. 34 can be rewritten as:

$$\left(\frac{f_0^2}{P}\right)^2 \sum_n \frac{\left\langle \Psi_f^0 \middle| V_0 \middle| \Phi_n^{0(0)} \right\rangle \left\langle \Psi_n^0 \middle| V_0 \middle| \Phi_i^{0(0)} \right\rangle}{E_i - E_n + i\eta} = \left(\frac{f_0^2}{P}\right)^2 \left\langle \Psi_f^0 \middle| V_0 \middle| \Phi_n^{0(0)} \right\rangle \left(\frac{f_0^2}{P}\right)^{-1} \times \left\langle \Psi_n^0 \middle| \left(E_i - H^0_{p=0} + i\eta\right)^{-1} \middle| \Phi_n^{0(0)} \right\rangle \left\langle \Psi_n^0 \middle| V_0 \middle| \Phi_i^{0(0)} \right\rangle, \tag{35}$$

where we applied the property of completeness, Eq. 9.

By substituting Eq. 35 into Eq. 34, we obtain the following expression for operator $\hat{T}$:

$$\hat{T} = \left(\frac{f_0^2}{P}\right) V_0 + \left(\frac{f_0^2}{P}\right) V_0 \left(\frac{f_0^2}{P}\right)^{-1} \left(E_i - H^0_{p=0} + i\eta\right)^{-1} \left(\frac{f_0^2}{P}\right) V_0 + \left(\frac{f_0^2}{P}\right) V_0 \left(\frac{f_0^2}{P}\right)^{-1} \left(E_i - H^0_{p=0} + i\eta\right)^{-1} \left(\frac{f_0^2}{P}\right) V_0 \left(\frac{f_0^2}{P}\right)^{-1} \times \left(E_i - H^0_{p=0} + i\eta\right)^{-1} \left(\frac{f_0^2}{P}\right) V_0 + \cdots \tag{36}$$

T-matrix can be found as a solution to Eq. 36 by successive approximations to the following operator equation:

$$\hat{T} = V_0^{\mathbb{N}} + V_0^{\mathbb{N}} \left(\frac{f_0^2}{P}\right)^{-1} \left(E_i - H^0_{p=0} + i\eta\right)^{-1} \hat{T}, \tag{37}$$

where $V_0^{\mathbb{N}} = \left(\frac{f_0^2}{P}\right) V_0$ is a renormalized perturbation operator.

The transition probability per unit of time is given by

$$w_{fi} = \frac{\left| \left\langle \Psi_f^0 \middle| S \middle| \Phi_i^{0(0)} \right\rangle \right|^2}{\lim_{\tau\to\infty} \int_{-\tau}^{\tau} \mathrm{d}t} = \frac{2\pi}{\hbar} \delta(E_f - E_i) \left| \left\langle \Psi_f^0 \middle| \hat{T} \middle| \Phi_i^{0(0)} \right\rangle \right|^2, \tag{38}$$

where we used Eq. 33.

To obtain an expression for the cross section of scattering events and reactions, we divide the result of Eq. 38 by the flux density of incident particles: $j_i = \hbar k_i/\mu_i$, where k_i is the wavevector of the relative movement of the incident particles and μ_i is their reduced mass:

$$\sigma_{fi} = \frac{2\pi\mu_i}{\hbar^2 k_i} \delta(E_f - E_i) \left| \left\langle \Psi_f^0 \middle| \hat{T} \middle| \Phi_i^{0(0)} \right\rangle \right|^2. \tag{39}$$

When the final state is within the continuous spectrum, the transition probability given by Eq. 38 must be multiplied by the number of final states in the volume per unit energy interval $\rho(E_f)$:

$$w_{fi} = \frac{2\pi}{\hbar} \delta(E_f - E_i) \left| \left\langle \Psi_f^0 \middle| \hat{T} \middle| \Phi_i^0 \right\rangle \right|^2 \rho(E_f). \tag{40}$$

By integration over all the possible energy of the final states, the formula for the probability of a scattering event per unit of time given by Eq. 40 can be transformed into an expression which accounts for all intercenter exchange contributions.

6 Collisions with exchange of electrons

The strength of the interaction between particles during collisions is described by a scattering cross section, or a differential cross section. The differential scattering cross section is obtained by substituting the given $\rho(E_f)$ into Eq. 40 and dividing the result by the flux density of the incident particles j_i. In this section, we derive the expression for $\rho(E_f)$, and consequently, for the differential cross section.

In the following, we consider the collision associated with the redistribution of electrons, as for example the collisions of positive ions with neutral atoms accompanied by charge transfer. The initial Hamiltonian of the system corresponds to the initial distribution of the electrons between the centers (permutation $p = 0$):

$$H_0^{p=0} = -\frac{\hbar^2}{2\mu_i} \nabla_i^2 + H_i^{p=0}(r_1, r_2, \ldots)_i, \tag{41}$$

which is the sum of the operator describing the kinetic energy of the relative motion (with reduced mass) and the operator of internal state of the colliding atoms (molecules), index i denotes the initial state.

For the initial state, the energy eigenvalues E_i and eigenvector $|\Phi_i)$, accounting for spin distribution, amount to

$$E_i = -\frac{\hbar^2}{2\mu_i} k_i^2 + \varepsilon_{n_i} \tag{42}$$

$$|\Phi_i^0) = \Phi_i(\vec{R} - \vec{r}_1, \vec{R} - \vec{r}_2, \vec{R} - \vec{r}_3 \ldots) \chi(\xi_1, \xi_2; \xi_3 \ldots) \exp(i\vec{k}_i \vec{R}), \tag{43}$$

where $\vec{R}$ is vector originating at one colliding particle and pointing to the other colliding particle, and its absolute value R is the distance between colliding particles.

As introduced above, see Eq. 11, the symmetric Hamiltonian form describing the final state can be written as

$$\widehat{H}_{0f} = \sum_{p=0}^{P} H_f^{0(p)} \Lambda_f^{(p)}$$
$$H_f^{0(p)} = -\frac{\hbar^2}{2\mu_f} \nabla_f^2 + H_f^p(r_1, r_2, \ldots)_f \tag{44}$$

The energy eigenvalues E_f and antisymmetric eigenvector of $\bar{H}_{0f}$, accounting for the permutations are given by

$$E_f = -\frac{\hbar^2}{2\mu_i}k_f^2 + \varepsilon_{n_f} \tag{45}$$

$$\left|\Psi_f^0\right\rangle = \hat{A}\Phi_f(\vec{R}-\vec{r}_1,\vec{R}-\vec{r}_2,\vec{R} - \vec{r}_3\ldots)\chi(\xi_1,\xi_2;\xi_3\ldots)\exp(i\vec{k}_f\vec{R}). \tag{46}$$

The number of the final states per unit energy interval for scattering in the direction of the unit vector $\vec{n}_f$ in the element of solid angle $\mathrm{d}\Omega$ is given by the expression: $\mathrm{d}\rho(E_f) = \frac{\mu_f k_f}{(2\pi)^3\hbar^2}\mathrm{d}\Omega$. By substituting $\mathrm{d}\rho(E_f)$ into Eq. 40, we obtain:

$$\frac{\mathrm{d}\sigma_{fi}}{\mathrm{d}\Omega} = j^{-1}\frac{\mathrm{d}w_{fi}}{\mathrm{d}\Omega} = \frac{\mu_i\mu_f k_f}{\left(2\pi\hbar^2\right)^2 k_i}\left|\left\langle\Psi_f^0\middle|\hat{T}\middle|\Phi_i^0\right\rangle\right|^2. \tag{47}$$

The transition operator $\hat{T}$ given by Eq. 37 can be rewritten in the form

$$\hat{T} = V_0^{\mathbb{N}} + V_0^{\mathbb{N}}\left(\frac{f_0^2}{P}\right)^{-1}(E_i - H + i\eta)^{-1}V_0^{\mathbb{N}}, \tag{48}$$

where H is the total Hamiltonian of the system, see Appendix 2.

7 Scattering of proton by lithium atom with electron exchange

In this section, we demonstrate how the obtained relations can be applied to a practical problem of proton scattering on Lithium atom: $\mathrm{Li} + p \rightarrow \mathrm{Li}^+ + \mathrm{H}$. $\vec{R}$ is vector originating at proton and pointing to Lithium atom. Figure 1 illustrates the arrangement of the particles.

As the initial permutation ($p = 0$), we assume the following arrangement: three electrons of the Lithium atom and the incident proton. We label the electrons by 1, 2, and 3.

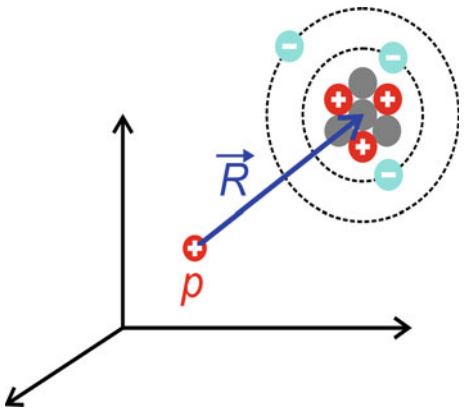

Fig. 1 Arrangement of the particles in the proton–lithium atom collision

The relative motion of the proton and the atom is determined by the operator of kinetic energy $(-\frac{\hbar^2}{2\mu}\nabla^2_{p-\mathrm{Li}})$. Interaction between proton and the atom is determined by the operator:

$$V_0 \equiv V(1,2,3) = -\frac{e^2}{r_{p1}} - \frac{e^2}{r_{p2}} - \frac{e^2}{r_{p3}} + \frac{3e^2}{R}. \tag{49}$$

The motion of electrons is described by the Hamiltonian $H(1,2,3) = -\frac{\hbar^2}{2m}\left(\nabla_1^2 + \nabla_2^2 + \nabla_3^2\right) - \frac{Ze^2}{r_{Li1}} - \frac{Ze^2}{r_{Li2}} - \frac{Ze^2}{r_{Li3}}$ whose antisymmetric eigenfunction with respect to intra-atomic electron permutations is given by

$$\Phi_{Li}(\vec{R}-\vec{r}_1,\vec{R}-\vec{r}_2,\vec{R}-\vec{r}_3)\otimes\chi(\xi_1,\xi_2;\xi_3) = \frac{1}{f_{Li}}(\Psi_{Li1}(\vec{r}_1,\vec{r}_2,\vec{r}_3)\mathrm{X}_{Li1}(1,2,3) + \Psi_{Li2}(\vec{r}_1,\vec{r}_2,\vec{r}_3)\mathrm{X}_{Li2}(1,2,3)) \tag{50}$$

and corresponds to the energy eigenvalues ε_n. Antisymmetrization of the atomic wavefunction given by Eq. 50 over intra-atomic electrons permutations is performed using four independent Young's operators corresponding to the Young diagram depicted in Fig. 1: $\omega_{11}^{[21]}$; $\omega_{12}^{[21]}$; $\omega_{21}^{[21]}$; $\omega_{22}^{[21]}$. Here, the superscripts [21] describe the ordering of empty boxes in the Young diagram: two boxes in the upper row and one box in the bottom row, and the subscripts describe the filling of the boxes [26]. For example,

$$\omega_{11}^{[21]} = \frac{1}{\sqrt{12}}(2 + 2P_{12} - P_{23} - P_{13} - P_{123} - P_{132}) \quad \text{and}$$
$$\omega_{12}^{[21]} = (P_{23} - P_{13} - P_{123} + P_{132}).$$

P_{12} denotes the permutation of electrons 1 and 2; P_{123} denotes the cyclic permutation of electrons 1, 2, and 3.

The components of the spatial parts of the eigenfunction in Eq. 50 are given by

$$\Psi_{\mathrm{Li}1}(\vec{r}_1,\vec{r}_2,\vec{r}_3) = \omega_{11}^{[21]}\phi_{1s}(\vec{R}-\vec{r}_1)\phi_{1s}(\vec{R}-\vec{r}_2)\varphi_{2s}(\vec{R}-\vec{r}_3);$$
$$\Psi_{\mathrm{Li}2}(\vec{r}_1,\vec{r}_2,\vec{r}_3) = \omega_{12}^{[21]}\phi_{1s}(\vec{R}-\vec{r}_1)\phi_{1s}(\vec{R}-\vec{r}_2)\varphi_{2s}(\vec{R}-\vec{r}_3) = 0 \tag{51}$$

and the corresponding spin parts are

$$\mathrm{X}_{\mathrm{Li}1} = \omega_{22}^{[21]}\chi(123) = \omega_{22}^{[21]}|\alpha1\beta2\alpha3\rangle = \frac{1}{\sqrt{12}}\{2|\alpha1\beta2\alpha3\rangle + |\alpha1\alpha2\beta3\rangle + |\alpha1\beta2\alpha3\rangle - 2|\beta1\alpha2\alpha3\rangle - |\alpha1\alpha2\beta3\rangle - |\beta1\alpha2\alpha3\rangle\} = \frac{\sqrt{3}}{2}\{|\alpha1\beta2\alpha3\rangle - |\beta1\alpha2\alpha3\rangle\}$$
$$\mathrm{X}_{\mathrm{Li}2} = \omega_{21}^{[21]}\chi(123) = \omega_{21}^{[21]}|\alpha1\beta2\alpha3\rangle = \frac{1}{2}\{-|\alpha1\alpha2\beta3\rangle + |\alpha1\beta2\alpha3\rangle - |\alpha1\alpha2\beta3\rangle + |\beta1\alpha2\alpha3\rangle\} = \frac{1}{2}\{-2|\alpha1\alpha2\beta3\rangle + |\alpha1\beta2\alpha3\rangle + |\beta1\alpha2\alpha3\rangle\}. \tag{52}$$

The Hamiltonian of the unperturbed system corresponding to the initial permutation of electrons is $H_0^{p=0} = H(1,2,3) - \frac{\hbar^2}{2\mu}\nabla^2_{p-\mathrm{Li}}$.

In the initial state, the motion of the proton and the Lithium atom relative to the center of mass are described as a plane wave with the wavevector of relative motion $\vec{k}_i$. Similarly, in the final state, the motion of the Hydrogen atom and the Lithium ion is described as a plane wave with the wavevector of relative motion $\vec{k}_f$.

The initial state is described by the function

$$\begin{aligned}\left|\Phi_i^0\right) &= \Phi_{\mathrm{Li}}(\vec{R}-\vec{r}_1,\vec{R}-\vec{r}_2,\vec{R}-\vec{r}_3)\otimes\chi(\xi_1,\xi_2;\xi_3)\exp(i\vec{k}_i\vec{R})\\ &= \frac{1}{f_{\mathrm{Li}}}(\Psi_{\mathrm{Li1}}(\vec{r}_1,\vec{r}_2,\vec{r}_3)\mathrm{X}_{\mathrm{Li1}}(1,2,3)+\Psi_{\mathrm{Li2}}(\vec{r}_1,\vec{r}_2,\vec{r}_3)\\ &\quad \mathrm{X}_{\mathrm{Li2}}(1,2,3))\exp(i\vec{k}_i\vec{R}).\end{aligned} \tag{53}$$

Here, the factor f_{Li} is found from the normalization condition, which, after some calculations, results in

$$\begin{aligned}f_{\mathrm{Li}}^2 &= \{\langle\Psi_{\mathrm{Li1}}(\vec{r}_1,\vec{r}_2,\vec{r}_3)|\Psi_{\mathrm{Li1}}(\vec{r}_1,\vec{r}_2,\vec{r}_3))\langle\mathrm{X}_{\mathrm{Li1}}|\mathrm{X}_{\mathrm{Li1}}\rangle\\ &\quad+\langle\Psi_{\mathrm{Li2}}(\vec{r}_1,\vec{r}_2,\vec{r}_3)|\Psi_{\mathrm{Li2}}(\vec{r}_1,\vec{r}_2,\vec{r}_3))\langle\mathrm{X}_{\mathrm{Li2}}|\mathrm{X}_{\mathrm{Li2}}\rangle\} = 4\end{aligned} \tag{53a}$$

and thus $f_{\mathrm{Li}} = 2$.

The antisymmetric vector of the final state is obtained by applying the normalized Young operator [26] to the wavefunction of the Hydrogen–Lithium-ion system:

$$\begin{aligned}\left|\Phi_f^0\right) &= \Phi_{\mathrm{Li}^+}(\vec{R}_f-\vec{r}_1,\vec{R}_f\\ &\quad-\vec{r}_2)\Phi_{\mathrm{H}}(\vec{r}_3)\chi(\xi_1,\xi_2;\xi_3)\exp(i\vec{k}_f\vec{R}_f)\end{aligned} \tag{54}$$

and (for the open channel $\frac{\hbar^2k_f^2}{2\mu} = \varepsilon_i - \varepsilon_n + \frac{\hbar^2k_i^2}{2\mu} \geq 0$) is given by

$$\begin{aligned}\left|\Psi_f^0\right\rangle &= \frac{1}{f_0}(\Psi_1(\vec{r}_1,\vec{r}_2,\vec{r}_3)\mathrm{X}_1(1,2,3)+\Psi_2(\vec{r}_1,\vec{r}_2,\vec{r}_3)\\ &\quad \mathrm{X}_2(1,2,3))\exp(i\vec{k}_f\vec{R}).\end{aligned} \tag{55}$$

For a three-electron system, where two electrons both occupy the $1s^2$ orbital in a singlet state, there is only one Young diagram possible, as depicted in Fig. 2a. This Young diagram allows the two possible combinations shown in Fig. 2b, c.

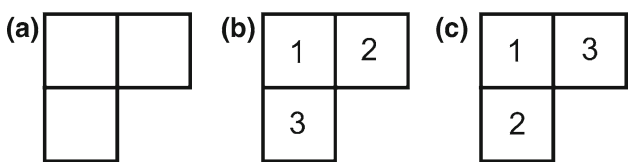

Fig. 2 Young diagrams for three-electron system. **a** Young diagram, **b** and **c** filled Young tableaux with two possible combinations

After applying the Young operators to the functions described by Eq. 54, the spatial parts of the antisymmetric wavefunction of Hydrogen atom–Lithium-ion system can be expressed as:

$$\begin{aligned}\Psi_1(\vec{r}_1,\vec{r}_2;\vec{r}_3) &= \omega_{11}^{[21]}\Phi_{\mathrm{Li}^+}(\vec{R}-\vec{r}_1,\vec{R}-\vec{r}_2)\Phi_{\mathrm{H}}(\vec{r}_3)\\ &= \frac{1}{\sqrt{12}}(2+2P_{12}-P_{23}-P_{13}-P_{123}-P_{132})\\ &\quad\times\Phi_{\mathrm{Li}^+}(\vec{R}-\vec{r}_1,\vec{R}-\vec{r}_2)\Phi_{\mathrm{H}}(\vec{r}_3).\\ \Psi_2(\vec{r}_1,\vec{r}_2;\vec{r}_3) &= \omega_{12}^{[21]}\Phi_{\mathrm{Li}^+}(\vec{R}-\vec{r}_1,\vec{R}-\vec{r}_2)\Phi_{\mathrm{H}}(\vec{r}_3)\\ &= (P_{23}-P_{13}-P_{123}+P_{132})\Phi_{\mathrm{Li}^+}\\ &\quad\times(\vec{R}-\vec{r}_1,\vec{R}-\vec{r}_2)\Phi_{\mathrm{H}}(\vec{r}_3).\end{aligned} \tag{56}$$

The related spin parts are

$$\begin{aligned}\mathrm{X}_1 &= \omega_{22}^{[21]}\chi(123) = \frac{1}{\sqrt{12}}\{2\chi_{\mathrm{Li}^+}(12)\chi_{\mathrm{H}}(3)+\chi_{\mathrm{Li}^+}(13)\chi_{\mathrm{H}}(2)\\ &\quad-2\chi_{\mathrm{Li}^+}(21)\chi_{e^+}(3)+\chi_{\mathrm{Li}^+}(32)\chi_{\mathrm{H}}(1)\\ &\quad-\chi_{\mathrm{Li}^+}(23)\chi_{\mathrm{H}}(1)-\chi_{\mathrm{Li}^+}(31)\chi_{\mathrm{H}}(2)\},\\ \mathrm{X}_2 &= \omega_{21}^{[21]}\chi(123) = \frac{1}{2}\{-\chi_{\mathrm{Li}^+}(13)\chi_{\mathrm{H}}(2)+\chi_{\mathrm{Li}^+}(32)\chi_{\mathrm{H}}(1)\\ &\quad-\chi_{\mathrm{Li}^+}(23)\chi_{\mathrm{H}}(1)+\chi_{\mathrm{Li}^+}(31)\chi_{\mathrm{H}}(2)\}.\end{aligned} \tag{57}$$

The normalization factor f_0 in Eq. 55 is

$$\begin{aligned}f_0 &= \langle\Psi_1(\vec{r}_1,\vec{r}_2,\vec{r}_3)\mathrm{X}_1(1,2,3)+\Psi_2(\vec{r}_1,\vec{r}_2,\vec{r}_3)\mathrm{X}_2(1,2,3)|\\ &\quad\times\Phi_{\mathrm{Li}^+}(\vec{R}-\vec{r}_1,\vec{R}-\vec{r}_2)\Phi_{\mathrm{H}}(\vec{r}_3)\chi(\xi_1,\xi_2;\xi_3),\big).\end{aligned} \tag{58}$$

By taking into account the orthogonality of the wavefunction spin parts, the normalization factor f_0 is reduced to the expression

$$\begin{aligned}f_0 = \Big\{&\langle\Psi_1(\vec{r}_1,\vec{r}_2,\vec{r}_3)|\Psi_{\mathrm{Li}^+}(\vec{r}_1,\vec{r}_2,)\psi_{\mathrm{H}}\vec{r}_3)\frac{\sqrt{3}}{2}\\ &+\langle\Psi_2(\vec{r}_1,\vec{r}_2,\vec{r}_3)|\Psi_{\mathrm{Li}^+}(\vec{r}_1,\vec{r}_2,)\psi_{\mathrm{H}}\vec{r})\frac{1}{2}\Big\}.\end{aligned} \tag{59}$$

By substituting Eqs. 56 and 57 into Eq. 58, the normalization factor f_0 is found to be

$$\begin{aligned}f_0 = \int d^3R e^{\left(i(\vec{k}_f-\vec{k}_i)\cdot\vec{R}\right)}&\\ \times\Big\{&2\Phi_{Li^+}(\vec{R}-\vec{r}_1,\vec{R}-\vec{r}_2)\Phi_H(\vec{r}_3)+2\Phi_{Li^+}(\vec{R}-\vec{r}_2,\vec{R}-\vec{r}_1)\Phi_H(\vec{r}_3)\rangle\\ &-\Phi_{Li^+}(\vec{R}-\vec{r}_1,\vec{R}-\vec{r}_3)\Phi_H(\vec{r}_2)-\Phi_{Li^+}(\vec{R}-\vec{r}_3,\vec{R}-\vec{r}_1)\Phi_H(\vec{r}_2)\\ &-\Phi_{Li^+}(\vec{R}-\vec{r}_2,\vec{R}-\vec{r}_3)\Phi_H(\vec{r}_1)-\Phi_{Li^+}(\vec{R}-\vec{r}_3,\vec{R}-\vec{r}_1)\Phi_H(\vec{r}_2)\\ &\times\left|\Phi_{Li^+}(\vec{R}-\vec{r}_1,\vec{R}-\vec{r}_2)\Phi_H(\vec{r}_3)\right\rangle\cdot\frac{\sqrt{3}}{2}+\Phi_{Li^+}(\vec{R}-\vec{r}_1,\vec{R}-\vec{r}_3)\\ &\times\Phi_H(\vec{r}_2)-\Phi_{Li^+}(\vec{R}-\vec{r}_3,\vec{R}-\vec{r}_2)\Phi_H(\vec{r}_1)-\Phi_{Li^+}(\vec{R}-\vec{r}_2,\vec{R}-\vec{r}_3)\\ &\times\Phi_H(\vec{r}_1)\rangle+\Phi_{Li^+}(\vec{R}-\vec{r}_3,\vec{R}-\vec{r}_1)\Phi_H(\vec{r}_2)\left|\Phi_{Li^+}(\vec{R}-\vec{r}_1,\vec{R}-\vec{r}_2)\right.\\ &\times\Phi_H(\vec{r}_3)\rangle\frac{1}{2}\Big\}.\end{aligned} \tag{60}$$

By substituting Eq. 53 and Eq. 54-a into Eq. 47, we find the differential cross section for the singlet state:

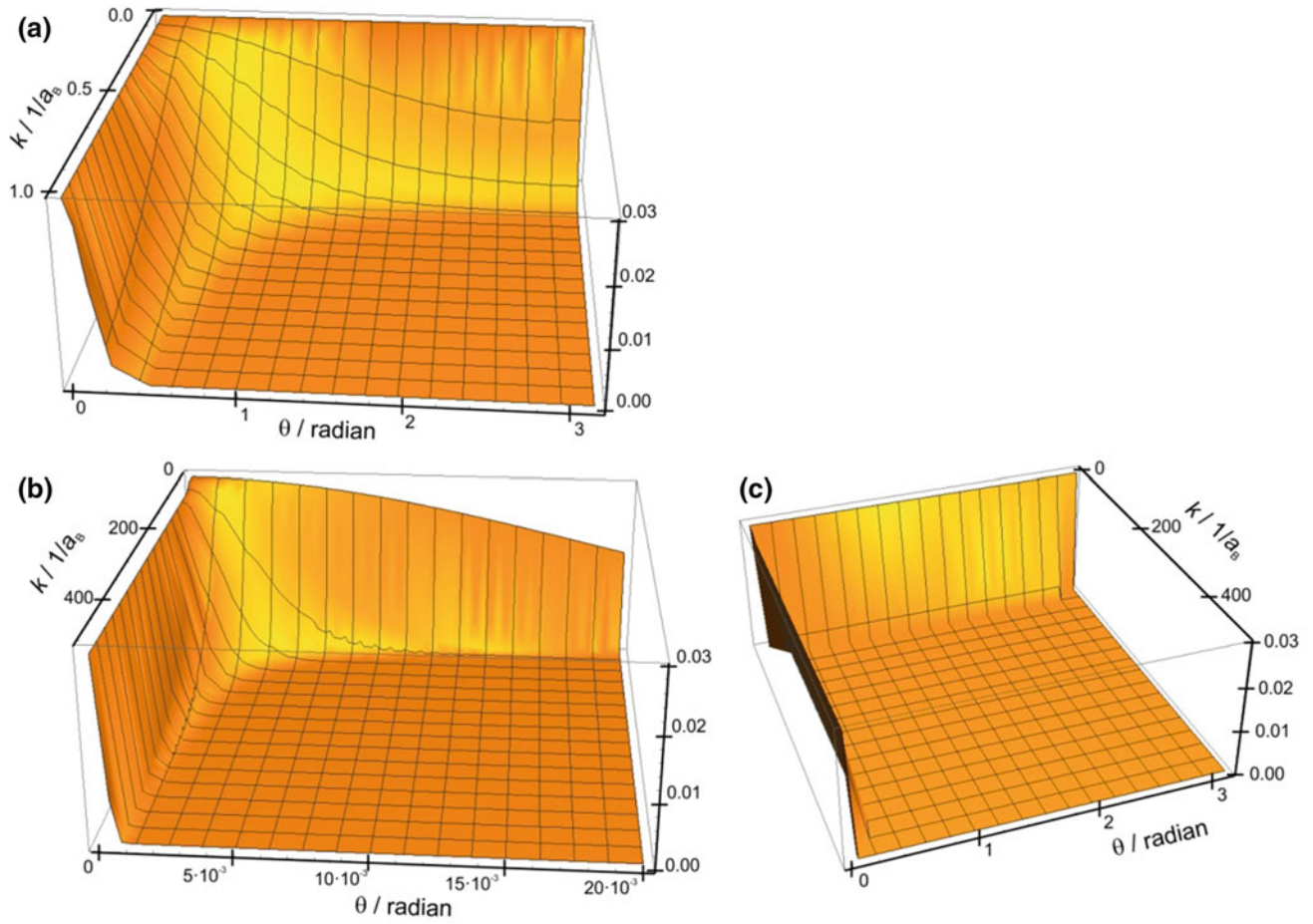

Fig. 3 Simulated differential cross section $\frac{d\sigma_{fi}}{d\Omega}$ (cm^2/sr). **a** Differential cross section, for the relative moving energy $E < 0.1$ eV in the range $\theta = (0, \pi)$. **b** The peak of differential cross section observed in the range $k = (0{,}500)$, corresponding to the relative moving energy $0 < E < 2$ keV and $\theta = (0, 0.2)$. **c** Differential cross section, for the relative moving energy $0 < E < 2$ keV and $\theta = (0, \pi)$

$$\frac{d\sigma_{if}}{d\Omega} = \frac{\mu_i \mu_f k_f}{\left(2\pi\hbar^2 |f_0 f_{Li}|\right)^2 k_i} \times \left| \left\langle (\Psi_1 \cdot \mathrm{X}_1 + \Psi_2 \cdot \mathrm{X}_2(1,2,3)) \exp(i\vec{k}_f \vec{R}) \right| \times \hat{T} \left| (\Psi_{Li1} \cdot \mathrm{X}_{Li1} + \Psi_{Li2} \cdot \mathrm{X}_{Li2}(1,2,3)) \exp(i\vec{k}_i \vec{R}) \right\rangle \right|^2. \quad (61)$$

Here, the transition operator $\hat{T}$ is given by Eq. 48, where we used

$$H = H_0^{p=0} + V^{p=0} = H(1,2,3) - \frac{\hbar^2}{2\mu} \nabla^2_{p-Li} - \frac{e^2}{r_{p1}} - \frac{e^2}{r_{p2}} - \frac{e^2}{r_{p3}} + \frac{3e^2}{R}, \quad (62)$$

and

$$V_0^{\mathbb{N}} = \left(\frac{f_0^2}{P}\right) \quad V_0 = \left(\frac{f_0^2}{6}\right) \left(- \frac{e^2}{r_{p1}} - \frac{e^2}{r_{p2}} - \frac{e^2}{r_{p3}} + \frac{3e^2}{R} \right). \quad (63)$$

The differential cross section given by Eq. 47, becomes in the first approximation

$$\frac{d\sigma_{fi}}{d\Omega} = \frac{\mu_i \mu_f k_f}{\left(2\pi\hbar^2\right)^2 k_i} \left| \left(\frac{f_0^2}{6}\right) \left\langle \Psi_f^0 \middle| V_0 \middle| \Phi_i^0 \right\rangle \right|^2, \quad (64)$$

where $\mu_i = \frac{M_{\mathrm{Li}} m_p}{(M_{\mathrm{Li}} + m_p)} = 1606.79\, m_e$ and $\mu_f = \frac{M_{\mathrm{Li}*} M_{\mathrm{H}}}{(M_{\mathrm{Li}*} + M_{\mathrm{H}})} = 1607.54\, m_e$ are the reduced mass of the incident particles, the lithium atom and proton at the beginning of scattering process and the lithium ion and hydrogen atom at the end of the scattering process. The solution to the matrix element in Eq. 64 is provided in Appendix 3. Here, we would like to emphasize the advantages of applying the EPT method. The matrix element given by Eq. 64 contains the exchange and superexchange integrals, contained in the second, third, and fourth terms in Eq. 64. These integrals take into account the permutations of the electrons between the atoms. The signs of these integrals are defined by the Young diagrams and depend on the total spin value.

The differential cross section given by Eq. 64 is plotted as a function of the scattering angle θ and k in Fig. 3, where k in the elastic scattering approximation is given by $k = k_i = k_f$. Here, and in what follows, we use Hartree atomic units, where k is measured in reciprocal Bohr radius units ($1/a_B$).

Figure 4 shows the simulated $\frac{d\sigma_{fi}}{d\theta} = \int_0^{2\pi} \frac{d\sigma_{fi}}{d\Omega} d\varphi \cdot \sin\theta$ as a function of the scattering angle θ at different energies of the incident proton. In insets of Fig. 4c, d, one can observe regions of a "twisted ridge" for certain values of k and θ. It has been previously reported that under similar conditions, but when an alpha particle is colliding with a Lithium atom [27], the differential cross section has a smooth appearance without ridges.

To find the total cross section, we apply the optical theorem, which states that $\sigma_{fi} = \frac{4\pi}{k} \mathrm{Im} f(\theta)|_{\theta=0}$ [1, 2], where the scattering amplitude $f(\theta)$ is given by $f(\theta) = -\frac{\mu_f}{2\pi\hbar^2} \left\langle \Psi_f^0 \middle| V_0 \middle| \Phi_i^0 \right\rangle$:

$$\sigma_{fi} = -\frac{2\mu_f}{k\hbar^2} \mathrm{Im}\left(\left\langle \Psi_f^0 \middle| V_0 \middle| \Phi_i^0 \right\rangle \right)_{\theta=0}. \quad (65)$$

The total cross section σ_{fi} is plotted in Fig. 5 and also summarized in Table 1, where the values of the cross section obtained in this paper are compared to those obtained from experimental [22, 24, 25] and theoretical publications [26, 27].

In the limit of long wavelengths ($k < 1$), the matrix element in the total cross section given by Eq. 65 is too large and cannot be simplified to a short expression. Therefore, first, the differential cross section for $k < 1$ was approximated by

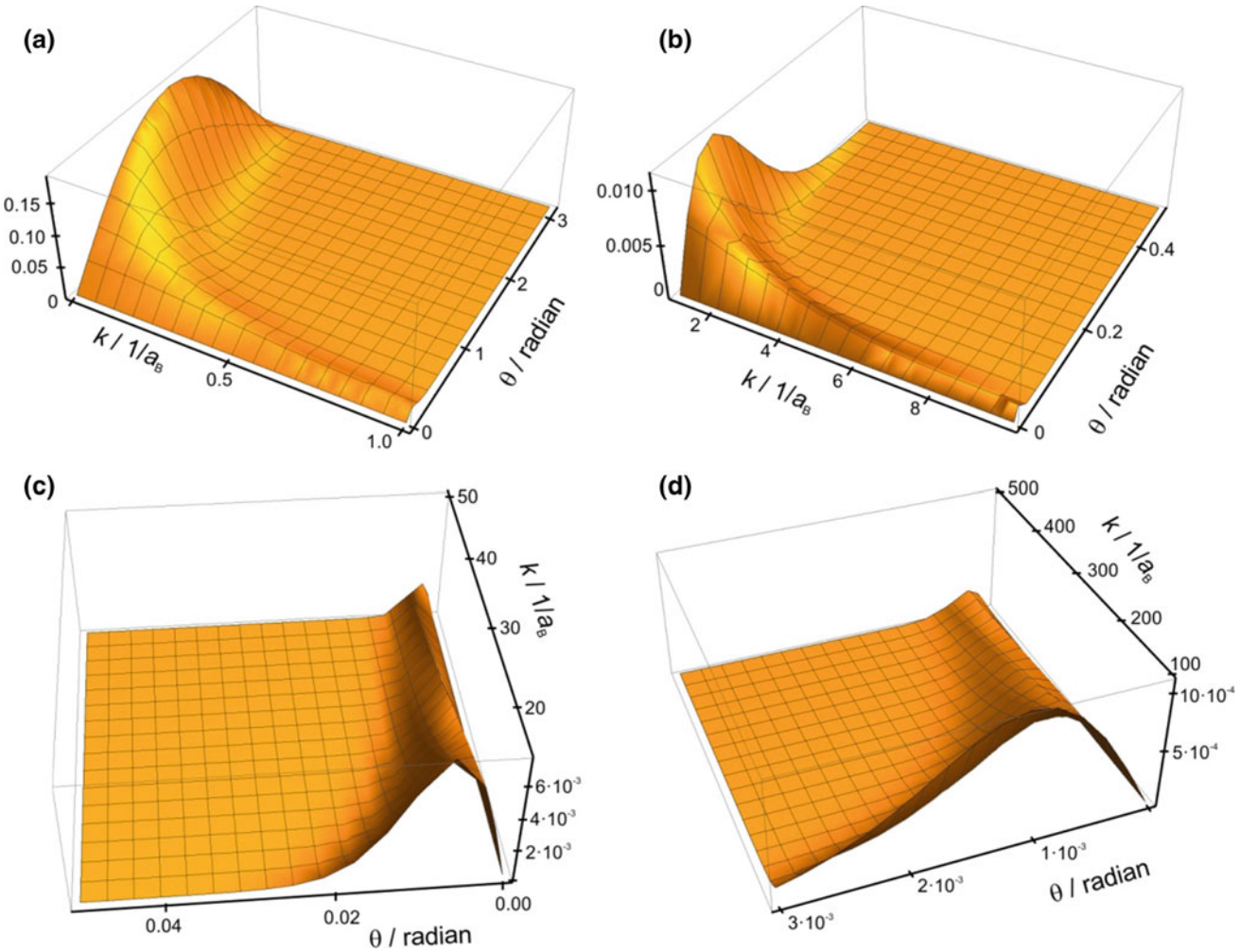

Fig. 4 Simulated differential cross section $\frac{d\sigma_{fi}}{d\Omega} \cdot 2\pi \cdot \sin\theta$ (cm^2/rad) at different relative moving energies E as a function of k and θ. **a** $E < 0.01$ eV (i.e., $k < 1.1$ $1/a_B$) and $\theta = (0, \pi)$. **b** $E < 1$ eV (i.e., $k < 10$ $1/a_B$) and $\theta = (0, \pi/6)$. **c** $E < 22$ eV (i.e., $k < 50$ $1/a_B$) and $\theta = (0, \pi/60)$. **d** $25 < E < 2000$ eV (i.e., $50 < k < 500$ $1/a_B$) and $\theta = (0, \pi/100)$

$$\frac{d\sigma_{fi}}{d\Omega}(k<1)=\frac{1.7\times10^{-10}}{0.25\times10^{-16}}\pi \cdot\left|\frac{-9+i\left(62.5k\cdot\sin(\theta/2)-144(k\cdot\sin(\theta/2))^3\right)}{1.6^2(0.6+4k^2)^2}+10\right|^2 =6.8\times10^6\pi \cdot\left|\frac{-9+i\left(62.5k\cdot\sin(\theta/2)-144(k\cdot\sin(\theta/2))^3\right)}{1.6^2(0.6+4k^2)^2}+10\right|^2. \quad (66)$$

and then it was integrated over θ and φ. The result amounts to

$$\sigma_{fi}(k<1)=6.8\cdot\pi \cdot\frac{\left(7812.5k^2-18000k^5+20736k^6+4(6.36+102.4k^2)^2\right)}{(0.6+4k^2)^2}, \quad (67)$$

and is plotted in Fig. 5a.

In the limit of short wavelengths ($k > 5$), the imaginary part of the scattering amplitude, as follows from Eq. 65, amounts to

$$\mathrm{Im}[f(\theta)]=\frac{\mu_f}{2\pi\hbar^2}\cdot\frac{10.8}{2\pi^3} \times\left\{\frac{\left(625+144k^2\sin^2\left[\frac{\theta}{2}\right]\right)\left(16k^2\sin^2\left[\frac{\theta}{2}\right]-2.8^2\right)+151\times22.4k^2\sin^2\left[\frac{\theta}{2}\right]}{\left(16k^2\sin^2\left[\frac{\theta}{2}\right]+2.8^2\right)} +\frac{0.9\left(\left(2k\sin\left[\frac{\theta}{2}\right]\right)^3-486k\sin\left[\frac{\theta}{2}\right]\right)}{\left(0.81+4k^2\sin^2\left[\frac{\theta}{2}\right]\right)^3}\right\}. \quad (68)$$

This gives the expression for the total cross section in atomic units, that is in Bohr radius squared

$$\sigma_{fi}(k>5)=\frac{4\pi}{k}\mathrm{Im}f(\theta)|_{\theta=0}=\frac{1}{k}\frac{\mu_f}{\hbar^2}\cdot\frac{10.8}{\pi^3}\cdot625 \quad (69)$$

The total cross section for short wavelengths ($k > 5$) given by Eq. 69 is plotted in Fig. 5b–e.

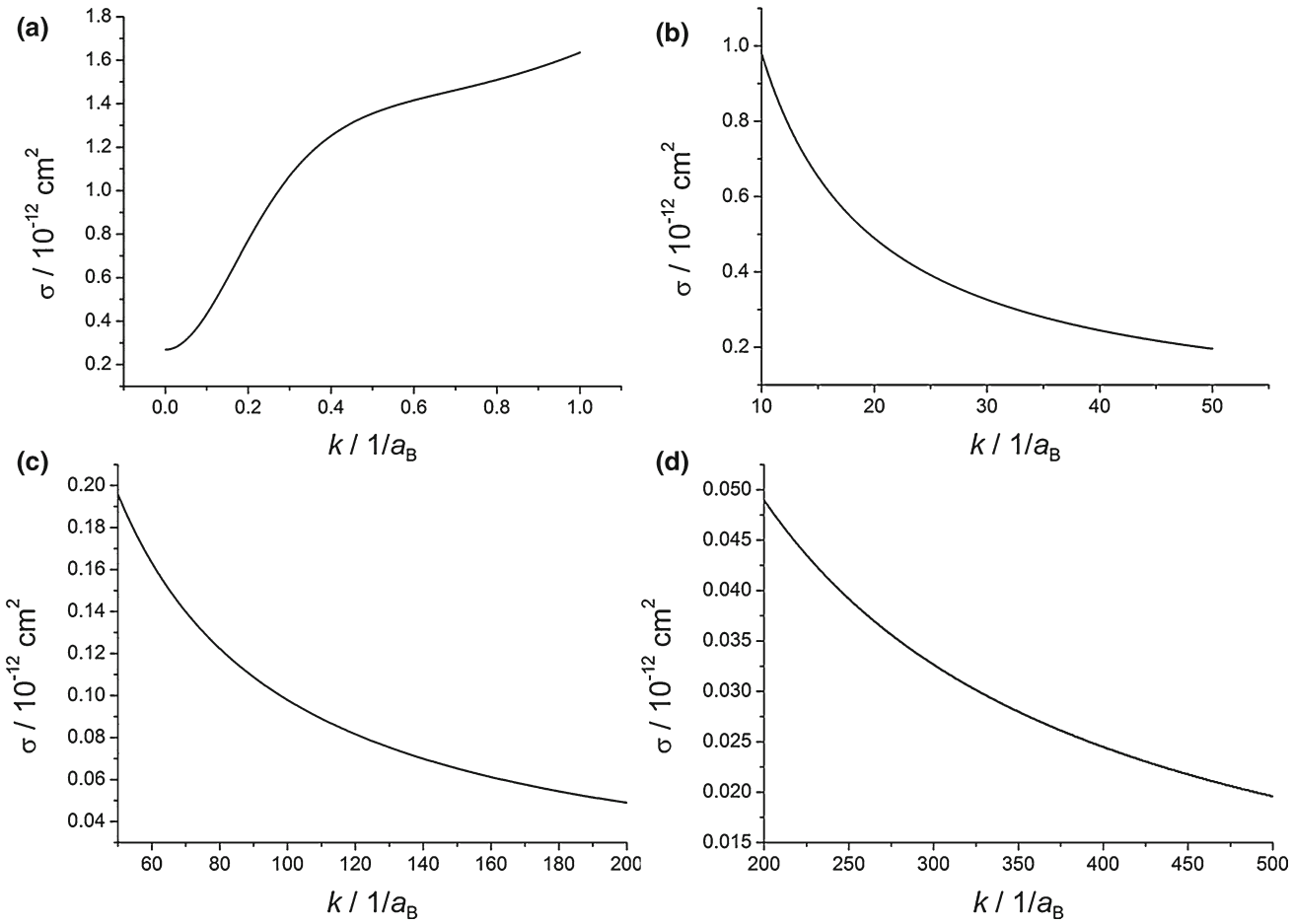

Fig. 5 Total cross section σ_{fi} of proton scattering on a lithium atom for the incident energy ranging: **a** $E < 0.01$ eV ($k < 1$ $1/a_B$), **b** $E = 0.0.87$–21.6 eV ($k = 10$–50 $1/a_B$), **c** $E = 21.6$–346 eV ($k = 50$–200 $1/a_B$), **d** $E = 346$–2161 eV ($k = 200$–500 $1/a_B$)

Table 1 Summary of total cross section as a function of the relative collision energy E

v (cm/s)	E (eV)	k ($1/a_B$)	σ (cm^2) Li–H$^+$ as calculated from Eqs. 62 and 64	σ (cm^2) Li–He^{2+} [27]	σ (cm^2) Li–Li$^+$ He–He$^+$ H–H$^+$ [26]	σ (cm$^{2)}$ He–He$^+$ [22, 24, 25]
2.5×10^5	0.22	5	2.0×10^{-13}	5×10^{-13}		
5×10^5	0.87	10	1.5×10^{-13}	1.30×10^{-13}		
7.5×10^5	1.95	15	7.5×10^{-14}	5.8×10^{-14}	2.6×10^{-14}	
					3.5×10^{-15}	
					6.2×10^{-15}	
1×10^6	3.45	20	5.3×10^{-14}	32.5×10^{-15}		
1.25×10^6	5.4	25	4.5×10^{-14}	26.4×10^{-15}		
2.5×10^6	21.6	50	2.3×10^{-14}	17×10^{-15}	2.2×10^{-14}	
					2.8×10^{-15}	
					5×10^{-15}	
5×10^6	86.4	100	1.0×10^{-14}	10×10^{-15}		
7.5×10^6	195	150	7.0×10^{-15}	8.75×10^{-15}	18×10^{-15}	
					2.1×10^{-15}	
					3.8×10^{-15}	
1×10^7	345	200	6.5×10^{-15}	8×10^{-15}		
2.5×10^7	2161	500	2.5×10^{-15}	5.6×10^{-15}		
5×10^7	8646	1000	1.0×10^{-15}	5.32×10^{-15}		
1×10^8	3458	2000	6.5×10^{-16}	5.24×10^{-15}		5×10^{-16}
1.5×10^8	77,821	3000	4×10^{-16}	5.22×10^{-15}		3.5×10^{-16}
2×10^8	138,348	4000	3.6×10^{-16}	5.21×10^{-15}		2.7×10^{-16}
2.5×10^8	216,169	5000	3×10^{-16}	5.21×10^{-15}		2×10^{-16}
3×10^8		6000	2×10^{-16}	5.20×10^{-15}		1×10^{-16}

Here, v (cm/s) is the speed of the relative motion. The relative collision energy is calculated as $E = \frac{k^2\hbar^2}{2\mu_i}$, and the relative collision speed is calculated as $v = \frac{\hbar k}{\mu_i}$

8 Conclusions

The formalism of the time-dependent exchange perturbation theory is developed in an invariant form. It allows the scattering processes of complex particles (atoms, molecules) to be described, taking into account the indistinguishability of electrons participating in multicenter collisions, even in cases where the permutations of electrons occur between different centers and are associated with non-orthogonal states. This formalism is applicable to cases of restructuring colliding particles, such as ion charge exchange processes.

Appendix 1

We apply $\widehat{O}_i = 1 - \left|\Psi_i^0\right\rangle(\Phi_i|$ to both sides of equation Eq. 12:

$$-\frac{\hbar}{i}\left|\dot{\Psi}^{(1)}(t)\right\rangle = \widehat{H}_0\left|\Psi^{(1)}(t)\right\rangle + \widehat{V}(t)\left|\Psi_i^0\right\rangle \tag{70}$$

where we use the expansion given by Eq. 13:

$$\left|\Psi^{(1)}(t)\right\rangle = \sum_n C_n(t)\exp\left(-\frac{i}{\hbar}E_n t\right)\left|\Psi_n^0\right\rangle \tag{71}$$

The resulting equation can now be written as

$$-\frac{\hbar}{i}\sum_n \dot{C}_n(t)\exp\left(-\frac{i}{\hbar}E_n t\right)\widehat{O}_i\left|\Psi_n^0\right\rangle = \exp\left(-\frac{i}{\hbar}E_i t\right)\widehat{O}_i\widehat{V}\left|\Psi_i^0\right\rangle, \tag{72}$$

where prime denotes that the term with $n = i$ is excluded.

Next, we use the completeness property of the antisymmetrized basis (see Eq. 4) and rewrite the right side of Eq. 72 as

$$\exp\left(-\frac{i}{\hbar}E_i t\right)\cdot\frac{f_0}{P}\sum_n \left|\Psi_n^0\right\rangle\left(\Phi_n^{0(0)}\right|\widehat{O}_i\widehat{V}\left|\Psi_i^0\right\rangle \tag{73}$$

Because $\left(\Phi_i^{0(0)}\right|\widehat{O}_i = \left(\Phi_i^{0(0)}\right| - \left(\Phi_i^{0(0)}\right|\Psi_i^0\rangle\left(\Phi_i^{0(0)}\right| \equiv 0$, the term at $n = i$, is excluded, which is signified by the prime on the summation sign.

Rearranging Eq. 72, we obtain

$$\sum_n \left\{ -\frac{\hbar}{i}\dot{C}_n(t) - \frac{f_0}{P}\left(\Phi_n^{0(0)}\middle|\bar{O}_i\bar{V}\middle|\Psi_i^0\right\rangle \exp(-i\omega_{in}t)\right\}\bar{O}_i\left|\Psi_n^0\right\rangle = 0. \quad (74)$$

The last equation is fulfilled when the expression in the curly brackets equals zero for all n. This, in turn, leads to an equation for $\dot{C}_n(t)$:

$$-\frac{\hbar}{i}\dot{C}_n(t) = \frac{f_0}{P}\exp(-i\omega_{ni}t)\left(\Phi_n^{0(0)}\middle|\bar{O}_i\bar{V}\middle|\Psi_i^0\right\rangle, \quad (75)$$

where we introduced $\frac{1}{\hbar}(E_i - E_n) = \omega_{in}$.

Appendix 2

Operator $\hat{T}$ satisfies Eq. 48:

$$\hat{T} = V_0^{\mathbb{N}} + V_0^{\mathbb{N}}\left(\frac{f_0^2}{P}\right)^{-1}\left(E_i - H_{p=0}^0 + i\eta\right)^{-1}\hat{T}, \quad (76)$$

which can be re-arranged to:

$$V_0^{\mathbb{N}} = \left(\hat{1} - V_0^{\mathbb{N}}\left(\frac{f_0^2}{P}\right)^{-1}\left(E_i - H_{p=0}^0 + i\eta\right)^{-1}\right)\hat{T}$$

$$V_0^{\mathbb{N}} = \left(\left(E_i - H_{p=0}^0 + i\eta\right)\left(\frac{f_0^2}{P}\right) - V_0^{\mathbb{N}}\right)\left(\frac{f_0^2}{P}\right)^{-1}\left(E_i - H_{p=0}^0 + i\eta\right)^{-1}\hat{T}. \quad (77)$$

Taking into account that the total Hamiltonian of the system

$$H = H_{p=0}^0 + V_{p=0} = H_p^0 + V_p, \quad (78)$$

is invariant with respect to permutations of electrons between atoms:

$$H = H_0^{p=0} + V^{p=0} = -\frac{\hbar^2}{2\mu_i}\nabla_i^2 + H_i^{p=0}(r_1, r_2, \ldots)_i + V^{p=0}. \quad (79)$$

We further re-arrange Eq. 77:

$$V_0^{\mathbb{N}} = (E_i - H + i\eta)\left(\frac{f_0^2}{P}\right)\left(\frac{f_0^2}{P}\right)^{-1}\left(E_i - H_{p=0}^0 + i\eta\right)^{-1}\hat{T}$$

$$\left(\frac{f_0^2}{P}\right)\left(E_i - H_{p=0}^0 + i\eta\right)\left(\frac{f_0^2}{P}\right)^{-1}(E_i - H + i\eta)^{-1}V_0^{\mathbb{N}} = \hat{T}$$

$$\left(\frac{f_0^2}{P}\right)\left(E_i - H_{p=0}^0 + V_0 - V_0 + i\eta\right)\left(\frac{f_0^2}{P}\right)^{-1}(E_i - H + i\eta)^{-1}V_0^{\mathbb{N}} = \hat{T}$$

$$V_0^{\mathbb{N}}\left(\frac{f_0^2}{P}\right)^{-1}(E_i - H + i\eta)^{-1}V_0^{\mathbb{N}} + \left(\frac{f_0^2}{P}\right)\left(E_i - H_{p=0}^0 - V_0 + i\eta\right)\left(\frac{f_0^2}{P}\right)^{-1} \times (E_i - H + i\eta)^{-1}V_0^{\mathbb{N}} = \hat{T}$$

to the final expression for operator $\hat{T}$:

$$V_0^{\mathbb{N}}\left(\frac{f_0^2}{P}\right)^{-1}(E_i - H + i\eta)^{-1}V_0^{\mathbb{N}} + V_0^{\mathbb{N}} = \hat{T}. \quad (80)$$

Appendix 3

The initial states of the electrons in the Lithium atom are given by [28] where the parameters α and β are taken from [29]

$$\phi_{1s}(\vec{R} - \vec{r}_i) = (\alpha_1^3/\pi)^{1/2}\exp\left(-\alpha_1|\vec{R} - \vec{r}_i|\right), \quad i = 1, 2$$
$$\varphi_{2s^1}(\vec{R} - \vec{r}_3) = (\alpha_2^3/8\pi)^{1/2}(1 - 0.5\alpha_2|\vec{R} - \vec{r}_3|) \times \exp\left(-0.5\alpha_2|\vec{R} - \vec{r}_3|\right), \quad (81)$$

where $\alpha_1 = 2.698, \alpha_2 = 0.795$.

The final states of the electrons in the Helium-like Lithium ion are described by

$$\phi^*(\vec{R} - \vec{r}_i) = (\alpha^{*3}/\pi)^{1/2}\exp(-\alpha^*|\vec{R} - \vec{r}_i|), \quad i = 1, 2$$
where $\alpha^* = 1.692$. (82)

The final state of the electron in the Hydrogen atom is described by the single-electron wavefunction:

$$\psi_H(r) = (\pi)^{-1/2}\exp(-\beta r); \quad \beta = 1 \quad (83)$$

Here, α, α^*, and β are given in reciprocal Bohr radius units, and R is in Bohr radius units.

The first-order correction to the S-matrix elements given by Eq. 31 becomes:

$$\begin{aligned}\left\langle\Psi_f^0\middle|V_0^{\mathbb{N}}\middle|\Phi_i^0\right\rangle = {} & \frac{1}{f_0}\frac{1}{f_{\mathrm{Li}}}\Big(\sqrt{3}\langle\Psi_1(\vec{r}_1,\vec{r}_2,\vec{r}_3)|V_0^{\mathbb{N}}\mathrm{e}^{\left(i(\vec{k}_f-\vec{k}_i)\cdot\vec{R}_{I,II}\right)} \\ & \times|\Psi_{\mathrm{Li}1}(\vec{r}_1,\vec{r}_2,\vec{r}_3)) \\ & + \frac{3}{2}\langle\Psi_2(\vec{r}_1,\vec{r}_2,\vec{r}_3)|V_0^{\mathbb{N}}\mathrm{e}^{\left(i(\vec{k}_f-\vec{k}_i)\cdot\vec{R}_{I,II}\right)}|\Psi_{\mathrm{Li}2}(\vec{r}_1,\vec{r}_2,\vec{r}_3))\Big) \\ = {} & \frac{4}{\sqrt{3}}\frac{1}{P}\frac{f_0}{f_{\mathrm{Li}}}\Big\{\left\langle\Phi_{\mathrm{Li}^+}(\vec{R}-\vec{r}_1,\vec{R}-\vec{r}_2)\Phi_H(\vec{r}_3)\middle|V_0\mathrm{e}^{\left(i(\vec{k}_f-\vec{k}_i)\cdot\vec{R}_{I,II}\right)}\right. \\ & \left|(\phi_{1s}(\vec{R}-\vec{r}_1)\phi_{1s}(\vec{R}-\vec{r}_2)\varphi_{2s}(\vec{R}-\vec{r}_3)\right) \\ & - \left\langle\Phi_{\mathrm{Li}^+}(\vec{R}-\vec{r}_1,\vec{R}-\vec{r}_2)\Phi_H(\vec{r}_3)\middle|V_0\mathrm{e}^{\left(i(\vec{k}_f-\vec{k}_i)\cdot\vec{R}_{I,II}\right)}\right. \\ & \times\left|\phi_{1s}(\vec{R}-\vec{r}_3)\phi_{1s}(\vec{R}-\vec{r}_2)\varphi_{2s}(\vec{R}-\vec{r}_1)\right)) \\ & - \left\langle\Phi_{\mathrm{Li}^+}(\vec{R}-\vec{r}_3,\vec{R}-\vec{r}_2)\Phi_H(\vec{r}_1)\middle|V_0\mathrm{e}^{\left(i(\vec{k}_f-\vec{k}_i)\cdot\vec{R}_{I,II}\right)}\right. \\ & \times\left|(\phi_{1s}(\vec{R}-\vec{r}_1)\phi_{1s}(\vec{R}-\vec{r}_2)\varphi_{2s}(\vec{R}-\vec{r}_3)\right) \\ & + \left\langle\Phi_{\mathrm{Li}^+}(\vec{R}-\vec{r}_3,\vec{R}-\vec{r}_2)\Phi_H(\vec{r}_1)\middle|V_0\mathrm{e}^{\left(i(\vec{k}_f-\vec{k}_i)\cdot\vec{R}_{I,II}\right)}\right. \\ & \left.\left.\times\left|\phi_{1s}(\vec{R}-\vec{r}_3)\phi_{1s}(\vec{R}-\vec{r}_2)\varphi_{2s}(\vec{R}-\vec{r}_1)\right)\right)\Big\}\end{aligned} \quad (84)$$

where we used the orthogonality of the spin parts of the wavefunctions.

The matrix element $\langle \Psi_f^0 | V_0 | \Phi^0{}_i \rangle$. in Eq. 64 can be rewritten as

$$\begin{aligned}
\left\langle \Psi_f^0 \middle| V_0 \middle| \Phi_i^0 \right\rangle &= \frac{4}{\sqrt{3}} \frac{1}{P} \frac{f_0}{f_{\mathrm{Li}}} \int d^3R \mathrm{e}^{\left(i(\vec{k}_f - \vec{k}_i)\cdot\vec{R}\right)} \\
&\times \left\{ \Delta_{1s^*1s} \left[\left(\frac{6}{R} \Delta_{1s^*1s} S_{1s'2s} - 2A_{1s'2s}\Delta_{1s^*1s} - 4K_{1s^*1s} S_{1s'2s} \right) \right.\right. \\
&\left. - \left(S_{1s'2s} \left(\frac{3}{R} \Delta_{1s^*1s} - K_{1s^*1s} - K_{1s^*2s} \right) - A_{1s'1s}\Delta_{1s^*2s} \right) \right] \\
&- \Delta_{1s^*1s}\Delta_{1s^*2s} \left(\frac{3S_{1s'1s}}{R} - A_{1s'1s} \right) + S_{1s'1s} (K_{1s^*1s}\Delta_{1s^*2s} \\
&\left. + K_{1s^*2s}\Delta_{1s^*1s}) \right\}, \qquad (85)
\end{aligned}$$

where we introduced the following symbols for integrals

$$\begin{aligned}
\Delta_{1s^*1s} &= \langle \phi^* | \phi_{1s^1} \rangle \\
\Delta_{1s^*2s} &= \langle \phi^* | \phi_{2s^1} \rangle \\
S_{1s'1s} &= \langle \psi_{He^*}(\vec{r}) | \phi_{1s}(\vec{R} - \vec{r}) \rangle , \\
S_{1s'2s} &= \langle \psi_{He^*}(\vec{r}) | \phi_{2s}(\vec{R} - \vec{r}) \rangle \\
K_{1s^*1s} &= \langle \phi^* | \frac{1}{r} | \phi_{1s^1} \rangle \\
K_{1s^*2s} &= \langle \phi^* | \frac{1}{r} | \phi_{2s^1} \rangle \\
A_{1s'1s} &= \langle \psi_{\mathrm{He}^*}(\vec{r}) | \frac{1}{r} | \phi_{1s}(\vec{R} - \vec{r}) \rangle \\
A_{1s'2s} &= A_{1s'1s} = \langle \psi_{\mathrm{He}^*}(\vec{r}) | \frac{1}{r} | \phi_{2s}(\vec{R} - \vec{r}) \rangle .
\end{aligned} \qquad (86)$$

All these integrals have analytical expressions, and they are listed below.

The normalization factor in Eq. 64 is found as follows:

$$\begin{aligned}
f_0 &= \frac{4}{3} \times \langle 4\phi^*(\vec{R} - \vec{r}_1) \cdot \phi^*(\vec{R} - \vec{r}_2) \cdot \psi_{He^*}(r_3) - 3\phi^*(\vec{R} - \vec{r}_1) \\
&\quad \cdot \phi^*(\vec{R} - \vec{r}_3) \cdot \psi_{He^*}(r_2) - \phi^*(\vec{R} - \vec{r}_3) \cdot \phi^*(\vec{R} - \vec{r}_2) \cdot \psi_{He^*}(r_1) | \\
&\quad \left| \mathrm{e}^{\left(i(\vec{k}_f - \vec{k}_i)\cdot\vec{R}\right)} (\phi_{1s}(\vec{R} - \vec{r}_1)\phi_{1s}(\vec{R} - \vec{r}_2)\varphi_{2s}(\vec{R} - \vec{r}_3) - \phi_{1s} \right. \\
&\quad \left. \times (\vec{R} - \vec{r}_3)\phi_{1s}(\vec{R} - \vec{r}_2)\varphi_{2s}(\vec{R} - \vec{r}_1)) \right\rangle \\
&= \frac{20}{3} \int d^3R \mathrm{e}^{\left(i(\vec{k}_f - \vec{k}_i)\cdot\vec{R}\right)} \{ \Delta_{1s^*1s}\Delta_{1s^*1s}S_{1s'2s} - \Delta_{1s^*1s}\Delta_{1s^*2s}S_{1s'1s} \}
\end{aligned} \qquad (87)$$

$$\begin{aligned}
\Delta_{1s^*1s} &= \langle \phi^* | \phi_{1s^1} \rangle = \frac{8(\alpha\alpha^*)^{3/2}}{(\alpha + \alpha^*)^3} \\
\Delta_{1s^*2s} &= \langle \phi^* | \phi_{2s^1} \rangle = \frac{8\left(\frac{\alpha}{2}\alpha^*\right)^{3/2}}{\left(\frac{\alpha}{2} + \alpha^*\right)^3} \left(1 - \frac{3\alpha}{\alpha + 2\alpha^*} \right) \\
S_{1s'1s} &= \langle \psi_{He^*}(\vec{r}) | \phi_{1s}(\vec{R} - \vec{r}) \rangle \\
&= \frac{8(\alpha\beta)^{3/2}}{\beta^2 - \alpha^2} \mathrm{sh}\left[\frac{R}{2}(\alpha - \beta) \right] e^{-\frac{R}{2}(\alpha+\beta)} \\
&\quad \times \left(\frac{1}{\alpha + \beta} + \frac{\mathrm{cth}\frac{R}{2}(\alpha - \beta)}{\alpha - \beta} - \frac{8\alpha\beta}{R\left(\alpha^2 - \beta^2\right)^2} \right)
\end{aligned} \qquad (88)$$

$$\begin{aligned}
S_{1s'2s} &= \langle \psi_{He^*}(\vec{r}) | \phi_{2s}(\vec{R} - \vec{r}) \rangle \\
&= \frac{(\alpha\beta)^{3/2}}{\sqrt{2}} \frac{R \cdot \mathrm{sh}\left[\frac{R}{2}\left(\frac{\alpha}{2} - \beta\right)\right] e^{-\frac{R}{2}\left(\frac{\alpha}{2} - \beta\right)}}{\beta^2 - \left(\frac{\alpha}{2}\right)^2} \\
&\quad \times \left\{ \frac{4}{R\left(\frac{\alpha}{2} + \beta\right)} \frac{8\alpha\beta}{R^2\left(\left(\frac{\alpha}{2}\right)^2 - \beta^2\right)^2} + \frac{4\mathrm{cth}\left[\frac{R}{2}\left(\frac{\alpha}{2} - \beta\right)\right]}{R\left(\frac{\alpha}{2} - \beta\right)} \right. \\
&\quad - \frac{\alpha\left(1 - \mathrm{cth}\left[\frac{R}{2}\left(\frac{\alpha}{2} - \beta\right)\right]\right)}{R\left(\frac{\alpha}{2} + \beta\right)} - \frac{2\alpha\left(3 - \mathrm{cth}\left[\frac{R}{2}\left(\frac{\alpha}{2} - \beta\right)\right]\right)}{R\left(\frac{\alpha}{2} + \beta\right)^2} \\
&\quad - \frac{12\alpha}{R^2\left(\left(\frac{\alpha}{2}\right) + \beta\right)^3} + \frac{12\alpha}{R^2\left(\left(\frac{\alpha}{2}\right) - \beta\right)^3} + \frac{\alpha\left(1 - \mathrm{cth}\left[\frac{R}{2}\left(\frac{\alpha}{2} - \beta\right)\right]\right)}{R\left(\frac{\alpha}{2} - \beta\right)} \\
&\quad \left. - \frac{2\alpha\left(1 + \mathrm{cth}\left[\frac{R}{2}\left(\frac{\alpha}{2} - \beta\right)\right]\right)}{R\left(\left(\frac{\alpha}{2}\right)^2 - \beta^2\right)} + \frac{2\alpha\left(1 - 3\mathrm{cth}\left[\frac{R}{2}\left(\frac{\alpha}{2} - \beta\right)\right]\right)}{R\left(\frac{\alpha}{2} - \beta\right)^2} \right\}
\end{aligned} \qquad (89)$$

$$\begin{aligned}
K_{1s^*1s} &= \left\langle \phi^* \middle| \frac{1}{r} \middle| \phi_{1s^1} \right\rangle = \frac{4(\alpha\alpha^*)^{3/2}}{(\alpha + \alpha^*)^2} \mathrm{sh}\left[\frac{R}{2}(\alpha + \alpha^*) \right] e^{-\frac{R}{2}(\alpha + \alpha^*)} \\
&\quad \times \left(1 + \frac{4}{R(\alpha + \alpha^*)} - \mathrm{cth}\left[\frac{R}{2}(\alpha + \alpha^*) \right] \right)
\end{aligned} \qquad (90)$$

$$\begin{aligned}
A_{1s'1s} &= \langle \psi_{He^*}(\vec{r}) | \frac{1}{r} | \phi_{1s}(\vec{R} - \vec{r}) \rangle \\
&= \frac{4(\alpha\beta)^{3/2}}{\left(\alpha^2 - \beta^2\right)} \mathrm{sh}\left[\frac{R}{2}(\alpha - \beta) \right] e^{-\frac{R}{2}(\alpha + \beta)} \\
&\quad \times \left(1 + \frac{4\alpha}{R\left(\alpha^2 - \beta^2\right)} - \mathrm{cth}\left[\frac{R}{2}(\alpha - \beta) \right] \right) \\
K_{1s^*2s} &= \langle \phi^* | \frac{1}{r} | \phi_{2s^1} \rangle = \frac{\sqrt{2}(\alpha\alpha^*)^{3/2}}{\left(\frac{\alpha}{2} + \alpha^*\right)^2} \\
&\quad \mathrm{sh}\left[\frac{R}{2}\left(\frac{\alpha}{2} + \alpha^* \right) \right] e^{-\frac{R}{2}\left(\frac{\alpha}{2} + \alpha^*\right)} \\
&\quad \times \left(1 + \frac{4}{R\left(\frac{\alpha}{2} + \alpha^*\right)} - \mathrm{cth}\left[\frac{R}{2}\left(\frac{\alpha}{2} + \alpha^* \right) \right] \right. \\
&\quad \left. - \frac{R\alpha}{2}\left(1 - \mathrm{cth}\left[\frac{R}{2}\left(\frac{\alpha}{2} + \alpha^* \right) \right] \right) \right. \\
&\quad \left. - \frac{2\alpha\left(1 - \mathrm{cth}\left[\frac{R}{2}\left(\frac{\alpha}{2} + \alpha^*\right)\right]\right)}{\left(\frac{\alpha}{2} + \alpha^*\right)} - \frac{6\alpha}{R\left(\frac{\alpha}{2} + \alpha^*\right)^2} \right) \\
A_{1s'2s} &= A_{1s'1s} = \left\langle \psi_{He^*}(\vec{r}) \middle| \frac{1}{r} \middle| \phi_{2s}(\vec{R} - \vec{r}) \right\rangle \\
&= \frac{\sqrt{2}(\alpha\beta)^{3/2}}{\left(\frac{\alpha}{2}\right)^2 - \beta^2} \mathrm{sh}\left[\frac{R}{2}\left(\frac{\alpha}{2} - \beta \right) \right] e^{-\frac{R}{2}\left(\frac{\alpha}{2} + \beta\right)} \\
&\quad \times \left\{ 1 - \mathrm{cth}\left[\frac{R}{2}\left(\frac{\alpha}{2} - \beta \right) \right] - \frac{R\alpha}{2}\left(1 - \mathrm{cth}\left[\frac{R}{2}\left(\frac{\alpha}{2} - \beta \right) \right] \right) \right. \\
&\quad - \frac{\alpha\left(1 - \mathrm{cth}\left[\frac{R}{2}\left(\frac{\alpha}{2} - \beta\right)\right]\right)}{\left(\frac{\alpha}{2} + \beta\right)} - \frac{\alpha\left(1 - \mathrm{cth}\left[\frac{R}{2}\left(\frac{\alpha}{2} - \beta\right)\right]\right)}{\left(\frac{\alpha}{2} - \beta\right)} \\
&\quad \left. - \frac{2\alpha}{R\left(\frac{\alpha}{2} + \beta\right)^2} - \frac{2\alpha}{R\left(\frac{\alpha}{2} - \beta\right)^2} \right\}
\end{aligned} \qquad (91)$$

References

1. Abrikosov AA, Gor'kov LP, Dzyaloshinskiy IE (1962) Quantum field theory techniques in statistical physics. Fizmatgiz, Moscow
2. Davydov AS (1969) Quantum mechanics. Pergamon Press, Oxford
3. Wu T, Ohmura T (1962) Quantum theory of scattering
4. Moshinsky M, Seligman TH (1971) Ann Phys 66:311
5. Mayer I (1983) Towards a "Chemical" Hamiltonian. Int J Quantum Chem 23(3):341–363
6. Surjan PR (1989) Second quantized approach to quantum chemistry (An elementary introduction). Springer, Berlin
7. Orlenko EV, Rumyantsev VV (1995) The effect of particle identity on a new type of weak localization. J Phys: Condens Matter 7(18):3557–3564
8. Rumyantsev VV, Orlenko EV, Libenson BN (1997) Nature of coherent enhancement of inelastic electron scattering from disordered media. Zeitschrift für Physik B Condensed Matter 103(1):53–60
9. Kohn W, Becke AD, Parr RG (1996) Density functional theory of electronic structure. J Phys Chem 100(31):12974–12980
10. Bockstedte M, Kley A, Neugebauer J, Scheffler M (1997) Density-functional theory calculations for poly-atomic systems: electronic structure, static and elastic properties and ab initio molecular dynamics. Comput Phys Commun 107(1–3):187–222
11. Fuchs M, Scheffler M (1999) Ab initio pseudopotentials for electronic structure calculations of poly-atomic systems using density-functional theory. Comput Phys Commun 119(1):67–98
12. Huix-Rotllant M, Natarajan B, Ipatov A, Wawire CM, Deutsch T, Casida ME (2010) Assessment of noncollinear spin-flip Tamm-Dancoff approximation time-dependent density-functional theory for the photochemical ring-opening of oxirane. Phys Chem Chem Phys 12(39):12811–12825
13. Salvador P, Mayer I (2004) Second-order Moller-Plesset perturbation theory without basis set superposition error. II. Open-shell systems. J Chem Phys 120(13):5882–5889
14. Mammino L, Kabanda MM (2009) A study of the intramolecular hydrogen bond in acylphloroglucinols. Theochem-J Mol Struct 901(1–3):210–219
15. Kaplan IG (2006) Intermolecular interactions: physical picture, computational methods, and model potentials. Wiley, New York
16. Orlenko EV, Rumyantsev AA (1990) Perturbation theory for intercenter electron exchange and superexchange with degeneracy. J Exp Theor Phys 97(2):439–448
17. Orlenko EV, Latychevskaia T (1998) The method of exchange perturbation theory as applied to magnetic ordering in high-Tc materials. J Exp Theor Phys 86(6):1167–1176
18. Orlenko EV, Orlova TS, Orlenko FE, Zegrya GG (2011) Exchange perturbation theory for multiatomic electron system and its application to spin arrangement in manganite chains. Adv Phys Chem 2011:868610
19. Orlenko EV, Ershova EV, Orlenko FE (2013) Invariant exchange perturbation theory for multicenter systems and its application to the calculation of magnetic chains in manganites. J Exp Theor Phys 117(4):674–690
20. Orlenko EV, Matisov BG (1999) Superexchange pairing and magnetic ordering in cuprate superconductors. Phys Solid State 41(12):1951–1955
21. Rumyantsev AA, Orlenko EV (1990) Time-dependent exchange perturbation theory. Sov Phys Tech Phys 35:409–413
22. Orlenko EV, Matisov BG (2000) Exchange-induced self-polarization of an electron beam. Tech Phys Lett 26(9):806–809
23. Orlenko EV, Matisov BG (2006) Coherent amplification of beams of atoms inelastically scattered by the Bose-Einstein condensate. Tech Phys 51(1):1–10
24. Ritchie AB (1968) Perturbation theory for exchange interactions between atoms and molecules I. Phys Rev 171(1):125–127
25. Rumyantsev AA (1973) Perturbation theory with allowance for exchange forces. J Exp Theor Phys 65(3):926
26. Kaplan IG (1975) Symmetry of many-electron systems. Academic, New York
27. Orlenko EV, Evstafev AV, Orlenko FE (2015) Invariant exchange perturbation theory for multicenter systems: time-dependent perturbations. J Exp Theor Phys 120(2):296–311. (Zhurnal Eksperimental'noi i Teoreticheskoi Fiziki 147(2):338–355)
28. Flurry RL Quantum chemistry. An introduction. Prentice-Hall, Englewood Cliffs
29. Gombas P, Szondy T (1970) Solutions of the simple self-consistent field for atoms. Acad. Kiodo, Budapest

Theor Chem Acc (2015) 134:21
DOI 10.1007/s00214-015-1621-y

REGULAR ARTICLE

On the definition of molecular dynamic magnetizability

Paolo Lazzeretti

Received: 23 August 2014 / Accepted: 16 January 2015 / Published online: 5 February 2015

Abstract The possibility of defining a second-rank tensor $\xi_{\alpha\beta}$, which would account for the frequency-dependent magnetizability of a molecule in the presence of an optical field, represented as a monochromatic wave, has been investigated. It has been shown that, whereas the electric dipole moment induced by the incident wave is origin independent, the magnetic dipole depends on the origin and cannot be rationalized via a function $M_\alpha = \xi_{\alpha\beta}B_\beta$ of the magnetic field B_β. This result was arrived at using time-dependent perturbation theory, within dipole, quadrupole, and octopole approximations for the interaction Hamiltonian, employing a series of relationships, which describe the change of molecular response tensors in a change of origin of the coordinate system.

Keywords Dynamic magnetizability · Molecular electric and magnetic dipoles induced by optical fields · Conditions for equivalence in a coordinate translation · Properties invariant of the origin

1 Introduction

The Kramers–Heisenberg (KH) formula provides a definition of the dynamic electric dipole polarizability of an atom in the presence of monochromatic radiation oscillating with frequency ω [1–4]. The KH expression is extended to a molecule introducing a second-rank tensor [5–7] $\alpha_{\alpha\beta}(-\omega;\omega)$, symmetric and origin independent: Its components do not vary in a translation of the coordinate system in which they are measured or calculated. Such a feature constitutes a major physical requirement, since origin-independent atomic and molecular macroscopic observables are sharply defined and experimentally accessible: A measurement is not generally conceivable for quantities which change in a translation of reference framework [8]. Typical examples are provided by the interaction energy W of a molecule in the presence of static fields, and by the permanent electric dipole moment $\mathcal{M}_\alpha^{(0)}$, if the molecule is electrically neutral. The dipole moment of molecular ions depends on the origin of the coordinate system [9]. However, it is calculated [10] and measured [11], assuming conventionally the origin on the center of mass (CM) of the ion.

The static magnetizability $\xi_{\alpha\beta} \equiv \xi_{\alpha\beta}(0;0)$ of atoms and molecules is "invariant of the origin", as shown by Van Vleck [12]. Arrighini et al. [13] reported fundamental relationships for translational invariance of $\xi_{\alpha\beta}$, which are a restatement of the Thomas–Reiche–Kuhn sum rule for oscillator strength within the dipole velocity gauge and an extension of the Condon sum rule [14] for rotational strength [8, 15, 16]. However, the diamagnetic and paramagnetic contributions to static magnetizability and static nuclear magnetic shielding depend on the origin of the reference system. Nonetheless, experimental estimates of paramagnetic contributions are obtained within the inertial principal axis system by microwave spectroscopy [17]. If the total diagonal components of the magnetizability tensor can also be measured, the numerical value of the corresponding diamagnetic contribution can be extracted [17].

Apart from remarkable exceptions of this kind, translationally invariant theoretical definitions are usually

Published as part of the special collection of articles derived from the 9th Congress on Electronic Structure: Principles and Applications (ESPA 2014).

P. Lazzeretti (✉)
Dipartimento di Scienze Chimiche e Biologiche, Università degli Studi di Modena e Reggio Emilia, Via Campi 183, 41100 Modena, Italy
e-mail: lazzeret@unimore.it

required for a meaningful evaluation of response properties via computational procedures of quantum mechanics.

Within the "dipole approximation" (DA) [18], according to which the vector potential in the radiation gauge and hence the electric field E_α are uniform over the molecular dimensions, also the induced electric dipole oscillating with the same frequency ω,

$$\mathcal{M}_\alpha = \alpha_{\alpha\beta} E_\beta \tag{1}$$

is origin independent and experimentally measurable. Within the next higher "quadrupole approximation" (QA) [15], assuming that the first spatial derivatives of the vector potential, and consequently, the magnetic field B_α and the electric field gradient $E_{\beta\alpha} \equiv \nabla_\beta E_\alpha$ of the impinging radiation are uniform [19], one obtains for diamagnetic molecules [5, 15][1]

$$\mathcal{M}_\alpha = \alpha_{\alpha\beta} E_\beta + \kappa'_{\alpha\beta} \dot{B}_\beta \omega^{-1} + \alpha_{\alpha,\beta\gamma} E_{\gamma\beta}, \tag{2}$$

introducing two additional property tensors, a mixed electric dipole–magnetic dipole polarizability $\kappa'_{\alpha\beta}(-\omega;\omega)$ and an electric dipole–electric quadrupole polarizability $\alpha_{\alpha,\beta\gamma}(-\omega;\omega)$.

Within the QA, Eq. (1) is inadequate: An origin-independent $\mathcal{M}_\alpha$ should be calculated by Eq. (2), taking also the second and third term on the r.h.s. into account [15]. In addition, one should recall that, in a translation of origin of the coordinate system,

$$\boldsymbol{r}' \to \boldsymbol{r}'' = \boldsymbol{r}' + \boldsymbol{d}, \tag{3}$$

in which both $\boldsymbol{r}'$ and $\boldsymbol{r}''$ are inside the molecular domain, the electric and magnetic fields at the different origins are related by

$$E_\alpha(\boldsymbol{r}'') = E_\alpha(\boldsymbol{r}') + E_{\beta\alpha}(\boldsymbol{r}') d_\beta + \frac{1}{2} E_{\gamma\beta\alpha}(\boldsymbol{r}') d_\beta d_\gamma + \cdots, \tag{4}$$

$$B_\alpha(\boldsymbol{r}'') = B_\alpha(\boldsymbol{r}') + B_{\beta\alpha}(\boldsymbol{r}') d_\beta + \frac{1}{2} B_{\gamma\beta\alpha}(\boldsymbol{r}') d_\beta d_\gamma + \cdots \tag{5}$$

The shift vector $\boldsymbol{d}$ in Eq. (3) is arbitrary. However, consistently with the long-wavelength approximation for monochromatic light, one may assume that $|\boldsymbol{d}|$ is smaller than the wavelength λ. With the proviso that this condition is fulfilled, truncated forms of Eqs. (4) and (5), corresponding to dipole, quadrupole, and octopole approximations outlined in Sect. 1, will also be considered on discussing the origin dependence of the induced moments, together with those reported in Sect. 5, describing the change of molecular response properties in a displacement (3).

A relationship analogous to Eq. (1),

$$M_\alpha = \xi_{\alpha\beta} B_\beta \tag{6}$$

has been proposed by Raab and de Lange [20] to define the magnetic dipole induced by the magnetic field of the monochromatic radiation, where $\xi_{\alpha\beta}(-\omega;\omega)$ is a second-rank symmetric tensor. These authors attempted at evaluating an origin-independent definition for $\xi_{\alpha\beta}$, analogous to the KH's, as a physically acceptable expression for the frequency-dependent magnetizability (FDM) of a molecule, via a linear combination of molecular polarizability tensors of the appropriate (electric octopole–magnetic quadrupole) multipole order [20–24]. Another approach had been previously used by considering the constitutive relations for the material constants [25]. Frequency-dependent magnetizabilities have been estimated by other authors [26–28]. These topics constituted the object of a PhD thesis [29].

However, according to Helgaker et al. [30], the theory for FDM remains an unresolved question. According to these authors, the derivation of the origin-independent dynamic magnetizability by Raab and de Lange [20] is based on ad hoc (but physically reasonable) conditions to be fulfilled rather than on exact conditions [30]. The correct definition of FDM is still regarded as a brain teaser.

In fact, it is necessary to delve more deeply into the problems concerning a suitable quantum mechanical definition of molecular dynamic magnetizability. One should consider a few fundamental points in connection with Eq. (6) within the "octopole approximation" (OA), explicitly adopted by considering a linear combination of polarizability tensors of electric octopole–magnetic quadrupole order [20], namely

1. the conditions for translational invariance of the total induced magnetic dipole M_α, implying its precise definition and pertaining to its measurability, should preliminarily be investigated in the light of previous results reported by Buckingham and Stiles [31],
2. in the presence of optical fields, contributions to M_α, Eq. (6), arising from the electronic interaction with the electric field gradient of the incident wave, and having the same order of magnitude as those induced by B_α, should not be omitted [19],
3. within the OA, terms up to the electric octopole and magnetic quadrupole should consistently be retained also in the electronic interaction Hamiltonian, Eq. (12) hereafter. To any higher-order approximation, one should congruously take into account higher spatial derivatives of both electric and magnetic fields,
4. within the OA retained by Raab and de Lange [20], the magnetic field on the r.h.s. of Eq. (6) cannot be consid-

[1] In Eq. (2) and throughout this paper, the fields and their spatial derivatives are evaluated at the origin of the coordinate system and a dot denotes a time derivative.

ered uniform and it should be allowed to vary according to Eq. (5), assuming a constant value of $B_{\alpha\beta}$, as well as a constant $E_{\alpha\beta\gamma}$, all over the molecular domain.

The scope of the present work is to investigate the points 1–4. A semiclassical approach is adopted, using a quantized form of electronic operators and the nonquantized description of the electromagnetic fields via the Maxwell equations. The Bloch multipolar gauge [32] has been used to define operators suitable to describe the molecular interaction with nonhomogeneous time-dependent perturbations.

The paper is arranged as follows. The electronic operators defined via a multipole expansion based on the Bloch gauge [8, 15, 16, 32, 33] are reported in Sect. 2. The expressions for the induced electric and magnetic dipole moments are reported in Sects. 3 and 4, together with those of a number of response tensors. Formulae describing the change of molecular tensors in a translation of reference system are given in Sect. 5.

The translational invariance of induced electric and magnetic dipole moments is investigated in Sect. 6, allowing for a fundamental assumption of perturbation theory, both time-independent and time-dependent, according to which the electromagnetic field and its derivatives are explicitly referred to an *arbitrary* origin of the coordinate system within the definition of the interaction Hamiltonian, Eq. (12) [19, 32, 34]. The fact that the origin can be chosen ad libitum is related to the need for a theory valid under translation of axes, Eq. (3), which implies that there is no preferential reference frame, and that the descriptions of the phenomenology given by two different (virtual) observers, each using his own coordinate system, K' and K'', with origins $\boldsymbol{r}'$ and $\boldsymbol{r}''$ respectively, are both legitimate. In particular, the nature of the *passive* transformation, Eq. (3), under which the molecule is kept in a fixed position in space, means that the results of measurements and calculations of properties operated in K' and K'' are physically equivalent. The order of magnitude of the physical quantities taken into account within different approximations is investigated in Sect. 7.

It was found that, whereas the frequency-dependent electric dipole is independent of the origin, the frequency-dependent magnetic dipole varies linearly with the distance between the origins of different coordinate systems, at variance with the implicit assumption of Ref. [20] and the conclusions reported previously assuming a $\boldsymbol{d}$ shift smaller than the molecular size [15, 16]. Therefore, as in the case of the electric dipole moment of ions [10, 11], or separate diamagnetic and paramagnetic contributions to static magnetic properties [17], a convention should be proposed to choose a certain coordinate system, e.g., with origin the molecular CM, to report values of the frequency-dependent induced magnetic dipole. Concluding remarks are presented in Sect. 8.

2 Electromagnetic multipole moment operators and the interaction Hamiltonian

We will consider a neutral molecule with n electrons and N nuclei localized near the origin of a coordinate system. The basic theory employed to determine its response properties in optical fields has been presented in previous papers [8, 15, 16, 33]. The notation adopted in these references is employed throughout the present article. SI units and the Einstein convention of summing over two repeated Greek subscripts are used.

The expressions for the electric dipole, electric quadrupole, electric octopole, magnetic dipole, and magnetic quadrupole operators consistent with the Bloch gauge [32] can be found elsewhere [8, 15, 16]. Equivalent definitions have been presented by other authors [35–38]. In addition, the gauge usually referred to as Poincaré's [18, 39–43] provides a power series for the vector potential equivalent to Bloch's [44–47].

Within the multipolar Bloch gauge [32] for the vector potential, the operator for the "perturbed" magnetic dipole moment becomes [33, 48, 49]

$$\hat{m}'_\alpha = -\frac{e}{2m_\mathrm{e}}\epsilon_{\alpha\beta\gamma}\sum_{i=1}^{n}(r_\beta\hat{\pi}_\gamma)_i = -\frac{e}{2m_\mathrm{e}}\sum_{i=1}^{n}\hat{\lambda}_{i\alpha} = \hat{m}_\alpha + \hat{\chi}^{\mathrm{d}}_{\alpha\beta}B_\beta + \hat{\chi}^{\mathrm{d}}_{\alpha\beta;\gamma}B_{\gamma\beta}, \tag{7}$$

introducing the electronic mechanical momentum operator [8, 15, 16]

$$\hat{\pi}_\alpha = \hat{p}_\alpha + eA_\alpha, \tag{8}$$

the corresponding angular momentum operator in the presence of magnetic field

$$\hat{\lambda}_\alpha = \hat{l}_\alpha + e\epsilon_{\alpha\beta\gamma}r_\beta A_\gamma, \tag{9}$$

and including terms up to the first spatial derivative of the magnetic field in Eq. (7). The operators for diamagnetic contributions to magnetic dipole and magnetic quadrupole magnetizabilities are [48, 49]

$$\hat{\chi}^{\mathrm{d}}_{\alpha\beta} = -\frac{e^2}{4m_\mathrm{e}}\sum_{i=1}^{n}\left(r^2\delta_{\alpha\beta} - r_\alpha r_\beta\right)_i, \tag{10}$$

$$\hat{\chi}^{\mathrm{d}}_{\alpha\beta;\gamma} = -\frac{e^2}{6m_\mathrm{e}}\sum_{i=1}^{n}\left[\left(r^2\delta_{\alpha\beta} - r_\alpha r_\beta\right)r_\gamma\right]_i, \tag{11}$$

denoting by $r^2 = r_\alpha r_\alpha$ the squared modulus of the electronic position vector. In these relationships, a semicolon separates sets of symmetric indices, which can be freely permuted within each set. The first-order interaction Bloch Hamiltonian [32] can be written in the form

$$H^{(1)} = -\hat{\mu}_\alpha E_\alpha - \hat{\mu}_{\alpha\beta} E_{\beta\alpha} - \hat{m}'_\alpha B_\alpha - \hat{\mu}_{\alpha\beta\gamma} E_{\gamma\beta\alpha} - \hat{m}'_{\alpha\beta} B_{\beta\alpha}, \tag{12}$$

including terms up to the electric octopole $\hat{\mu}_{\alpha\beta\gamma}$ and magnetic quadrupole $\hat{m}'_{\alpha\beta}$. Analogous terms result from the same order of expansion of the vector potential within the approach of Stephens [19].

In the definitions (7) and (12), all the electronic operators, the fields, and their derivatives are defined with respect to a given origin of the coordinate system [19, 34]. In the following, it is assumed that such an origin can arbitrarily be chosen.

The perturbation is represented as a monochromatic plane wave propagating in the z direction. The electric field $\boldsymbol{E}$ and the magnetic induction $\boldsymbol{B}$ are sinusoidal functions of position and time. In real form, indicating by $\boldsymbol{k}$ the wave vector whose magnitude is the wave number

$$k = 2\pi/\lambda = \omega/c,$$

and by $\tilde{\boldsymbol{x}}$, $\tilde{\boldsymbol{y}}$ the unit vectors parallel to the x and y axes, the transverse fields

$$\boldsymbol{E}(z,t) = E_0 \cos(kz - \omega t + \delta)\tilde{\boldsymbol{x}}, \tag{13}$$

$$\boldsymbol{B}(z,t) = B_0 \cos(kz - \omega t + \delta)\tilde{\boldsymbol{y}}, \tag{14}$$

are perpendicular to the direction of propagation and oscillate in the zx and yz planes, respectively [50]. They are in phase and mutually orthogonal, and their amplitudes are related by

$$B_0 = \frac{k}{\omega} E_0 = \frac{1}{c} E_0. \tag{15}$$

Within the long-wavelength approximation, it is assumed that the spatial extent of the electron cloud of the molecule is small compared with the distance characterizing the spatial variations of the vector potential $\boldsymbol{A}$ (and hence $\boldsymbol{E}$ within the DA), e.g., with respect to the wavelength λ of the impinging radiation [18].

3 Induced electric dipole moment

A series of relationships for the dynamic electric dipole moment induced by the monochromatic wave is obtained by time-dependent perturbation theory [51], substituting the electric dipole operator $\hat{\mu}_\alpha$ in the general formula [5, 8, 15, 16, 34] for the expectation value of a quantum mechanical operator in the perturbed state $|\Phi_a\rangle$. The arbitrary origin is denoted by **0** in the following equations. Within the DA approximation,

$$\Delta\langle\hat{\mu}_\alpha\rangle = \alpha_{\alpha\beta} E_\beta(\mathbf{0},t) + \alpha'_{\alpha\beta}\dot{E}_\beta(\mathbf{0},t)\omega^{-1} \equiv \mathcal{M}_\alpha, \tag{16}$$

within the QA approximation,

$$\begin{aligned}\Delta\langle\hat{\mu}_\alpha\rangle = {} & \alpha_{\alpha\beta} E_\beta(\mathbf{0},t) + \alpha'_{\alpha\beta}\dot{E}_\beta(\mathbf{0},t)\omega^{-1} \\ & + \kappa_{\alpha\beta} B_\beta(\mathbf{0},t) + \kappa'_{\alpha\beta}\dot{B}_\beta(\mathbf{0},t)\omega^{-1} \\ & + \alpha_{\alpha,\beta\gamma} E_{\gamma\beta}(\mathbf{0},t) + \alpha'_{\alpha,\beta\gamma}\dot{E}_{\gamma\beta}(\mathbf{0},t)\omega^{-1} \equiv \mathcal{M}_\alpha,\end{aligned} \tag{17}$$

within the OA approximation

$$\begin{aligned}\Delta\langle\hat{\mu}_\alpha\rangle = {} & \alpha_{\alpha\beta} E_\beta(\mathbf{0},t) + \alpha'_{\alpha\beta}\dot{E}_\beta(\mathbf{0},t)\omega^{-1} \\ & + \kappa_{\alpha\beta} B_\beta(\mathbf{0},t) + \kappa'_{\alpha\beta}\dot{B}_\beta(\mathbf{0},t)\omega^{-1} \\ & + \alpha_{\alpha,\beta\gamma} E_{\gamma\beta}(\mathbf{0},t) + \alpha'_{\alpha,\beta\gamma}\dot{E}_{\gamma\beta}(\mathbf{0},t)\omega^{-1} \\ & + \kappa_{\alpha,\beta\gamma} B_{\gamma\beta}(\mathbf{0},t) + \kappa'_{\alpha,\beta\gamma}\dot{B}_{\gamma\beta}(\mathbf{0},t)\omega^{-1} \\ & + \alpha_{\alpha,\beta\gamma\delta} E_{\delta\gamma\beta}(\mathbf{0},t) + \alpha'_{\alpha,\beta\gamma\delta}\dot{E}_{\delta\gamma\beta}(\mathbf{0},t)\omega^{-1} \equiv \mathcal{M}_\alpha.\end{aligned} \tag{18}$$

To avoid misunderstanding, the uniformity of E_α within DA, of B_α and $E_{\alpha\beta}$ within QA, and of $B_{\alpha\beta}$ and $E_{\alpha\beta\gamma}$ within OA, is meant in connection with the expression for the interaction Hamiltonian, Eq. (12). However, on applying time-dependent perturbation theory [34, 51], the time derivative of the electric field appears in the second term of Eq. (16), which, according to the Maxwell equation $\dot{\boldsymbol{E}} = c^2 \boldsymbol{\nabla} \times \boldsymbol{B}$, implies that it accounts for nonuniformity of the magnetic field, limited to the antisymmetric components of the magnetic field gradient. On the other hand, for a diamagnetic molecule, the second term vanishes, as $\alpha'_{\alpha\beta}$ is a null tensor, unless the function $|a\rangle$ contains an imaginary contribution, that is, it corresponds to a magnetic field perturbed electronic state [5]. In such a case, the second term describes nonlinear response [52]. Therefore, there is no contradiction between Eq. (16) and the concept of dipole approximation, according to which only terms linear in E_α are included in the interaction Hamiltonian, Eq. (12). Analogous considerations can be made within Eqs. (17) and (18), since, assuming linear response, there is no mixing of terms involving unprimed $\alpha_{\alpha\beta}, \kappa_{\alpha\beta}, \ldots$ and primed $\alpha'_{\alpha\beta}, \kappa'_{\alpha\beta}, \ldots$ tensors.

The explicit definitions of the response properties appearing in Eqs. (16)–(18) are given hereafter, assuming a transparent medium, indicating by $|a\rangle$ the nondegenerate reference state, by $|j\rangle$ the excited states eigenfunctions of the unperturbed Hamiltonian $H^{(0)}$, and denoting by $\Re$ and $\Im$ the real and imaginary parts:

Electric dipole polarizability

$$\alpha_{\alpha\beta} = \frac{1}{\hbar} \sum_{j \neq a} \frac{2\omega_{ja}}{\omega_{ja}^2 - \omega^2} \Re\{\langle a|\hat{\mu}_\alpha|j\rangle\langle j|\hat{\mu}_\beta|a\rangle\}, \tag{19}$$

$$\alpha'_{\alpha\beta} = -\frac{1}{\hbar} \sum_{j \neq a} \frac{2\omega}{\omega_{ja}^2 - \omega^2} \Im\{\langle a|\hat{\mu}_\alpha|j\rangle\langle j|\hat{\mu}_\beta|a\rangle\}. \tag{20}$$

Electric dipole–magnetic dipole polarizability

$$\kappa_{\alpha\beta} = \frac{1}{\hbar}\sum_{j\neq a}\frac{2\omega_{ja}}{\omega_{ja}^2-\omega^2}\Re\{\langle a|\hat{\mu}_\alpha|j\rangle\langle j|\hat{m}_\beta|a\rangle\}, \tag{21}$$

$$\kappa'_{\alpha\beta} = -\frac{1}{\hbar}\sum_{j\neq a}\frac{2\omega}{\omega_{ja}^2-\omega^2}\Im\{\langle a|\hat{\mu}_\alpha|j\rangle\langle j|\hat{m}_\beta|a\rangle\}. \tag{22}$$

Electric dipole–electric quadrupole polarizability

$$\alpha_{\alpha,\beta\gamma} = \frac{1}{\hbar}\sum_{j\neq a}\frac{2\omega_{ja}}{\omega_{ja}^2-\omega^2}\Re\{\langle a|\hat{\mu}_\alpha|j\rangle\langle j|\hat{\mu}_{\beta\gamma}|a\rangle\}, \tag{23}$$

$$\alpha'_{\alpha,\beta\gamma} = -\frac{1}{\hbar}\sum_{j\neq a}\frac{2\omega}{\omega_{ja}^2-\omega^2}\Im\{\langle a|\hat{\mu}_\alpha|j\rangle\langle j|\hat{\mu}_{\beta\gamma}|a\rangle\}. \tag{24}$$

Electric dipole–magnetic quadrupole polarizability

$$\kappa_{\alpha,\beta\gamma} = \frac{1}{\hbar}\sum_{j\neq a}\frac{2\omega_{ja}}{\omega_{ja}^2-\omega^2}\Re\{\langle a|\hat{\mu}_\alpha|j\rangle\langle j|\hat{m}_{\beta\gamma}|a\rangle\}, \tag{25}$$

$$\kappa'_{\alpha,\beta\gamma} = -\frac{1}{\hbar}\sum_{j\neq a}\frac{2\omega}{\omega_{ja}^2-\omega^2}\Im\{\langle a|\hat{\mu}_\alpha|j\rangle\langle j|\hat{m}_{\beta\gamma}|a\rangle\}. \tag{26}$$

Electric dipole–electric octopole polarizability

$$\alpha_{\alpha,\beta\gamma\delta} = \frac{1}{\hbar}\sum_{j\neq a}\frac{2\omega_{ja}}{\omega_{ja}^2-\omega^2}\Re\{\langle a|\hat{\mu}_\alpha|j\rangle\langle j|\hat{\mu}_{\beta\gamma\delta}|a\rangle\}, \tag{27}$$

$$\alpha'_{\alpha,\beta\gamma\delta} = -\frac{1}{\hbar}\sum_{j\neq a}\frac{2\omega}{\omega_{ja}^2-\omega^2}\Im\{\langle a|\hat{\mu}_\alpha|j\rangle\langle j|\hat{\mu}_{\beta\gamma\delta}|a\rangle\}. \tag{28}$$

4 Induced magnetic dipole moment

The dynamic magnetic dipole moment induced by the monochromatic wave is expressed via relationships analogous to Eqs. (16)–(18), obtained by substituting $\hat{m}'_\alpha$, Eq. (7), in the general formula from perturbation theory [5, 15, 16]. The DA relationship for this property is

$$\Delta\langle\hat{m}_\alpha\rangle = \kappa_{\beta\alpha}E_\beta - \kappa'_{\beta\alpha}\dot{E}_\beta\omega^{-1} \equiv M_\alpha. \tag{29}$$

Within the QA approximation

$$\begin{aligned}\Delta\langle\hat{m}'_\alpha\rangle &= \kappa_{\beta\alpha}E_\beta - \kappa'_{\beta\alpha}\dot{E}_\beta\omega^{-1}\\ &+ \chi_{\alpha\beta}B_\beta + \chi'_{\alpha\beta}\dot{B}_\beta\omega^{-1}\\ &+ D_{\alpha,\beta\gamma}E_{\gamma\beta} + D'_{\alpha,\beta\gamma}\dot{E}_{\gamma\beta}\omega^{-1} \equiv M_\alpha,\end{aligned} \tag{30}$$

within the OA approximation,

$$\begin{aligned}\Delta\langle\hat{m}'_\alpha\rangle &= \kappa_{\beta\alpha}E_\beta - \kappa'_{\beta\alpha}\dot{E}_\beta\omega^{-1}\\ &+ \chi_{\alpha\beta}B_\beta + \chi'_{\alpha\beta}\dot{B}_\beta\omega^{-1}\\ &+ D_{\alpha,\beta\gamma}E_{\gamma\beta} + D'_{\alpha,\beta\gamma}\dot{E}_{\gamma\beta}\omega^{-1}\\ &+ \chi_{\alpha,\beta\gamma}B_{\gamma\beta} + \chi'_{\alpha,\beta\gamma}\dot{B}_{\gamma\beta}\omega^{-1}\\ &+ D_{\alpha,\beta\gamma\delta}E_{\delta\gamma\beta} + D'_{\alpha,\beta\gamma\delta}\dot{E}_{\delta\gamma\beta}\omega^{-1} \equiv M_\alpha.\end{aligned} \tag{31}$$

The response tensors appearing in Eqs. (29) and (30) are defined hereafter:

Diamagnetic contribution to dipole magnetizability

$$\chi^{\mathrm{d}}_{\alpha\beta} = \left\langle a|\hat{\chi}^{\mathrm{d}}_{\alpha\beta}|a\right\rangle, \tag{32}$$

Paramagnetic contribution to dipole magnetizability

$$\chi^{\mathrm{p}}_{\alpha\beta} = \frac{1}{\hbar}\sum_{j\neq a}\frac{2\omega_{ja}}{\omega_{ja}^2-\omega^2}\Re\{\langle a|\hat{m}_\alpha|j\rangle\langle j|\hat{m}_\beta|a\rangle\}, \tag{33}$$

$$\chi'_{\alpha\beta} = -\frac{1}{\hbar}\sum_{j\neq a}\frac{2\omega}{\omega_{ja}^2-\omega^2}\Im\{\langle a|\hat{m}_\alpha|j\rangle\langle j|\hat{m}_\beta|a\rangle\}, \tag{34}$$

Total dipole magnetizability

$$\chi_{\alpha\beta} = \chi^{\mathrm{p}}_{\alpha\beta} + \chi^{\mathrm{d}}_{\alpha\beta} = \chi_{\beta\alpha}. \tag{35}$$

Magnetic dipole–electric quadrupole polarizability

$$D_{\alpha,\beta\gamma} = \frac{1}{\hbar}\sum_{j\neq a}\frac{2\omega_{ja}}{\omega_{ja}^2-\omega^2}\Re\{\langle a|\hat{m}_\alpha|j\rangle\langle j|\hat{\mu}_{\beta\gamma}|a\rangle\}, \tag{36}$$

$$D'_{\alpha,\beta\gamma} = -\frac{1}{\hbar}\sum_{j\neq a}\frac{2\omega}{\omega_{ja}^2-\omega^2}\Im\{\langle a|\hat{m}_\alpha|j\rangle\langle j|\hat{\mu}_{\beta\gamma}|a\rangle\}. \tag{37}$$

Diamagnetic contribution to magnetic dipole–magnetic quadrupole polarizability

$$\chi^{\mathrm{d}}_{\alpha\beta;\gamma} = \left\langle a|\hat{\chi}^{\mathrm{d}}_{\alpha\beta;\gamma}|a\right\rangle = \chi^{\mathrm{d}}_{\beta\alpha;\gamma}, \tag{38}$$

Paramagnetic contribution to magnetic dipole–magnetic quadrupole polarizability

$$\chi^{\mathrm{p}}_{\alpha,\beta\gamma} = \frac{1}{\hbar}\sum_{j\neq a}\frac{2\omega_{ja}}{\omega_{ja}^2-\omega^2}\Re\{\langle a|\hat{m}_\alpha|j\rangle\langle j|\hat{m}_{\beta\gamma}|a\rangle\}, \tag{39}$$

$$\chi'_{\alpha,\beta\gamma} = -\frac{1}{\hbar}\sum_{j\neq a}\frac{2\omega}{\omega_{ja}^2-\omega^2}\Im\{\langle a|\hat{m}_\alpha|j\rangle\langle j|\hat{m}_{\beta\gamma}|a\rangle\}, \tag{40}$$

Total magnetic dipole–magnetic quadrupole polarizability

$$\chi_{\alpha,\beta\gamma} = \chi^{\mathrm{p}}_{\alpha,\beta\gamma} + \chi^{\mathrm{d}}_{\alpha\beta;\gamma} \equiv \chi_{\beta\gamma,\alpha}. \tag{41}$$

Magnetic dipole–electric octopole polarizability

$$D_{\alpha,\beta\gamma\delta} = \frac{1}{\hbar}\sum_{j\neq a}\frac{2\omega_{ja}}{\omega_{ja}^2-\omega^2}\Re\{\langle a|\hat{m}_\alpha|j\rangle\langle j|\hat{\mu}_{\beta\gamma\delta}|a\rangle\}, \tag{42}$$

$$D'_{\alpha,\beta\gamma\delta} = -\frac{1}{\hbar}\sum_{j\neq a}\frac{2\omega}{\omega_{ja}^2-\omega^2}\Im\{\langle a|\hat{m}_\alpha|j\rangle\langle j|\hat{\mu}_{\beta\gamma\delta}|a\rangle\}. \tag{43}$$

In the absence of an external magnetic field, the electronic wave functions may be chosen to be real, so that, for instance [5],

$$\alpha'_{\alpha\beta} = \alpha'_{\alpha,\beta\gamma} = \alpha'_{\alpha,\beta\gamma\delta} = \kappa_{\alpha\beta} = \kappa_{\alpha,\beta\gamma} = \chi'_{\alpha\beta} = \chi'_{\alpha,\beta\gamma} = 0.$$

For diamagnetic molecules, assuming that the wave function $|a\rangle$ corresponds to a magnetic field perturbed state, nonvanishing primed tensors such as $\alpha'_{\alpha\beta}$, $\chi'_{\alpha\beta}$ should be replaced by higher-rank tensors [52].

5 Change of response properties and equivalence conditions in a translation of coordinates

Let us consider a translation of origin of the coordinate system defined via Eq. (3). Using Eqs. (4) and (5), off-diagonal hypervirial theorems [8, 15, 16, 33, 53], the Maxwell equations in the absence of sources, and related expressions, e.g.,

$$B_{\alpha\alpha} = 0, \quad \dot{B}_\alpha = -\epsilon_{\alpha\beta\gamma}E_{\beta\gamma}, \quad \dot{B}_{\delta\alpha} = -\epsilon_{\alpha\beta\gamma}E_{\delta\beta\gamma}, \tag{44}$$

$$B_\alpha\omega = \epsilon_{\alpha\beta\gamma}\dot{E}_{\beta\gamma}\omega^{-1}, \quad B_{\delta\alpha}\omega = \epsilon_{\alpha\beta\gamma}\dot{E}_{\delta\beta\gamma}\omega^{-1}, \tag{45}$$

and the harmonicity conditions

$$\ddot{E}_\alpha = -\omega^2 E_\alpha, \quad \ddot{B}_\alpha = -\omega^2 B_\alpha, \tag{46}$$

it is proven in Sect. 6 that the electric dipole induced in the electron cloud by optical fields is origin independent within DA, QA, and OA. An analogous discussion is presented for the induced magnetic dipole in the same section. However, a preliminary analysis has been made to weigh the magnitude of the admissible shift vectors within the DA and QA in Sect. 5.1. The transformation laws for some response tensors are given in Sect. 5.2.

5.1 Magnitude of origin-shift vectors

The electric field gradient obtained by differentiating Eq. (13),

$$E_{zx} = \frac{\omega}{c}E_0\sin\left[\omega\left(t-\frac{z}{c}\right)\right], \tag{47}$$

for $\omega = 3.198\times10^{15}$ rad s^{-1}, corresponding to the sodium D-line, i.e., for $\lambda = 5.890\times10^{-7}$ m, is as big as $1.067\times10^7 E_0$, measured in Vm^{-2} for E_0 in Vm^{-1}. Thus, if it is assumed within the DA that the electric field is uniform over the molecular dimensions, so that only the first term in the interaction Hamiltonian, Eq. (12), is retained, in principle, it should consistently be admitted that $d_\beta \approx 0$ in Eq. (4) in order for the origin to be legitimately chosen anywhere inside the charge distribution. However, for the (2*R*)-*N*-methyloxaziridine chiral molecule considered in Sect. 7, the nuclear skeleton is completely contained in a cube of 5×10^{-10} m; thus, a shift d_β of the same magnitude can be safely chosen.

For molecules of size comparable with λ, within the QA, that is, assuming that the electric field gradient is spatially uniform so that the electric field varies linearly in the molecular domain, one can infer that there is an upper bound to the shift vector, $d_\beta < 1\times10^{-8}$ m in Eq. (4). In fact, let us assume that the electric field, Eq. (13), as a function of z, varies sinusoidally for $t = 0$ and $\delta = -\pi/2$. Since $\sin\alpha \approx \alpha$ for $\alpha = \omega z/c$ varying in the interval 0–0.1 rad, one has that $0 \le z \le 1\times10^{-8}$ m. Therefore, within the QA, different origins in Eq. (3) should be separated by a distance varying within this range.

5.2 Translation of frequency-dependent response tensors

Equations describing the change of a number of relevant operators in a coordinate translation are found elsewhere [15, 16, 48, 49]. For the response properties, a series of relationships is reported hereafter:

Electric dipole–magnetic dipole polarizability

$$\kappa_{\alpha\beta}(\boldsymbol{r}'') = \kappa_{\alpha\beta}(\boldsymbol{r}') + \frac{\omega}{2}\epsilon_{\beta\gamma\delta}\alpha'_{\alpha\gamma}d_\delta, \tag{48}$$

$$\kappa'_{\alpha\beta}(\boldsymbol{r}'') = \kappa'_{\alpha\beta}(\boldsymbol{r}') - \frac{\omega}{2}\epsilon_{\beta\gamma\delta}\alpha_{\alpha\gamma}d_\delta. \tag{49}$$

Electric dipole–electric quadrupole polarizability

$$\alpha_{\alpha,\beta\gamma}(\boldsymbol{r}'') = \alpha_{\alpha,\beta\gamma}(\boldsymbol{r}') - \frac{1}{2}\left(\alpha_{\alpha\beta}d_\gamma + \alpha_{\alpha\gamma}d_\beta\right), \tag{50}$$

$$\alpha'_{\alpha,\beta\gamma}(\boldsymbol{r}'') = \alpha'_{\alpha,\beta\gamma}(\boldsymbol{r}') - \frac{1}{2}\left(\alpha'_{\alpha\beta}d_\gamma + \alpha'_{\alpha\gamma}d_\beta\right). \tag{51}$$

Electric dipole–magnetic quadrupole polarizability

$$\begin{aligned}\kappa_{\alpha,\beta\gamma}(\boldsymbol{r}'') = {}& \kappa_{\alpha,\beta\gamma}(\boldsymbol{r}') \\ & - \kappa_{\alpha\beta}(\boldsymbol{r}')d_\gamma + \frac{1}{3}\delta_{\beta\gamma}\kappa_{\alpha\delta}(\boldsymbol{r}')d_\delta \\ & - \frac{\omega}{3}\epsilon_{\beta\delta\epsilon}\alpha'_{\alpha,\gamma\epsilon}(\boldsymbol{r}')d_\delta + \frac{\omega}{3}\epsilon_{\beta\delta\epsilon}\alpha'_{\alpha\epsilon}d_\gamma d_\delta,\end{aligned} \tag{52}$$

$$\kappa'_{\alpha,\beta\gamma}(\boldsymbol{r}'') = \kappa'_{\alpha,\beta\gamma}(\boldsymbol{r}') - \kappa'_{\alpha\beta}(\boldsymbol{r}')d_\gamma + \frac{1}{3}\delta_{\beta\gamma}\kappa'_{\alpha\delta}(\boldsymbol{r}')d_\delta + \frac{\omega}{3}\epsilon_{\beta\delta\epsilon}\alpha_{\alpha,\gamma\epsilon}(\boldsymbol{r}')d_\delta - \frac{\omega}{3}\epsilon_{\beta\delta\epsilon}\alpha_{\alpha\epsilon}d_\gamma d_\delta. \quad (53)$$

Electric dipole–electric octopole polarizability

$$\alpha_{\alpha,\beta\gamma\delta}(\boldsymbol{r}'') = \alpha_{\alpha,\beta\gamma\delta}(\boldsymbol{r}') - \frac{1}{3}\left[\alpha_{\alpha,\beta\gamma}(\boldsymbol{r}')d_\delta + \alpha_{\alpha,\beta\delta}(\boldsymbol{r}')d_\gamma + \alpha_{\alpha,\gamma\delta}(\boldsymbol{r}')d_\beta\right] + \frac{1}{6}\left(\alpha_{\alpha\beta}d_\gamma d_\delta + \alpha_{\alpha\gamma}d_\beta d_\delta + \alpha_{\alpha\delta}d_\beta d_\gamma\right), \quad (54)$$

$$\alpha'_{\alpha,\beta\gamma\delta}(\boldsymbol{r}'') = \alpha'_{\alpha,\beta\gamma\delta}(\boldsymbol{r}') - \frac{1}{3}\left[\alpha'_{\alpha,\beta\gamma}(\boldsymbol{r}')d_\delta + \alpha'_{\alpha,\beta\delta}(\boldsymbol{r}')d_\gamma + \alpha'_{\alpha,\gamma\delta}(\boldsymbol{r}')d_\beta\right] + \frac{1}{6}\left(\alpha'_{\alpha\beta}d_\gamma d_\delta + \alpha'_{\alpha\gamma}d_\beta d_\delta + \alpha'_{\alpha\delta}d_\beta d_\gamma\right). \quad (55)$$

Dipole magnetizability

$$\chi_{\alpha\beta}(\boldsymbol{r}'') = \chi_{\alpha\beta}(\boldsymbol{r}') - \frac{\omega}{2}\left[\epsilon_{\alpha\gamma\delta}\kappa'_{\gamma\beta}(\boldsymbol{r}') + \epsilon_{\beta\gamma\delta}\kappa'_{\gamma\alpha}(\boldsymbol{r}')\right]d_\delta + \frac{\omega^2}{4}\epsilon_{\alpha\gamma\delta}\epsilon_{\beta\lambda\mu}\alpha_{\gamma\lambda}d_\delta d_\mu, \quad (56)$$

$$\chi_{\alpha\alpha}(\boldsymbol{r}'') = \chi_{\alpha\alpha}(\boldsymbol{r}') - \omega\epsilon_{\alpha\beta\gamma}\kappa'_{\beta\alpha}(\boldsymbol{r}')d_\gamma + \frac{\omega^2}{4}\alpha_{\beta\gamma}(d^2\delta_{\beta\gamma} - d_\beta d_\gamma), \quad (57)$$

$$\chi'_{\alpha\beta}(\boldsymbol{r}'') = \chi'_{\alpha\beta}(\boldsymbol{r}') + \frac{\omega}{2}\left[\epsilon_{\alpha\gamma\delta}\kappa_{\gamma\beta}(\boldsymbol{r}') - \epsilon_{\beta\gamma\delta}\kappa_{\gamma\alpha}(\boldsymbol{r}')\right]d_\delta + \frac{\omega^2}{4}\epsilon_{\alpha\gamma\delta}\epsilon_{\beta\lambda\mu}\alpha'_{\gamma\lambda}d_\delta d_\mu. \quad (58)$$

Magnetic dipole–magnetic quadrupole polarizability

$$\chi_{\alpha,\beta\gamma}(\boldsymbol{r}'') = \chi_{\alpha,\beta\gamma}(\boldsymbol{r}') - \chi_{\alpha\beta}d_\gamma + \frac{1}{3}\delta_{\beta\gamma}\chi_{\alpha\delta}d_\delta - \left[\frac{\omega}{3}\epsilon_{\beta\delta\epsilon}D'_{\alpha,\gamma\epsilon}(\boldsymbol{r}') - \frac{\omega}{2}\epsilon_{\alpha\delta\epsilon}\kappa'_{\epsilon,\beta\gamma}(\boldsymbol{r}')\right]d_\delta - \left[\frac{\omega}{3}\epsilon_{\beta\delta\epsilon}\kappa'_{\epsilon\alpha}(\boldsymbol{r}') + \frac{\omega}{2}\epsilon_{\alpha\delta\epsilon}\kappa'_{\epsilon\beta}(\boldsymbol{r}')\right]d_\gamma d_\delta + \frac{\omega}{6}\epsilon_{\alpha\delta\epsilon}\left[\delta_{\beta\gamma}\kappa'_{\epsilon\eta}(\boldsymbol{r}') + \omega\epsilon_{\beta\eta\theta}\alpha_{\epsilon,\gamma\theta}(\boldsymbol{r}')\right]d_\delta d_\eta - \frac{\omega^2}{6}\epsilon_{\alpha\delta\epsilon}\epsilon_{\beta\eta\theta}\alpha'_{\epsilon\theta}d_\gamma d_\delta d_\eta. \quad (59)$$

$$\chi'_{\alpha,\beta\gamma}(\boldsymbol{r}'') = \chi'_{\alpha,\beta\gamma}(\boldsymbol{r}') - \chi'_{\alpha\beta}d_\gamma + \frac{1}{3}\delta_{\beta\gamma}\chi'_{\alpha\delta}d_\delta + \left[\frac{\omega}{3}\epsilon_{\beta\delta\epsilon}D_{\alpha,\gamma\epsilon}(\boldsymbol{r}') - \frac{\omega}{2}\epsilon_{\alpha\delta\epsilon}\kappa_{\epsilon,\beta\gamma}(\boldsymbol{r}')\right]d_\delta - \left[\frac{\omega}{3}\epsilon_{\beta\delta\epsilon}\kappa_{\epsilon\alpha}(\boldsymbol{r}') - \frac{\omega}{2}\epsilon_{\alpha\delta\epsilon}\kappa_{\epsilon\beta}(\boldsymbol{r}')\right]d_\gamma d_\delta - \frac{\omega}{6}\epsilon_{\alpha\delta\epsilon}\left[\delta_{\beta\gamma}\kappa_{\epsilon\eta}(\boldsymbol{r}') - \omega\epsilon_{\beta\eta\theta}\alpha'_{\epsilon,\gamma\theta}(\boldsymbol{r}')\right]d_\delta d_\eta - \frac{\omega^2}{6}\epsilon_{\alpha\delta\epsilon}\epsilon_{\beta\eta\theta}\alpha'_{\epsilon\theta}d_\gamma d_\delta d_\eta. \quad (60)$$

Magnetic dipole–electric quadrupole polarizability

$$D_{\alpha,\beta\gamma}(\boldsymbol{r}'') = D_{\alpha,\beta\gamma}(\boldsymbol{r}') - \frac{1}{2}\left[\kappa_{\beta\alpha}(\boldsymbol{r}')d_\gamma + \kappa_{\gamma\alpha}(\boldsymbol{r}')d_\beta\right] + \frac{\omega}{2}\epsilon_{\alpha\delta\epsilon}\alpha'_{\epsilon,\beta\gamma}(\boldsymbol{r}')d_\delta - \frac{\omega}{4}\epsilon_{\alpha\delta\epsilon}\left(\alpha'_{\epsilon\beta}d_\gamma + \alpha'_{\epsilon\gamma}d_\beta\right)d_\delta, \quad (61)$$

$$D'_{\alpha,\beta\gamma}(\boldsymbol{r}'') = D'_{\alpha,\beta\gamma}(\boldsymbol{r}') + \frac{1}{2}\left[\kappa'_{\beta\alpha}(\boldsymbol{r}')d_\gamma + \kappa'_{\gamma\alpha}(\boldsymbol{r}')d_\beta\right] - \frac{\omega}{2}\epsilon_{\alpha\delta\epsilon}\alpha_{\epsilon,\beta\gamma}(\boldsymbol{r}')d_\delta + \frac{\omega}{4}\epsilon_{\alpha\delta\epsilon}\left(\alpha_{\beta\epsilon}d_\gamma + \alpha_{\gamma\epsilon}d_\beta\right)d_\delta. \quad (62)$$

Magnetic dipole–electric octopole polarizability

$$D_{\alpha,\beta\gamma\delta}(\boldsymbol{r}'') = D_{\alpha,\beta\gamma\delta}(\boldsymbol{r}') - \frac{1}{3}\left[D_{\alpha,\beta\gamma}(\boldsymbol{r}')d_\delta + D_{\alpha,\gamma\delta}(\boldsymbol{r}')d_\beta + D_{\alpha,\beta\delta}(\boldsymbol{r}')d_\gamma\right] + \frac{\omega}{2}\epsilon_{\alpha\eta\epsilon}\alpha'_{\epsilon,\beta\gamma\delta}(\boldsymbol{r}')d_\eta + \frac{1}{6}\left[\kappa_{\beta\alpha}(\boldsymbol{r}')d_\gamma d_\delta + \kappa_{\gamma\alpha}(\boldsymbol{r}')d_\beta d_\delta + \kappa_{\delta\alpha}(\boldsymbol{r}')d_\beta d_\gamma\right] - \frac{\omega}{6}\epsilon_{\alpha\eta\epsilon}\left[\alpha'_{\epsilon,\beta\gamma}(\boldsymbol{r}')d_\delta + \alpha'_{\epsilon,\gamma\delta}(\boldsymbol{r}')d_\beta + \alpha'_{\epsilon,\beta\delta}(\boldsymbol{r}')d_\gamma\right]d_\eta + \frac{\omega}{12}\epsilon_{\alpha\eta\epsilon}\left(\alpha'_{\epsilon\beta}d_\gamma d_\delta + \alpha'_{\epsilon\gamma}d_\beta d_\delta + \alpha'_{\epsilon\delta}d_\beta d_\gamma\right)d_\eta, \quad (63)$$

$$D'_{\alpha,\beta\gamma\delta}(\boldsymbol{r}'') = D'_{\alpha,\beta\gamma\delta}(\boldsymbol{r}') - \frac{1}{3}\left[D'_{\alpha,\beta\gamma}(\boldsymbol{r}')d_\delta + D'_{\alpha,\gamma\delta}(\boldsymbol{r}')d_\beta + D'_{\alpha,\beta\delta}(\boldsymbol{r}')d_\gamma\right] - \frac{\omega}{2}\epsilon_{\alpha\eta\epsilon}\alpha_{\epsilon,\beta\gamma\delta}(\boldsymbol{r}')d_\eta - \frac{1}{6}\left[\kappa'_{\beta\alpha}(\boldsymbol{r}')d_\gamma d_\delta + \kappa'_{\gamma\alpha}(\boldsymbol{r}')d_\beta d_\delta + \kappa'_{\delta\alpha}(\boldsymbol{r}')d_\beta d_\gamma\right] + \frac{\omega}{6}\epsilon_{\alpha\eta\epsilon}\left[\alpha_{\epsilon,\beta\gamma}(\boldsymbol{r}')d_\delta + \alpha_{\epsilon,\gamma\delta}(\boldsymbol{r}')d_\beta + \alpha_{\epsilon,\beta\delta}(\boldsymbol{r}')d_\gamma\right]d_\eta - \frac{\omega}{12}\epsilon_{\alpha\eta\epsilon}\left(\alpha_{\epsilon\beta}d_\gamma d_\delta + \alpha_{\epsilon\gamma}d_\beta d_\delta + \alpha_{\epsilon\delta}d_\beta d_\gamma\right)d_\eta. \quad (64)$$

Table 1 Conversion factors from a.u. to SI units

Quantity	Symbol	Numerical value	Unit
$\alpha_{\alpha\beta}$	$e^2a_0^2/E_\mathrm{h}$	$1.6487772536 \times 10^{-41}$	Fm^2
$\alpha_{\alpha,\beta\gamma}$	$e^2a_0^3/E_\mathrm{h}$	$8.724953446 \times 10^{-52}$	Fm^3
$\alpha_{\alpha,\beta\gamma\delta}$	$e^2a_0^4/E_\mathrm{h}$	$4.617046510 \times 10^{-62}$	Fm^4
$\kappa'_{\alpha\beta}$	$e^2a_0^3/\hbar$	$3.607015578 \times 10^{-35}$	$\mathrm{Fm}^3\,\mathrm{s}^{-1}$
$\kappa'_{\alpha,\beta\gamma}$	$e^2a_0^4/\hbar$	$1.908750435 \times 10^{-45}$	$\mathrm{Fm}^4\,\mathrm{s}^{-1}$
$\chi_{\alpha\beta}$	$e^2a_0^2/m_\mathrm{e}$	$7.891036433 \times 10^{-29}$	JT^{-2}
$\chi_{\alpha,\beta\gamma}$	$e^2a_0^3/m_\mathrm{e}$	$4.175756632 \times 10^{-39}$	$\mathrm{JT}^{-2}\,\mathrm{m}$
$D'_{\alpha,\beta\gamma}$	$e^2a_0^4/\hbar$	$1.908750435 \times 10^{-45}$	$\mathrm{Fm}^4\,\mathrm{s}^{-1}$
$D'_{\alpha,\beta\gamma\delta}$	$e^2a_0^5/\hbar$	$1.010067227 \times 10^{-55}$	$\mathrm{Fm}^5\,\mathrm{s}^{-1}$

From CODATA compilation [57]

6 Variation of frequency-dependent moments in a coordinate translation

Within the DA, the electric field is assumed to be uniform over the molecular dimensions and the frequency-dependent electric dipole polarizability, Eqs. (19) and (20), is invariant in the translation of reference frame defined via Eq. (3). Therefore, the induced electric dipole, Eq. (16), stays the same, that is,

$$\Delta\langle\hat{\mu}_\alpha(\boldsymbol{r}'')\rangle = \Delta\langle\hat{\mu}_\alpha(\boldsymbol{r}')\rangle. \tag{65}$$

This result is also obtained within the next higher QA approximation taking into account Eqs. (4), (21)–(24), and (48)–(51), that is, the induced electric dipole approximated via Eq. (17) is translationally invariant. The same conclusion is arrived at for the induced electric dipole, Eq. (18), within the OA, allowing for Eqs. (4), (5), and the full series of relationships (48)–(55) describing the change of the response tensors, Eqs. (21)–(28).

For the induced orbital magnetic dipole within the DA, Eq. (29), allowing for the harmonicity condition characterizing the electric field of the monochromatic wave, Eq. (46), and for Eqs. (48)–(49), one finds [8]

$$\Delta\langle\hat{m}'_\alpha(\boldsymbol{r}'')\rangle = \Delta\langle\hat{m}'_\alpha(\boldsymbol{r}')\rangle + \frac{1}{2}d_\gamma\epsilon_{\alpha\beta\gamma}\frac{\partial}{\partial t}\Delta\langle\hat{\mu}_\beta(\boldsymbol{r}')\rangle. \tag{66}$$

The origin $\boldsymbol{r}'$ of the induced electric dipole on the r.h.s. of Eq. (66) may be dropped owing to its translational invariance, Eq. (65).

In a previous paper [8], it was erroneously assumed that the second term on the r.h.s. of Eq. (66), being a time derivative, could be eliminated by time averaging. In fact, time averaging would also eliminate $\Delta\langle\hat{m}'_\alpha\rangle$ on both sides of Eq. (66) because of the periodic nature of all the quantities involved. Thus, the magnetic moment formally depends on the origin if there is a time-dependent electric dipole. Equation (66) generalizes a result previously reported by Buckingham and Stiles [31].

For a diamagnetic chiral molecule, characterized by nonvanishing diagonal components of $\kappa'_{\alpha\beta}$, there are components of the induced electric and magnetic dipoles in the same α direction, i.e., $\Delta\langle\hat{\mu}_\alpha\rangle$ and $\Delta\langle\hat{m}'_\alpha\rangle$. However, they do not mix in Eq. (66), because of the Levi-Civita tensor in the second term on the r.h.s. of Eq. (66). This term vanishes for a translation in the direction of either the electric or magnetic dipoles oscillating at right angles to the wave vector $\boldsymbol{k}$. Therefore, origin translations should be considered only for $d_z \neq 0$.

Equation (66) is also obtained within QA, allowing for Eqs. (48), (49), (56), (58), (61), and (62), and within the OA, using Eqs. (48), (49), and the full series, Eqs. (56)–(64). The second term of Eq. (66) is related to the oscillating mechanical momentum [15, 54] induced in the electrons by the monochromatic wave, e.g., within the QA,

$$\begin{aligned}\Delta\langle\hat{\Pi}_\alpha\rangle &= o_{\alpha\beta}E_\beta + o'_{\alpha\beta}\dot{E}_\beta\omega^{-1} + o_{\alpha,\beta\gamma}E_{\gamma\beta} \\ &\quad + o'_{\alpha,\beta\gamma}\dot{E}_{\gamma\beta}\omega^{-1} + v_{\alpha\beta}B_\beta + v'_{\alpha\beta}\dot{B}_\beta\omega^{-1} \\ &\equiv \frac{m_\mathrm{e}}{e}\Big[\alpha'_{\alpha\beta}E_\beta\omega - \alpha_{\alpha\beta}\dot{E}_\beta + \alpha'_{\alpha,\beta\gamma}E_{\gamma\beta}\omega \\ &\quad -\alpha_{\alpha,\beta\gamma}\dot{E}_{\gamma\beta} + \kappa'_{\alpha\beta}B_\beta\omega - \kappa_{\alpha\beta}\dot{B}_\beta\Big] \\ &= -\frac{m_\mathrm{e}}{e}\frac{\partial}{\partial t}\Delta\langle\hat{\mu}_\alpha\rangle,\end{aligned} \tag{67}$$

defining the total electronic operator

$$\hat{\boldsymbol{\Pi}} = \sum_{i=1}^{n}\hat{\boldsymbol{\pi}}_i,$$

according to Eq. (8), so that Eq. (66) is rewritten in the form

$$\Delta\langle\hat{m}'_\alpha(\boldsymbol{r}'')\rangle = \Delta\langle\hat{m}'_\alpha(\boldsymbol{r}')\rangle + \frac{e}{2m_\mathrm{e}}d_\beta\epsilon_{\alpha\beta\gamma}\Delta\langle\hat{\Pi}_\gamma\rangle. \tag{68}$$

Using Eqs. (4) and (48)–(51), it is immediately verified that $\Delta\langle\hat{\Pi}_\alpha\rangle$ is origin independent, in accord with Eq. (65).

The origin dependence of the induced magnetic dipole moment, Eqs. (66) and (68), is related to a corresponding relationship involving the total angular momentum in the presence of nonuniform magnetic field

$$\hat{\Lambda}_\alpha = \sum_{i=1}^{n}\hat{\lambda}_{i\alpha} = \hat{L}_\alpha + I_{\alpha\beta}\Omega_\beta + \cdots,$$

see Eq. (9). The operator for the moment of inertia of the electrons

$$\hat{I}_{\alpha\beta} = m_\mathrm{e}\sum_{i=1}^{n}(r^2\delta_{\alpha\beta} - r_\alpha r_\beta)_i$$

is coupled to the electronic Larmor frequency

$$\Omega_\alpha = \frac{e}{2m_e} B_\alpha$$

in the second term on the r.h.s.

Eventually, a relation analogous to Eq. (66) has been obtained for the dipole moments induced by a precessing nuclear moment [55].

7 Orders of magnitude

The magnitude of the contributions to the electric and magnetic dipoles induced in the (2*R*)-*N*-methyloxaziridine chiral molecule has been estimated from near Hartree–Fock theoretical predictions obtained in a recent investigation [56]. Quantities given there in a.u. are converted into SI by factors reported in Table 1. Within the QA, taking $\alpha_{xx} = 7.225 \times 10^{-40}$ Fm^2, $\kappa'_{xy} = 1.191 \times 10^{-35}$ Fm^3 s^{-1}, $\alpha_{x,xz} = 9.894 \times 10^{-52}$ Fm^3, and $\lambda = 5.890^{-7}$ m, one finds the three contributions

$$\begin{aligned} &7.225 \times 10^{-40} E_0 \cos\left[\omega\left(t - \frac{z}{c}\right)\right] \\ &- 3.973 \times 10^{-44} E_0 \sin\left[\omega\left(t - \frac{z}{c}\right)\right] \\ &+ 1.056 \times 10^{-44} E_0 \sin\left[\omega\left(t - \frac{z}{c}\right)\right] \end{aligned}$$

to $\mathcal{M}_x$, Eq. (17), measured in Cm for E_0 in Vm^{-1}. The second and third contributions, arising, respectively, from the time derivative of the magnetic field and from the electric field gradient, are $\delta = -\pi/2$ out-of-phase and four orders of magnitude smaller than the dominant first contribution from the electric field of the incident wave.

For the induced magnetic dipole, using $\chi_{yy} = -5.786 \times 10^{-28}$ JT^{-2} from Ref. [56], and assuming $E_0 = 1 \times 10^5$ Vm^{-1} in Eq. (13), one has $B_0 = 3.336 \times 10^{-4}$ T from Eq. (15). Thus, the contributions to M_y, Eq. (30), expressed in JT^{-1}, respectively, from the time derivative of the electric field and from the magnetic field, are

$$\begin{aligned} &1.191 \times 10^{-30} \sin\left[\omega\left(t - \frac{z}{c}\right)\right] \\ &- 1.930 \times 10^{-31} \cos\left[\omega\left(t - \frac{z}{c}\right)\right]. \end{aligned}$$

The contribution from the time derivative of the electric field gradient, with $D'_{y,zx}$ in a.u., see Table 1 for the conversion factor to SI units, is

$$2.036 \times 10^{-33} D'_{y,zx} \cos\left[\omega\left(t - \frac{z}{c}\right)\right] \text{JT}^{-1}.$$

Applying Eq. (66) and using computed values [56], one obtains

$$\begin{aligned} M_y(\boldsymbol{r}'') &= -\left[\kappa'_{xy}(\boldsymbol{r}')\omega^{-1} + \frac{1}{2} d_z \alpha_{xx}\right] \dot{E}_x \\ &= -(3.724 \times 10^{-51} + 3.613 \times 10^{-40} d_z) \dot{E}_x, \end{aligned}$$

in which the second term is much greater than the first one unless $d_z \approx 0$ according to the DA, as expounded in Sect. 5.1. Therefore, within the DA, the induced magnetic dipole moment M_y should be referred to an origin chosen by some reasonable criterion, e.g., the CM or the center of electron charge, and considered approximately invariant of the origin.

Within the QA, the magnetic dipole moment induced in the *y* direction is

$$M_y = -\kappa'_{xy} \dot{E}_x \omega^{-1} + \chi_{yy} B_y + D'_{y,xz} \dot{E}_{zx} \omega^{-1}$$

and from Eq. (66)

$$M_y(\boldsymbol{r}'') = M_y(\boldsymbol{r}') - \frac{1}{2} d_z (\alpha_{xx} \dot{E}_x + \kappa'_{xy} \ddot{B}_y \omega^{-1} + \alpha_{x,xz} \dot{E}_{zx}),$$

then for the terms depending on the magnetic field, with $\ddot{B}_y = -\omega^2 B_y$,

$$\begin{aligned} &\left(\chi_{yy} + \frac{1}{2} d_z \kappa'_{xy} \omega\right) B_y \\ &\quad = -\left(5.786 \times 10^{-28} - 3.809 \times 10^{-20} d_z\right) B_y \end{aligned}$$

and for the terms depending on the time derivative of the electric field gradient

$$\begin{aligned} &\left(D'_{y,xz} \omega^{-1} - \frac{1}{2} d_z \alpha_{x,xz}\right) \dot{E}_{zx} \\ &\quad = \left(5.969 \times 10^{-61} D'_{y,xz}(\text{a.u.}) - 4.947 \times 10^{-52} d_z\right) \dot{E}_{zx}. \end{aligned}$$

From these results, one can arrive at plausible conclusions on the magnitude of the allowed shift vectors $\boldsymbol{d}$ separating different origins within the QA: The contribution to M_y provided by the magnetic field B_y can be considered virtually independent of the origin for $d_z \approx \pm 2.5 \times 10^{-10}$ m from the CM, e.g., for a shift comparable with the molecular size, see Sect. 5.1 and previous references [15, 16].

For a freely tumbling (2*R*)-*N*-methyloxaziridine chiral molecule in disordered phase, from calculated [56] average quantities $\alpha_{av} = (1/3)\alpha_{\alpha\alpha} = 6.103 \times 10^{-40}$ Fm^2 and $\kappa'_{av} = (1/3)\kappa'_{\alpha\alpha} = -6.190 \times 10^{-37}$ Fm^3 s^{-1}, and assuming $E_0 = 1 \times 10^5$ Vm^{-1} in Eq. (13), the contributions to the electric and magnetic dipoles induced in the *x* direction are

$$\mathcal{M}_x = \alpha_{av} E_x = 6.103 \times 10^{-35} \cos\left[\omega\left(t - \frac{z}{c}\right)\right] \text{Cm}$$

and

$$M_x = -\kappa'_{av} \dot{E}_x \omega^{-1} = -6.190 \times 10^{-32} \sin\left[\omega\left(t - \frac{z}{c}\right)\right] \text{JT}^{-1}.$$

These properties are origin independent within the DA owing to the translational invariance of α_{av} and κ'_{av}. Estimates of electric and magnetic dipole moments induced in a freely tumbling (2*R*)-*N*-methyloxaziridine molecule within the QA can further be obtained using calculated average magnetizability [56] $\chi_{av} = (1/3)\chi_{\alpha\alpha} = -6.418 \times 10^{-28}$ JT^{-2} and $\alpha'_{\alpha,\beta\gamma}\epsilon_{\alpha\beta\gamma} = 0 = D'_{\alpha,\beta\gamma}\epsilon_{\alpha\beta\gamma}$.

8 Concluding remarks

Allowing for approximations of increasing order to the interaction Hamiltonian, within the framework of time-dependent perturbation theory, relationships have been obtained, which define the electric and magnetic dipoles induced in the electrons of a molecule by a monochromatic wave represented classically via the Maxwell equations. As the electronic operators, the electromagnetic field, and its spatial derivatives appearing in the interaction Hamiltonian, Eq. (12), explicitly depend on the origin of the coordinate system, we compared theoretical expressions of induced dipole moments arrived at by two different observers in distinct reference systems K' and K'', with parallel axes and origins $\boldsymbol{r}'$ and $\boldsymbol{r}''$ respectively. Each observer evaluates the induced moments using his own reference system, that is, his local interaction Hamiltonian. The molecule acted upon by the electromagnetic fields lies in a fixed position in space: Due to the nature of passive transformation relating K' and K'', and to nonexistence of a preferential coordinate system, the two alternative "pictures" must be fully equivalent. In particular, the observable induced moments predicted or measured by different observers are expected to be the same.

The induced electric dipole, rationalized via molecular response tensors of increasing rank coupled to fields and spatial field derivatives, Eqs. (16)–(18), is origin independent. The induced magnetic dipole, similarly expressed via intrinsic molecular tensors, Eqs. (29)–(31), formally depends on the distance between two different origins of the coordinate system multiplied by the partial time derivative of the induced electric dipole.

None of the three expressions, Eqs. (29)–(31), arrived at in this study for the magnetic dipole moment induced in a molecule by optical fields, can be cast in the form of Eq. (6),

$$M_\alpha = \xi_{\alpha\beta}B_\beta.$$

In fact, within the dipole approximation, according to which the electric field of a monochromatic wave is spatially uniform over the molecular domain, the magnetic field simply does not appear in Eq. (29). In the relationship obtained via the quadrupole approximation, Eq. (30), that is, assuming spatially uniform magnetic field and electric field gradient within the interaction Hamiltonian, Eq. (12), the term depending on B_α cannot be separated from the contribution of the same magnitude depending on $\dot{E}_{\alpha\beta}$. Within the next octopole approximation of spatially uniform magnetic field gradient $B_{\alpha\beta}$ and electric field second derivative $E_{\alpha\beta\gamma}$ within the interaction Hamiltonian, Eq. (12), other higher-rank tensors must be included in the expression for the induced magnetic dipole.

These results would seem to imply that a quantum mechanical definition of frequency-dependent second-rank magnetizability of the form $\xi_{\alpha\beta}(-\omega;\omega)$ is not accessible. The tensor $\chi_{\alpha\beta}(-\omega;\omega)$ in Eqs. (30), (31), (33) and (35) is the quantum mechanical FDM.

References

1. Kramers HA, Heisenberg W (1925) Z Phys 31:681
2. Dirac PAM (1927) Proc R Soc Lond Ser A 114:243
3. Breit G (1932) Rev Mod Phys 4:504
4. Wijers C (2004) Phys Rev A 70:063807
5. Buckingham AD (1967) Adv Chem Phys 12:107
6. Bogaard MP, Orr BJ (1975) Electric dipole polarisabilities of atoms and molecules. In: Buckingham AD (ed) International review of science. Molecular structure and properties. Physical chemistry series two, vol 2. Butterworths, London, pp 149–194
7. Buckingham AD (1978) Basic theory of intermolecular forces: applications to small molecules. In: Pullman B (ed) Intermolecular interactions: from diatomics to biopolymers. Wiley, Chichester, pp 1–67
8. Lazzeretti P (2014) Int J Quantum Chem 114:1364
9. Landau LD, Lifshitz EM (1979) The classical theory of fields, 4th revised english edition. Pergamon Press, Oxford
10. Rosmus P (1979) Theor Chim Acta 51:359
11. Laughlin KB, Blake GA, Cohen RC, Hovde DC, Saykally RJ (1987) Phys Rev Lett 58:996
12. Vleck JHV (1932) The theory of electric and magnetic susceptibilities. Oxford University Press, Oxford
13. Arrighini GP, Maestro M, Moccia R (1968) J Chem Phys 49:882
14. Condon EU (1937) Rev Mod Phys 9:432
15. Lazzeretti P (1989) Adv Chem Phys 75:507
16. Lazzeretti P (2003) Electric and magnetic properties of molecules. In: Wilson S (ed) Handbook of molecular physics and quantum chemistry, part 1, chapt 3, vol 1. Wiley, Chichester, pp 53–145
17. Flygare WH (1974) Chem Rev 74:653
18. Cohen-Tannoudji C, Dupont-Roc J, Grynberg G (1989) Photon and atoms. Wiley, New York
19. Stephens PJ (1970) J Chem Phys 52:3489
20. Raab RE, De Lange OL (2006) Mol Phys 104:1925
21. Raab RE, de Lange OL (2005) Multipole theory in electromagnetism. Oxford Science, Oxford
22. de Lange OL, Raab RE, Welter A (2012) J Math Phys 53:013513
23. de Lange OL, Raab RE, Welter A (2012) J Math Phys 53:073518
24. Welter A, Raab RE, de Lange OL (2013) J Math Phys 54:023512
25. Graham EB, Raab RE (2000) Proc R Soc Lond 456:1193
26. Autschbach J, Ziegler T (2002) J Chem Phys 116:891
27. Yoshizawa T, Hada M (2007) J Comput Chem 28:740
28. Krykunov M, Autschbach J (2007) J Chem Phys 126:024101
29. Anelli M (2010) Frequency-dependent magnetizability, University of Tromsø Faculty of Science and Technology, Department of Physics and Technology, http://hdl.handle.net/10037/2961

30. Helgaker T, Coriani S, Jørgensen P, Kristensen K, Olsen J, Ruud K (2012) Chem Rev 112:543
31. Buckingham AD, Stiles PJ (1974) Acc Chem Res 7:258 see, in particular, Eq. A3 and the analysis reported in the Appendix
32. Bloch F (1961) Zur wirkung äußerer elektromagnetischer felder auf kleine systeme. In: Bopp F (ed) W. Heisenberg und die Physik Unserer Zeit, Friedr. Wieveg & Son, Braunschweig, pp 93–102
33. Provasi PF, Pagola GI, Ferraro MB, Pelloni S, Lazzeretti P (2014) J Phys Chem A 118:6333
34. Eyring H, Walter J, Kimball GE (1944) Quantum chemistry. Wiley, New York
35. Buckingham AD, Stiles PJ (1972) Mol Phys 24:99
36. Barron LD, Gray CG (1973) J Phys A Math Nucl Gen 6:59
37. Woolley RG (1973) J Phys B Atom Mol Phys 6:L97
38. Craig DP, Thirunamachandran T (1984) Molecular quantum electrodynamics. Academic Press, New York
39. Valatin JG (1954) Proc R Soc Lond A 222:93
40. Brittin WE, Smythe WR, Wyss W (1982) Am J Phys 50:693
41. Skagerstram B-SK (1983) Am J Phys 51:1148
42. Kobe DH (1982) Am J Phys 50:128
43. Saue T (2002) Post Dirac–Hartree–Fock methods—properties. In: Schwerdtfeger P (ed) Relativistic electronic structure theory. Part 1. Fundamentals. Elsevier, Amsterdam, p 332
44. Stewart AM (1999) J Phys A Math Nucl Gen 32:6091
45. Stewart AM (2000) J Phys A Math Nucl Gen 33:9165
46. Stewart AM (2000) Aust J Phys 53:613
47. Stewart AM (2003) Euro J Phys 24:519
48. Lazzeretti P (1993) Theor Chim Acta 87:59
49. Faglioni F, Ligabue A, Pelloni S, Soncini A, Lazzeretti P (2004) Chem Phys 304:289
50. Griffiths DJ (1999) Introduction to electrodynamics. Prentice Hall, Upper Saddle River, 07458, p 303
51. Langhoff PW, Epstein ST, Karplus M (1972) Rev Mod Phys 44:602
52. Buckingham AD, Parlett LC (1994) Science 264:1748
53. Epstein ST (1974) The variation method in quantum chemistry. Academic Press, New York
54. Lazzeretti P, Bertocchi P (1987) Chem Phys Lett 138:465
55. Lazzeretti P, Soncini A, Zanasi R (2008) Theor Chem Acc 119:99
56. Caputo MC, Pelloni S, Lazzeretti P (2015) Int J Quantum Chem (submitted)
57. Mohr PJ, Taylor BN, Newell DB (2008) Rev Mod Phys 80:633

Theor Chem Acc (2015) 134:9
DOI 10.1007/s00214-014-1611-5

REGULAR ARTICLE

Toward (car)borane-based molecular magnets

Josep M. Oliva · Diego R. Alcoba · Ofelia B. Oña · Alicia Torre · Luis Lain · Josef Michl

Received: 18 October 2014 / Accepted: 19 December 2014 / Published online: 18 January 2015

Abstract In a previous work, we reported the electronic structure of dimer diradicals composed of two $S = ½$ *closo*-carborane $CB_{11}H_{12}^{\cdot}$ structural units (Theor. Chem. Acc. (2013) 132: 1329). That work has been extended here in order to describe a linear dimer, a linear and a cyclical trimer, and a tetrahedral structure of these units connected by means of a $–CH_2–$ bridge. A mapping of the resulting spin states onto a Heisenberg spin Hamiltonian is proposed for these new chains providing the evaluation of spin-exchange coupling constants.

Keywords Carboranes · Spin population · Heisenberg spin Hamiltonian · Heisenberg coupling constants

Published as part of the special collection of articles derived from the 9th Congress on Electronic Structure: Principles and Applications (ESPA 2014).

J. M. Oliva (✉)
Instituto de Química-Física "Rocasolano", Consejo Superior de Investigaciones Científicas, 28006 Madrid, Spain
e-mail: j.m.oliva@iqfr.csic.es

D. R. Alcoba
Departamento de Física, Facultad de Ciencias Exactas y Naturales, Universidad de Buenos Aires, Buenos Aires, Argentina

D. R. Alcoba
Instituto de Física de Buenos Aires, Consejo Nacional de Investigaciones Científcas y Técnicas, Ciudad Universitaria, 1428 Buenos Aires, Argentina

O. B. Oña
Instituto de Investigaciones Fisicoquímicas Teóricas y Aplicadas, Universidad Nacional de La Plata, CCT La Plata, Consejo Nacional de Investigaciones Científicas y Técnicas, Diag. 113 y 64 (S/N), Sucursal 4, CC 16, 1900 La Plata, Argentina

A. Torre · L. Lain
Departamento de Química Física, Facultad de Ciencia y Tecnología, Universidad del País Vasco, Apdo. 644, 48080 Bilbao, Spain

J. Michl
Institute of Organic Chemistry and Biochemistry, Academy of Sciences of the Czech Republic, 166 10 Prague 6, Czech Republic

1 Introduction

The magnetic properties in individual molecules, connected to the total spin S of the system, can be manifested macroscopically with properties such as ferromagnetism, antiferromagnetism, and ferrimagnetism [1]. Molecular magnets encompass active fields of research within current and future fundamental and applied sciences [2], such as spintronics, quantum computing, information storage, and nanomedicine [3–5].

As regards to polyhedral heteroborane clusters and particularly the very stable icosahedral carboranes [6], little is known about their magnetic properties. In 1996, Michl et al. [7] obtained the crystal structure of a carborane-based stable free radical: dodecamethylcarba-*closo*-dodecaboranyl $(CB_{11}Me_{12})^{\cdot}$. According to their measurements using electron-spin resonance (ESR) spectroscopy, one can flip

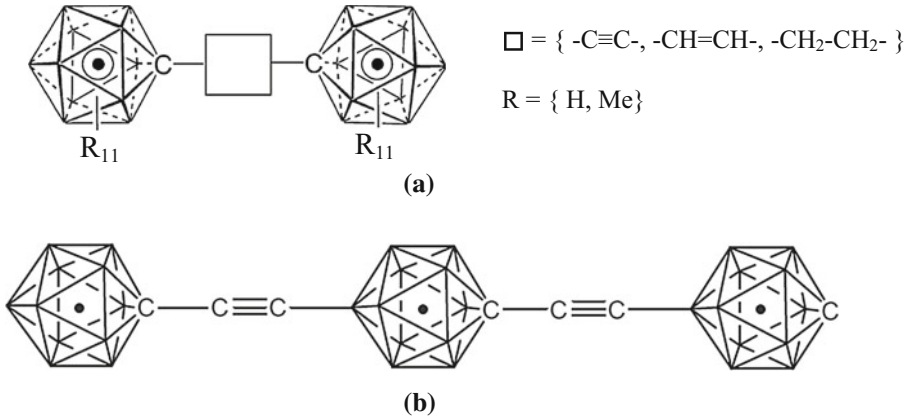

Fig. 1 **a** Two icosahedral $(CB_{11}R_{12})^{\cdot}$ radicals connected through the carbon atom from the icosahedral cage with different bridge units □ = {–C≡C–, –CH=CH–, $–CH_2–CH_2–$} and substituents *R* on each non-connected vertex of the cage, with *R* = {H, Me}. **b** Three carborane radical units $CB_{11}H_{12}^{\cdot}$ connected through the carbon cage atom with acetylene bridge units, with the same cage orientation. In all cases, the *dot* represents an unpaired electron

the spin of the unpaired electron of this radical using a magnetic field of 37 Gauss, which corresponds to a radiofrequency of 104 MHz. Later on, in 2007, these radical units were experimentally connected by means of acetylene and ethylene bridges [8], through the carbon atom of each carborane cage, as displayed in Fig. 1a, with bridge units {–C≡C–} and {–CH=CH–}. In this work [8], they did not report on ESR measurements for the diradicals. The electronic structure of singlet ($S = 0$) and triplet ($S = 1$) electronic states derived from the simplified systems of Fig. 1a was then analyzed, where each methyl group was simplified with a hydrogen atom, with acetylene [9], ethylene, and ethane [10] bridge units (Fig. 1a, with □ = {–C≡C–, –CH=CH–, $–CH_2–CH_2–$} and R = H). The quantum chemical computations showed that the ground state of the diradicals, independently from the bridge unit, is of singlet nature with a very close—almost degenerate—triplet state, {0.004, 0.080, 0.0005 eV} above in energy for the bridge units □ = {–C≡C–, –CH=CH–, $–CH_2–CH_2–$}, respectively.

One can proceed further from Fig. 1a and connect the simplified carborane cage $CB_{11}H_{12}^{\cdot}$ in 1D, 2D, and 3D [11]. From a theoretical point of view, elongation of the 1D chain was carried out by connecting three carborane units with acetylene bridge units, as shown in Fig. 1b, thus having three unpaired electrons, one on each cage [11]. The electronic structure computations showed that for the linear triradical, the ground state is of high-spin nature ($S = 3/2$), with a doublet state ($S = 1/2$) lying 0.013 eV above in energy.

As we shall explain below (vide infra Results ad Discussion), one can further consider the possibility of connecting the radical carborane cages (as magnetic units with $S = 1/2$) with methylene as a bridge unit, into different architectural constructs in 1D, 2D, and 3D. In this work, we will consider a "linear" dimer, a "linear" and "cyclic" three-unit structure, and a "tetrahedral" (four-unit) structure. The reason for generating such structures stems from the possibility of determining the electronic structure for the low-lying spin states of the system. Hence, one could then map these results onto a Heisenberg spin Hamiltonian, thus allowing the connection between experimental and theoretical studies of these polyradical networks [12, 13]. This approach has been applied even to large systems [14] requiring the determination of the corresponding coupling constants.

The organization of this article is as follows. Section 2 summarizes the theoretical concepts and the notation used in this work. In Sect. 3, we report the computational details and the results found in four carborane compounds with different geometrical arrangements as well as the corresponding discussion. Finally, in the last section, we point out the concluding remarks of this work.

1.1 The theoretical models

The phenomenological Heisenberg spin Hamiltonian in Eq. 1 predicts the energy of the different spin states of a many-electron system, provided the spin and electron (orbital) degrees of freedom are independent from each other,

$$\hat{H} = E_0 - 2\sum_{A<B} J_{AB}\hat{S}_A\hat{S}_B \tag{1}$$

where E_0 is a constant meaning the origin of the energy scale chosen for that model; *A* and *B* are the magnetic sites within the system, J_{AB} is the coupling constant between them, and $\hat{S}_A$ and $\hat{S}_B$ are the spin operators assigned to those centers.

In Noodleman's treatment [15, 16], the expectation values of the Hamiltonian $\hat{H}$ in Eq. 1 are calculated through Slater determinants. One of these determinants is the highest pure spin multiplet (*HS*) in which all its orbitals are singly occupied with spin up (a ferromagnetic disposal). The other determinants are mixed spin symmetry and lowered spin symmetry; they are denominated broken-symmetry (*BS*) states possessing singly occupied orbitals with spin down (an antiferromagnetic disposal). Consequently, the differences in the energies corresponding to the determinants are

$$E_{HS} - E_{BS} = -2 \sum_{A<B} J_{AB} \left[\left\langle \hat{S}_A \hat{S}_B \right\rangle^{HS} - \left\langle \hat{S}_A \hat{S}_B \right\rangle^{BS} \right] \quad (2)$$

There are different possibilities to formulate the *BS* determinants so that Eq. 2 constitutes a system of linear equations in the variables J_{AB} provided that the two-center expectation values $\langle \hat{S}_A \hat{S}_B \rangle^{HS}$ and $\langle \hat{S}_A \hat{S}_B \rangle^{BS}$ individually, or their differences $(\langle \hat{S}_A \hat{S}_B \rangle^{HS} - \langle \hat{S}_A \hat{S}_B \rangle^{BS})$, have previously been evaluated. The information on the spin attributed to the fragments *A* and *B* may be obtained from the partitioning of the expectation values of the spin operator

$$\left\langle \hat{S}^2 \right\rangle = \sum_A \sum_B \left\langle \hat{S}_A \hat{S}_B \right\rangle \quad (3)$$

The one-center local spin (*LS*) quantity $\langle \hat{S}_A^2 \rangle$ allows one to determine the spin state of an atom or group of atoms in a molecule or cluster, while the spin correlation between fragments *A* and *B* is described by the expectation value $\langle \hat{S}_A \hat{S}_B \rangle$. This value provides an important tool for linking experimental results interpreted in terms of the Heisenberg spin Hamiltonian to quantum chemical calculations. We will consider the general algebraic expression for $\langle \hat{S}_A \hat{S}_B \rangle$ reported in Refs. [17–21]. The terms $\langle \hat{S}_A^2 \rangle$ and $\langle \hat{S}_A \hat{S}_B \rangle$ (arising from the spin atomic operator formulation) will be identified, respectively, with $\langle \hat{S}^2 \rangle_A$ and $\langle \hat{S}^2 \rangle_{AB}$ in those references.

We have constructed these systems of equations with each of the determinants of type *BS,* which represent all possible spin orientations of the individual centers plus the determinant that describes the *HS* state. In our scheme, each cage of the $CB_{11}H_{12}^{\cdot}$ radical, which possesses an unpaired electron, has been regarded as a magnetic site while the contribution of the bridges $–CH_2–$ has been neglected. We have evaluated the different coupling constants J_{AB} (as well as the E_0 quantity) in systems of two, three, and four magnetic sites that have been summarized in the following subsections. Likewise, we have followed the working hypothesis considering the magnetic sites as equivalent (whenever possible), and consequently, only a few different coupling constants must be evaluated. The spin symmetry of the multiplet states has been identified with the S_z quantum number of the *HS* and *BS* Slater determinants. In order to describe the four polyradicals mentioned in the Introduction, we have considered the cases described below.

1.1.1 Two magnetic sites system

The general solution of the Hamiltonian consists of one single *J* for two singlet (*S*) and triplet (*T*) states

$$E_T = E_0 + J_{12} \left\langle \hat{S}^2 \right\rangle_{12}^{T}$$

$$E_s = E_0 + J_{12} \left\langle \hat{S}^2 \right\rangle_{12}^{S}$$

1.1.2 Three magnetic sites systems

In this case, the general solution of the Hamiltonian yields two doublet (D_1 and D_2) and one quartet states (*Q*).

One single *J*:

$$E_Q = E_0 + J_{12} \left\langle \hat{S}^2 \right\rangle_{12}^{Q} + J_{13} \left\langle \hat{S}^2 \right\rangle_{13}^{Q} + J_{23} \left\langle \hat{S}^2 \right\rangle_{23}^{Q}$$

$$E_D = E_0 + J_{12} \left\langle \hat{S}^2 \right\rangle_{12}^{D} + J_{13} \left\langle \hat{S}^2 \right\rangle_{13}^{D} + J_{23} \left\langle \hat{S}^2 \right\rangle_{23}^{D}$$

$$J_{12} = J_{23}; J_{12} = J_{13}$$

Two different *Js*:

$$E_Q = E_0 + J_{12} \left\langle \hat{S}^2 \right\rangle_{12}^{Q} + J_{13} \left\langle \hat{S}^2 \right\rangle_{13}^{Q} + J_{23} \left\langle \hat{S}^2 \right\rangle_{23}^{Q}$$

$$E_{D_1} = E_0 + J_{12} \left\langle \hat{S}^2 \right\rangle_{12}^{D_1} + J_{13} \left\langle \hat{S}^2 \right\rangle_{13}^{D_1} + J_{23} \left\langle \hat{S}^2 \right\rangle_{23}^{D_1}$$

$$E_{D_2} = E_0 + J_{12} \left\langle \hat{S}^2 \right\rangle_{12}^{D_2} + J_{13} \left\langle \hat{S}^2 \right\rangle_{13}^{D_2} + J_{23} \left\langle \hat{S}^2 \right\rangle_{23}^{D_2}$$

$$J_{12} = J_{23}$$

1.1.3 Four magnetic sites system

One single *J*:

In the four magnetic site system case, a singular value decomposition may also be used to solve the resulting overdetermined system of linear equations [22], which arises from considering the different spin configurations (*Q* now means quintuplet)

$$E_Q = E_0 + J_{12} \left\langle \hat{S}^2 \right\rangle_{12}^{Q} + J_{13} \left\langle \hat{S}^2 \right\rangle_{13}^{Q} + J_{14} \left\langle \hat{S}^2 \right\rangle_{14}^{Q} + J_{23} \left\langle \hat{S}^2 \right\rangle_{23}^{Q} + J_{24} \left\langle \hat{S}^2 \right\rangle_{24}^{Q} + J_{34} \left\langle \hat{S}^2 \right\rangle_{34}^{Q}$$

$$E_T = E_0 + J_{12} \left\langle \hat{S}^2 \right\rangle_{12}^{T} + J_{13} \left\langle \hat{S}^2 \right\rangle_{13}^{T} + J_{14} \left\langle \hat{S}^2 \right\rangle_{14}^{T} + J_{23} \left\langle \hat{S}^2 \right\rangle_{23}^{T} + J_{24} \left\langle \hat{S}^2 \right\rangle_{24}^{T} + J_{34} \left\langle \hat{S}^2 \right\rangle_{34}^{T}$$

$$E_S = E_0 + J_{12} \left\langle \hat{S}^2 \right\rangle_{12}^{S} + J_{13} \left\langle \hat{S}^2 \right\rangle_{13}^{S} + J_{14} \left\langle \hat{S}^2 \right\rangle_{14}^{S} + J_{23} \left\langle \hat{S}^2 \right\rangle_{23}^{S} + J_{24} \left\langle \hat{S}^2 \right\rangle_{24}^{S} + J_{34} \left\langle \hat{S}^2 \right\rangle_{34}^{S}$$

$$J_{12} = J_{13}; J_{12} = J_{14}; J_{12} = J_{23}; J_{12} = J_{24}; J_{12} = J_{34}; J_{23} = J_{24}; J_{23} = J_{34}; J_{24} = J_{34}$$

The determination of coupling constants solving these linear equation systems is based on the previous evaluation

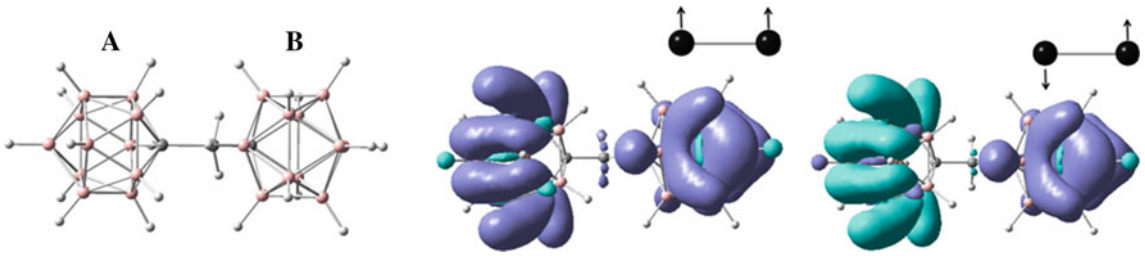

Fig. 2 Geometrical arrangement and calculated spin densities of the linear dimer constituted by two carborane radical units $CB_{11}H_{12}^{\cdot}$ connected through the carbon cage atoms with an methylene bridge unit

Table 1 Local spin populations, energies (au), $\langle \hat{S}^2 \rangle$ expectation values, and coupling constants (in cm^{-1}) for the linear dimer studied in this work in the *HS* and *BS* states

Local spins					
HS state			*BS* state		
	A	B		A	B
A	0.746	0.248	A	0.745	−0.244
B	0.248	0.753	B	−0.244	0.746
	Energy		$<\hat{S}^2>$	$J_{AB}(YA)$	$J_{AB}(LS)$
HS state	−675.703373		2.0076	6.004	6.101
BS state	−675.703345		1.0073		

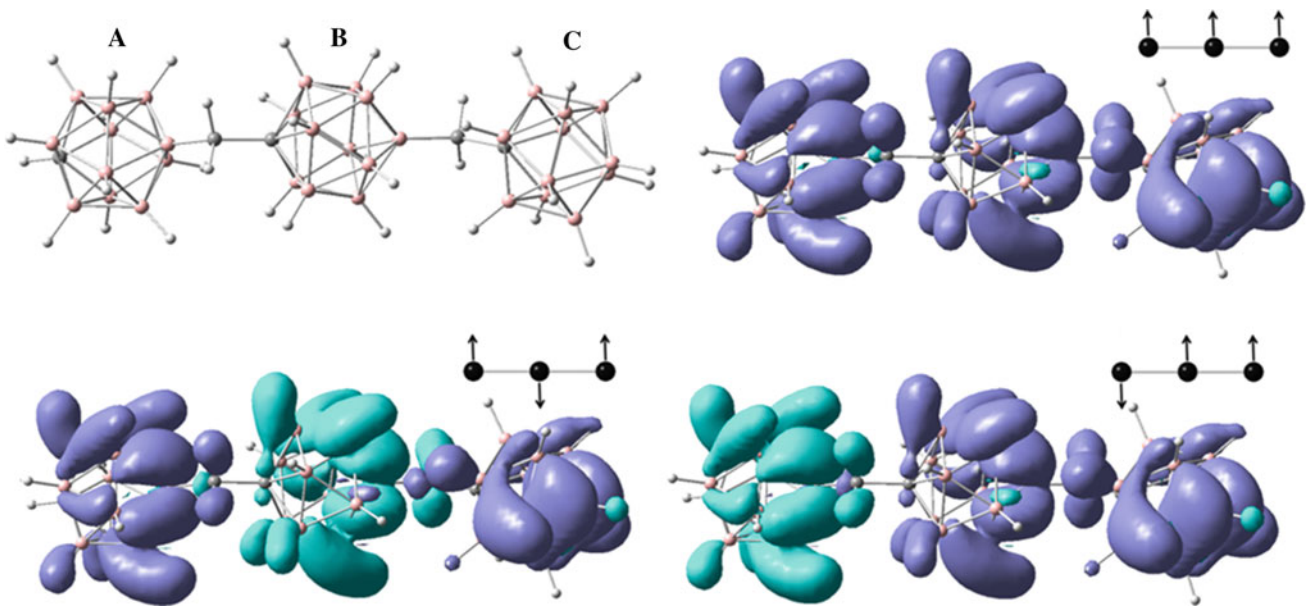

Fig. 3 Geometrical arrangement and calculated spin densities of the linear trimer constituted by three carborane radical units $CB_{11}H_{12}^{\cdot}$ connected through the carbon cage atoms with an methylene bridge unit

of the local spin (*LS*) quantities $\langle \hat{S}_A \hat{S}_B \rangle$ according to the algorithms reported in Refs. [17–21]. Alternatively, in the case of a unique *J* constant, these quantities can also be calculated using the Yamaguchi (*YA*) procedure [23–25] in which the coupling constants are evaluated in terms of energies and spin-squared expectation values

$$J_{AB}(YA) = \frac{E_{HS} - E_{BS}}{\left\langle \hat{S}^2 \right\rangle^{HS} - \left\langle \hat{S}^2 \right\rangle^{BS}} \tag{4}$$

In the next section, we report values for the constants *Js* arising from both approaches.

Table 2 Local spin populations, energies (au), $\langle \hat{S}^2 \rangle$ expectation values, and coupling constants (in cm^{-1}) for the linear trimer ($D_{\infty h}$-like) studied in this work in the *HS* and two *BS* states

Local spins							
HS state				*BS*1 state			
	A	B	C		A	B	C
A	0.713	0.232	0.241	A	0.701	−0.223	0.235
B	0.232	0.708	0.240	B	−0.223	0.688	−0.229
C	0.241	0.240	0.753	C	0.235	−0.229	0.745

*BS*2 state			
	A	B	C
A	0.702	−0.227	−0.239
B	−0.227	0.694	0.236
C	−0.239	0.236	0.752

	Energy	$\langle \hat{S}^2 \rangle$	$J_{AB}(LS)$	$J_{AC}(LS)$
HS state	−1032.644247	3.7600	−65.279	21.875
*BS*1 state	−1,032.644799	1.7449		
*BS*2 state	−1,032.644619	1.7450		

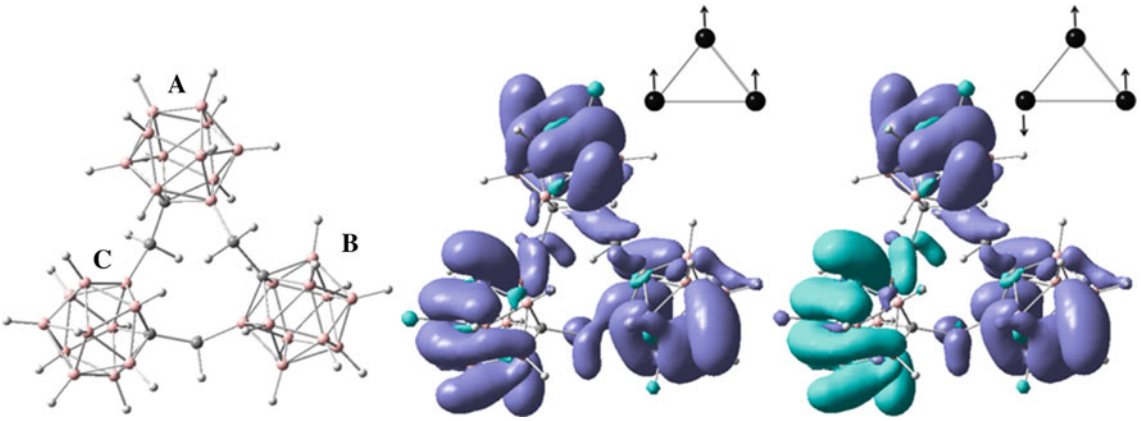

Fig. 4 Geometrical arrangement and calculated spin densities of the cyclical trimer constituted by three carborane radical units $CB_{11}H_{12}$ connected through the carbon cage atoms with methylene bridge units

Table 3 Local spin populations, energies (au), $\langle \hat{S}^2 \rangle$ expectation values, and coupling constants (in cm^{-1}) for the linear trimer (D_{3h}-like) studied in this work in the *HS* and *BS* states

Local spins							
HS state				*BS* state			
	A	B	C		A	B	C
A	0.725	0.237	0.236	A	0.721	0.230	-0.229
B	0.237	0.723	0.234	B	0.230	0.715	−0.225
C	0.236	0.234	0.721	C	−0.229	−0.225	0.712

	Energy	$\langle \hat{S}^2 \rangle$	$J_{AB}(YA)$	$J_{AB}(LS)$
HS state	−1,070.728919	3.7612	−6.301	−6.779
BS state	−1,070.728977	1.7611		

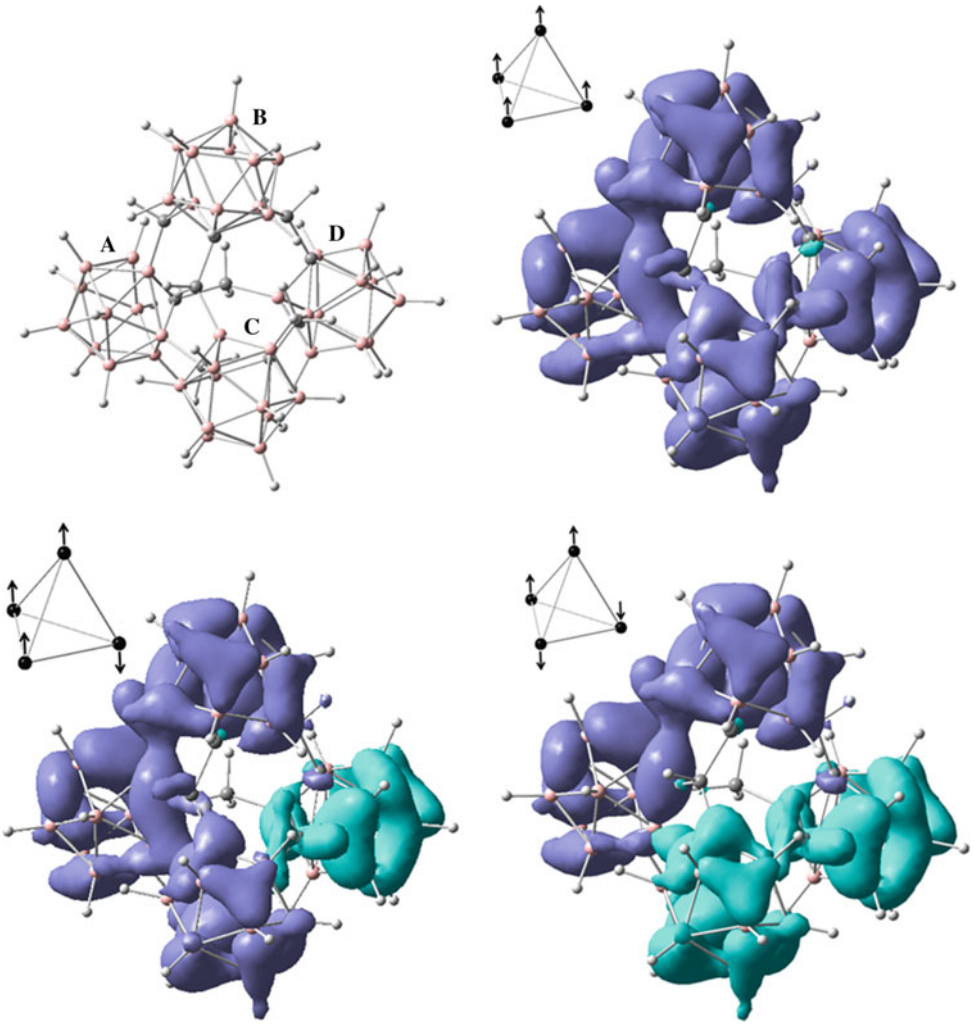

Fig. 5 Geometrical arrangement and calculated spin densities of the tetramer constituted by four carborane radical units $CB_{11}H_{12}^{\cdot}$ connected through the carbon cage atoms with an methylene bridge

2 Results and discussion

As stated above in the Introduction, we chose the methylene bridge unit for connecting the radical carborane cages. This choice was made in order to provide separated spin densities on each magnetic unit (carborane cage) so that one can map these results onto a Heisenberg spin Hamiltonian. We successfully found solutions with a predetermined spin orientation on each cage for the dimers, using acetylene (–C≡C–) and ethylene (–CH=CH–) bridge units. However, for larger systems, such as triangular architectures, we could not find this kind of states. Notwithstanding, these solutions can be found with a methylene bridge unit. We now turn to the description of these molecular architectures.

The determination of the spin density matrices, their corresponding spin densities, and the energies E_{HS} and E_{BS} required in the *LS* and *YA* treatments has been carried out at unrestricted Becke-3-parameter-Lee–Yang–Parr functional levels (UB3LYP) using the Gaussian 09 [26] package and the atomic basis sets 6-31G(d). In all the systems, the geometries were optimized for the *HS* state at UB3LYP/6-31G(d) level. The evaluation of the one- and two-center local spins, $\langle \hat{S}_A^2 \rangle$ and $\langle \hat{S}_A \hat{S}_B \rangle$, respectively, was performed in subsequent steps using our own codes. Likewise, the solutions of the above-mentioned linear equations have been obtained from the Mathematica 9.0 [27].

The results corresponding to the linear dimer $[(CB_{11}H_{11})^{\cdot}–CH_2–(CB_{11}H_{11})^{\cdot}]$ are shown in Fig. 2 and Table 1, where *A* and *B* stand for the left and right moieties, respectively. This figure also indicates the two possible orientations of the cage spins. As can be observed, both states *HS* (triplet) and *BS* (singlet) present $\langle \hat{S}_A^2 \rangle$ quantities close to 0.75 [the canonical value is 1/2 (1 + 1/2)] meaning the two electrons are well localized in each cage. The signs of the two-center local spin components $\langle \hat{S}_A \hat{S}_B \rangle$ positive for the triplet state and negative for the singlet one confirm the predictions found in previous works [10] being their absolute values close to 0.25 (i.e., 1/2·1/2). The energies found are very similar indicating a near degenerate situation.

Table 4 Local spin populations, energies (au), $<\hat{S}^2>$ expectation values, and coupling constants (in cm^{-1}) for the tetramer studied in this work in the *HS* and two *BS* states

Local spins								
HS state					*BS*1 state			
	A	B	C	D		A	B	C	D
A	0.683	0.234	0.221	0.205	A	0.672	0.226	0.196	−0.194
B	0.234	0.735	0.235	0.218	B	0.226	0.721	0.210	−0.208
C	0.221	0.235	0.687	0.206	C	0.196	0.210	0.646	−0.180
D	0.205	0.218	0.206	0.626	D	−0.194	−0.208	−0.180	0.605

*BS*2 state				
	A	B	C	D
A	0.593	0.189	−0.176	−0.167
B	0.189	0.700	−0.213	−0.202
C	−0.176	−0.213	0.637	0.188
D	−0.167	−0.202	0.188	0.605

	Energy	$<\hat{S}^2>$	$J_{AB}(YA)(HS/BS2)$	$J_{AB}(LS)$(overdet)
HS state	−1,503.830274	6.0136	−132.798	−149.162
*BS*1 state	−1,503.831593	2.9927		
*BS*2 state	−1,503.832744	1.9312		

Although in this treatment the *HS* state has been formulated by means of Slater determinants, the spin contamination is very low and the coupling constants predicted by our method are in agreement with those provided by the Yamaguchi method. We have also determined the local spins corresponding to the bridge unit considered as a whole; the values found are $\langle\hat{S}_A^2\rangle = 0.0043$ and $\langle\hat{S}_A\hat{S}_B\rangle = 0.0011$ for the *HS* state and $\langle\hat{S}_A^2\rangle = 0.0043$ $\langle\hat{S}_A\hat{S}_B\rangle = 0.0018$ for the *BS* one. These values turn out to be negligible, and consequently, the bridge units are not considered in the computations.

In Fig. 3 and Table 2, we report the results found for the linear trimer composed of three units $CB_{11}H_{120}^{\cdot}$ bonded with two methylene groups: $[(CB_{11}H_{11})^{\cdot}–CH_2–(CB_{11}H_{10})^{\cdot}–CH_2–(CB_{11}H_{11})^{\cdot}]$. In this Table, the A, B, C moieties start from left to right as indicated in Fig. 3. The three different spin orientations of this system provide a *HS* quartet and the two different *BS* doublets. From a qualitative point of view, these results show that the electronic distribution is similar to that described in the previous system, exhibiting well-localized electrons in each cage. The energies of these states (the *HS* quartet and the two *BS* doublets) are also near degenerate, although the spin contamination is higher than in the previous compound. The negative sign of the coupling constant J_{AB} shows the ferromagnetic character of the adjacent *A* and *B* moieties while J_{AC} (positive) presents an antiferromagnetic behavior [28]. The local spins of the bridge units for this compound are also negligible and consequently have been omitted.

This triradical has also been studied with a triangular arrangement bonded with three methylene groups: $[(CB_{11}H_{10})^{\cdot}–CH_2]_3$. The results are shown in Fig. 4 and Table 3. The compound symmetry allows one to describe this aggregate by means of a *HS* state (quartet) and a *BS* one (doublet) that arise from the corresponding spin coupling. No significant differences between its *HS* and *BS* energies have been found with respect to the linear trimer, indicating the independency of each magnetic site and the small gap between the energies of those states; the spin contaminations are also similar to those found in the linear trimer. A weak ferromagnetic interaction is also observed between the adjacent moieties in agreement with the Yamaguchi treatment.

The results for the tetraradical system with a tetrahedrical arrangement, $[(CB_{11}H_9)^{\cdot}–CH_2]_4$, are shown in Fig. 5 and Table 4 in which the two *BS* states refer to the two lowest energies. This system presents one-center spin populations $\langle\hat{S}_A^2\rangle$ lower than the other elements of this series of radicals what can be interpreted as a higher interaction between the magnetic sites. Likewise, one can observe higher differences in energies between all states confirming that interpretation. The Yamaguchi coupling constant has been evaluated using the *HS* and *BS*2 states due to the last one, that is, the ground state. In this polyradical, the resulting linear equation system mentioned in Sect. 2, which allows to determine the coupling constants in the local spin approach, turns to be overdetermined, which has been indicated in Table 4. This system presents local spin values for the bridge unit (the highest ones of this series) $\langle\hat{S}_A^2\rangle = 0.0064$ and $\langle\hat{S}_A\hat{S}_B\rangle = 0.0507$ (for the *HS* state) and $\langle\hat{S}_A^2\rangle = 0.0001$ and $\langle\hat{S}_A\hat{S}_B\rangle = 0.0177$ (for the *BS* state); again, these values can be neglected as in the case of above-mentioned simplest linear dimer $(CB_{11}H_{12}^{\cdot})_2–CH_2$ compound.

We should emphasize that for all the studied systems in this work, the largest differences between two values for $\langle \hat{S}_A^2 \rangle$ corresponding to equivalent centers are within 0.109 in the *HS* state; the largest differences between $\langle \hat{S}_A \hat{S}_B \rangle$ expectation values are within 0.029; these small values confirm that the regular linear, triangular, and tetrahedral arrangements are suitable for the proposed systems.

3 Concluding remarks

In this work, we have studied a series of polyradicals derived from the connection of two, three, and four carborane radicals $CB_{11}H_{12}^{\cdot}$ bonded by methylene groups within several geometrical arrangements. This study extends and complements our previous determinations, based on local spins, on this type of radicals bonded by ethane, ethylene, and acetylene bridges. The results obtained from local spin populations and energy evaluations show a low interaction between these radicals when the bridge unit is a methylene group as well as a negligible interaction between the bridge units and the magnetic sites. The quantitative determination of coupling constants arising from our method, based on the direct partitioning of the spin-squared expectation value $\langle \hat{S}^2 \rangle$, yields values of similar magnitude to those obtained from the Yamaguchi procedure. These results confirm the ability of our local spin technique to determine electronic structures and magnetic behaviors on this type of chains within the Heisenberg Hamiltonian framework.

In future works, one could also consider spin polarization effects [29], well known from simple radicals and diradicals, in order to better understand the magnetic properties of the systems studied in this work and further polyradical molecular architectures derived from the s = 1/2 icosahedral carborane magnetic unit $(CB_{11}H_{12})^{\cdot}$. Other chemical compounds with magnetic activity are currently being studied in our laboratories.

Acknowledgments This study has been financially supported by the Projects CTQ2009-13652 (MICINN, Spain), i-COOP-2013 COOP20040 (Consejo Superior de Investigaciones Científicas), UBACYT 20020100100197 (Universidad de Buenos Aires, Argentina), PIP No. 11220090100061 (Consejo Nacional de Investigaciones Científicas y Técnicas, Argentina), GIU12/09 and UFI11/07 (Universidad del País Vasco, Spain). We thank the Universidad del País Vasco and the Consejo Superior de Investigaciones Científicas for allocation of computational resources.

References

1. Coronado E, Delhaes P, Gatteschi D, Miller JS (eds) (1996) Molecular magnetism: from molecular assemblies to devices. Kluwer, Dordrecht
2. Datta SN, Trindle CO, Illas F (2014) Theoretical and computational aspects of magnetic organic molecules. Imperial College, London
3. Dunbar KR (2012) Inorg Chem 51:12055
4. Gómez-Coca S, Urtizberea A, Cremades E, Alonso PJ, Camón A, Ruiz E, Luis F (2014) Nat Commun 5:4300
5. Rajca A, Wang Y, Boska M, Paletta JT, Olankitwanit A, Swanson MA, Mitchell DG, Eaton SS, Eaton GR, Rajca S (2012) J Am Chem Soc 134:15724
6. Grimes RN (2011) Carboranes. Elsevier, Amsterdam
7. King BT, Noll BC, McKinley AJ, Michl J (1996) J Am Chem Soc 118:10902
8. Eriksson L, Vyakaranam K, Ludvík J, Michl J (2007) J Org Chem 72:2351
9. Oliva JM, Serrano-Andrés L, Havlas Z, Michl J (2009) J Mol Struct (Theochem) 912:13
10. Oliva JM, Alcoba DR, Lain L, Torre A (2013) Theor Chem Acc 132:1329
11. Oliva JM (2012) Adv Quantum Chem 64:105
12. Neese F (2009) Coord Chem Rev 253:526
13. Oka H, Kouno H, Tanaka H (2007) J Mater Chem 17:1209
14. Ciofini I, Daul C (2003) Coord Chem Rev 238:187
15. Noodleman L (1981) J Chem Phys 74:5737
16. Noodleman L, Davidsom ER (1986) Chem Phys 109:131
17. Alcoba DR, Lain L, Torre A, Bochicchio RC (2009) Chem Phys Lett 470:136
18. Torre A, Alcoba DR, Lain L, Bochicchio RC (2010) J Phys Chem A 114:2344
19. Alcoba DR, Torre A, Lain L, Bochicchio RC (2011) Chem Phys Lett 504:236
20. Alcoba DR, Torre A, Lain L, Bochicchio RC (2011) J Chem Theory Comput 7:3560
21. Alcoba DR, Torre A, Lain L, Oña OB, Oliva JM (2014) Int J Quantum Chem 114:952
22. Zein S, Kalhor MP, Chibotaru LF, Chermette H (2009) J Chem Phys 131:224316
23. Yamaguchi K, Takahara Y, Fueno T (1986) In: Smith H, Schaefer HF, Morokuma K (eds) Applied quantum chemistry. Reidel, Dordrecht
24. Soda T, Kitagawa Y, Onishi T, Takano Y, Shigeta Y, Nagao H, Yohioka Y, Yamaguki K (2000) Chem Phys Lett 319:223
25. Shoji M, Koizumi K, Kitagawa Y, Kawakami T, Yamanaka S, Okumura M, Yamaguchi K (2006) Chem Phys Lett 432:343
26. Frisch MJ et al (2009) Gaussian 09, revision D.01. Gaussian Inc., Wallingford
27. Mathematica, Version 9.0 (2012) Wolfram Research, Inc., Champaign, IL
28. Ciofini I, Adamo C, Barone V, Berthier G, Rassat A (2005) Chem Phys Lett 309:133
29. Kessler J (1976) Polarized Electrons. Springer, Berlin

Theor Chem Acc (2015) 134:7
DOI 10.1007/s00214-014-1605-3

REGULAR ARTICLE

Theoretical analysis of vibrational modes in uranyl aquo chloro complexes

F. Izquierdo-Ruiz · J. M. Menéndez · J. M. Recio

Received: 5 August 2014 / Accepted: 10 December 2014 / Published online: 15 January 2015

Abstract The electronic structure of uranyl-based complexes of water and chlorine, with the general formula $[UO_2(H_2O)_xCl_y]^{2-y}$ ($y = 1, 2, 3, 4$; $x + y = 4, 5$), have been computed both in vacuo and in aqueous solution. Within the density functional theory framework, total and relative energies (including basis set superposition error corrections), equilibrium geometries, and vibrational frequencies were determined and briefly compared with available experimental and previous theoretical data. New results on vibrational modes of these complexes are emphasized. Our focus is on the trend exhibited by the frequency of the stretching mode (ν_s) associated to the uranyl moiety at different chlorine concentrations. A charge transfer index (CT) accounting for the number of electrons transferred from the ligands to UO_2^{2+} is used to rationalize this trend. According to our most accurate calculations, ν_s is red-shifted at a rate between 15 and 20 cm^{-1} per 0.1 e transferred. Interestingly enough, a linear trend is displayed using CT as the correlating parameter.

Keywords Uranyl-type complexes · DFT calculations · Vibrational modes

Published as part of the special collection of articles derived from the 9th Congress on Electronic Structure: Principles and Applications (ESPA 2014).

F. Izquierdo-Ruiz · J. M. Menéndez · J. M. Recio (✉)
Departamento de Química Física y Analítica, Universidad de Oviedo, 33006 Oviedo, Spain
e-mail: jmrecio@uniovi.es

F. Izquierdo-Ruiz
e-mail: izquierdofernando@uniovi.es

J. M. Menéndez
e-mail: jmenendezmontes@gmail.com

1 Introduction

Uranyl aquo chloro complexes play a decisive role in the mobility and transport of uranium, as revealed by a number of well-documented mineralization processes and giant deposits formed under hydrothermal conditions [1, 2]. It is also known that high quantities of uranium in chloride-brines require pH values between 2.5 and 4.5 [3]. In this acidic environments, the presence of complexes with a general chemical formula $[UO_2(H_2O)_xCl_y]^{2-y}$ ($y = 1, 2, 3, 4$; $x + y = 4, 5$) has been identified, though the questions of which is the composition and which is the total number of ligands of the species at a given chlorinity still remain open.

Experimental observations using Raman spectroscopy [4] conclude that a perfect linear trend (with a negative slope) fits how the frequency of the symmetric stretching mode (ν_s) of the uranyl moiety evolves as the number of anionic ligands (n) increases: $\nu_s\,(cm^{-1}) = -A\,n + 870$, with $A\,(cm^{-1})$ depending on the nature of the ligand and taking a value of 4 in the case of uranyl chloro complexes. Based on this relationship, Dargent et al. [5] were able to resolve the relative abundance of uranyl species containing up to five chloride anions at different temperatures and chlorinities. Their results led to a set of complexation constants showing an overall but not complete agreement with previous experimental values.

From the theoretical side, the UO_2^{2+} moiety alone or coordinated with different ligands or crystalline ions have been the subject of a number of electronic structure calculations. Vallet et al. [6–8] and Matsika and Pitzer [9] have analyzed in detail wavefunction-based methodologies and embedded models with the main focus on the description of excited electronic states of uranyl. Using the density functional theory (DFT) approximation, Siboulet et al.

[10] carried out a careful study of solvent models proposing a charge transfer parameter to account for the shift of the uranyl stretching frequency as the number of water ligands increases. More recently, Buhl et al. [11] performed a thorough investigation of uranyl complexes of water and chloro in aqueous solution using DFT. Only one stretching frequency was reported since "this property is probably a poor indicator for coordination number in uranyl chloride complexes".

Our contribution is aimed at providing a general interpretation of the behavior of the frequency associated with the vibrational symmetric mode of uranyl (ν_s) in terms of parameters regardless the nature of the ligand. A detailed analysis of the vibrational modes of the calculated aquo chloro complexes is also reported. First principles cluster in vacuo calculations and in different cluster-in-the-solvent models have been carried out on a number of uranyl-type aquo chloro complexes containing up to five ligands. Optimized geometries, vibrational frequencies and relative stabilities are obtained. It can be seen that the charge transfer parameter earlier proposed by Siboulet et al. [10] provides a guide for the redshift trend observed for the symmetric U–O vibration mode as the number of chloride ligands increases in uranyl-type complexes. The charge transfer produces a reduction in the (positive) charge of uranyl, which leads to a weakening of the U–O bond and, therefore, a decreasing in the frequency of the stretching mode. Traditional charges (Mulliken [12]), values from NBO analysis (NPA charges) [13, 14], and results from the analysis of the topology of the electron density (Bader [15]) were computed to validate our correlating index with satisfactory results.

This paper contains three more sections. Next, a summary of the computational parameters used in our density functional theory calculations will be given. In Sect. 3, we provide a general description of vibrational modes and frequencies of the uranyl aquo chloro complexes followed by the analysis of the correlating charge transfer parameter describing how ν_s decreases as the number of chloro ligands increases. Main conclusions are presented in the last section.

2 Computational aspects

Cluster in vacuo (gas phase) and cluster-in-the-solvent calculations have been performed for all the aquo chloro complexes depicted in Fig. 1. Notice the self-explanatory nomenclature that will be used throughout the next sections ('w' refers to water molecules, 'cl' to chlorine ligands, and subscripts 'c' and 't' stand for *cis*- and *trans*-like configurations of the ligands). All the calculations were performed within the framework of DFT using B3LYP [16, 17] with basis sets aug-cc-pVDZ [18] in H, O, and Cl, and a relativistic corrected Stuttgart pseudopotential for 60 electrons with an associated basis set for U [19]. The election of the level of calculation follows the deep and thorough study of Jong et al. [20] in uranyl. We notice that the B3LYP functional was also used in the works on aquo- and chloro complexes of uranyl by Siboulet et al. [10] and Buhl et al. [11], respectively. Calculated geometries for gas phase clusters were re-optimized at the cluster-in-the-solvent type of calculation using a polarizable continuum model (PCM) [21–25] as implemented in the Gaussian09 code [26]. The dielectric constant used for water in the calculations (78.3553, defect value) is the experimental value at 298 K.

All the computational parameters chosen, as well as the PCM model, are well-known standard options described with detail in the literature [26]. In addition to the PCM approach, we have also considered a hybrid model in which

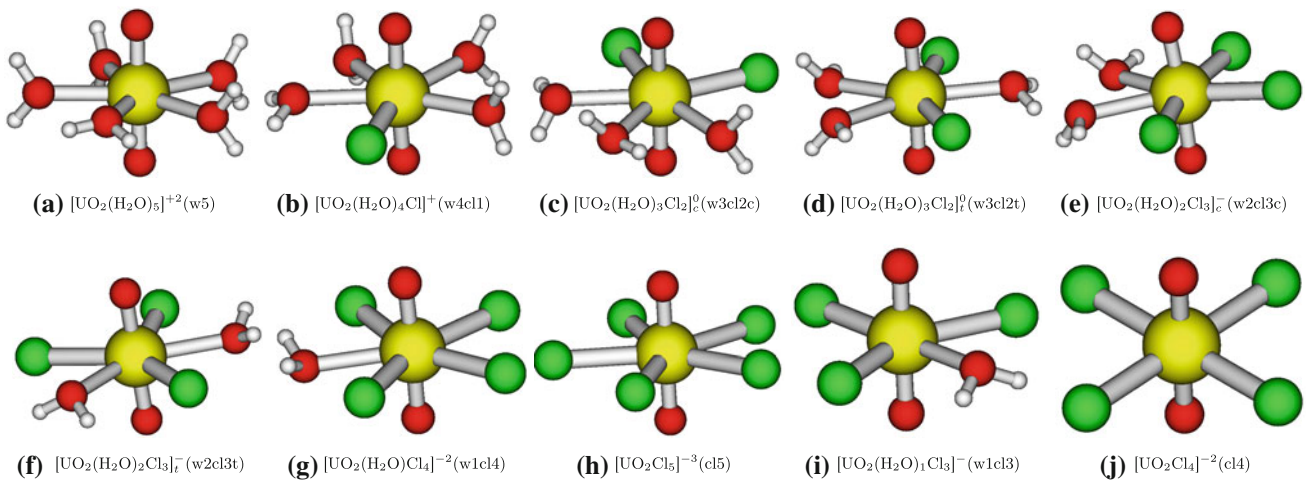

Fig. 1 Uranyl aquo chloro complexes considered in this work. w, cl, c and t, stands for water, chlorine, *cis* and *trans*, respectively. In this ball and stick representations, *yellow*, *red*, *white* and *green colors stand*, respectively, for U, O, H, and Cl

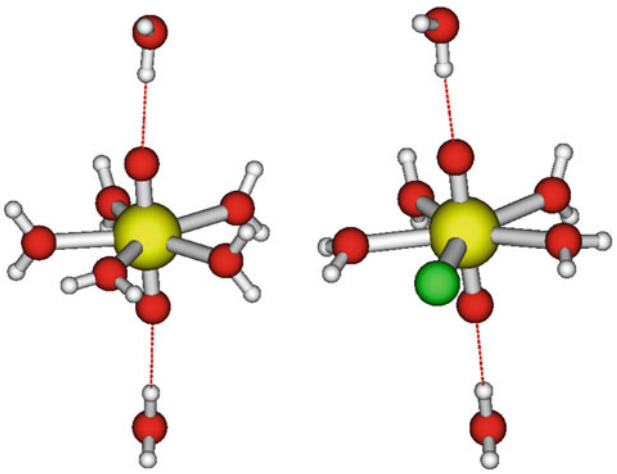

Fig. 2 Quantum mechanical clusters used in our hybrid-PCM model for $[UO_2(H_2O)_5]^{2+}$ and $[UO_2(H_2O)_4Cl]^{1+}$ complexes. Same color pattern as in Fig. 1

two water molecules of the solvent were explicitly included in the quantum mechanical clusters of $[UO_2(H_2O)_5]^{2+}$ and $[UO_2(H_2O)_4Cl]^{+}$. For these two clusters, it seems reasonable to take into account the presence of solvation water molecules approaching the axial positions of uranyl (see Fig. 2), whereas this is less probable for complexes with a greater number of chlorine ligands. The consideration of explicit water molecules only in axial configurations follows the conclusions of the thorough study of Siboulet et al. [10] concerning second hydration sphere models. Other cluster models including another coordinations involving water molecules in the equatorial plane are not competitive (and do not introduce meaningful changes on vibrational frequencies) with respect to the ones shown in Fig. 2. Notice that all the ligands of the complex are in an equatorial plane with the linear UO_2^{2+} moiety perpendicular to it.

In all the calculated clusters, Mulliken analysis [12], charges from NPA [13, 14], and Bader charges [15] from the analysis of the topology of the electron density were computed to evaluate the charges of all the chemical species involved in the complexes. Accurate values, except for the hydrogen atoms, have been obtained. This drawback does not affect our analysis since we are interested in the charge transferred to UO_2^{2+}, and it is evaluated as the difference between its nominal charge (+2) and the computed charge of the uranyl moiety in the corresponding complex.

3 Results and discussion

An extensive theoretical study involving all the complexes considered in this work was previously carried out by Buhl et al. [11] using similar computational parameters. We refer to this work for a detailed description of the equilibrium geometries and their relative energies of the complexes both in gas phase and considering the PCM approach to the solvent since our results are almost identical as the ones reported by Buhl et al. At this last level of calculation, the U–O distance in uranyl ranges from 1.76 Å in w5 to 1.78 in cl4, U–Cl distances are clustered around 2.75 ± 0.1 Å (lower value in w4cl1, greater value in cl5) and U–OH_2 distances varies between 2.45 Å in w5 to 2.61 Å in w1cl4. Besides the total agreement of our independent simulations with the results of Buhl et al. [11], the comparison with the average values provided by EXAFS experiments [27] is also very good. EXAFS distances are $d_{U-O} = 1.76 \pm 0.02$ Å, $d_{U-Cl} = 2.71 \pm 0.02$ Å, and $d_{U-OH_2} = 2.41 \pm 0.02$ Å. We should stress that these experimental values are the same regardless the positions and the number of water and chlorine ligands in the complex. Thus, theoretical calculations provide a richer description of the geometry of these species. It is also worth to remark that structural data from X-ray experiments in crystalline structures containing the $UO_2Cl_4^{2-}$ complex, as in $Cs_2UO_2Cl_4$ [28], are almost coincident with the above values: $d_{U-O} = 1.776$ Å, $d_{U-Cl} = 2.670$ Å.

The accurate description of the computed equilibrium geometries allows us to perform with confidence the evaluation of the vibrational modes associated with all of these complexes. Although our focus is on the symmetric stretching U–O mode, we will provide a detailed description of the rest of the modes in three steps. In the first one, and for simplicity (no water ligands are present), we discuss the $UO_2Cl_4^{2-}$ complex. Sketches of its vibrational modes are displayed in Fig. 3. We have used the following symbols to characterize how the atoms move (see arrows in Fig. 3) in a given vibrational mode: symmetric stretching (SS), antisymmetric stretching (AS), bending (B), wagging (W), rocking (R) and twisting (Tw). Given the D_{4h} point group symmetry, the fifteen vibrational modes of this complex can be decomposed into the following irreducible representations:

$$2A_{1g} + 2A_{1u} + B_{1g} + B_{2g} + B_{2u} + E_g + 3E_u. \quad (1)$$

Except the two stretching modes associated with uranyl (with values around 900 cm^{-1}), all the vibrational modes of this complex present low frequencies. This is due to either the great reduced mass of the atoms involved (U, Cl) or the weakness of the force constants of all the non stretching-like modes. Thus, twisting, bending and wagging modes involving U and Cl are the lowest frequency modes (around 100 cm^{-1}), followed by stretching modes of U–Cl bonds (around 200 cm^{-1}) and rocking and bending ones of U–O bonds (up to 250 cm^{-1}).

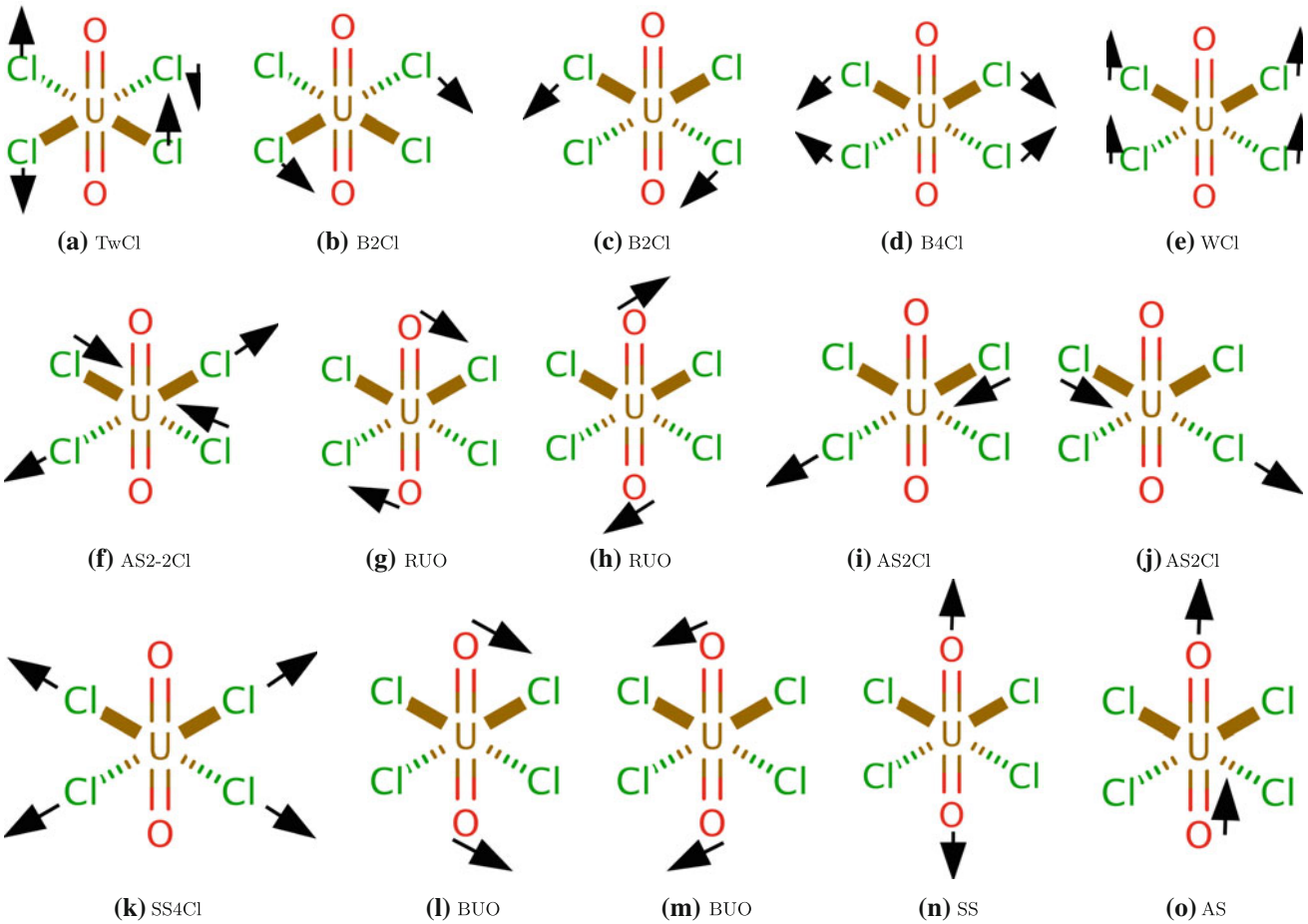

Fig. 3 Sketches of the vibrational modes of cl4 cluster. U displacements are not shown

A more detailed general analysis involving compounds with water molecules can be done in a second step. We start with the frequencies of modes that are common to all the complexes. These modes can be grouped again depending on the type of atomic displacements as: twisting, wagging, rocking, bending and stretching (breathing, Br, is the symmetric stretching). This sequence roughly follows an increasing trend in the frequencies (see Fig. 4). In each group, frequencies are represented by bars following the sequence from cl5 to w5. Along the series, the charge transfer decreases since the number of Cl ligands becomes lower. Twisting and wagging frequencies have values up to 110 cm^{-1}, bending ones up to 200 cm^{-1}, UO_2^{2+} rocking modes ranges from 140 up to 200 cm^{-1}, UO_2^{2+} bending modes lie between 210 and 260 cm^{-1}, and stretching modes including the breathing mode have frequencies up to 330 cm^{-1}. There are not clear patterns with the ligands in all these frequencies except in the stretching modes of the U–L bond that show increasing values following the expected decrease in the charge transfer. Thus, we point out the difference for this frequency between cl5 (around 200 cm^{-1}) and w5 complexes (around 330 cm^{-1}) in the breathing mode.

In the third step, we describe vibrations related to the water ligands. Each water molecule in the complex introduces six new normal modes that can be classified as: (1) librations or bending of the U–OH_2 bonds with values up to 600 cm^{-1}, (2) H–O–H bending modes with frequencies around 1,600 cm^{-1}, and (3) the well-known symmetric and antisymmetric O–H stretching modes at 3,700 and 3,800 cm^{-1}, respectively. In Fig. 5, these stretching frequencies are collected for all the water containing complexes. In general, as the number of water molecules increases, both symmetric and antisymmetric frequencies increase. This can be explained as an inductive effect of the greater positive charge of the U atom as the number of Cl decreases, thus increasing the strength of the bond with the oxygen atom of the water ligand. Notice that a lowering of the symmetry down to the C_1 point group can be displayed for some of these aquo chloro complexes.

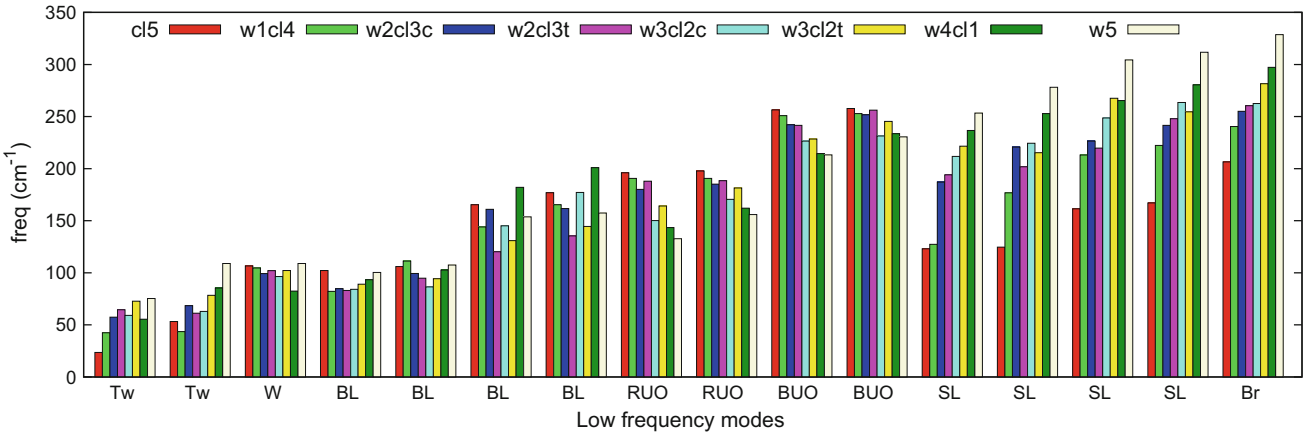

Fig. 4 Low frequency modes of 5-coordinated aquo chloro complexes of uranyl. *L* stands for ligand, other *symbols* explained in the text

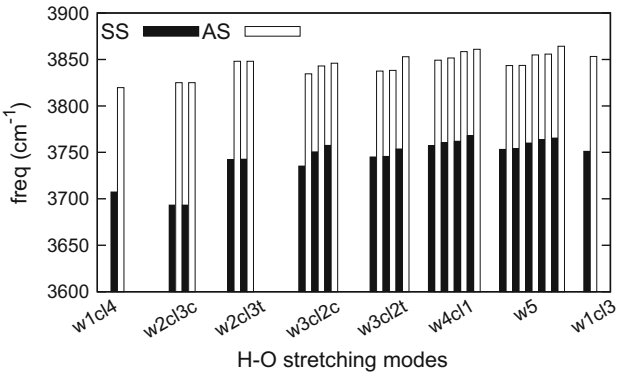

Fig. 5 Symmetric and antisymmetric stretching H–O modes

Table 1 Vibrational frequencies (cm^{-1}) of the symmetric stretching mode (subscript s) and antisymmetric stretching mode (subscript a) of uranyl in the complexes explored in this work

Complex	In $vacuo_s$	PCM_s	Exp. [4]	In $vacuo_a$	PCM_a
UO_2^{2+}	1,036	928	–	1,135	1,006
w5	941	922	870	1,030	984
w7	–	910	870	–	968
w4cl	903	890	866	989	954
w6cl	–	880	866	–	940
w3cl2c	883	870	862	968	936
w3cl2t	890	874	862	976	940
w2cl3c	868	859	858	952	925
w2cl3t	879	860	858	965	926
w1cl4	–	848	854	–	916
cl5	855	840	850	944	909
w1cl3	873	863	858	959	930
cl4	854	841	854	940	909

Experimental values (Exp.) are for the symmetric stretching modes

Let us focus now on the symmetric stretching vibrational mode associated with the U–O bonds of the UO_2^{2+} moeity in all the complexes studied. Results from in vacuo and PCM calculations for all the uranyl complexes are collected in Table 1, along with values from w7 and w6cl hybrid models that include explicitly two extra water molecules in the w5 and w4cl quantum mechanical clusters. Overall, the fair agreement with the experimental values of the in vacuo results improves if we consider the solvent. Values from the hybrid model are also closer to the experimental ones. Considering our most accurate results, only the computed frequency of the complex without chlorine ligands is noticeably overestimated, which may be due to the lack of a second hydration sphere, as discussed by Siboulet et al. [10]. For all the other complexes, deviations from the experimental values lower than 3 % were obtained. We have checked the use of a scale factor to correct these deviations [29–32]. The calculated scale factors taking into account all the complexes is 0.985. Since our cluster-in-the-solvent values show both over and underestimations with respect to the experimental values, there is not an overall improvement in the corrected figures that could justify the introduction of this correction.

Being the theory–experiment comparison of the absolute values important, what we want to analyze in detail here is the trend exhibited by this A_{1g} frequency as the number of chlorine ligands increases. This parameter leads to a perfect linear trend of the experimental frequencies, though it is also to be pointed out that there is not explicit consideration of how many water molecules belong to each of the considered complexes. Efforts toward a parametrization of the redshift of this frequency using the number of anionic ligands to the uranyl moeity were also performed for OH^-, F^-, etc. [4, 33, 34]. From the theoretical side, it is also possible to propose a more general parameter

Table 2 Calculated Q_B (Bader charges, first row) and Q_N charges (NPA charges, second row) in *e* units for each complex, along with the corresponding CT_i parameter (see text for definition), according to our cluster-in-the-solvent PCM results

Complex	U	O	Cl	UO_2	CT
UO_2^{2+}	3.562	−0.781	–	2.000	0
	3.812	−0.906	–	2.000	0
w5	3.124	−0.858	–	1.408	0.592
	3.088	−0.819	–	1.451	0.549
w7	3.141	−0.842	–	1.457	0.542
	–	–	–	–	–
w4cl	3.047	−0.882	−0.685	1.283	0.716
	2.950	−0.837	−0.676	1.276	0.724
w6cl	3.048	−0.873	−0.647	1.302	0.698
	–	–	–	–	–
w3cl2c	2.978	−0.898	−0.713	1.182	0.818
	2.833	−0.849	−0.697	1.134	0.866
w3cl2t	2.999	−0.896	−0.713	1.197	0.803
	2.858	−0.847	−0.716	1.164	0.836
w2cl3c	2.932	−0.911	−0.741	1.110	0.890
	2.762	−0.857	−0.730	1.047	0.953
w2cl3t	2.937	−0.911	−0.740	1.114	0.886
	2.778	−0.858	−0.740	1.061	0.939
w1cl4	2.891	−0.924	−0.768	1.044	0.956
	2.732	−0.870	−0.764	0.992	1.008
cl5	2.853	−0.933	−0.798	0.987	1.013
	2.717	−0.877	−0.793	0.964	1.036
w1cl3	2.938	−0.903	−0.732	1.132	0.868
	2.805	−0.854	−0.727	1.096	0.904
cl4	2.846	−0.925	−0.749	0.996	1.004
	2.672	−0.870	−0.733	0.932	1.068

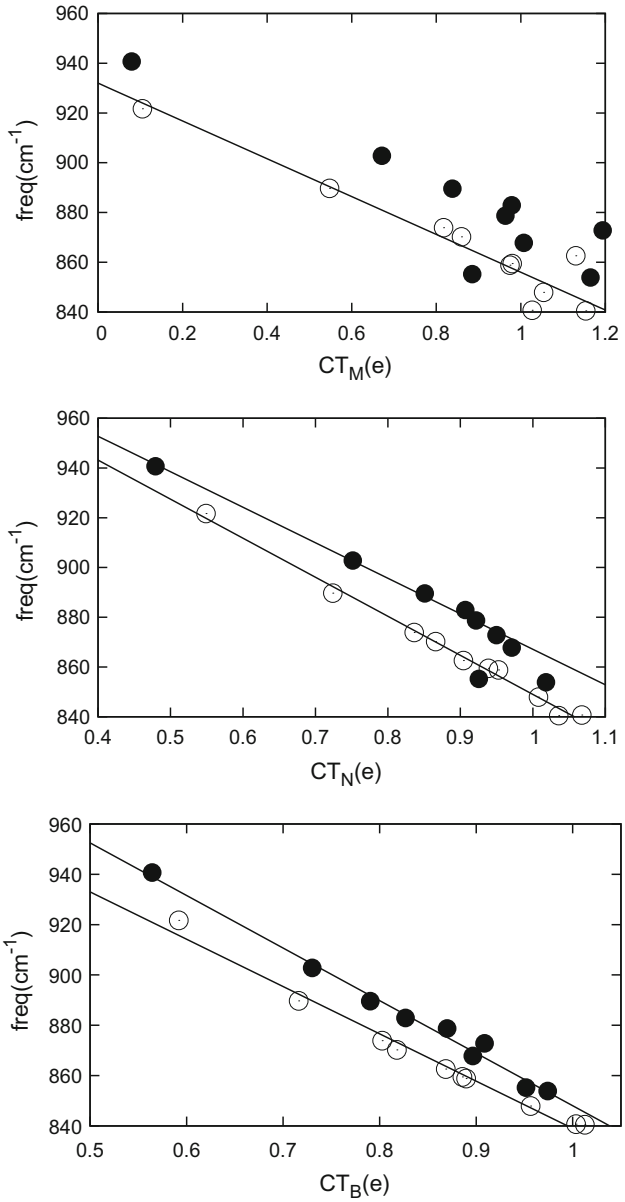

Fig. 6 Frequencies of the symmetric stretching mode of UO_2^{2+} versus the charge transfer parameter computed with Mulliken (*top*), NPA (*center*) and Bader (*bottom*) charges. *Solid* and *empty symbols* stand for in vacuo and PCM calculations, respectively

independent on the nature of the ligand. As Siboulet et al. have shown in uranyl aquo complexes, the charge transfer from the water ligands to the oxygen atoms of the uranyl moeity can be used as a good correlating index. A question arises concerning how this charge transfer parameter is evaluated.

Three different approaches, Mulliken, NPA and topological (Bader) charges, were used in our work to calculate the electron populations associated with all the atomic species of the complexes. We define the charge transfer parameter (CT) as the difference between the nominal charge of uranyl (+2) and the actual charge of UO_2 in the complex: $CT_i = 2 - Q_i(UO_2)$, with i = M, N and B for Mulliken, NPA and Bader charges, respectively. NPA and Bader charges are collected in Table 2. Whereas Mulliken population analysis may present basis set dependence, NPA usually provides a meaningful chemical picture, and topological charges are unequivocally defined and tend to show stable values with respect to the computational parameters chosen in the calculations. Similar drawbacks of the Mulliken approach were also posed by Siboulet et al. [10] in their charge transfer analysis of uranyl water complexes using the NPA approach. It is to be noted that the difference between calculated CT_N and CT_B values for a given complex is usually lower than 0.05 *e*. For the sake of comparison, topological charges from experimental electron densities in $Cs_2UO_2Cl_4$ crystal [28] are given: 2.751 (U), 0.774

(Cs), −0.923 (O), and −0.605 (Cl), all in e units. In this crystal, the total charge of UO_2 is +0.905 e, and the charge transfer is $CT_B = 1.095\,e$. All these values are close to the ones we obtain for the $[UO_2Cl_4]^{-2}$ complex (see last two rows of Table 2).

In Fig. 6, we plot how the frequency of the SS mode (in cm^{-1}) evolves with the charge transfer evaluated with Mulliken charges (top), NPA charges (center) and Bader charges (bottom). It is apparent that values stand on a linear trend in all the cases (r close to 0.99) when results from cluster-in-the-solvent using the PCM model are considered:

$$\nu_s(\text{PCM}) = -76 \times CT_M + 932, \quad r = 0.985 \tag{2}$$

$$\nu_s(\text{PCM}) = -157 \times CT_N + 1006, \quad r = 0.994 \tag{3}$$

$$\nu_s(\text{PCM}) = -188 \times CT_B + 1027, \quad r = 0.985. \tag{4}$$

In the case of Mulliken charges (Fig. 6 top), points from fourfold coordinated complexes (cl4 and w1cl3) are clearly outliers and have not been included in the fitting. Besides, the asymptotic behavior (1,036 cm^{-1}, see Table 1) is not correct. Using Q_M, it is not possible to find a linear trend for gas phase frequencies. In the case of NPA charges (Fig. 6 center), points from fourfold coordinated complexes and the cl5 complex were excluded from the fitting for the in vacuo case, but in the PCM case all the compounds are included. It is possible to see that the fitting in both cases (Fig. 6 center) is quite good and reproduces reasonably well the reference state (isolated uranyl cation). The quality of the fittings is also very good and stable when Q_B charges are computed with the more robust topological approach. See how for in vacuo calculations (Fig. 6 bottom), a linear fitting is also obtained using CT_B with similar slope and asymptotic limit (close to the value of the reference uranyl ion of 1,036 cm^{-1}) as in the PCM situation, and without leaving out any data. The expressions of the linear fittings for in vacuo results using NPA and Bader charges are:

$$\nu_s\ (\text{in vacuo}) = -143 \times CT_N + 1010, \quad r = 0.994 \tag{5}$$

$$\nu_s\ (\text{in vacuo}) = -209 \times CT_B + 1057, \quad r = 0.988 \tag{6}$$

It is very satisfactory to have obtained analogous results from both, in vacuo and PCM-like calculations either with the topological or with NPA charges. The rate the frequency of this symmetric stretching mode is red-shifted is predicted between 15 and 20 cm^{-1} for each 0.1 e transferred to the UO_2^{2+} moiety. The final remark that has to be stressed from our results is that, in coincidence with Siboulet et al., we have found a high correlation between the charge transferred from the ligands to the UO_2^{2+} moiety and the SS vibrational frequency exhibited by a variety of uranyl aquo chloro complexes.

4 Conclusions

Quantum mechanical calculations at both in vacuo and PCM approximations provide a reasonable description of the geometry, the energetics, and the vibrational modes of uranyl aquo chloro complexes, in agreement with other theoretical and experimental studies. In addition, simulations provide a more detailed information on the structure–properties relationship.

Calculated frequencies of the symmetric and antisymmetric UO_2^{2+} stretching modes change with the number of water and chlorine ligands of the complex. We have found that both modes behave very similarly, having the antisymmetric mode higher wavenumber values. The calculated trend agrees with the one observed in other experimental studies, although, specially at low chlorine coordinations, some deviations appear probably related to effects of the second hydration sphere. Using Mulliken population analysis, NBO analysis and Bader topological partition of space, we propose a charge transfer parameter, CT, that accounts for the decrease of the charge supported by the uranyl moiety in the aquo chloro complexes. Our calculations reveal that CT is a good correlating parameter for the redshift experienced by these frequencies when the number of chlorine ligands increases. Whereas Mulliken charges do not lead to an overall satisfactory picture, the CT_B parameter evaluated with the Bader approach and NPA charges provide good linear fittings that allow us quantifying the redshift rate in 20 cm^{-1} per 0.1 e transferred (Bader) and 15 cm^{-1} per 0.1 e transferred (NPA).

Acknowledgments Financial support from Spanish MINECO under Project CTQ2012-38599-C02-01 and Spanish Consolider-Ingenio 2010 program under Project CSD2007-00045 is gratefully acknowledged. FIR thanks Principado de Asturias FICYT and FPU program from MECD for a Ph.D. grant.

References

1. Cuney M (2009) Miner Depos 44:3
2. Richard A, Pettke T, Cathelineau M, Boiron MC, Mercadier J, Cuney M, Derome D (2010) Terra Nova 22:303
3. Richard A, Rozcypal C, Mercadier J, Banks DA, Cuny M, Boiron MC, Cathelineau M (2011) Nat Geosci 5:142
4. Nguyen-Trung C, Begun GM, Palmer DA (1992) Inorg Chem 31:5280
5. Dargent M, Dubessy J, Truche L, Bazarkina EF, Nguyen-Trung C, Robert P (2013) Eur J Mineral 25:765
6. Réal F, Vallet V, Marian C, Walhgren U (2007) J Chem Phys 127:214302
7. Wahlin P, Danilo C, Vallet V, Réal F, Flament JP, Wahlgren U (2008) J Chem Theor Comput 4:569
8. Réal F, Gomes ASP, Visscher L, Vallet V, Ephrain E (2009) J Phys Chem A 113:12504
9. Matsika S, Pitzer RM (2001) J Phys Chem A 105:637
10. Siboulet B, Marsden CJ, Vitorge P (2006) Chem Phys 326:289

11. Buhl M, Sieffert N, Golubnychiy V, Wipff G (2008) J Phys Chem A 112:2428
12. Mulliken RS (1955) J Chem Phys 23:1833
13. Glendening ED, Reed AE, Carpenter JE, Weinhold F (1998) NBO version 3.1
14. Reed AE, Curtiss LA, Weinhold F, Aas W (1988) Chem Rev 88:899
15. Bader RW (1990) Atoms in molecules: a quantum theory. Oxford Publications, Oxford
16. Becke AD (1993) J Chem Phys 98:5648
17. Lee C, Yang W, Parr RG (1988) Phys Rev B 37:785
18. Dunning TH (1989) J Chem Phys 90:1007
19. Dolg M, Wedig U, Stoll H, Preuss H (1987) J Chem Phys 86:866
20. de Jong WA, Harrison RJ, Nichols JA, Dixon DA (2001) Theor Chem Acc 107:22
21. Cances E, Mennucci B, Tomasi J (1997) J Chem Phys 107:3032
22. Mennucci B, Cances E, Tomasi J (1997) J Chem Phys 106:5151
23. Mennucci B, Cances E, Tomasi J (1997) J Phys Chem B 101:10506
24. Tomasi J, Mennucci B, Cances E (1999) J Mol Struct 464:211
25. Tomasi J, Mennucci B, Cammi R (2005) Chem Rev 105:2999
26. Frisch MJ et al (2010) Gaussian 09; Gaussian Inc., Wallingford, vol revision B 01
27. Henning C, Tutschku J, Rosberg A, Bernhard G, Scheinost AC (2005) Inorg Chem 44:6655
28. Zhurov VV, Zhurova EA, Stash AI (2011) J Phys Chem A 115:13016
29. Scott AP, Radom L (1996) J Phys Chem 100:16502
30. Ming WW (1996) Chem Phys Lett 256:391
31. Merrick JP, Moran D, Radom L (2007) J Phys Chem 111:11683
32. Johnson RD III (2013) NIST Computational chemistry comparison and benchmark database. NIST standard reference database 101. http://cccbdb.nist.gov
33. Tshusima S, Suzuki A (1999) J Mol Struct 487:33
34. Gu JF, Lu CH, Chen WK, Xu Y, Zheng JD (2009) Acta Phys Chim Sin 25:655

Theor Chem Acc (2015) 134:56
DOI 10.1007/s00214-015-1658-y

REGULAR ARTICLE

Theoretical study of nonlinear optical properties of cobalt bis (dicarbollide) derivatives: the effect of substituents

Georgia M. A. Junqueira[1] · **Fernando Sato**[1]

Received: 27 October 2014 / Accepted: 28 March 2015 / Published online: 14 April 2015

Abstract In the present work, molecular first-order hyperpolarizability (β_{tot}) and dipole moment (d) are obtained at B3LYP/6–31G(d,p) level of theory by coupled perturbed Hartree–Fock method within the static approach. The investigated molecules are a series of substituted cobalt bis (dicarbollide) derivatives: Hydrogens bonded to the two carbon atoms are replaced by acceptor and donor electron substituents. Correlations between the Hammett electronic parameters of the substituents and the molecular properties are tested. Among them, the named push–pull compounds produced the largest calculated values of β_{tot} and d. The UV–Vis spectra are reported for all studied compounds.

Keywords Cobalt bis (dicarbollide) derivatives · NLO properties · Hammett electronic parameters · Absorption spectrum

1 Introduction

The chemistry of carboranes has been widely studied due to peculiar structural and electronic fundamental properties [1–8]. The strong bonds between carborane and metal combined with high electronic delocalization provide great stability and diverse applications of these compounds [3, 7] in medicine [9–12] and materials sciences [13–20]. An interesting feature of the boron-based cages, due to high electronic and thermal stability, delocalized structures and easy functionalization, is the potential application in nonlinear optics (NLO) [3, 5, 21]. Generally, molecules with NLO applications are systems with acceptor and donor electron groups in its extremities (push–pull type), high values of first-order hyperpolarizability (β) and permanent dipole moment (d). The second-order responses can be enhanced by increasing the electronic asymmetry or the conjugation length between the extremity groups [22, 23]. Besides, the structure must be non-centrosymmetric, and the molecules must present absorption at wavelength greater than 400 nm for second harmonic generation (SHG), to avoid re-absorption of the converted light [24]. The energy (E) of a molecular system under an external electric field $\mathbf{F}$ can be written as Eq. (1), where $E(0)$ is the energy of the system in the absence of an external field, and F_i are the components of the applied field [25]:

$$E(\mathbf{F}) = E(0) - \sum_i dF_i - \sum_{i,j} \frac{1}{2!}\alpha_{ij}F_iF_j - \sum_{i,j,k} \frac{1}{3!}\beta_{ijk}F_iF_jF_k - \sum_{i,j,k,l} \frac{1}{4!}\gamma_{ijkl}F_iF_jF_kF_l - \cdots \quad (1)$$

The dipole moment (d), the linear polarizability (α), and the first- and second-order hyperpolarizabilities (β and γ) play a significant role mainly in the study of NLO properties [24, 26, 27].

The NLO behavior of icosahedral carboranes has been investigated for more than 20 years [14]. Studies in this area involving carboranes include synthesis of novel compounds [14, 18] and NLO properties' calculations [5, 8, 15–17, 21, 28]. For example, a new class of dodecaboranes ($[B_{12}H_{11}–C_2B_{10}H_{11}]^{2-}$) with potential application as NLO materials was proposed through *ab initio* calculations

Published as part of the special collection of articles derived from the 9th Congress on Electronic Structure: Principles and Applications (ESPA 2014).

✉ Georgia M. A. Junqueira
junqueira.georgia@gmail.com

[1] Departamento de Física, Universidade Federal de Juiz de Fora, Juiz de Fora, MG 36036-900, Brazil

[16]. In addition, Grüner et al. [18] obtained a derivative [12-$C_7H_6^+$–$CB_{11}H_{11}^-$] with β ten times larger than *p*-nitroaniline (9.2×10^{-30} cm^5/esu) [24]. Recently, we studied the role played by substituent effects on NLO properties of dicarba-*closo*-dodecarboranes isomers 1,2-(*ortho*-), 1,7-(*meta*-) and 1,12-(*para*-) $C_2B_{10}H_{12}$ [8]. In such a study, among the analyzed isomers, the para-derivatives were found to be the most sensitive by replacements and with the larger values of β_{tot}. Moreover, the results from Ref. [8] suggested the investigated compounds as potential molecules for NLO applications, since the β_{tot} values are more than twice the corresponding for *p*-nitroaniline. The cobalt bis (dicarbollide) anion [3-Co-(1,2-$C_2B_9H_{11})_2$]$^-$ (Fig. 1) besides being the most investigated metallaheteroborane sandwich compound, it presents potential application in NLO [29–31].

Here, our aim is to study the substituent effects on NLO properties of a series of cobalt bis (dicarbollide) derivatives: [3-Co-(1,2-$C_2B_9H_9)_2$RX]$^-$ (where R, X = H, NH_2, NO_2, CH_3, OCH_3, Ph, Cl) (see Fig. 2). Thus, NLO quantities will be obtained at DFT level of theory and correlations between Hammett electronic parameters [32] of the substituents ($\sum \sigma_p$) and ln(β_{tot}) will be tested. In addition, UV–Vis spectrum will be reported for all studied compounds. The paper is organized as follows: In Sect. 2, we describe the computational procedures. The results are reported and discussed in Sect. 3, and the concluding remarks are included in Sect. 4.

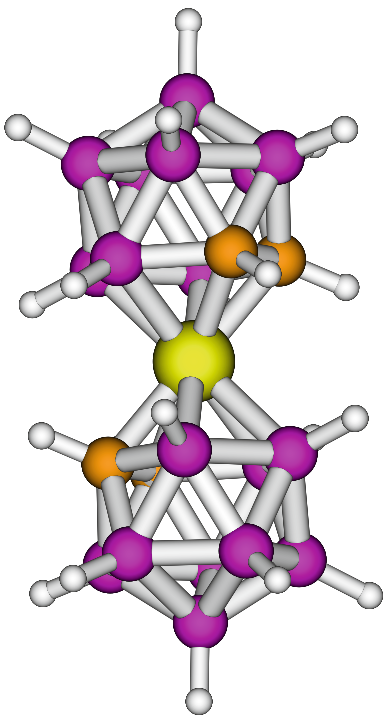

Fig. 1 B3LYP/6−31G(d,p) optimized structure of cobalt bis (dicarbollide) anion [3-Co-(1,2-$C_2B_9H_{11})_2$]$^-$

2 Computational procedures

The geometries of all studied molecules were fully optimized in the gas phase using density functional theory (DFT) with the B3LYP functional employing standard split valence basis set with inclusion of polarization and diffuse functions [6−31+G(d,p)]. Molecular first-order hyperpolarizabilities (β_{tot}) and dipole moments (d) were calculated using the B3LYP[6−31+G(d,p)] level of theory using the coupled perturbed Hartree–Fock (CPHF) [33] method within the static approach.

The first-order hyperpolarizability β is a tensor with 27 components. The tensor components β_{ijk} (with $i = x, y, z$; $j = x, y, z$ and $k = x, y, z$) are generally reducible when considering the symmetry properties. Through Kleinman symmetry ($\beta_{ij} = \beta_{ji}$) [34], the calculation provides 10 components. In the present paper, we obtain the three independent values for β components β_i ($i = x, y, z$) [Eq. (2)] and then solve the complete expression for calculating the magnitude of the β_{tot}, the molecular first-order hyperpolarizability [24] [Eq. (3)].

$$\beta_i = \beta iii + 1/3 \sum_{j \neq i} (\beta_{ijj} + \beta_{jij} + \beta_{jji}) \quad i = x, y, z; \quad j = x, y, z \tag{2}$$

$$\beta_{tot} = (\beta_x^2 + \beta_y^2 + \beta_z^2)^{1/2} \tag{3}$$

For all derivatives, excitation energies and oscillator strengths were calculated in two different ways: (a) by means of time-dependent DFT (TD-DFT) approach using GAUSSIAN-03 [35] (b) using the semiempirical ZINDO/S within the INDO/CIS approach, as implemented in the ORCA program [36–41]. The optimization of geometries and NLO calculations were performed using GAUSSIAN-03 [35].

3 Results and discussion

In this paper, we studied 13 derivatives of cobalt bis (dicarbollide) anion (Fig. 1). The analyzed series are depicted in Fig. 2: [3-Co-(1,2-$C_2B_9H_9)_2$RX]$^-$ (where R, X = H, NH_2, NO_2, CH_3, OCH_3, Ph, Cl). The calculated molecular hyperpolarizabilities (β_{tot}) as well as the dipole moments (d) are reported in Table 1.

Besides, correlations between properties and the Hammett electronic parameters [32] were obtained. A negative value of σ_p corresponds to substituent electron donor relative to the hydrogen atom and a positive σ_p an electron acceptor group relative to the hydrogen atom. The cooperative effect of both groups is described by the summation of individual σ_p ($\sum \sigma_p$).

In Table 1, the set of substituents are gathered in addition to $\sum \sigma_p$ [32]. Here this global parameter covers a

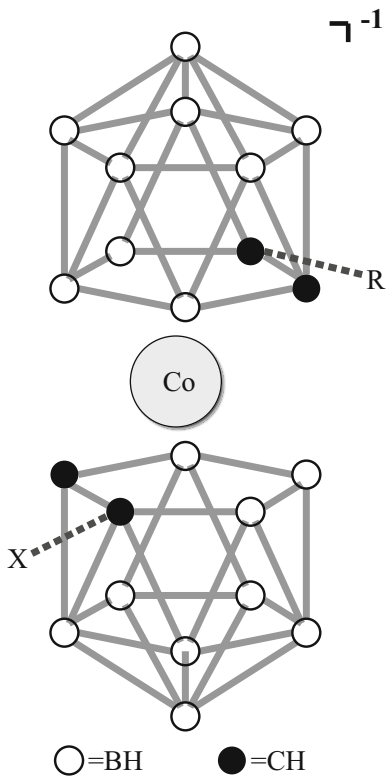

Fig. 2 Scheme of studied structures of cobalt bis (dicarbollide) $[3\text{-Co-}(1,2\text{-}C_2B_9H_9)_2RX]^-$. Hydrogen atoms attached to carbon atoms will be replaced by acceptor and donor electron groups, **R** and **X**, where R, X = H, NH_2, NO_2, CH_3, OCH_3, Ph, Cl

Table 1 Hyperpolarizabilities ($\beta_{tot} \times 10^{-30}$ cm^5/esu) and dipole moments (d, Debye) in parenthesis, obtained to analyzed series

R	X	$\sum\sigma_p$	$\beta_{tot}(d)$ $[Co\text{-}(1,2\text{-}C_2B_9H_9RX)_2]^-$	β_{tot} $(1,4\text{-}C_6H_4RX)$
NH_2	NH_2	−1.32	7.9 7 (2.41)	–
H	NH_2	−0.66	15.7 (1.43)	0.55
H	CH_3	−0.17	8.29 (1.26)	<0.2
Ph	Ph	−0.02	21.6 (3.82)	–
H	Ph	−0.01	14.4 (4.05)	–
H	H	0	0.0 (0.0)	0
NH_2	NO_2	+0.12	20.2 (1.95)	9.2
H	Cl	+0.23	13.3 (0.56)	<0.2
H	OCH_3	+0.34	27.4 (2.62)	<0.2
H	COH	+0.42	13.0 (1.90)	0.8
OCH_3	NO_2	+0.44	27.4 (2.68)	–
CH_3	NO_2	+0.61	18.6 (3.06)	2.1
H	NO_2	+0.78	9.81 (2.21)	1.9
NO_2	NO_2	+1.56	4.09 (2.17)	–

Experimental values of β_{tot} for para-substituted benzenes[47] are included for comparison

broad range of electronic effect with values from −1.32 (strong electron donor effect) to +1.56 (strong electron acceptor effect). In accordance with the results from Table 1, such NLO properties are found to be very sensitive to the type of pair substituent of the derivatives. For example, while the unsubstituted compound displays both β_{tot} and d nulls, the NLO quantities change from 7.97×10^{-30} cm^5/esu and 2.41 Debye $[Co(C_2B_9H_9)_2HNH_2]^-$ to 27.4×10^{-30} cm^5/esu and 2.62 Debye $[Co(C_2B_9H_9)_2OCH_3NO_2]^-$.

Some studies [8, 42–46] have reported relationships among NLO quantities and some Hammett electronic parameters [32]. In a previous study [8], we found that β_{tot} values of the 1,12-(*para*-) dicarba-*closo*-dodecarboranes push–pull compounds were enhanced by two orders of magnitude when compared to unsubstituted dodecarboranes.

In order to improve the investigation of the influence of substituents on NLO properties of $[3\text{-Co-}(1,2\text{-}C_2B_9H_9)_2RX]^-$ compounds, plots of molecular first-order hyperpolarizability (β_{tot}) as a function of Hammett electronic parameters, $\sum\sigma_p$, were obtained (Fig. 3). Furthermore, β_{tot} values of ($C_2B_{10}H_{10}RX$) [8] (where R, X = H, NH_2, NO_2, CH_3, OCH_3, Ph, Cl) are also depicted in Fig. 3. A similar profile can be noted between β_{tot} correlations of $C_2B_{10}H_{10}RX$ isomers [8] and $[3\text{-Co-}(1,2\text{-}C_2B_9H_9)_2RX]^-$ coordination compounds (see Fig. 3). This fact shows how the type of pair substituent substantially affects such properties. Besides, an enhancement of the NLO properties of substituted coordination compounds comparing to obtained values for isomer derivatives can be observed. Moreover, in Ref. [21], the authors have found that halogen and organic group substituted

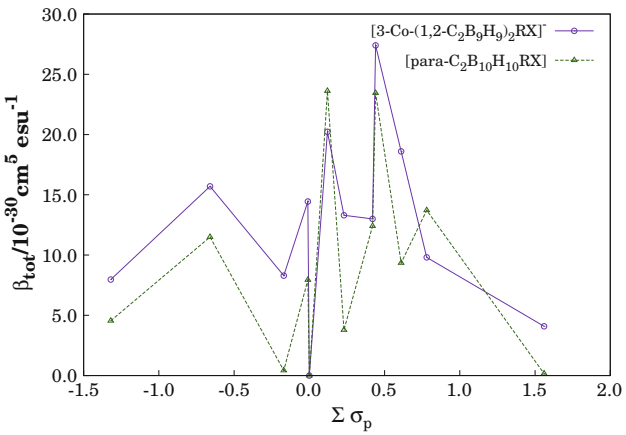

Fig. 3 Molecular hyperpolarizabilities (β_{tot}) of cobalt bis (dicarbollide) compounds $[3\text{-Co-}(1,2\text{-}C_2B_9H_9)_2RX]^-$ and -para dicarba-*closo*-dodecarboranes ($C_2B_{10}H_{12}$) versus Hammett electronic parameters of substituents

ortho- 12-vertex-*closo*-carboranes exhibits β_{tot} values enhanced by one order of magnitude when compared to the original isomers.

For comparison effects, in Table 1 are included β_{tot} experimental values of substituted benzenes [47]. Notice that β_{tot} of mono-substituted benzenes: $C_6H_5CH_3$ ($<0.2 \times 10^{-30}$ cm^5/esu) and $C_6H_5NH_2$ (0.55×10^{-30} cm^5/esu) are enhanced in the para-substituted compounds: 1,4-$C_6H_4CH_3NO_2$ (2.1×10^{-30} cm^5/esu) and 1,4-$C_6H_4NH_2NO_2$ (9.2×10^{-30} cm^5/esu). Also, an analogous behavior for studied series: [3-Co-(1,2-$C_2B_9H_9)_2HCH_3]^-$ (8.29×10^{-30} cm^5/esu) and [3-Co-(1,2-$C_2B_9H_9)_2HNH_2]^-$ (15.7×10^{-30} cm^5/esu) is improved to [3-Co-(1,2-$C_2B_9H_9)_2CH_3NO_2]^-$ (18.6×10^{-30} cm^5/esu) and [3-Co-(1,2-$C_2B_9H_9)_2NH_2NO_2]^-$ (20.2×10^{-30} cm^5/esu), when one hydrogen atom was changed for one NO_2 group.

It can be verified from Table 1 and Fig. 3 that the compounds with larger β_{tot} usually have a pair substituent with $\sum \sigma_p > 0$. Moreover, it can be noted that higher values of β_{tot} were obtained for [3-Co-(1,2)-$C_2B_9H_9)_2$ RX]$^-$ with $R, X = CH_3, NO_2$ [18.6×10^{-30} cm^5/esu]; NH_2, NO_2[20.2×10^{-30} cm^5/esu] and OCH_3, NO_2 [27.4×10^{-30} cm^5/esu]. These derivatives can be considered push–pull systems because they contain as pair substituent one electron acceptor and one electron donor group.

Since SHG depends on the development of NLO materials with a wide transparent region in the ultraviolet, the study of UV–Vis spectra of the molecules with potential NLO properties is desirable.

The experimental electronic absorption spectrum [48] of [Co–Co–(1,2-$C_2B_9H_{11})_2]^-$, in methanol solution, exhibits four principal bands: 445, 345, 293 and 216 nm, where the weak absorption at 445 nm is the responsible for the orange color of this compound.

Initially, by means of TD-DFT and ZINDO/S calculations, the UV–Vis spectra were computed for the unsubstituted compound [3-Co-(1,2-$C_2B_9H_{11})_2]^-$ ($\sum \sigma_p = 0$) (Fig. 4). In addition, the experimental data [48] are depicted in Fig. 4. We can observe from Fig. 4 that TD-DFT results are in better agreement with the experiment than ZINDO/S data. Both calculations produce the $\lambda_{max} = 276$ nm, shifted around -17 nm with respect to the experiment ($\lambda_{max} = 293$ nm). However, the values of molar absorptivity (ϵ) obtained with ZINDO/S were overestimated. Similarly to the experimental data [48] and Bühl et al. [30] theoretical work, in our study, the largest intensity was observed close to 300 nm for the unsubstituted compound. Moreover, as well as Ref. [30], from our findings, the absorption near 450 nm is very weak compared to the other strong bands in the UV region. This fact can be explained because both theoretical calculations were carried out considering [3-Co-(1,2-$C_2B_9H_{11})_2]^-$ with C_{2h} symmetry, and some of these transitions can be allowed when the symmetry is reduced [30].

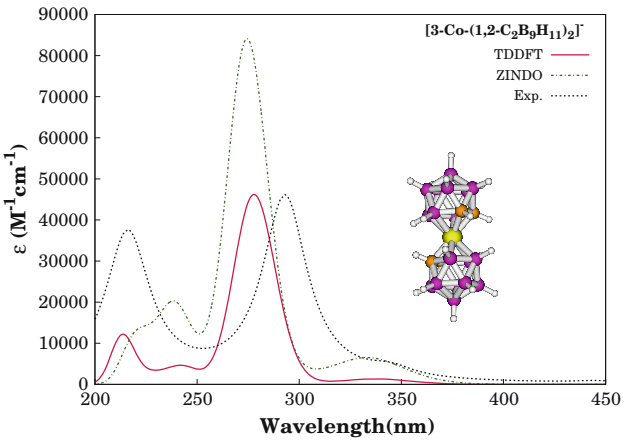

Fig. 4 Theoretical (this work) and experimental [48] UV–Vis spectra of cobalt bis (dicarbollide) anion [3-Co-(1,2-$C_2B_9H_{11})_2]^-$

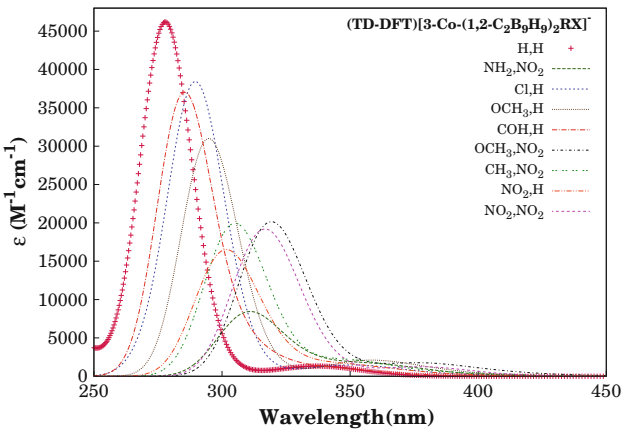

Fig. 5 UV spectra of cobalt bis (dicarbollide) compounds [3-Co-(1,2-$C_2B_9H_9)_2$RX]$^-$: unsubstituted (H,H) and with substituents $\sum \sigma_p > 0$. TD-DFT calculations

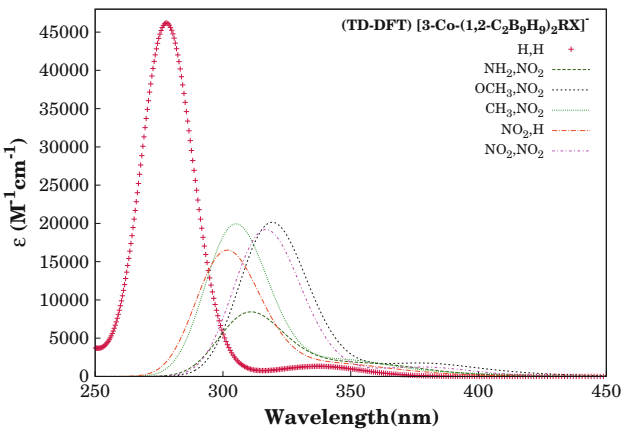

Fig. 6 UV spectra of cobalt bis (dicarbollide) compounds [3-Co-(1,2-$C_2B_9H_9)_2$RX]$^-$: unsubstituted (H,H) and with substituents R,X = H, NO_2. TD-DFT calculations

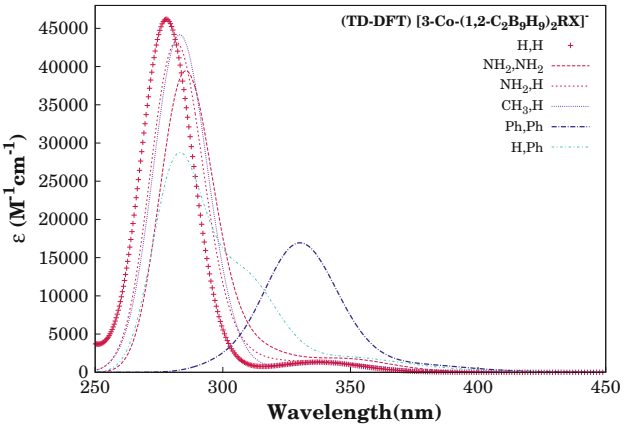

Fig. 7 UV–Vis spectra of cobalt bis (dicarbollide) compounds $[3\text{-Co-}(1,2\text{-}C_2B_9H_9)_2RX]^-$: unsubstituted (H,H) and with substituents $\sum \sigma_p < 0$. TD-DFT calculations

From here on, correlations between the Hammett parameters [32] of substituents and electronic absorption (TD-DFT) of the substituted compounds will be studied (Figs. 5, 6, 7). The spectra performed with ZINDO/S were omitted here.

The UV–Vis absorption spectra for compounds in which substituents are electron acceptor ($\sum \sigma_p > 0$) are reported in Fig. 5 and compared with the unsubstituted compound. There, we can notice an increase in charge transfer (CT), characterized by a bathochromic shift[1] on the CT maximum absorption wavelength.

Moreover, such a displacement is more significant in spectra of the compounds where at least one of the substituents is the nitro group (NO_2) (Fig. 6). This can be rationalized as follows: NO_2 is strongly electron withdrawing, and its presence provides larger intramolecular CT. Such a CT appears to be responsible for the electronic absorption near 445 nm. Figure 6 displays also the so mentioned absorption band (@445 nm), with rather small, but not zero, intensity.

With the exception of the compound with R, X = Ph, Ph, we do not observe any significant shift in spectra of the derivatives with substituents with $\sum \sigma_p > 0$ (Fig. 7). The peculiar behavior of phenyl radicals in carboranes has been studied [49]. Electron-accepting capability of carboranes is greatly improved when are added phenyl radicals [49].

Finally, when the absorption spectra of the 13 derivatives are analyzed (Fig. 2), the band next to 445 nm is not observed for any compounds with substituents having $\sum \sigma_p < 0$ (see Fig. 7).

Here we used the same methodology of previous work with the $C_2B_{10}H_{10}RX$ isomers [8], for comparison purposes. Therefore, neither the frequency dependence nor solvent effects in the properties were performed in this study.

[1] Bathochromic shift is a change of spectral band position in the absorption of a molecule to a longer wavelength. This effect is also commonly called a redshift.

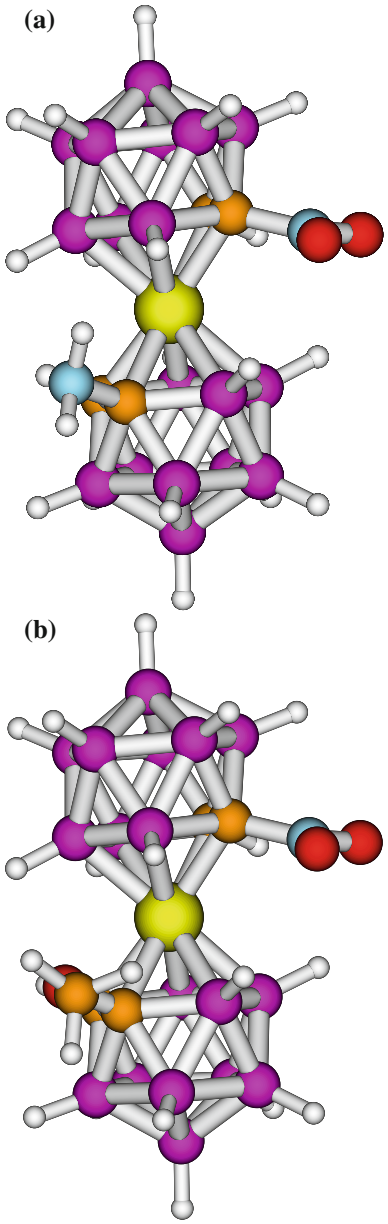

Fig. 8 B3LYP/6−31G(d,p) optimized structures of cobalt bis (dicarbollide) compounds with their respective β_{tot} **a** $[3\text{-Co-}(1,2\text{-}C_2B_9H_9)_2NH_2NO_2]^-$ $[20.2 \times 10^{-30}\,cm^5/esu]$ and **b** $[3\text{-Co-}(1,2\text{-}C_2B_9H_9)_2OCH_3NO_2]^-$ $[27.4 \times 10^{-30}\,cm^5/esu]$

4 Conclusions

In the present work, we studied the role played by substituent on NLO properties for a series of substituted cobalt bis (dicarbollide) $[3\text{-Co-}(1,2\text{-}C_2B_9H_9)_2RX]^-$ derivatives

(R, X $= H, NH_2, NO_2, CH_3, OCH_3, Ph, Cl$) (Fig. 2). The obtained NLO properties were strongly affected by replacements, compared to the unsubstituted anion, [3-Co-(1,2-$C_2B_9H_{11})_2]^-$ with C_{2h} symmetry.

The larger values of β_{tot} were obtained for push–pull compounds: [3-Co-(1,2-$C_2B_9H_9)_2CH_3NO_2]^-$ [18.6×10^{-30} cm^5/esu]; NH_2, NO_2 [20.2×10^{-30} cm^5/esu] and OCH_3, NO_2 [27.4×10^{-30} cm^5/esu]. In Fig. 8, examples of compounds with larger values of β_{tot} are depicted.

We identify a systematic bathochromic shift of intramolecular charge transfer bands only related to the compounds containing $\sum \sigma_p > 0$ pair substituents.

Through our findings, it can be verified that the UV–Vis transition near 450 nm essentially originates from CT and the presence of the NO_2 group provides an enhancement of this intramolecular energy transfer (see Figs. 5, 6).

Since these species are considered archetype of all metallaheteroboranes, the finding of new compounds and the development of novel molecular architectures are of fundamental importance in NLO research. Thus, our work suggest these cobalt bis (dicarbollide) derivatives as potential molecules for the design of the NLO materials, since these molecules exhibit β_{tot} values more than twice the corresponding for *p*-nitroaniline, large *d* values, excellent chemical and thermal stability and high optical transparency.

Acknowledgments We are indebted to Conselho Nacional de Desenvolvimento Científico e Tecnológico (CNPq) and Coordenação de Aperfeiçoamento de Pessoal de Nível Superior (CAPES) for financial support. G.M.A.J. acknowledges Maikel Y. Ballester for valuable discussions about this work.

References

1. Grimes RN (1987) Pure Appl Chem 59:847
2. Fister TT, Vila FD, Seidler GT, Svec L, Linehan JC, Cross JO (2008) J Am Chem Soc 130:925
3. Grimes RN (2000) Coord Chem Rev 200:773
4. Junqueira GMA, Rocha LC, Cotta VT, Cesar ET (2012) Chem Phys Lett 538:54
5. Fàrras P, Juárez-Pérez EJ, Lepsik M, Luque R, Núñez R, Teixidor F (2012) Chem Soc Rev 41:3445
6. Choi S, Byun Y (2013) J Organomet Chem 733:49
7. Grimes RN (2013) J Organomet Chem 747:4
8. Junqueira GMA, Sato F (2014) J Mol Model 20:2275
9. Kozisek M, Cigler P, Lepsik M, Fanfrlik J, Rezacova P, Brynda J, Pokorna J, Plesek J, Grüner B, Vaclavikova KSJ, Kral V, Konvalinka J (2008) J Med Chem 51:4839
10. Rezacova P, Pokorna J, Brynda J, Kozisek M, Cigler P, Lepsik M, Fanfrlik J, Rezac J, Saskova KG, Sieglova I, Plesek J, Sicha V, Gruener B, Oberwinkler H, Sedlacek J, Kraeusslich HG, Hobza P, Kral V, Konvalinka J (2009) J Med Chem 52:7132
11. Nakamura H, Yasui Y, Ban HS (2013) J Organomet Chem 747:189
12. Tan JJ, Cong XJ, Hu LM, Wang CX, Jia L, Liang XJ (2010) Drug Discov Today 15:186
13. Balaz S, Caruso AN, Platt NP, Dimov DI, Boag NM, Brand JI, Losovyj YB, Dowben PA (2007) J Phys Chem B 111:7009
14. Murphy D, Mingos D, Forward J (1993) J Mater Chem 3(1):67
15. McKinney J, McQuillan F, Chen H, Hamor T, Jones C, Slaski M, Cross G, Harding C (1997) J Organomet Chem 547:253
16. Abe J, Nemoto N, Nagase Y, Shirai Y, Iyoda T (1998) Inorg Chem 37:172
17. Base K, Tierney M, Fort A, Muller J, Grinstaff M (1999) Inorg Chem 38:287
18. Grüner B, Janousek Z, King BT, Woodford JN, Wang CH, Vsetecka V, Michl J (1999) J Am Chem Soc 121:3122
19. Dalby KJ, Erhardt DES, McIntosh RD, Macgregor S, Rae K, Rosair GM, Settels V, Welch AJ, Hodson BE, McGrath TD, Stone FGA (2007) J Am Chem Soc 129:3302
20. Kennedy R, Clingerman D, Morris W, Wilmer C, Sarjeant A, Stern CL, O'Keeffe M, Snurr R, Hupp JT, Farha O, Mirkin CA (2014) Cryst Growth Des 14:1324
21. Fan M, Sun S, Qiu Y, Liu X, Su Z (2011) Int J Quantum Chem 111:1039
22. Chen CT, Marder SR, Cheng L (1994) J Am Chem Soc 116:3117
23. Law K (1995) J Phys Chem 99:9818
24. Kanis DR, Ratner MA, Marks TJ (1994) Chem Rev 94:195
25. Buckingham AD (2007) Adv Chem Phys 12:107
26. Zyss J, Ledouxs I (1994) Chem Rev 94:77
27. Kobus J, Moncrieff D, Wilson S (2007) J Phys B At Mol Opt Phys 40:877
28. Qiu YQ, Liu XD, Sun SL, Fan M, Su ZM, Wang RS (2008) J Mol Struct (THEOCHEM) 863:66
29. Mortimer M, Knobler C, Hawthorne MF (1996) Inorg Chem 35:5750
30. Bühl M, Hnyk D, Machácek J (2005) Chem Eur J 11:4109
31. Chevrot G, Schurhammer R, Wipff G (2006) J Phys Chem B 110:9488
32. Hansch C, Leo A, Taft RW (1991) Chem Rev 91:165
33. Dykstra CE, Jasien PG (1984) Chem Phys Lett 109:388
34. Kleinman DA (1962) Phys Rev 128:1761
35. Frisch MJ, Trucks GW, Schlegel HB, Scuseria GE, Robb MA, Cheeseman JR, Montgomery Jr JA, Vreven T, Kudin KN, Burant JC, Millam J, Iyengar SS, Tomasi J, Barone V, Mennucci B, Cossi M, Scalmani G, Rega N, Petersson GA, Nakatsuji H, Hada M, Ehara M, Toyota K, Fukuda R, Hasegawa J, Ishida M, Nakajima T, Honda Y, Kitao O, Nakai H, Klene M, Li X, Knox JE, Hratchian HP, Cross JB, Adamo C, Jaramillo J, Gomperts R, Stratmann RE, Yazyev O, Austin AJ, Cammi R, Pomelli C, Ochterski JW, Ayala PY, Morokuma K, Voth GA, Salvador P, Dannenberg JJ, Zakrzewski VG, Dapprich S, Daniels AD, Strain MC, Farkas O, Malick DK, Rabuck AD, Raghavachari K, Foresman JB, Ortiz JV, Cui Q, Baboul AG, Clifford S, Cioslowski J, Stefanov BB, Liu G, Liashenko A, Piskorz P, Komaromi I, Martin RL, Fox DJ, Keith T, Al-Laham MA, Peng CY, Nanayakkara A, Challacombe M, Gill PMW, Johnson B, Chen W, Wong MW, Gonzalez C, Pople JA (2003) Gaussian 03 Revision B.05. Gaussian Inc., Pittsburg
36. Neese F (2012) The ORCA program system. Wiley Interdiscip Rev Comput Mol Sci 2:73
37. Petrenko T, Kossmann S, Neese F (2001) J Chem Phys 134:054116
38. Petrenko T, Kossmann S, Neese F (2009) New J Phys 11:015001
39. Grimme S, Neese F (2007) J Chem Phys 127:154116
40. Petrenko T, Ray K, Wieghardt K, Neese F (2006) J Am Chem Soc 128:4422
41. Neese F, Olbrich G (2002) Chem Phys Lett 362:170
42. Junqueira GMA, Da Silva AM (2010) Int J Quantum Chem 110:489
43. Sastre A, Diaz-Garcia MA, del Rey B, Dhenaut C, Zyss J, Ledoux I, Agullo-Lopez F, Torres T (1997) J Phys Chem A 101:9773

44. Park G, Cho BR (2004) J Phys Org Chem 17:169
45. Park G, Cho BR (2005) J Phys Org Chem 18:264
46. Barzoukas M, Fort A, Klein G, Serbutoviez C, Oswald L, Nicoud JF (1992) Chem Phys 164:395
47. Cheng LT, Tam W, Stevenson SH, Meredith GR, Rikken G, Marder SR (1991) J Phys Chem 95:10631
48. Hawthorne M, Young D, Andrews T, Howe D, Pilling RL, Pitts A, Reintjes M, Warren LF Jr, Wegener PA (1968) J Am Chem Soc 90:879
49. Jin GF, Hwang JH, Lee JD, Wee KR, Suh IH, Kang SO (2013) Chem. Commun. 49:9398. doi:10.1039/C3CC45313H

Theor Chem Acc (2015) 134:22
DOI 10.1007/s00214-015-1622-x

REGULAR ARTICLE

The driving force role of ruthenacyclobutanes

Sai Vikrama Chaitanya Vummaleti · Luigi Cavallo · Albert Poater

Received: 5 November 2014 / Accepted: 16 January 2015 / Published online: 7 February 2015

Abstract DFT calculations have been used to determine the thermodynamic and kinetic preference for ruthenacyclobutanes resulting from the experimentally proposed interconversion pathways (olefin and alkylidene rotations) through the investigation of cross-metathesis reaction mechanism for neutral Grubbs catalyst, $RuCl_2(=CHEt)$ NHC (**A**), with ethylene and 1-butene as the substrates. Our results show that although the proposed interconversions are feasible due to the predicted low energy barriers (2-6 kcal/mol), the formation of ruthenacyclobutane is kinetically favored over the competitive reactions involving alkylidene rotations. In comparison with catalyst **A**, the reaction energy profile for cationic Piers catalyst $[RuCl_2(=CHPCy_3)NHC^+]$ (**B**) is more endothermic in nature with both ethylene and 1-butene substrates.

Keywords Olefin metathesis · Metallacycle · Ruthenium · Ruthenacyclobutane · DFT calculations

Published as part of the special collection of articles derived from the 9th Congress on Electronic Structure: Principles and Applications (ESPA 2014).

Electronic supplementary material The online version of this article (doi:10.1007/s00214-015-1622-x) contains supplementary material, which is available to authorized users.

S. V. C. Vummaleti · L. Cavallo
Physical Sciences and Engineering Division, Kaust Catalysis Center, King Abdullah University of Science and Technology, Thuwal 23955-6900, Saudi Arabia

A. Poater (✉)
Institut de Química Computacional i Catàlisi and Departament de Química, Universitat de Girona, Campus Montilivi, 17071 Girona, Catalonia, Spain
e-mail: albert.poater@udg.edu

Abbreviations

SIMes	1,3-Bis(2,4,6-trimethylphenyl)-4,5-dihydroimidazolin-2-ylidene
DMDAM	Dimethyl diallyl malonate

1 Introduction

Olefin metathesis is a powerful method for the clean, reliable, and efficient construction of carbon–carbon bonds in synthetic chemistry [1–5]. As a testimony to its importance, metathesis reaction is widely used in the preparation of fine chemicals [6–8], biologically active compounds [9–12], new functionalized materials, and various polymers [13–16]. Therefore, it has become one of the most relevant reactions for organic synthesis. The reaction takes place only in the presence of a suitable transition-metal catalyst. In particular, well-defined ruthenium catalysts **1** and **2** (see Scheme 1) have received significant attention due to their high reactivity, commercial availability, and functional group tolerance [17–19].

The mechanism of ruthenium-catalyzed olefin metathesis has been extensively studied, based on the principal steps occur according to the Chauvin mechanism [20], where the transformation of a metal–alkylidene complex and a coordinated olefin into a four-membered metallacycle, whose opening in the forward direction leads to the formation of the observed products. The first experimental [21–25] and theoretical insights [26–30] in regard to the mechanism were achieved since the late 1990s. Since these studies, DFT calculations have been extensively used to clarify many aspects of Ru-catalyzed olefin metathesis [31–54], and efforts have been made to validate computational protocols [55–63]. To this end, we recently reported a highly accurate computational and rather cheap recipe, M06/TZVP//BP86/SVP (PCM, $P = 1{,}354$ atm) [64].

Scheme 1 Olefin metathesis ruthenium catalysts

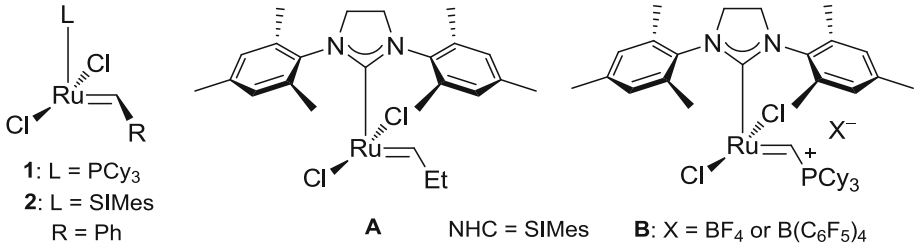

Despite a large number of notable studies in the past two decades, the nature of the metallacyclobutane intermediate, particularly with regard to the stereochemical orientation of the ligands, still remains elusive. These insights have greater implications toward olefin metathesis catalyst and reaction design. To fill this gap, in 2005, Piers and co-workers reported the first direct observation of a ruthenametallacycle upon the reaction of catalyst **B** (see Scheme 1) with ethylene metathesis at −50 °C [65]. These species are usually detected at low temperatures (experiments are performed between −40 and −80 °C) by means of NMR spectroscopy [65–69]. In the subsequent years [66–69], Wenzel and Grubbs reported several ruthenacyclobutanes (α-mono- and α,α-disubstituted species (both *cis* and *trans*)) arising from the reaction between **B** and different terminal olefins. Additionally, they found that the ruthenacyclobutanes to be dynamic structures that proceed through a series of nonproductive metallacycle formations/cycloreversions prior to olefin exchange. Overall, the study summarizes that alkylidene dynamics, in addition to differential metallacycle stability, play a role in the stereochemical outcome of an olefin metathesis reaction.

Herein, we report the cross-metathesis reaction mechanism as well as the experimentally proposed interconversion pathways (olefin and alkylidene rotations) for $RuCl_2$(=CHEt)NHC (**A**) using ethylene and 1-butene as the substrates. In addition, we report metathesis mechanism for [$RuCl_2$(=CHPCy_3)NHC$^+$] (**B**) using ethylene and 1-butene. A recent DFT study by Jaque et al. [70] about the nature of metallacycles in olefin metathesis elucidates why the α,β-disubstituted species are not detected experimentally, whereas α-mono-substituted and α,α-disubstituted species are detected even at low temperatures (−40 and −80 °C). To sum up, their mechanistic insights reveal that the absence of the β-mono- α,β-disubstituted species is due to their less thermodynamic stability compared to α-mono- and α,α-disubstituted species. Bearing in mind these results here, we strengthen the study about the relative stability of the 14 electron (14e$^-$) species, plus the next 16 electron species (16e$^-$), either the coordination intermediate or the metallacycle, unraveling the mechanistic insights by DFT calculations of the data of Grubbs et al. [66–69].

2 Computational details

All the DFT static calculations were performed with the Gaussian09 set of programs [71]. The electronic configuration of the molecular systems was described with the standard split-valence basis set with a polarization function of Ahlrichs and co-workers for H, C, N, and Cl (SVP keyword in Gaussian) [72]. For Ru, we used the small-core, quasi-relativistic Stuttgart/Dresden effective core potential, with an associated valence basis set contracted (standard SDD keywords in Gaussian09) [73–75]. The geometry optimizations were performed without symmetry constraints, and the characterization of the located stationary points was performed by analytical frequency calculations. The BP86 functional was employed in the geometry optimization. The reported free energies, ΔG, were built through single-point energy calculations in solvent on the BP86/SVP geometries using both BP86 (given in brackets) and M06 (given without brackets) functionals [76]. Solvent effects were included with the PCM model using CH_2Cl_2 as solvent [77, 78]. To these BP86/TZVP and M06/TZVP electronic energies in solvent, zero-point energy and thermal corrections were included from the gas-phase frequency calculations at the BP86/SVP level.

3 Results

Figure 1 shows the most stable species and the free energy for $RuCl_2$(=CHEt)NHC (**A**)-mediated olefin metathesis reaction with ethylene as the substrate. Going into detail, the first step we considered here is the coordination of ethylene to the metal in 14e$^-$ catalyst species, **A**, to give the intermediate **I**, which lies 3.3 kcal/mol above **A** and requires the overcoming of a barrier of 7.9 kcal/mol. Then, a barrierless step in terms of Gibbs free energy drives intermediate **I** to the stable metallacycle complex **II**, lying 8.4 kcal/mol below **I** and 5.1 kcal/mol below **A** plus the free olefin substrate, respectively. The next step corresponds to the ring opening of metallacycle **II**, leading to the formation of a second coordination intermediate **III**, requires an energy barrier of 10.7 kcal/mol from **II**. From an energetic point of view, intermediate **III** is 9.5 kcal/mol less stable relative to **II**. In the final step, release of alkene

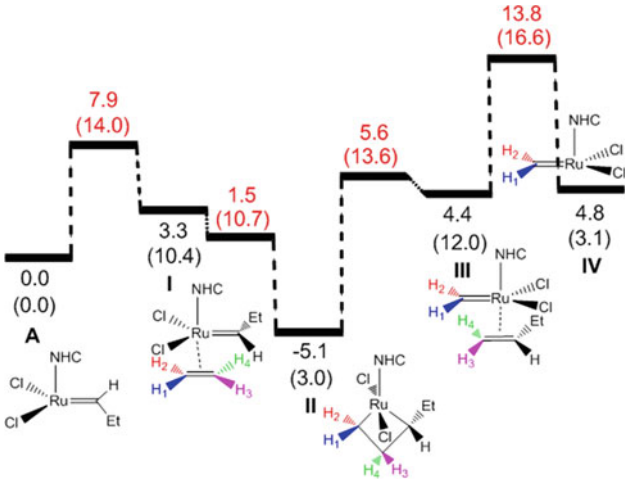

Fig. 1 Computed stationary points for the olefin metathesis reaction pathway for $RuCl_2$(=CHEt)NHC (**A**) with ethylene as a substrate

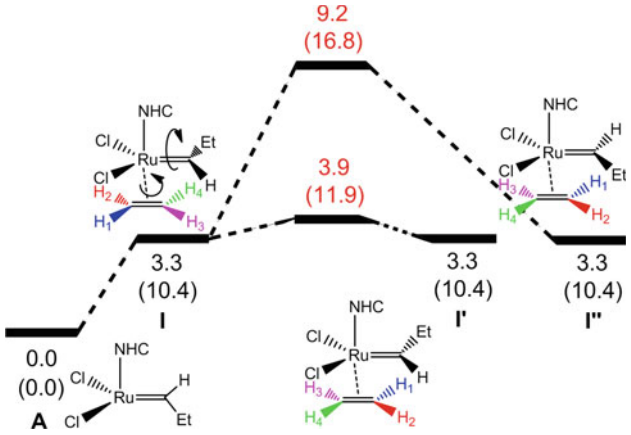

Fig. 2 Possible competitive reactions of the studied ethylene metathesis reaction mechanism in Fig. 1

from **III** results in the formation of a second $14e^-$ species **IV**, overcoming a barrier of 9.4 kcal/mol above **III**. This complex **IV** is 4.8 kcal/mol higher in energy with respect to **A**, suggesting that overall reaction pathway is slightly endothermic in nature. This endothermicity might be attributed in part to the differential stability of carbenes, i.e., phenylidene in **A** is more stable when compared to methylidene in **IV**, due to the fact that the carbene carbon for **IV** is more electrophilic. However, a point worth mentioning here is that the BP86 calculated ΔG values follow the same trend as M06.

Having completed the description of the $RuCl_2$(=CHEt)NHC (**A**)-mediated catalytic cycle, we now focus on the alternative deactivation reactions that could decrease the yield of the above studied reaction pathway (see Fig. 2). Rotation of ethylene around the metal-olefin axis in intermediate **I** is nearly barrierless, requiring only .6 kcal/mol. On the contrary, rotation of =CHEt alkylidene group together with the olefin rotation requires a slightly higher barrier of 5.9 kcal/mol above **I**, which is 1.5 kcal/mol less expensive than the single rotation of =CHEt alkylidene group. These predicted barriers are lower in energy when compared to the upper barrier **II** → **III** (10.7 kcal/mol) in Fig. 1, suggesting that the studied rotation reactions would be feasible even at low experimental temperatures (−45 °C). However, it is clear that the formation of metallacycle complex **II** is much easier when compared to the formation of rotational isomers of **I**, **I′**, and **I″**, since the former step is a barrierless reaction.

To understand the effect of olefin substrate, we describe here the reaction mechanism up to metallacycle formation for catalyst **A** using 1-butene as the substrate and the corresponding energy profile is shown in Fig. 3. Overall, the results obtained for 1-butene are similar to that of ethylene

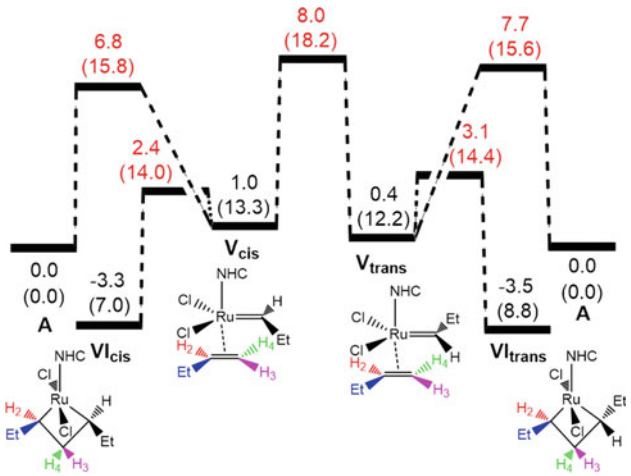

Fig. 3 Computed stationary points for the olefin metathesis reaction pathway for $RuCl_2$(=CHEt)NHC (**A**) with 1-butene as a substrate

presented in Fig. 1. In detail, coordination of 1-butene to metal in **A** leads to the formation of coordination intermediates $\mathbf{V_{cis}}$ and $\mathbf{V_{trans}}$, followed by a cyclization step gives rise to metallacycles $\mathbf{VI_{cis}}$ and $\mathbf{VI_{trans}}$, respectively. From an energy point of view, intermediates $\mathbf{V_{cis}}$ and $\mathbf{V_{trans}}$ are nearly isoenergetic and require the overcoming of a barrier of 6.8 ($\mathbf{A} \rightarrow \mathbf{V_{cis}}$) and 7.7 kcal/mol ($\mathbf{A} \rightarrow \mathbf{V_{trans}}$), respectively. These barriers are comparable to the **A** → **I** barrier (7.9 kcal/mol) for ethylene in Fig. 1. An important result here is that the interconversion of $\mathbf{V_{cis}}$ and $\mathbf{V_{trans}}$ (i.e., rotation of alkylidene group) requires a barrier of ≈7.5 kcal/mol, which is much higher in energy when compared to the barrier of ≈2 kcal/mol required for formation of respective metallacycles, $\mathbf{VI_{cis}}$ and $\mathbf{VI_{trans}}$. This observation clearly suggests that formation of metallacycle is favored over the interconversion of coordination intermediates.

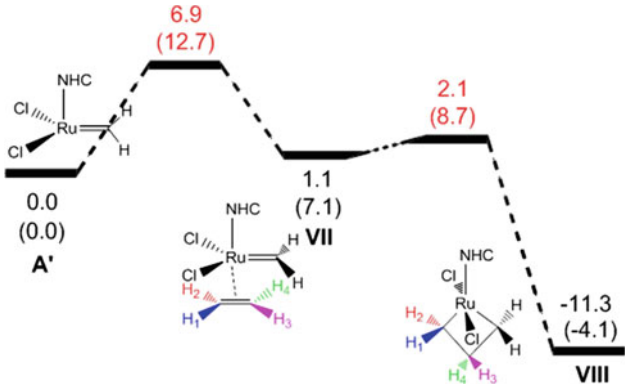

Fig. 4 Computed stationary points up to metallacycle formation for $RuCl_2(=CH_2)NHC$ (**A′**)-mediated olefin metathesis with ethylene substrate

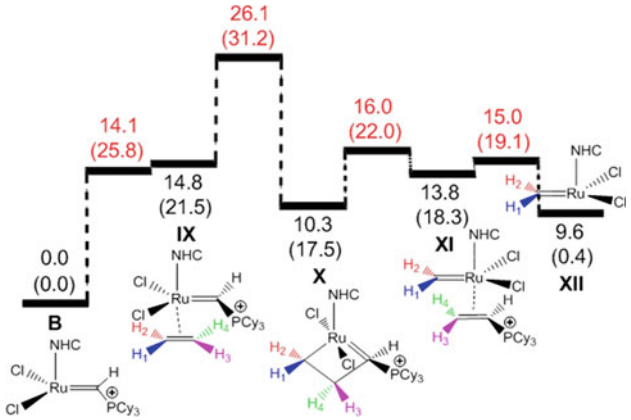

Fig. 5 Computed stationary points for $RuCl_2(=CHPcy_3)NHC^+$ (**B**)-mediated olefin metathesis with ethylene substrate

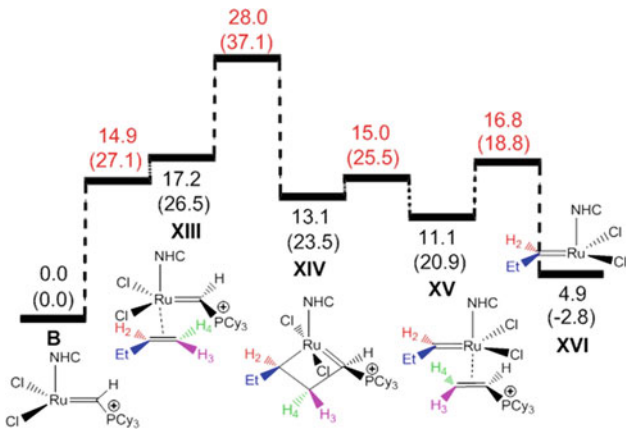

Fig. 6 Computed stationary points for $RuCl_2(=CHPcy_3)NHC^+$ (**B**)-mediated olefin metathesis with 1-butene substrate

Additionally, we studied the relative thermodynamic stability of metallacycles, $\mathbf{VI_{cis}}$ and $\mathbf{VI_{trans}}$, by replacing the "Et" group by "Me." The results indicate that, in the presence of less steric Me group, the stability of $\mathbf{VI_{cis}}$ and $\mathbf{VI_{trans}}$ metallacycles is reversed, i.e., the latter is 1.5 kcal/mol more stable than the former.

Next, we describe the effect of alkylidene group for the reaction mechanism given in Fig. 1 using $RuCl_2(=CH_2)$ NHC catalyst (**A′**) and ethylene as the substrate. The reaction energy profile up to metallacycle formation is shown in Fig. 4. In detail, the coordination intermediate **VII** is 2.2 kcal/mol more stable than the similar intermediate for **A** (**I** in Fig. 1). Additionally, the predicted barrier **A′** → **I** is 1.0 kcal/mol lower in energy relative to **A** → **I**. Next, the metallacycle **VIII** is 6.2 kcal/mol more stable than the **II** and requires a low barrier of 1.0 kcal/mol from **VII**. This relative high stability of **VIII** with respect to **A′** might be associated with the increase in the electron density around the metal center as Solans-Monfort and Jaquet et al. have recently rationalized in detail by the decompostion of the bonding energy [70]. This stabilization of the metallacycle is not that important with ylidene groups able to interact with the ruthenium such as ethylidene in **A**, or phenylidene [39, 79]. On the contrary, the presence of the $=CH_2$ moiety on **VIII** makes the reaction pathway more exothermic when compared to the presence of the more sterically demanding =CHEt group in species **VI**.

For comparison with Grubbs catalyst **A**, we studied the reaction mechanism for cationic Piers catalyst $[RuCl_2(=CHPCy_3)NHC^+]$ (**B**) using ethylene as the substrate (see Fig. 5). The main results can be summarized as follows: In the case of **B**, the coordination intermediate (**IX**) and metallacycle (**X**) complex are thermodynamically less stable (11.5 and 15.4 kcal/mol, respectively) relative to the similar complexes (**I** and **II**) for **A** in Fig. 1; additionally, the first barrier **B** → **IX** is placed 6.2 kcal/mol higher in energy when compared to the corresponding barrier **I** → **II** for **A**. Similarly, the barrier for the formation of metallacycle **X** (**IX** → **X**) is predicted to be 11.3 kcal/mol above **IX**, while for **A**, this reaction is barrierless. In contrast to the first two barriers, the predicted barrier for metallacycle opening step (**X** → **XI**) is 3.7 kcal/mol lower in energy relative to the **II** → **III** barrier for **A**. Taking together, these observations suggest that catalyst **B**-mediated ethylene metathesis reaction is less exothermic in nature when compared to catalyst **A**.

Finally, to understand the effect of olefin substrate, we investigated the reaction mechanism presented in Fig. 5 for **B** using 1-butene (see Fig. 6). By comparing the two reaction energy profiles given in Figs. 5 and 6, it is evident that substrate 1-butene results in the formation of less thermodynamically stable (by ≈3.0 kcal/mol) coordination intermediate (**XIII**) and metallacycle (**XIV**) when compared to ethylene. Of course, this can be attributed to the higher sterical hindrance of 1-butene relative to ethylene. On the

other hand, the upper barrier that corresponds to the formation of metallacycle is almost similar for both substrates (≈11.0 kcal/mol); however, the metallacycle ring opening step barrier is 3.8 kcal/mol lower in energy for 1-butene than ethylene.

4 Conclusions

In summary, using DFT calculations, we have reported the olefin metathesis reaction mechanism for neutral Grubbs catalyst, $RuCl_2$(=CHEt)NHC (**A**), with ethylene and 1-butene as the substrates. Our results show that for both substrates, formation of metallacyclobutane is kinetically favored over the possible competitive alkylidene rotations. Additionally, in the case of ethylene metathesis reaction, we observed that the presence of less steric $=CH_2$ group on catalyst **A** makes the reaction pathway more exothermic when compared to the relatively high steric =CHEt group. Finally, for comparison, we investigated the reaction mechanism for cationic Piers catalyst [$RuCl_2(=CHPCy_3)NHC^+$] (**B**) using ethylene and 1-butene. Different from catalyst **A**, **B** displays a more endothermic reaction energy profile. The differences in the thermodynamics of the metathesis reaction between **A** and **B** can be attributed to the charged nature of the later complexes, appealing for future new catalysts, able to take profit of these rather unstable metallacycle intermediates, remarkable in opposition to the Schrock catalysts [80–82].

Acknowledgments A.P. thanks the Spanish MINECO for a Ramón y Cajal contract (RYC-2009-05226) and a José Castillejo fellowship (CAS14/00165), and European Commission for a Career Integration Grant (CIG09-GA-2011-293900).

References

1. Grubbs RH (2003) Handbook of olefin metathesis. Wiley, Weinheim, Germany
2. Vougioukalakis GC, Grubbs RH (2009) Chem Rev 110:1746–1787
3. Samojowicz C, Bieniek M, Grela K (2009) Chem Rev 109:3708–3742
4. Fürstner A (2000) Angew Chem Int Ed 39:3012–3043
5. Keitz BK, Endo K, Patel PR, Herbert MB, Grubbs RH (2012) J Am Chem Soc 134:693–699
6. Connon SJ, Blechert S (2003) Angew Chem Int Ed 42:1900–1923
7. Pozgan F, Dixneuf PH (2007) Metathesis chemistry: from nanostructure design to synthesis of advanced materials, vol 243. Springer, Dordrecht, The Netherlands, pp 195–222
8. Mele G, Li J, Vasapollo G (2008) Chim Oggi 26:72–74
9. Giudici RE, Hoveyda AH (2007) J Am Chem Soc 129:3824–3825
10. Keitz BK, Grubbs RH (2010) Organometallics 29:403–408
11. Stenne B, Timperio J, Savoie J, Dudding T, Collins SK (2010) Org Lett 12:2032–2035
12. Schmidt B, Staude L (2009) J Org Chem 74:9237–9240
13. Leitgeb A, Wappel J, Slugovc C (2010) Polymer 51:2927–2946
14. Bielawski CW, Grubbs RH (2007) Prog Polym Sci 32:1–29
15. Mol JC (2004) J Mol Catal A Chem 213:39–45
16. Baughman TW, Wagener KB (2005) Adv Polym Sci 76:1–42
17. Adlhart C, Chen P (2004) J Am Chem Soc 126:3496–3510
18. Tallarico JA, Bonitatebus PJ Jr, Snapper ML (1997) J Am Chem Soc 119:7157–7158
19. Anderson DR, Hickstein DD, O'Leary DJ, Grubbs RH (2006) J Am Chem Soc 128:8386–8387
20. Hérisson PJL, Chauvin Y (1971) Die Makromol Chem 141:161–176
21. Dias EL, Nguyen ST, Grubbs RH (1997) J Am Chem Soc 119:3887–3897
22. Sanford MS, Ulman M, Grubbs RH (2001) J Am Chem Soc 123:749–750
23. Sanford MS, Love JA, Grubbs RH (2001) J Am Chem Soc 123:6543–6554
24. Adlhart C, Hinderling C, Baumann H, Chen P (2000) J Am Chem Soc 122:8204–8214
25. Adlhart C, Chen P (2000) Helv Chim Acta 83:2192–2196
26. Vyboishchikov SE, Bühl M, Thiel W (2002) Chem Eur J 8:3962–3975
27. Cavallo L (2002) J Am Chem Soc 124:8965–8973
28. Aagaard OM, Meier RJ, Buda F (1998) J Am Chem Soc 120:7174–7182
29. Bernardi F, Bottoni A, Miscione GP (2000) Organometallics 19:5529–5532
30. Adlhart C, Chen P (2002) Angew Chem Int Ed 41:4484–4487
31. Stewart IC, Benitez D, O'Leary DJ, Tkatchouk E, Day MW, Goddard WA, Grubbs RH III (2009) J Am Chem Soc 131:1931–1938
32. van Rensburg WJ, Steynberg PJ, Meyer WH, Kirk MM, Forman GS (2004) J Am Chem Soc 126:14332–14333
33. Correa A, Cavallo L (2006) J Am Chem Soc 128:13352–13353
34. Webster CE (2007) J Am Chem Soc 129:7490–7491
35. Benitez D, Tkatchouk E, Goddard WA III (2008) Chem Commun 6194–6196
36. Mathew J, Koga N, Suresh CH (2008) Organometallics 27: 4666–4670
37. Barbasiewicz M, Szadkowska A, Bujok R, Grela K (2006) Organometallics 25:3599–3604
38. Poater A, Cavallo L (2010) J Mol Catal A Chem 324:75–79
39. Poater A, Ragone F, Correa A, Cavallo A (2011) Dalton Trans 40:11066–11069
40. Leitgeb A, Abbas M, Fischer RC, Poater A, Cavallo L, Slugovc C (2012) Catal Sci Technol 2:1640–1643
41. Falivene L, Poater A, Cazin CSJ, Slugovc C, Cavallo L (2013) Dalton Trans 42:7312–7317
42. Credendino R, Poater A, Ragone F, Cavallo L (2011) Catal Sci Technol 1:1287–1297
43. Bantreil X, Poater A, Urbina-Blanco CA, Bidal YD, Falivene L, Randall RAM, Cavallo L, Slawin AMZ, Cazin CSJ (2012) Organometallics 31:7415–7426
44. Poater A, Bahri-Lalehac N, Cavallo L (2011) Chem Commun 47:6674–6676
45. Poater A, Cosenza B, Correa A, Giudice S, Ragone F, Scarano V, Cavallo L (2009) Eur J Inorg Chem 1759–1766
46. Benitez D, Goddard WA III (2005) J Am Chem Soc 127:12218–12219
47. Liu P, Xu X, Dong X, Keitz BK, Herbert MB, Grubbs RH, Houk KN (2012) J Am Chem Soc 134:1464–1467
48. Costabile C, Mariconda A, Cavallo L, Longo P, Bertolasi V, Ragone F, Grisi F (2011) Chem Eur J 17:8618–8629
49. Núñez-Zarur F, Solans-Monfort X, Rodríguez-Santiago L, Sodupe M (2012) Organometallics 31:4203–4215
50. Nuñez-Zarur F, Solans-Monfort X, Pleixats R, Rodríguez-Santiago L, Sodupe M (2013) Chem Eur J 19:14553–14565
51. Núñez-Zarur F, Solans-Monfort X, Rodríguez-Santiago L, Sodupe M (2013) ACS Catal 3:206–218

52. Benitez D, Tkatchouk E, Goddard WA III (2009) Organometallics 28:2643–2645
53. Martinez H, Pere Miró P, Charbonneau P, Hillmyer MA, Cramer CJ (2012) ACS Catal 2, 2547–2556
54. Rowley CN, van der Eide EF, Piers WE, Woo TK (2008) Organometallics 27:6043–6045
55. Kulkarni AD, Truhlar DG (2011) J Chem Theory Comput 7:2325–2332
56. Zhao Y, Truhlar DG (2009) J Chem Theory Comput 5:324–333
57. Zhao Y, Truhlar DG (2007) Org Lett 9:1967–1970
58. Zhao Y, Truhlar DG (2011) Chem Phys Lett 502:1–13
59. Zhao Y, Truhlar DG (2008) Acc Chem Res 41:157–167
60. Occhipinti G, Bjørsvik H-R, Jensen VR (2006) J Am Chem Soc 128:6952–6954
61. Minenkov Y, Singstad A, Occhipinti G, Jensen VR (2012) Dalton Trans 41:5526–5541
62. Tsipis AC, Orpen AG, Harvey JN (2005) Dalton Trans 2849–2858
63. Occhipinti G, Hansen FR, Törnroos KW, Jensen VR (2013) J Am Chem Soc 135:3331–3334
64. Poater A, Pump E, Vummaleti SVC, Cavallo L (2014) J Chem Theory Comput 10:4442–4448
65. Romero PE, Piers WE (2005) J Am Chem Soc 127:5032–5033
66. Wenzel AG, Grubbs RH (2006) J Am Chem Soc 128:16048–16049
67. Romero PE, Piers WE (2007) J Am Chem Soc 129:1698–1704
68. Van der Eide EF, Piers WE (2010) Nat Chem 2:571–576
69. Wenzel AG, Blake G, VanderVelde DG, Grubbs RH (2011) J Am Chem Soc 133:6429–6439
70. Paredes-Gil K, Solans-Monfort S, Rodríguez-Santiago L, Sodupe M, Jaque P (2014) Organometallics. doi:10.1021/om500718a
71. Gaussian 09, Revision D.01, Frisch MJ, Trucks GW, Schlegel HB, Scuseria GE, Robb MA, Cheeseman JR, Scalmani G, Barone V, Mennucci B, Petersson GA, Nakatsuji H, Caricato M, Li X, Hratchian HP, Izmaylov AF, Bloino J, Zheng G, Sonnenberg JL, Hada M, Ehara M, Toyota K, Fukuda R, Hasegawa J, Ishida M, Nakajima T, Honda Y, Kitao O, Nakai H, Vreven T, Montgomery JA Jr, Peralta JE, Ogliaro F, Bearpark M, Heyd JJ, Brothers E, Kudin KN, Staroverov VN, Kobayashi R, Normand J, Raghavachari K, Rendell A, Burant JC, Iyengar SS, Tomasi J, Cossi M, Rega N, Millam NJ, Klene M, Knox JE, Cross JB, Bakken V, Adamo C, Jaramillo J, Gomperts R, Stratmann RE, Yazyev O, Austin AJ, Cammi R, Pomelli C, Ochterski JW, Martin RL, Morokuma K, Zakrzewski VG, Voth GA, Salvador P, Dannenberg JJ, Dapprich S, Daniels AD, Farkas Ö, Foresman JB, Ortiz JV, Cioslowski J, Fox DJ (2009) Gaussian, Inc., Wallingford, CT
72. Schaefer A, Horn H, Ahlrichs R (1992) J Chem Phys 97:2571–2577
73. Haeusermann U, Dolg M, Stoll H, Preuss H (1993) Mol Phys 78:1211–1224
74. Kuechle W, Dolg M, Stoll H, Preuss H (1994) J Chem Phys 100:7535–7542
75. Leininger T, Nicklass A, Stoll H, Dolg M, Schwerdtfeger P (1996) J Chem Phys 105:1052–1059
76. Zhao Y, Truhlar D (2008) Theor Chem Acc 120:215–241
77. Barone V, Cossi M (1998) J Phys Chem A 102:1995–2001
78. Tomasi J, Persico M (1994) Chem Rev 94:2027–2094
79. Urbina-Blanco CA, Poater A, Lebl T, Manzini S, Slawin AMZ, Cavallo L, Nolan SP (2013) J Am Chem Soc 135:7073–7079
80. Solans-Monfort X (2014) Dalton Trans 43:4573–4586
81. Poater A, Solans-Monfort X, Clot E, Copéret C, Eisenstein O (2006) Dalton Trans 3077–3087
82. Poater A, Solans-Monfort X, Clot E, Copéret C, Eisenstein O (2007) J Am Chem Soc 129:8207–8216

Theor Chem Acc (2015) 134:20
DOI 10.1007/s00214-015-1620-z

REGULAR ARTICLE

Study of electron transport in polybenzenoid chains covalently attached to gold atoms through unsaturated methylene linkers

Nicolás Ramos-Berdullas · Ana M. Graña · Marcos Mandado

Received: 15 November 2014 / Accepted: 16 January 2015 / Published online: 3 February 2015

Abstract It is well recognized that chemical properties such as aromaticity influence strongly the transport of electrons within a molecule. Since these properties are calculated from equilibrium wave functions, methods relying on equilibrium electronic distributions to determine the electron transport, such as those stemmed from the energy–time uncertainty relation, may be suitable to connect chemical concepts and electron transport. Here, we explore the relation of molecular conductance with the electric response and aromatic stabilization of molecular junctions formed with chains of polybenzenoid units attached to gold atoms through unsaturated methylene carbons. We have found that voltage dependence of conductance stems from the amount of electrons promoted by the electric potential from occupied to virtual molecular orbitals. We also show that aromaticity assists the electron transport when it arises from resonant polarized structures. Otherwise, aromaticity decreases electron transport as reported in previous theoretical and experimental works.

Keywords Molecular conductors · Electron transport · Aromaticity · Quantum chemistry

1 Introduction

Due to its proximity to graphene nanoribbon structures and properties, chains constructed with polybenzenoid hydrocarbons (PBHs) constitute a very interesting target for molecular electronics. Not in vain has benzene, the simplest one, triggered off a continuous growth in the field [1]. Recently, the progress in techniques for fabrication, characterization and manipulation of individual molecules linked to metallic electrodes made possible to consider a larger variety of systems and linkers such as π-conjugated oligomers with covalent carbon–metal contacts [2–4]. However, as pointed out by Chen and Tao [1], there exists a huge amount of more complex aromatic hydrocarbons than benzene with great potential as possible conductors that have not been explored yet.

Theoretical approaches can help hugely on this task, namely they can link the electronic structure characteristics of molecular junctions with its conducting ability at different transport regimes. However, the search for a suitable method yielding current/voltage profiles in agreement with experiments still continues being a challenge [5–19]. The main problem is the realistic description of the whole molecular device, which may suppose a serious drawback due to the lack of atomic-scale information and the delimitation of the 'extended molecule' [20]. Another problem is the treatment of the electronic levels, which depending on the type of molecule–metal contacts may imply a strong delocalization along the whole electrode–molecule–electrode system. Most of the methods employed nowadays for the calculation of the electric conductance in molecular junctions are based on the Landauer formalism [21, 22], where the transport is directly obtained from the transmission probability between two electron reservoirs. This formalism in combination with the non-equilibrium Green's function (NEGF) method provides the best approach to the calculation of the conductance [11–13]. However, the calculation of the transmission matrix requires consideration of the electronic states of the molecule and the electrodes

Published as part of the special collection of articles derived from the 9th Congress on Electronic Structure: Principles and Applications (ESPA 2014).

N. Ramos-Berdullas · A. M. Graña · M. Mandado (✉)
Department of Physical Chemistry, University of Vigo, Lagoas-Marcosende s/n, 36310 Vigo, Spain
e-mail: mandado@uvigo.es

almost independently. Thus, the mixing of the atomic states of the molecule and the metal atoms from the electrodes could not be taken into account accurately, particularly when strong covalent contacts are established. More precisely, the molecular orbitals (MOs) from the molecule are just considered as the available channels for the electron transmission.

The fundamental problems mentioned above open the door for the formulation of other approaches non-based on the transmission matrix. Good examples are those based on the uncertainty relation [20–25], which is in the origin of the quantum conductance limit. Advantages of these approaches are: the simple implementation of the current calculation, which requires only equilibrium ab initio electronic structure calculations, the possibility to treat metal and molecular states on the same footing, allowing for a correct mixing of the corresponding orbitals and the easy link that can be established with magnitudes calculated from equilibrium electron densities such as electron delocalization or electron polarization. On the other hand, disadvantages are related to the bulk nature of the electrodes, which may be hardly accounted for within these approaches, even when using relatively large metallic clusters to represent them. Also, the polarization at the molecular tips in the perturbed system leads to an underestimation of the current compared to a continuous steady-state flow of electrons. In addition, inherent to the uncertainty principle fundamentals, the calculated current may just represent an upper bound limit [20].

Besides the disadvantages mentioned above, which limits its application to a qualitative level when confronting with experimental results, the equilibrium electronic structure foundation of this approach allows establishing interesting relations between conductance and well-known chemical concepts such as aromaticity or bond order. Up to now, such connections were limited to a qualitative framework, using in most cases arguments based on the chemical graph theory [26, 27]. For instance, based on the analysis of the molecular electric response in terms of electron charge polarization, energetic stabilization and electron delocalization, some of us recently predicted the high electric conductance of a new oligophenyl chain [28]. The outstanding conductance of this chain was rationalized in terms of energetically accessible polarized Kekulé structures. These polarized structures are stabilized by a large electron delocalization/aromaticity within the molecular skeleton and act as electron transfer channels from the negative electrode to the molecule and from the molecule to the positive electrode (this situation is depicted in Scheme 1).

In a very recent work, we also proposed a simple computational tool to calculate the amount of electrons promoted from occupied orbitals to unoccupied ones by the external electric potential and qualitatively relate it with the molecular electric conductance [29]. In addition, this electron promotion may be obtained from the eigenvectors and eigenvalues of the deformation density matrix. These eigenvectors were called electron deformation orbitals (EDOs). The EDOs represent the channels available for the transfer of electrons between different molecular regions. In metallic wires and the oligophenyl chains studied in Ref. [28], it was shown that only one of these channels (the one with the largest eigenvalue) accounts for an effective electron transport between the contacts with the electrodes. The corresponding eigenvectors provided almost the whole magnitude of the total electron promotion. Similar ideas were previously employed to analyse the charge transfer in the formation of chemical bonds [30] and electronic transitions [31]. Such electron promotion is intrinsically connected with the main ideas of the band theory of conductivity in materials with non-overlapped bands, such as semiconductors or molecular scale devices.

In the present work, we extend our analysis to chains constructed with different polybenzenoid structures as building units attached to gold atoms at the tips through a methylene carbon bridge. The molecule–electrode contact used for this study is the same as that proposed in our previous work, and we have taken also the xylylene chain as reference model to construct the new polybenzenoid chains. The main aim of this work is to generalize at quantitative level the relationships previously found between electric response properties and electric conductance to more complex PBHs and derive explicit expressions relating both. Relationships between aromatic stability measures and conductivity are also obtained and rationalized in

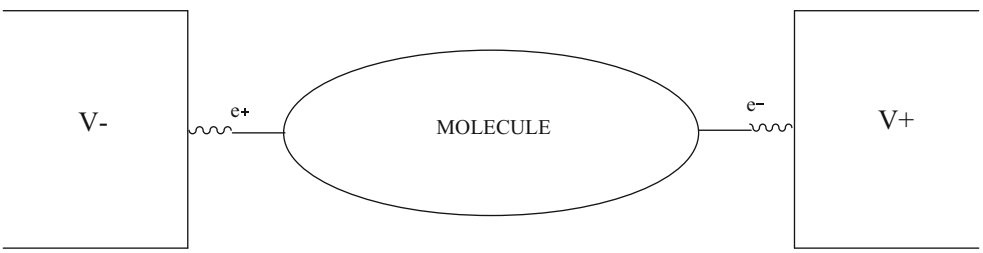

Scheme 1 Representation of the electron transfer between a negative and a positive electrode through a molecule polarized at the contacts

terms of a simplified model based on energetically accessible polarized Kekulé structures.

2 Methodology

We have analysed four different chains formed by polybenzenoid units, all displaying a similar central backbone. The way to construct the chains analysed in this work is schematically represented in Fig. 1. In this figure, the central backbone together with the methylene linkers and the gold atoms is represented by solid bonds, whereas bonds/rings added to construct the additional chains are represented by dashed bonds. The number of units is indicated in the figure with the letter '**n**' and was varied from 1 to 6. The xylylene chains (***p*X2** following the nomenclature employed in Ref. [28] but **C1** in this work) are constructed with the central backbone alone. As mentioned in the introduction section, these oligophenyl chains were already considered in a previous work and will serve as reference structure for this work. Three additional chains were included here, constructed following three different ring sequences in Fig. 1. These sequences are identified in the figure by the letters assigned to the different benzene rings. Thus, we have analysed chains constructed following the ring sequences: [abac][abac]… (**C2**), [ab][ab]… (**C3**) and [abc][abc]… (**C4**). The second one generates the well-known series of polyphenantrenes. In this work to make an explicit mention to a particular molecular chain, we employ a nomenclature formed first by the series of chains to which it bellows (**C1**, **C2**, **C3** or **C4**) and followed by the length of the chain (from **n1** to **n6**).

All the structure and wave function calculations were carried out with the density functional theory (DFT) at the B3PW91/LANLD2Z level as implemented in the Gaussian 09 program suite [32]. We have performed full geometry optimizations for all the chains considered. Although it has been reported that hybrid functionals lead to overestimation of the electron delocalization, the most important point in this work is to describe correctly the relative changes among the different systems investigated. The effect of this overestimation is expected to be substantially cancelled in relative terms since the electronic characteristics of the different polybenzenoid chains investigated in this work are similar. The systems were subjected to an external electric potential, V, which ranged from 0 to 5 V. The electric potential was simulated by applying a constant electric field of the appropriate intensity along the longitudinal axis of the system.

The current intensity, I, was calculated with our revised expression [24] of the Ortiz and Seminario's approach [20] (Eq. 1).

$$I = \frac{2\Delta q_{\mathrm{E-E}}\Delta E_{\mathrm{def}}}{\hbar} \tag{1}$$

This expression includes the electrode–electrode charge transfer, $\Delta q_{\mathrm{E-E}}$, which is defined as the lowest value of the charge transferred from or to the molecule at the right or left contacts; the difference between both values just represents electron charge accumulation/depletion in the molecule. The second term, ΔE_{def}, is the deformation energy, which is defined as the energy change associated with the electron deformation induced by the external voltage. The calculation of these terms is implemented in an own Fortran code that reads the one-electron integrals from Gaussian 09. The electric conductance, G, was obtained from analytical fitting of the I/V curves and later derivation according to Eq. (2),

$$G(V) = \frac{\mathrm{d}I}{\mathrm{d}V} \tag{2}$$

where the voltage dependence of the conductance, G, is explicitly stated.

The magnitude of G depends on the availability of low-energy unoccupied (virtual) MOs from high-energy occupied ones. In other words, conduction occurs when partially filled delocalized levels can be created. Promotion of electrons from occupied to unoccupied MOs, $N_{\mathrm{occ}\rightarrow\mathrm{vir}}$, by the external electric potential V is then the first condition for conduction, and its magnitude must be intrinsically related to G. Both the energy gap and the MO symmetry govern this electron promotion. In addition, since these MOs form the available channels to transport electrons throughout the molecule, the atomic orbitals from the metal must contribute significantly in their linear combination in order to have an effective transport between electrodes. In other words, the MOs must be largely delocalized within the whole electrode–molecule–electrode system.

$N_{\mathrm{occ}\rightarrow\mathrm{vir}}$ has been calculated following Eq. (7) of Ref. [29]. This quantity may be simply obtained from the diagonal elements of the electron deformation density matrix (induced by the external voltage), d^{I}_{it} when constructed in the basis of unperturbed MOs.

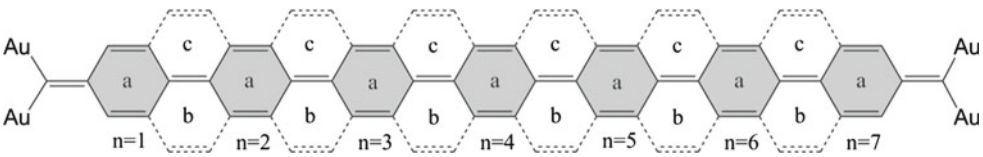

Fig. 1 Schematic representation of the molecular chains studied in this work (see text for details)

$$N_{\mathrm{occ}\rightarrow\mathrm{vir}} = \sum_{i=N_{\mathrm{occ}}+1}^{N_T} d_{ii}^{l} \tag{3}$$

The summation in Eq. (3) runs over all the unoccupied MOs. Alternatively, $N_{\mathrm{occ}\rightarrow\mathrm{vir}}$ may be obtained from the coefficients of the virtual orbitals in the EDOs [29]. These EDOs are obtained by diagonalization of the electron deformation density matrix (difference between the perturbed and unperturbed density matrices) and represent accumulation and depletion of electron density. They are grouped in pairs, where each EDO has the same eigenvalue but opposite sign. Each pair may be viewed as an electron transfer channel induced by the external electric field, where the electrons are transferred from the EDO with the negative eigenvalue to the corresponding EDO with the positive one.

In this work, as in our previous works [24, 28], we have analysed the *I*/*V* profiles, confirming that for all the molecular devices investigated the current–voltage curves satisfy the following non-ohmic relation,

$$I = \beta V^{\alpha} (\text{with } \alpha \approx 3) \tag{4}$$

giving rise to the following approximated expression for G,

$$G(V) \approx 3\beta V^2 \tag{5}$$

In addition, we have also explored the relation between $N_{\mathrm{occ}\rightarrow\mathrm{vir}}$, given by Eq. (3), and V. In all the systems investigated here, this relation matches perfectly the expression,

$$N_{\mathrm{occ}\rightarrow\mathrm{vir}}(V) = \beta' V^{\alpha'} (\text{with } \alpha' \approx 2) \tag{6}$$

which combined with Eq. (5) leads to the following approximated expression for G.

$$G(V) \approx 3\gamma N_{\mathrm{occ}\rightarrow\mathrm{vir}}(V) \left(\text{with } \gamma = \beta/\beta'\right) \tag{7}$$

Equation (7) reveals that dependence of the electric conductance on the external electric potential stems from the electron promotion from occupied to virtual orbitals, which, as expected, increases with the voltage strength. As will be shown in the following section, the empirical relations given by Eqs. (4) and (6) were derived from quasi-perfect analytical fittings of the calculated data.

On the other hand, six-centre indices were also calculated for the benzene rings using Mulliken atomic domains and an own Fortran code. This code reads the density matrix from a

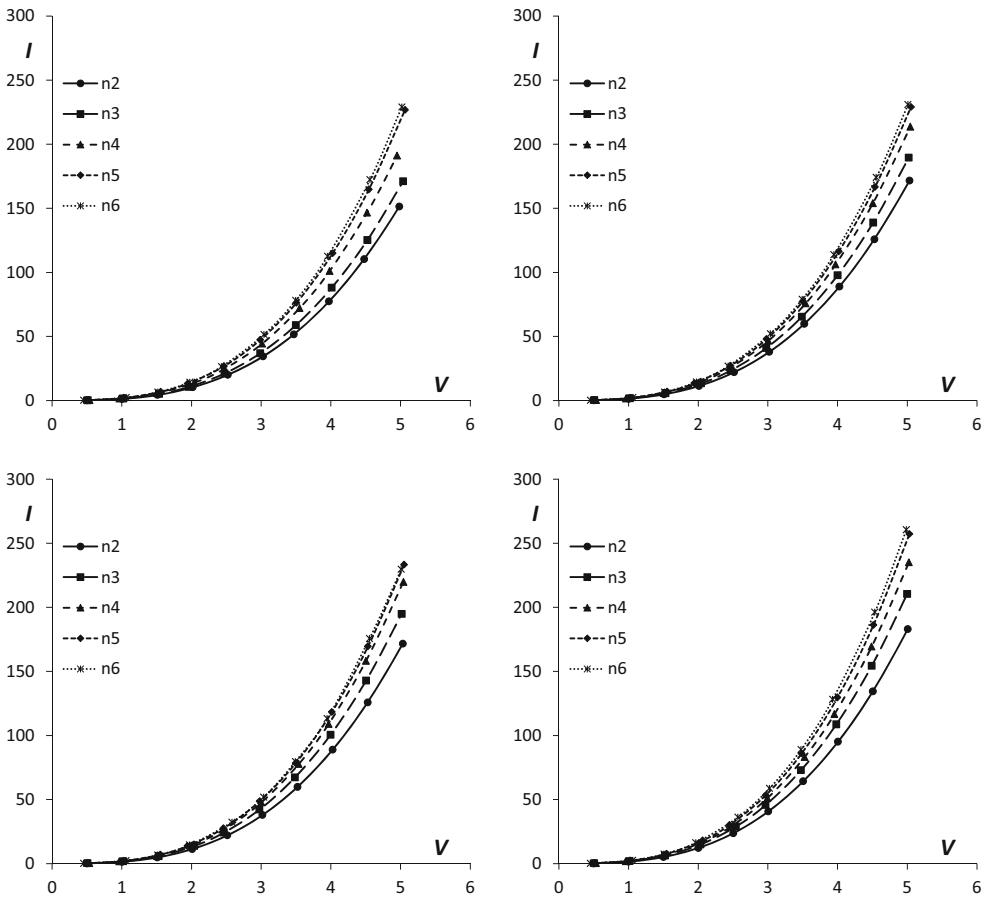

Fig. 2 *I*/*V* profiles obtained for chains **C1** (*top left*), **C2** (*top right*), **C3** (*bottom left*) and **C4** (*bottom right*). *I* in μA and *V* in Volts

Table 1 Parameters α and β (see Eq. 4) and α' and β' (see Eq. 6), obtained by analytical fitting of the I/V and $N_{occ\rightarrow vir}/V$ curves depicted in Figs. 2 and 7

	N2	N3	N4	N5	N6
Chain1					
β	1.2604	1.4113	1.6573	1.8019	1.8636
$\beta'(\times 10^2)$	0.8977	1.0694	1.1330	1.0773	1.0545
α	2.9840	2.9757	2.9742	2.9841	2.9830
α'	1.9939	2.0020	2.0168	2.0383	2.0349
r^2	0.999998	0.99998	0.999994	0.999998	0.999998
$r^{2\prime}$	0.999998	0.9999995	0.99994	0.9998	0.9998
Chain2					
β	1.4021	1.5862	1.7503	1.8400	1.8877
$\beta'(\times 10^2)$	0.9164	1.0818	1.1391	1.1186	1.1100
α	2.9806	2.9735	2.9769	2.9822	2.9859
α'	2.0002	2.0086	2.0190	2.0370	2.0379
r^2	0.999994	0.99998	0.99998	0.999995	0.999997
$r^{2\prime}$	0.999991	0.9999994	0.99993	0.9998	0.9998
Chain3					
β	1.4021	1.6370	1.7962	1.8702	1.9012
$\beta'(\times 10^2)$	0.9162	1.0835	1.1154	1.0924	1.0805
α	2.9806	2.9733	2.9786	2.9839	2.9820
α'	2.0009	2.0105	2.0267	2.0416	2.0453
r^2	0.999994	0.99998	0.999992	0.999997	0.99998
$r^{2\prime}$	0.999990	0.999998	0.99993	0.9998	0.9998
Chain4					
β	1.5321	1.7917	1.9438	2.0686	2.1644
$\beta'(\times 10^2)$	0.9498	1.1189	1.1664	1.2088	1.2193
α	2.9762	2.9721	2.9781	2.9863	2.9829
α'	1.9905	2.0087	2.0348	2.0572	2.0468
r^2	0.99998	0.99998	0.999991	0.9999993	0.999998
$r^{2\prime}$	0.999998	0.99998	0.99994	0.9997	0.9997

In the table, it is shown the square of the Pearson coefficient obtained from each fitting

Gaussian-formatted checkpoint file. A multicentre index provides the electron delocalization within the array of atoms to which it is calculated and can be employed to measure the aromaticity of a given ring in a polycyclic system [33, 34]. In addition, the six-centre delocalization indices calculated for the benzene rings in a PBH may serve to estimate the magnitude of the total resonance energy through the value of the effective scaled electron delocalization (ESED) [34, 35]. ESED represents the magnitude of the total aromaticity in a polycyclic aromatic hydrocarbon and was successfully correlated with other indices of total aromaticity based on energetic magnitudes (aromatic stabilization energies [34] or resonance energies [35]) or magnetic magnitudes [34] (total nucleus independent chemical shifts, NICS). In this work, we have compared the electric conductance with the ESED values for the different molecular structures.

3 Results and discussion

3.1 Electric conductance and aromatic stabilization

The I/V profiles obtained within the range 0–5 V for all the molecular chains are depicted in Fig. 2. The current intensity follows in all cases the non-ohmic regime reflected by Eq. (4), and the parameters α and β in this equation, obtained by analytical fitting, are given in Table 1. All the curves obtained fit perfectly to the form of Eq. (4) within the range of electric potential employed, as it is reflected by the values of the Pearson coefficient also shown in the Table. Moreover, $\alpha \approx 3$ for all the systems, displaying deviations smaller than 0.03. This is not only a characteristic of the molecular chains considered here since the same value of α was recently found for other molecular devices such as benzene-1,4-dithiolate [24] and other oligophenyl chains [28]. Then, the values of β may be employed alone as a measure of the relative ease of different molecular junctions to conduct electrons through the central molecular chain at a certain applied voltage. From the values of β in Table 1, one can infer that the current increases with the length of the chain even though the difference tends to decrease for the longest chains (**n5** and **n6**) in all cases. This is an unexpected result for semiconducting molecules, characteristic of some graphene nanoribbons with metallic behaviour (zigzag type and armchair type with $N = 3p - 1$, being N the number of elementary cells, here 1 for **C1** and 2 for **C4**, and p an integer number) [36]. However, in Ref. [28], we showed how this behaviour is only found when the linker is an unsaturated methylene carbon atom attached to two gold atoms from the electrode. This kind of linker modifies completely the π electronic structure and the electric response of the oligophenyl chain. In Ref. [29], we showed that replacing a segment of gold atoms in a metallic wire by a **C1** chain of equivalent length provokes almost no changes in its electric response (analysed in terms of EDOs). Similar oligophenyl chains with direct contact to a gold atom or linked to the electrode through a saturated carbon atom were shown to display the characteristic exponential decay of the conductance with the chain length. Thus, this result does not seem to be an artefact of the approach employed here and would not have to conflict with previous studies using the NEGF method.

On the other hand, following chains of similar length, one can observe that the magnitude of β increases in the order **C1** < **C2** < **C3** < **C4**. The translation of these results to the electric conductance through Eq. (5) is reflected in the G/V profiles of Fig. 3. These plots provide essentially the same information as the I/V plots, but in this case, the convergence of the conductance at the longest chains is even more evident. This increase in G is related to the magnitude of the electron delocalization of the molecule,

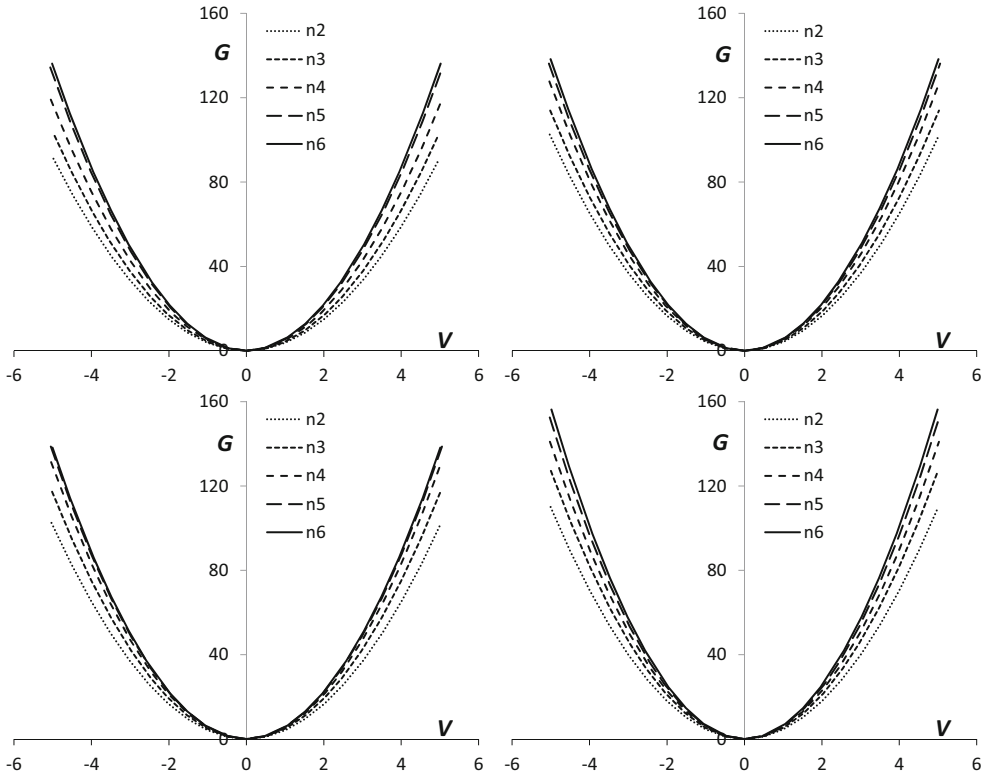

Fig. 3 *G*/*V* profiles obtained for chains **C1** (*top left*), **C2** (*top right*), **C3** (*bottom left*) and **C4** (*bottom right*). *G* in μS and *V* in Volts

which in turn rules the relative stabilization of the polarized structure represented in Scheme 1 and responsible of the electron transfer between electrodes. Thus, in all the systems investigated, this polarized structure is formed after reorganization of the π electrons within the polycyclic conjugated system. Such reorganization gives rise to a central polycyclic hydrocarbon stabilized by the aromaticity of the benzene rings. In Fig. 4, we have only represented the main resonance forms together with the total number of polarized Kekulé structures (*K*) for the largest chain (**n6**). The values of the scaled six-centre electron delocalization indices for each ring in all the molecular chains are also presented in Fig. 4. The summation of these values for all the rings provides the total ESED. The ESED values per electron, ESED/*N*, are strongly related to the β parameter as can be deduced from the representation shown in Fig. 5.

Some important conclusions may be drawn in the wake of the ring electron delocalization and total electron delocalization of Figs. 4 and 5. The most important one is that ESED/*N* values are closely related to the relative ability of the different molecular chains to transport electrons. A similar relation, although qualitative, was previously found by us for hydrocarbon chains [28]. However, for the first time, we are able to recognize the exact role played by aromaticity in the molecular electric conductance. Thus, only when ground state aromaticity is linked to stable polarized resonance structures, one can assert that it facilitates the electron transport. On the contrary, aromaticity becomes an opposite factor when these polarized structures destroy it [28]. Closely related to this point, interference effects raising from ring electron currents which opposes to electron transmission in aromatic molecules have been theoretically investigated [37, 38]. Also, experimental evidences of a negative relation between aromaticity and conductance have been reported recently [39, 40]. Results of Ref. [28] and those presented here set up the conditions at which aromaticity becomes a reinforcing or an opposing factor to the electron transport.

Following the same idea, electron delocalization can also explain the slightly higher conductance of **C3** chains with respect to **C2**. As it is well known, polyphenantrenes are more aromatic than the corresponding linear polyacenes and increasing the number of zigzags in a linear chain of a polyacene increases also its aromaticity. This can be extended to the relative aromatic stability of **C2** and **C3** chains. Thus, the values of the scaled ring electron delocalization shown in Fig. 4 indicate that the main difference between both chains stems from the low aromaticity of the rings 'b' and 'c' in **C2**. Besides this quantitative observation and according to the polarized Kekulé structures of Fig. 4, conjugated circuits are

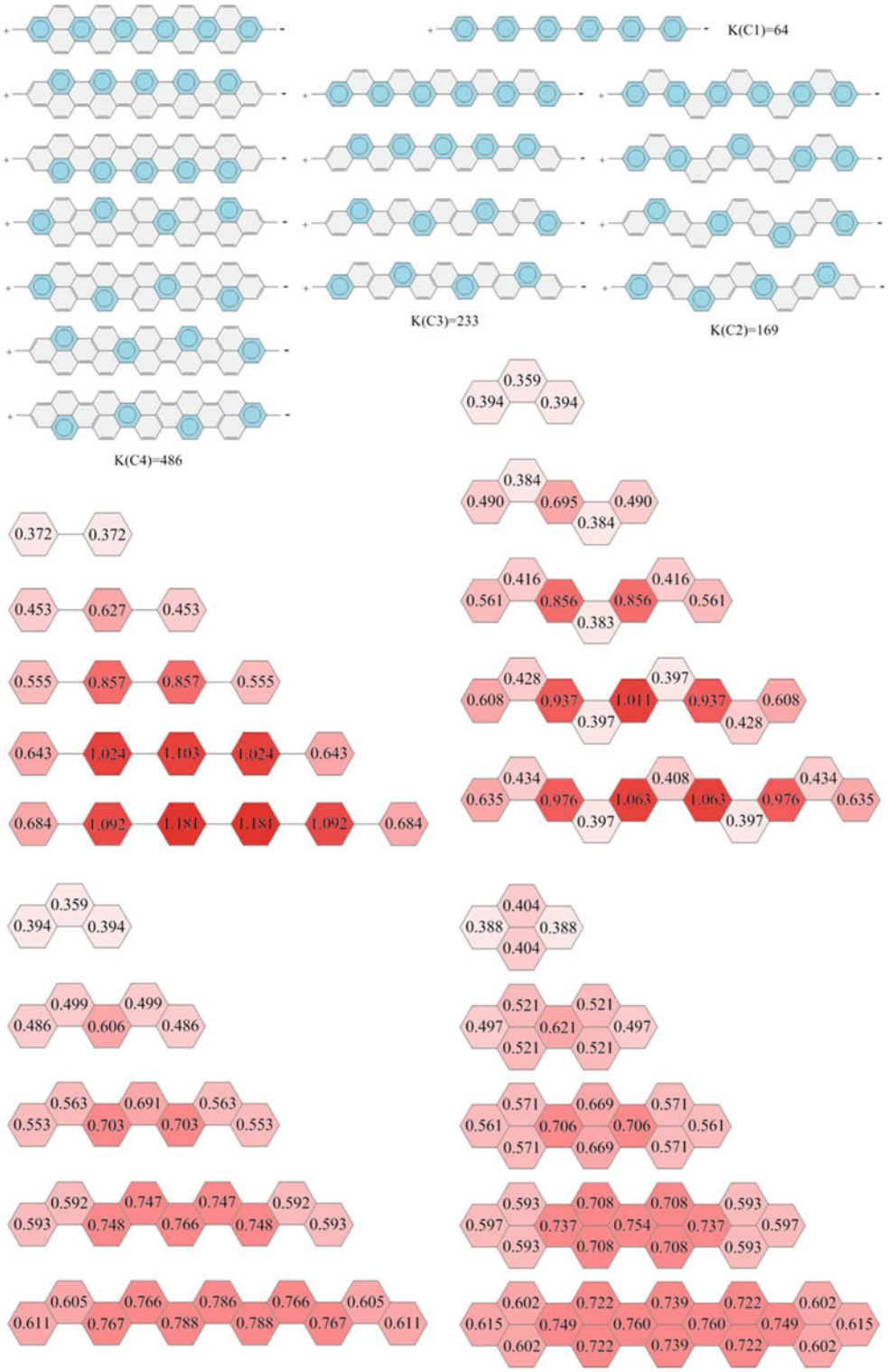

Fig. 4 Main resonant polarized structures for **n6** chains and the corresponding number of Kekulé structures (*top*) and scaled six-centre indices for all the chains studied

more concentrated on the rings of type 'a' in **C2** than in **C3**, so that the expected aromaticity of rings 'b' and 'c' is lower in the former. Additionally, the number of polarized Kekulé structures is larger in **C3** than in **C2**, so explaining qualitatively the larger aromatic stability of the former.

3.2 Electric conductance and occupied–virtual electron promotion

Electric conductance in molecular electronics is usually explained within the context of MO theories. Here, we have applied a recently developed method of analysis of

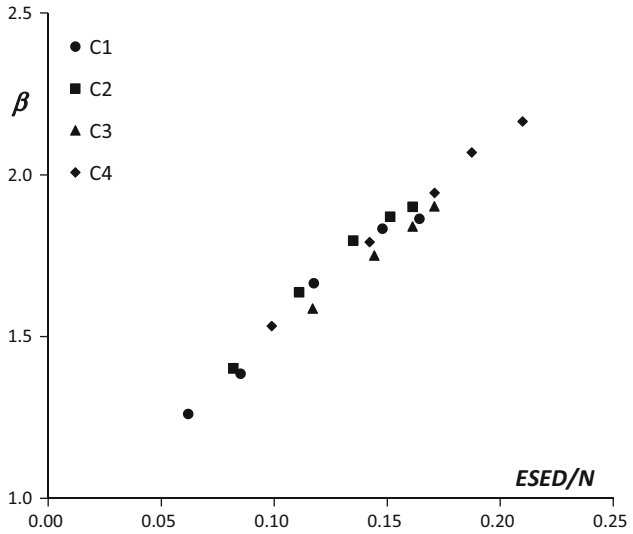

Fig. 5 Parameter β (see Eq. 4; Table 1) versus the total scaled electron delocalization per electron, ESED/*N*

the molecular electric response in terms of EDOs [29]. In this method, the electron deformation density induced by the electric potential is transformed into the basis of unperturbed MOs (occupied + virtual) and later diagonalized to get a set of EDOs constructed as linear combination of them. The electric potential creates partially filled states in the occupied and virtual MO bands, representing the holes and the electrons, respectively, carrying the charge from one contact to the other. By means of these deformation orbitals, it is possible to quantify the magnitude of $N_{\mathrm{occ}\rightarrow\mathrm{vir}}$ [29], or more simply using Eq. (3) as we have done in this work.

The shape of the main EDOs (those with the largest eigenvalues) in **n6** chains calculated at the highest voltage (5 V) (where the electron transfer is also largest) is shown in Fig. 6. The direction of the electron transport is explicitly indicated in the figure. The EDOs are grouped in pairs [29] with positive and negative eigenvalues of the same magnitude; the figure represents the sum of the squares of

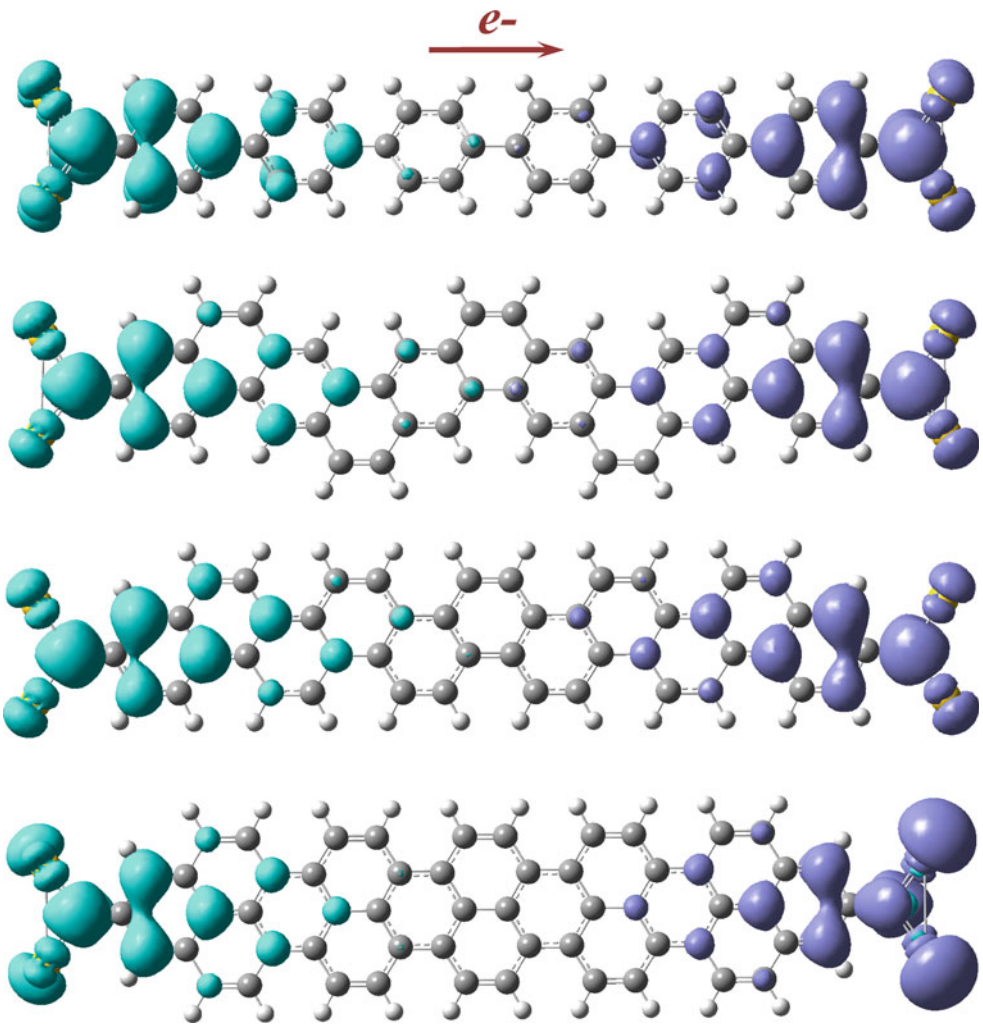

Fig. 6 Representation of the electron transfer associated with the main pair of EDOs in chains, from top to bottom, **C1n6**, **C2n6**, **C3n6** and **C4n6**, obtained for an external electric potential of 5 V

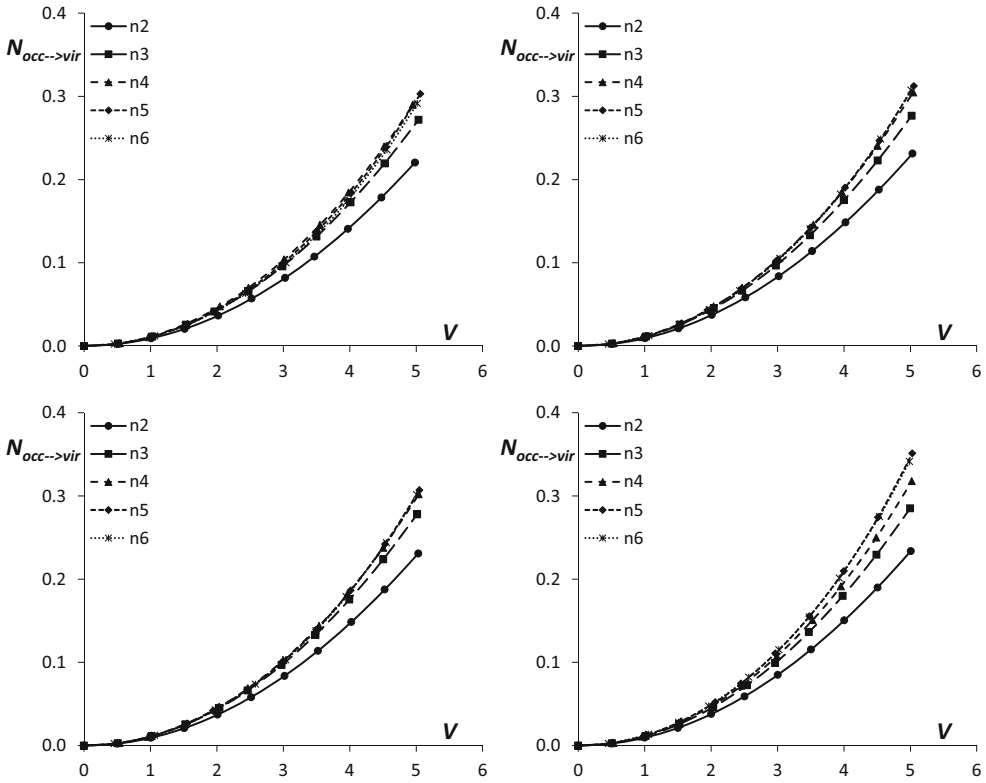

Fig. 7 $N_{occ\rightarrow vir}/V$ profiles obtained for chains **C1** (*top left*), **C2** (*top right*), **C3** (*bottom left*) and **C4** (*bottom right*). $N_{occ\rightarrow vir}$ in au and V in Volts

the EDOs forming the pair. As discussed in Refs. [24, 29], the main pair of EDOs carries almost all the relevant information for the study of the molecular conductance.

In this work, we have explored the relation of $N_{occ\rightarrow vir}$ with V. The representations of $N_{occ\rightarrow vir}$ versus V are depicted in Fig. 7. They clearly show an almost perfect quadratic dependence of $N_{occ\rightarrow vir}$ with V (see Eq. 6). The parameters obtained for each particular correlation, including the Pearson's coefficient, are given in Table 1. As one can see, all the correlations are excellent in view of the Pearson's coefficients and the values of α', the latter very close to 2 in all cases. As mentioned in the previous section, combination of Eqs. (5) and (6) leads to Eq. (7) and to the linear dependence of the electric conductance, G, with $N_{occ\rightarrow vir}$. We have checked the correctness of Eq. (7) by confronting both magnitudes for all the chains within the range of 0–5 V. The plots generated are shown in Fig. 8. It is clear from the figure that the voltage dependence certainly comes from the value of $N_{occ\rightarrow vir}$ since the linear correlations found are perfect within the range of 0–2.5 V. For larger voltages, the linear dependence deviates slightly, which could indicate a limit for the calculation of the current intensity using the approach employed here. It should be remarked that the calculation of I is based on the uncertainty relation. Here, the deformation energy employed [24] is calculated up to second order, and then for large perturbations, it may lead to non-negligible errors. However, there is no need to go further than second order as it is unusual to employ voltages higher than 2 V in molecular electronic devices.

Another interesting result is that the size of the chain seems to have little influence in the correlation of G and $N_{occ\rightarrow vir}$. Thus, all the data may be enclosed within the same fitting equation at low voltage. Only **C1** chains display non-negligible deviations that are appreciated at lower voltages. This may be due to the non-planar structure adopted by these molecules [28]. Thus, the unhindered rotation of adjacent phenyl rings around the bridge CC bond in **C1** makes possible to adopt alternated conformations, which introduces additional structural factors that may have effect on the electron transport. On the contrary, **C2**, **C3** and **C4** are all perfectly planar molecules with structural features more transferable along chains of different length. In fact, it can be observed in the plot corresponding to the **C1** chains how the magnitude of the slope does not increase with the length of the chain but follows an arbitrary order, so that it is not the length what modifies the $G/N_{occ\rightarrow vir}$ relation.

In order to confirm that the $G/N_{occ\rightarrow vir}$ linear dependence is not an isolated fact but it also occurs to very different molecular junctions, we have compared both magnitudes in benzene-1,4-dithiolate attached to gold clusters on top and bridge conformations. We recently investigated the electric

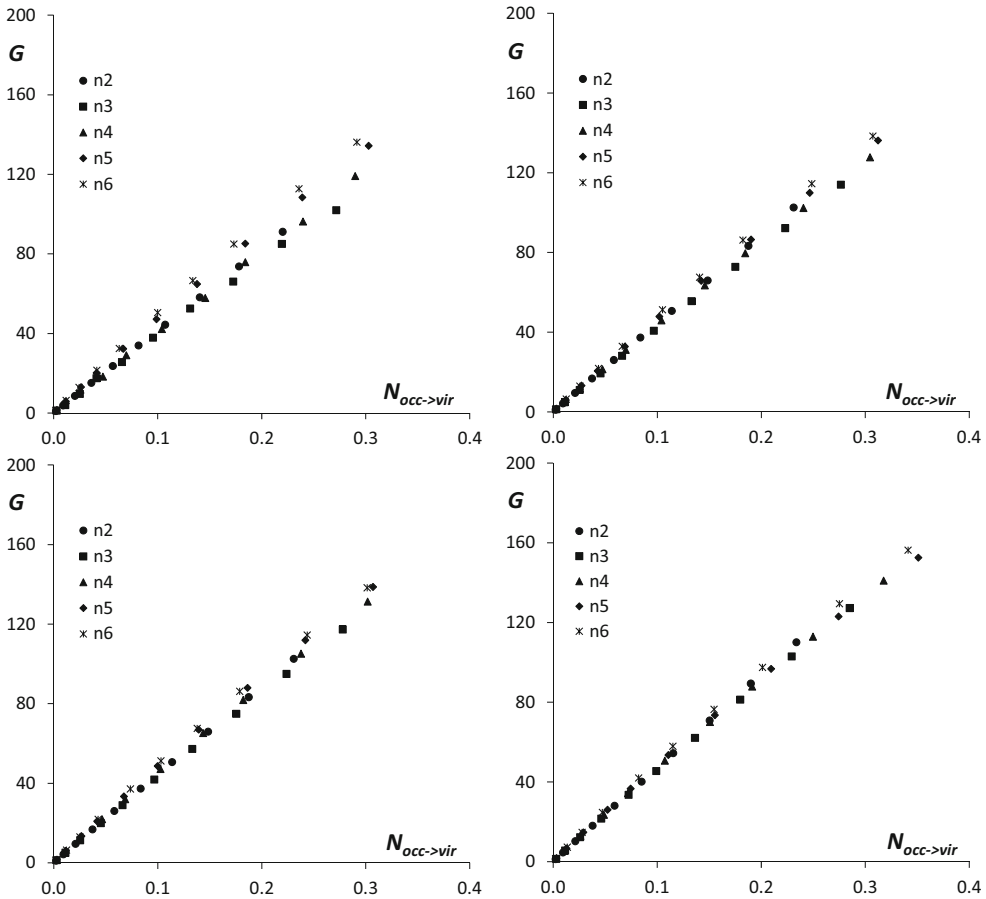

Fig. 8 $G/N_{\mathrm{occ}\rightarrow\mathrm{vir}}$ profiles obtained for chains **C1** (*top left*), **C2** (*top right*), **C3** (*bottom left*) and **C4** (*bottom right*). G in μS and $N_{\mathrm{occ}\rightarrow\mathrm{vir}}$ in au

response of this junction using EDOs; however, we did not go into detail about the role played by $N_{\mathrm{occ}\rightarrow\mathrm{vir}}$ in the conductance. As one can see in Fig. 9, a perfect linear dependence holds in these systems independently of the type of contact. The voltage dependence of G is then a reflection of the voltage dependence of $N_{\mathrm{occ}\rightarrow\mathrm{vir}}$. As mentioned before, $N_{\mathrm{occ}\rightarrow\mathrm{vir}}$ represents the number of electrons and holes created in the unoccupied and occupied MOs, respectively, which could be compared with the magnitude of charge carriers at mesoscopic and macroscopic level. The relation between electric conductance and charge carriers is well known in macroscopic and mesoscopic systems as conductivity is directly proportional to the density of carriers [41], which may be controlled by the gate voltage in systems that display a nonzero energy gap such as semiconductors.

In molecular junctions, once the charge carriers are created, the electron transport between the electrodes will depend on the contact conductance, which in turn depends on the effective 'overlap' between the electronic states of the molecule and the metal. Thus, it is possible to have a low conductance with a significant number of carriers if the movement of such is limited to the molecular region and probability to cross the molecule–metal contact is small. Since the systems considered here display a covalent molecule–metal contact, the contact conductance will depend on the delocalization of the atomic orbitals from the metal and the molecule in the frontier occupied and virtual MOs. This is explicitly accounted for in the expression of the current by the electrode–electrode charge transfer term, which is defined as the lowest value of the charge transferred between the metal and the molecule at the right and left contacts.

The ideas exposed above are illustrated in Fig. 10. The linear combination of frontier orbitals generates electron accumulations and holes which allow electron transport from one side of the system to the other in both directions. In the absence of an external electric potential, the average of states Ψ_3 (positive combination) and Ψ_4 (negative combination) leads to zero conduction. However, application of an electric potential favours one of the polarized states, Ψ_3 or Ψ_4, depending on its polarization, leading to an effective transport across the molecule. Thus, in this simplified model, the accessibility of states Ψ_3 and Ψ_4 is a key factor to display a high electric conductance as well as a significant contribution of the contact atoms from the electrode.

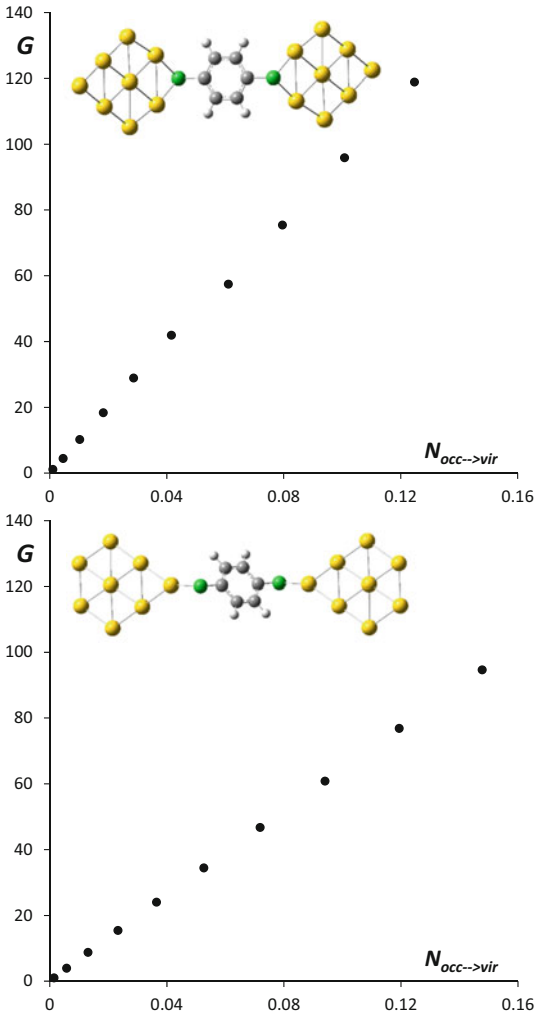

Fig. 9 $G/N_{occ\rightarrow vir}$ profiles obtained for benzene-1,4-dithiolate attached to gold clusters on bridge (*top*) and top (*bottom*) conformations. G in μS and $N_{occ\rightarrow vir}$ in au

In the same figure, the electron densities associated with Ψ_1 (HOMO orbital), Ψ_3 and Ψ_4 are plotted for **C1n2;** from these plots, it is clear what regions are associated with positive and negative charges.

An equivalent qualitative explanation of the electron transport in these systems can be given using chemical graphs based on Kekulé structures. Here, the charge carriers are accounted for by the polarized Kekulé structures, some of them depicted at the top of Fig. 4 for **n6**. As mentioned before, these polarized structures represent the transport channels and have a certain weight in the total VB wave function. In the absence of an external electric potential, they are equally weighted with their counterparts (structures with the opposite polarization). On the contrary, in the presence of a nonzero electric potential, the structures with polarization in the field direction increase in weight, leading to an effective transport. As discussed before, the relative weight that polarized Kekulé structures play in the total wave function is quantitatively reflected on the values of the electron delocalization per electron. The larger the weight of polarized Kekulé structures, the larger the electron delocalization per electron. It is then expected to reach a maximum of the electric conductance when the electron delocalization per electron reaches also its maximum, condition that should be achieved for large chains. Although the size of the systems investigated here is too small to observe clearly such behaviour, for **n5** and **n6,** one can glimpse a trend to reduce the conductance jump compared with the smaller chains **n2**, **n3** and **n4**. However, in order to confirm this trend, we have performed calculations at the minimal basis set level for polyphenantrene chains up to **n35**. In Fig. 11, the values of β are represented against K. The latter is given in a nonlinear scale since the number of Kekulé structures grows hugely with the number

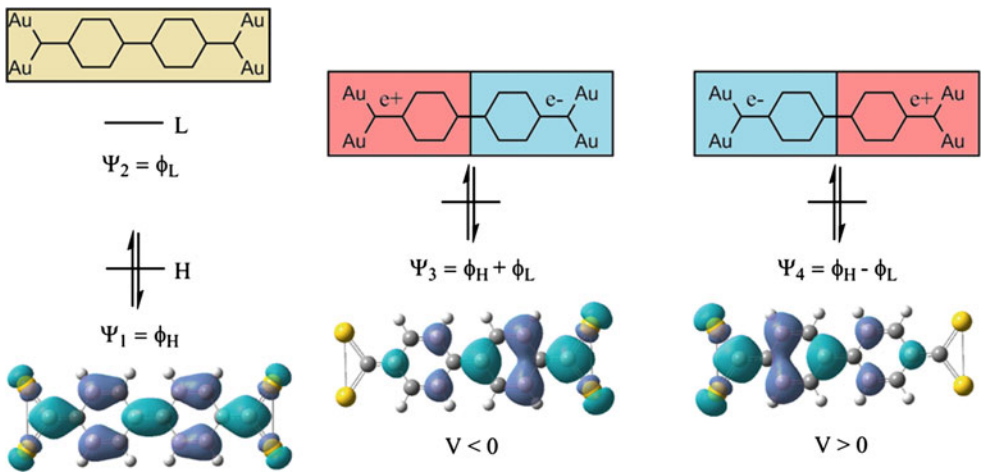

Fig. 10 Schematic representation of the charge transport channels obtained by combination of HOMO and LUMO MOs. In the figure are shown these combinations for the **C1n2** chain

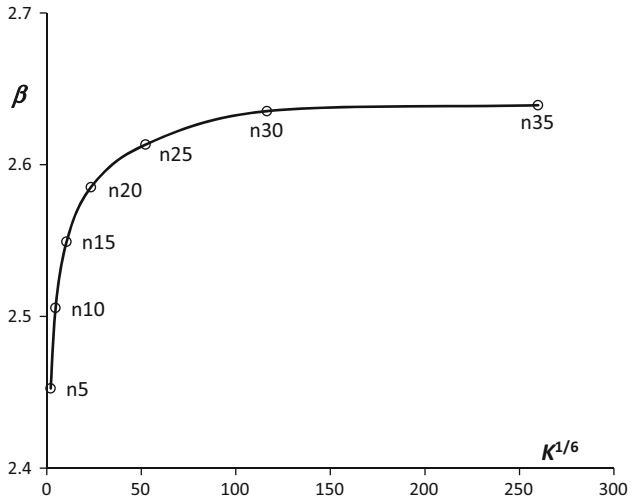

Fig. 11 Parameter β (see Eq. 4) versus the number of Kekulé structures K for chains of polyphenantrenes of lengths ranging from 5 to 35 units

of units n, following the series $[2 \times 3^{(n-1)}]$. In the plot, it is clear the asymptotic behaviour of β, reflecting the electric conductance does reach a maximum.

4 Conclusions

In the present work, strong links between chemical concepts and molecular electric conductance via aromaticity and electron polarization have been established in a quantitative sense for the first time. Thus, the relation between aromaticity as linked to cyclic electron delocalization and electric conductivity in molecular conductors based on polybenzenoid chains has been explored and conditions for the enhancement mechanism of the conductance revealed. Thus, aromatic stabilization significantly contributes to the molecular electric conductance as long as it arises from superposition of resonant polarized structures, which act as charge transport channels upon an external electric perturbation. To satisfy this condition in molecular junctions is crucial the kind of contact established between the molecule and the metal electrode. Covalent C-metal contacts through methylene linkers allow a perfect delocalization of positive and negative charges throughout the electrode–molecule–electrode system assisting charge transport upon the action of an external electric potential.

Interpretation of the electric conductance in terms of charge carriers created by mixing electron states of occupied and virtual MOs has been provided. An empirical linear relation between electric conductance and the number of electrons promoted by the electric potential from occupied to virtual electronic states has been found. This relation allows establishing a direct connection between conduction in macroscopic and mesoscopic systems and conduction in molecular systems through the concept of charge carrier density.

The quantitative relations found have been also rationalized in terms of chemical graphs and a simplified model based on Kekulé structures. This is a definite link between bare chemical concepts for understanding the electronic structure and the intricate molecular electric response in oligophenyl conductors.

Acknowledgments We thank Centro de Supercomputacion de Galicia (CESGA) for providing access to its computational facilities and Xunta de Galicia for funding this research through Project INCITE10TMT314014PR.

References

1. Chen F, Tao NJ (2009) Acc Chem Res 42:429–438
2. Schneebeli ST, Kamenetska M, Cheng Z, Skouta R, Friesner RA, Venkataraman L, Breslow R (2011) J Am Chem Soc 133:2136–2139
3. Cheng ZL, Skouta R, Vazquez H, Widawsky JR, Schneebeli S, Chen W, Hybertsen MS, Breslow R, Venkataraman L (2011) Nat Nanotechnol 6:353–357
4. Chen W, Widawsky JR, Vazquez H, Schneebeli ST, Hybertsen MS, Breslow R, Venkataraman L (2011) J Am Chem Soc 133:17160–17163
5. Emberly E, Kirczenow G (1999) Nanotechnology 10:285–289
6. Yaliraki SN, Kemp M, Ratner MA (1999) J Am Chem Soc 121:3428–3434
7. Yaliraki SN, Roitberg AE, Gonzalez C, Mujica V, Ratner MA (1999) J Chem Phys 111:6997–7002
8. Choi HJ, Ihm J (1999) Phys Rev B 59:2267–2275
9. Di VM, Pantelides ST, Lang ND (2000) Phys Rev Lett 84:979–982
10. Derosa PA, Seminario JM (2001) J Phys Chem B 105:471–481
11. Taylor J, Guo H, Wang J (2001) Phys Rev B 63:245407/1–245407/13
12. Xue Y, Datta S, Ratner MA (2002) Chem Phys 281:151–170
13. Brandbyge M, Mozos J-L, Ordejón P, Taylor J, Stokbro K (2002) Phys Rev B 65:165401/1–165401/17
14. Delaney P, Greer JC (2004) Phys Rev Lett 93:036805/1–036805/4
15. Kurth S, Stefanucci G, Almbladh CO, Rubio A, Gross EKU (2005) Phys Rev B 72:035308/1–035308/13
16. Rocha AR, García-Suárez VM, Bailey S, Lambert C, Ferrer J, Sanvito S (2006) Phys Rev B 73:085414/1–085414/22
17. Toher C, Sanvito S (2007) Phys Rev Lett 99:056801/1–056801/4
18. Toher C, Sanvito S (2008) Phys Rev B 77:155402/1–155402/12
19. Goyer F, Ernzerhof M, Zhuang M (2007) J Chem Phys 126:144104/1–144104/8
20. Ortiz DO, Seminario JM (2007) J Chem Phys 127:111106/1–111106/3
21. Landauer R (1957) IBM J Res Dev 1:223–231
22. Büttiker M, Imry Y, Landauer R, Pinhas S (1985) Phys Rev B 31:6207–6215
23. Seminario JM (2007) J Phys B: At Mol Opt Phys 40:F275–F276
24. Ramos-Berdullas N, Mandado M (2014) J Phys Chem A 118:3827–3834
25. Szarek P, Suwannawong S, Doi K, Kawano S (2013) J Phys Chem C 117:10809–10817

26. Fowler PW, Pickup BT, Todorova TZ (2011) Pure Appl Chem 83:1515–1528
27. Morikawa T, Narita S, Klein DJ (2005) Chem Phys Lett 402:554–558
28. Ramos-Berdullas N, Mandado M (2013) Chem Eur J 19:3646–3654
29. Mandado M, Ramos-Berdullas N (2014) J Comput Chem 35:1261–1269
30. Mitoraj M, Michalak A, Ziegler T (2009) J Chem Theor Comput 5:962–975
31. Martin RL (2003) J Chem Phys 118:4775–4777
32. Gaussian 09, Revision D01, Frisch MJ, Trucks GW, Schlegel HB, Scuseria GE, Robb MA, Cheeseman JR, Scalmani G, Barone V, Mennucci B, Petersson GA, Nakatsuji H, Caricato M, Li X, Hratchian HP, Izmaylov AF, Bloino J, Zheng G, Sonnenberg JL, Hada M, Ehara M, Toyota K, Fukuda R, Hasegawa J, Ishida M, Nakajima T, Honda Y, Kitao O, Nakai H, Vreven T, Montgomery JA Jr, Peralta JE, Ogliaro F, Bearpark M, Heyd JJ, Brothers E, Kudin KN, Staroverov VN, Kobayashi R, Normand J, Raghavachari K, Rendell A, Burant JC, Iyengar SS, Tomasi J, Cossi M, Rega N, Millam NJ, Klene M, Knox JE, Cross JB, Bakken V, Adamo C, Jaramillo J, Gomperts R, Stratmann RE, Yazyev O, Austin AJ, Cammi R, Pomelli C, Ochterski JW, Martin RL, Morokuma K, Zakrzewski VG, Voth GA, Salvador P, Dannenberg JJ, Dapprich S, Daniels AD, Farkas Ö, Foresman JB, Ortiz JV, Cioslowski J, Fox DJ (2009) Gaussian, Inc, Wallingford CT
33. Bultinck P, Ponec R, Van Damme S (2005) J Phys Org Chem 18:706–718
34. Mandado M, Gonzalez-Moa MJ, Mosquera RA (2007) J Comput Chem 28:127–136
35. Mandado M, Gonzalez-Moa MJ, Mosquera RA (2007) J Comput Chem 28:1625–1633
36. Chen X, Wang H, Wan H, Song K, Zhou G (2011) J Phys: Condens Matter 23:315304/1–315304/8
37. Ernzerhof M, Bahmann H, Goyer F, Zhuang M, Rocheleau P (2006) J Chem Theory Comput 2:1291–1297
38. Solomon GC, Herrmann C, Hansen T, Mujica V, Ratner MA (2010) Nat Chem 2:223–228
39. Quinn JR, Foss FW, Venkataraman L, Hybertsen MS, Berlow R (2007) J Am Chem Soc 129:6714–6715
40. Chen W, Li H, Widawsky JR, Appayee C, Venkataraman L, Breslow R (2014) J Am Chem Soc 136:918–920
41. Datta S (1995) Electronic Transport in Mesoscopic Systems. In: Ahmed H, Pepper M, Broers A (eds) Cambridge studies in semiconductor physics and microelectronic engineering: 3. Cambridge University Press, Cambridge

Theor Chem Acc (2015) 134:60
DOI 10.1007/s00214-015-1661-3

REGULAR ARTICLE

Revisiting the mechanism and the influence of the excitation wavelength on the surface-enhanced Raman scattering of the pyridine–Ag_{20} system

Nicolás Ramos-Berdullas[1] · Diego López-Carballeira[1] · Marcos Mandado[1] · Ignacio Pérez-Juste[1]

Received: 4 January 2015 / Accepted: 2 April 2015 / Published online: 16 April 2015

Abstract This work presents the application of a recent decomposition scheme of the Raman tensor into molecule and surface contributions to the study of the static and resonance Raman spectra of pyridine adsorbed on a Ag_{20} cluster, a typical probe for the theoretical study of surface-enhanced Raman scattering (SERS) spectra. The results obtained show that both the chemical and electromagnetic enhancements observed are related to changes on the polarizability and polarizability derivatives of the pyridine molecule. No significant contributions from the surface and from vibrational intermolecular coupling are found. Since similar incident lights produce remarkably different SERS spectra, the effect of excitation wavelength on the spectra of the PY–Ag_{20} complexes is also scrutinized. From the computed Raman excitation profiles and from the analysis of the electron density changes upon electronic transitions, it is established that the differences found can be related to the amount of electron density transferred from the silver cluster to pyridine upon excitation and to the distance between both units. These findings suggest that a proper knowledge of the effect of the excitation wavelength is necessary for obtaining a reliable theoretical interpretation of surface-enhanced Raman spectra.

Keywords Surface-enhanced Raman spectroscopy · Density functional theory · Adsorption · Pyridine–silver complexes

1 Introduction

Since its discovery [1], surface-enhanced Raman scattering (SERS) has proven to be one of the most sensitive spectroscopic techniques for molecular detection and studying adsorption on metal surfaces [2–7]. Despite the great amount of interest received among researchers, there is still controversy about the origin of the huge enhancement of Raman activity induced by the proximity to a metal surface, but it is generally accepted that there are two main qualitative contributions to the signal enhancement, named electromagnetic (EM) and chemical (CM). The electromagnetic enhancement is due to the existence of surface plasmon resonances as a consequence of collective excitations of electrons in the conduction band of the metal. The chemical term could comprise several enhancements due to the ground-state chemical interactions between the molecule and the metal, the resonance Raman enhancement if the excitation wavelength is resonant with a molecular transition and the charge-transfer resonance Raman enhancement if the excitation wavelength is resonant with a transition between the molecule and the metal. All the mechanisms are not independent of each other, but the electromagnetic contribution is considered to be the dominant term and the chemical contribution provides additional enhancement required to explain the enhancements observed experimentally [8–10].

Due to the difficulties arising from the simultaneous combination of effects, few works have been dedicated to the development of theories to explain the importance of

Published as part of the special collection of articles derived from the 9th Congress on Electronic Structure: Principles and Applications (ESPA 2014).

✉ Ignacio Pérez-Juste
uviqpipj@uvigo.es

[1] Departamento de Química Física, Facultad de Química, Universidade de Vigo, 36310 Vigo, Spain

the different contributions to the SERS effect. Lombardi and Birke proposed a unified expression for SERS, which contains three terms representing the surface plasmon resonance, the metal–molecule charge-transfer resonance at the Fermi level and an allowed molecular resonance, illustrating the coupling between the different terms [11]. Jensen and co-workers employed time-dependent density functional theory based on a short-time approximation to obtain Raman scattering cross sections and analysed the importance of the different contributions to Raman enhancement [12, 13]. These theoretical methods focused on finding the origin of the contributions to the polarizability and polarizability derivatives that give rise to Raman intensities considering a supermolecular approach for the metal surface–adsorbate systems. From a different approach, we have recently proposed the partition of the Raman tensor into molecule and surface contributions to study the possibility of Raman enhancement caused by carbon surfaces [14]. The results obtained for pyridine as adsorbate showed the importance of the electromagnetic term and unveiled the existence of vibrational coupling between the adsorbate and the surface and how both factors must be taken into account to properly understand the computed SERS spectra.

In this work, we present the results of our decomposition scheme of the Raman tensor on the study of the static and resonance Raman spectra of pyridine (PY) adsorbed on a Ag_{20} cluster, a prototype model for the study of SERS [3, 15–24]. It will be shown that both the chemical and electromagnetic enhancements observed on the Raman spectra of PY–Ag_{20}, despite their different origins, are related to polarizability changes of the pyridine molecule. Finally, the analysis of the electron density deformations taking place upon electronic transitions will be used to explain the differences observed on the resonance spectra obtained with different excitation wavelengths.

2 Computational methods

On the basis of previous studies [19, 23, 25, 26], two different structures for the PY–Ag_{20} complexes were chosen in this work, one with the pyridine molecule interacting with a planar surface of the Ag_{20} tetrahedron (S-complex) and another with the pyridine molecule pointing to the vertex of the Ag_{20} cluster (V-complex) (Fig. 1). Both geometries were constrained to Cs symmetry and were oriented in such a way that the pyridine molecule is located on the yz-plane, with the y-axis oriented along the Ag–N bond and the x-axis perpendicularly oriented out of the molecular plane.

All computations presented in this paper were done employing density functional theory (DFT) methods implemented in the Gaussian 09 package [27]. The functional

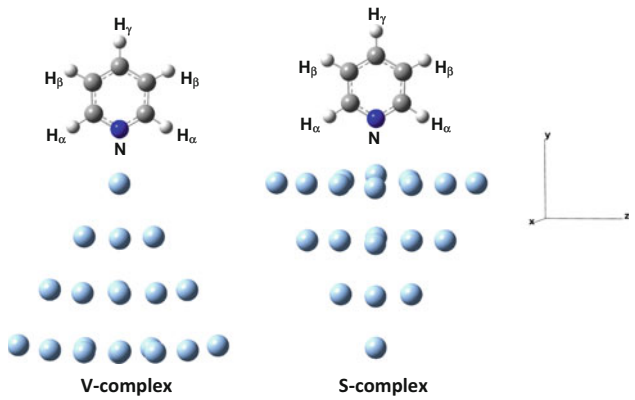

Fig. 1 Structures of the PY–Ag_{20} complexes and atom notation in pyridine

selected was M06-2X [28] in combination with the LANL2DZ basis set and the corresponding core pseudopotential for the silver atoms, and the triple zeta 6−311++G** basis set for the atoms in pyridine. The choice of the M06-2X functional follows from our previous studies about the adsorption on carbon-based substrates and the possibility of these compounds to be substrates for SERS spectra [29]. Therefore, we consider this paper as a test for the M06-2X/LANL2DZ/6−311++G** method for the study of metallic cluster–organic compounds interactions and SERS spectra.

Full geometrical optimizations have been performed for both complexes, and they were characterized as energy minima by means of their harmonic vibrational analysis. Vibrational assignments were obtained by using the VEDA program, which generates an optimized set of internal coordinates based on the molecular structure and provides a potential energy distribution (PED) for the quantitative analysis of vibrational spectra [30, 31]. Time-dependent DFT (TD–DFT) calculations were employed to obtain the excitation spectra of the complexes, and those transitions with larger oscillator strengths were chosen for obtaining the frequency-dependent Raman spectra. Since it is well known that frequency-dependent Raman spectra can diverge at exact resonance conditions [12, 32], we have also computed a large number of pre-resonance spectra by small detuning of the excitation frequency to analyse the influence of the excitation wavelength on the theoretical Raman signal enhancements [32–34].

In this work, we have obtained separately the polarizability tensors of pyridine and silver cluster within the complexes using the Hilbert space of the basis functions. To compute the molecule and surface contributions, the total polarizability tensor is calculated from the derivative of the dipole moment with respect to an external electric field given by

$$\alpha = \frac{\mathrm{d}\mu}{\mathrm{d}E} \tag{1}$$

For a small constant electric field, Eq. 1 can be approximately written as

$$\alpha \approx \frac{\mu_{ind}}{E} \tag{2}$$

where μ_{ind} represents the induced dipole moment. This induced dipole can be calculated from the electron deformation density, ρ^{def}, and the position operator, $\vec{r}$, as

$$\mu_{ind} = \int \rho^{def}(\vec{r})\vec{r}\mathrm{d}\vec{r} \tag{3}$$

The electric polarizability is then a tensor with components defined in terms of the electric field orientation and position operator. Thus, each component is given by

$$\alpha_{\sigma\sigma'} = \frac{1}{E_\alpha}\int \rho^{def}(\vec{r})\sigma'\mathrm{d}\sigma' \tag{4}$$

where σ and σ′ represent Cartesian components (x, y or z). By expanding Eq. 4 in terms of density matrix elements for a given basis set, we obtain

$$\alpha_{\sigma\sigma'} = \frac{1}{E_\alpha}\sum_{\mu\nu}\left(D^{E_\sigma}_{\mu\nu} - D_{\mu\nu}\right)\int \varphi_\mu(\vec{r})\sigma'\varphi_\nu(\vec{r})\mathrm{d}\sigma' \tag{5}$$

where $D_{\mu\nu}$ and $D^{E_\sigma}_{\mu\nu}$ are, respectively, density matrix elements before and after the application of the electric field, and φ_μ and φ_ν the corresponding basis functions. The first summation in Eq. 5 may be split into terms containing basis functions of the molecule and those belonging to the surface, leading to a decomposition of the polarizability tensor into molecule $\left(\alpha^M_{\sigma\sigma'}\right)$ and surface $\left(\alpha^S_{\sigma\sigma'}\right)$ contributions

$$\alpha^M_{\sigma\sigma'} = \frac{1}{E_\sigma}\sum_{\mu\in M}\sum_{\nu}\left(D^{E_\sigma}_{\mu\nu} - D_{\mu\nu}\right)\int \varphi_\mu(\vec{r})\sigma'\varphi_\nu(\vec{r})\mathrm{d}\sigma' \tag{6}$$

$$\alpha^S_{\sigma\sigma'} = \frac{1}{E_\sigma}\sum_{\mu\in S}\sum_{\nu}\left(D^{E_\sigma}_{\mu\nu} - D_{\mu\nu}\right)\int \varphi_\mu(\vec{r})\sigma'\varphi_\nu(\vec{r})\mathrm{d}\sigma' \tag{7}$$

This partitioning scheme of the polarizability tensor depends both on the coordinates' origin and on the basis set employed, so that its utility is restricted to the analysis of 'relative' distributed polarizabilities where the coordinates' origin and basis set remain unchanged. Thus, in this work we have always employed the coordinates' origin and the basis set of the complex in the calculation of the polarizability even for the isolated pyridine.

Raman intensities in this paper are given as Raman activities (in $\mathrm{Å}^4$/amu) since the profiles of Raman spectra are almost similar to those obtained from Raman scattering cross sections. Raman activities are obtained from the Raman tensor, and for systems composed of molecules adsorbed on surfaces, we have recently proposed to split the Raman tensor into molecule and surface contributions [14]. Such splitting of the Raman tensor leads to a decomposition of the Raman activity into molecule, surface and intermolecular contributions. Thus, the Raman activity for a given vibrational mode k, R_k, is given by the following expression [7],

$$R_k = 45\bar{\alpha}^2_k + 7\bar{\gamma}^2_k \tag{8}$$

where $\bar{\alpha}^2_k$ and $\bar{\gamma}^2_k$ are the isotropic and anisotropic invariants of the Raman tensor, $\hat{R}_k$, whose expressions are given by

$$\bar{\alpha}^2 = \frac{1}{9}\left[\alpha^2_{xx} + \alpha^2_{yy} + \alpha^2_{zz} + 2\alpha_{xx}\alpha_{yy} + 2\alpha_{xx}\alpha_{zz} + 2\alpha_{yy}\alpha_{zz}\right] \tag{9}$$

$$\bar{\gamma}^2 = \left[\alpha^2_{xx} + \alpha^2_{yy} + \alpha^2_{zz} - \alpha_{xx}\alpha_{yy} - \alpha_{xx}\alpha_{zz} - \alpha_{yy}\alpha_{zz}\right] + 3\left[\alpha^2_{xy} + \alpha^2_{xz} + \alpha^2_{yz}\right] \tag{10}$$

On the other hand, the Raman tensor for a normal mode k, $\hat{R}_k$, may be expressed in terms of the normalized atomic displacements, φ^n_k, the polarizability derivatives with respect to the corresponding unnormalized atomic displacements $\left(\frac{\partial\hat{\alpha}}{\partial\xi^{\sigma}}\right)$ and the reduced mass, μ_k, as

$$\hat{R}_k = \frac{1}{\sqrt{\mu_k}}\sum_{n=1}^{3N}\phi^n_k\left(\frac{\partial\hat{\alpha}}{\partial\xi^n}\right) \tag{11}$$

Since the summation in Eq. 11 runs over the 3 N atomic Cartesian coordinates (N being the number of nuclei), one can then decompose the Raman tensor into atomic contributions as

$$\hat{R}_k = \sum_{I=1}^{N_{at}} R^I_k = \sum_{I=1}^{N_{at}}\frac{1}{\sqrt{\mu_k}}\sum_{\sigma=1}^{3}\phi^{I_\sigma}_k\left(\frac{\partial\hat{\alpha}}{\partial\xi^{I_\sigma}}\right) \tag{12}$$

where I represents an atom. Grouping the atoms in Eq. 12 in those belonging to the molecule and surface separately, the Raman tensor becomes split into molecule and surface parts.

$$\hat{R}_k = \hat{R}^M_k + \hat{R}^S_k = \sum_{I\in M}\frac{1}{\sqrt{\mu_k}}\sum_{\sigma=1}^{3}\phi^{I_\sigma}_k\left(\frac{\partial\hat{\alpha}}{\partial\xi^{I_\sigma}}\right) + \sum_{I\in S}\frac{1}{\sqrt{\mu_k}}\sum_{\sigma=1}^{3}\phi^{I_\sigma}_k\left(\frac{\partial\hat{\alpha}}{\partial\xi^{I_\sigma}}\right) \tag{13}$$

Taking into account that the isotropic and anisotropic invariants represented in Eqs. 9 and 10 are obtained from products of Raman tensor components, they can be represented by a sum of molecule (M), surface (S) and intermolecular (MS)

contributions, the latter arising from the crossed products of the components of $\hat{R}_k^M$ and $\hat{R}_k^S$ of Eq. 13. By introducing this partitioning of the isotropic and anisotropic invariants in Eq. 8, one obtains the following expression for the Raman activity,

$$R_k = R_k^M + R_k^S + R_k^{MS} = \left[45(\bar{\alpha}_k^M)^2 + 7\left(\bar{\gamma}_k^M\right)^2\right] + \left[45(\bar{\alpha}_k^S)^2 + 7\left(\bar{\gamma}_k^S\right)^2\right] + \left[45(\bar{\alpha}_k^{MS})^2 + 7\left(\bar{\gamma}_k^{MS}\right)^2\right] \quad (14)$$

As will be seen below, for the PY–Ag_{20} complexes studied in this paper it is convenient to present together the last two terms of Eq. 14.

3 Results and discussion

3.1 Geometrical optimization and electronic spectra

The optimized structures for the PY–Ag_{20} complexes are those depicted in Fig. 1. No significant differences were found between the geometries of pyridine in both complexes. However, the M06-2X-computed distances between the nitrogen atom and the closest silver atom are 2.422 Å for the V-complex and 2.532 Å for the S-complex. The intermolecular distance for the S-complex is only slightly smaller than that obtained by Zhao et al. [19] employing BP86/TZP computations (2.46 Å), but there is a significant reduction in the intermolecular distance for the V-complex (2.66 Å). It must be also noted that the geometries reported here were characterized as energy minima by analysis of their harmonic vibrational frequencies, that is, no negative vibrational frequencies were found, while Zhao et al. reported small imaginary frequencies for both complexes associated with numerical inaccuracies because of the grid employed.

The results in Table 1 show that binding energies for both complexes are similar, with a small preference for the adsorption through the vertex in the V-complex (−12.7 and −10.2 kcal/mol, BSSE-corrected values). Remarkably, the binding energies reported here are stronger than those by Zhao et al. (−8.87 and −1.31 kcal/mol), in particular for the S-complex [19]. The differences are probably related to the reduction in the intermolecular distance predicted by M06-2X computations.

Interaction energies have been analysed by means of the natural energy decomposition analysis (NEDA) method included within the NBO method of Weinhold and coworkers [35–37]. The interaction energy is divided into three components, $\Delta E = EL + CT + CO$, which includes an electrical contribution (*EL*) arising from electrostatic, polarization and self-polarization energies, a stabilizing charge-transfer contribution (*CT*) due to the difference between the energies of the total and localized charge densities, and a core term (*CO*) accounting for the intermolecular Pauli repulsion, electron exchange and correlation effects [36]. According to the NEDA results, charge transfer is the main stabilizing contribution followed by the electrical contribution and both of them overcome the core destabilization term. Remarkably, although the electrical term is similar in both complexes, there is a larger preference for the S-complex due to charge transfer, and the analysis of the NPA charges indicates that pyridine in the S-complex receives charge (0.014 e) from the Ag cluster while donates charge (0.038 e) to the Ag cluster in the V-complex. These results are not in complete agreement with the Voronoi deformation density charges reported by Zhao et al. [19], who stated that charge is always transferred from pyridine to the silver cluster in both complexes.

Table 1 Binding energies (in kcal/mol) for the PY–Ag_{20} complexes

Energy	V-complex	S-complex
Binding	−13.60	−11.62
Binding (BSSE corrected)	−12.72	−10.17
Electrical (EL)	−40.60	−40.50
Charge transfer (CT)	−142.63	−161.71
Core (CO)	170.51	192.04

NEDA decomposition of the interaction energies (see text for details)
EL, *CT* and *CO* are BSSE-corrected values

Table 2 Excitation energies, oscillator strengths, symmetries and components of the transition dipole moment (in a.u.) for some selected electronic transitions of the PY–Ag_{20} complexes

	Energies	*f*	sym	μ_x	μ_y	μ_z
V-complex	3.366 eV (368.3 nm)	2.94	A″	0.00	0.00	5.97
	3.368 eV (368.1 nm)	2.95	A′	5.95	0.55	0.00
	3.417 eV (362.9 nm)	2.85	A′	0.53	−5.81	0.00
S-complex	3.325 eV (372.8 nm)	2.38	A″	0.00	0.00	5.41
	3.333 eV (371.9 nm)	2.32	A′	5.33	−0.21	0.00
	3.363 eV (368.6 nm)	2.25	A′	−0.20	5.23	0.00
	3.367 eV (368.3 nm)	0.59	A′	−1.58	−2.15	0.00
	3.399 eV (364.7 nm)	0.07	A″	0.00	0.00	0.91
	3.429 eV (361.6 nm)	0.23	A′	0.67	−1.53	0.00

Table 3 Vibrational frequencies (in cm^{-1}) and vibrational assignments for isolated pyridine and PY–Ag_{20} complexes

PY	V-complex	S-complex		Description and PED
613.8	634.4 (20.7)	628.1 (14.3)	Ring deformation	(92 % Ring CCC bending)
669.7	666.3 (−3.4)	667.0 (−2.6)	Ring deformation	(84 % Ring bending)
763.4	766.5 (3.2)	760.5 (−2.9)	CH out of plane	(50 % Ring torsion out of plane + 36 % CH torsion out of plane)
1021.9	1039.2 (17.3)	1032.4 (10.5)	Ring deformation	(70 % Ring bending + 24 % ring stretching)
1059.9	1059.2 (−0.7)	1059.3 (−0.6)	Ring breathing	(73 % Ring stretching + 23 % CH bending)
1103.4	1104.5 (1.2)	1102.7 (−0.7)	Ring CH bending	(49 % Ring stretching + 37 % CH bending)
1254.2	1252.2 (−2.0)	1249.0 (−5.1)	Ring CH bending	(69 % CH bending + 25 % ring stretching)
1287.9	1294.2 (6.4)	1293.7 (5.8)	Ring stretching	(80 % Ring stretching + 14 % CH ring bending)
1487.8	1493.4 (5.6)	1490.1 (2.3)	Ring CH twisting	(59 % CH bending + 36 % ring stretching)
1527.6	1530.6 (3.0)	1527.8 (0.2)	Ring CH twisting	(57 % Ring bending + 39 % ring stretching)
1664.2	1663.3 (−0.9)	1662.0 (−2.2)	Ring stretching	(72 % Ring stretching)
1668.7	1678.9 (10.2)	1674.5 (5.8)	Ring C=C stretching	(68 % Ring stretching + 25 % CH bending)

Values in parenthesis are the frequency shifts due to complexation

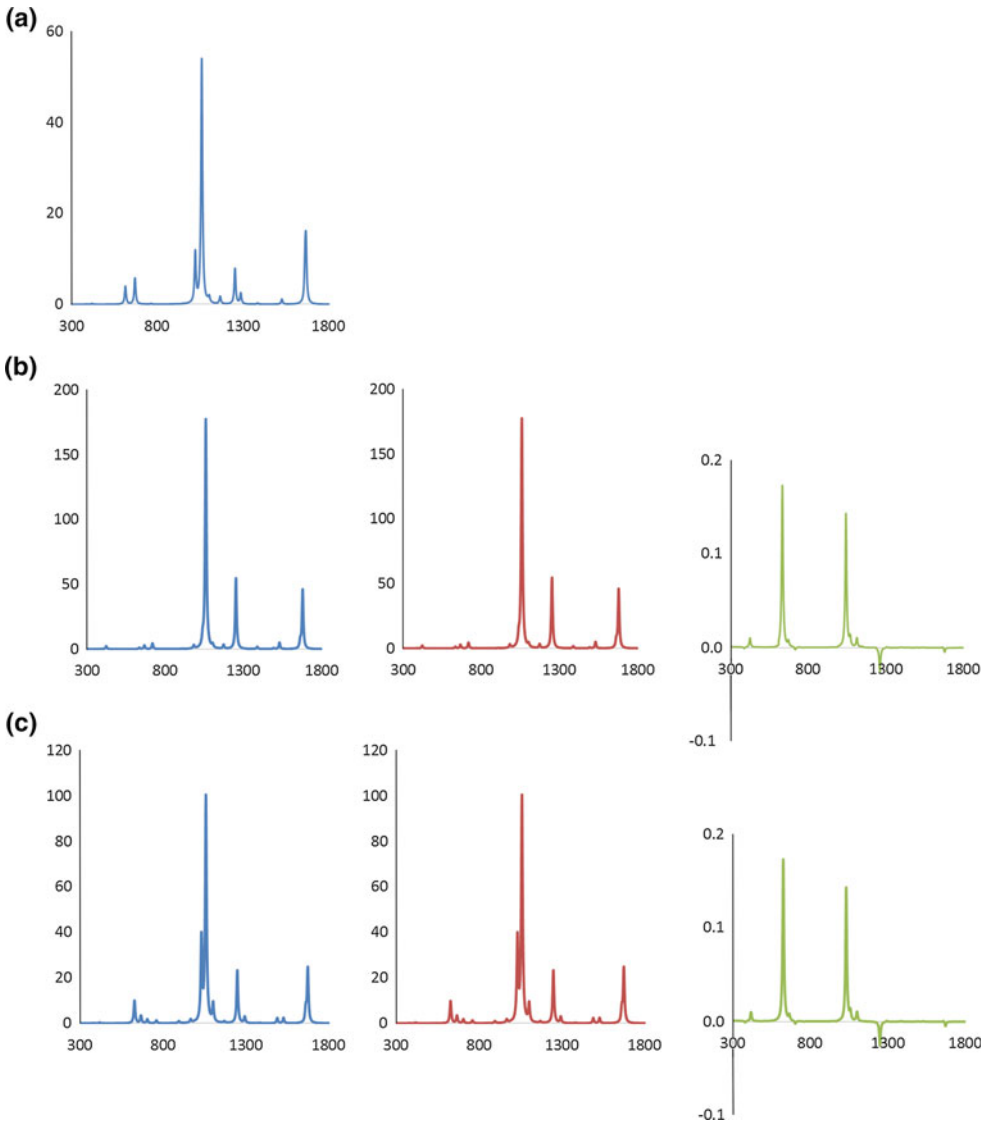

Fig. 2 Static Raman spectra of isolated pyridine and the PY–Ag_{20} complexes (*blue lines*). Separated contributions from pyridine and from the (surface + molecule−surface) terms to the Raman activity (*red* and *green lines*, respectively; see text for details). Wavenumbers are in cm^{-1}, and intensities are given as Raman activities ($Å^4$ amu^{-1}). **a** Pyridine; **b** V-complex; **c** S-complex

Table 4 Polarizability tensor components and isotropic polarizability (in a.u.) for the Ag_{20} cluster and pyridine isolated and forming complexes, total values for the S- and V-complexes and contributions from the pyridine atoms (see Fig. 1 for notation)

	Isolated		V-complex			Atomic contributions						
	Ag_{20}	PY	Total	Ag_{20}	PY	N	C_α	C_β	C_γ	H_α	H_β	H_γ
α_{xx}	995.7	25.7	1028.0	1014.0 (1.02)	14.0 (0.55)	−2.28	4.16	3.27	2.35	−0.50	0.00	0.11
α_{yy}	1007.0	66.3	1142.0	919.7 (0.91)	222.3 (3.35)	−68.14	−14.56	9.57	6.11	−30.20	92.23	170.30
α_{zz}	995.4	69.3	1060.0	1006.6 (1.01)	53.4 (0.77)	0.35	−3.54	−4.11	−1.87	14.07	20.83	0.43
α	999.4	53.7	1076.7	980.1 (0.98)	96.6 (1.80)	−23.36	−4.65	2.91	2.20	−5.54	37.69	56.95
	Isolated		S-complex			Atomic contributions						
	Ag_{20}	PY	Total	Ag_{20}	PY	N	C_α	C_β	C_γ	H_α	H_β	H_γ
α_{xx}	996.1	28.2	1020.0	1011.3 (1.01)	8.7 (0.31)	−1.04	1.85	2.82	1.32	−0.56	0.04	0.08
α_{yy}	999.6	66.8	1144.0	995.0 (0.99)	149.0 (2.23)	−22.34	−17.69	3.85	−2.35	−21.46	60.37	123.50
α_{zz}	996.3	70.8	1039.0	1001.0 (1.01)	38.0 (0.54)	1.06	−2.24	−3.65	−1.82	6.84	18.28	0.36
α	997.3	55.3	1067.7	1002.4 (1.01)	65.2 (1.18)	−7.44	−6.03	1.01	−0.95	−5.06	26.23	41.31

The values between brackets are the ratios between the values for adsorbed and isolated species. The values for the isolated species are computed with the geometries in their corresponding complexes

We have computed the electronic spectra for both complexes, and the main transitions found are given in Table 2. In agreement with previous studies, M06-2X computations predict three intense transitions for the S- and V-complexes located around 3.3–3.4 eV, which correspond to the splitting of the degenerated signal of the Ag_{20} cluster because of the loss of symmetry when the complexes are formed. The analysis of the orbitals involved indicates that these intense transitions are mainly centred on the silver cluster. On the other hand, the energy separation between these metallic transitions is similar in both complexes (about 0.05 eV), what suggests that the electron density change in the silver cluster upon adsorption is very similar in both complexes. For the S-complex, three additional weaker excitations at slightly higher energies (3.37, 3.40 and 3.43 eV) have been also found, and from the analysis of the molecular orbitals, it can be concluded that these signals correspond to electronic transitions from orbitals in the silver cluster to unoccupied molecular orbitals of pyridine. Following Zhao et al. [19], these transitions correspond to charge-transfer transitions, but it must be remarked that at the BP86/TZP level, they were found at lower energies (around 2.6 eV) and they were much weaker ($f < 0.04$) than those presented here.

3.2 Static Raman spectra

As can be seen in Table 3 and Fig. 2, in the 400–1800 cm^{-1} region, the Raman spectrum for isolated pyridine is dominated by a ring breathing at 1060 cm^{-1}, a ring C=C stretching at 1669 cm^{-1}, a ring deformation at 1022 cm^{-1}, a ring C–H bending at 1254 cm^{-1} and two ring deformations of smaller intensity at 670 and 614 cm^{-1}.

When pyridine is adsorbed on the silver cluster, significant changes can be observed in the Raman spectra. Thus, the spectrum for the V-complex is dominated only by three signals at 1059, 1252 and 1679 cm^{-1}, with intensities enhanced by a factor of 3.5–7 if compared to the spectrum of isolated pyridine. All these three vibrations correspond to ring vibrations, but with a noticeable contribution from the hydrogen atoms and the most remarkable shift (+10 cm^{-1}) corresponds to the signal at 1679 cm^{-1}, maybe because in this case the ring C=C stretch is largely combined with the C–H bending of the hydrogen atoms close to the Ag atom at the vertex of the cluster.

For the S-complex, the static Raman spectrum is again dominated by the signal at 1059 cm^{-1} and the signals at 1249 and 1674 cm^{-1}, but the overall intensities are enhanced only by factor of 2–3 with respect to the signals in isolated pyridine. Two additional signals at 1032 and 628 cm^{-1} are also well distinguished in the spectrum. The intensity of these signals is also enhanced by a factor of about 2–3, and they are positively shifted by about 10–15 cm^{-1} compared to pyridine. These signals, however, correspond to ring deformations without contribution of the hydrogen atoms.

To analyse these different behaviours, we focused initially on the changes of the polarizabilities for the complexes and on the contributions from the pyridine molecule. The results obtained for the polarizability components and the isotropic polarizability for the pyridine molecule and the silver cluster isolated and adsorbed on the surfaces are shown in Table 4. It can be seen that negligible changes occur on the isotropic polarizability of the silver cluster, reducing from 999 to 980 a.u. in the V-complex and increasing from 997 to 1002 a.u. in the S-complex. However, the

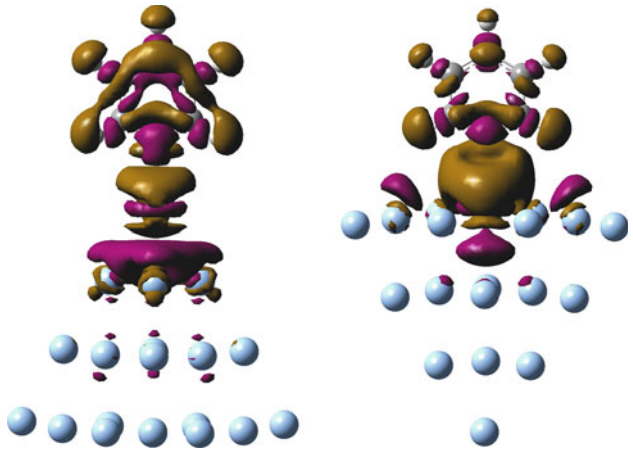

Fig. 3 Electron density change ($\Delta\rho = \rho_{complex} - \rho_{PY} - \rho_{Ag_{20}}$) due to complexation. Isosurface value of 0.0004 a.u. with enhanced density in *magenta* and reduced density in *brown*

isotropic polarizability of pyridine always increases considerably due to the adsorption on the silver cluster. Thus, the value for pyridine in the V-complex (96 a.u.) almost doubles that of isolated pyridine (54 a.u.), while in the S-complex (65 a.u.) it is around 20 % larger that in pyridine. This increase in the polarizability of pyridine due to adsorption explains the overall increase in intensity found in the static Raman spectra for both complexes and the larger enhancements observed in the signals for the V-complex.

The analysis of the components of the polarizability tensor shows that the main change of the polarizability takes place in the α_{yy} term, which increases by a factor of 2–3 with respect to the value of isolated pyridine, while the α_{xx} and α_{zz} components decrease. Furthermore, the values in Table 4 also indicate that contributions from the hydrogen atoms to the α_{yy} components are the largest ones and this would explain why vibrations involving hydrogen atoms are specially enhanced due to adsorption. Finally, it must be remarked that the contributions from the H_β and H_γ atoms in the V-complex are considerably larger than in the S-complex and there is also a significant increase in the contribution from the nitrogen atom. These trends can be related to the change of the electron density experimented by the pyridine molecule due to complexation, represented in Fig. 3, where it can be seen that most of the changes take place along the y direction.

Following the procedure indicated above, we have also obtained separately the R^M, R^S and R^{MS} contributions to the static Raman activity of the pyridine molecule and the theoretical Raman spectra obtained with those contributions were also included in Fig. 2. It can be seen that the Raman spectra of the complexes are almost equal to the contributions arising exclusively from the pyridine, since the combined contributions from the silver cluster and the intermolecular interactions are negligible (note the different scales in Fig. 2). This finding reinforces the idea that the signal enhancement observed in the static Raman spectra of the PY–Ag_{20} complexes, usually known as chemical enhancement, is only due to the changes of the polarizability of pyridine when it is adsorbed. On the other hand, these results indicate the absence of intermolecular vibrational coupling of pyridine with the silver cluster, probably due to the large atomic weight of the silver nuclei. It must be noted here that we have also recently found that the intermolecular vibrational coupling might become important and affect significantly Raman spectra if the surface is composed of lighter atoms as carbon [14].

3.3 Resonance Raman spectra

It has been established in previous studies that, for small clusters, excitations at wavelengths corresponding to electronic transitions on the metal can be considered as a model to the plasmon excitation responsible for the electromagnetic Raman enhancement observed in metals [19, 24, 26]. Therefore, the Raman spectra obtained at incident wavelengths around the absorption maxima for the V- and S-complexes are shown in Fig. 4, and it can be seen that there is a significant dependence of the Raman profiles on the excitation wavelength. For the V-complex, the SERS spectra for excitations at 369 and 368 nm are similar and the most intense signal corresponds to the ring C–H bending at 1252 cm^{-1}. However, for the excitation at 363 nm, the Raman spectrum is completely different and the most intense signals correspond to the ring stretch at 1679 cm^{-1}. On the other hand, the SERS spectrum for the S-complex obtained with an excitation at 373 nm is dominated by the signal at 1252 cm^{-1} and the signals at 1679, 1039 and 1059 cm^{-1} are of similar intensity. However, for excitations at 372 and 369 nm Raman spectra are dominated by the signal at 1679 cm^{-1}, followed by signals at 1249 and 1059 cm^{-1}, and the signal at 634 cm^{-1} can be also appreciated. Remarkably, the enhanced Raman spectra of the S-complex obtained with excitations at 362, 365 and 368 nm, which correspond to charge-transfer transitions from orbitals in the silver cluster to unoccupied molecular orbitals of pyridine, are similar to those at 369 and 372 nm. As in the static case, the decomposition of the Raman activities in molecule + surface contributions (see Fig. 4) shows that the contributions from the metallic cluster are always several orders of magnitude smaller than that of pyridine and do not contribute significantly to the total Raman profile. Therefore, it can be concluded that the differences in the SERS spectra are exclusively originated from the contribution of the polarizability derivatives with respect to the pyridine atoms.

To further check the influence of the excitation wavelength on the SERS spectra, we have obtained the excitation

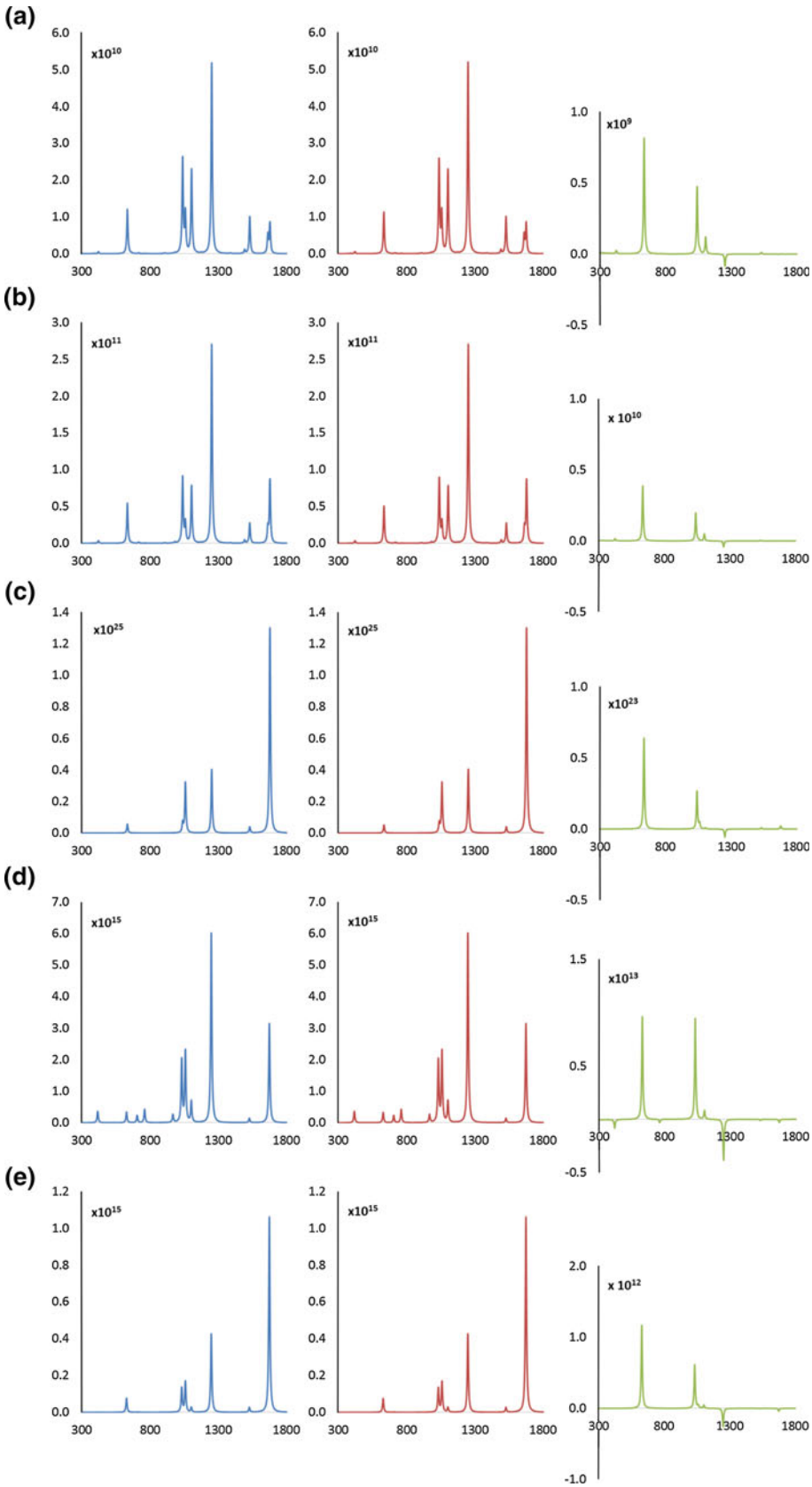

Fig. 4 Resonance Raman spectra for PY–Ag_{20} complexes (*blue lines*). Separated contributions from pyridine and from the (surface + molecule−surface) terms to the Raman activity (*red* and *green lines*, respectively; see text for details). Wavenumbers are in cm^{-1}, and intensities are given as Raman activities ($Å^4$ amu^{-1}). **a** V-complex—excitation wavelength 369 nm; **b** V-complex—excitation wavelength 368 nm; **c** V-complex—excitation wavelength 363 nm; **d** S-complex—excitation wavelength 373 nm; **e** S-complex—excitation wavelength 372 nm; **f** S-complex—excitation wavelength 369 nm; **g** S-complex—excitation wavelength 368 nm; **h** S-complex—excitation wavelength 365 nm; **i** S-complex—excitation wavelength 362 nm

Fig. 4 continued

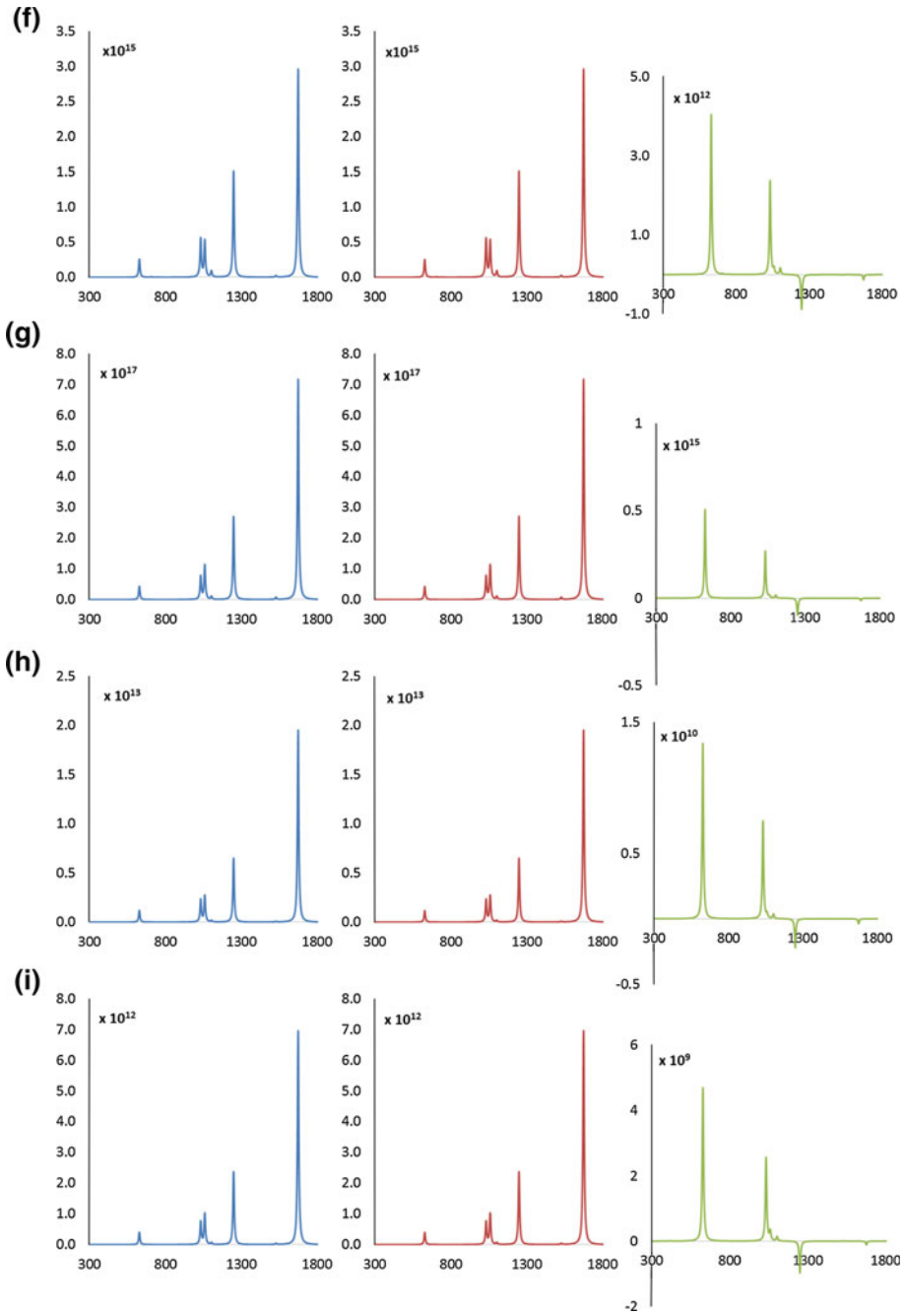

profiles for some of the most intense vibrational signals by detuning the excitation wavelength around the absorption maxima. The results obtained are plotted in Fig. 5, and it can be observed that, for the V-complex, the enhancement factors (EF) for the main vibrational modes follow the trend EF(1679) > EF(1252) > EF(1059), but there is an inversion between the signals at 1252 and 1679 cm^{-1} in the interval between 367 and 370 nm. In a similar way, the enhancement factors for the main vibrational modes of the S-complex follow the trend EF(1674) > EF(1249) > EF(628) > EF(1032) > EF(1059), and there is a change to EF(1249) > EF(1674) > EF(1032) > EF(628) > EF(1059) between 373 and 375 nm. Two main conclusions can be achieved from the results in the figure. On the one hand, it is clear that the use of excitation wavelengths at pre-resonance conditions will predict Raman profiles in agreement with those obtained at resonance conditions, but special care should be taken in the cited inversion interval. On the other hand, the enhancement factors predicted at pre-resonance conditions are expected to be larger for the S-complex. This can be proved by inspection of Fig. 5 and checking, for instance, that the enhancement factors for excitations wavelengths

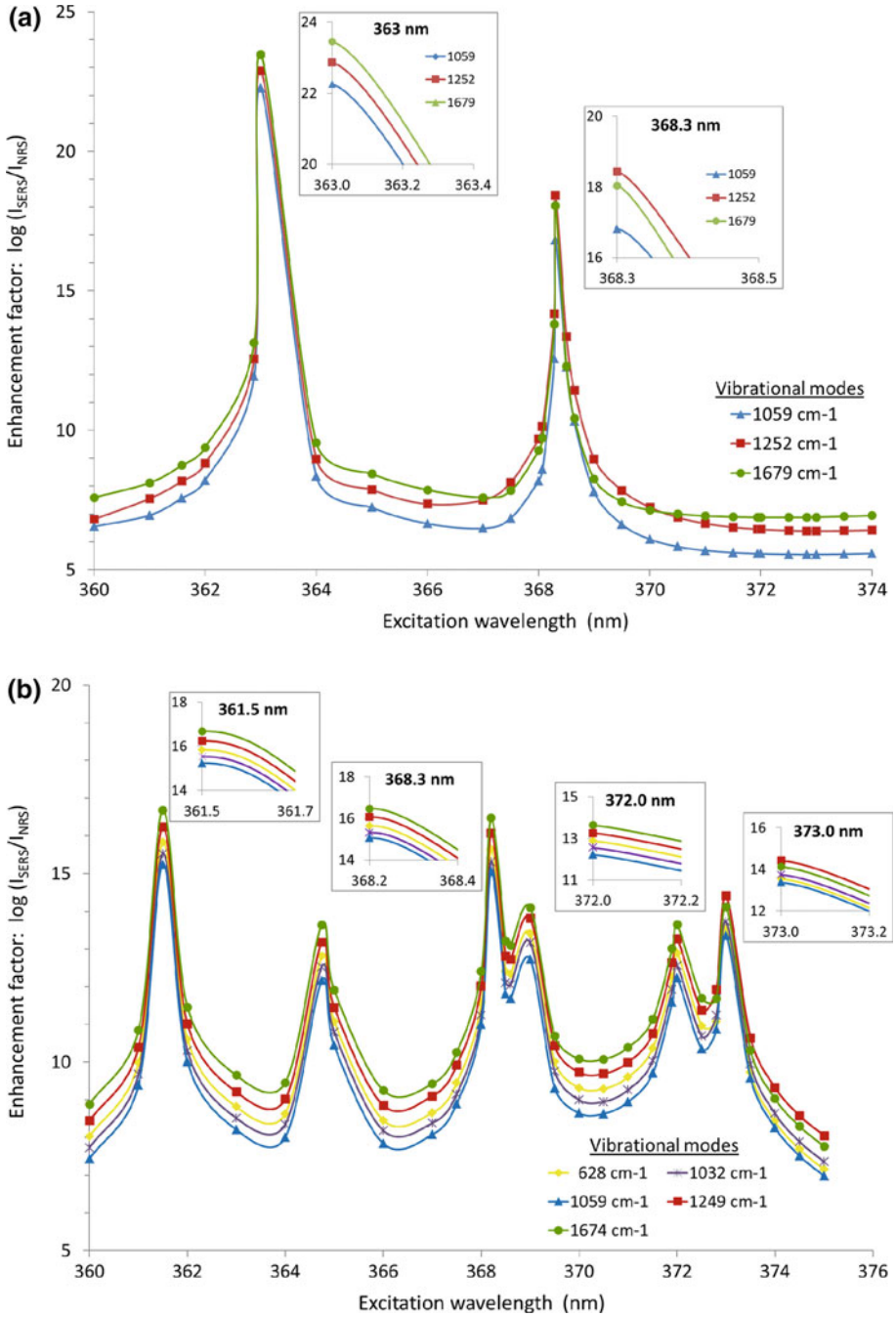

Fig. 5 Raman excitation profiles for some selected vibrational modes of the PY–Ag_{20} complexes. **a** V-complex; **b** S-complex

at 360 and 366 nm, which are far from resonance in both complexes, are always larger for the S-complex than for the V-complex.

In must be remarked here that the Raman excitation profiles presented in Fig. 5 are more resolved than those reported by Zhao et al. [19] employing time-dependent damping computations. We believe that the introduction of a damping in the TDDFT computations blurs out the electronic levels involved in the electronic transitions and, although the procedure avoids numerical problems during the TD–DFT calculations and can be adjusted to obtain Raman intensities in agreement with experimental results, introduces a significant uncertainty that may cause a loss of information in the resonance Raman spectra predicted theoretically.

To explain all the previous observations, we have also analysed the change of the electronic density during the electronic transitions for both complexes and represented them in Fig. 6. For the excitations at 369 and 368 nm, it can be seen that the electron density in the V-complex only changes on a face of the silver cluster along the z and x directions, respectively. However, for the transition at

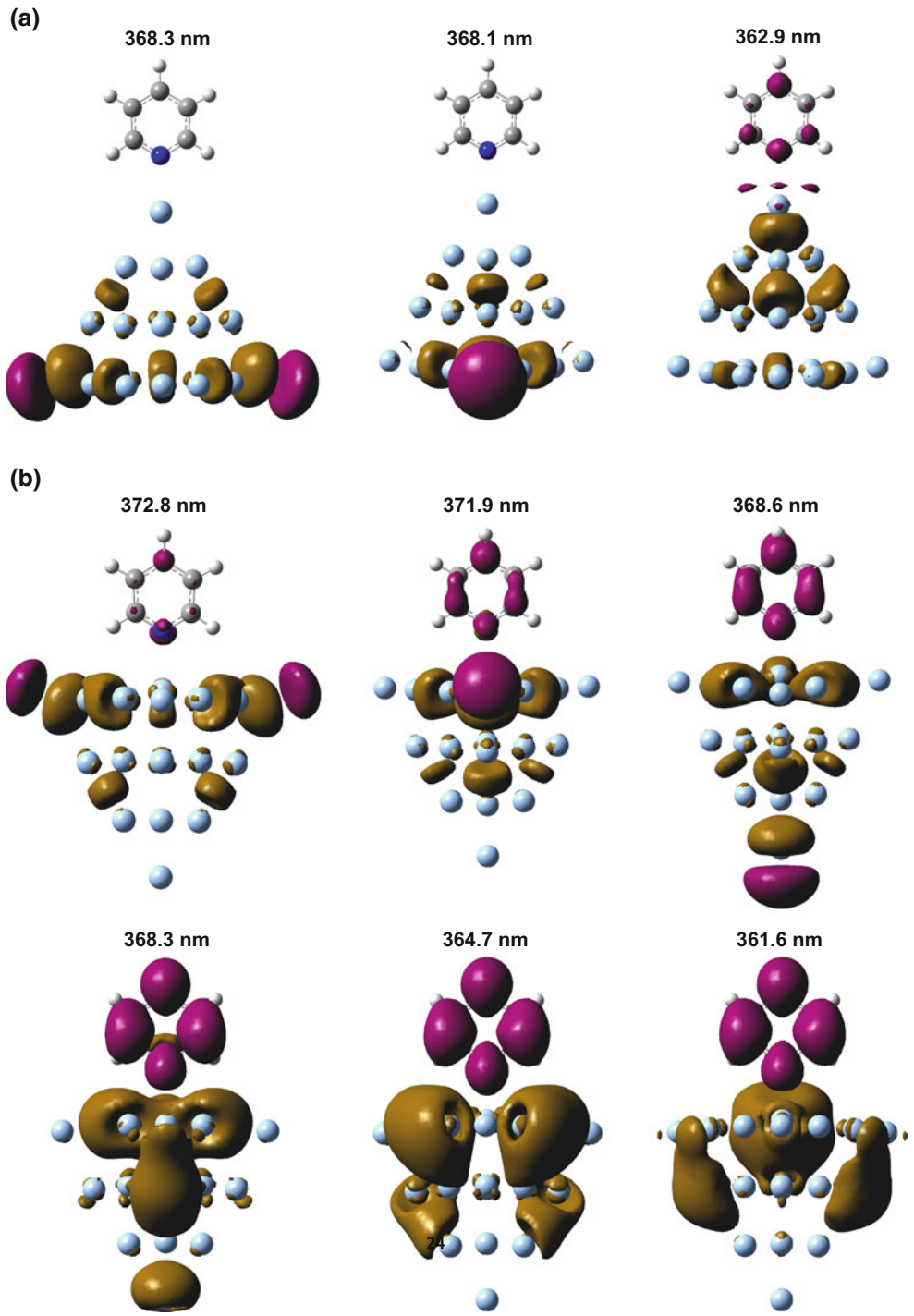

Fig. 6 Electron density deformations in the PY–Ag_{20} complexes due to the electronic transitions employed in the calculation of the resonance Raman spectra. Isosurface values of 0.0004 a.u. with enhanced densities in *magenta* and reduced densities in *brown*. **a** V-complex; **b** S-complex

363 nm, the electron density on the cluster changes along the *y* direction and causes an increase in electron density on some of the atoms of pyridine. As a consequence, it is the ring stretch at 1679 cm^{-1} the most enhanced signal because it possesses a considerable contribution of the carbon atoms of the ring.

In a similar way, for the excitations at 369 and 372 in the S-complex, the change of the electron density mainly takes place along the *y* and *x* direction, respectively, but there is also a clear increase in the electron density in the pyridine ring and, as a consequence, the ring stretch at 1674 cm^{-1} appears at the most intense signal with an enhancement

factor around 10^{15} with respect to the static spectra. However, for excitation at 373 nm, the amount of electron density shifted to the pyridine ring is smaller and the intensity of the signals at 1249 and 1674 cm^{-1} is inverted.

The above observations suggest that the reason for the differences observed in the resonance and pre-resonance spectra of the V- and S-complexes depends mainly on the amount of electron density transferred to pyridine during the electronic transition, and this could be related to the distance between the silver cluster and the pyridine ring. Thus, for both complexes, excitations with electron density shifts along the *y* direction always increase significantly the electron density of pyridine and the ring stretch is the most enhanced signal in the SERS spectra. On the other hand, the electronic transitions along the *x* and *z* directions in both complexes always occur with charge shifts on the surface of the cluster, but the amount of density transferred depends notably on the distance to pyridine: since the silver atoms on the surface of the S-complex are closer to pyridine, more electron density is transferred and the signal enhancements for the S-complex are several orders of magnitude larger than in the V-complex.

The same explanation can be also employed to explain the SERS profiles obtained with excitations at 368, 365 and 362 nm. The deformations of the electron density associated with these excitations agree with those expected for charge-transfer transitions since there is a noticeable electron density shift from the silver cluster towards pyridine (see Fig. 6). As a consequence, all these transitions increase the electron density in the ring framework of pyridine, and the most enhanced signals in the resonance Raman spectra are again the ring stretchings at 1674–1679 cm^{-1}.

4 Conclusions

In this paper, we have presented a detailed interpretation of the static and resonance Raman spectra of pyridine adsorbed on a Ag_{20} cluster using DFT (M06-2X) calculations. To this purpose, we have employed a decomposition method that allowed us to obtain separately the contributions from pyridine and the silver cluster to the Raman activity. The application of the method to the static Raman spectra of the V- and S-complexes permitted to conclude that the chemical enhancement observed in the static Raman spectra is only due to the increase in the polarizability of pyridine when adsorbed on the metal. In an analogous way, the computed electromagnetic and charge-transfer enhancements observed in the resonance Raman spectra can be explained only considering the Raman activities of pyridine. For both static and resonance Raman spectra, the contribution of the silver cluster is negligible and no significant contribution from vibrational intermolecular coupling was found.

The dependence on the excitation wavelength of the SERS spectra of the PY–Ag_{20} complexes has been also analysed since similar incident lights produce remarkably different spectra. We have found that the Raman spectra obtained at resonance and pre-resonance conditions are similar, and both complexes present a narrow interval of excitation wavelengths where the enhancement factors of certain vibrational signals change significantly. From the analysis of the changes of the electron density during electronic transitions, it has been established that the differences observed depend on the amount of electron density transferred to pyridine during the electronic transition, and this could be related to the distance between the surface of the cluster and the pyridine ring. Finally, the strong dependence on the excitation wavelength found in the SERS spectra of the PY–Ag_{20} complexes indicates that a proper knowledge of the effect of the excitation wavelength is very convenient for obtaining a reliable theoretical interpretation of surface-enhanced Raman spectra. Furthermore, understanding the influence of the excitation wavelength could be of great importance in future experimental work as the availability of tunable lasers improves.

References

1. Fleischmann M, Hendra PJ, Mcquillan AJ (1974) Chem Phys Lett 26:163–166
2. Van Duyne RP (1974) Chemical and biochemical applications of lasers, Chapter 5, vol 4. Academic Press, New York
3. Albrecht MG, Creighton JA (1977) J Am Chem Soc 99:5215–5217
4. Jeanmaire DL, Van Duyne RP (1977) J Electroanal Chem 84:1–20
5. Kneipp K, Wang Y, Kneipp H, Perelman LT, Itzkan I, Dasari RR, Feld MS (1997) Phys Rev Lett 78:1667–1670
6. Nie SM, Emory SR (1997) Science 275:1102–1106
7. Le Ru EC, Etchegoin PG (2009) Principles of surface-enhanced Raman spectroscopy and related plasmonic effects, Whole, vol Book. Elsevier, Boston
8. Campion A, Kambhampati P (1998) Chem Soc Rev 27:241–250
9. Jensen L, Aikens CM, Schatz GC (2008) Chem Soc Rev 37:1061–1073
10. Lombardi JR, Birke RL (2008) J Phys Chem C 112:5605–5617
11. Lombardi JR, Birke RL (2009) Accounts Chem Res 42:734–742
12. Jensen L, Autschbach J, Schatz GC (2005) J Chem Phys 122:224115
13. Jensen L, Zhao LL, Autschbach J, Schatz GC (2005) J Chem Phys 123:174110
14. Ramos-Berdullas N, López-Carballeira D, Perez-Juste I, Mandado M (2015) Submitted
15. Golab JT, Sprague JR, Carron KT, Schatz GC, Vanduyne RP (1988) J Chem Phys 88:7942–7951
16. Li WH, Li XY, Yu NT (1999) Chem Phys Lett 305:303–310
17. Corni S, Tomasi J (2001) Chem Phys Lett 342:135–140
18. Vivoni A, Birke RL, Foucault R, Lombardi JR (2003) J Phys Chem B 107:5547–5557
19. Zhao LL, Jensen L, Schatz GC (2006) J Am Chem Soc 128:2911–2919
20. Cardini G, Muniz-Miranda M, Pagliai M, Schettino V (2007) Theor Chem Acc 117:451–458
21. Jensen L, Zhao LL, Schatz GC (2007) J Phys Chem C 111:4756–4764

22. Wu D-Y, Liu X-M, Duan S, Xu X, Ren B, Lin S-H, Tian Z-Q (2008) J Phys Chem C 112:4195–4204
23. Morton SM, Jensen L (2009) J Am Chem Soc 131:4090–4098
24. Gaff J, Franzen S (2012) Chem Phys 397:34–41
25. Zhao LL, Jensen L, Schatz GC (2006) Nano Lett 6:1229–1234
26. Aikens CM, Schatz GC (2006) J Phys Chem A 110:13317–13324
27. Frisch MJ, Trucks GW, Schlegel HB, Scuseria GE, Robb MA, Cheeseman JR, Scalmani G, Barone V, Mennucci B, Petersson GA, Nakatsuji H, Caricato M, Li X, Hratchian HP, Izmaylov AF, Bloino J, Zheng G, Sonnenberg JL, Hada M, Ehara M, Toyota K, Fukuda R, Hasegawa J, Ishida M, Nakajima T, Honda Y, Kitao O, Nakai H, Vreven T, Jr. JAM, Peralta JE, Ogliaro F, Bearpark M, Heyd JJ, Brothers E, Kudin KN, Staroverov VN, Kobayashi R, Normand J, Raghavachari K, Rendell A, Burant JC, Iyengar SS, Tomasi J, Cossi M, Rega N, Millam JM, Klene M, Knox JE, Cross JB, Bakken V, Adamo C, Jaramillo J, Gomperts R, Stratmann RE, Yazyev O, Austin AJ, Cammi R, Pomelli C, Ochterski JW, Martin RL, Morokuma K, Zakrzewski VG, Voth GA, Salvador P, Dannenberg JJ, Dapprich S, Daniels AD, Farkas Ö, Foresman JB, Ortiz JV, Cioslowski J, Fox DJ (2009) Gaussian 09, Revision A.02; Gaussian Inc., Wallingford CT
28. Zhao Y, Truhlar DG (2008) Theor Chem Acc 120:215–241
29. Ramos-Berdullas N, Perez-Juste I, Van Alsenoy C, Mandado M (2015) Phys Chem Chem Phys 17:575–587
30. Jamroz MH (2004–2010) Vibrational energy distribution analysis, (VEDA 4), Warsaw
31. Jamroz MH (2013) Spectrochim Acta A 114:220–230
32. Norman P, Bishop DM, Jensen HJA, Oddershede J (2001) J Chem Phys 115:10323–10334
33. Hermida-Ramon JM, Guerrini L, Alvarez-Puebla RA (2013) J Phys Chem A 117:4584–4590
34. Sanchéz-Lozano M, Mandado M, Pérez-Juste I, Hermida-Ramón JM (2014) ChemPhysChem 15:4067–4076
35. Weinhold F (1998) Natural bond orbital methods. In: Schleyer PVR, Allinger NL, Clark T et al (eds) Encyclopedia of computational chemistry, vol 3. Wiley, Chichester, UK, pp 1792–1811
36. Glendening ED (2005) J Phys Chem A 109:11936–11940
37. Glendening ED, Badenhoop JK, Reed AE, Carpenter JE, Bohmann JA, Morales CM, Weinhold F (2001) NBO 5.0.; Theoretical Chemistry Institute, University of Wisconsin, Madison

Theor Chem Acc (2015) 134:67
DOI 10.1007/s00214-015-1666-y

REGULAR ARTICLE

Effect of van der Waals interactions in the DFT description of self-assembled monolayers of thiols on gold

José L. C. Fajín[1] · Filipe Teixeira[1] · José R. B. Gomes[2] · M. Natália D. S. Cordeiro[1]

Received: 14 November 2014 / Accepted: 13 April 2015 / Published online: 3 May 2015

Abstract The structure and energetic properties of self-assembled monolayers (SAMs) of alkanethiol derivatives (simple alkanethiols, mercaptoalkanoic acids and aminoalkanethiols with different chain length) adsorbed on the metallic Au(111) surface are investigated through periodic DFT calculations. To sort out the effect of van der Waals (vdW) interactions on the DFT calculations, the results of the standard GGA–PBE functional are compared with those obtained with approaches including the vdW interactions such as those incorporating the Grimme's (GGA–PBE-D2) and the Tkatchenko–Scheffler's (GGA–PBE-TS) schemes, as well as with the optB86b-vdW density functional. The most significant difference between the two sets of results appears for the adsorption energies per thiol molecules: The standard functional predicts energy values 30–40 % lower than those obtained when the van der Waals interactions are taken into account. This is certainly due to a better description of the lateral interactions between the chains of the thiols when including the van der Waals effects. Differences are also found between the adsorption energies predicted by density functionals taking into account the vdW corrections, with values increasing in the order GGA–PBE-D2 < GGA–PBE-TS < optB86b-vdW. Furthermore, the functionals considering dispersion interactions favor much more tilted orientations of the SAMs over the surface with respect to those found using the standard GGA functional (the SAMs' tilt angles increase from 17°–24° to 37°–46°), being the former in closer agreement with available experimental data. In contrast, the SAMs' precession angle and monolayer thickness are less affected by the type of DFT exchange–correlation functional employed. In the case of low surface coverage, the chains of the thiols adopt more tilted configurations and tend to lay side-down onto the surface.

Keywords Gold (111) surface · Thiols · Periodic density functional theory · van der Waals effects

1 Introduction

Self-assembled monolayers (SAMs) of thiols on metallic surfaces have been and still are being extensively studied due to their practical applications and functionalities. This kind of SAMs has been used namely as modifiers of metal electrodes, with variation of the metal electrode functionality with the SAM used [1–4], or as modifiers, which confer magnetic properties to the metal surface [5]. In addition, they have been applied as agents for the growth of thin films [6], C_{60} islands [7] or neuronal cells [8], of the immobilization of nanoparticles [9] or β-cyclodextrins [10], and for the aggregation of nanoparticles [11]. Other important applications of these SAMs include their use as sensors and biosensors [12], or even as reactants that can act in reactions on surfaces [13]. Following these important

Published as part of the special collection of articles derived from the 9th Congress on Electronic Structure: Principles and Applications (ESPA 2014).

✉ José L. C. Fajín
jfajin@fc.up.pt

✉ M. Natália D. S. Cordeiro
ncordeir@fc.up.pt

[1] LAQV@REQUIMTE, Department of Chemistry and Biochemistry, Faculty of Sciences, University of Porto, 4169-007 Porto, Portugal

[2] CICECO, Department of Chemistry, University of Aveiro, Campus Universitário de Santiago, 3810-193 Aveiro, Portugal

applications, several research works have dealt with the study of the thiol SAMs' structure [14–25] or with the development of new techniques aimed at creating patterned surfaces [26–28]. It has been found that desorption studies are very useful in the study of the SAMs' structure [29, 30].

It is well documented that thiols adsorb dissociatively on gold surfaces through their sulfur atoms upon breakage of the S–H bond [31–36] and form SAMs when the coverage is near to the monolayer. The formation of the SAMs is affected by the presence of surface defects [33, 37], by the thiol chain length which can distress the SAMs functionality [38–41], by the thiol terminal groups [42] which can lead to lateral interactions, by the formation of surface oxides [43–45] or by the thiol concentration [31, 46, 47]. Furthermore, the presence of adatoms on the surface has been claimed as an important factor toward the formation of thiol SAMs on gold surfaces [48–51], and, in particular, it has been found that methanethiol leads to a strong surface reconstruction during its adsorption [52].

The thiols used in the preparation of SAMs are usually alkanethiols [21, 27, 47, 53] or alkanethiols with the other end of the alkyl chain terminated with an organic acid group [54] or with an amino group [8, 9]. SAMs formed by mixing different types of alkanethiols are also quite common [28, 55]. The terminal group of the thiols can be altered by X-ray irradiation [56] or by photooxidation [57]. Despite that alkanethiols, aminoalkanethiols and mercaptoalkanoic acids are by far the most employed and investigated, other types of thiols such as thiophenethiols [58–63] have also been used for fabricating SAMs.

The important applications of thiol SAMs attracted also the attention of the theoreticians who focused their work in studies of their formation and resulting structures. Different theoretical methods have been employed in such studies, being widely spread in this field molecular dynamics (MD) simulations [42, 64–71] and density functional theory (DFT) [34, 39, 50, 72–79] calculations. The former methods are able to extract information on the dynamics of the formation of the SAMs at the atomic level, as well as their follow-on structural properties, whereas the latter ones are more useful for the study of bond formation or lateral interactions among the thiol chains in the SAMs. Monte Carlo simulations have also been used in the study of thiol SAMs [80].

These theoretical methods are then particularly helpful for verifying many aspects of the packing and phase behavior of SAMs and may provide a detailed description of the SAM structures. For example, both allow an easy estimation of parameters like the tilt and precession angles of the thiol chains into the SAMs or the monolayer thickness. The tilt angle corresponds to the angle between the thiol chain and the normal to the surface in the adsorption point, while the precession angle corresponds to the angle between the thiol chain projection into the *xy* plane (surface) and the *x*-axis (for additional information please refer to Fig. 2 of Ref. [81]). The tilted SAMs' structures are adopted to maximize the interaction between chains, and normally thiol SAMs exhibit tilt angles between 20° and 35° depending on the type of chains [15, 33, 40, 47, 53, 64, 82, 83]. In addition, it has been suggested that the tilt angle of the thiol chains depends on parameters such as the temperature, the nanoparticle size, the chain length (only for short thiols, <20 CH_2 groups) [69] and the deposition of metals on the surface [84]. Here, it should be mentioned that the reconstruction of the surface detected in MD simulations has been checked to be an artifact caused by the potential used in such simulations, by comparison with the reconstructed (postulated as unstable) and unreconstructed SAMs energies using DFT [65].

All the results obtained so far within DFT theoretical studies of SAMs resorted to standard DFT functionals, which do not account for van der Waals dispersion forces. In this work, we go one step ahead in the theoretical study of thiols SAMs onto a gold (111) surface by determining their binding energies and structures, through periodic DFT calculations with and without the consideration of van der Waals (vdW) forces. Three different types of thiol SAMs are compared namely: alkanethiols SAMs (hexane-1-thiol or undecane-1-thiol), SAMs formed by thiols terminated in an organic acid group (6-mercaptohexanoic acid and 11-mercaptoundecanoic acid) and SAMs formed by thiols terminated in an amino group (6-aminohexane-1-thiol and 11-aminoundecane-1-thiol). In fact, these thiols were chosen because they arise as the most frequently used in the preparation of SAMs on gold [9, 10, 28, 46, 55]. Additionally, with this selection of thiols, we also consider the most habitually chain lengths and terminal groups (methyl, carboxylic or amino) of thiol SAMs on gold.

This work is organized as follows. The computational methods are described in detail in Sect. 2, while the calculated results are reported and discussed in Sect. 3. Finally, the most important conclusions are summarized in Sect. 4.

2 Computational details

2.1 DFT approach

All the DFT calculations were carried out with the VASP 5.3.3 computer code [85–87], together with the GGA–PBE density functional proposed by Perdew et al. [88] to obtain the electron density. Due to the predictable effect of the dispersion forces in the calculations, these were considered in this work by using the Grimme's (GGA–PBE-D2) [89], the Tkatchenko–Scheffler's (GGA–PBE-TS) [90] schemes and by the consideration of the optB86b-vdW density

functional [91]. D2 corrections employed the common C_6 Grimme's parameters for the H, C, O, S and N atoms, while the C_6 parameter for gold was taken from Ref. [92] (14.99 J nm^6 mol^{-1}) where it was optimized for the interaction of thiols with the Au(111) surface. The expression for the dispersion energy in the TS method is essentially the same that used in the D2 method; however, the dispersion coefficients and damping function are charge-density dependent. Therefore, this method is able to account for variations in vdW contributions of atoms due to their local chemical environment [90]. The optB86b-vdW is a density functional that approximately takes into account the dispersion forces, and is framed in the scheme of the non-local van der Waals density functional (vdW-DF) of Dion but where the exchange functional was optimized for the correlation part [91]. For additional details on these approaches and applications, please refer to the recent review by Prates Ramalho et al. [93].

The effect of core electrons on the valence shells was described using the projected augmented-wave (PAW) method due to Blöch [94] and further implemented by Kresse and Joubert [95], together with a plane-wave basis set used to span the valence electronic states. The cutoff energy for the plane waves was 415 eV, found to be sufficient for energy and geometry convergence in previous works concerning adsorptions and reactions on gold surfaces [96, 97]. In addition, the conjugate-gradient algorithm was used for the relaxation of the ions during the spin-polarized calculations, and a 3 × 3 × 1 Monkhorst–Pack *k*-points grid was used for the integrals in the Brillouin zone for a correct energy convergence.

2.2 Slab models

The infinite Au(111) gold surface was modeled using the three-dimensional (3D) periodic-slab approach, being the same approach used to model the interaction of this surface with the thiol SAMs considered in this work.

The initial positions of the gold atoms in the slab used for the generation of the Au(111) surface by its repetition in the three spatial dimensions were obtained using the lattice parameter for bulk gold taken from a previous work [98]. Following on, bulk gold was cut along the (111) plane for obtaining a slab with three layers of gold atoms and forming a (3 × 3) unit cell with respect to the minimal unit cell for the (111) Miller index surface. The unit cell represented by this slab is a hexagonal prism with the angle between the *x*- and *y*-axes being 120° and the two other involving the *xz*- and *yz*-axes of exactly 90°. The resulting Au(111) surface model contains 27 gold atoms and assures that the adsorption energy of the thiols is converged with respect to the slab thickness. The Au(111) surface is characterized by four different adsorption positions, i.e., *top*, *bridge*, *fcc* hollow (above a subsurface octahedral cavity) and *hcp* hollow (above a subsurface tetrahedral cavity) sites. A representation of these adsorption sites can be seen in Fig. 1.

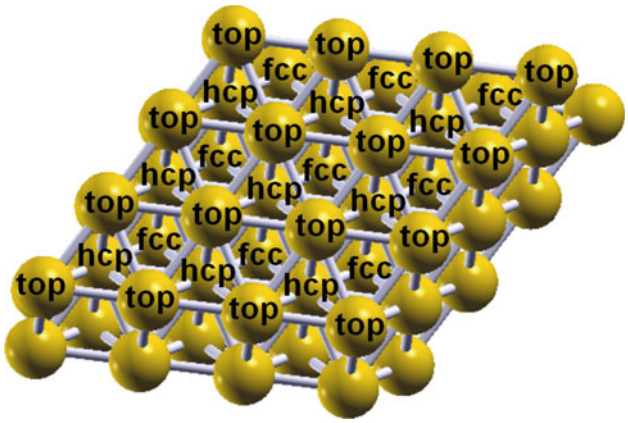

Fig. 1 Top, hollow hcp and hollow fcc adsorption sites on the Au(111) surface. Bridge sites correspond to the *lines* connecting top sites

It was necessary to consider three thiol molecules in each gold slab to obtain the correct thiol SAMs' configurations during the replication of the unit cell. Models with only one thiol chain on the slab and corresponding to the 1/3 ML coverage were also built in order to consider the coverage effects in the thiols adsorption. In both situations, the positions of the gold and thiol atoms were completely relaxed.

3 Results and discussion

3.1 Structure of thiol SAMs adsorbed onto the Au(111) surface

The most stable configurations for the thiol SAMs were determined, starting from several initial trial configurations and adsorption sites of the Au(111) surface (Fig. 1), by energy minimizations to sample minima corresponding to equilibrium structures. We considered the adsorption of the thiols in thiolated form since it is well established that the S–H bond breaks during the adsorption of thiols on gold surfaces [31–36] leading to H_2 formation [34].

The adsorption energies per thiol molecule (E_{ads}) of the thiols forming the SAMs were computed by the following expression:

$$E_{ads} = (E_{slab-(thiol)_n} - E_{slab} - n \times E_{thiol})/n \quad (1)$$

where E_{slab} refers to the electronic energy of the gold slab used, E_{thiol} to the molecular electronic energy on the gas phase of the correspondent thiol molecule in thiolated form and $E_{slab-(thiol)_n}$ to the electronic energy of the

correspondent slab-thiol supersystem; n is 3 or 1 for 1 ML or 1/3 ML surface coverages, respectively, and it refers to the number of thiol molecules per slab considered. Consequently, the adsorption energies E_{ads} are given per thiol molecule and negative values mean energetically favored adsorptions. Additionally, in the case of the 1 ML surface coverage (i.e., $n = 3$), Eqs. 2, and 3,

$$E_{\text{int\_Au-S}} = (E_{\text{slab}-(\text{thiol})_n} - E_{\text{slab}} - E_{(\text{thiol})_n})/n \quad (2)$$

$$E_{\text{int\_thiol-thiol}} = (E_{\text{slab}-(\text{thiol})_n} - E_{\text{slab}} - n \times E_{(\text{thiol})})/n \quad (3)$$

were employed to calculate the Au–sulfur interaction energy per thiol molecule, $E_{\text{int\_Au–S}}$ and the interchains interaction energy per thiol molecule, $E_{\text{int\_thiol–thiol}}$ for thiols forming the SAMs. In these equations, $E_{\text{slab}-(\text{thiol})_n}$, n and E_{slab} are as in Eq. (1), while $E_{(\text{thiol})_n}$ corresponds to the total energy of the thiol molecules frozen in their optimized geometries onto the Au(111) surface but without the 27 Au atoms of the metal slab, and $E_{(\text{thiol})}$ corresponds to the total energy of a single thiol chain frozen in its optimized geometry on the slab (i.e., without two of the three thiol molecules and the gold surface). Note that the sum of the values determined using Eqs. (2) and (3) does not correspond exactly to the value obtained with Eq. (1) because the thiol molecule used as reference in the latter equation is fully optimized in vacuum, while in the former cases, frozen geometries of the thiols in their adsorbed states are employed.

We began our investigation by determining the most favorable configurations for the adsorption of two representative alkanethiols on the Au(111) surface, i.e., the hexane-1-thiol and the undecane-1-thiol. The results concerning to the alkanethiol adsorption energies, tilt and precession angles of the thiol chains and monolayer thickness for the most stable structures of these alkanethiol SAMs on Au(111) are given in Table 1. In Fig. 2, we present the most favorable configurations for these thiols, computed by using the GGA–PBE-D2 functional (these structures are similar to those obtained using GGA–PBE-TS and optB86b-vdW). As it can be seen, the packing of the alkanethiols forming a compact monolayer is characterized by the alkanethiols adsorbed through their sulfur atoms on bridge positions and adopting a tilted structure similar to that obtained experimentally for the hexane-1-thiol closely packed phase [46] or to that found through MD simulations [81]. These tilted structures allow for better interactions between the chains with concomitant stabilization of the system. In the case of the structures relaxed with functionals taking into account the dispersion forces, the tilt angles calculated with the GGA–PBE-D2, GGA–PBE-TS and optB86b-vdW are, respectively, 45.7°, 45.0° and 44.8° for hexane-1-thiol, and 40.8°, 41.4° and 41.5° for undecane-1-thiol SAMs. These values are higher than those attained without taking

Table 1 Adsorption energies (E_{ads}, given per thiol molecule in eV) and structural properties for the most stable configuration of the studied thiol SAMs on Au(111) calculated with the PBE, PBE-D2, TS and optB86b-vdW methods

Type of thiol SAM	E_{ads}				Θ (°)				χ (°)				d (Å)			
	PBE	PBE-D2	TS	optB86b-vdW	PBE	PBE-D2	TS	optB86b-vdW	PBE	PBE-D2	TS	optB86b-vdW	PBE	PBE-D2	TS	optB86b-vdW
Hexane-1-thiol	−1.78	−2.52	−2.75	−2.92	17.5°	45.7°	45.0°	44.8°	45.5°	45.1°	45.3°	45.2°	8.26	5.48	5.55	5.56
Undecane-1-thiol	−1.75	−2.94	−3.47	−3.61	23.5°	40.8°	41.4°	41.5°	13.1°	5.1°	4.7°	4.6°	13.95	10.78	10.72	10.70
6-Mercaptohexanoic acid	−2.00	−2.82	−3.07	−3.21	23.1°	41.1°	40.3°	40.5°	16.4°	23.4°	23.4°	23.4°	8.14	5.83	5.91	5.90
11-Mercaptoundecanoic acid	−2.08	−3.27	−3.65	−3.92	24.2°	37.3°	37.6°	37.6°	3.7°	5.1°	5.1°	5.1°	13.98	11.34	11.31	11.30
6-Aminohexane-1-thiol	−1.75	−2.63	−2.98	−3.08	16.3°	46.1°	43.0°	46.0°	43.1°	48.9°	46.2°	43.8°	8.64	6.33	5.77	5.44
11-Aminoundecane-1-thiol	−1.79	−3.06	−3.64	−3.78	20.9°	43.9°	40.9°	41.0°	48.1°	51.3°	50.1°	50.2°	14.59	11.15	10.79	10.78

The Θ, χ angles and thiol layer thickness were determined as in Ref. [81]

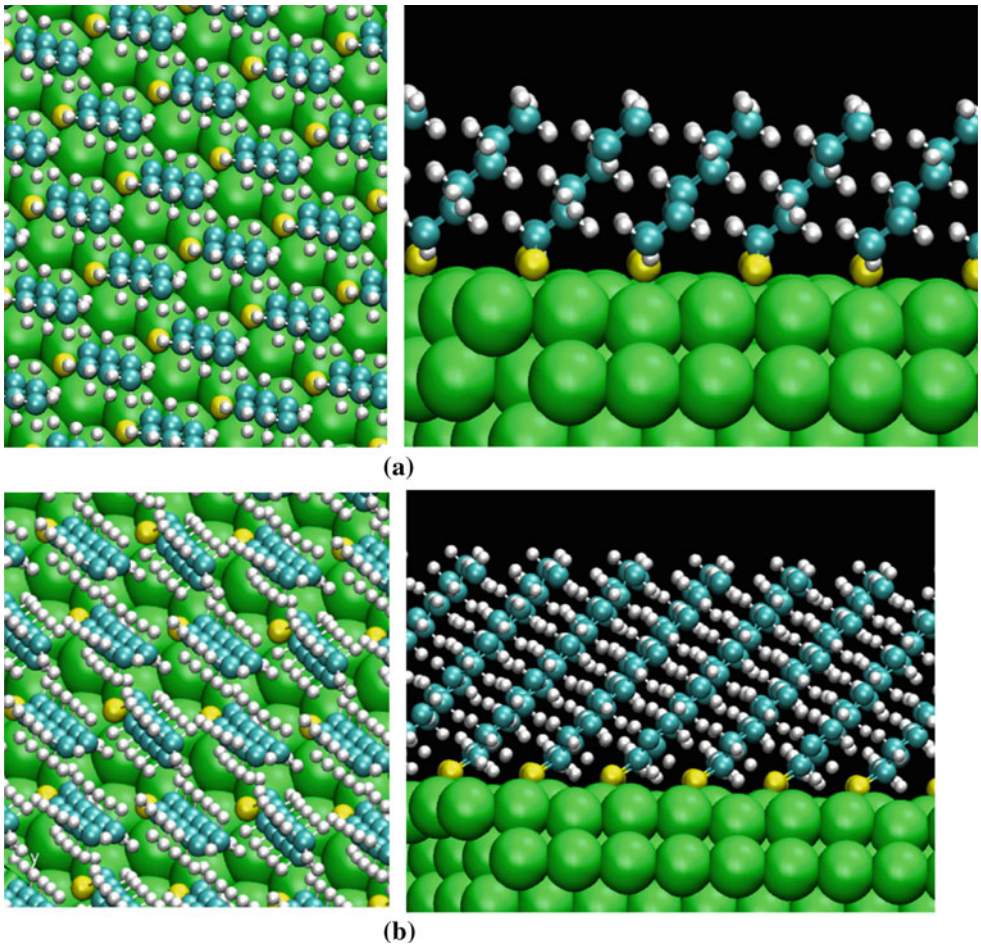

Fig. 2 Top (*left*) and side (*right*) views of the most stable SAMs obtained with the PBE-D2 approach for hexane-1-thiol (**a**) and undecane-1-thiol (**b**) on Au(111). *Green* stands for gold, *yellow* for sulfur, *blue* for carbon and *white* for hydrogen

into account the vdW forces (GGA–PBE functional), i.e., 17.5° and 23.5°, respectively. The tilt angle (GGA–PBE) for the undecanethiol SAM on Au(111) is similar to the experimental values found for the hexadecane-1-thiol SAM (22°) [53] and for the decane-1-thiol SAM (20°) [76]. Nevertheless, for the hexane-1-thiol SAM, the tilt angle computed with GGA-PBE is slightly lower than that obtained through MD simulations (23°) [81]. Moreover, the precession angles obtained indicate that the hexane-1-thiols adopt a next–next-nearest-neighbor (NNNN) tilt direction [99], and, in the case of the undecane-1-thiol SAM, the chains are oriented as in nearest-neighbor (NN) and NNNN configurations. To sum up, it seems that the inclusion of van der Waals forces in the calculations leads to an excessive tilt of the SAM chains, but the precession angle and the monolayer thickness are less affected. Interestingly, the values obtained for angles and thickness with the GGA–PBE-D2, GGA–PBE-TS and optB86b-vdW functionals are very similar, indicating that these quantities do not depend on the strategy employed to introduce the effects of the dispersion interactions in the DFT calculations.

The adsorption energies per thiol molecule are 0.42 eV (GGA–PBE-D2), 0.72 eV (GGA–PBE-TS) and 0.69 eV (optB86b-vdW) more negative for the SAMs with undecane-1-thiol than for the SAMs with hexane-1-thiol, showing the importance of the lateral interactions between the thiols in the SAMs. Such increment in the adsorption energy on going from the hexane to the undecane chain is not found when the calculations are performed with the GGA-PBE approach (cf. Table 1). The adsorption energy difference between undecane-1-thiol and hexane-1-thiol increases in the order GGA–PBE $\ll$ GGA–PBE-D2 < GGA–PBE-TS $\approx$ optB86b-vdW. This ordering is similar to that found for adsorption energies of the thiols (i.e., GGA–PBE < GGA–PBE-D2 < GGA–PBE-TS < optB86b-vdW), which suggests that the contribution of the dispersion interactions arising from the optB86b-vdW method is larger than those arising from the consideration of the other computational approaches.

We also examined the effect of the inclusion of the van der Waals forces in the thiols interatomic distances. All the interatomic distances for the most stable configuration of each thiol (alkanethiols, aminoalkanethiol and mercaptoalkanoic acids) SAMs are presented in the schemes depicted in Fig. 3. Some interatomic distances between atoms in different thiol chains are also provided to show the hydrogen

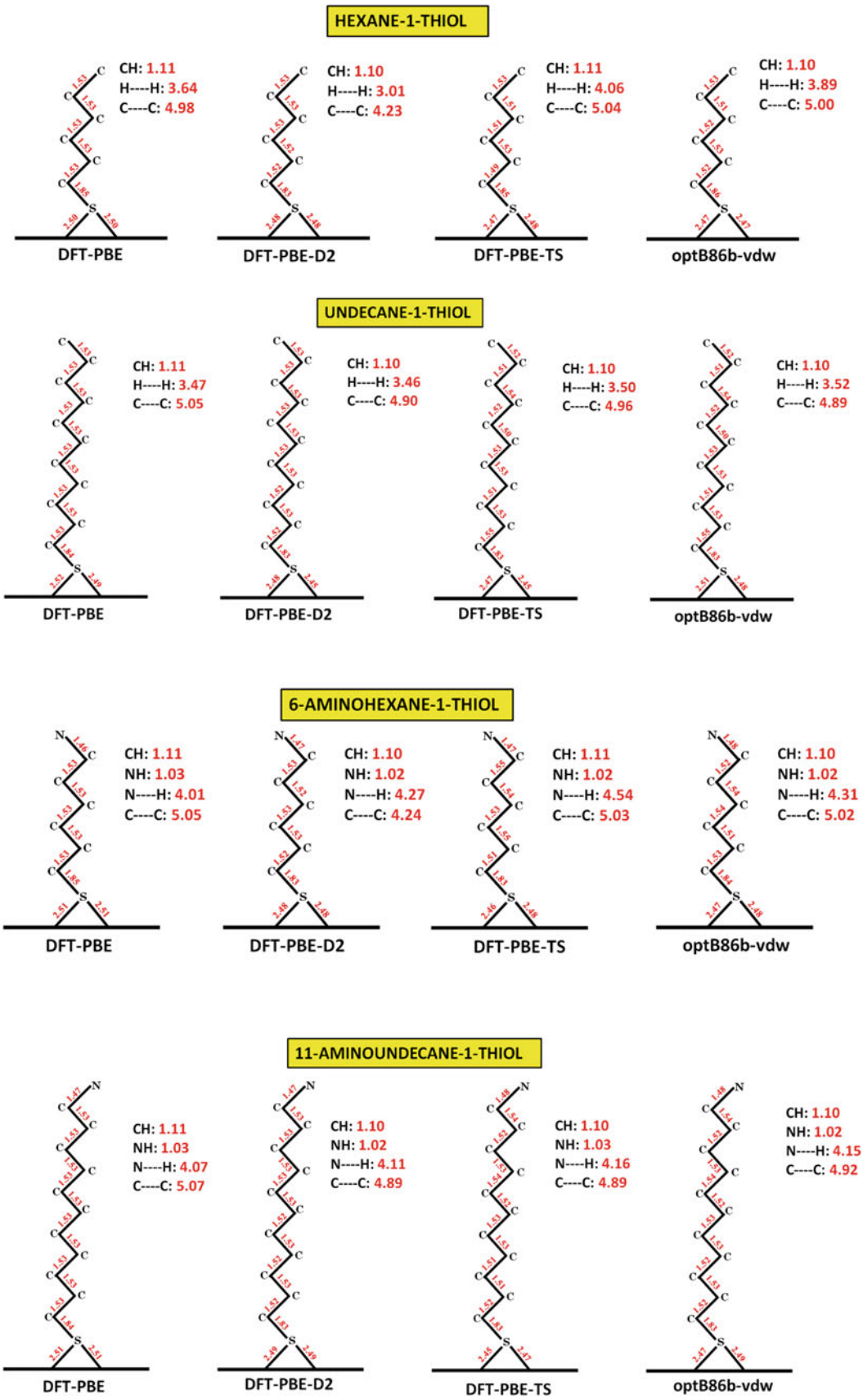
HEXANE-1-THIOL
CH: 1.11
H----H: 3.64
C----C: 4.98
DFT-PBE
CH: 1.10
H----H: 3.01
C----C: 4.23
DFT-PBE-D2
CH: 1.11
H----H: 4.06
C----C: 5.04
DFT-PBE-TS
CH: 1.10
H----H: 3.89
C----C: 5.00
optB86b-vdw
UNDECANE-1-THIOL
CH: 1.11
H----H: 3.47
C----C: 5.05
DFT-PBE
CH: 1.10
H----H: 3.46
C----C: 4.90
DFT-PBE-D2
CH: 1.10
H----H: 3.50
C----C: 4.96
DFT-PBE-TS
CH: 1.10
H----H: 3.52
C----C: 4.89
optB86b-vdw
6-AMINOHEXANE-1-THIOL
CH: 1.11
NH: 1.03
N----H: 4.01
C----C: 5.05
DFT-PBE
CH: 1.10
NH: 1.02
N----H: 4.27
C----C: 4.24
DFT-PBE-D2
CH: 1.11
NH: 1.02
N----H: 4.54
C----C: 5.03
DFT-PBE-TS
CH: 1.10
NH: 1.02
N----H: 4.31
C----C: 5.02
optB86b-vdw
11-AMINOUNDECANE-1-THIOL
CH: 1.11
NH: 1.03
N----H: 4.07
C----C: 5.07
DFT-PBE
CH: 1.10
NH: 1.02
N----H: 4.11
C----C: 4.89
DFT-PBE-D2
CH: 1.10
NH: 1.03
N----H: 4.16
C----C: 4.89
DFT-PBE-TS
CH: 1.10
NH: 1.02
N----H: 4.15
C----C: 4.92
optB86b-vdw

◀ **Fig. 3** Interatomic distances (Å) for the bonds in the thiols of SAMs on gold (labels CH, NH and OH) and shortest interatomic distances between atoms in neighboring thiols (labels H–H, C–C and O–H)

contacts (N–H or O–H distances) established between thiols terminal groups and to measure the distance between thiol chains (H–H or C–C distances). In general, for alkanethiol SAMs the inclusion of the van der Waals forces with any of the three approaches considered in this work has a weak influence in the thiols interatomic distances and their values are similar to those computed with the GGA-PBE approach. Still, the C–C and H–H distances computed with the GGA–PBE-D2 approach are ~0.2–0.7 Å shorter than those calculated with the GGA–PBE approach, while those calculated with the GGA–PBE-TS and optB86b-vdw functionals are slightly shorter in the case of the SAMs with hexane-1-thiol or slightly longer in the case of the SAMs with undecane-1-thiol when compared with those calculated with the standard GGA–PBE approach. However, striking differences are seen in the case of the distances between the sulfur and the gold surface, which become shorter after the consideration of the van der Waals interactions.

Following on, we studied the formation of SAMs on Au(111) of two thiols terminated with an amino group, i.e., the 6-aminohexane-1-thiol and the 11-aminoundecane-1-thiol. The most favorable configurations for the 6-aminohexane-1-thiol and 11-aminoundecane-1-thiol SAMs are shown in Fig. 4. The 6-aminohexane-1-thiol and 11-aminoundecane-1-thiol SAMs are characterized by thiols adsorbed on bridge positions through their S atoms and being the thiol chains tilted with respect to the surface normal. The tilt angles are similar to those obtained for the alkanethiol SAMs, i.e., 16.3°, 46.1°, 43.0° and 46.0°, with GGA–PBE, GGA–PBE-D2, GGA–PBE-TS and optB86b-vdW, respectively, in the case of the 6-aminohexane-1-thiol chains and 20.9°, 43.9°, 40.9° and 41.0° in the case of the 11-aminoundecane-1-thiol chains, being in both cases the GGA-PBE values closer to the experimental value (i.e., 26°) [82]. As in the case of simple alkanethiol SAMs, the inclusion of the van der Waals corrections seems to overestimate the tilt angles and it also leads to the differentiation between the adsorption energies for long and short aminoalkanethiol SAMs. This is in concordance with a better estimation of the interaction among the thiol chains when van der Waals forces are included in the calculations. In

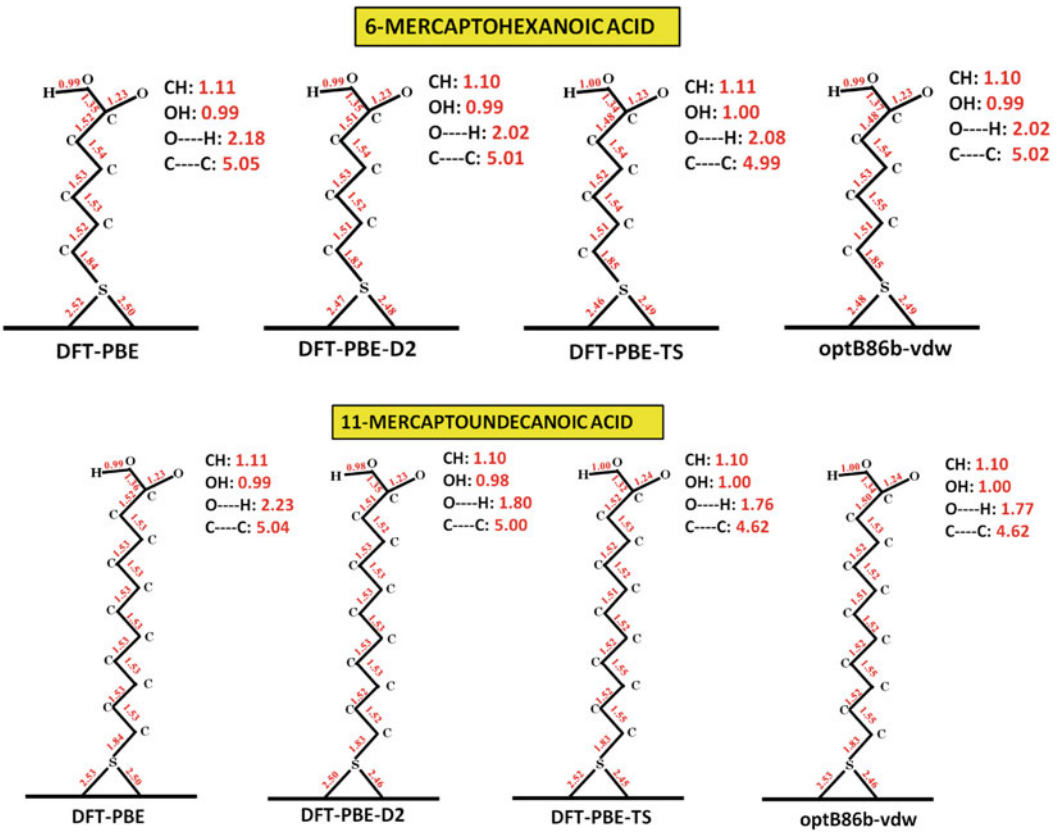

Fig. 3 continued

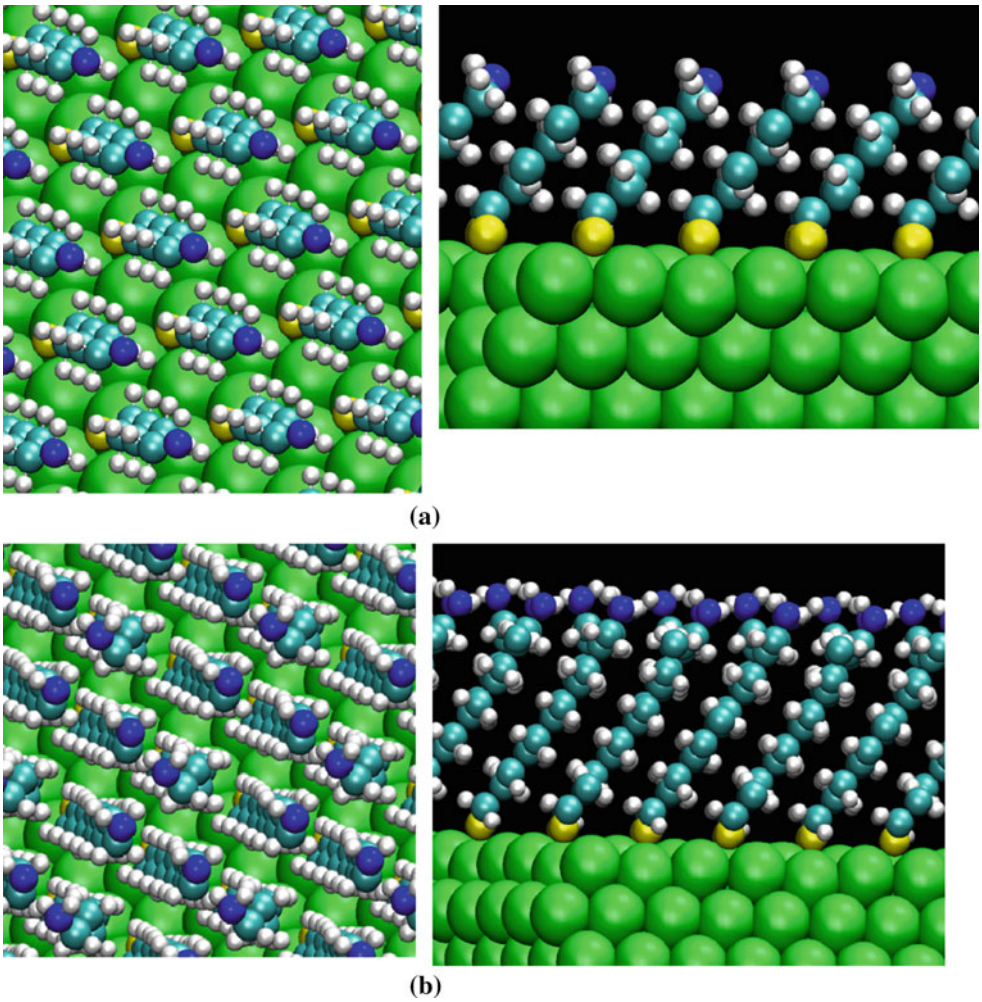

Fig. 4 Top (*left*) and side (*right*) views of the most stable SAMs obtained with the PBE-D2 approach for 6-aminohexane-1-thiol (**a**) and 11-aminoundecane-1-thiol (**b**) on Au(111). *Green* stands for gold, *yellow* for sulfur, *light-blue* for carbon, *dark-blue* for nitrogen and *white* for hydrogen

fact, the interatomic distance (C–C) between carbon atoms in different aminoalkanethiol chains for 11-aminoundecane-1-thiol is shorter by about 0.2 Å when van der Waals forces are considered in the calculations, while the distances in the thiol chains are almost the same (see schemes for aminoalkanethiols interatomic distances in Fig. 3). For SAMs with the 6-aminohexane-1-thiol, the GGA–PBE-D2 functional predicts shorter C–C distances than those calculated with the GGA–PBE functional but the values obtained with GGA–PBE-TS and optB86b-vdw functionals are similar to those obtained with the GGA–PBE approach. The effects in the precession angles and in monolayer thicknesses are more modest when van der Waals interactions are considered. Interestingly, the angles and thicknesses predicted by the calculations with GGA–PBE-D2, GGA–PBE-TS and optB86b-vdW functionals are similar, but the adsorption energies increase in the order GGA–PBE-D2 < GGA–PBE-TS < optB86b-vdW. The adsorption energy differences between 11-aminoundecane-1-thiol and 6-aminohexane-1-thiol become more negative in the same order, more precisely by 0.43 eV (GGA–PBE-D2), 0.66 eV (GGA–PBE-TS) and 0.70 eV (optB86b-vdW) showing again that the dispersion effects are more pronounced in the case of the calculations employing the optB86b-vdW functional. The precession angles obtained indicate that the SAMs of the aminothiols adopt NNNN configurations. In addition, as it can be seen in Fig. 4, the most favorable structures for the SAMs of the aminoalkanethiols are characterized by perpendicular orientation of the amino groups to the direction of the chain tilt in the case of 6-aminohexane-1-thiol and by the formation of hydrogen bonds between amino groups of neighboring aminoalkanethiols in the case of the 11-aminoundecane-1-thiol.

The orientations on the surface calculated for the SAMs of the 6-mercaptohexanoic and 11-mercaptoundecanoic acids are analogous to those described above for those obtained with the hexane-1-thiol and undecane-1-thiol compounds, respectively. According to previous MD simulations [64], there are several possible orientations of the carboxyl terminal groups of these SAMs. The configurations of the SAMs of 6-mercaptohexanoic and 11-mercaptoundecanoic acids (Fig. 5) obtained with DFT in this

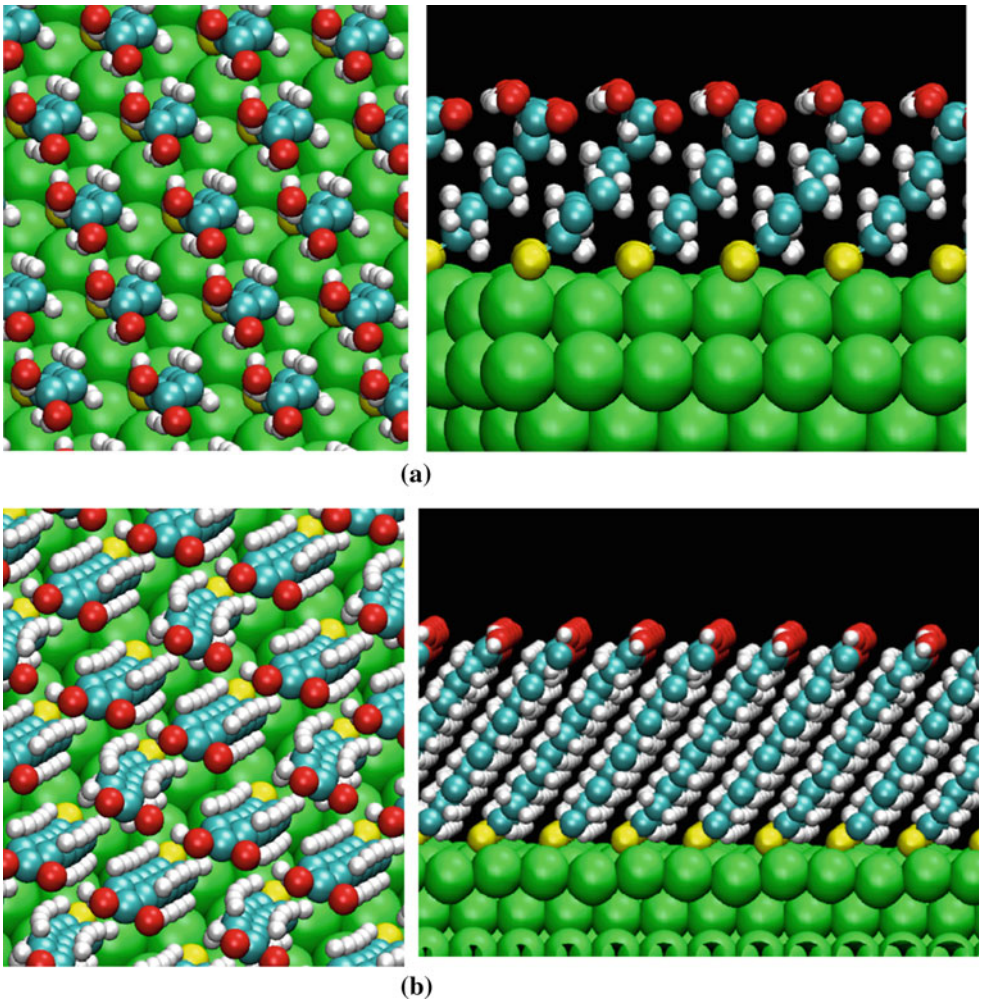

Fig. 5 Top (*left*) and side (*right*) views of the most stable SAMs obtained with the PBE-D2 approach form 6-mercaptohexanoic acid (**a**) and 11-mercaptoundecanoic acid (**b**) on Au(111). *Green* stands for gold, *yellow* for sulfur, *light-blue* for carbon, *red* for oxygen and *white* for hydrogen

work resemble intermediate configurations between the two extreme cases reported in Ref. [64]. In these SAMs, the 6-mercaptohexanoic and the 11-mercaptoundecanoic acids are adsorbed on bridge positions through their sulfur atoms and adopting tilted structures. In the case of 6-mercaptohexanoic acid, the tilt angles are 23.1°, 41.1°, 40.3° and 40.5°, with GGA-PBE, GGA-PBE-D2, GGA-PBE-TS and optB86b-vdW, respectively, while in the case of the 11-mercaptoundecanoic acid, the tilt angles are 24.2°, 37.3°, 37.6° and 37.6°, with GGA–PBE, GGA–PBE-D2, GGA–PBE-TS and optB86b-vdW, respectively. The angles obtained with the standard GGA–PBE are closer to the classical MD values in Ref. [64] than when the comparison is made with the approaches incorporating the van der Waals interactions. Once again, the inclusion of the van der Waals forces corrections seems to overestimate the tilt angles of the thiol chains of the SAMs. The higher adsorption energies predicted by the DFT–PBE-D2, DFT–PBE-TS and optB86b-vdw functionals are in concordance with the interatomic distances presented in the schemes of Fig. 3 for the mercaptoalkanoic acids studied here. The O–H distance between different thiols is shorter, about 0.2–0.4 Å when van der Waals forces are considered in the calculations, i.e., the hydrogen bond between different thiol chains is stronger when van der Waals forces are considered in the calculations. Interestingly, C–C distances are not significantly affected by the inclusion of the van der Waals forces in the calculations in the case of the SAMs based on mercaptoalkanoic acids.

The effect of the consideration in the calculations of the vdW forces on the values of the precession angles and monolayer thicknesses is more modest. The values obtained for the precession angles indicate that the 6-mercaptohexanoic acid adopts a configuration between NNNN and next-nearest-neighbor (NNN) into its SAM while the 11-mercaptoundecanoic acid adopts a configuration more close to NN [99]. In the case of the mercaptoalkanoic acids SAMs, the adsorption energy per thiol molecule is higher in the compounds with the longer alkyl chains even when van der Waals interactions are not considered (cf. Table 1). This must be related to the formation of more efficient hydrogen bonds between the carboxylic terminal in the

Table 2 Estimation of the contribution for the adsorption energy of the Au–sulfur ($E_{int\_Au–S}$, eV) and interchains ($E_{int\_thiol–thiol}$, eV) interactions obtained with the PBE-D2 approach

Type of thiol SAM	$E_{int\_Au–S}$	$E_{int\_thiol–thiol}$
Hexane-1-thiol	−2.37	−0.63
Undecane-1-thiol	−2.36	−1.07
6-Mercaptohexanoic acid	−2.34	−0.97
11-Mercaptoundecanoic acid	−2.33	−1.46
6-Aminohexane-1-thiol	−2.37	−0.71
11-Aminoundecane-1-thiol	−2.39	−1.25

SAMs obtained with the thiols with larger alkyl chains and also with the fact that these interactions, which are correctly described with the GGA-PBE approach, are much more favorable than the dispersive interactions between the chains.

The contributions of the lateral chain–chain and of the sulfur–metal interactions for SAMs obtained with the six different compounds considered in this work calculated with Eqs. (2) and (3) are reported in Table 2. As it can be seen, the Au–sulfur interaction clearly dominates over lateral interchains interaction for all the thiols. It is also found that the Au–sulfur interaction is not dependent on the type of thiol used to obtain the SAM as can be concluded by the similar values calculated for this interaction for all the thiols considered. Lateral interchain interactions depend on the chain length (−0.63 eV for hexane-1-thiol vs −1.07 eV for undecane-1-thiol; −0.97 eV for 6-mercaptohexanoic acid vs −1.46 eV for 11-mercaptoundecanoic acid; −0.71 eV for 6-aminohexane-1-thiol vs −1.25 eV for 11-aminoundecane-1-thiol) and on the thiol terminal group (−0.63 eV for hexane-1-thiol vs −0.71 eV for the 6-aminohexane-1-thiol vs −0.97 eV for the 6-mercaptohexanoic acid; −1.07 eV for undecane-1-thiol vs −1.25 eV for 11-aminoundecane-1-thiol vs −1.46 eV for the 11-mercaptoundecanoic acid). Lateral interactions in thiols with terminal carboxylic groups are stronger than lateral interactions between thiols with terminal amino groups, and the latter are stronger than lateral interactions in alkanethiols.

Finally, we also investigated with the GGA–PBE-D2 method the adsorption of the six thiols at 1/3 ML coverage where the formation of SAMs is not possible. The optimized configurations are represented in Fig. 6, and the adsorption energies are given in Table 3. As it can be seen in Fig. 6, the thiols with shorter chains adopt configurations with tilt angles much larger than those discussed above (values between 60° and 80°). These configurations allow a better interaction of the thiol with the gold surfaces being this

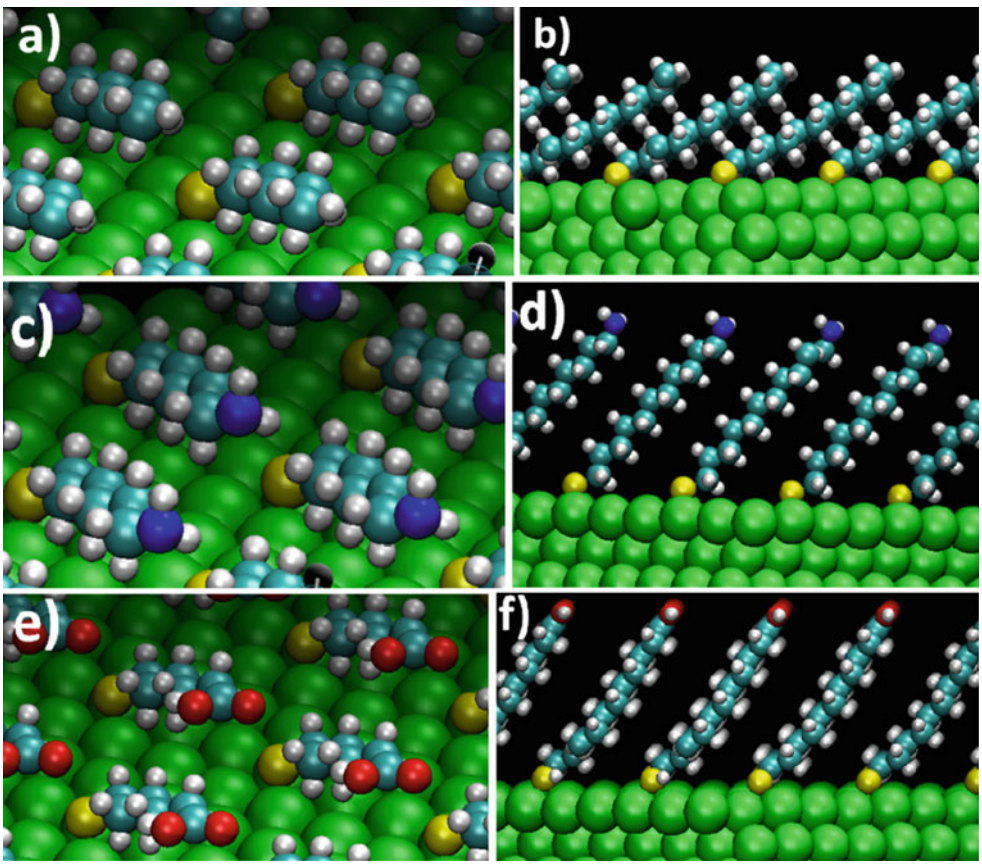

Fig. 6 Views of optimized configurations for different thiols adsorption at 1/3 ML coverage: **a** hexane-1-thiol, **b** undecane-1-thiol, **c** 6-aminohexane-1-thiol, **d** 11-aminoundecane-1-thiol, **e** 6-mercaptohexanoic acid and **f** 11-mercaptoundecanoic acid. *Green* stands for gold, *yellow* for sulfur, *light-blue* for carbon, *dark-blue* for nitrogen, *red* for oxygen and *white* for hydrogen

Table 3 Adsorption energies (E_{ads}, given per thiol molecule in eV) and structural properties for the most stable configuration of the different thiols on Au(111) at 1/3 ML coverage calculated with the PBE-D2 approach

Type of thiol SAM	E_{ads}	Θ (°)	χ (°)	d (Å)
Hexane-1-thiol	−2.49	67.1°	55.7°	3.05
Undecane-1-thiol	−2.63	63.2°	12.4°	5.76
6-Mercaptohexanoic acid	−2.75	61.3°	12.9°	3.82
11-Mercaptoundecanoic acid	−2.32	38.1°	0.9°	11.17
6-Aminohexane-1-thiol	−2.57	77.4°	33.1°	1.99
11-Aminoundecane-1-thiol	−2.16	41.5°	44.2°	11.59

The Θ, χ angles and thiol layer thickness were determined as in Ref. [81]

result similar to that obtained in Ref. [100] for methanethiol adsorption at low coverage. The adsorption energies reported in Table 3 for the thiols with shorter chains are similar to those obtained for the same thiols at the 1 ML coverage which indicates that the magnitude of the interaction of the chains with the gold surface is similar to the chain–chain interactions in the SAMs. In the case of the thiols having larger chains, the lateral interaction of their chains with the surface and among them is not possible (tilt angles are of about 40°) and the adsorption energies for these thiols are lower than those for the same thiols in the SAMs.

4 Conclusions

In this work, DFT calculations were carried out to elucidate the structure of SAMs of thiols on the Au(111) surface. SAMs with different terminal groups and chain lengths are addressed, namely (1) terminated in a methyl group: hexane-1-thiol and undecane-1-thiol; (2) terminated in an amino group: 6-aminohexane-1-thiol and 11-aminoundecane-1-thiol; and (3) terminated in a carboxylic group: 6-mercaptohexanoic acid and 11-mercaptoundecanoic acid. In order to assess the effect of the van der Waals interactions upon the results of the DFT calculations, the results pertaining to a common GGA approach, i.e., using the PBE exchange–correlation functional, are compared to those obtained with approaches including dispersion interactions, namely the PBE-D2, the PBE-TS and the optB86b-vdw functionals. The thiol SAMs are characterized by the tilt of the thiols chains which favors the interaction among the thiol chains and terminal groups. The consideration of the van der Waals forces in the calculations leads to a higher tilt of the thiol chains with values about 40° and to larger adsorption energies when compared to the values obtained without the consideration of the van der Waals interactions. Tilt angles calculated with the former approach (PBE) are closer to experimental and theoretical MD results reported in the literature than those obtained with the latter methods (PBE-D2, PBE-TS, optB86b-vdw functionals). The structures obtained for the SAMs with the PBE-D2, PBE-TS and optB86b-vdW functionals are similar, but adsorption energies increase from the former to the latter. Thus, it can be concluded that the inclusion of the van der Waals interactions in the calculations overestimate the tilt angle. Finally, the inclusion of the van der Waals forces in the calculations leads to different adsorption energies for long and short thiols possessing the same terminal group, which is related to a better description of the interactions between the thiol chains and also among thiol terminal groups.

Acknowledgments Thanks are due to Fundação para a Ciência e Tecnologia (FCT), Lisbon, Portugal, and to FEDER for financial support to REQUIMTE (projects Pest-C/EQB/LA0006/2013 and NORTE-07-0124-FEDER-000067-NANOCHEMISTRY) and to CICECO (project Pest-C/CTM/LA0011/2013) and for *Programa Investigador FCT*. This work is supported also by FCT through project PTDC/QUI–QUI/117439/2010 (FCOMP-01-0124-FEDER-020977) co-financed by *Programa COMPETE*. JLCF acknowledges FCT for the grant SFRH/BPD/64566/2009 co-financed by the *Programa Operacional Potencial Humano* (POPH)/*Fundo Social Europeu* (FSE); *Quadro de Referência Estratégico Nacional 2009–2013 do Governo da República Portuguesa*.

References

1. Domínguez CSH, Quintana C, Vicente J, Hernández P, Hernández L (2008) Talanta 74:1014–1019
2. Dong X-D, Lu J, Cha C (1995) Bioelectrochem Bioenerg 36:73–76
3. Guo C, Boullanger P, Jiang L, Liu T (2008) Colloid Surf B 62:146–150
4. Kondo M, Nakamura Y, Fujii K, Nagata M, Suemori Y, Dewa T, Iida K, Gardiner AT, Cogdell RJ, Nango M (2007) Biomacromolecules 8:2457–2463
5. Crivillers N, Mas-Torrent M, Vidal-Gancedo J, Veciana J, Rovira C (2008) J Am Chem Soc 130:5499–5506
6. Pattanaik G, Shao W, Swami N, Zangari G (2009) Langmuir 25:5031–5038
7. Li F, Tang L, Zhou W, Guo Q (2009) J Phys Chem C 113:17899–17903
8. Palyvoda O, Bordenyuk AN, Yatawara AK, McCullen E, Chen C-C, Benderskii AV, Auner GW (2008) Langmuir 24:4097–4106
9. Jacobsen V, Zhu T, Knoll W, Kreiter M (2005) Eur J Inorg Chem 2005:3683–3690
10. Campiña JM, Martins A, Silva F (2009) Electrochem Acta 55:90–103
11. Lim I-IS, Ip W, Crew E, Njoki PN, Mott D, Zhong C-J, Pan Y, Zhou S (2007) Langmuir 23:826–833
12. Taylor AD, Ladd J, Etheridge S, Deeds J, Hall S, Jiang S (2008) Sens Actuator B 130:120–128
13. Waring C, Bagot PAJ, Räisänen MT, Costen ML, McKendrick KG (2009) J Phys Chem A 113:4320–4329
14. Dubois C, Stellacci F (2008) J Phys Chem C 112:7431–7435
15. Dubois LH, Zegarski BR, Nuzzo RG (1993) J Chem Phys 98:678–688

16. Laiho T, Leiro JA (2008) Surf Interface Anal 40:51–59
17. Müller-Meskamp L, Karthäuser S, Waser R, Homberger M, Simon U (2008) Langmuir 24:4577–4580
18. Oh SY, Chung CM, Kim DH, Lee SG (2008) Colloid Surf A 313–314:600–603
19. Okabayashi N, Konda Y, Komeda T (2008) Phys Rev Lett 100:217801
20. Béthencourt MI, Srisombat L-O, Chinwangso P, Lee TR (2009) Langmuir 25:1265–1271
21. Sharma M, Komiyama M, Engstrom JR (2008) Langmuir 24:9937–9940
22. Silien C, Buck M, Goretzki G, Lahaye D, Champness NR, Weidner T, Zharnikov M (2009) Langmuir 25:959–967
23. Staub R, Toerker M, Fritz T, Schmitz-Hübsch T, Sellam F, Leo K (2000) Surf Sci 445:368–379
24. Ge Y, Weidner T, Ahn H, Whitten JE, Zharnikov M (2009) J Phys Chem C 113:4575–4583
25. Subramanian S, Sampath S (2007) Anal Bioanal Chem 388:135–145
26. Lamb BM, Barrett DG, Westcott NP, Yousaf MN (2008) Langmuir 24:8885–8889
27. Pace G, Petitjean A, Lalloz-Vogel M-N, Harrowfield J, Lehn J-M, Samorì P (2008) Angew Chem Int Ed 47:2484–2488
28. Phong PH, Tomono H, Nishi N, Yamamoto M, Kakiuchi T (2008) Electrochim Acta 53:4900–4906
29. Hayashi T, Wakamatsu K, Ito E, Hara M (2009) J Phys Chem C 113:18795–18799
30. Srisombat L-O, Zhang S, Lee TR (2010) Langmuir 26:41–46
31. Nadler R, Sánchez-de-Armas R, Sanz JF (2011) Comput Theoretical Chem 975:116–121
32. Hattori S, Kano S, Azuma Y, Majima Y (2010) J Phys Chem C 114:8120–8125
33. Cossaro A, Mazzarello R, Rousseau R, Casalis L, Verdini A, Kohlmeyer A, Floreano L, Scandolo S, Morgante A, Klein ML, Scoles G (2008) Science 321:943–946
34. Tielens F, Santos E (2010) J Phys Chem C 114:9444–9452
35. Kankate L, Turchanin A, Gölzhäuser A (2009) Langmuir 25:10435–10438
36. Sellers H, Ulman A, Shnidman Y, Eilers JE (1993) J Am Chem Soc 115:9389–9401
37. Cortés E, Rubert AA, Benitez G, Carro P, Vela ME, Salvarezza RC (2009) Langmuir 25:5661–5666
38. Desikan R, Armel S, Meyer HM III, Thundat T (2007) Nanotechnology 18:424028
39. Torres E, Blumenau AT, Biedermann PU (2011) Chem Phys Chem 12:999–1009
40. Fenter P, Eberhardt A, Liang KS, Eisenberger P (1997) J Chem Phys 106:1600–1608
41. Fenter P, Eisenberger P, Liang KS (1993) Phys Rev Lett 70:2447–2450
42. Li T-W, Chao I, Tao Y-T (1998) J Phys Chem B 102:2935–2946
43. Sung I-H, Kim D-E (2004) Tribol Lett 17:835–844
44. Tsai M-Y, Lin J-C (2001) J Colloid Interface Sci 238:259–266
45. Woodward JT, Walker ML, Meuse CW, Vanderah DJ, Poirier GE, Plant AL (2000) Langmuir 16:5347–5353
46. Noh J, Hara M (2011) RIKEN Rev: focused on nanotechnology in RIKEN II 38:49–51
47. Terrill RH, Tanzer TA, Bohn PW (1998) Langmuir 14:845–854
48. Kautz NA, Kandel SA (2009) J Phys Chem C 113:19286–19291
49. Kautz NA, Kandel SA (2008) J Am Chem Soc 130:6908–6909
50. Torres E, Biedermann PU, Blumenau AT (2009) Int J Quantum Chem 109:3466–3472
51. Wang J-G, Selloni A (2009) J Phys Chem C 113:8895–8900
52. Maksymovych P, Sorescu DC, Yates JT (2006) Phys Rev Lett 97:146103 (1–4)
53. Rosu DM, Jones JC, Hsu JWP, Kavanagh KL, Tsankov D, Schade U, Esser N, Hinrichs K (2009) Langmuir 25:919–923
54. Mendoza SM, Arfaoui I, Zanarini S, Paolucci F, Rudolf P (2007) Langmuir 23:582–588
55. Chuang W-H, Lin J-C (2007) J Biomed Mater Res A 82:820–830
56. Iqbal P, Critchley K, Attwood D, Tunnicliffe D, Evans SD, Preece JA (2008) Langmuir 24:13969–13976
57. Lee S-H, Lin W-C, Kuo C-H, Karakachian M, Lin Y-C, Yu B-Y, Shyue J-J (2010) J Phys Chem C 114:10512–10519
58. Fadda AA, Abdel-Latif E, El-Mekawy RE (2009) Eur J Med Chem 44:1250–1256
59. Ge Y, Whitten JE (2008) J Phys Chem C 112:1174–1182
60. Sändig N, Biscarini F, Zerbetto F (2008) J Phys Chem C 112:19516–19520
61. Harpham MR, Süzer O, Ma C-Q, Bäuerle P, Goodson T III (2009) J Am Chem Soc 131:973–979
62. Tang ML, Mannsfeld SCB, Sun Y-S, Becerril HA, Bao Z (2009) J Am Chem Soc 131:882–883
63. Nogues C, Lang P, Desbat B, Buffeteau T, Leiserowitz L (2008) Langmuir 24:8458–8464
64. Duffy DM, Harding JH (2005) Langmuir 21:3850–3857
65. Alkis S, Jiang P, Wang L-L, Roitberg AE, Cheng H-P, Krause JL (2007) J Phys Chem C 111:14743–14752
66. Bhatia R, Garrison BJ (1997) Langmuir 13:765–769
67. Bhatia R, Garrison BJ (1997) Langmuir 13:4038–4043
68. Dirama TE, Johnson JA (2007) Langmuir 23:12208–12216
69. Ghorai PK, Glotzer SC (2007) J Phys Chem C 111:15857–15862
70. Mar W, Klein ML (1994) Langmuir 10:188–196
71. Jia J, Huang YD, Long J, He JM, Zhang HX (2009) App Surf Sci 255:6451–6459
72. Carro P, Creus AH, Muñoz A, Salvarezza RC (2010) Langmuir 26:9589–9595
73. Lee H-H, Ružele Ž, Malysheva L, Onipko A, Gutés A, Björefors F, Valiokas R, Liedberg B (2009) Langmuir 25:13959–13971
74. Grönbeck H, Häkkinen H, Whetten RL (2008) J Phys Chem C 112:15940–15942
75. Grönbeck H (2010) J Phys Chem C 114:15973–15978
76. Leng J-C, Lin L-L, Song X-N, Li Z-L, Wang C-K (2009) J Phys Chem C 113:18353–18357
77. Majumder C (2008) Langmuir 24:10838–10842
78. Fletcher MC, Vivoni A, Moore MM, Lui J, Caldwell J, Prokes SM, Glembocki O, Hosten CM (2008) Surf Sci 602:1614–1621
79. Rajaraman G, Caneschi A, Gatteschi D, Totti F (2010) J Mater Chem 20:10747–10754
80. Alexiadis O, Daoulas KC, Mavrantzas VG (2008) J Phys Chem B 112:1198–1211
81. Szefczyk B, Franco R, Gomes JANF, Cordeiro MNDS (2010) J Mol Struct: Theochem 946:83–87
82. Campiña JM, Martins A, Silva F (2007) J Phys Chem C 111:5351–5362
83. Battaglini N, Repain V, Lang P, Horowitz G, Rousset S (2008) Langmuir 24:2042–2050
84. Epple M, Bittner AM, Kuhnke K, Kern K, Zheng W-Q, Tadjeddine A (2002) Langmuir 18:773–784
85. Kresse G, Hafner J (1993) Phys Rev B 47:558–561
86. Kresse G, Furthmüller J (1996) Comput Mater Sci 6:15–50
87. Kresse G, Furthmüller J (1996) Phys Rev B 54:11169–11186
88. Perdew JP, Burke K, Ernzerhof M (1996) Phys Rev Lett 67:3865–3868
89. Grimme S (2006) J Comput Chem 27:1787–1799
90. Tkatchenko A, Scheffler M (2009) Phys Rev Lett 102:073005
91. Klimeš J, Bowler DR, Michaelides A (2010) J Phys: Cond Matt 22:022201
92. Andersson MP (2013) J Theor Chem 2013:327839

93. Prates Ramalho JP, Gomes JRB, Illas F (2013) RSC Adv 3:13085–13100
94. Blöchl PE (1994) Phys Rev B 50:17953–17979
95. Kresse G, Joubert D (1999) Phys Rev B 59:1758–1775
96. Fajín JLC, Cordeiro MNDS, Gomes JRB (2011) Chem Comm 47:8403–8405
97. Fajín JLC, Gomes JRB, Cordeiro MNDS (2013) Langmuir 29:8856–8864
98. Fajín JLC, Cordeiro MNDS, Gomes JRB (2007) J Phys Chem C 111:17311–17321
99. Rai B, Sathish P, Malhotra CP, Pradip, Ayappa KG (2004) Langmuir 20:3138–3144
100. Fertitta E, Voloshina E, Paulus B (2014) J Comput Chem 35:204–213

Theor Chem Acc (2015) 134:37
DOI 10.1007/s00214-015-1639-1

REGULAR ARTICLE

Structural relaxation effects on the lowest $4f-5d$ transition of Ce^{3+} in garnets

Quan Manh Phung · Zoila Barandiarán · Luis Seijo

Received: 13 November 2014 / Accepted: 16 February 2015 / Published online: 27 February 2015

Abstract The role of structural relaxations on the energy of the lowest $4f-5d$ transition of Ce^{3+} in garnets is studied by means of *ab initio* calculations. This study completes previous studies on the roles of the interactions of the Cerium impurity with its first neighbors and with the rest of the solid hosts, before the relaxations take place. Periodic boundary conditions density functional theory calculations (DFT) and second-order perturbation theory spin–orbit coupling embedded-cluster wave function theory calculations (WFT) have been performed in the garnets $Y_3Al_5O_{12}$, $Lu_3Al_5O_{12}$, $Y_3Ga_5O_{12}$, $Lu_3Ga_5O_{12}$, and $Ca_3Sc_2Si_3O_{12}$ doped with Ce^{3+}. The local relaxation effects on the $4f-5d$ transition are similar in the WFT and DFT calculations. They produce a blue shift in Al and Ga garnets in which Ce substitutes for smaller Y and Lu cations, which is found to be basically due to the local expansions around the impurity, with only minor contributions from angular relaxations. Atomic relaxations of more distant neighbors enhance the blue shift. Although the embedding effects of the undistorted garnets are known to make the differences between the $4f-5d$ transition in Al and Ga garnets, we find that the structural relaxations are responsible for the small differences between the $4f-5d$ transition in $Y_3Al_5O_{12}$:Ce^{3+} and $Lu_3Al_5O_{12}$:Ce^{3+}, and in $Y_3Ga_5O_{12}$:Ce^{3+} and $Lu_3Ga_5O_{12}$:Ce^{3+}.

Keywords Ce · YAG · Garnets · $4f-5d$ transitions · Ab initio · Defect · Relaxation

1 Introduction

Yttrium aluminum garnet $Y_3Al_5O_{12}$ (YAG) doped with Ce^{3+} is a well-known phosphor used in energy-efficient solid-state white lighting devices based on InGaN blue LED [1, 2]. The facts that its Ce^{3+} $4f \rightarrow 5d$ blue absorption is well adapted to the blue LED emission and its $5d \rightarrow 4f$ emission is yellow [3] and can be mixed with residual blue from the LED to produce white light make the YAG:Ce^{3+} phosphor useful in LED-based illumination devices and a widely studied material. The convenience of producing white light warmer than the cool bluish white light so obtained boosted the search for alternative phosphors with better efficiencies and color-rendering indexes, and, in particular, for new phosphors with red-shifted emission. New Ce^{3+}-doped garnets (with general formula $A_3B'_2B''_3O_{12}$) are on focus in this respect and the search along this line led, for instance, to the discoveries of the $Lu_2CaMg_2Si_3O_{12}$:Ce^{3+} orange phosphor [4] and the $Ca_3Sc_2Si_3O_{12}$:Ce^{3+} green phosphor [5]. Besides illumination, Ce^{3+}-doped garnets find other applications such as scintillation [6], which is important in medical imaging.

Ab initio calculations can be of great help in the search for new red phosphors because of their ability to pinpoint the factors that govern the light absorptions and emissions.

Published as part of the special collection of articles derived from the 9th Congress on Electronic Structure: Principles and Applications (ESPA 2014).

Q. M. Phung
Department of Chemistry, KU Leuven, Celestijnenlaan 200F, 3001 Leuven, Belgium

Z. Barandiarán · L. Seijo
Departamento de Química, Universidad Autónoma de Madrid, 28049 Madrid, Spain

Z. Barandiarán · L. Seijo (✉)
Instituto Universitario de Ciencia de Materiales Nicolás Cabrera, Universidad Autónoma de Madrid, 28049 Madrid, Spain
e-mail: luis.seijo@uam.es

For example, they have provided an explanation to the fact that the $5d \rightarrow 4f$ emission of Ce^{3+} in YAG is blue shifted upon Ga-codoping and red-shifted upon La-codoping, although both codopants produce lattice expansions [3, 7, 8]: Whereas Ga does not substitute for Al in any preferent site and the lattice expansion it produces lowers the Ce^{3+} $5d$ splitting and shifts the $5d_1$ level to higher energies, La substitutions for Y are more stable near Ce, and the larger La $5p$ and $6s$ orbitals produce an increment of the Pauli repulsion on Ce^{3+}, which increases its $5d$ splitting and shifts its $5d_1$ level to lower energies [9, 10].

Previously, we have shown that the 12 energy levels of the $4f^1$ and $5d^1$ configurations of Ce^{3+} in 21 $A_3B'_2B''_3O_{12}$ garnets of Al, Ga, and Si ($B'' = Al, Ga, Si$), obtained in *ab initio* embedded-cluster calculations after a hypothetical *undistorted substitution*, provide useful data and information on differences in these levels between Ce^{3+}-doped garnets and garnet families [11, 12]. This is interesting because such calculations simply demand to compute the energy levels of the Ce_A substitutional defect at fixed experimental structures of the undoped garnet hosts, which means avoiding computationally demanding optimizations of the defective solids in the ground and excited states. The two main findings of these two previous *ab initio* studies were the following: Among the six components of the actual D_2 field experienced by Ce^{3+} when it is doped in garnets, only the cubic O_h and tetragonal D_{4h} (ditetragonal–dipyramidal) components lower the $5d_1-4f_1$ energy difference significantly [11]. Also, the undistorted host effects play a very important role in the differentiation of the $4f_1 \rightarrow 5d_1$ transition in different garnet families (of Al, Ga, and Si) [12].

Here, we complete the previous works with an *ab initio* study on the effect of the *structural relaxation* on the lowest Ce^{3+} $4f \rightarrow 5d$ transition. This relaxation takes place after Ce^{3+} substitutes for A in the undoped garnet $A_3B'_2B''_3O_{12}$ and creates a Ce_A substitutional defect. Altogether, the undistorted substitution effect and the structural relaxation effect give the total change of a $4f \rightarrow 5d$ transition of Ce^{3+} when it is incorporated into the solid host. We study the materials $Y_3Al_5O_{12}$:Ce^{3+}, $Lu_3Al_5O_{12}$:Ce^{3+}, $Y_3Ga_5O_{12}$:Ce^{3+}, and $Lu_3Ga_5O_{12}$:Ce^{3+}, which allow to compare Y/Lu and Al/Ga substitutions, and $Ca_3Sc_2Si_3O_{12}$:Ce^{3+}, which is the only Ce^{3+}-doped normal Si garnet with available $4f \rightarrow 5d_1$ experimental data. The results support that the undistorted host effect dominates the differences in $4f-5d$ transitions between Ce^{3+}-doped garnet families. Local relaxations are found to provide small corrections that can explain the small $4f-5d$ differences in similar materials, like $Y_3Al_5O_{12}$:Ce^{3+} and $Lu_3Al_5O_{12}$:Ce^{3+}.

We give the methodological details in Sect. 2, show and discuss the results in Sect. 3, and present the conclusions in Sect. 4.

2 Method

We performed *ab initio* wave function theory (WFT) embedded-cluster calculations with the MOLCAS suite of programs [13]. These are two-step spin–orbit coupling calculations on the $(CeO_8)^{13-}$cluster. In the first step, we used the many-electron scalar relativistic second-order Douglas–Kroll–Hess (DKH) Hamiltonian [14, 15]. We performed state-average complete-active-space self-consistent-field [16–18] (SA-CASSCF) calculations with the active space that results from distributing the open-shell electron in 13 active molecular orbitals with main character Ce $4f, 5d, 6s$. This provided occupied and empty molecular orbitals to feed subsequent multistate second-order perturbation theory calculations (MS-CASPT2) [19–22], where the dynamic correlation of 73 electrons (the $5s, 5p, 4f, 5d, 6s$ electrons of Ce and $2s, 2p$ electrons of the O atoms) was taken into account. In the second step, spin–orbit coupling effects were included by adding the atomic mean-field integrals (AMFI) approximation of the DKH spin–orbit coupling operator [23] to the Hamiltonian and performing restricted-active-space state-interaction spin–orbit calculations (RASSI-SO) [24] with the previously computed SA-CASSCF wave functions and MS-CASPT2 energies. All the calculations are all-electron, with atomic natural orbital (ANO) relativistic basis sets for Cerium [25] and Oxygen [26], with respective contractions $(25s22p15d11f4g)/[10s8p5d4f2g]$ and $(14s9p4d3f)/[4s3p2d1f]$. The Hamiltonian of the $(CeO_8)^{13-}$ cluster was supplemented with the *ab initio* model potential (AIMP) embedding Hamiltonians [27] of the $Y_3Al_5O_{12}$, $Lu_3Al_5O_{12}$, $Y_3Ga_5O_{12}$, $Lu_3Ga_5O_{12}$, and $Ca_3Sc_2Si_3O_{12}$ garnets obtained in Refs. [12, 28] (YAG). These embedding potentials add host electrostatic effects (long-range point-charge Madelung contributions and short-range charge density Coulomb contributions), exchange effects, and Pauli repulsion effects (non-orthogonality contributions due to cluster–host antisymmetry requirements) onto the otherwise isolated cluster. Electron correlation effects between the cluster and the host are excluded from these calculations. The embedding Hamiltonians are made of total-ion embedding AIMPs representing the A, B′, and B″ cations and the O^{2-} anions, which are obtained in self-consistent embedded-ions (SCEI) [29] Hartree–Fock (HF) calculations on the undoped garnets at their experimental structures [160 atom body-centered cubic unit cell (80 atom primitive cell) of the $Ia\bar{3}d$ (230) space group, with 8 formula units of $A_3B'_2B''_3O_{12}$; see Ref. [12] for specific structural data]. They are located at the ionic sites within a cube made of $3 \times 3 \times 3$ unit cells and centered on Ce^{3+}, and the embedding potential is completed with a set of $\sim 10^5$ additional point charges situated at lattice sites, generated by the method of Gellé and

Lepetit [30] in order to closely reproduce the Ewald potential [31] within the cluster.

In a set of frozen-lattice embedded-cluster WFT calculations, experimental ionic sites were used in the 27 unit cells surrounding Ce^{3+} in all the garnets, and the D_2 structures of the $(CeO_8)^{13-}$ clusters were optimized at the spin–orbit level of calculation, RASSI-SO. This was done in the $4f^1$ ground state, $1\Gamma_5$, and in the lowest excited state of the $5d^1$ configuration, $8\Gamma_5$. We used an iterative sequential optimization in specific directions, which was stopped when a relative change smaller than 10–5 was found in two iterations. The specific directions chosen were the six D_2 totally symmetric displacements of the CeO_8 moiety $S_1 - S_6$ defined in Ref. [12], which are Ce–O bond stretching (S_1, S_2), bond bending (S_3, S_4), and bond twisting (S_5, S_6) D_2 deformations of a reference CeO_8 cube. We calculated the energy differences between the $8\Gamma_5(5d^1)$ and $1\Gamma_5(4f^1)$ states at these structures using the same level of theory, RASSI-SO.

In separate calculations, following the procedure of Ref. [9], we used periodic boundary conditions density functional theory (PBC-DFT) calculations in order to obtain ground-state structures of the undoped garnets and of the Ce^{3+}-doped garnets. At the DFT structures of the latter, we computed the energy differences $E[8\Gamma_5(5d^1)] - E[1\Gamma_5(4f^1)]$ using the embedded-cluster RASSI-SO WFT method described above. With this DFT-WFT combined procedure, we computed the effects of CeO_8 relaxations and of full lattice relaxations on the Ce^{3+} $4f-5d$ energy differences.

The details of the PBC-DFT calculations are the following. We used the Projector Augmented-Wave Method (PAW) [32, 33] implemented in the VASP code [34–37] with the generalized gradient approximation (GGA) functional PW91 [38], a converged cutoff energy of 520 eV, and a k-point mesh of $4 \times 4 \times 4$. For the Ce^{3+}-doped garnets, we used the GGA+U approach [39] with an effective Hubbard parameter for the localized Ce $4f$ of $U_{eff} = 6$ eV, as proposed by Ning et al. [40] in $LuAlO_3$:Ce^{3+}. The structures of the undoped garnets were constrained to the $Ia\bar{3}d$ space group. In the Ce^{3+}-doped garnets, Ce substitutes for A at one of the 24(c) unit cell sites with D_2 local symmetry, and we used the C222 space group in order to maintain the local symmetry.

3 Results and discussion

We have calculated the crystal structures of the undoped garnets $Y_3Al_5O_{12}$, $Lu_3Al_5O_{12}$, $Y_3Ga_5O_{12}$, $Lu_3Ga_5O_{12}$, and $Ca_3Sc_2Si_3O_{12}$ at the PBC-DFT PW91 level. The results are shown in Table 1. The theoretical lattice constants show deviations from the experiments of about +1 %, which are common in calculations of this type; the largest deviation is +1.1 % in $Y_3Ga_5O_{12}$. The theoretical values of the oxygen special position parameters, x_O, y_O, z_O, also show deviations under or of around 1 %, except 1.5 and 3.3 % in the x_O and y_O values of $Y_3Ga_5O_{12}$, and 1.8 and 2.2 % in the y_O values of $Y_3Al_5O_{12}$ and $Lu_3Al_5O_{12}$. The good overall agreement suggests that taking an experimental structure or a theoretical structure as a starting point to study structural relaxations around a Ce_A substitutional defect should yield similar results.

In Table 2, we summarize the values of the lowest Ce^{3+} $4f-5d$ transition $[1\Gamma_5(4f^1) \rightarrow 8\Gamma_5(5d^1)]$, calculated at the RASSI-SO WFT level using different structures for the doped garnets: (A) the experimental structure of the undoped garnet; (B) the structure resulting from local relaxation of the CeO_8 moiety in RASSI-SO embedded-cluster calculations using the embedding potential of an unrelaxed host with the experimental structure; (C) the structure resulting from local relaxation of the CeO_8 moiety in PBC-DFT calculations where the rest of the atoms

Table 1 Experimental and calculated crystallographic data of the studied garnets: lattice constant a and special position (h) of the $Ia\bar{3}d$ (230) space group x_O, y_O, z_O

Garnet		a(Å)	x_O	y_O	z_O
$Y_3Al_5O_{12}$	Exp. (Ref. [47])	12.000	–0.0306	0.0512	0.1500
	DFT PBE (Ref. [48])	12.114	–0.0306	0.0519	0.1491
	DFT PW91 (this work)	12.096	–0.0308	0.0503	0.1490
$Y_3Ga_5O_{12}$	Exp. (Ref. [49])	12.273	–0.0274	0.0546	0.1493
	DFT PW91 (this work)	12.403	–0.0278	0.0564	0.1501
$Lu_3Al_5O_{12}$	Exp. (Ref. [47])	11.906	–0.0294	0.0537	0.1509
	DFT PW91 (this work)	11.936	–0.0291	0.0525	0.1498
$Lu_3Ga_5O_{12}$	Exp. (Ref. [47])	12.188	–0.0252	0.0570	0.1506
	DFT PW91 (this work)	12.263	–0.0254	0.0576	0.1513
$Ca_3Sc_2Si_3O_{12}$	Exp. (Ref. [50])	12.250	–0.0400	0.0501	0.1589
	DFT PW91 (this work)	12.363	–0.0400	0.0499	0.1585

Table 2 Energies of the lowest $4f-5d$ transition of Ce^{3+} in several garnets [$1\Gamma_5(4f^1) \rightarrow 8\Gamma_5(5d^1)$, in cm^{-1}] calculated at the RASSI-SO WFT level using different ground-state structures, which are indicated

Material	Exp. [Ref.]	Ground-state structure				
		A[a]	B[b]	C[c]	D[d]	E[e]
		Experimental undistorted host	WFT relaxed CeO_8[f]	DFT relaxed CeO_8[g]	DFT undistorted host	DFT relaxed CeO_8 and host[h]
$Y_3Al_5O_{12}:Ce^{3+}$	22,000 [3]	22,520	23,390 (+870)	23,640 (+1120)	23,310	24,960 (+1650)
$Y_3Ga_5O_{12}:Ce^{3+}$	23,800 [3]	24,450	25,290 (+840)	25,460 (+1010)	25,260	26,940 (+1680)
$Lu_3Al_5O_{12}:Ce^{3+}$	22,470 [51]	22,100	23,420 (+1320)	23,720 (+1620)	22,500	24,970 (+2470)
$Lu_3Ga_5O_{12}:Ce^{3+}$		24,110	25,410 (+1300)	25,700 (+1590)	24,460	26,880 (+2420)
$Ca_3Sc_2Si_3O_{12}:Ce^{3+}$	22,200 [5]	24,370	21,590 (–2780)	24,200 (–170)	25,010	25,690 (+680)

Maxima of the lowest $4f-5d$ experimental absorption bands are also given

[a] Undistorted garnet with experimental structure

[b] WFT ground-state relaxed structure of the CeO_8 moiety in an unrelaxed host with the experimental structure

[c] DFT ground-state relaxed structure of the CeO_8 moiety in an unrelaxed host with the experimental structure

[d] Undistorted garnet with DFT calculated structure

[e] DFT calculated structure after full relaxation of the CeO_8 moiety and the host structure

[f] WFT local relaxation effect is given in parentheses

[g] DFT local relaxation effect is given in parentheses

[h] DFT full relaxation effect is given in parentheses

are fixed at their positions in the experimental structure of the undoped garnet; (D) the PBC-DFT structure of the undoped garnet; and (E) the structure resulting from full atomic relaxation of the Ce^{3+}-doped garnet in PBC-DFT calculations. The change experienced by the $4f-5d$ transition from A to B is the local relaxation effect calculated at the RASSI-SO WFT level, and, from A to C, is the local relaxation effect calculated at the PBC-DFT PW91 level; both effects can be compared. The change from D to E is the full relaxation effect calculated at the PBC-DFT PW91 level. These changes are shown in parentheses in Table 2.

We aim at discussing the role of the structural relaxation effect on the $4f-5d$ lowest excitation and its comparison with the role of the undistorted host effect. We also aim at linking the relaxation effect with the details of the atomic relaxations; for this, we will use the structures obtained for the CeO_8 moieties, which are given in Tables 3 and 4. In Table 3, we show the D_2 structures of the CeO_8 moiety obtained at different relaxation levels. This structure has 6 degrees of freedom, and it is described here in terms of two perpendicular CeO_4 crosses that compose the CeO_8 moiety (Fig. 1): One of them is part of the $-A\text{-}B''O_4-A\text{-}B''O_4$ – tight chains of a $A_3B'_2B''_3O_{12}$ garnet (these chains exist along each cartesian direction of the cubic unit cell); [41] it is called the axial cross, and it is shown with red oxygens in Fig. 1, where the chain axis is shown in green. The other CeO_4 cross is perpendicular to the chain axis; it is called the equatorial cross, and it is shown with yellow oxygens in Fig. 1. Both crosses are defined in terms of the respective Ce–O distances, $d(Ce–O_a)$ and $d(Ce–O_e)$, bond angles α_a and α_e, and torsion or dihedral angles ϕ_a and ϕ_e. Deeper insight can be drawn from the structures as described in Table 4, in terms of a reference CeO_8 cube of arbitrary Ce–O distance, e.g., $d_{ref} = 2.34$ Å, and six D_2 distortions S_1–S_6 (or, equivalently, in terms of a non-arbitrary cube of Ce–O distance d_{cube} and five non-cubic D_2 distortions S_2–S_6) [11, 12]. In effect, it was shown in Ref. [11] that, although the six coordinates are important for the sets of seven $4f^1$ and five $5d^1$ levels, the lowest $4f-5d$ transition only changes significantly with S_1 and S_3 (or d_{cube} and S_3), which are the O_h breathing of the cube and its the D_{4h} tetragonal distortion (also described as symmetric bond stretching and symmetric bond bending of the two CeO_4 crosses) [11]. These two atomic displacement coordinates are shown in the top of Fig. 1. In the bottom of the figure, we show how the energy of the lowest $4f-5d$ transition depends on them, according to RASSI-SO calculations on the $(CeO_8)^{13-}$ cluster embedded in a cubic field: [11] Shortening the cubic Ce–O distance has the largest impact on the lowering the energy of the lowest $4f-5d$ transition; increasing the absolute value of the D_{4h} tetragonal distortion also lowers its energy. This transition energy is basically independent on the remaining atomic displacement coordinates coherent with a D_2 structure: S_2, S_4, S_5, and S_6 (of respective symmetries D_{2h}, D_{2h}, D_4, and D_{2d}, Ref. [11]).

In Table 2, we observe that the structural relaxation effect on the $4f-5d$ lowest excitation energy of Ce^{3+}-doped Al and Ga garnets is a blue shift (column E). This

Table 3 Local structure of the CeO_8 moiety in Ce^{3+}-doped garnets (AO_8 moiety in undoped garnets)

Structure [a]	d(Ce–O_a)	α_a	ϕ_a	d(Ce–O_e)	α_e	ϕ_e	$\langle d$(Ce−O)$\rangle$
$Y_3Al_5O_{12}:Ce^{3+}$							
A	2.303	71.7	35.8	2.432	73.7	23.7	2.368
B	2.375	71.7	40.2	2.451	71.9	20.7	2.413 (+0.045)[b]
C	2.390	72.0	35.9	2.474	73.6	21.1	2.432 (+0.064)[c]
D	2.329	71.9	37.1	2.467	73.7	22.7	2.398
E	2.420	71.3	36.6	2.525	74.4	21.6	2.473 (+0.075)[d]
$Y_3Ga_5O_{12}:Ce^{3+}$							
A	2.340	73.9	33.1	2.440	75.2	23.1	2.390
B	2.410	72.6	35.7	2.456	73.1	22.0	2.433 (+0.043)[b]
C	2.426	73.8	29.4	2.469	75.6	22.9	2.448 (+0.058)[c]
D	2.363	73.8	31.9	2.459	75.4	23.9	2.411
E	2.460	73.3	30.8	2.525	76.2	23.1	2.493 (+0.082)[d]
$Lu_3Al_5O_{12}:Ce^{3+}$							
A	2.276	72.3	33.1	2.383	74.3	24.8	2.330
B	2.375	72.0	38.7	2.428	72.3	20.7	2.402 (+0.072)[b]
C	2.389	72.5	33.6	2.451	74.7	21.9	2.420 (+0.090)[c]
D	2.283	72.6	34.5	2.402	74.5	23.6	2.343
E	2.419	71.5	34.3	2.492	75.4	22.2	2.456 (+0.113)[d]
$Lu_3Ga_5O_{12}:Ce^{3+}$							
A	2.303	74.7	30.3	2.393	76.4	24.4	2.348
B	2.412	73.0	34.5	2.438	73.6	22.0	2.425 (+0.077)[b]
C	2.424	74.3	27.0	2.459	77.2	23.7	2.442 (+0.094)[c]
D	2.318	74.5	29.3	2.399	76.2	25.2	2.359
E	2.453	73.6	27.8	2.511	78.0	23.8	2.482 (+0.123)[d]
$Ca_3Sc_2Si_3O_{12}:Ce^{3+}$							
A	2.389	64.4	32.4	2.532	69.7	33.4	2.461
B	2.374	61.8	28.2	2.451	66.4	43.5	2.413 (–0.048)[b]
C	2.402	64.9	31.2	2.494	69.7	33.3	2.448 (–0.013)[c]
D	2.412	64.6	32.8	2.556	69.6	33.0	2.484
E	2.448	63.5	33.9	2.542	70.1	32.5	2.495 (+0.011)[d]

Taking one of the three perpendicular −A-B″O_4−A-B″O_4– tight chains of a $A_3B'_2B''_3O_{12}$ garnet [41] as a reference, the moiety is made of an axial CeO_4 cross and an equatorial CeO_4 cross (cf. red atoms and yellow atoms in Fig. 1, respectively). d(Ce–O_a) is the Ce–O distance in the axial CeO_4 cross, α_a is the O_{a1}–Ce–O_{a2} angle, and ϕ_a is the dihedral angle between the two planes of the axial cross, O_{a1}–Ce–O_{a2} and O_{a3}–Ce–O_{a4}. d(Ce–O_e), α_e, and ϕ_e are the equivalent quantities of the equatorial cross. $\langle d$(Ce-O)$\rangle$ stands for the average Ce–O distance; its change upon cluster and full structure relaxations are given in parenthesis. Distances are given in Å and angles in degree

[a] The structure labels correspond to Table 2

[b] WFT local relaxation effect (difference between B and A) is given in parentheses

[c] DFT local relaxation effect (difference between C and A) is given in parentheses

[d] DFT full relaxation effect (difference between E and D) is given in parentheses

blue shift is already produced by the local relaxation of the CeO_8 moiety (columns B and C) and is enhanced by the relaxation of the rest of the host.

Let us discuss the local relaxations. Comparing B and C, we see that the local relaxation effects on the $4f-5d$ transition are similar in the WFT and DFT calculations, the DFT results leading to slightly higher energies. The local relaxation effect is basically the same in Al and Ga garnets with the same A cation. However, it clearly depends on this cation (its associated blue shift is roughly 500 cm^{-1} higher in Lu garnets than in their Y partners). The latter dependence seems to be responsible for the value of the experimental transition in $Lu_3Al_5O_{12}:Ce^{3+}$ being slightly higher than in $Y_3Al_5O_{12}:Ce^{3+}$: The undistorted host calculations give a lower value. The dependence with the A cation is explained with the structural data in Table 4. We only need to analyze the O_h and D_{4h} components of the D_2 structure, S_1 and S_3, if we keep in mind that the values of S_2, S_4, S_5,

Table 4 Local structure of the CeO_8 moiety in Ce^{3+}-doped garnets (AO_8 moiety in undoped garnets) expressed in terms of a Ce–O distance in a garnet-specific reference CeO_8 cube, d_{cube}, and its D_2 distortions, $S_2 - S_6$, as defined in Refs. [11, 12]

Structure [a]	d_{cube}	(S_1)	S_2	S_3	S_4	S_5	S_6
$Y_3Al_5O_{12}:Ce^{3+}$							
A	2.339	–0.0019	–0.2094	0.0156	–0.1018	1.0099	–0.1613
B	2.381 (+0.042)[b]	0.1166	–0.1572	–0.0493	–0.0794	1.0409	–0.3098
C	2.405 (+0.066)[c]	0.1830	–0.1537	0.0293	–0.0999	0.9954	–0.2279
D	2.368	0.0805	–0.2295	0.0213	–0.1064	1.0272	–0.2044
E	2.443 (+0.075)[d]	0.2924	–0.1821	0.0294	–0.1512	1.0315	–0.2221
$Y_3Ga_5O_{12}:Ce^{3+}$							
A	2.363	0.0647	–0.1629	0.1338	–0.0757	0.9876	–0.1440
B	2.405 (+0.042)[b]	0.1832	–0.0989	0.0277	–0.0638	1.0145	–0.2238
C	2.423 (+0.060)[c]	0.2361	–0.0736	0.1628	–0.0784	0.9474	–0.0965
D	2.385	0.1264	–0.1520	0.1421	–0.0751	0.9926	–0.1106
E	2.467 (+0.082)[d]	0.3578	–0.1059	0.1615	–0.1176	0.9935	–0.1097
$Lu_3Al_5O_{12}:Ce^{3+}$							
A	2.303	–0.1042	–0.1683	0.0555	–0.0866	0.9766	–0.1044
B	2.372 (+0.069)[b]	0.0894	–0.1202	–0.0190	–0.0741	1.0179	–0.2904
C	2.394 (+0.091)[c]	0.1526	–0.1136	0.0844	–0.1063	0.9756	–0.1782
D	2.315	–0.0696	–0.1911	0.0718	–0.0932	0.9876	–0.1457
E	2.428 (+0.113)[d]	0.2488	–0.1279	0.0734	–0.1597	1.0038	–0.1756
$Lu_3Ga_5O_{12}:Ce^{3+}$							
A	2.322	–0.0520	–0.1378	0.1961	–0.0727	0.9580	–0.0755
B	2.398 (+0.076)[b]	0.1632	–0.0668	0.0579	–0.0626	0.9946	–0.2087
C	2.418 (+0.096)[c]	0.2203	–0.0514	0.2309	–0.0996	0.9294	–0.0389
D	2.333	–0.0194	–0.1209	0.1879	–0.0677	0.9577	–0.0454
E	2.457 (+0.124)[d]	0.3300	–0.0823	0.2354	–0.1508	0.9598	–0.0391
$Ca_3Sc_2Si_3O_{12}:Ce^{3+}$							
A	2.426	0.2445	–0.1978	–0.3354	–0.1407	1.0895	0.0850
B	2.370 (–0.056)[b]	0.0857	–0.0685	–0.5333	–0.0623	1.1235	0.2844
C	2.415 (–0.011)[c]	0.2129	–0.1240	–0.3151	–0.1266	1.0663	0.0873
D	2.450	0.3110	–0.2016	–0.3358	–0.1405	1.0997	0.0714
E	2.460 (+0.010)[d]	0.3386	–0.1378	–0.3592	–0.1970	1.1087	0.0471

The values of the O_h breathing distortion from a common reference cube with $d_{ref} = 2.34$ Å, S_1, are also given; note that two valid alternatives to define the oxygen structure of a CeO_8 moiety with D_2 symmetry are as follows: (d_{cube}, $S_1 = 0$, S_2, S_3, S_4, S_5, S_6) and ($d_{cube} = d_{ref}$, S_1, S_2, S_3, S_4, S_5, S_6); note also that $S_1 = \sqrt{8}(d_{cube} - d_{ref})$. S_1 and S_3 are illustrated in Fig. 1. Changes of d_{cube} upon cluster and full structure relaxations are given in parenthesis. All quantities are given in Å

[a] The structure labels correspond to Table 2

[b] WFT local relaxation effect (difference between B and A) is given in parentheses

[c] DFT local relaxation effect (difference between C and A) is given in parentheses

[d] DFT full relaxation effect (difference between E and D) is given in parentheses

and S_6 are irrelevant for the lowest $4f-5d$ transition [11]. We can observe that the changes in the tetragonal component are small, so that the most important contribution comes from the breathing mode S_1. So, the larger blue shifts of the DFT vs. WFT are just due to their larger values of S_1 or, in other words, to their larger Ce–O distance in their respective reference cubes, d_{cube}. Also, the larger blue shift in Lu garnets vs. Y garnets is just due to their larger d_{cube}. Although d_{cube} is different than the average Ce–O distance in the garnet, $\langle d(\text{Ce–O})\rangle$, we can observe in Table 3 that both of them experience similar changes from garnet to garnet. The positive increments in d_{cube} and $\langle d(\text{Ce–O})\rangle$ are measures of the expansion of the O_8 shell when the Ce_A substitutional defect is created, and they qualitatively follow the ionic radii mismatch (although they are smaller): +0.17 Å in Ce_{Lu} and +0.12 Å in Ce_Y, using Shannon's

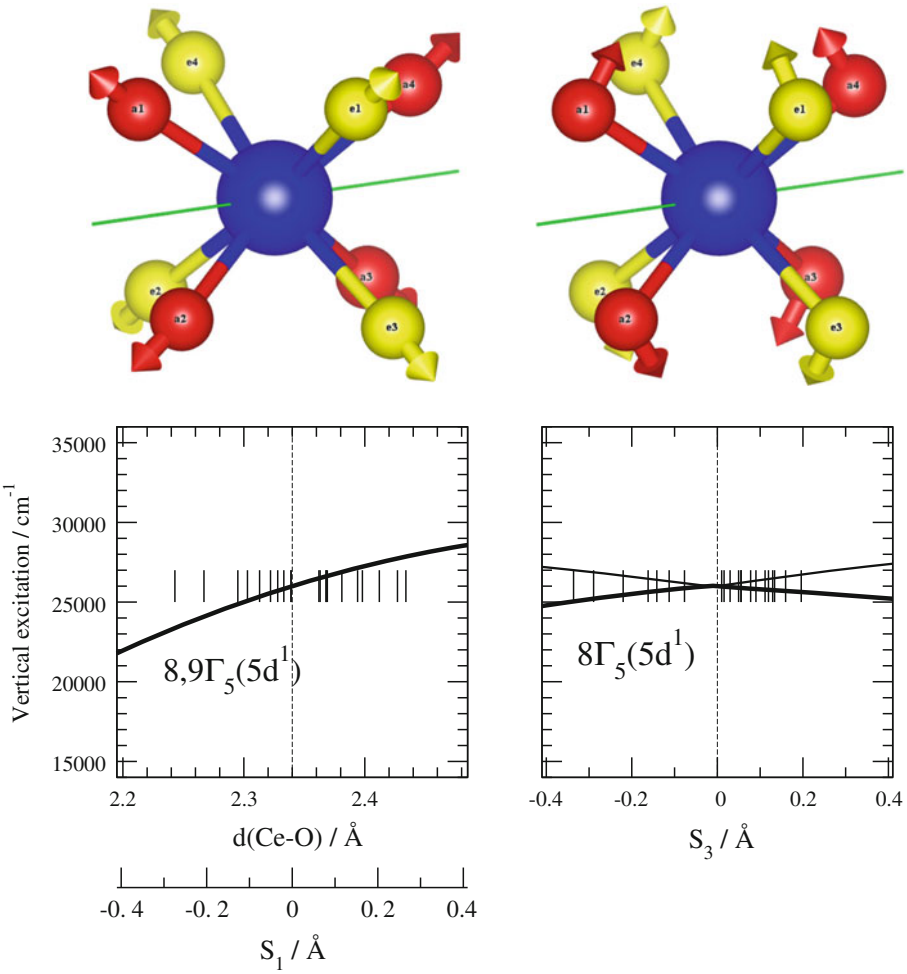

Fig. 1 *Top* Cubic O_h breathing (S_1, symmetric bond stretching; *left*) and tetragonal D_{4h} (S_3, symmetric bond bending; *right*) atomic displacements which keep the D_2 symmetry of the CeO_8 moiety. The red atoms are the oxygens of the axial CeO_4 cross: along the C_2 symmetry axis that relates O_{a1} with O_{a2} and O_{a3} with O_{a4} (shown in *green*) lies a tight –A-B″O_4–A-B″O_4– chain of the $A_3B'_2B''_3O_{12}$ garnet [41]. The yellow atoms are the oxygens of the equatorial CeO_4 cross. *Bottom* Dependence of the energy of the lowest $4f-5d$ transition, $1\Gamma_5(4f^1) \rightarrow 8\Gamma_5(5d^1)$, on the S_1 and S_3 atomic displacements (Ref. [11], RASSI-SO calculations on the $(CeO_8)^{13-}$ cluster embedded in a cubic field)

eightfold coordination ionic radii [42] 1.143 Å (Ce^{3+}), 1.019 Å (Y^{3+}), 0.977 Å (Lu^{3+}).

We may recall that EXAFS experiments on Ce^{3+}-doped garnets are able to provide two Ce–O distances [43], but not the six independent structural parameters of the CeO_8 moiety. This leads us to remark that the facts that the cubic component of the actual D_2 field alone is sufficient to explain the shift of the $4f-5d$ transition due to structural relaxations and that d_{cube} (directly associated with such cubic field) experiences similar changes than the average Ce–O distance $\langle d(\text{Ce–O})\rangle$ suggest that EXAFS data on Ce^{3+}-doped garnets should correlate well with their lowest $4f-5d$ transition.

In $Ca_3Sc_2Si_3O_{12}$:Ce^{3+}, the CeO_8 relaxation induces a red shift of the $4f-5d$ transition, in opposition to the other garnets. Such shift is dominated by the contraction of the O shell, which does not follow the +0.02 Å ionic radii mismatch (Ca^{2+} has a 1.12 Å ionic radius in eightfold coordination) [42] but is caused by the additional attraction of the oxygens for the positive charge created by the substitution of Ca^{2+} by Ce^{3+}. The WFT calculation leads to a larger contraction than the DFT calculation, and consequently to a larger red shift. In this case, the WFT calculation also gives a larger increment of the absolute value of S_3 than in other cases, which enhances the red shift.

The atomic relaxation beyond the O_8 shell also has an impact on the $4f-5d$ excitation: It results from a direct effect and from an indirect effect via the additional relaxation of the O_8 shell it brings. The overall effect can be estimated in DFT calculations as the difference between the DFT full relaxation effect (column E in parentheses) and the DFT local relaxation effect (column C in parenthesis). It means an additional blue shift that amounts 500–800 cm^{-1} and does not have important implications making differences between different garnets. This blue shift enhances the one due to the local relaxations in Al and Ga garnets and overtakes the local relaxation red shift of $Ca_3Sc_2Si_3O_{12}$:Ce^{3+}. The $4f-5d$ blue shift induced by the full relaxation around the Ce_A defect is opposite to the important red shift brought about by the undistorted host effect [12]; however, it does not play an important role at differentiating between garnet families, which seems to be controlled by the undistorted host embedding effects [12]. On the other hand, the relaxation-induced blue shifts move the $4f-5d$ transitions away from experiments in overall; the higher overall agreement of the undistorted host calculations

Table 5 Local structure of the CeO_8 moiety in Ce^{3+}-doped garnets in the lowest state of its $5d^1$ configuration ($8\Gamma_5(5d^1)$ or $5d_1$), as calculated at the WFT (RASSI-SO) relaxed CeO_8 level

	d(Ce–O_a))	α_a	ϕ_a	d(Ce−O_e)	α_e	ϕ_e	$\langle d$(Ce−O)$\rangle$
$Y_3Al_5O_{12}$:Ce^{3+}	2.358	71.3	40.8	2.435	71.0	21.0	2.397 (–0.017)
$Y_3Ga_5O_{12}$:Ce^{3+}	2.396	72.4	36.1	2.439	72.2	22.2	2.418 (–0.016)
$Lu_3Al_5O_{12}$:Ce^{3+}	2.360	71.8	39.1	2.412	71.5	20.9	2.386 (–0.016)
$Lu_3Ga_5O_{12}$:Ce^{3+}	2.399	72.8	34.7	2.420	72.7	22.1	2.410 (–0.016)
$Ca_3Sc_2Si_3O_{12}$:Ce^{3+}	2.350	61.5	29.1	2.432	65.5	44.6	2.391 (–0.022)
	d_{cube}	(S_1)	S_2	S_3	S_4	S_5	S_6
$Y_3Al_5O_{12}$:Ce^{3+}	2.365 (–0.016)	0.0702	–0.1593	–0.0880	–0.0642	1.0413	–0.3138
$Y_3Ga_5O_{12}$:Ce^{3+}	2.389 (–0.016)	0.1394	–0.0967	–0.0071	0.0439	1.0111	–0.2283
$Lu_3Al_5O_{12}$:Ce^{3+}	2.356 (–0.016)	0.0454	–0.1202	–0.0542	–0.0567	1.0155	–0.2927
$Lu_3Ga_5O_{12}$:Ce^{3+}	2.383 (–0.015)	0.1214	–0.0614	0.0258	–0.0404	0.9889	–0.2120
$Ca_3Sc_2Si_3O_{12}$:Ce^{3+}	2.347 (–0.023)	0.0185	–0.0732	–0.5685	–0.0415	1.1335	0.2798

See captions of Tables 3 and 4 for the meaning of the structural parameters. Distances and atomic displacements $S_1 - S_6$ are given in Å; angles are given in degree. Changes on the cubic Ce–O distances, d_{cube}, and average Ce–O distances, $\langle d$(Ce–O)$\rangle$, with respect to the corresponding ground-state data are given in parentheses

is the result of a compensation of errors. The fine differences between Ce^{3+}-doped garnets are better reproduced when the structural relaxations are taken into account.

We have also included here (Table 5) the results of the RASSI-SO WFT structural optimizations of the CeO_8 moieties in the lowest state of its $5d^1$ configuration, $8\Gamma_5(5d^1)$. These results do not provide information on the role of the relaxation effects compared with the undistorted host effects; they only do on the different relaxation effects in the $4f^1$ ground state and the first $5d^1$ excited state. Comparison of the results with the corresponding B entries in Tables 2 and 3 show small changes with respect to the ground state in the angles and in the non-cubic O_8 atomic displacements. The changes in the Ce–O distances, which are shown in parentheses in Table 5, are all negative. These bond contractions associated with the lowest $f \rightarrow d$ excitation are known and expected in lanthanide and actinide compounds and materials: They have been reported for the first time in Pa^{4+}-doped Cs_2ZrCl_6 (Ref. [44]); they have been explained as due to the superposition of three factors (the small relevance of the change in orbital size during the excitation, the ligand field stabilization of the most stable $5d$ orbital, and the larger charge transfer from the ligands to the $4f$ shell in the excited state); [45] and they have been found in all the *ab initio* calculations performed up to date in such materials with the methods used in this paper [46].

4 Conclusions

We have discussed the role of structural relaxations on the lowest $4f-5d$ excitation of Ce^{3+}-doped garnets, based on *ab initio* RASSI-SO WFT calculations of the transition energy performed on the $(CeO_8)^{13-}$ cluster under the effects of quantum mechanical embedding potentials of $Y_3Al_5O_{12}$, $Lu_3Al_5O_{12}$, $Y_3Ga_5O_{12}$, $Lu_3Ga_5O_{12}$, and $Ca_3Sc_2Si_3O_{12}$. We used locally relaxed structures calculated at the WFT and DFT levels and globally relaxed DFT structures.

Local relaxation effects on the $4f-5d$ transition are similar in the WFT and DFT calculations. They contribute with a blue shift in Ce^{3+}-doped Al and Ga garnets in which Ce substitutes for smaller Y and Lu cations. The angular relaxations do not play a significant role in this blue shift, which is basically due to the local expansion around Ce. The full relaxation of more distant neighbors, which is calculated at the DFT level, enhances the blue shift.

Whereas the embedding effects of the undistorted hosts make the lowest $4f-5d$ transition different in different garnet families, the relaxation effects are responsible for the small differences of the transition in closely related garnets where Ce^{3+} substitutes for different cations, like $Y_3Al_5O_{12}$:Ce^{3+} and $Lu_3Al_5O_{12}$:Ce^{3+}.

Acknowledgments This work was partly supported by a grant from Ministerio de Economía y Competitivad, Spain (Dirección General de Investigación y Gestión del Plan Nacional de I+D+I, MAT2011-24586). QMP thanks the Erasmus Mundus Master in Theoretical Chemistry and Computational Modelling (TCCM) and the Flemish Science Foundation (FWO) for financial support.

References

1. Nakamura S, Fasol G (1997) The blue laser diode: GaN based light emitters and lasers. Springer, Berlin

2. Jüstel T, Nikol H, Ronda C (1998) Angew Chem Int Ed 37:3084
3. Blasse G, Bril A (1967) J Chem Phys 47:5139
4. Setlur AA, Heward WJ, Gao Y, Srivastava AM, Chandran RG, Shankar MV (2006) Chem Mater 18:3314
5. Shimomura Y, Honma T, Shigeiwa M, Akai T, Okamoto K, Kijima N (2007) J Electrochem Soc 154:J35
6. Weber MJ (2002) J Lumin 100:35
7. Holloway WW, Kestigian M (1969) J Opt Soc Am 59:60
8. Pan YX, Wang W, Liu GK, Skanthakumar S, Rosenberg RA, Guo XZ, Li KK (2009) J Alloys Compd 488:638
9. Muñoz-García AB, Seijo L (2010) Phys Rev B 82:184118
10. Muñoz-García AB, Pascual JL, Barandiarán Z, Seijo L (2010) Phys Rev B 82:064114
11. Seijo L, Barandiarán Z (2013a) Opt Mater 35:1932
12. Seijo L, Barandiarán Z (2013b) Phys Chem Chem Phys 15:19221
13. Karlström G, Lindh R, Malmqvist PA, Roos BO, Ryde U, Veryazov V, Widmark PO, Cossi M, Schimmelpfennig B, Neogrady P et al (2003) Comput Mater Sci 28:222
14. Douglas M, Kroll NM (1974) Ann Phys (NY) 82:89
15. Hess BA (1986) Phys Rev A 33:3742
16. Roos BO, Taylor PR, Siegbahn PEM (1980) Chem Phys 48:157
17. Siegbahn PEM, Heiberg A, Roos BO, Levy B (1980) Phys Scr 21:323
18. Siegbahn PEM, Heiberg A, Almlöf J, Roos BO (1981) J Chem Phys 74:2384
19. Andersson K, Malmqvist P-A, Roos BO, Sadlej AJ, Wolinski K (1990) J Phys Chem 94:5483
20. Andersson K, Malmqvist P-A, Roos BO (1992) J Chem Phys 96:1218
21. Zaitsevskii A, Malrieu J-P (1995) Chem Phys Lett 233:597
22. Finley J, Malmqvist P-A, Roos BO, Serrano-Andrés L (1998) Chem Phys Lett 288:299
23. Hess BA, Marian CM, Wahlgren U, Gropen O (1996) Chem Phys Lett 251:365
24. Malmqvist PA, Roos BO, Schimmelpfennig B (2002) Chem Phys Lett 357:230
25. Roos BO, Lindh R, Malmqvist PA, Veryazov V, Widmark PO (2008) J Chem Phys 112:11431
26. Roos BO, Lindh R, Malmqvist PA, Veryazov V, Widmark PO (2005) J Phys Chem A 108:2851
27. Barandiarán Z, Seijo L (1988) J Chem Phys 89:5739
28. Gracia J, Seijo L, Barandiarán Z, Curulla D, Niemansverdriet H, van Gennip W (2008) J Lumin 128:1248
29. Seijo L, Barandiarán Z (1991) J Chem Phys 94:8158
30. Gellé A, Lepetit M-B (2008) J Chem Phys 128:244716
31. Ewald PP (1921) Ann Phys 369:253
32. Blöchl PE (1994) Phys Rev B 50:17953
33. Kresse G, Joubert D (1999) Phys Rev B 59:1758
34. Kresse G, Hafner J (1993) Phys Rev B 47:558
35. Kresse G, Hafner J (1994) Phys Rev B 49:14251
36. Kresse G, Furthmüller J (1996a) Comput Mater Sci 6:15
37. Kresse G, Furthmüller J (1996b) Phys Rev B 54:11169
38. Perdew JP, Chevary JA, Vosko SH, Jackson KA, Pederson MR, Singh DJ, Fiolhais C (1992) Phys Rev B 46:6671
39. Dudarev SL, Botton GA, Savrasov SY, Humphreys CJ, Sutton AP (1998) Phys Rev B 57:1505
40. Ning L, Yang F, Duan C, Zhang Y, Liang J, Cui Z (2012) J Phys Condens Matter 24:05502
41. Muñoz-García AB, Seijo L (2011) J Phys Chem A 115:815
42. Shannon RD (1976) Acta Crystallogr A 32:751
43. Ghigna P, Pin S, Ronda C, Speghini A, Piccinelli F, Bettinelli M (2011) Opt Mater 34:19
44. Seijo L, Barandiarán Z (2001) J Chem Phys 115:5554
45. Barandiarán Z, Seijo L (2003) J Chem Phys 119:3785
46. Barandiarán Z, Seijo L (2015) In: Dolg N (ed) Computational methods in lanthanide and actinide chemistry. Wiley, New York
47. Euler F, Bruce JA (1965) Acta Crystallogr 19:971
48. Muñoz-García AB, Anglada E, Seijo L (2009) Int J Quantum Chem 109:1991
49. Nakatsuka A, Yoshiasa A, Takeno S (1995) Acta Crystallogr B 51:737
50. Quartieri S, Oberti R, Boiocchi M, Dalconi MC, Boscherini F, Safonova O, Woodland AB (2006) Am Mineral 91:1240
51. Ogieglo JM, Zych A, Ivanovskikh KV, Jüstel T, Ronda CR, Meijerink A (2012) J Phys Chem A 116:8464

Theor Chem Acc (2014) 133:1578
DOI 10.1007/s00214-014-1578-2

REGULAR ARTICLE

A local topological view of pressure-induced polymorphs in SiO_2

A. Morales-García · M. Marqués · J. M. Menéndez · R. Franco · V. G. Baonza · J. M. Recio

Received: 24 July 2014 / Accepted: 4 September 2014 / Published online: 24 October 2014

Abstract By means of the quantum theory of atoms in molecules (QTAIM), we carry out a microscopic analysis of the response to hydrostatic pressure (p) of α-quartz, coesite, stishovite, $CaCl_2$-type, and α-PbO_2-type polymorphs of silica (SiO_2). According to QTAIM atomic charges, there is not a substantial change in the ionic character of the bonding network (often described as polar covalent) along the pressure-induced polymorphic sequence. Atomic volumes (V_i) reveal that Si atoms remain with similar values regardless the polymorph, whereas oxygen follows the same volume collapses as the unit cells upon phase transformations. The inert character of Si is also displayed when local pressures ($p_i = -\frac{dE}{dV_i}$, E is the energy per formula unit) are computed. We obtain linear trends ($p_{Si} = 9.40\,p$ and $p_O = 2.22\,p$) with a greater slope in the case of Si, illustrating its greater resistance to reduce its volume as pressure is applied. QTAIM also allows the evaluation of the atomic contributions to the bulk compressibility. Interestingly enough, we found a change in the atom showing the lowest compressibility, which is silicon in low-pressure phases but oxygen for stishovite and post-stishovite polymorphs.

Keywords DFT calculations · High pressure · QTAIM · Silica

Published as part of the special collection of articles derived from the 9th Congress on Electronic Structure: Principles and Applications (ESPA 2014).

A. Morales-García (✉) · V. G. Baonza
MALTA-Consolider Team and Departamento de Química Física I, Universidad Complutense de Madrid, 28040 Madrid, Spain
e-mail: amoralesg@quim.ucm.es

V. G. Baonza
e-mail: vgbaonza@quim.ucm.es

M. Marqués
MALTA-Consolider Team and Departamento de Física Teórica y Óptica, Universidad de Valladolid, Valladolid, Spain
e-mail: miriam.marques@uva.es

J. M. Menéndez · R. Franco · J. M. Recio (✉)
MALTA-Consolider Team and Departamento de Química Física y Analítica, Universidad de Oviedo, 33006 Oviedo, Spain
e-mail: jmrecio@uniovi.es

R. Franco
e-mail: ruth@uniovi.es

1 Introduction

Silica arouses a great attraction in diverse fields such as Geophysics and Materials Science. Despite its simple chemical composition, SiO_2, silica shows a rich polymorphism induced by pressure and temperature. The polymorphic sequence, α-quartz → coesite → stishovite → $CaCl_2$-type → α-PbO_2-type, has been the subject of many experimental and theoretical studies (see for example [1, 2] and references therein). Transition phase properties and equation of state parameters have been reported, but little is known concerning the microscopic contribution to phase stability of the two, oxygen and silicon, sublattices.

Since its origin [3, 4], the quantum theory of atoms in molecules (QTAIM) has evolved into a valuable tool for the chemical interpretation of results from quantum chemical computations. As regards high-pressure silica polymorphs, a number of QTAIM studies have addressed the characterization of the Si-O bond providing general correlations between bond lengths and the electron densities at the bond critical points (see the work of Gibbs et al. [5] and references therein). Prencipe and Nestola [6] also stressed the role played by O-O interactions in the cohesion of these structures. Recently, Merli and Sciascia [7] performed

topological analysis of the electron density concerning pressure-induced phase transformations/amorphization of silica in the framework of the catastrophe theory. They concluded that this analysis is a powerful method for the investigation and the prediction of phase changes induced by pressure or temperature.

In our particular application of QTAIM, we emphasize that this tool also provides a particular division of real space into atomic basins where volumes, electron populations, and other quantum mechanical observables can be obtained using the appropriate operator density. In this way, atomic contributions add up leading to values of macroscopic properties. Thus, this partition allows the splitting of the unit cell volume, the thermodynamic pressure, and the bulk compressibility of all the pressure-induced polymorphs of silica into local contributions associated with Si and O. It is our main goal here to use this decomposition in order to shed light into the role played by both sublattices in the response and stabilization of the different phases as hydrostatic pressure is applied.

Three more sections complete this manuscript. Next, we briefly describe the computational details used in our electronic structure calculations, with a short review of main AIM concepts used in our study. We continue with the results section, where we discuss bulk and local properties of silica along the pressure-induced polymorphic sequence. Finally, a summary of the main conclusions will be presented.

2 Computational aspects

2.1 Total energy and equation of state

First-principles electronic structure calculations for the α-quartz ($P3_221$, [8]), coesite ($C2/c$, [9]), stishovite ($P4_2/mnm$, [10]), $CaCl_2$-type ($Pnnm$, [11]), and α-PbO_2 -type ($Pbcn$, [11]) polymorphs (space groups in brackets with references to detailed descriptions of the corresponding unit cells) were performed under the generalized gradient approximation (GGA) of the density functional theory (DFT), as implemented in the Vienna *ab initio* simulation package (VASP) [12]. The projector-augmented wave (PAW) all electron description of the electron–ion–core interactions [13, 14] and the exchange and correlation functional proposed by Perdew–Burke–Ernzerhof (PBE) [15] were used. The energies were converged with respect to the k-points density [16] ($8 \times 8 \times 6$, $4 \times 2 \times 4$, $6 \times 6 \times 8$, $6 \times 6 \times 8$, and $6 \times 6 \times 6$ for α-quartz, coesite, stishovite, $CaCl_2$-type, and α-PbO_2, respectively) and the plane-wave cutoff (600 eV), to ensure convergence of the total energy within 10^{-3} eV. Full relaxations of geometrical parameters were carried out in all polymorphs.

Numerical and analytical (Vinet) [17] equations of state were used to describe the calculated energy–volume (E,V) points of each structure, all the values refer to one formula unit. From these fittings, we are able to provide pressure–volume (p–V) data, equation of state (EOS) parameters (bulk modulus, B_0, and its pressure derivative, B_0', both evaluated at zero pressure), and enthalphy ($H - p$) curves. H is the appropriate thermodynamic potential to determinate phase stability at static conditions (zero temperature and zero-point vibrational contributions neglected). These calculations have been performed with the GIBBS2 code [18, 19]. Within the framework of the quasiharmonic approximation, we have included the effect of thermal effects on the calculated static transition pressures using a Debye model that only requires the knowledge of the static energy obtained from the above VASP calculations.

2.2 Atoms in molecules formalism. Local properties

To investigate the bonding and topological properties, the electron density obtained from VASP calculations was taken as input to the CRITIC2 code [20, 21]. We have to consider that in a calculation with pseudopotentials, the valence density is not optimal. To avoid this problem, we carry out single-point calculations on the relaxed structures of SiO_2 to compute total atomic charges using the LAECHG keyword in VASP. Thus, we are sure that the electron density is the appropriate for each case. Applying QTAIM formalism, unit cell volumes are partitioned into atomic basins surrounded by surfaces where the flux of the gradient of the electron density is zero. To perform the integration of the basins, we apply the method of Yu and Trinkle [22]. The algorithm, which is implemented in CRITIC2 code, is based on the assignment of integration weights to each point in the numerical grid by evaluating the flow of the gradient using the neighboring points. This algorithm is extremely efficient and robust and is strongly recommended in the case of fields on a grid.

Our analysis of bulk properties in terms of local contributions is thus based on the accurate partition of the cell volume into basin or atomic-like volumes: $V = \sum_i V_i$. Two different local properties will be discussed: local pressures and local compressibilities. The first one involves the first derivative of the energy with respect to the atomic volume in a formally equivalent way as in the definition of the total macroscopic thermodynamic pressure (p). An expression relating local and thermodynamic pressure can be thus easily derived [23]:

$$p_i = -\frac{\mathrm{d}E}{\mathrm{d}V_i}, \quad \frac{1}{p} = \frac{1}{p_{\mathrm{Si}}} + \frac{2}{p_{\mathrm{O}}}. \tag{1}$$

The compressibility and bulk modulus of the crystal are defined as:

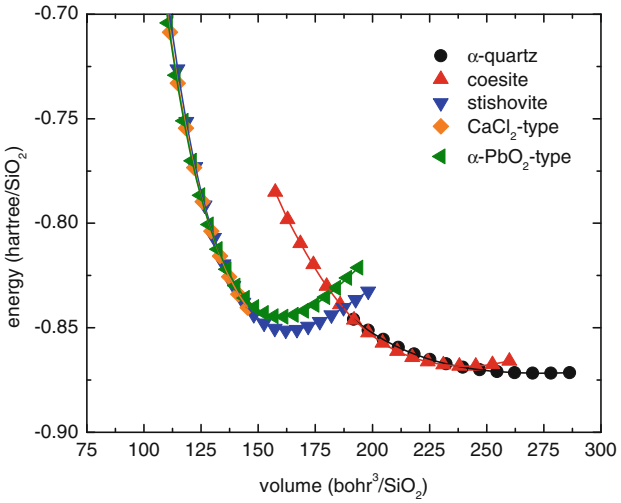

Fig. 1 Calculated energy–volume curves per formula unit for SiO_2 polymorphs

Table 1 Calculated (first row, this work) and experimental (second row, [27] for α-quartz, coesite, and stishovite; [26] for $CaCl_2$-type and α-PbO_2-type) unit cell parameters

Phase	α-quartz	coesite	stishovite	$CaCl_2$	α-PbO_2
a (Å)	5.017	7.223	4.225	3.848	3.751
	4.916	7.136	4.179	3.982	3.716
b (Å)		12.494		4.015	4.697
		12.384		3.802	4.751
c (Å)	5.508	7.239	2.691	2.557	4.198
	5.405	7.186	2.666	2.525	4.118
β (°)		120.23			
		120.38			
c/a	1.098	1.002	0.637	0.665	1.120
	1.100	1.007	0.638	0.634	1.108
V (Å^3)	40.02	35.27	24.01	19.76	18.49
	37.71	34.23	23.30	19.14	18.16

$$\kappa = \frac{1}{B} = -\frac{1}{V}\left(\frac{\partial V}{\partial P}\right), \tag{2}$$

with an also equivalent definition for the local compressibility:

$$\kappa_i = \frac{1}{B_i} = -\frac{1}{V_i}\left(\frac{\partial V_i}{\partial P}\right). \tag{3}$$

The relationship between bulk and local compressibilities can be derived from the second derivative of the energy with respect to the atomic volumes. The bulk magnitude, by these equations, results from averaging the local compressibilities in such a way that the contribution from a basin is proportional to the volume fraction occupied by the basin in the crystal [24]:

$$\kappa = \sum_i f_i \kappa_i, \quad \frac{1}{B} = \sum_i f_i \frac{1}{B_i}, \tag{4}$$

where $f_i = V_i/V$ is the fraction of the cell volume occupied by the ith basin.

3 Results and discussion

3.1 Structure, stability, and equation of state

Figure 1 shows calculated total energies as a function of volume per formula unit for α-quartz, coesite, stishovite, $CaCl_2$-type, and α-PbO_2-type polymorphs. Two volume regimes can be distinguished: (i) high volumes (around 225−300 bohr^3) for phases with tetrahedral environments surrounding Si atom and (ii) low volumes (around 130−170 bohr^3), where the structures are characterized by octahedral and higher oxygen coordination environments for Si. Equilibrium lattice parameters for the minimum energy structures are collected in Table 1. We observe the expected slight overestimation of our PBE-calculated values when compared with the experimental data, with differences of the order of few units (2–3 %) on the average. For post-stishovite structures ($CaCl_2$-type and α-PbO_2-type), we compare with available experimental lattice parameters at high pressure (85 and 120 GPa, respectively). Murakami et al. [25] demonstrated that the $CaCl_2$-type silica is a stable post-stishovite phase at high temperature which experienced a phase transition to the α-PbO_2-type structure above 121 GPa at 2,400 K. This fact is consistent with previous studies [11, 26] and our calculations (see below).

In Table 2, the calculated EOS parameters along with data from other works are collected. The most compressible structures are those in which the SiO_4 unit is present, while the lowest compressible ones correspond to stishovite and post-stishovite structures. According to the calculated results in stishovite and $CaCl_2$-type, their EOS fittings are very similar due to the fact that full structural optimization in $CaCl_2$-type structure up to around 30 GPa leads to a strained unit cell that is finally relaxed back to the tetragonal (rutile) phase. The same results were also observed in a previous study [28], and it is related to the second-order phase transition character claimed for the transformation involving these polymorphs (see below).

From these static energy calculations, we can determine the transition pressures between polymorphs. At 0 K, enthalpy (H) is the thermodynamic potential appropriate to calculate the stability under pressure:

$$H = E + pV \quad \text{and} \quad p = -\left(\frac{\partial E}{\partial V}\right)_T \tag{5}$$

Table 2 Calculated (first row) equation of state parameters for SiO_2 polymorphs

Phase	E_0	V_0	B_0	B'_0
α-Quartz	0	40.55	30.0	5.1
Exp [27]	–	37.71	34-37	5.99
Coesite	0.0943	35.55	90.4	5.3
Exp [27]	–	33.43	94	6.1
Stishovite	0.5584	24.15	258.4	6.1
Exp [27]	–	23.3	313.00	2.8–6
$CaCl_2$-type	0.5577	24.16	262.8	6.1
LDA [29]	–	23.58	258.4	4.61
α-PbO_2-type	0.7328	23.68	290.9	4.4
LDA [29]	–	22.78	324.4	4.23

E_0, V_0, B_0, and B'_0 are the zero-pressure energy (hartree) with respect to the α-quartz phase, volume ($Å^3$), bulk modulus (GPa), and its pressure derivative

Experimental (Ref. [27] for α-quartz, coesite, and stishovite) and LDA calculated (Ref. [29] for $CaCl_2$-type and α-PbO_2-type) data are included for comparison

Attending to the lowest enthalpy at a given pressure, α-quartz is the stable phase from 0 to 4.4 GPa, where coesite starts to be stable. Coesite structure undergoes a phase transition to stishovite at 7.0 GPa (see Fig. 2, left), a value similar to the one reported in previous studies [27]. Stishovite is the polymorph with the highest range of stability, and this phase is stable between 7.0 and 55.0 GPa, where it undergoes a phase transition to an orthorhombic structure ($CaCl_2$-type). Following, a transition from this structure ($CaCl_2$-type) to the α-PbO_2-type one is predicted at 97.0 GPa (see Fig. 2, right). Overall, the calculated transition pressures are also in good agreement with previous calculated and available experimental data [25, 27, 30].

We found negligible changes in volume and atomic displacements from the stishovite to the $CaCl_2$-type structure at the transition pressure, suggesting a second-order phase transition character (no discontinuity in volume occurs at the transition). The enthalpy of the orthorhombic phase relative to that of the tetragonal phase is zero at 55 GPa and then becomes increasingly negative at higher pressures, favoring the $CaCl_2$-type structure for silica (see Fig. 2, right).

Murakami et al. [25] concluded in their study that the transition pressure from $CaCl_2$-type to α-PbO_2-type is represented by a linear equation: $p(\text{GPa}) = 98 + (0.0095 \pm 0.0016) \times T(\text{K})$. Considering that our calculation is carried out at static conditions ($T = 0$ K), the extrapolated athermal value for this transition pressure would be 98 GPa. Our study estimates 97 GPa, giving a good agreement between theory and experiment.

We further estimate the effect of temperature in these transitions by means of a quasiharmonic Debye model, which is a reasonable one in terms of accuracy and computational cost [19]. The knowledge of the static energy is enough to build the vibrational Helmholtz free energy at any temperature in this model. At 300 K, we observe this sequence: α-quartz $\rightarrow$ stishovite $\rightarrow$ $CaCl_2$-type $\rightarrow$ α-PbO_2-type at pressures 9.62, 56.35, and 114.59 GPa, respectively. The inclusion of thermal effects entails the vanishing of α-quartz $\rightarrow$ coesite transformation, comparing with the static results.

3.2 Chemical bonding. Local properties

Our topological analysis of the computed core-valence electron density (see above) is firstly used to calculate total charges of Si and O in SiO_2 polymorphs. We confirm that all polymorphs behave as ionic compounds, as it

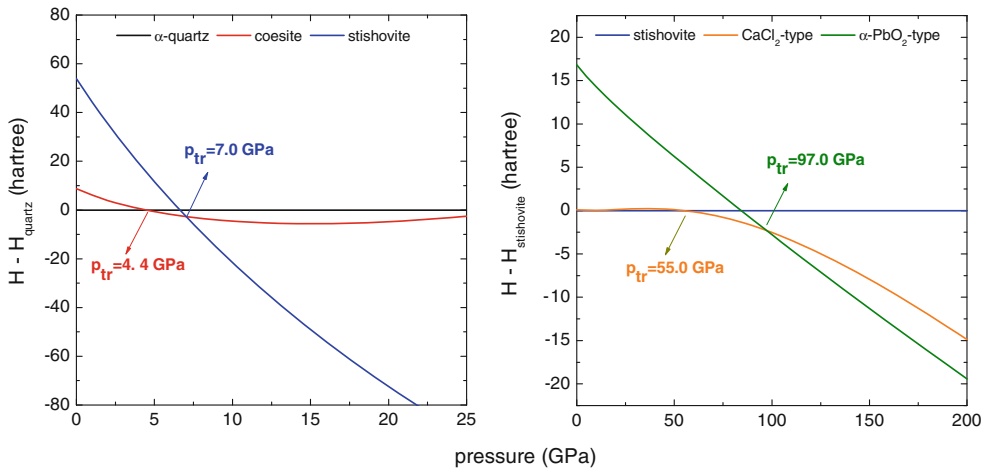

Fig. 2 Calculated enthalpy–pressure curves for SiO_2 polymorphs

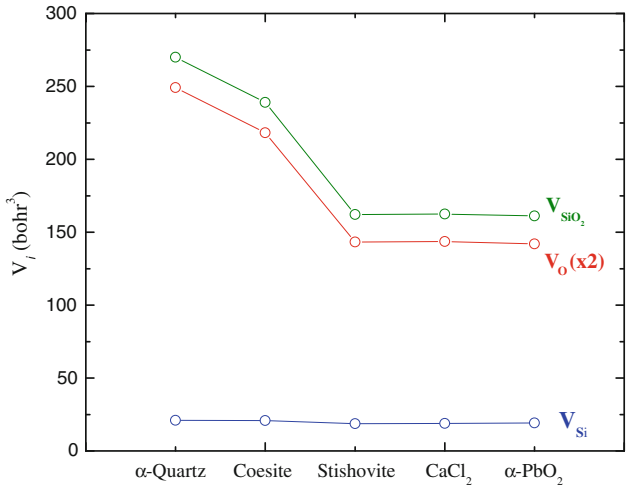

Fig. 3 Atomic and crystal volumes per formula unit along the polymorphic sequence

Table 3 QTAIM topological volumes and charges in silica polymorphs at 0 GPa

Polymorph	V_{Si}	V_O	Q_{Si}	Q_O	α
α-Quartz	20.92	124.57	3.20	−1.60	80.0
Coesite	20.78	109.12	3.20	−1.60	79.8
Stishovite	18.75	71.65	3.19	−1.60	79.8
$CaCl_2$-type	18.80	71.80	3.19	−1.60	79.7
α-PbO_2-type	19.21	70.98	3.19	−1.60	79.8

α is the degree of global ionicity index. Atomic units are used

is indicated by the topological charges (see Table 3). This result has been observed in our recent study of the transformation path from α-cristobalite to stishovite [2]. There, we follow the chemical bonding reorganization along the transition using the electron localization function (ELF) and conclude that the bonding presents a highly ionic character (see figures 9–11 of that article). Moreover, calculated Bader's volumes and charges are perfectly in correspondence with previous studies [29]. Deviations from nominal charge values are observed, with Si displaying a net charge of around $+3.20\,e$ and O $-1.60\,e$. We can propose a single parameter, α, describing the global charge transfer by averaging the ratios between the topological charges (Q_i) and the nominal oxidation states (OS, +4 for Si, −2 for O) [31]:

$$\alpha = \frac{1}{N}\sum_{i=1}^{N}\frac{Q(i)}{OS(i)} \tag{6}$$

where i runs over the N non-equivalent atoms in the unit cell. According to this index, the degree of global ionicity remains constant along the silica high-pressure sequence. It is also in concordance with the high difference in electronegativity between oxygen (3.44) and Si (1.90) according to Pauling's scale.

In Fig. 3, the volume of each basin along the polymorphic sequence is displayed. The most remarkable result from this plot is the equivalent trend displayed by both the bulk and the oxygen curves, whereas the Si volume remains always with a similar value. It is not only the fact that most of the unit cell is occupied by oxygen atoms (see also Tables 3, 4), but also the uniform value of the occupation fraction of oxygen in all the polymorphs. Two regions can be observed. The first region is associated with tetrahedral environment surrounding Si atom in α-quartz and coesite phases, and the second one corresponds to octahedral and higher coordinated Si environments in stishovite and post-stishovite structures. Connecting both, the transformation from coesite to stishovite provides a representative example of the general picture. The calculated volume collapse ($\Delta V/V_i$, Δ means final minus initial structures and i is the initial one) is around 32 % at 0 GPa. We notice that in our previous study on the α-cristobalite to stishovite transition mechanism, the calculated volume collapse associated with the same changes in atomic coordinations was around 48 % at 0 GPa [2]. Compared with the volume reductions of the atoms, calculated values are 10 and 34 % for Si and O basins, respectively, at 0 GPa. These values clearly indicate that the accommodation of the electron density of the O atoms is the key to understand the stabilization of the stishovite phase. The most efficient packing involving higher atomic coordinations in the stishovite polymorph is achieved thanks mostly to the reduction of the space occupied by the electron density associated with oxygen.

This reduction can also be quantified calculating the local pressures of both Si and O atoms in all the polymorphs. When a solid is subdued to compression, its volume reduction (ΔV, Δ means here difference of pressure for the same structure) depends on the mechanical resistance of the solid [23]. Using the splitting of the cell volume into different atomic contributions, we can relate the mechanical resistance of the solid with the atomic–mechanical resistance of each basin. To do this, we analyze the energy–volume curves of each basin (Si and O) and bulk (SiO_2). We understand that the volume change (bulk or atomic) correlates with the corresponding mechanical resistance in such a way that the lower volume reduction the greater the resistance. In the case of stishovite (Fig. 4), it is apparent that for the same increase in energy, the reduction of volume is lower for Si, then for O, and then for the bulk. Notice that $\Delta V_{Si} + \Delta V_O = \Delta V$. This is then the same decreasing order of the corresponding mechanical resistances.

Taking into account the definition of p and p_i (thermodynamic and local pressure, respectively, $p = -(\frac{\partial E}{\partial V})_T$ and $p_i = -(\frac{\partial E}{\partial V_i})_T$), the greater pressure corresponds to the smaller volume reduction, and, therefore, to the greater

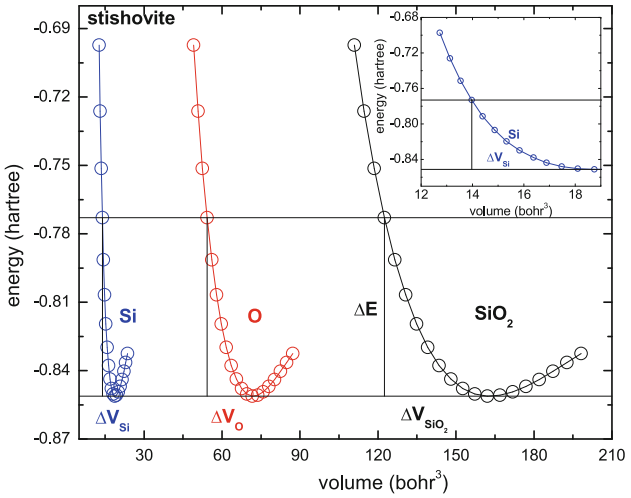

Fig. 4 Total energy *versus* atomic and crystal volumes per formula unit for stishovite. The *inset* displays a zoom view of the Si plot

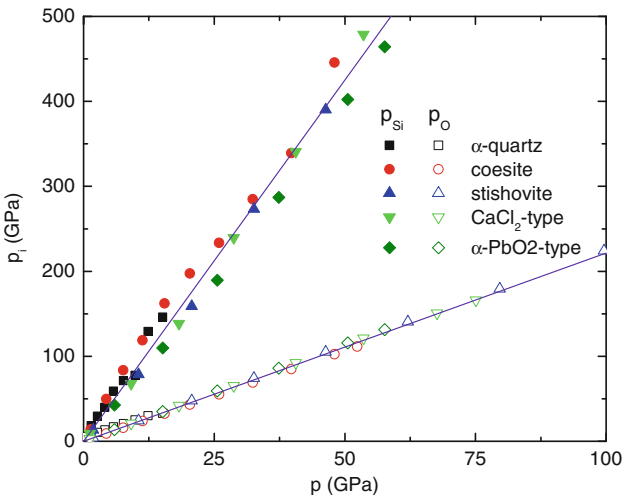

Fig. 5 Local pressures *versus* thermodynamic pressure for Si and O in all polymorphs

mechanical resistance of the atom (or bulk). As we have seen, Si has the lowest value of this reduction, followed by O and by the bulk. Under these proposals, Si atoms are the ones with the greatest local pressure or the greatest mechanical resistance upon compression in the silica polymorphs. What is more interesting is that we can establish a relationship between the local atomic-like pressure and the macroscopic thermodynamic pressure as suggested by the plot in Fig. 5. Two trends are observed, one for Si and other for O, $p_{Si} = 9.40p$ and $p_O = 2.22p$, respectively. The slopes clearly demonstrate the different mechanical resistances of both atoms, around 9.4 for Si and 2.2 for O. Looking at Fig. 5, as far as similarities are concerned, the lower the pressure the greater the ability of both atoms to reduce their volumes. The most important conclusion from these plots is the fact that not only all the points can be grouped in two very well-defined curves, one associated with Si and one with O, but also these trends are simple linear equations. Maybe, this behavior could continue even if we consider the calculated local pressures of other silica polymorphs, like the pyrite-like structure. This regularity calls for universal trends under pressure for silica polymorphs. This kind of universal behavior has been detected, for example, in the zinc blende-rock salt transition path of several II-VI, III-V, and IV-IV compounds [32].

Finally, we analyze the QTAIM partition of the compressibility and bulk modulus taking into account the contribution of Si and O basins to the crystal. Based on the partition of the cell volume into basin volumes (see Sect. 2), we collect in Table 4 the calculated results for all SiO_2 polymorphs. Small differences in B_0 values with respect to results discussed in previous subsections are mostly due to errors in the integrated volumes of the atomic basins. These differences are too small to influence the analysis of the partition. We observe that in low-pressure phases, the compressibility of oxygen is higher than that of silicon. This is the expected result given the greater size (and relative lower electron density) of oxygen. It is also in concordance with previous studies on other oxides and ionic crystals [24, 33], where the anionic species were found to be significantly easier to compress than the cations. However, this behavior changes in the high-pressure polymorphs of silica.

Table 4 QTAIM partition of the macroscopic zero-pressure compressibility and bulk modulus of SiO_2 into atomic basin contributions

	f_i	κ_i (TPa^{-1})	B_i (GPa)
α-Quartz			
Si	0.077	4.37	228.56
O	0.923	33.48	29.87
	Total	31.24	32.01
Coesite			
Si	0.088	5.77	173.29
O	0.912	10.60	94.33
	Total	10.17	98.33
Stishovite			
Si	0.116	4.49	222.56
O	0.884	3.68	271.73
	Total	3.77	265.25
$CaCl_2$-type			
Si	0.116	4.47	223.51
O	0.884	3.66	273.21
	Total	3.75	266.67
α-PbO_2-type			
Si	0.119	4.49	222.80
O	0.881	3.46	288.95
	Total	3.58	279.09

In stishovite and post-stishovite structures, the compressibility of Si is slightly lower than that of O. From α-quartz to α-PbO_2-type, there is a significant reduction of the compressibility of O (from 30 to 3 TPa^{-1}), whereas the compressibility of Si remains with values around 4.5 ± 1 TPa^{-1}. As a result, an inversion on the order of the atom with the lowest compressibility is found along the polymorphic sequence. It is to be noticed that this inversion correlates with the change of Si and O coordinations from 4 and 2 to 6 and 3, respectively. We can then speculate that the leading role of oxygen as the active atom in the pressure-induced polymorphism has to be shared with Si for those phase transitions at very high pressures.

Nevertheless, it is to be noticed that the values of the macroscopic compressibility are always, regardless the pressure stability range of the polymorph, much more similar to the corresponding values of oxygen than to the silicon ones. This is a consequence of the occupation factor (see Table 4). As we noticed above, the oxygen atoms occupy most of the cell volume, around 90 % as average in all polymorphs. According to Eq. 4, oxygen dominates the atomic contribution to the macroscopic compressibility in all polymorphs, and one can approximate the compressibility of any of the SiO_2 polymorphs by the corresponding compressibility of oxygen.

4 Conclusions

Silica high-pressure sequence, α-quartz $\rightarrow$ coesite $\rightarrow$ stishovite $\rightarrow$ $CaCl_2$-type $\rightarrow$ α-PbO_2-type, is studied by first-principles calculations. At static conditions, α-quartz transforms to coesite at 4.5 GPa, coesite–stishovite transition happens at 7.0 GPa, and stishovite transforms into $CaCl_2$-type at 55 GPa. This polymorph undergoes a phase transformation to α-PbO_2-type at 97 GPa. Structural properties and mechanical properties are evaluated, yielding a good agreement with previous theoretical and experimental studies. Pressure promotes great volume reductions in silica polymorphs such as α-quartz and coesite that display low bulk modulus. On the other hand, stishovite and post-stishovite structures are less compressible (high bulk modulus). Stishovite-$CaCl_2$-type transition occurs without changes in the volume suggesting a second-order phase transition.

By QTAIM analysis, we calculated electron population and volumes associated with Si and O basins. An ionic picture of all the polymorphs is obtained. Oxygen is the atom that occupies most of the space of the unit cell with an almost constant contribution. This fact has implications on the different chemical activity of Si and O as hydrostatic pressure is applied. Regarding volume collapses, the oxygen atom exhibits the same trend as the bulk along the polymorphic sequence. After local pressures are evaluated, we can conclude that the volume occupied by the electron density of O is easier to reduce under pressure than that of Si. This lower mechanical resistance follows a linear trend with respect to the external hydrostatic pressure with a slope around 2.20, being the corresponding one for Si 9.4. A second consequence of the high occupation factor (around 90 % of the space) of oxygen is the similar compressibility of this atom compared with the macroscopic value in all the polymorphs: $\kappa(SiO_2) \approx \kappa(O)$ and $B(SiO_2) \approx B(O)$. This result is compatible with the inversion in the order of the atomic compressibilities along the polymorphic sequence. The compressibility of oxygen decreases from the low-pressure phases to the post-stishovite polymorphs where Si has a higher value.

Acknowledgments Financial support from Spanish MINECO under Project CTQ2012-38599-C02 and the Spanish Consolider Program (CSD2007-00045) is gratefully acknowledged. AMG thanks Spanish government for a PhD-FPI grant.

References

1. Kingma KJ, Cohen RE, Hemley RJ, Mao HK (1995) Nature 374:243–245
2. Salvadó MA, Pertierra P, Morales-García A, Menéndez JM, Recio JM (2013) J Phys Chem C 117:8950–8958
3. Bader RFW (1990) Atoms in molecules. Oxford University Press, Oxford
4. Bader RFW (1991) Chem Rev 91:893–928
5. Gibbs GV, Ross NL, Cox DF, Rosso KM, Iversen BB, Spackman MA (2014) Phys Chem Miner 41:17–25
6. Prencipe M, Nestola F (2005) Phys Chem Miner 32:471–479
7. Merli M, Sciascia L (2013) Phys Chem Miner 40:455–466
8. Levien L, Prewitt CT (1981) Am Miner 66(324):333
9. Smyth JR, Smith JV, Artioli G, Kvick A (1987) J Phys Chem 91:988–992
10. Sugiyama M, Endo S, Koto K (1987) Miner J Jpn 13:455–466
11. Teter DM, Hemley RJ, Kresse G, Hafner J (1998) Phys Rev Lett 80:2145–2148
12. Kresse G, Furthmuller J (1996) Phys Rev B 54:11169–11186
13. Blöch PE (1994) Phys Rev B 50:17953–17979
14. Kresse G, Joubert D (1999) Phys Rev B 59:1758–1775
15. Perdew JP, Burke K, Ernzerhof M (1996) Phys Rev Lett 77:3865–3868
16. Monkhorts HJ, Pack JD (1976) Phys Rev B 13:5188–5192
17. Vinet P, Rose JH, Ferrante J, Smith JR (1989) J Phys Condens Matter 1:1941–1963
18. Otero-de-la-Roza A, Luaña V (2011) Comput Phys Commun 182:1708–1720
19. Otero-de-la-Roza A, Abbasi-Pérez D, Luaña V (2011) Comput Phys Commun 182:2232–2248
20. Otero-de-la-Roza A, Blanco MA, Martín Pendás A, Luaña V (2009) Comput Phys Commun 180:157–166
21. Otero-de-la-Roza A, Johnson ER, Luaña V (2014) Comput Phys Commun 185:1007–1018
22. Yu M, Trinkle DR (2011) J Chem Phys 134:064111/1-8
23. Ouahrani T, Menéndez JM, Marqués M, Contreras-García J, Baonza VG, Recio JM (2012) Europhys Lett 98:56002/1-6

24. Martín Pendás A, Costales A, Blanco MA, Recio JM, Luaña V (2000) Phys Rev B 62:13970–13978
25. Murakami M, Hirose K, Ono S, Ohiski M (2003) Geophys Res Lett 30:11/1-4
26. Ono S, Hirose K, Murakami M, Isshiki M (2002) Earth Planet Sci Lett 197:187–192
27. Demuth T, Jeanvoine Y, Hafner J, Angyan JG (1999) J Phys Condens Matter 11:3833–3874
28. Karki BB, Warren MC, Stixrude L, Ackland GJ, Crain J (1997) Phys Rev B 55:3465–3471
29. Oganov AR, Gillan MJ, Price GD (2005) Phys Rev B 71:064104/1-8
30. Andrault D, Fiquet G, Guyot F, Hanfland M (1998) Science 282:720–724
31. Mori-Sánchez P, Martín Pendás A, Luaña V (2002) J Am Chem Soc 124:14721–14723
32. Miao MS, Lambrecht RL (2005) Phys Rev Lett 94:225501/1-4
33. Recio JM, Franco R, Martín Pendás A, Blanco MA, Pueyo L, Pandey R (2001) Phys Rev B 63:184101/1-6

Theor Chem Acc (2014) 133:1586
DOI 10.1007/s00214-014-1586-2

REGULAR ARTICLE

Noncovalent interactions in dimers and trimers of SO_3 and CO

Luis Miguel Azofra · Ibon Alkorta · Steve Scheiner

Received: 28 August 2014 / Accepted: 10 October 2014 / Published online: 22 October 2014

Abstract The SO_3:CO heterodimer has been found by ab initio calculations to form a complex in which the C lone pair of CO interacts with the π*(SO) antibond via the π-hole lying directly above the S atom of SO_3. The binding energy of this complex is 4.3 kcal/mol, with Coulombic attraction as its main component. There is also a secondary minimum, with half that strength, wherein the CO molecule is rotated so that it is its O atom that interacts with SO_3. The most stable SO_3:$(CO)_2$ heterotrimer has the two CO molecules approaching the S atom from above and below the SO_3 plane with the C atoms of the CO interacting with the S of the SO_3. A strong chalcogen bond between SO_3 molecules is the dominant feature of the $(SO_3)_2$:CO trimer, supplemented by a S···C chalcogen bond in the SO_3:CO dimer.

Keywords Chalcogen bonds · S···C bonds · S···O bonds · π-Hole

1 Introduction

Noncovalent bonds [1], such as hydrogen [2–5], halogen [6–11], pnicogen [12–20] or tetrel [21–24] interactions, are essential ingredients in the structure adopted by bimolecular complexes and by numerous single molecules, as these bonds can represent large fractions of the forces between segments that are not directly covalently bonded to one another. Chalcogen bonds (YB) [25–38] are noncovalent interactions, which arise when an atom of the chalcogen family (Y), e.g., O, S, Se or Te, acting as Lewis acid, is drawn toward another electronegative atom, acting as Lewis base, due in part to the anisotropic distribution of electron density around Y [39]. The electrostatic attractions within these chalcogen bonds are supplemented by charge transfer from the lone pair(s) of the electron donor atom into the σ* or π* antibonding Z–Y orbitals (where Z is covalently bonded to Y), which tend to weaken and lengthen the latter Z–Y bond [40–43].

The present work examines the complexes formed between SO_3 and CO, as well as their 1:2 and 2:1 heterotrimers. Understanding the behavior of these molecules when interacting with one another is important to the basic knowledge of the various noncovalent forces. The work documents the primary attractive force to be a surprisingly strong chalcogen bond between a lone pair of the C (or O) atom of CO and the π-hole of SO_3 via its π*(SO) antibonding orbitals.

2 Computational details

The structure, energy and properties of the SO_3:CO heterodimers, and the SO_3:$(CO)_2$ and $(SO_3)_2$:CO heterotrimers, were studied through the use of the second-order Møller–Plesset perturbation theory (MP2) [44] with the aug-cc-pVTZ basis set [45, 46]. In all cases, vibrational frequencies were calculated in order to verify that the structures obtained correspond to true minima and to obtain the zero point vibrational energy (ZPE). Also, binding energies for the heterodimers were corrected by the counterpoise

Published as part of the special collection of articles derived from the 9th Congress on Electronic Structure: Principles and Applications (ESPA 2014).

L. M. Azofra (✉) · I. Alkorta
Instituto de Química Médica, CSIC, Juan de la Cierva, 3, 28006 Madrid, Spain
e-mail: luisazofra@iqm.csic.es

S. Scheiner
Department of Chemistry and Biochemistry, Utah State University, Logan, UT 84322-0300, USA

procedure [47]. All calculations were carried out via the GAUSSIAN09 program (revision D.01) [48].

Binding energies, E_b, were computed as the difference in energy between the complex on one hand and the sum of the energies of the isolated optimized monomers on the other. In order to obtain more accurate values, single point coupled-cluster CCSD(T) [49]/aug-cc-pV*X*Z (X = T, Q) calculations from the optimized MP2/aug-cc-pVTZ minima were performed via MOLPRO program [50].

The many-body procedure [51, 52] was applied to the trimers (Eq. 1) whereby the binding energy can be expressed as:

$$E_b = E_r + \Sigma\Delta^2 E + \Delta^3 E \quad (1)$$

where E_r represents the energy arising from the monomers' deformation and $\Delta^n E$ is the nth complex term (n = 2 for dimers and 3 for trimers). $\Delta^3 E$ represents the total cooperativity in the full trimer.

Atoms in molecules (AIM) [53, 54] theory at the MP2/aug-cc-pVTZ level, and natural bond orbital (NBO) [55] theory with the ωB97XD [56] functional and the aug-cc-pVTZ basis set, were applied to analyze the noncovalent interactions, using the AIMAll [57] and NBO6.0 [58] programs. The appearance of an AIM bond critical point (BCP) between centers of different monomers supports the presence of an attractive bonding interaction, which can also be examined by NBO charge transfer between orbitals of different fragments [53, 59].

The molecular electrostatic potential (MEP) on the 0.001 au electron density isosurface at MP2/aug-cc-pVTZ level was analyzed for the monomers via the WFA-SAS program [60]. Also, for the heterodimers, the electron density shift (EDS) maps were calculated as the difference between the electron density of the complex and the sum of those of the monomers in the geometry of the complex.

The interaction energy of each SO_3:CO heterodimer was decomposed via DFT-SAPT calculations at the PBE0 [61]/aug-cc-pVTZ level with the MOLPRO program [50]. The DFT-SAPT interaction energy, $E^{\text{DFT-SAPT}}$, is obtained as the sum of five components (Eq. 2): electrostatic (*ES*), exchange (*EX*), induction (*IND*), dispersion (*DISP*) and higher-order contributions (δ_{HF}) [62].

$$E^{\text{DFT-SAPT}} = ES + EX + IND + DISP + \delta_{HF} \quad (2)$$

3 Results and discussion

3.1 Monomers

Sulfur trioxide (SO_3) and carbon monoxide (CO) adopt D_{3h} and $C_{\infty v}$ symmetry, respectively. Their molecular electrostatic potential (MEP) on the 0.001 au electron density isosurface is illustrated in Fig. 1. The black dots represent maxima on the surface. In the case of SO_3, these maxima occur directly above and below the S atom, so may be referred to as π-holes. The cylindrical symmetry of CO leads to an equatorial belt of positive MEP around the middle of the molecule, represented by the series of black dots. The values of the MEP maxima for the SO_3 and CO molecules are 52.8 and 10.9 kcal/mol, respectively. The green dots indicate the positions of minima on the MEP. These points occur in the approximate positions of the O lone pairs in SO_3 and are rather shallow with a value of −9.0 kcal/mol. The minima occur on the two extensions of the CO axis, with the one on the C end somewhat more negative at −14.0 kcal/mol versus only −4.1 kcal/mol for the O terminus. The more negative C end is verified by the calculated dipole moment of CO, which is 0.254 D at MP2/aug-cc-pVTZ level, close to the experimental value of 0.11 D [63]. As described below, the positions of these extrema in the MEP act to guide the molecules into their respective dispositions in the dimers and trimers.

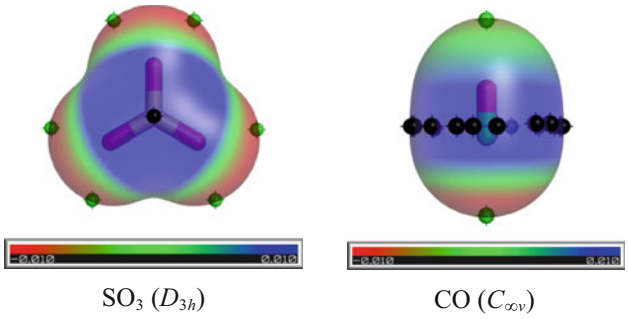

Fig. 1 Molecular electrostatic potential (MEP) on the 0.001 au electron density isosurface for the SO_3 and CO monomers, both calculated at the MP2/aug-cc-pVTZ level. The *red* and *blue colors* indicate negative and positive regions, respectively, varying between −0.010 and +0.010 au. *Black* and *green dots* indicate the location of the ESP maxima and minima, respectively, on the surface. The *black dots* for CO represent an equatorial belt of cylindrical symmetry

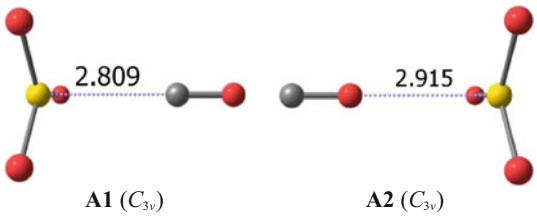

Fig. 2 Structures of the two SO_3:CO heterodimers optimized at the MP2/aug-cc-pVTZ level. *Broken blue lines* connect interacting moieties corroborated by AIM. Interatomic distances in Å

3.2 SO_3:CO heterodimers

The potential energy surface (PES) of the SO_3:CO heterodimers contains two minima (see Fig. 2). CO approaches the S atom from above via its C atom in the more stable

Table 1 Binding energy, E_b, for the SO_3:CO heterodimers at the MP2/aug-cc-pVTZ and CCSD(T)/aug-cc-pVXZ (X = T, Q; single point) levels

Dimer	MP2				CCSD(T)[a]
	E_b^b	E_b + BSSE[c]	ΔH	ΔG	E_b
A1	−4.74 (−3.85)	−3.90	−3.69	3.57	−4.34 (−4.20)
A2	−2.15 (−1.69)	−1.56	−1.22	4.36	−2.47 (−2.26)

Also, enthalpy, ΔH, and Gibbs free energy, ΔG, for the association reactions at room temperature (298 K) and at MP2/aug-cc-pVTZ computational level are shown. All quantities in kcal/mol

[a] CCSD(T)/aug-cc-pVTZ//MP2/aug-cc-pVTZ and, in parentheses, CCSD(T)/aug-cc-pVQZ//MP2/aug-cc-pVTZ computational levels

[b] Zero point vibrational energy corrections (ZPE) added in parentheses

[c] Basis set superposition error (BSSE)

Table 2 Natural bond orbital parameters [$E(2)$ in kcal/mol] at ωB97XD/aug-cc-pVTZ level, and AIM descriptors (electron density, ρ_{BCP}, and its Laplacian at the BCP, both in au) at MP2/aug-cc-pVTZ computational level for the noncovalent interactions present in the indicated dimers and **B1**–**B3** trimers

Complex	NBO		AIM	
	Donor lone pair	$E(2)$	ρ_{BCP}	$\nabla^2\rho_{BCP}$
A1	C	6.24	0.020	0.055
A2	O	1.10	0.010	0.045
B1	C, C	5.40, 5.40	0.016, 0.016	0.049, 0.049
B2	C, O	6.20, 1.17	0.019, 0.009	0.052, 0.041
B3	O, O	1.21, 1.21	0.010, 0.010	0.044, 0.044

Sum of all the $C_{lp}/O_{lp} \rightarrow \pi^*(SO)$ components for a same type interaction

complex, **A1**, while the approach is via the O atom in **A2**. In either case, the interactions can be described as the approach of a negative minimum in the MEP of CO toward the positive π-hole above S. The greater stability of **A1** is consistent with the more negative minimum near the C atom, as well as the 0.1 Å shorter intermolecular distance. No dimers in which the O lone pairs from SO_3 interact with the positive belt in CO have found, due to the very poor electrostatic power of this last region.

The energetics of the two complexes are displayed in Table 1 which shows the binding energy of **A1** to be roughly twice that of **A2**, both before and after zero point energies basis set superposition errors (BSSE) are added in. Raising the level of correlation from MP2 to CCSD(T) reduces the binding energy of **A1** and raises that of **A2**, but by small amounts in either case. As can be seen in Table 1 about E_b at CCSD(T) level, small differences arise from the change in the aug-cc-pVTZ and aug-cc-pVQZ basis sets. The more stable OC···SO_3 complex is bound by approximately the same amount as the water dimer [64], the paradigm of classic H-bonding. The succeeding columns indicate that ΔH is rather similar to the ZPE-corrected binding energy. ΔG, on the other hand, is positive at 298 K, less so for **A1** than for **A2**. This thermodynamic quantity is negative for temperatures below −121 K for **A1**, and below −208 K for **A2**.

In addition to a simple electrostatic attraction, Table 2 reports measures of a stabilizing charge transfer between the two molecules. The NBO value of $E(2)$ represents an energetic assessment of the charge transfer from the C/O lone pair of CO in **A1/A2**, to a π* antibonding orbital of SO_3. There is a fairly large $E(2)$ of 6.24 kcal/mol for **A1**, and a smaller but still significant $E(2)$ of 1.10 kcal/mol for **A2**. The last two columns of Table 2 present the values of the electron density ρ and its Laplacian $\nabla^2\rho$ at the C/O···S bond critical point as determined by AIM analysis. Consistent with the other trends, both of these measures of bond strength are larger for **A1** than for **A2**.

The decomposition of the total interaction energy into its constituent parts was calculated via DFT-SAPT, and the results are reported in Table 3. The electrostatic force represents the strongest attractive component for **A1**, followed by dispersion and then by induction. Electrostatic is much smaller in **A2** and is in fact surpassed by dispersion, with induction again playing a much more minor role. The smaller Coulombic attraction in **A2** is understandable based on the CO dipole moment, which is repelled by the SO_3 quadrupole moment.

Another result of the formation of a dimer is the shift of electron density that accompanies the complexation. These shifts are displayed in Fig. 3 where electron density increments are denoted in purple and losses in green. The patterns for both **A1** and **A2** are similar, but again they are attenuated in **A2**. A gain is observed in the C/O atom that is approaching the SO_3 molecule from above, and a loss on the other atom of CO. This pattern is verified by NBO atomic charges wherein the atom of CO interacting directly with SO_3 acquires additional charge, at the expense of the other atom. There is an internal shift of density from the region immediately above the S atom of SO_3 toward the three O atoms, a redistribution consistent with the NBO atomic charges. It would appear from Fig. 3 that the latter internal polarization of SO_3 is considerably smaller in **A2,** while the changes within CO are fairly similar from **A1** to **A2**, again all consonant with NBO atomic charge patterns. In terms of the amount of charge transferred between molecules, from CO to SO_3, both Fig. 3 and the NBO atomic charges suggest that there is very little transfer in **A2**, as most of the density rearrangement is internal, particularly within CO.

Dipole moments of the complexes also reflect charge redistribution. The dipole of the CO monomer is 0.254 D, in the $^-$C–O$^+$ direction. This moment is increased more

Table 3 Interaction energy components (kcal/mol) for the SO_3:CO heterodimers, calculated using the DFT-SAPT (PBE0/aug-cc-pVTZ) methodology

Complex	*ES*	*EX*	*IND*	*DISP*	δ_{HF}	$E^{DFT\text{-}SAPT}$
A1	−7.62	12.00	−2.13	−4.15	−1.40	−3.30
A2	−2.01	3.26	−0.55	−2.12	−0.28	−1.70

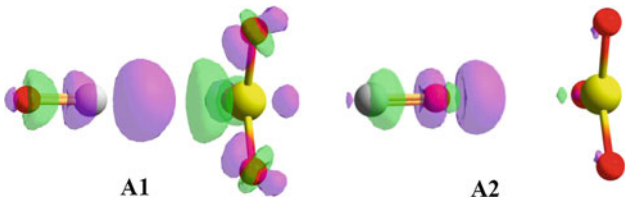

Fig. 3 Electron density shifts in SO_3:CO dimers caused by formation of complex. Contours represent the ±0.001 au surface; increase in *purple* and decrease in *green*

Table 4 Changes in internal bond lengths (mÅ) and vibrational frequencies (cm^{-1}) of monomers upon formation of dimers and **B1**-**B3** trimers

Complex	R(C≡O)	ν(C≡O)	R(S=O)	ν_{st}(S=O)[a]
A1	−2.5	21	−1.7	10
A2	0.8	−2	1.0	−4
B1	−1.9	16, 16	−2.2	16
B2	−2.5, 0.5	20, −1	−2.2	13
B3	0.8	−3, −3	−1.4	7

In monomers, R(C≡O) = 1.1390 Å and ν(C≡O) = 2,110 cm^{-1}; R(S=O) = 1.4451 Å, ν_{st} = 1,036 cm^{-1}

[a] Symmetric stretching frequency

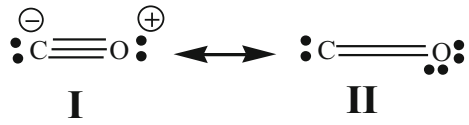

Scheme 1 Lewis structure analysis in the CO monomer

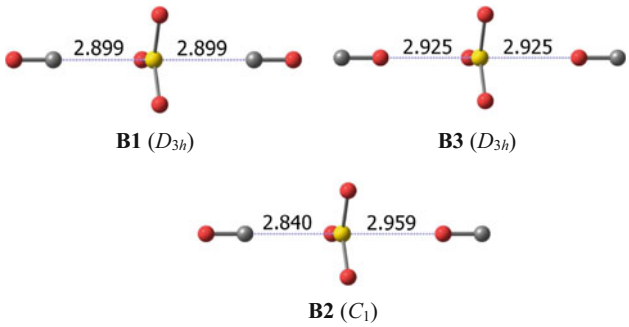

Fig. 4 Structures of the SO_3:$(CO)_2$ heterotrimers optimized at the MP2/aug-cc-pVTZ level. *Broken blue lines* connect interacting moieties corroborated by AIM. Interatomic distances in Å

than fourfold in complex **A1**, which is consistent with the shift of density from O to C in Fig. 3. This same figure shows the opposite polarization, from C to O, in **A2**. This polarization indeed reverses the dipole of CO, to $^{+}C–O^{-}$, with a magnitude of 0.149 D.

Even weak noncovalent interactions are known to induce perturbations in the internal properties of the monomers. Table 4 lists the changes in the internal bond lengths and vibrational frequencies that occur upon forming dimers **A1** and **A2**. It is first notable that these two structures influence the monomers in opposite ways. In structure **A1**, the bonds of both molecules become shorter and the frequencies shift to the blue. The changes are of opposite sign in **A2** and smaller in magnitude.

There are perhaps several ways to understand these trends. With respect to CO, the largest shift in orbital occupancy upon forming the **A1** dimer is a 28 me drop in the C lone pair orbital. A pictorial examination of this orbital shows a node in the region between the C and O atoms, which may be characterized as antibonding character. The loss of density from this orbital may thus be associated with an enhanced C–O bond strength, which leads to the observed bond contraction and blue shift. The loss of occupancy of the O lone pair in **A2** is very small, less than 1 me, so is consistent with the very small changes in the CO bond strength markers in Table 4.

Another and less rigorous manner of understanding these patterns is associated with a simple Lewis structure analysis. One may consider the bonding of CO to consist of a resonance between a triple-bonded structure I with opposite charges on the two atoms, as shown in Scheme I, and II which contains two neutral atoms connected by a double bond (see Scheme 1). The shift in charge which amplifies the charge separation in **A1** would tend to push the equilibrium between I and II toward I, and the stronger triple bond contained therein.

3.3 SO_3:$(CO)_2$ heterotrimers

Upon adding a second CO monomer to the SO_3:CO dimer, the potential energy surface was searched in two steps: (1)

Table 5 Many-body analysis (kcal/mol) for the SO_3:$(CO)_2$ heterotrimers calculated at MP2/aug-cc-pVTZ level

Comp.	E_r	E_{12}	E_{13}	E_{23}	$\Sigma\Delta^2E$	Δ^3E	E_b
B1	0.03	−4.65	−4.65	−0.01	−9.31	0.55	−8.73
B2	0.07	−4.79	−2.14	−0.01	−6.94	0.22	−6.64
B3	0.00	−2.15	−2.15	−0.06	−4.36	0.05	−4.31

Subscripts 1, 2 and 3 refer to SO_3, CO(1), and the second CO monomer [CO(2)], respectively. Binding energies in **A1** and **A2** dimers are −4.74 and −2.15 kcal/mol, respectively

using the **A1** and **A2** dimers as starting points and (2) beginning with fresh initial starting points. For this second purpose, the coalescence-kick program was employed, which provides a fully objective searching protocol [65]. The three minima in Fig. 4 resulted from this combined approach. All three resemble the dimers in that the CO molecules approach SO_3 both from above and below. In the most stable **B1**, S is attacked by C atoms, by O atoms in **B3**, and by one of each in **B2**. The order of stability follows the dimer pattern that the C atom is favored over O to form a S···C chalcogen bond. The very weak interactions between CO monomers precluded formation of SO_3:$(CO)_2$ heterotrimers where a pair of CO molecules interact with one another. Indeed, $(CO)_2$ homodimers are described in the literature as bound by only very weak van der Waals bonds [66–68].

There is evidence of negative cooperativity in the S···X bond lengths. Whereas R(S···C) = 2.809 Å in **A1**, it is elongated in the trimers; likewise, the S···O bonds in the trimers are longer that its value of 2.915 Å in **A2**. This mutual weakening effect may be understood first on the basis that SO_3 serves as double electron acceptor in the trimers. A related description might utilize the weakening of the SO_3 π-hole upon its complexation with the first CO molecule. For example, the π-hole in the SO_3 monomer has a magnitude of 52.8 kcal/mol, which is reduced to 44.6 in **A1** and 50.8 in **A2**.

Other evidence of antagonistic behavior is observed in the electronic structure. It may be noted from Table 2 that the $E(2)$ $C_{lp} \rightarrow \pi^*(SO)$ charge transfer energy of the **A1** dimer of 6.24 kcal/mol is reduced in the trimers, although there is a slight rise in the $O_{lp} \rightarrow \pi^*(SO)$ quantities. The AIM measures in the last two columns also show a bond weakening upon going from dimer to trimer.

The changes in the internal parameters provide further support of negative cooperativity. The CO bond length contraction of 2.5 mÅ in **A1** is reduced in **B1**, and the 0.8 mÅ stretch in **A2** is lowered to 0.5 in **B2**, with similar patterns noted in ν(C≡O). On the other hand, the 1.7 mÅ contraction of R(S=O) in **A1** is amplified to 2.2 mÅ in **B1** and **B2**, suggesting that the effects of one CO molecule upon the central SO_3 are enhanced by a second CO on the other side of the trimer. This same amplification is observed in the symmetric SO stretching frequency.

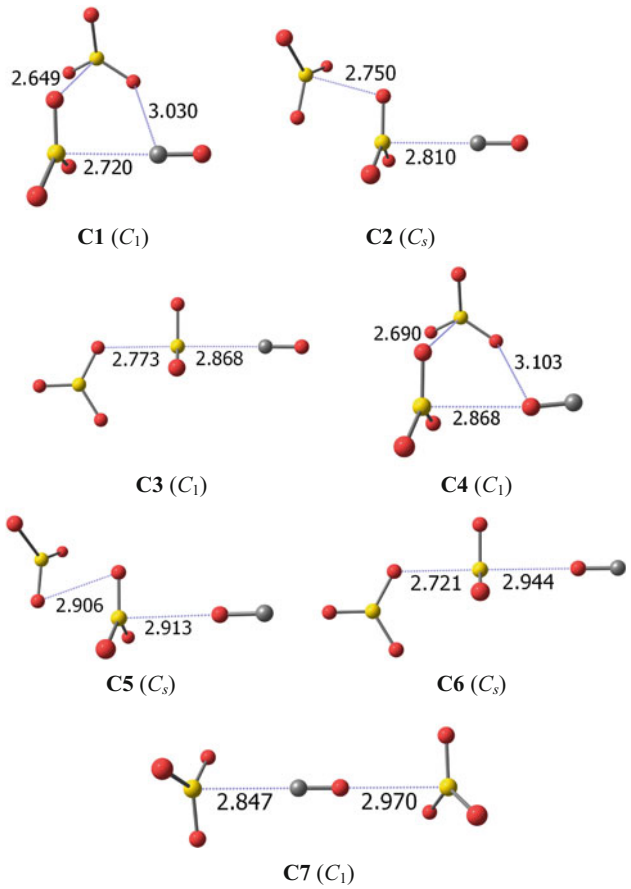

Fig. 5 Structures of $(SO_3)_2$:CO heterotrimers optimized at the MP2/aug-cc-pVTZ level. *Broken blue lines* connect interacting moieties corroborated by AIM. Interatomic distances in Å

The many-body analysis for the SO_3:$(CO)_2$ heterotrimers reported in Table 5 shows first that the interaction energies of the **A1** and **A2** dimers are changed very little when placed in the context of pairwise interactions E_{12} and E_{13} in the trimers. The small changes in the geometry have a negligible energetic effect, as is clear from the very small values of E_r in the first column of Table 5. The third-order term, Δ^3E, which represents the total cooperativity is positive in all cases, again confirming the negative cooperativity. Note that this term is largest for the most strongly bound trimers.

3.4 $(SO_3)_2$:CO heterotrimers

As for the SO_3:$(CO)_2$ complexes, the inclusion of a second SO_3 monomer was performed: (1) through the **A1** and **A2** dimers and (2) beginning with fresh initial starting points. SO_3 molecules can engage in relatively strong noncovalent bonds [37]. For that reason, the six most stable minima of the seven found on the $(SO_3)_2$:CO potential energy surface in Fig. 5 include stabilizing interactions between the SO_3 monomers. Structure **C1**, for example, includes a S···O chalcogen bond between SO_3 molecules as the shortest contact, as well as a S···C contact reminiscent of that in dimer **A1**, and a longer C···O contact. Structure **C1**, like **C4**, could best be described as a cyclic geometry. In **C2**, **C3**, and **C5**, SO_3 occupies a central position, whereas CO is located between the two SO_3 molecules in **C7**.

The changes induced in the CO monomer by formation of these heterotrimers are documented in Table 6. There is a clear pattern of CO bond contraction and blue shifts in **C1**, **C2**, **C3**, and **C7**, with opposite, albeit smaller, changes in **C4**–**C6**. Consistent with the results for the dimers, the former set of trimers all involves interaction of the C atom of CO, while the O atom participates in the bonding in the latter set.

Table 6 Changes in internal bond lengths (mÅ) and vibrational frequencies (cm^{-1}) of monomers upon formation of dimers and **C1**–**C7** trimers

Complex	R(C≡O)	ν(C≡O)
C1	−3.3	27
C2	−2.7	22
C3	−2.2	18
C4	1.0	−3
C5	0.8	−3
C6	0.6	−2
C7	−1.8	19

In monomers, R(C≡O) = 1.1390 Å and ν(C≡O) = 2,110 cm^{-1} ; R(S=O) = 1.4451 Å, ν_{st} = 1,036 cm^{-1}

The many-body analysis of the seven $(SO_3)_2$:CO heterotrimers in Table 7 shows first that the distortion energy remains low, here less than 0.4 kcal/mol. Again, the bimolecular terms representing OC···SO_3 and CO···SO_3 interactions are quite similar to their values in the **A1** and **A2** dimers. While generally small, the cooperativity term Δ^3E is negative in many cases, indicating a synergistic effect, but especially large in **C1**. Not surprisingly, positive values of Δ^3E are characteristic of structures where the central molecule plays the role of either double electron acceptor (**C3** and **C6**) or donor (**C7**).

Due in part to their cyclic nature, the structure of NBO charge transfers in the $(SO_3)_2$:CO heterotrimers is more complicated than in those of the preceding structures. The values of $E(2)$ are displayed in Table 8, along with their donor and acceptor orbitals. The stability of **C1** can be traced to a pair of important transfers. The largest is the $C_{lp} \rightarrow \pi^*(SO)$ transfer involving CO, followed closely by an $O_{lp} \rightarrow \pi^*(SO)$ chalcogen bond between two SO_3 molecules. And indeed, these $C_{lp} \rightarrow \pi^*(SO)$ transfers are typically more substantial than the chalcogen bonds between SO_3 molecules. As in the dimers, the $C_{lp} \rightarrow \pi^*(SO)$ values of $E(2)$ are consistently much larger than $O_{lp} \rightarrow \pi^*(SO)$.

Another manifestation of the synergistic effects in some of these trimers can be seen in the values of $C_{lp} \rightarrow \pi^*(SO)$ $E(2)$, which was equal to 6.24 kcal/mol in **A1**. This quantity exceeds this value in **C1** and **C2**. In both of these structures, the second SO_3 molecule engages in a S···O chalcogen bond with the first SO_3, which retrieves electron density from it, and thereby enhancing its π-hole, and also permitting a larger charge transfer from the C lone pair.

4 Summary

The C atom of CO attacks the SO_3 molecule from directly above the SO_3 plane, to form a S···C chalcogen bond. This interaction is largely electrostatic in nature, with the negative end of the CO dipole advancing toward the π-hole that lies above the S atom. It is supplemented by the charge

Table 7 Many-body analysis (kcal/mol) for the $(SO_3)_2$:CO heterotrimers calculated at the MP2/aug-cc-pVTZ level

Comp.	E_r	E_{12}	E_{13}	E_{23}	$\Sigma\Delta^2E$	Δ^3E	E_b
C1	0.39	−4.78	−4.82	−1.01	−10.60	−0.86	−11.08
C2	0.18	−4.90	−4.77	−0.20	−9.87	−0.09	−9.78
C3[a]	0.08	−4.60	−0.03	−4.71	−9.34	0.38	−8.89
C4	0.14	−4.75	−2.11	−0.75	−7.61	−0.26	−7.73
C5	0.14	−5.03	−2.14	−0.07	−7.24	−0.02	−7.12
C6	0.11	−4.73	−0.06	−2.14	−6.93	0.13	−6.69
C7	0.05	−4.76	0.10	−2.13	−6.79	0.40	−6.35

Subscripts 1, 2 and 3 refer to $SO_3(1)$, the second SO_3 monomer [$SO_3(2)$], and the CO monomer, respectively

[a] **C3** contains one very small imaginary frequency of 8*i* cm^{-1}

Table 8 NBO values of E(2) (kcal/mol) at the ωB97XD/aug-cc-pVTZ level for the noncovalent interactions present in the $(SO_3)_2$:CO heterotrimers

Complex	Donor/Acc.	Type	$E(2)$
C1	$SO_3(2)/SO_3(1)$	$O_{lp} \rightarrow \pi^*(SO)$	10.74
	$SO_3(1)/CO$	$O_{lp} \rightarrow \pi^*(CO)$	0.69
	$CO/SO_3(1)$	$C_{lp} \rightarrow \pi^*(SO)$	11.39
C2	$SO_3(2)/SO_3(1)$	$O_{lp} \rightarrow \pi^*(SO)$	4.46
	$SO_3(1)/SO_3(2)$	$O_{lp} \rightarrow \pi^*(SO)$	2.58
	$CO/SO_3(1)$	$C_{lp} \rightarrow \pi^*(SO)$	7.24
C3	$SO_3(2)/SO_3(1)$	$O_{lp} \rightarrow \pi^*(SO)$	4.55
	$CO/SO_3(1)$	$C_{lp} \rightarrow \pi^*(SO)$	5.79
C4	$SO_3(2)/SO_3(1)$	$O_{lp} \rightarrow \pi^*(SO)$	4.90
	$CO/SO_3(1)$	$O_{lp} \rightarrow \pi^*(SO)$	0.59
C5	$SO_3(2)/SO_3(1)$	$O_{lp} \rightarrow \pi^*(SO)$	3.38
	$SO_3(1)/SO_3(2)$	$O_{lp} \rightarrow \pi^*(SO)$	3.26
	$CO/SO_3(1)$	$O_{lp} \rightarrow \pi^*(SO)$	1.34
C6	$SO_3(2)/SO_3(1)$	$O_{lp} \rightarrow \pi^*(SO)$	5.14
	$CO/SO_3(1)$	$O_{lp} \rightarrow \pi^*(SO)$	1.16
C7	$CO/SO_3(1)$	$C_{lp} \rightarrow \pi^*(SO)$	5.93
	$CO/SO_3(2)$	$O_{lp} \rightarrow \pi^*(SO)$	0.83

$SO_3(1)$ and $SO_3(2)$ refer to the derived and nonderived SO_3 structure in dimers for the $(SO_3)_2$:CO heterotrimers, in each case

transfer from the C lone pair into the π*(SO) antibonding system, as well as a sizable dispersion contribution. In total, the binding energy of this heterodimer is between 4 and 5 kcal/mol, similar to the H-bond energy of the water dimer. A secondary minimum occurs if the CO molecule is rotated around so that its O atom attacks the S of SO_3, but this structure is more weakly bound.

This same S···O chalcogen bond is the guiding feature in the global minimum of the SO_3:$(CO)_2$ heterotrimer. The C atoms of the two CO molecules simultaneously approach the S of SO_3 from above and below. This assembly leads to a minor degree of negative cooperativity, as the central SO_3 molecule serves as double electron acceptor. In the case of the $(SO_3)_2$:CO trimer, there are two strong noncovalent bonds present. In the first place, there is the same S···C chalcogen bond that is the common feature of the dimer. This interaction is supplemented by an equally strong S···O chalcogen bond between the pair of SO_3 molecules. Due to its cyclic structure, with each of the three molecules acting as both electron donor and acceptor, this complex exhibits a synergistic positive cooperativity that amounts to nearly 1 kcal/mol.

In addition to the global minima, the potential energy surface of each heterotrimer contains a number of secondary minima as well. The stability of each can be explained on the basis of charge transfers and alignment of positive with negative extremes of the molecular electrostatic potentials.

Acknowledgments This work has been supported by the CTQ2012–35513–C02–02 (MINECO) project. LMA thanks the MICINN for a PhD grant (No. BES–2010–031225). Computer, storage and other resources from the CTI (CSIC) and from the Division of Research Computing in the Office of Research and Graduate Studies at Utah State University are gratefully acknowledged.

References

1. Hobza P, Müller-Dethlefs K (2009) Non-covalent interactions. The Royal Society of Chemistry, Cambridge
2. Schuster P, Zundel G, Sandorfy C (1976) The hydrogen bond. Recent developments in theory and experiments. North-Holland Publishing Co., Amsterdam
3. Scheiner S (1997) Hydrogen bonding: a theoretical perspective. Oxford University Press, New York
4. Grabowski SJ (2006) Hydrogen bonding—new insights. Springer, Dordrecht
5. Gilli G, Gilli P (2009) The nature of the hydrogen bond. Oxford University Press, Oxford
6. Lommerse JPM, Stone AJ, Taylor R, Allen FH (1996) J Am Chem Soc 118:3108–3116
7. Metrangolo P, Resnati G (2008) Science 321:918–919
8. Zierkiewicz W, Michalska D, Zeegers-Huyskens T (2010) Phys Chem Chem Phys 12:13681–13691
9. Adhikari U, Scheiner S (2012) Chem Phys Lett 532:31–35
10. Politzer P, Murray JS, Clark T (2013) Phys Chem Chem Phys 15:11178–11189
11. Solimannejad M, Malekani M, Alkorta I (2013) J Phys Chem A 117:5551–5557
12. Tschirschwitz S, Lonnecke P, Hey-Hawkins E (2007) Dalton Trans 14:1377–1382
13. Bühl M, Kilian P, Woollins JD (2011) ChemPhysChem 12:2405–2408
14. Del Bene JE, Alkorta I, Sanchez-Sanz G, Elguero J (2011) Chem Phys Lett 512:184–187
15. Scheiner S (2011) J Phys Chem A 115:11202–11209
16. Zahn S, Frank R, Hey-Hawkins E, Kirchner B (2011) Chem Eur J 17:6034–6038
17. Adhikari U, Scheiner S (2012) Chem Phys Lett 536:30–33
18. Scheiner S (2012) Acc Chem Res 46:280–288
19. Alkorta I, Elguero J, Del Bene JE (2013) J Phys Chem A 117:4981–4987
20. Azofra LM, Alkorta I, Elguero J (2014) ChemPhysChem. doi:10.1002/cphc.201402086
21. Alkorta I, Rozas I, Elguero J (2001) J Phys Chem A 105:743–749
22. Azofra LM, Altarsha M, Ruiz-López MF, Ingrosso F (2013) Theor Chem Acc 132:1326
23. Bauzá A, Mooibroek TJ, Frontera A (2013) Angew Chem Int Ed 52:12317–12321
24. Grabowski SJ (2014) Phys Chem Chem Phys 16:1824–1834
25. Minyaev RM, Minkin VI (1998) Can J Chem 76:776–788
26. Rosenfield RE, Parthasarathy R, Dunitz JD (1977) J Am Chem Soc 99:4860–4862
27. Burling FT, Goldstein BM (1992) J Am Chem Soc 114:2313–2320
28. Iwaoka M, Takemoto S, Tomoda S (2002) J Am Chem Soc 124:10613–10620
29. Werz DB, Gleiter R, Rominger F (2002) J Am Chem Soc 124:10638–10639
30. Bleiholder C, Werz DB, Köppel H, Gleiter R (2006) J Am Chem Soc 128:2666–2674
31. Sánchez-Sanz G, Alkorta I, Elguero J (2011) Mol Phys 109:2543–2552

32. Jabłoński M (2012) J Phys Chem A 116:3753–3764
33. Sánchez-Sanz G, Trujillo C, Alkorta I, Elguero J (2012) ChemPhysChem 13:496–503
34. Adhikari U, Scheiner S (2014) J Phys Chem A 118:3183–3192
35. Azofra LM, Scheiner S (2014) J Phys Chem A 118:3835–3845
36. Azofra LM, Alkorta I, Scheiner S (2014) J Chem Phys 140:244311
37. Azofra LM, Alkorta I, Scheiner S (2014) Phys Chem Chem Phys 16:18974–18981
38. Bauzá A, Alkorta I, Frontera A, Elguero J (2013) J Chem Theory Comput 9:5201–5210
39. Cavallo G, Metrangolo P, Pilati T, Resnati G, Terraneo G (2014) Cryst Growth Des 14:2697–2702
40. Goettel JT, Chaudhary P, Hazendonk P, Mercier HPA, Gerken M (2012) Chem Commun 48:9120–9122
41. Murray J, Lane P, Clark T, Riley K, Politzer P (2012) J Mol Model 18:541–548
42. Azofra LM, Scheiner S (2014) J Chem Phys 140:034302
43. Azofra LM, Scheiner S (2014) Phys Chem Chem Phys 16:5142–5149
44. Møller C, Plesset MS (1934) Phys Rev 46:618–622
45. Dunning THJ (1989) J Chem Phys 90:1007–1023
46. Woon DE, Dunning TH (1993) J Chem Phys 98:1358–1371
47. Boys SF, Bernardi F (1970) Mol Phys 19:553–566
48. Frisch MJ, Trucks GW, Schlegel HB, Scuseria GE, Robb MA, Cheeseman JR, Scalmani G, Barone V, Mennucci B, Petersson GA, Nakatsuji H, Caricato M, Li X, Hratchian HP, Izmaylov AF, Bloino J, Zheng G, Sonnenberg JL, Hada M, Ehara M, Toyota K, Fukuda R, Hasegawa J, Ishida M, Nakajima T, Honda Y, Kitao O, Nakai H, Vreven T, Montgomery J, J. A., Peralta JE, Ogliaro F, Bearpark M, Heyd JJ, Brothers E, Kudin KN, Staroverov VN, Kobayashi R, Normand J, Raghavachari K, Rendell A, Burant JC, Iyengar SS, Tomasi J, Cossi M, Rega N, Millam NJ, Klene M, Knox JE, Cross JB, Bakken V, Adamo C, Jaramillo J, Gomperts R, Stratmann RE, Yazyev O, Austin AJ, Cammi R, Pomelli C, Ochterski JW, Martin RL, Morokuma K, Zakrzewski VG, Voth GA, Salvador P, Dannenberg JJ, Dapprich S, Daniels AD, Farkas Ö, Foresman JB, Ortiz JV, Cioslowski J, Fox DJ, GAUSSIAN09, Revision D.01, Wallingford CT, 2009
49. Pople JA, Head-Gordon M, Raghavachari K (1987) J Chem Phys 87:5968–5975
50. Werner H-J, Knowles PJ, Manby FR, Schütz M, Celani P, Knizia G, Korona T, Lindh R, Mitrushenkov A, Rauhut G, Adler TB, Amos RD, Bernhardsson A, Berning A, Cooper DL, Deegan MJO, Dobbyn AJ, Eckert F, Goll E, Hampel C, Hesselmann A, Hetzer G, Hrenar T, Jansen G, Köppl C, Liu Y, Lloyd AW, Mata RA, May AJ, McNicholas SJ, Meyer W, Mura ME, Nicklaß A, Palmieri P, Pflüger K, Pitzer R, Reiher M, Shiozaki T, Stoll H, Stone AJ, Tarroni R, Thorsteinsson T, Wang M, Wolf A, MOLPRO 2012.1, 2012
51. Xantheas SS, Dunning TH (1993) J Chem Phys 99:8774–8792
52. Xantheas SS (1994) J Chem Phys 100:7523–7534
53. Bader RFW (1990) Atoms in molecules: a quantum theory. Clarendon Press, Oxford
54. Popelier PLA (2000) Atoms in molecules. An introduction. Prentice Hall, Harlow
55. Weinhold F, Landis CR (2005) Valency and bonding. A natural bond orbital donor-acceptor perspective. Cambridge Press, Cambridge
56. Chai J-D, Head-Gordon M (2008) Phys Chem Chem Phys 10:6615–6620
57. Keith TA, AIMAll (Version 13.11.04), Overland Park KS, USA, 2013
58. Glendening ED, Badenhoop JK, Reed AE, Carpenter JE, Bohmann JA, Morales CM, Landis CR, Weinhold F, NBO 6.0, Madison, USA, 2013
59. Rozas I, Alkorta I, Elguero J (2000) J Am Chem Soc 122:11154–11161
60. Bulat F, Toro-Labbé A, Brinck T, Murray J, Politzer P (2010) J Mol Model 16:1679–1691
61. Perdew JP, Burke K, Ernzerhof M (1996) Phys Rev Lett 77:3865–3868
62. Chałasiński G, Szczęśniak MM (2000) Chem Rev 100:4227–4252
63. Muenter JS (1975) J Mol Spectrosc 55:490–491
64. Reimers JR, Watts RO, Klein ML (1982) Chem Phys 64:95–114
65. Sergeeva AP, Averkiev BB, Zhai H-J, Boldyrev AI, Wang L-S (2011) J Chem Phys 134:224304
66. van der Pol A, van der Avoird A, Wormer PES (1990) J Chem Phys 92:7498–7504
67. Brookes MD, McKellar ARW (1999) J Chem Phys 111:7321–7328
68. Vissers GWM, Wormer PES, van der Avoird A (2003) Phys Chem Chem Phys 5:4767–4771

Theor Chem Acc (2015) 134:1587
DOI 10.1007/s00214-014-1587-1

REGULAR ARTICLE

Is the structure of hydroxide dihydrate $OH^-(H_2O)_2$? An ab initio path integral molecular dynamics study

Yudai Ogata · Yukio Kawashima · Kaito Takahashi · Masanori Tachikawa

Received: 31 July 2014 / Accepted: 15 October 2014 / Published online: 4 November 2014

Abstract We carried out ab initio path integral molecular dynamics simulations at room temperature for $OH^-(H_2O)_n$ ($n = 1, 2$) clusters to elucidate the ionic hydrogen bond structure with full thermal and nuclear quantum effects. We found that the hydrogen-bonded proton is located near the water molecule in the case of $n = 2$, while the proton is located at the center between hydroxide ion and the water molecule in the case of $n = 1$. Thus, the solvated hydroxide structure $HO{-}H\cdots OH$ is found in $n = 2$, while the proton sharing hydroxide structure $HO\cdots H\cdots OH$ is in $n = 1$. We found that the nature of hydrogen bonds significantly changes with the number of water molecules around the hydroxide. We also compared these results with those of $F^-(H_2O)_n$ ($n = 1, 2$) clusters.

Keywords Water cluster · Hydroxide ion · Nuclear quantum effect · Path integral molecular dynamics · Ionic hydrogen bond

Published as part of the special collection of articles derived from the 9th Congress on Electronic Structure: Principles and Applications (ESPA 2014).

Y. Ogata · M. Tachikawa (✉)
Graduate School of Nanobioscience, Yokohama City University, Yokohama 236-0027, Japan
e-mail: tachi@yokohama-cu.ac.jp

Y. Kawashima
RIKEN Advanced Institute for Computational Science, Kobe 650-0047, Japan

K. Takahashi
Institute of Atomic and Molecular Sciences, Academia Sinica, P.O. Box 23-166, Taipei 10617, Taiwan, ROC

1 Introduction

Hydroxide OH^-, fluoride F^-, or chloride Cl^- anions are well known to play an important role in aqueous chemistry. Many studies have targeted the quantification of molecular level hydration structure of anion–water clusters to understand its interesting characteristics such as the anomalously high mobility in aqueous solution [1–19]. These anions form ionic hydrogen bonds (IHBs), strong and short hydrogen bond relative to typical hydrogen bonds, with the first solvation shell water molecules. Therefore, the following difficulties arise in describing these anion–water clusters: large flexibility, and large anharmonicity of strong and short IHB. These difficulties have prevented elucidation of the detailed conformations of anion–water clusters.

Experimental vibrational spectra for water clusters with fluoride or hydroxide ions, $F^-(H_2O)_n$ and $OH^-(H_2O)_n$ ($n = 1$–5), were reported by Johnson and co-workers [3]. These vibrational spectra have shown that the first solvent shell includes four and three water molecules forming IHBs with the fluoride and hydroxide ions, respectively. Efforts have been made to assign the experimental spectra by theoretical studies employing conventional normal mode analysis with electronic structure calculations [9–13, 16]. Also, in the case of the IHBs between anion and one water molecule, it is clarified that the order of the IHB strengths is $OH^- > F^- > Cl^-$ from experimental vibrational spectra [15].

On theoretical grounds, for fluoride ion-water clusters $F^-(H_2O)_n$, Kawashima et al. carried out ab initio path integral molecular dynamics (PIMD) simulations included both nuclear quantum and thermal effects [5, 6]. They found that the hydrogen-bonded proton is located around the center between two heavy atoms, $F^-\cdots H\cdots OH$, in the case of $n = 1$. They also suggested that the two

structures were mixed in the case of $n = 2$; where one hydrogen-bonded proton is localized on a water molecule, $F^- \cdots HOH$, and the other proton is located around the center of the two heavy atoms, $F^- \cdots H \cdots OH$. For chloride ion-water clusters $Cl^-(H_2O)_n$, Wang et al. [8] carried out semi-empirical PIMD simulation. The hydrogen-bonded protons are localized on a water molecule, $Cl^- \cdots HOH$, regardless of the number of hydrogen-bonded water molecules. The difference among these two anions reflects the strength of IHBs: Fluoride ion with stronger IHB has the donor hydrogen closer to the acceptor anion, while IHB of chloride ion has the character similar to a typical hydrogen bond.

From the above relationship on $F^-(H_2O)_2$ and $Cl^-(H_2O)_2$, it can be expected that the hydrogen-bonded proton in hydroxide anion and water will be located at the center of the hydrogen bond, as similar to fluoride anion clusters due to the stronger IHB. In fact, in the case of $OH^-(H_2O)$, Zundel-type proton sharing hydroxide structure, $OH^- \cdots H^+ \cdots OH^-$, was suggested by both experimental vibrational and theoretical path integral studies [3, 18, 19]. From these studies, it is known that the proton sharing geometry are more dominant in $OH^-(H_2O)$ than that in $F^-(H_2O)$. However, for $OH^-(H_2O)_2$, questions still remain whether the structure will be $HOH \cdots OH^- \cdots HOH$, like the chloride system, or $HO \cdots H \cdots OH^- \cdots H \cdots OH$, like the fluoride systems.

For $OH^-(H_2O)_2$ Morita and Takahashi reported theoretical vibrational spectra obtained by multidimensional local mode calculations including anharmonic, thermal, and partial nuclear quantum effects [16]. They assigned the experimental peaks [3] as the first overtone of the IHB OH stretching vibration. In their study, they used two stable conformations of $OH^-(H_2O)_2$, but the experimental spectra could not be fully reproduced. One may wonder that the failure in the previous work for $n = 2$ may be due to the existence of $OH^- \cdots H^+ \cdots OH^- \cdots H_2O$ or $OH^- \cdots H_3O^+ \cdots OH^-$ structures, which may obtained in only PIMD simulations, and such investigation is highly beneficial to understand geometries of hydrogen-bonded water clusters systematically.

Since the previous application of the powerful PIMD method was limited to $n = 1$, we perform PIMD simulation of $OH^-(H_2O)_2$ to elucidate the IHB structures with full treatment of thermal and nuclear quantum effects in this study. We also carry out PIMD simulation for the case of $n = 1$ to compare the hydrogen bond structures with $n = 2$ and to understand the effect of the additional ion-water hydrogen bond on the IHB. We also compare the hydrogen-bonded structures in hydroxide ion-water clusters to that in our previous results of fluoride ion-water clusters [5, 6].

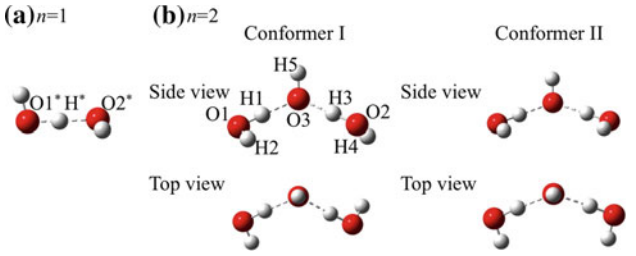

Fig. 1 Schematic illustrations of stable conformers for $OH^-(H_2O)_n$ ($n = 1, 2$) obtained by electronic structure calculations

2 Computational details

We carried out ab initio PIMD simulations for $OH^-(H_2O)_n$ ($n = 1, 2$). Here, both oxygen and hydrogen are treated as quantum mechanical particles by beads expansion. PIMD simulations were performed at 300 K with massive Nosé–Hoover chain thermostat [20] to achieve canonical ensemble in the same manner as in our previous works [18, 21–23]. For $n = 1$ and 2, PIMD simulation was performed for 200,000 steps with 16 beads after a thermal equilibration of 5,000 steps using time step size of 0.1 fs. All electronic structure calculations in the PIMD simulation were performed by B3LYP functional [24, 25] with TZVP basis set with the resolution of identity approximation (RI-B3LYP/TZVP) [26, 27] in TURBOMOLE package [28]. Figure 1 shows the schematic illustrations of (a) $OH^-(H_2O)$ and (b) $OH^-(H_2O)_2$ optimized by the conventional electronic structure calculations, with atomic numberings.

In this article, we focus on the relative positions of IHB hydrogen atoms to analyze the hydrogen bond structure. We introduce δH^* for $n = 1$, and $\delta H1$ and $\delta H3$ for $n = 2$ as the proton transfer coordinates defined by

$$\delta H^* = R_{O1^*H^*} - R_{O2^*H^*} \tag{1}$$

$$\delta H1/\delta H3 = R_{O1H1/O2H3} - R_{O3H1/O3H3} \tag{2}$$

respectively. Negative δH values correspond to structures with hydrogen-bonded proton localized to a water molecule ($OH^- \cdots HOH$). $\delta H = 0$ corresponds to structures with proton shared by the two heavy atoms ($OH^- \cdots H^+ \cdots OH^-$). We also analyzed the heavy atom distance of the hydrogen bonds between $O1^*$ and $O2^*$ atoms ($R_{O1^*O2^*}$) in $n = 1$, and the distances between O1 and O3 atoms (R_{O1O3}) and that between O2 and O3 atoms (R_{O2O3}) in $n = 2$.

To quantify the accuracy of our present calculation level, in Table 1, we compare the values of δH^*, $\delta H1$, $\delta H3$, $R_{O1^*O2^*}$, R_{O1O3}, and R_{O2O3} obtained by RI-B3LYP/TZVP level, as well as those previously reported by MP2/6-311++G(3df,3pd) level [16]. The δH^* value in $n = 1$ of RI-B3LYP/TZVP level is 0.002 Å. This indicates that

Table 1 Geometrical values obtained by electronic structure calculations (RI-B3LYP/TZVP and MP2/6-311 ++G(3df,3pd) levels), and average values obtained by PIMD simulations for $OH^-(H_2O)_n$ ($n = 1, 2$)

	$n = 1$				
	Static				PIMD
	RI-B3LYP		MP2		
δH^*	0.002		0.221		0.003 (6)
$R_{O1^*O2^*}$	2.457		2.463		2.500 (2)
	$n = 2$				
	Static conf. I		Static conf. II		PIMD
	RI-B3LYP	MP2	RI-B3LYP	MP2	
$\delta H1$	−0.509	−0.507	−0.494	−0.493	−0.512 (10)
$\delta H3$	−0.478	−0.485	−0.493	−0.493	−0.466 (6)
R_{O1O3}	2.582	2.565	2.574	2.559	2.613 (6)
R_{O2O3}	2.565	2.554	2.574	2.559	2.574 (6)

Statistical errors of average values are shown in parentheses. Values are given in Å

the potential energy curve of RI-B3LYP level along the proton transfer coordinate shows a quasi-symmetric single-well structure. The δH^* value obtained by MP2/6-311++G(3df,3pd) level is 0.221 Å, which shows a symmetric double-well structure. However, the barrier height of this potential energy curve is extremely small with a value of 0.05 kcal/mol. Thus, it can be said that a negligible barrier is found for $n = 1$. The values in $n = 2$ of RI-B3LYP/TZVP level give close agreement with that of MP2/6-311++G(3df,3pd) level. The differences are within ~0.02 Å. From these results, we are confident on the accuracy of RI-B3LYP/TZVP and will use this method for on-the-fly ab initio PIMD simulations.

3 Results and discussion

We first focus on the heavy atom distances of the hydrogen bonds between oxygen atoms in $n = 1$ and 2 to analyze the hydrogen bond structure and its character. Figure 2 shows the one-dimensional distributions of $R_{O1^*O2^*}$ in $n = 1$, and R_{OO}^{sum} (a sum of distributions with respect to R_{O1O3} and R_{O2O3}) in $n = 2$. The expectation values with their statistical errors are shown in Table 1. We found that the distribution of $R_{O1^*O2^*}$ in $n = 1$ is much shorter and much sharper than that of R_{OO}^{sum} in $n = 2$. The peak positions of each distribution in $n = 1$ and 2 are 2.485 and 2.575 Å, respectively. The distribution of $n = 2$ is found in the range of typical hydrogen bond, while for $n = 1$ it is extremely shorter. Furthermore, the distribution in $n = 2$ is much broader than that of $n = 1$, reflecting the floppy motion of the weaker hydrogen bond. We found a significant difference between the two systems.

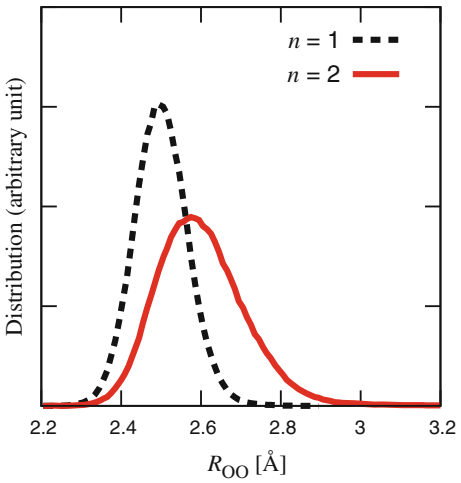

Fig. 2 One-dimensional distributions of $R_{O1^*O2^*}$ and R_{OO}^{sum} (a sum of distributions of R_{O1O3} and R_{O2O3}) for $OH^-(H_2O)_n$ ($n = 1, 2$)

We next analyze the relative position of the IHB proton, to understand the difference of the hydrogen bond character between the two systems. We show the distributions of the relative positions of the hydrogen-bonded protons between oxygen atoms δHs for $OH^-(H_2O)_n$ ($n = 1, 2$) in Fig. 3a. Here, we note that the distribution in $n = 2$ is the sum of the distributions of $\delta H1$ and $\delta H3$. The expectation values of δH^*, $\delta H1$, and $\delta H3$ and their statistical errors are shown in Table 1. The distribution of δH^* of $n = 1$ shows a single broad peak centered at 0.0 Å, which indicates that the hydrogen-bonded proton is delocalized and located at the center between the two oxygen atoms with frequent proton transfer.

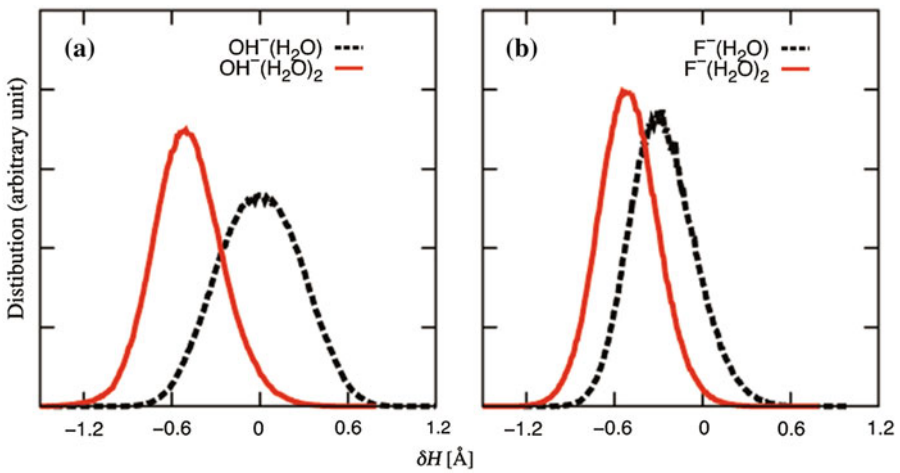

Fig. 3 One-dimensional distributions of δH^{*} and δH^{sum} (a sum of distributions of $\delta H1$ and $\delta H3$) for **a** $OH^{-}(H_2O)_n$ ($n = 1, 2$) and **b** $F^{-}(H_2O)_n$ ($n = 1, 2$)

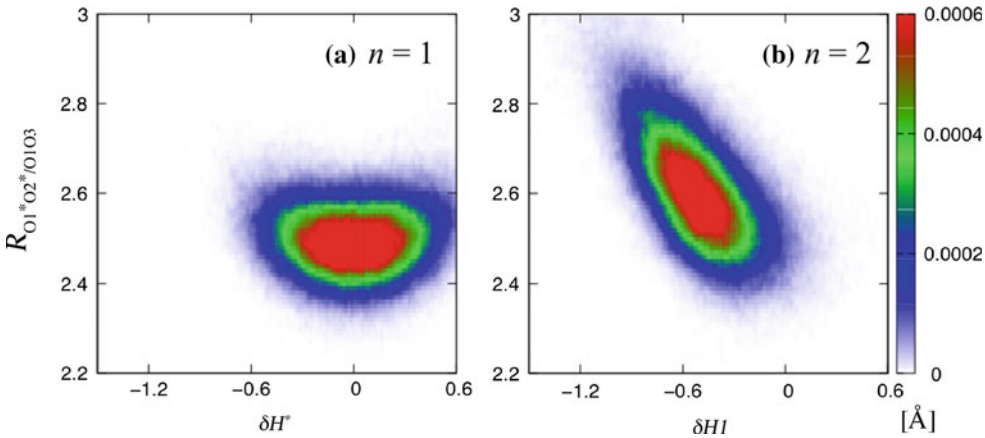

Fig. 4 Two-dimensional distributions with respect to **a** δH^{*} and $R_{O1^{*}O2^{*}}$, and **b** $\delta H1$ and R_{O1O3} for $OH^{-}(H_2O)_n$ ($n = 1, 2$), respectively

On the other hand, in the case of $n = 2$, the values of δHs are distributed around -0.5 Å, which indicates that the protons are localized near the water molecules. This tendency that the proton delocalizes in $n = 1$ and it localizes in $n = 2$ is also seen in protonated cation water clusters [18, 29, 30]. Similar to deprotonated anion–water cluster, $OH^{-}(H_2O)$ and $OH^{-}(H_2O)_2$, the protonated proton is delocalized between oxygen atoms in $H_3O^{+}(H_2O)$, while the protons are localized at oxygen atoms of water molecules in $H_3O^{+}(H_2O)_2$. Furthermore, the width of distributions in $n = 2$ is narrower than that in $n = 1$. This tendency is opposite to R_{OO}. Discussions on the tendency are given below in the two-dimensional distributions. Strictly speaking, very small proton transfer probability of 2.6 % was found in Fig. 3a. These difference in Fig. 3a arises from the frequent proton transfer seen in only $n = 1$. We found that protons localize in $n = 2$, as seen in cation water clusters.

In our previous studies [18, 19, 21–24], we gained insights of hydrogen bond structures by analyzing the relation between the relative position of the hydrogen-bonded proton and the heavy atomic distance. The correlation between these two structural parameters clarified the hydrogen bond character in the previous studies. Thus, here, we analyzed the hydrogen bond structure of $OH^{-}(H_2O)_n$ ($n = 1, 2$) in a similar manner. The two-dimensional distributions with respect to (a) δH^{*} and $R_{O1^{*}O2^{*}}$ in $n = 1$ and (b) $\delta H1$ and R_{O1O3} in $n = 2$ are shown in Fig. 4. In Fig. 4a of $n = 1$, large distribution is found in the region around $\delta H^{*} = \sim 0.0$ Å and $R_{O1^{*}O2^{*}} = \sim 2.5$ Å, which is symmetric in the $R_{O1^{*}O2^{*}}$ direction with proton located at the center of the hydrogen bond. The $R_{O1^{*}O2^{*}}$ value is the smallest at $\delta H^{*} = \sim 0.0$ Å, while the $R_{O1^{*}O2^{*}}$ elongates as the proton becomes closer to the oxygen atoms of water. Such distribution is due to the characteristic feature of so-called low-barrier hydrogen bonds (LBHB) reported in refs [17–19]: a short heavy atom distance and a position of proton located at the center of the hydrogen bond [18, 19, 21–23]. So for $n = 1$ inclusion of thermal and nuclear quantum effects causes the cluster to take $OH^{-}\cdots H^{+}\cdots OH^{-}$ structure, which is different from the previously suggested static minimum of $HOH\cdots OH^{-}$ [18, 19].

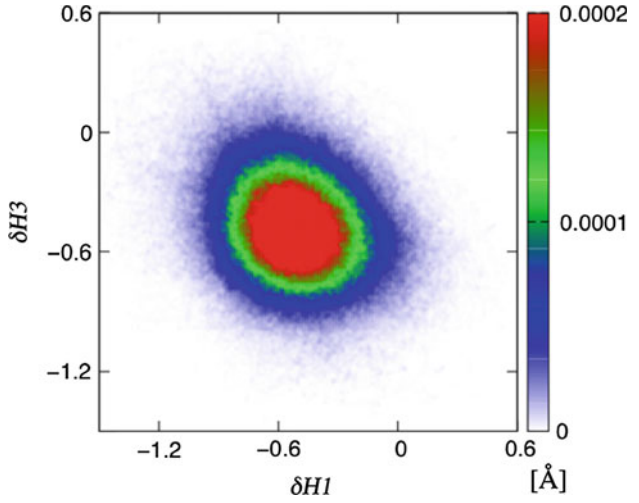

Fig. 5 Two-dimensional distribution with respect to $\delta H1$ and $\delta H3$ for $OH^-(H_2O)_2$

On the other hand, in Fig. 4b of $n = 2$, large distribution is found in the region around $\delta H^* = \sim -0.6$ Å and $R_{O1^*O2^*} = \sim 2.6$ Å. The proton lies near the oxygen of water molecules and the heavy atom distance becomes longer as the proton moves toward oxygen atoms. In addition, strong correlation is found between the relative position of the proton and the distance between two oxygen atoms in $n = 2$, while such tendency is not found in $n = 1$. The strong correlation is due to the fact that almost no proton transfer takes place in the case of $n = 2$. Therefore, in the case of $n = 2$, we are seeing a characteristic of a moderate hydrogen bond, not LBHB as in $n = 1$. In $n = 2$, the cluster stayed as a solvated hydroxide structure as found in the static calculations even including thermal and nuclear quantum effects.

We next analyzed the relationship between the two hydrogen bonds in $n = 2$ by the two-dimensional distribution between δH1 and δH3 shown in Fig. 5 to investigate the correlation between the two IHBs. From Fig. 5, we find that $\delta H1$ and $\delta H3$ fluctuate around the wide region centered at $\delta H1 = -0.4$ Å and $\delta H3 = -0.4$ Å. However, no distribution is found at the region around $\delta H1 = 0.0$ Å and $\delta H3 = 0.0$ Å. This indicates that in our PIMD simulation the probability of observing both hydrogen atoms near the hydroxide ion at the same time, the $HO^- \cdots H_3O^+ \cdots OH^-$ structure, is completely negligible. Since there are little distribution for either $\delta H1 = 0.0$ Å or $\delta H3 = 0.0$ Å, the formation of $OH^- \cdots H^+ \cdots OH^- \cdots H_2O$ structure is found to be a quite rare-event in our simulation.

Finally, we would like to focus on $OH^-(H_2O)_n$ and $F^-(H_2O)_n$ anion–water clusters. In these anion clusters, it is known that the hydrogen-bonded proton is located around the center of two heavy atoms relative to classical simulation in the case of $n = 1$. However, the systematic understanding on the difference between $n = 1$ and $n = 2$ is still not clear. So, we compare the distribution of δH in OH^- clusters to that in fluoride anion clusters. The one-dimensional distributions of $F^-(H_2O)_n$ ($n = 1, 2$) simulated in Refs. [5, 6] are shown in Fig. 3b. Note that the distribution in $n = 2$ is the sum of the distributions obtained by two hydrogen bonds, similar to R_{OO}^{sum} in hydroxide ion cluster. From Fig. 3a, b, the distribution of OH^- clusters is broader than that of F^- clusters regardless of the number of water molecules. Also, the positions of distributions move to a negative direction as the number of water molecules increases in both OH^- and F^- clusters. It means that the proton is located near the water molecules with increase in hydration. The peak positions of each distribution in Fig. 3 are 0.000 Å for $OH^-(H_2O)$, −0.505 Å for $OH^-(H_2O)_2$, −0.275 Å for $F^-(H_2O)$, and −0.545 Å for $F^-(H_2O)_2$, respectively. This means that hydroxide ion strongly withdraws the hydrogen-bonded proton from water molecules, therefore is a stronger proton acceptor than fluoride ion. This agrees with the order of the IHB strengths found in experiments [15]. We note that shifts of the δH values from $n = 1$ to $n = 2$ in hydroxide and fluoride ions are 0.505 and 0.270 Å, respectively. Such significant difference between the shift in hydroxide and fluoride ions come from the proton being at the center between the heavy atoms in $OH^-(H_2O)$ completely. In other words, it is indicated that a specific property seen in $n = 1$ of hydroxide ion decreases with the addition of the second water molecule. This trend indicates the magnitude of the redshift from $n = 2$ to $n = 1$ in OH^- clusters should be larger than that in F^- clusters in the experimental vibrational spectra [3, 15].

4 Conclusion

We carried out ab initio path integral molecular dynamics (PIMD) simulations for $OH^-(H_2O)_n$ ($n = 1, 2$) at 300 K to elucidate the ionic hydrogen bond structures. We found that the ionic hydrogen-bonded protons are located near the water molecules, and proton transfer structure is found to be quite rare in the case of $n = 2$, while the proton is located at the center between oxygen atoms in the case of $n = 1$. From these results, the hydrogen bond structure should be described as "$OH^- \cdots H^+ \cdots OH^-$" not "$OH^-(H_2O)$" in $n = 1$, but as "$OH^-(H_2O)_2$" in $n = 2$. Therefore, in the cluster of OH^- with water molecules, we found that the nature of hydrogen bonds is significantly changed with the number of hydrogen-bonded water molecules. Furthermore, we also found that the difference of the position of hydrogen-bonded proton between $n = 1$ and 2 in hydroxide cluster is quite larger than that in fluoride cluster by comparing the δH values. From these results, it is suggested that the magnitude of redshift of IHB OH

stretching vibration from $n = 2$ to $n = 1$ in $OH^-(H_2O)_2$ is greater than that in $F^-(H_2O)_2$.

Here, we analyzed the structure of ionic hydrogen bond in $n = 1$ and 2. We next aim to reproduce the vibrational spectra observed by Johnson and co-workers [3]. In that case, we need to perform simulation including nuclear quantum effect at various low temperatures of 50–150 K to reproduce the corresponding experimental condition. In the work of Suzuki et al. [19], the hydrogen delocalization for $OH^-(H_2O)$ was enhanced at lower temperature. The large nuclear quantum fluctuation at low temperature plays a key role in hydrogen delocalization. Therefore, in our future work, we plan to carry out PIMD simulation for $OH^-(H_2O)_2$ at various low temperatures and analyze the hydrogen bond structure in detail.

Acknowledgments Financial support was provided by Grant-in-Aid for Scientific Research and for the priority area by Ministry of Education, Culture, Sports, Science, and Technology, Japan for YK and MT. KT thanks Academia Sinica, National Center for High Performance Computing of Taiwan and Ministry of Science and Technology (NSC100-2113-M-001-004-MY2, NSC 102-2113-M-001-012-MY3) of Taiwan for support.

References

1. Agmon N (2000) Mechanism of hydroxide mobility. Chem Phys Lett 319:247–252
2. Tuckerman ME, Marx D, Parrinello M (2002) The nature and transport mechanism of hydrated hydroxide ions in aqueous solution. Nature 417:925–929
3. Robertson WH, Diken EG, Price A, Shin J-W, Johnson MA (2003) Spectroscopic Determination of the OH^- Solvation Shell in the $OH^-(H_2O)_n$ clusters. Science 299:1367–1372
4. Ludwig R (2003) New insight into the transport mechanism of hydrated hydroxide ions in water. Angew Chem Int Ed 42:258–260
5. Suzuki K, Tachikawa M, Shiga M (2010) Efficient ab initio path integral hybrid Monte Carlo based on the fourth-order Trotter expansion: application to fluoride ion-water cluster. J Chem Phys 132:144108
6. Kawashima Y, Suzuki K, Tachikawa M (2013) Ab initio Path integral simulations for the fluoride ion-water clusters: competitive nuclear quantum effect between—water and water-water hydrogen bonds. J Phys Chem A 117:5205–5210
7. Choi J-H, Kuwata KT, Cao Y-B, Okumura M (1998) Vibrational spectroscopy of the $Cl^-(H_2O)_n$ anion clusters, n = 1–5. J Phys Chem A 102:503–507
8. Wang Q, Suzuki K, Nagashima U, Tachikawa M, Yan S (2013) Path integral molecular dynamics study of nuclear quantum effect on small chloride water clusters of $Cl^-(H_2O)_{1-4}$. Chem Phys 419:229–236
9. Xantheas SS (1995) Theoretical study of hydroxide ion-water clusters. J Am Chem Soc 117:10373–10380
10. Baik J, Kim J, Majumdar D, Kim KS (1999) Structures, energetics, and spectra of fluoride–water clusters $F^-(H_2O)_n$, n = 1–6: Ab initio study. J Chem Phys 110:9116–9127
11. Chandhuri C, Wang Y-S, Jiang JC, Lee YT, Chang H-C, Niedner-Schatteburg G (2001) Infrared spectra and isomeric structures of hydroxide ion-water clusters $OH^-(H_2O)_{1-5}$: a comparison with $H_3O^+(H_2O)_{1-5}$. Mol Simul 99:1161–1173
12. Chaban GM, Xantheas SS, Gerber RB (2003) Anharmonic vibratinal spectroscopy of the $F^-(H_2O)_n$ complexes, n = 1, 2. J Phys Chem A 107:4952–4956
13. McCoy AB, Huang X, Carter S, Bowman JM (2005) Quantum studies of the vibrations in $H_3O_2^-$ and $D_3O_2^-$. J Chem Phys 123:064317
14. Samson CCM, Klopper W (2002) Ab initio calculation of proton barrier and binding energy of the $(H_2O)OH^-$ complex. J Mol Struc 586:201–208
15. Roscioli JR, Diken EG, Johnson MA, Horvath S, McCoy AB (2006) Prying apart a water molecule with anionic H-bonding: a comparative spectroscopic study of the X − H2O(X = OH, O, F, Cl, and Br) binary complexes in the 600–3800 cm–region. J Phys Chem A 110:4943–4952
16. Morita M, Takahashi K (2013) Multidimensional local mode calculations for the vibrational spectra of OH−(H2O)2 and OH−(H2O)2·Ar. Phys Chem Chem Phys 15:14973–14985
17. Tuckerman ME, Marx D, Klein LM, Parrinello M (1997) On the quantum nature of the shared proton in hydrogen bonds. Science 275:817–820
18. Tachikawa M, Shiga M (2005) Geometrical H/D Isotope effects on hydrogen bonds in charged water clusters. J Am Chem Soc 127:11908–11909
19. Suzuki K, Shiga M, Tachikawa M (2008) Temperature and isotope effects on water cluster ions with path integral molecular dynamics based on the fourth order Trotter expansion. J Chem Phys 129:144310
20. Martyna GJ, Klein ML, Tuckerman M (1992) Nosé–Hoover chains: the canonical ensemble via continuous dynamics. J Chem Phys 97:2635
21. Kawashima Y, Tachikawa M (2013) Nuclear quantum effect on intramolecular hydrogen bond of hydrogen maleate anion: an ab initio path integral molecular dynamics study. Chem Phys Lett 571:23–27
22. Kawashima Y, Tachikawa M (2014) Ab initio path integral molecular dynamics study of the nuclear quantum effect on out-of-plane ring deformation of hydrogen maleate anion. J Chem Theory Comput 10:153–163
23. Ogata Y, Daido M, Kawashima Y, Tachikawa M (2013) Nuclear quantum effects on protonated lysine with asymmetric low barrier hydrogen bond: an ab initio path integral molecular dynamics study. RSC Adv 3:25252–25257
24. Becke AD (1988) Density-functional exchange-energy approximation with correct asymptotic behaviour. Phys Rev A 38:3098–3100
25. Lee C, Yang W, Parr RG (1988) Development of the Colle-Salvetti correlation-energy formula into a functional of the electron density. Phys Rev B 37:785–789
26. Vahtras O, Almlöf J, Feyereisen MW (1993) Integral approximations for LCAO-SCF calculations. Chem Phys Lett 213:514–518
27. Feyereisen MW, Fitzgerald G, Komornicki A (1993) Use of approximate integrals in ab initio theory. An application in MP2 energy calculations. Chem Phys Lett 208:359–363
28. Ahlrichs R, Bär H, Häser M, Horn H, Kölmel C (1989) Electronic structure calculations on workstation computers: the program system turbomole. Chem Phys Lett 162:165–169
29. Kaledin M, Wood CA (2010) Ab initio studies of structural and vibrational properties of protonated water cluster $H_7O_3^+$ and its deuterium isotopologues: an application of driven molecular dynamics. J Chem Theory Comput 6:2525–2535
30. Parthasarathi R, Subramanian V, Sathyamurthy N (2007) Hydrogen bonding in protonated water clusters: an atoms-in-molecules perspective. J Phys Chem A 111:13287–13290

Theor Chem Acc (2015) 134:17
DOI 10.1007/s00214-014-1609-z

REGULAR ARTICLE

Solvation effects on electronic polarization and reactivity indices at the air–water interface: insights from a theoretical study of cyanophenols

Marilia T. C. Martins-Costa · Manuel F. Ruiz-Lopez

Received: 20 October 2014 / Accepted: 16 December 2014 / Published online: 31 January 2015

Abstract We report a theoretical analysis of solvation effects on the molecular properties of *ortho*, *meta,* and *para* cyanophenol isomers at the air–water interface. The study was carried out using a self-consistent image charge polarizable continuum model, which allows to get clear insights on the solvation process and to rationalize the calculated differences with respect to solvation in bulk water. The results show that polarization at the air–water interface cannot be compared to polarization in a bulk solvent of low or medium polarity, as sometimes claimed. Indeed, though the calculated induced dipole moments at the interface are always significantly smaller than the induced moments in bulk water, other reactivity indices such as the chemical potential experience the largest solvation effects at the interface. Moreover, the relationship between solvation energies and solute polarity at the interface is not as simple as in the case of bulk solvation. In this respect, the study emphasizes the key role of the topology of the electrostatic field created by the polarized medium because its high anisotropy at the interface makes the molecular properties to be very dependent on the relative orientation of the solute. These findings can explain the higher chemical and photochemical reactivity previously described for some molecules and radicals of atmospheric interest.

Keywords Aqueous interfaces · Solvation effects · Reactivity indices · Electronic polarization · Dielectric model · Cyanophenol

1 Introduction

In recent years, significant progress has been made toward the understanding of chemical reactions in bulk solvents but the study of reactions at liquid interfaces is still at an early stage. This issue is the key, however, to reach a better understanding of atmospheric and environmental chemistry because aqueous interfaces are ubiquitous on Earth. Thus, for instance, in recent studies carried out through combined QM/MM simulations [1–3] (QM/MM = Quantum Mechnics and Molecular Mechanics), we have shown that molecules adsorbed at the air–water interface undergo chemical and/or photochemical transformations that differ noticeably from gas-phase or bulk water reactions, which may present significant atmospheric impact. A paramount example is the case of the OH radical formation from ozone photolysis at the surface of cloud water droplets; we predicted this process to be enhanced by four orders of magnitude at the water surface (compared to gas-phase reactions), contributing to the oxidizing capacity of the troposphere on a global scale [3].

Central to the understanding of chemical reactivity on water surfaces is the study of electronic polarization effects. In general, the properties of compounds interacting with a liquid interface have been considered to be

Published as part of the special collection of articles derived from the 9th Congress on Electronic Structure: Principles and Applications (ESPA 2014).

Electronic supplementary material The online version of this article (doi:10.1007/s00214-014-1609-z) contains supplementary material, which is available to authorized users.

M. T. C. Martins-Costa · M. F. Ruiz-Lopez
SRSMC, University of Lorraine, BP 70239,
54506 Vandoeuvre-les-Nancy, France

M. T. C. Martins-Costa · M. F. Ruiz-Lopez (✉)
UMR 7565, CNRS, BP 70239, 54506 Vandoeuvre-les-Nancy, France
e-mail: Manuel.Ruiz@univ-lorraine.fr

intermediate between the two bulk phases. Moreover, some works have claimed that polarity at liquid interfaces is close to the arithmetic average of the polarity of the two bulk phases [4, 5], and that polarization effects at the air–water interface are similar to those observed in bulk butyl ether [4–6]. More recent sum-frequency generation (SFG) experiments [7] have shown, however, that polarization of some coumarin derivatives is strongly dependent on the relative orientation of the solute with respect to the interface, which in turn depends on the molecular shape and specific substituents of the derivative considered. Likewise, interface-sensitive vibrational SFG spectroscopy measurements [8] for *meta*- and *para*-cyanophenol revealed quite different orientations of the molecules with respect to the interface. These compounds have atmospheric and environmental relevance since some derivatives are widely used as bactericides and pesticides.

In this work, our aim was to rationalize the conclusions reached in previous theoretical and experimental studies trying to get further insights into the phenomenon of electronic polarization for molecules interacting with a water surface. We have carried out quantum mechanical calculations for three cyanophenol derivatives at the air–water interface, and in gas phase and bulk water for the sake of comparison. Since our objective was to get a better understanding of polarization effects (and the relationship with solute orientation) rather than getting very accurate data for specific systems, we chose a simple dielectric model. Dielectric models are widely used to study bulk solvation problems and are useful to obtain the main trends in modelling complex systems for which more elaborated approaches such as the combined QM/MM molecular dynamics simulation would be too costly.

2 Model

Dielectric models have often been described in the literature, and here, we will briefly summarize the main characteristics of our approach. A dielectric continuum medium is used to represent the solvent. It is polarized by the electronic and nuclear charge distributions of the solute, which in turn generates an electrostatic potential (the so-called reaction field) that interacts with the solute charges. The solute–solvent equilibrium polarization is obtained in a self-consistent calculation of the solute wave function. In the original method developed by Rivail and coworkers [9–13], a multipole moment expansion of the reaction field potential was implemented but different approaches have been proposed by Tapia and Goscinski [14, 15], Hilton-McCreery et al. [16], Tomasi and coworkers [17–19], and Cramer, Truhlar and coworkers [20–25] among others.

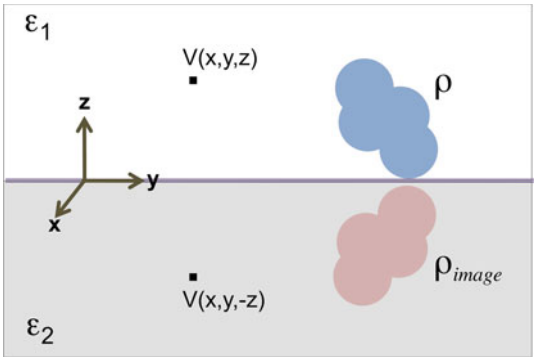

Fig. 1 Dielectric interface model illustrating the "image charge" method to calculate the electrostatic potential V

The widely used PCM (Polarizable Continuum Model) approach of the Pisa group has recently been extended [26] to the case of a diffuse dielectric interface, and expressions for the solvation energy contributions (electrostatics, dispersion, repulsion, and cavitation) have been provided. The SM5 family of universal solvation models of the Minnesota group has also been extended to determine the partitioning between the vapor phase and the macroscopic surface of liquid water [27].

In our approach, the reaction field is calculated using the "image charge" equations. Accordingly (see Fig. 1), the total potential V_{total} at (x, y, z) when a molecule of charge distribution ρ interacts with a planar interface (xy plane) is given by [28]:

$$V_{\text{total}}(x,y,z) = V(x,y,z) - \frac{\varepsilon_2 - \varepsilon_1}{\varepsilon_2 + \varepsilon_1} V(x,y,-z)$$

where V is the electrostatic potential generated by ρ in the medium of dielectric constant ε_1. The second term in the right expression corresponds to the reaction potential due to the dielectric ε_2 and is equivalent to the potential created at (x, y, z) by the image charge distribution ρ_{image}, scaled by the factor $(\varepsilon_2 - \varepsilon_1)/(\varepsilon_2 + \varepsilon_1)$. In this model, one assumes a perfectly planar interface separating two homogeneous dielectrics with all solute charges lying on one of the two dielectric media. In a more elaborated model, one could assume a diffuse interface in which the permittivity of the medium is position dependent and the solute can partially be embedded in the two media. Though this case can be treated [26], we chose the simple planar interface model because it provides a straightforward, intuitive picture of the solute polarization. As pointed out below, getting accurate results for solvation effects at interfaces does inevitably require the use of statistical simulations because one has to account for the large fluctuations associated with reorientational motions of the solute, as well as to the solute moving forth and back across the interface.

In the self-consistent image charge dielectric model (SCIC) used here, the reaction field potential is calculated from a molecular charge distribution that fits the electrostatic potential of the solute [29, 30]. The advantage of using this approximation (instead of carrying out a rigorous calculation of the molecular potential) is that errors due to penetration of the electronic density into the dielectric are avoided. The approximation has proven to provide very accurate solvation energies in the case of bulk solvation [11]. The solute is assumed to be "in contact" with the planar interface, the molecular envelop being defined by the atomic van der Waals radii multiplied by a standard factor 1.2, widely used in bulk solvation calculations. This factor was empirically introduced on the basis of different tests and calculations [19], but it can be derived from the relationship existing between liquid densities and van der Waals molecular volumes [11]. Energies and ground-state molecular properties are calculated at the B3LYP/6-311+G(d) level [31], although some calculations using other density functional methods and basis sets have been carried out to check the dependence of the results on the computational method. The molecular geometries have been optimized in gas phase without further optimization at the air–water interface or bulk water; moreover, only the most stable conformer in gas phase has been considered. This choice has been made because the main goal of the work was to discuss electronic polarization effects, which is facilitated by comparing electronic properties for the same geometries. Polarization effects are discussed in terms of induced dipole moment and modification of reactivity indices in conceptual density functional theory [32, 33], namely, the chemical potential μ, the hardness η, and the electrophilicity ω, corresponding to the following definitions:

$$\mu = \frac{1}{2}(\varepsilon_{\mathrm{HOMO}} + \varepsilon_{\mathrm{LUMO}})$$

$$\eta = (\varepsilon_{\mathrm{LUMO}} - \varepsilon_{\mathrm{HOMO}})$$

$$\omega = \frac{\mu^2}{\eta}$$

where $\varepsilon_{\mathrm{HOMO}}$ and $\varepsilon_{\mathrm{LUMO}}$ are the HOMO and LUMO energies of the molecule, respectively. Calculations have been carried out using the Gaussian 09 program [34] for the quantum mechanical computations and the code developed by us for SCIC calculations at dielectric interfaces. In the calculations presented below, we model the air–water interface by a dielectric interface; the dielectric constants of the two media are 1 and 78.4, corresponding, respectively, to the relative permittivity of vacuum and liquid water at 298 K.

3 Results

3.1 Energetics, preferred orientations

The electrostatic interaction energy as a function of the relative isomer interface orientation angles has been computed, and the corresponding potential energy surfaces (PES) are illustrated in Fig. 2. The figure also shows the most stable orientations predicted for the three isomers. In the case of the *para* isomer, we have selected two different orientations because they exhibit very close interaction energies. Table 1 summarizes the values for the CN bond—interface angles, interaction energies, dipole moments, and reactivity indices calculated for the most stable orientations.

In the case of the *ortho* and *meta* isomers, the molecule is oriented in such a way that the two polar groups (CN and OH) are in contact with the water surface, which is the expected result. In the case of the *para* isomer, such a situation is not possible and the most stable structures display only one polar group (either CN or OH) oriented toward the water surface [*para* (1) and *para* (2) orientations, respectively]. The calculated orientation for the *meta* isomer is in good agreement with the available SFG experiment [8], which predicts a polar angle θ in the range 96°–106° (θ is the angle formed by the CN bond, and the Z axis perpendicular to the interface; $\theta = 0°$ stands for CN bond vector pointing toward the air). In the case of the *para* isomer, the SFG experiments lead to θ values in the range 65°–80°, which are intermediate between the predicted values for the two *para* (1) and *para* (2) orientations. Our calculations suggest that in this case, there is not a single stable orientation of the molecule but two and that the SFG data do probably correspond to the average of two different signals.

The interaction energies in Table 1 show some interesting trends. Despite the similar polarity of the *ortho* and *meta* isomers, the *meta* isomer is much more stabilized at the interface. Note that it also displays a larger polarization than the *ortho* isomer, while in bulk solvent the two molecules display a similar induced moment. Likewise, despite the much higher polarity of the *para* derivative compared to the *ortho* and *meta* isomers, it does not display a larger interaction energy, as expected from basic considerations and confirmed by the calculations in bulk solution; in fact, the interaction energy value is intermediate between the *ortho* and *meta* isomer values. These trends were confirmed by single-point energy calculations using larger basis set (B3LYP/aug-cc-pVTZ calculations) or different density functionals (BLYP/6-311 + G(d) and PBE0/6-311 + G(d) calculations); in all cases, the absolute value of the solvation energy at the interface for the cyanophenol isomers remains in the range 2.6–2.8 kcal/mol (*ortho*), 5.0–5.5 kcal/

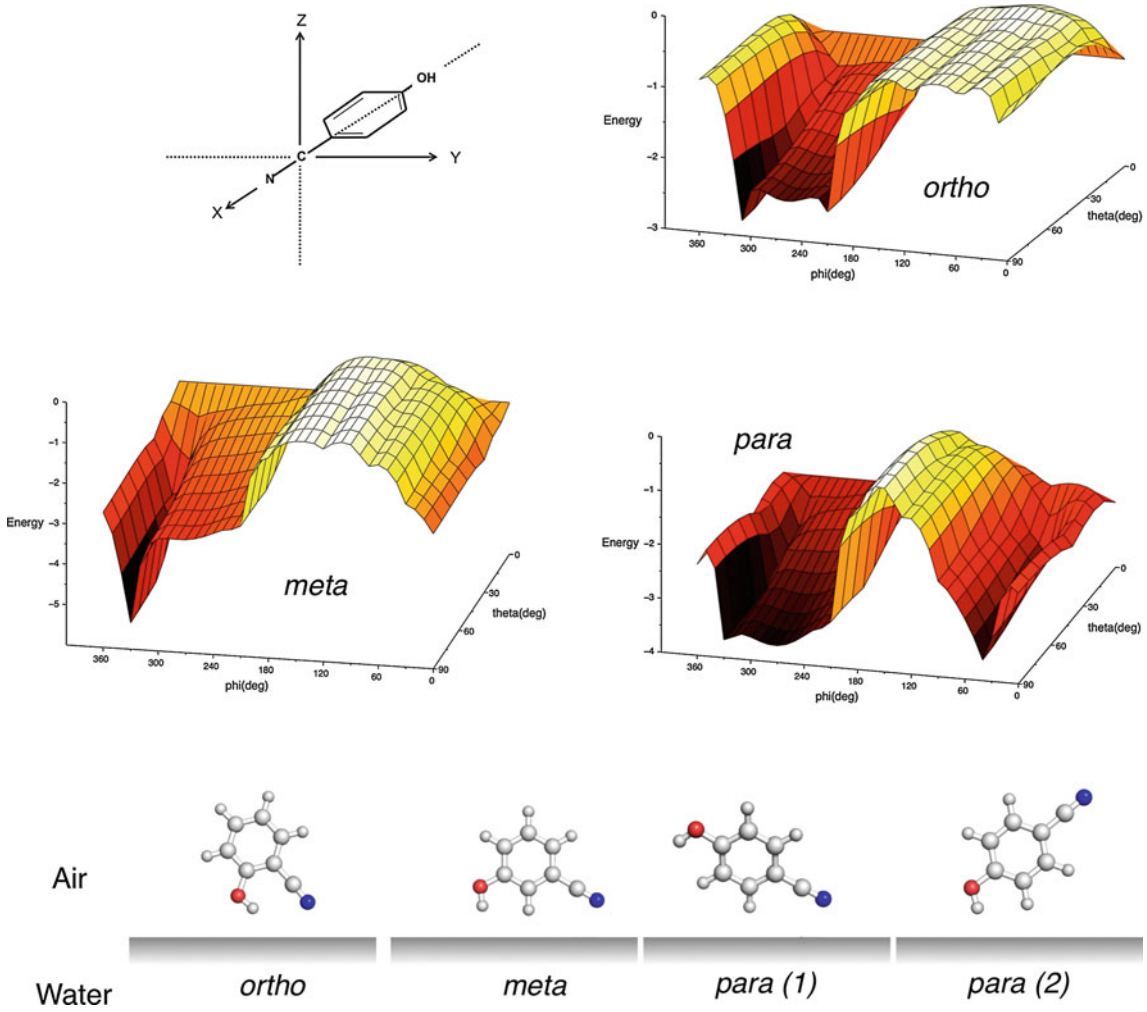

Fig. 2 Potential energy surfaces for the interaction of cyano phenol isomers with the air–water interface (dielectric model) and most stable orientations for each isomer. The Euler angles (ψ, θ, ϕ) are zero for the molecule in the *XY* plane and the CN bond oriented along the *X* axis, as illustrated in the case of the *para* isomer (we use the following convention: the first rotation (ψ) is done around the *Z* axis, the second one (θ) around the X' axis and the third one (ϕ) around the Z'' axis; rotations are done clockwise)

mol (*meta*), 3.7–3.8 kcal/mol (*para* (1)), and 3.2–3.8 kcal/mol (*para* (2)).

It is interesting to note also that the calculations reported in Table 1 and in Fig. 2 correspond to s-*cis* conformations of the OH group in the *ortho* and *meta* isomers because they are the most stable ones in the gas phase. However, one might wonder whether these conformers remain the most stable ones at the interface since one expects the s-*trans* conformer to display a larger polarity compared to the s-*cis* one, a trend which is confirmed by the calculations. Indeed, in gas phase, the dipole moment of the s-*trans* conformers amount 6.06 and 6.03 D for the *ortho* and *meta* isomers, respectively, (the dipole moments of the s-*cis* conformers are close to 3.6 D in both cases, see Table 1). Interestingly, the two isomers behave differently at the interface. While in the case of the *ortho* isomer, the s-*trans* conformer does display a larger stabilization ($E_{\text{s-trans}}$–$E_{\text{s-cis}}$ energy differences are 2.4 kcal/mol in gas phase and −0.3 kcal/mol at the interface); in the case of the *meta* isomer, the s-*cis* conformer displays the largest stabilization (energy differences are 0.2 kcal/mol in gas phase and 2.0 kcal/mol at the interface). These opposite trends can be explained by looking at the relative orientation of the conformers with respect to interface. In the case of the *ortho* isomer, the s-*trans* and s-*cis* conformer orientations are similar (CN-*Z* axis angle equals 130 and 140°, respectively) so that the two polar groups interact with the interface. In contrast, in the case of the *meta* isomer, the orientations are significantly different (CN-*Z* axis angle equals 180° and 120° for s-*trans* and s-*cis* conformers, respectively), so that in the case of the s-*trans* conformer, only the cyano group interacts with the interface.

Table 1 Calculated properties for different cyanophenol isomers in gas phase, in bulk water, and at the air–water interface

	Ortho	*Meta*	*Para*	
			(1)	(2)
CN-*Z* axis angle (°)	140	120	120	50
Electrostatic interaction energy (kcal/mol)	−2.79	−5.35	−3.80	−3.62
Dipole moment (*D*)				
Gas	3.58	3.57	5.26	
Interface	3.84	4.04	5.78	5.71
Bulk water	4.58	4.51	6.80	
μ (eV)				
Gas	−4.45	−4.46	−4.26	
Interface	−4.57	−4.40	−4.34	−3.98
Bulk water	−4.36	−4.36	−4.20	
η (eV)				
Gas	5.21	5.21	5.46	
Interface	5.18	5.16	5.45	5.44
Bulk water	5.17	5.09	5.40	
ω (eV)				
Gas	1.90	1.91	1.66	
Interface	2.01	1.88	1.73	1.46
Bulk water	1.83	1.86	1.64	

The molecular geometries are in all cases those optimized in gas phase

3.2 Reactivity indices

The analysis of solvation effects on reactivity indices is useful to rationalize the role that solute–solvent interactions play on chemical kinetics and reaction mechanisms. In Table 1, we have summarized the results obtained for the chemical potential, hardness, and electrophilicity of the different isomers in gas phase, in bulk water, and at the air–water interface.

As said in the introduction, it is usually accepted that polarization effects at liquid interfaces are intermediate between the effects in the two bulk phases, and that polarization at the air–water interface should be comparable to solvation effects in a low polar solvent. If one looks at the calculated dipole moments, our results confirm that the overall polarization of the solutes at the interface is significantly lower than in bulk water. Thus, the induced dipole moments at the interface range between 0.3 and 0.5 D, while in bulk water they range between 1 and 1.5 D.

This result, however, cannot be extrapolated to other electronic properties, as appears if one looks now at the reactivity indices. Inspection of data in Table 1 reveals that interface effects are sometimes significantly larger than solvation effects in bulk water. This is clearly the case for the chemical potential and for the electrophilicity

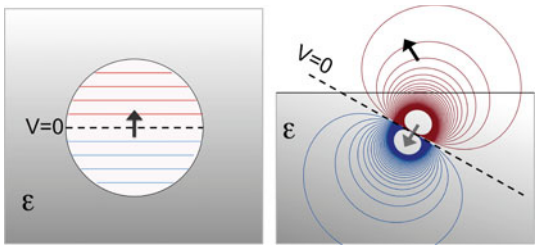

Fig. 3 Schematic representation of the reaction field electrostatic potential in the case of a simple model system: a point dipole interacting with a dielectric continuum medium. *Left*: dipole in a spherical cavity (Onsager's model for bulk solvation). *Right*: dipole in the vicinity of a planar interface

indices of the *para* isomer in orientation (2). These indices change slightly from gas phase to bulk water by +0.06 and −0.02 eV, while the change from gas phase to the interface is as large as +0.28 and −0.20 eV.

Furthermore, unexpected trends of the solvent effect at the air–water interface are noticed in some cases. As shown in the Table, all the isomers exhibit the same behavior under bulk water solvation, i.e., all the reactivity indices decrease in absolute value with respect to the gas phase, as intuitively expected. Instead, at the air–water interface, solvation effects may produce a decrease or an increase in the reactivity indices, depending on isomer and/or orientation. Specifically, the chemical potential and the electrophilicity indices for the *ortho* and *para* (1) isomers increase in absolute value, while all the other indices decrease, as found in bulk water. The relative solute interface orientation plays an important role, not only on the direction of the solvation effect, but also on its intensity. The *para* isomer undergoes a larger solvation effect in orientation (2), as shown for instance by the chemical potential, which increases (in absolute value) by 0.08 eV in orientation (1) but decreases by 0.28 eV in orientation (2). One can summarize these results by saying that in contrast to bulk solvation, the polarity of the molecule is not the key factor for determining the environment effect on reactivity.

4 Discussion and conclusions

The results presented above show that qualitative prediction of solvation effects on chemical reactivity at the air–water interface is not a straightforward matter. The different topology of the electrostatic potential in bulk water and at the water surface is a crucial factor that must be taken into account. To illustrate this point, let us consider the simplest case of a point dipole interacting with a dielectric continuum, as shown in Fig. 3. The dipole moment is assumed to be at a distance R from a planar dielectric interface or at the center of a spherical cavity of radius R immersed in a

dielectric medium and corresponding to Onsager's model for bulk solvation [35] (in both cases, the dielectric constant of vacuum is assumed for the region containing the point dipole). The solvent electrostatic potential at the center of the spherical cavity is zero, and the isopotential surfaces consist of equidistant parallel planes perpendicular to the dipole moment axis. In other words, the electric field inside the cavity is constant and parallel to the dipole moment. The situation is very different for a dipole interacting with a planar interface: The solvent electrostatic potential is nonzero at the position of the point dipole and, in general, the electric field is not parallel to the dipole moment. Note in addition that in this case, the isopotential surfaces are not parallel, and that the electric field is quite inhomogeneous, i.e., the dielectric polarization generates an electric field gradient. Detailed equations for the electric fields are reported in the supporting information since they can be useful to get an order of magnitude for the relative interface *versus* bulk electric field and solvation energy values, as a function of the dipole moment orientation.

In the case of general charge distributions in real molecules, the situation is obviously much more complicated but the point dipole moment model clearly demonstrates that electrostatic interactions in bulk or at the interface may lead to quite different solvation effects, even from qualitative considerations. In particular, one can expect that hydrogen bond donors will produce a polarization of the surface that will lead to the appearance of a "background" negative potential over the interface, while hydrogen bond acceptors will lead to a "background" positive potential. Such an electrostatic potential will produce an energy shift of the molecular orbitals, stabilizing or destabilizing them (positive or negative potential, respectively). Then, in the case of a hydrogen bond donor, one expects the HOMO and LUMO energy levels to rise and the chemical potential to increase in algebraic value. The opposite situation is expected for a hydrogen bond acceptor. The hardness of the system should not be much influenced by the electrostatic potential (a constant potential would not modify the HOMO–LUMO gap), and its change has to be mainly ascribed to the effect of the associated electric field.

Differences between orientations (1) and (2) of the *para* isomer can be rationalized by means of this simple model. In orientation (1), the cyano group is directed toward the surface, since this group is a hydrogen bond acceptor, a positive "background" potential is created over the surface stabilizing the solute's molecular orbitals. The chemical potential becomes more negative and the electrophilicity index increases. In the case of orientation (2), the alcohol group is oriented toward the surface. This group behaves as a proton donor, and the interface effect is the opposite of that observed for orientation (1). The study of the *para* cyanophenol isomer further indicates that particular attention has to be paid when interpreting data for molecular properties obtained at interfaces. Measured values correspond to averages that according to the preceding discussion can involve a wide dispersion of instantaneous properties along the reorientational dynamics of the solute. The comparison between theoretical and experimental values needs to take this question into account, as well as the fluctuations of the solute's position with respect to the average interface, which is not feasible using simple static dielectric models.

In summary, this work confirms and rationalizes the conclusions reported previously from SFG experiments claiming that polarization at the air–water interface cannot be compared to polarization in (bulk) low polar media. Our calculations emphasize the role of the topology of the electrostatic potential, as well as the crucial influence of the solute orientation with respect to the interface, showing that molecules of similar polarity and polarizabilities may undergo quite different solvation effects. A corollary of our study is that carrying out statistical simulations is compulsory in order to capture the complexity of interface solvation phenomena and to provide an accurate average of the (presumably large) fluctuations of the molecular properties.

References

1. Martins-Costa MTC, Anglada JM, Francisco JS, Ruiz-Lopez MF (2012) J Am Chem Soc 134:11821–11827
2. Martins-Costa MTC, Anglada JM, Francisco JS, Ruiz-Lopez MF (2012) Angew Chem Int Ed 51:5413–5417
3. Anglada JM, Martins-Costa M, Ruiz-Lopez MF, Francisco JS (2014) Proc Natl Acad Sci USA 111:11618–11623
4. Wang HF, Borguet E, Eisenthal KB (1998) J Phys Chem B 102:4927–4932
5. Wang HF, Borguet E, Eisenthal KB (1997) J Phys Chem A 101:713–718
6. Zimdars D, Eisenthal KB (2001) J Phys Chem B 105:3993–4002
7. Sen S, Yamaguchi S, Tahara T (2009) Angew Chem Int Ed 48:6439–6442
8. Soule MCK, Hore DK, Jaramillo-Fellin DM, Richmond GL (2006) J Phys Chem B 110:16575–16583
9. Rivail JL, Rinaldi D (1976) Chem Phys 18:233
10. Rinaldi D, Ruiz-López MF, Rivail JL (1983) J Chem Phys 78:834
11. Ruiz-Lopez MF (2008) In: Canuto S (ed) Solvation effects on molecules and biomolecules. Computational Methods and Applications. Springer, New York, pp 23–28
12. Dillet V, Rinaldi D, Rivail JL (1994) J Phys Chem 98:5034–5039
13. Tuñón I, Bertrán J, Ruiz-López MF, Rinaldi D (1996) J Comput Chem 17:148–155
14. Tapia O (1991) Theochem 72:59–72
15. Tapia O, Goscinski O (1975) Mol Phys 29:1653–1661
16. Hilton-McCreery J, Christoffersen RE, Hall GG (1976) J Am Chem Soc 98:7198–7202
17. Miertus S, Scrocco E, Tomasi J (1981) Chem Phys 55:117–129
18. Tomasi J, Persico M (1994) Chem Rev 94:2027–2094
19. Tomasi J, Mennucci B, Cammi R (2005) Chem Rev 105:2999–3093
20. Cramer CJ, Truhlar DG (1991) J Am Chem Soc 113:8305–8311
21. Liotard DA, Hawkins GD, Lynch GC, Cramer CJ, Truhlar DG (1995) J Comput Chem 16:422–440

22. Hawkins GD, Cramer CJ, Truhlar DG (1998) J Phys Chem B 102:3257–3271
23. Thompson JD, Cramer CJ, Truhlar DG (2005) Theor Chem Acc 113:107–131
24. Cramer CJ, Truhlar DG (2008) Acc Chem Res 41:760–768
25. Marenich AV, Cramer CJ, Truhlar DG (2009) J Phys Chem B 113:4538–4543
26. Mozgawa K, Mennucci B, Frediani L (2014) J Phys Chem C 118:4715–4725
27. Kelly CP, Cramer CJ, Truhlar DG (2004) J Phys Chem B 108:12882–12897
28. Durand E, Electrostatique III (1966) Méthodes de calcul diélectriques. Masson et Cie, Paris, pp 230–231
29. Besler BH, Merz KM, Kollman PA (1990) J Comput Chem 11:431–439
30. Singh UC, Kollman PA (1984) J Comput Chem 5:129–145
31. Becke AD (1993) J Chem Phys 98:5648–5652
32. Parr RG, Yang W (1989) Density-functional theory of atoms and molecules. Oxford University Press, New York
33. Geerlings P, De Proft F, Langenaeker W (2003) Chem Rev 103:1793–1873
34. Frisch MJ, Trucks GW, Schlegel HB, Scuseria GE, Robb MA, Cheeseman JR, Scalmani G, Barone V, Mennucci B, Petersson GA, Nakatsuji H, Caricato M, Li X, Hratchian HP, Izmaylov AF, Bloino J, Zheng G, Sonnenberg JL, Hada M, Ehara M, Toyota K, Fukuda R, Hasegawa J, Ishida M, Nakajima T, Honda Y, Kitao O, Nakai H, Vreven T, Montgomery JA Jr, Peralta JE, Ogliaro F, Bearpark MJ, Heyd J, Brothers EN, Kudin KN, Staroverov VN, Kobayashi R, Normand J, Raghavachari K, Rendell AP, Burant JC, Iyengar SS, Tomasi J, Cossi M, Rega N, Millam NJ, Klene M, Knox JE, Cross JB, Bakken V, Adamo C, Jaramillo J, Gomperts R, Stratmann RE, Yazyev O, Austin AJ, Cammi R, Pomelli C, Ochterski JW, Martin RL, Morokuma K, Zakrzewski VG, Voth GA, Salvador P, Dannenberg JJ, Dapprich S, Daniels AD, Farkas Ö, Foresman JB, Ortiz JV, Cioslowski J, Fox DJ (2009) Gaussian 09. Gaussian Inc, Wallingford
35. Böttcher CJF (1952) Theory of electric polarisation. Elsevier, Amsterdam

Theor Chem Acc (2015) 134:52
DOI 10.1007/s00214-015-1655-1

REGULAR ARTICLE

Electronic structure of kaempferol–Cu^{2+} coordination compounds: a DFT, QTAIM and NBO study in the gas phase

María del Carmen Ramírez Avi[1] · Ana África Márquez García[1] · Francisco Partal Ureña[1]

Received: 17 November 2014 / Accepted: 24 March 2015 / Published online: 5 April 2015

Abstract A DFT study on the molecular structure of a flavonoid, kaempferol, two anions and four copper complexes has been carried out. Three functionals, namely B3LYP, M06-2X and ωB97X-D, along with 6-311++G(2*d*,2*p*) basis set are applied to achieve this goal. The influence of metal coordination on the molecular and electronic structures of kaempferol and its anions is studied by applying quantum theory of atoms in molecules and natural bond order methodology.

Keywords DFT · QTAIM · NBO · Structure · Flavonoid · Kaempferol

1 Introduction

Flavonoids [1] are a group of phytochemicals with over 8000 individual compounds known. They act in plants as antioxidant, antimicrobials, photoreceptors, visual attractors, feeding repellents and for light screening. Many studies on these compounds have shown that flavonoids exhibit pharmacological and therapeutic activities, including antiallergenic, antiviral, anti-inflammatory and vasodilating actions. Most studies are devoted to their antioxidant activities [2–10] related to the presence of a double bond in position 2, a OH group in position 3, OH groups mainly in B ring and AC–B rings coplanarity (see Fig. 1b for nomenclature). However, it has been found that some of them have prooxidant activity [8].

From a theoretical point of view, studies are mainly devoted to the study of the molecular structure–antioxidant activity relationship. The most recent works are carried out at DFT/B3LYP level to achieve this goal (e.g. [11–19]).

Flavonoids are able to chelate with metal ions. Those metal complexes have shown a broader spectrum of pharmacological and therapeutics activities. However, their antioxidant–prooxidant activities, biological significance, molecular targets and mechanisms of actions are poorly understood. In addition, studies dealing with the molecular structure of those complexes have been carried out only for a limited number of flavonoid–metal cation couples [20–22].

The current work deals with the study of the molecular and the electronic structure of a flavonoid, kaempferol and the effect on these structures when it is chelate to Cu^{2+} cation. Kaempferol is found in tea, broccoli, cabbage, kale, beans, endive, leek, tomato, strawberries, grapes and in plants used in traditional medicine (e.g. *Ginkgo biloba*, *Tilia* spp, *Equisetum* spp, *Moringa oleifera*, *Sophora japonica* and *propolis*) [1]. Kaempferol has shown pharmacological activity in diabetes, asthma and carcinogenesis and is a good radical scavenger [23].

On the other hand, copper has been chosen because it plays an important role in several neurodegenerative diseases and in oxidative stress processes in the cell [24–27], in spite of its essential role in the biological functions of living organisms [28].

Molecular structures are optimised at DFT level using three functionals. The goal is to check how different functionals describe the molecular structures of neutral

Published as part of the special collection of articles derived from the 9th Congress on Electronic Structure: Principles and Applications (ESPA 2014).

✉ Francisco Partal Ureña
fpartal@ujaen.es

[1] Department of Physical and Analytical Chemistry, Faculty of Experimental Sciences, University of Jaén, Campus Las Lagunillas s/n, 23071 Jaén, Spain

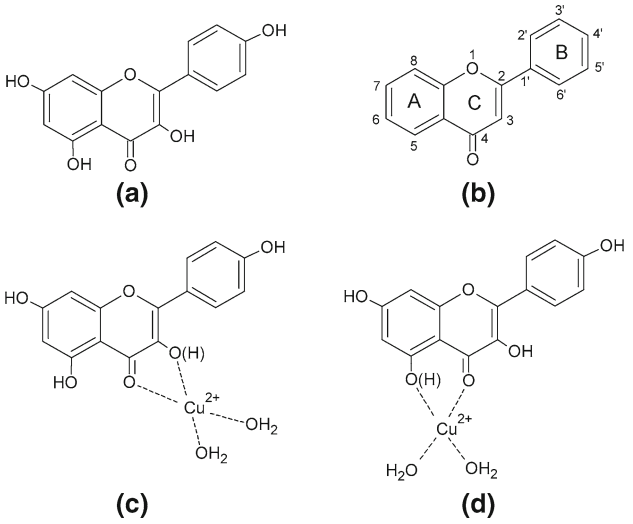

Fig. 1 Molecular structure of kaempferol (**a**), numbering (**b**) and molecular structures of coordination compounds (**c**, **d**) studied in the present work

kaempferol, two anions and four different coordination compounds.

Electronic structures of selected coordination compounds are studied using two different approach, quantum theory of atoms in molecules (QTAIM) [29–31] and natural bond order (NBO) method [32, 33]. To our knowledge, this sort of studies on flavonoids–metal complexes is scarce in the literature.

2 Computational details

Theoretical calculations based on density functional theory (DFT) were carried out using Gaussian 09 package [34]. Three functionals [35–38] were chosen to optimise the molecular structures of the seven systems under study in the present work, namely neutral kaempferol (K), two of its anions and four Cu^{2+} coordination compounds (Fig. 1) with and without the loss of a proton after coordination. Those functionals are the hybrid B3LYP [39], which is considered the standard functional in Chemistry for structures and molecular properties; the Minnesota M06-2X [40, 41], recommended by the developers for applications involving main-group elements (structures, thermochemistry, non-covalent interactions) and the long-range corrected ωB97X-D [42], which has shown to be somewhat superior to the results obtained by conventional DFT methods with respect to equilibrium geometries, reactions energies and charge transfer. The 6-311++G(2*d*,2*p*) basis set was used in all calculations.

In our study, the coordination number of copper was set to four following previous works [43, 44]. Flavonoids chelates to metals via O3 and O4 or O5 and O4 oxygen atoms (e.g. Refs. [20, 45–49]). In those studies, the proton from de hydroxyl involved in the coordination is lost. This loss is not always described in previous experimental works [21 and references therein], and in a recent Molecular Dynamics study on the coordination of 3-hydroxyflavone with alkaline metals, the proton is retained [50]. In our present work, these two possibilities are checked. Two water molecules were added to complete coordination sphere on Cu^{2+}.

Anions formed from the loss of the proton of hydroxyl 3OH (K3O) and 5OH (K5O) are studied to differentiate between anion formation and coordination effects.

Electronic structures of selected compounds were analysed at the B3LYP/6-311G(*d*,*p*) level. For this task are applied NBO method [32, 33], as implemented in Gaussian 09 [34], and QTAIM [29–31], using AIM2000 software [51].

Within the NBO method, molecular properties are depicted in terms of 'natural Lewis structures' with localised Lewis-like bonds. Residual resonance delocalisation effects are described as 'non-Lewis' bonds. NBO method provides links to elementary valency and bonding concepts in chemical species, i.e. bond type, hybridisation, bond order, charge transfer, resonance weights and atomic charges, among other.

On the other hand, QTAIM relates chemical concepts, as chemical structure, chemical bonding and chemical reactivity, to the topology of the electron density ($\rho(\mathbf{r})$) distribution of a chemical species. The electronic density surface presents maxima, minima and saddle points that are called critical points (CP) and can be divided in nuclear-(NCP), bond-(BCP), ring-(RCP) and cage-critical points (CCP). The classification can be done from the Laplacian of the electron density ($\nabla^2 \rho(\mathbf{r})$). The number and type of CP follow a strict topological relationship called Poincaré–Hopf rule, which for isolated molecules states that $n_{NCP} - n_{BCP} + n_{RCP} - n_{CCP} = 1$.

In the current study, five QTAIM descriptors were used to characterise interactions at selected bond critical points [31, 52–57]:

1. Electron density (ρ_b ($\mathbf{r_c}$)), related to bond orders and binding energies;
2. Laplacian of the density ($\nabla^2 \rho_b(\mathbf{r_c})$), which is the sum of the three curvatures of the density at the critical point, the two perpendicular to the bond path being negative (λ_1 and λ_2, $|\lambda_1| > |\lambda_2|$) and the third lying along the bond path being positive (λ_3). Its sign indicates concentration (negative sign) or depletion (positive sign) of the electronic distribution;
3. Ratio between the gradient kinetic energy density (G_b ($\mathbf{r_c}$)) and the electron density, G_b ($\mathbf{r_c}$)/ρ_b ($\mathbf{r_c}$), which was initially proposed as a criterion to distinguish between different types of bonds;

4. Absolute value of the ratio between the potential energy density (V_b ($\mathbf{r_c}$)) and the gradient kinetic energy density, $|V_b(\mathbf{r_c})/G_b(\mathbf{r_c})|$, which enables identification of atomic interactions;
5. Total electronic energy density ($H_b(\mathbf{r_c}) = G_b(\mathbf{r_c}) + V_b(\mathbf{r_c})$). It is negative for interactions with important electron sharing, and its magnitude reflects the degree of covalence of the interaction.

These five descriptors allowed us to describe interactions as 'shared shell' interactions, related to covalent ones, and 'closed shell' interactions, related to ionic ones:

- Closed shell interactions: $\rho_b(\mathbf{r_c}) < 0.1$ e a_o^{-3}, $\nabla^2\rho_b(\mathbf{r_c}) > 0$ e a_o^{-5}, $G_b(\mathbf{r_c})/\rho_b(\mathbf{r_c}) > 1$ a.u., $H_b(\mathbf{r_c}) > 0$ a.u., $|V_b(\mathbf{r_c})/G_b(\mathbf{r_c})| < 1$;
- Shared shell interactions: $\rho_b(\mathbf{r_c}) > 0.1$ e a_o^{-3}, $\nabla^2\rho_b(\mathbf{r_c}) < 0$ e a_o^{-5}, $G_b(\mathbf{r_c})/\rho_b(\mathbf{r_c}) < 1$ a.u., $H_b(\mathbf{r_c}) < 0$ a.u., $|V_b(\mathbf{r_c})/G_b(\mathbf{r_c})| > 2$.

In addition to those parameters, another one useful in the description of bonds properties is the ellipticity ε, defined as $(\lambda_1/\lambda_2) - 1$. Ellipticity is a measure of the π-character of a bond. Bonds cylindrically symmetrical, for example single C–C bonds, present an ellipticity equal to zero. Aromatic bonds in benzene have an ellipticity of 0.23 and double bond in ethylene of 0.45.

3 Results and discussion

3.1 Molecular structures of kaempferol and its anions

Selected structural parameters of kaempferol (K) and its anions (K3O and K5O) are shown in Table 1.

As can be seen, B3LYP calculations give a planar structure for kaempferol, in agreement with previous works [11, 12]. A similar planar structure has been found for quercetin [11, 13] and fisetin [14]. This planar structure was related to a hydrogen bonding between 3OH hydroxyl group and the 6H′ in the B ring (Fig. 1). On the other hand, M06-2X and ωB97X-D give a non-planar structure, with an angle between AC and B rings of 10° (ωB97X-D) and −8° (M06-2X). As shown in a next section, our calculations reveal that the hydrogen bonding between 3OH and 6H′ remains in this non-planar structure, and thus this hydrogen bonding cannot be responsible for coplanarity.

Aparicio [11] found that the O4···H5 hydrogen bonding was stronger than the O4···H3 one. This fact is confirmed by our calculations for the three functionals in a first step. As shown in Table 1, O4···H5 is shorter than O4···H3 about 0.250 Å.

Table 1 Selected structural parameters of kaempferol and its anions

Compound	Structural parameter[a]	B3LYP	M06-2X	ωB97X-D
K	C2–C1′	1.462	1.465	1.466
	C3–O3	1.356	1.352	1.349
	O3–H3	0.976	0.971	0.970
	C4–O4	1.257	1.244	1.246
	O4···H3	2.005	2.027	2.015
	C5–O5	1.340	1.335	1.333
	O5–H5	0.987	0.979	0.980
	O4···H5	1.756	1.785	1.765
	C7–O7	1.360	1.353	1.351
	O7–H7	0.962	0.960	0.958
	C4′–O4′	1.364	1.357	1.356
	O4′–H4′	0.962	0.960	0.958
	O3···H6′	2.160	2.155	2.172
	O1–C2–C1′–C2′	0	−8	−9
K3O	C2–C1′	1.449	1.452	1.454
	C3–O3	1.259	1.254	1.255
	C4–O4	1.255	1.244	1.244
	C5–O5	1.340	1.333	1.333
	O5–H5	1.016	1.014	1.004
	O4···H5	1.562	1.550	1.586
	C7–O7	1.379	1.370	1.368
	O7–H7	0.961	0.959	0.957
	C4′–O4′	1.387	1.379	1.377
	O4′–H4′	0.961	0.959	0.957
	O3···H6′	2.087	2.081	2.078
	O1–C2–C1′–C2′	0	0	0
K5O	C2–C1′	1.464	1.467	1.467
	C3–O3	1.354	1.350	1.347
	O3–H3	0.997	0.987	0.989
	C4–O4	1.249	1.237	1.240
	O4···H3	1.764	1.805	1.772
	C5–O5	1.246	1.237	1.238
	C7–O7	1.384	1.376	1.373
	O7–H7	0.962	0.960	0.957
	C4′–O4′	1.380	1.372	1.370
	O4′–H4′	0.961	0.959	0.957
	O3···H6′	2.181	2.155	2.169
	O1–C2–C1′–C2′	0	0	0

[a] Bond lengths in Å, torsion angle in degrees

As regards kaempferol anions (K3O and K5O), our calculations give a planar structure for both of them (Table 1) at all theoretical levels. On the other hand, K3O is lower in energy [E_o, obtained as the sum of electronic (E_e), and zero point corrected energies (ZPVE)] than K5O (by 22 kJ mol^{-1} according to B3LYP, and 16 kJ mol^{-1} according to M06-2X and ωB97X-D), in

agreement with the fact that O4···H5 is stronger than O4···H3.

The loss of the proton makes the corresponding C–O bond become shorter and the O4···H remaining hydrogen bond become stronger, as inferred from their shorter lengths. This point will be confirmed in a next section from the electronic structure study. B3LYP and ωB97X-D predict a higher shortening in K5O. However, M06-2X estimates a higher shortening in K3O.

In all the cases, C2–C1′ bond is shorter in K3O and does not change in KO5. The same is found for the O3···6H′ distance, fact that point out a strengthening of this interaction. These results show that the molecular structure is contracted in K3O with respect to neutral kaempferol. The effect of this contraction on the electronic structure of these species is described in a section below.

3.2 Molecular structure of coordination compounds when the proton is lost

All our calculations predict square planar (SP-4) geometry [58] for the O4–O5 coordination compound (C5O). However, in the case of the O3–O4 compound (C3O), B3LYP and M06-2X give tetrahedral geometry (T-4) and ωB97X-D predicts SP-4 one (Table 2). It is found in the literature [43, 44] that Cu^{2+} coordination number is five or four, and that in metalloproteins tends to bind in square planar (SP-4) or tetrahedral (T-4) structures, although the SP-4 structure is preferred [43].

B3LYP predicts C3O to be 11 kJ mol^{-1} lower in energy than C5O. The opposite is found by M06-2X and ωB97X-D, C5O being 25 and 9 kJ mol^{-1} lower in energy, respectively. Our calculations show discrepancies in both energy differences and complex with lower energy. In order to check if those discrepancies are due to the functional used or the predicted geometry, single-point calculations on the optimised structures at every level are carried out using the remaining functionals.

Unfortunately, structures that are local minimum at a level do not have to be true at another one, and imaginary frequencies could be found. As an example of this, the SP-4 structure predicted at ωB97X-D level for C5O presents four imaginary frequencies at B3LYP level even when the coordination structure predicted is the same. That is why energy comparison is done using electronic energy only, E_e. Results are shown in Table 3. As shown above, B3LYP predicts a change in the coordination geometry from C3O (T-4) to C5O (SP-4), C3O species being the lower in energy. M06-2X and ωB97X-D single-point calculations on those B3LYP structures predict C5O to be lower in energy. In addition, M06-2X predicts an energy difference between the two structures almost six times higher than B3LYP and ωB97X-D. The same pattern is found when single-point calculations at B3LYP and ωB97X-D levels are carried out on M06-2X structures (with the same change in coordination geometry than B3LYP), energy differences being a bit different from the former case. Only ωB97X-D structures (with no change in coordination geometry, SP-4) present the same pattern and energy differences when single-point calculations are carried out at the remaining levels (Table 3). Those facts show that the functional used is decisive in both predicted geometry and energy differences between C3O and C5O.

As regards AC–B rings coplanarity, B3LYP and M06-2X predict an almost coplanar structure of C3O and ωB97X-D

Table 2 Selected structural parameters of coordination compounds when the proton is lost

Coordination compound	Structural parameter[a]	B3LYP	M06-2X	ωB97X-D
C3O	Polyhedral symbol[b]	T-4	T-4	SP-4
	C2–C1′	1.436	1.431	1.454
	C3–O3	1.274	1.253	1.339
	C4–O4	1.261	1.247	1.306
	C5–O5	1.344	1.329	1.338
	O5–H5	0.982	0.974	0.967
	O4···H5	1.775	1.813	1.847
	C7–O7	1.345	1.337	1.339
	O7–H7	0.964	0.962	0.959
	C4′–O4′	1.344	1.336	1.345
	O4′–H4′	0.964	0.962	0.959
	O3···H6′	2.155	2.151	2.275
	Cu–O3	1.958	2.098	1.853
	Cu–O4	2.246	2.182	1.902
	O1–C2–C1′–C2′	2	4	−20
C5O	Polyhedral symbol	SP-4	SP-4	SP-4
	C2–C1′	1.451	1.455	1.455
	C3–O3	1.360	1.355	1.353
	C3–H3	0.967	0.964	0.962
	C4–O4	1.306	1.298	1.296
	O4···H3	2.043	2.052	2.050
	C5–O5	1.325	1.318	1.318
	C7–O7	1.349	1.342	1.340
	O7–H7	0.963	0.961	0.959
	C4′–O4′	1.350	1.346	1.344
	O4′–H4′	0.963	0.961	0.959
	O3···H6′	2.154	2.175	2.183
	Cu–O4	1.886	1.897	1.877
	Cu–O5	1.852	1.856	1.840
	O1–C2–C1′–C2′	−6	−14	−14

[a] Bond lengths in Å, torsion angle in degrees

[b] IUPAC nomenclature [58]

Table 3 Single-point energy differences (in kJ mol^{-1}) between coordination compounds

	B3LYP	M06-2X	ωB97X-D
E_e (C5O) − E_e (C3O)	**6**	−37	−7
	2	**−32**	−8
	−9	−10	**−8**
E_e (C5OH) − E_e (C3OH)	**−4**	−38	−19
	−2	**−41**	−19
	−11	0	**3**

In bold results from full optimised structures

a non-planar one (−20°). In the case of C5O, the three functionals give a non-planar structure (Table 2).

Results for C3O show a shortening in C2–C1′, C7–O7 and C4′–O4′ bonds with respect to K3O. At the same time, a lengthening in C4–O4 and O4···H5 bonds is predicted. B3LYP and ωB97X-D predict a lengthening in the C3–O3 bond. The same trends are found for C5O with respect to K5O.

All the functionals predict Cu–O distances in C5O shorter than in C3O and O4···H3 distances in C5O longer than O4···H5 ones in C3O, pointing out a weakening of this interaction in C5O with respect to C3O. C4′–O4′ and C7–O7 bonds present the same length. On the other hand, B3LYP and M06-2X predict longer C2–C1′ and C4–O4 bonds in C5O than in C3O in disagreement with ωB97X-D (Table 2).

3.3 Molecular structure of coordination compounds when the proton is retained

Predicted structures with O4–O3 coordinating pattern (C3OH) are non-planar, with optimised torsion angle values of −26° (B3LYP), −24° (M06-2X) and −33° (ωB97X-D) (Table 4). B3LYP and M06-2X give L-2 coordination geometries with Cu coordinating O4 and one water molecule and the other one out of the coordination sphere (Fig. 2). In contrast, ωB97X-D gives SP-4 geometry. Only ωB97X-D functional predicts both coordination number and geometry in agreement with previous experimental works [43, 44].

All the functionals predict almost coplanar structures of the compounds with coordinating pattern O4–O5 (C5OH). M06-2X gives T-4 and ωB97X-D SP-4 geometries. In the case of B3LYP, Cu–O5 distance is so longer that the optimised structure could be considered as a trigonal plane (TP-3) one. B3LYP gives both coordination number and geometry in disagreement with previous works [43, 44].

C5OH is lower in energy than C3OH from B3LYP (7 kJ mol^{-1}) and M06-2X (42 kJ mol^{-1}) calculations. A similar energy difference is predicted by ωB97X-D functional (3 kJ mol^{-1}).

As in the previous section, single-point calculations are carried out on the optimised structures to check the effect of geometry and functional in the predicted energy differences. As shown in Table 3, larger discrepancies in energy are found with optimised structures at B3LYP and M06-2X levels. With all the functionals, C5OH is lower in energy than C3OH with optimised structures B3LYP and M06-2X. When ωB97X-D structure is the optimised one, B3LYP predicts C5OH lower in energy than C3OH, in contrast to ωB97X-D. In addition, the same energy is predicted by

Table 4 Selected structural parameters of coordination compounds when the proton is retained

Coordination compound	Structural parameter[a]	B3LYP	M06-2X	ωB97X-D
C3OH	Polyhedral symbol[b]	L-2	L-2	SP-4
	C2–C1′	1.436	1.427	1.447
	C3–O3	1.334	1.325	1.405
	C4–O4	1.274	1.261	1.309
	C5–O5	1.320	1.315	1.333
	O5–H5	0.979	0.973	0.962
	O4···H5	1.785	1.823	1.929
	C7–O7	1.326	1.318	1.323
	O7–H7	0.967	0.965	0.961
	C4′–O4′	1.323	1.313	1.330
	O4′–H4′	0.967	0.966	0.960
	O3···H6′	2.515	2.476	2.565
	Cu–O3	2.853	2.742	1.992
	Cu–O4	1.896	1.951	1.868
	O1–C2–C1′–C2′	−26	−24	−33
C5OH	Polyhedral symbol	TP-3	T-4	SP-4
	C2–C1′	1.426	1.418	1.429
	C3–O3	1.319	1.309	1.347
	C3–H3	0.980	0.978	0.961
	C4–O4	1.262	1.245	1.342
	O4···H3	1.945	1.960	2.112
	C5–O5	1.357	1.353	1.401
	C7–O7	1.330	1.324	1.329
	O7–H7	0.965	0.964	0.960
	C4′–O4′	1.319	1.309	1.326
	O4′–H4′	0.968	0.967	0.961
	O3···H6′	2.156	2.141	2.120
	Cu–O4	1.936	2.050	1.841
	Cu–O5	2.821	2.353	1.967
	O1–C2–C1′–C2′	0	2	2

[a] Bond lengths in Å, torsion angle in degrees

[b] IUPAC nomenclature [58]

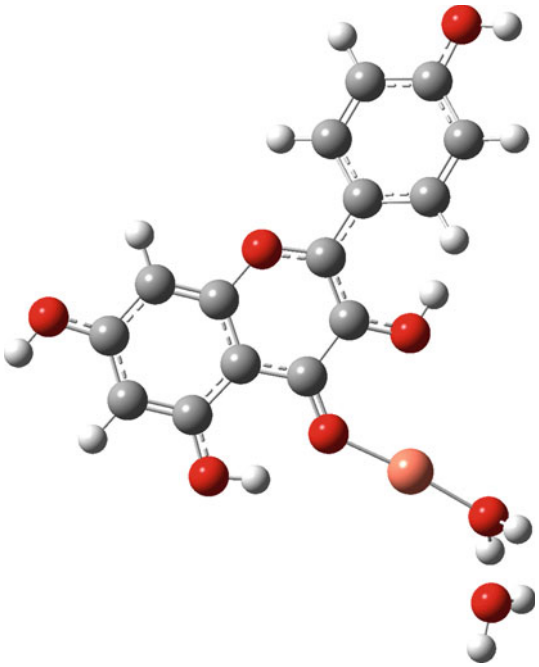

Fig. 2 Molecular structure of compound C3OH with L-2 coordination geometry

M06-2X for both compounds. The same conclusions as in the case of C3O and C5O can be inferred from these results, i.e. functionals are decisive in the prediction of both geometries and energy differences between compounds.

In C3OH, coordination causes a shortening of C2–C1′, C7–O7 and C4′–O4′ bonds with respect to neutral kaempferol. At the same time, C4–O4 and O4···H5 are lengthened. As regards C3–O3 and C5–O5 bonds, B3LYP and M06-2X predict a shortening of the bond lengths. On the other hand, ωB97X-D functional predicts a lengthening of the former and no change in the latter. All the functionals predict a longer O3···H6′ distance.

As far as C5OH is concerned, all the functionals estimate the lengthening of C5–O5 bond and the shortening of C3–O3, C2–C1′, C7–O7 and C4′–O4′ bonds after coordination. At the same time, they estimate a lengthening in O4···H3 and O3···H6′ distances.

3.4 Effects of coordination on the electronic structure of kaempferol and its anions: QTAIM and NBO results

As shown above, only ωB97X-D functional gives coordination number and geometry in agreement with previous works on Cu^{2+} coordination for all the cases. Thus, ωB97X-D structures are chosen to study how electronic distribution is affected by coordination.

In the present work, similar results are obtained to the ones presented in the work by Aparicio [11] for neutral kaempferol (Tables 5, 6; Fig. 3). The three hydrogen bondings in the former work, namely O4···H3, O4···H5 and C3···H6′, are found in our QTAIM study, and the order in strength O4···H5 > O4···H3 > C3···H6′ is reasserted. G/ρ values are lower than 1 as found in previous works on hydrogen bonding [24], and H has a negative value for O4···H5 BCP. This fact shows that this hydrogen bond presents some degree of covalency.

NBO results show a great electron delocalisation between rings, the percentage of non-Lewis structures being close to 3 %. A flow of charge between AC and B rings is described which makes AC ring to have a negative net charge and B ring a positive one.

Anions present similar molecular graphs as neutral kaempferol, bearing in mind that one hydrogen bond disappears in each case. In K3O, O4···H5 and C3···H6′ bonds are reinforced. In K5O, O4···H3 is reinforced and C3···H6′ remains without any change (Table 5). In both anions, the ellipticity of the C2–C1′ bond is higher than in neutral kaempferol ($\varepsilon = 0.156$ in K, 0.208 in K3O and 0.163 in K5O). In K3O, its value is close to the one for aromatic bonds in benzene ($\varepsilon = 0.23$) [31].

On the other hand, a new BCP is described between O4 and O5 in K5O (Fig. 4). This BCP remains when the calculations are carried out at the MP2 level, fact that discards an effect of B3LYP functional. This interaction is described by QTAIM parameters as 'close shell' (Table 5).

NBO results show a similar electron delocalisation in both anions and with respect to neutral kaempferol (Table 6). The whole negative charge is shared across the rings, and the NPA charges of O1, O3, O5, O7 and O4′ are increased with respect to neutral kaempferol, in contrast to NPA charge of O4. In addition, AC and B rings have negative net charges. Coordination with Cu^{2+} implies a new electronic redistribution in all the complexes, although non-Lewis structures percentages are similar to the values obtained in neutral kaempferol and its anions. Charge delocalisation from ligands to copper cation is predicted. Conversely, delocalisation from copper to ligands (back donation) is not significant. This fact makes Cu NPA charges to be between 1.345e and 1.395e and q(O4) to increase (Table 6). On the other hand, Cu–O bonds show QTAIM parameters intermediate between 'closed shell' and 'share shell' interactions (Table 5).

Cu–O4 shows a lower covalency degree than Cu–O3 and Cu–O5 in C3O and C5O, respectively. This fact can be related with a higher strength of Cu–O3 and Cu–O5 bonds and it is related to results from NBO analysis below. Ellipticity of C2–C1′ bond decreases in C3O with respect to K3O ($\varepsilon = 0.208$ in K3O, 0.161 in C3O) and is similar

Table 5 QTAIM descriptor values for selected BCP[a]

Compound	BCP	ρ	$\nabla^2\rho$	G/ρ	H	$\|V/G\|$
K	O4···H3	0.026	0.104	0.902	0.002	0.911
	O4···H5	0.041	0.127	0.838	−0.003	1.075
	C3···H6′	0.017	0.071	0.859	0.003	0.806
K3O	O4···H5	0.065	0.151	0.811	−0.015	1.287
	C3···H6′	0.024	0.086	0.808	0.002	0.877
K5O	O4···H3	0.045	0.138	0.835	−0.003	1.088
	O4···O5	0.011	0.040	0.841	0.001	0.927
	C3···H6′	0.017	0.070	0.846	0.003	0.811
C3O	O4···H5	0.033	0.117	0.877	0.0001	0.996
	C3···H6′	0.016	0.058	0.799	0.002	0.856
	Cu–O3	0.114	0.591	1.462	−0.019	1.114
	Cu–O4	0.098	0.535	1.480	−0.012	1.082
C5O	O4···H3	0.024	0.101	0.939	0.002	0.904
	C3···H6′	0.017	0.071	0.866	0.003	0.803
	Cu–O4	0.1031	0.580	1.532	−0.013	1.082
	Cu–O5	0.1152	0.625	1.520	−0.019	1.107
C3OH	O4···H5	0.027	0.100	0.867	0.001	0.952
	C3···C6′	0.011	0.044	0.822	0.002	0.800
	Cu–O3	0.075	0.422	1.478	−0.005	1.044
	Cu–O4	0.107	0.588	1.511	−0.015	1.093
C5OH	O4···H3	0.022	0.097	0.973	0.003	0.873
	C3···H6′	0.019	0.082	0.887	0.003	0.806
	Cu–O4	0.112	0.656	1.610	−0.017	1.092
	Cu–O5	0.078	0.464	1.553	−0.005	1.045

[a] Values in a.u

Table 6 Lewis and non-Lewis structures percentage and NPA charges from NBO calculation[a]

	K	K3O	K5O	C3O	C5O	C3OH	C5OH
Lewis	97.20	96.91	97.18	97.18	97.18	96.96	96.91
Non-Lewis	2.80	3.09	2.82	2.82	2.82	3.04	3.09
q(O1)	−0.474	−0.489	−0.508	−0.447	−0.449	−0.429	−0.440
q(O3)	−0.677	−0.718	−0.705	−0.829	−0.668	−0.761	−0.642
q(O4)	−0.684	−0.655	−0.650	−0.817	−0.813	−0.798	−0.816
q(O5)	−0.660	−0.691	−0.670	−0.651	−0.820	−0.623	−0.760
q(O7)	−0.654	−0.680	−0.691	−0.633	−0.634	−0.600	−0.609
q(O4′)	−0.660	−0.693	−0.683	−0.640	−0.639	−0.601	−0.590
q(Cu)	–	–	–	1.379	1.391	1.389	1.349
q(AC rings)	−0.052	−0.853	−0.939	−0.661	−0.686	0.178	0.099
q(B ring)	0.052	−0.147	−0.061	0.129	0.151	0.271	0.410

[a] NPA charges (q) in e

to ellipticity in neutral kaempferol ($\varepsilon = 0.156$). This bond shows similar values of ellipticity in C5O with respect to K5O and neutral kaempferol ($\varepsilon = 0.167$ in C5O, 0.163 in K5O and 0.156 in K). Besides, O4···H5 and O4···H3 interactions decrease their covalency in C3O and C5O, respectively, which point out a weakening of these hydrogen bonds after coordination.

NBO analysis describes C3O and C5O as systems with three independent units, namely two water molecules and the kaempferol anion–copper molecule. A dative bond is described in C3O between Cu and O3 ($\sigma = 0.8685\ (sp^{26.05})_O + 0.4958\ (sd^{5.60})_{Cu}$; 75.24 % O contribution, 24.58 % Cu contribution) and in C5O between Cu and O5 ($\sigma = 0.8735\ (sp^{21.44})_O + 0.4868\ (sd^{6.01})_{Cu}$; 76.31 % O

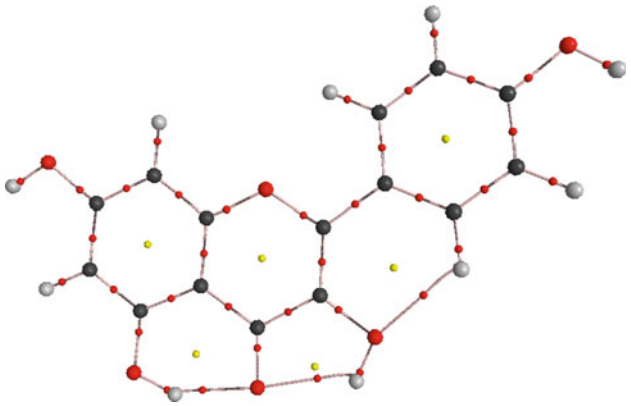

Fig. 3 Molecular graph of neutral kaempferol (in *red*, *small spheres*, *bond critical points* and in *yellow ring critical points*)

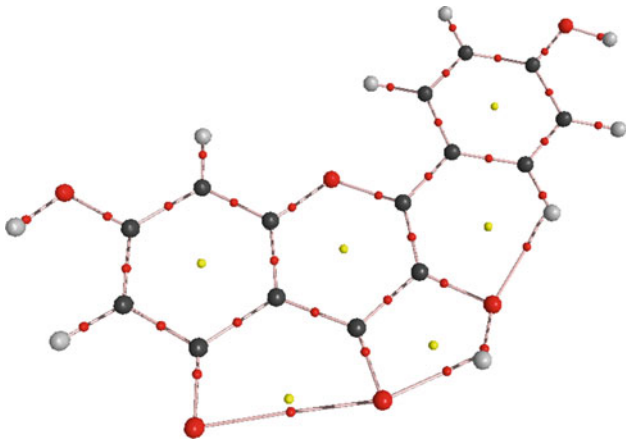

Fig. 4 Molecular graph of K5O anion (in *red*, *small spheres*, *bond critical points* and in *yellow ring critical points*)

contribution, 23.69 % Cu contribution). These results agree with higher covalency degree obtained from QTAIM analysis for these bonds and described in the previous paragraph. Besides, $n \rightarrow n^*$ interactions are found between valence lone pairs of O4, O3 and oxygen atoms of water molecules and one non-valence lone pair of Cu. In C3O, n^* Cu has *s* character and a population of 0.139e; in C5O, the lone pair has *p* character and a population of 0.002e.

On the other hand, AC rings have a negative net charge and B ring a positive one in both compounds (these two moieties are negatively charged in the anions, as shown above). The main charge flow goes from anions to the copper cation (0.468e and 0.465e in C3O and C5O, respectively). The charge flow from water molecules to copper is lower than 0.1e.

In addition, bonds described as single ones are C4–O4 (it is described as double in K, K3O and K5O), C3–O3

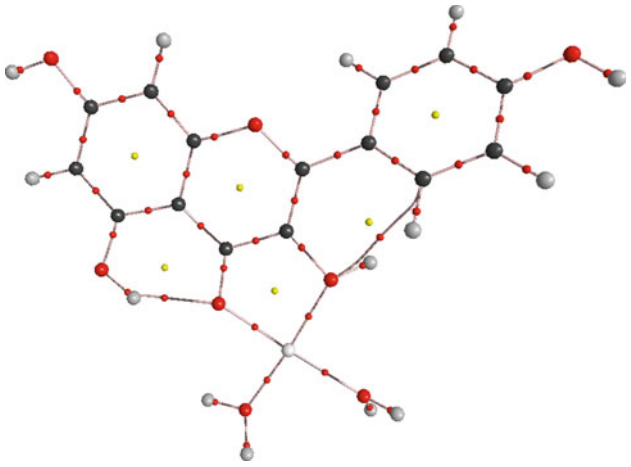

Fig. 5 Molecular graph of C3OH coordination compound (in *red*, *small spheres*, *bond critical points* and in *yellow ring critical points*)

(double in K3O and single in K5O) and C5–O5 (single in K3O and double in K5O).

As regards C3OH and C5OH, QTAIM analysis finds an increase in the 'close shell' character of O4···H5 and O4···H3, respectively (Table 5). This fact could be related to a weakening of these interactions. Besides, C2–C1′ ellipticity decreases in C3OH with respect to neutral kaempferol ($\varepsilon = 0.156$ in K, 0.149 in C3OH); conversely, in C5OH increases ($\varepsilon = 0.199$), and becomes closer to the value of aromatic bonds in benzene [31].

A new bond path is found in C3OH between C3 and C6′ atoms, and the bond path between C3 and H6′ disappears (Fig. 5). This bond path is found at the MP2 level, too. This interaction is described as a 'closed shell' one similar to O3···H6′.

NBO analysis describes the two complexes as composed of four independent units, and any dative bond is not found. Both AC and B moieties have a positive net charge. The main charge flow to copper is due to kaempferol (0.449e in C3OH and 0.509e in C5OH). The charge flow from water molecules to copper is lower than 0.1e as in C3O and C5O. Besides, the present analysis reveals that C4–O4 has single bond character in both complexes.

Finally, $n \rightarrow n^*$ interactions are found between valence lone pairs of O4, O3 and oxygen atoms of water molecules and one non-valence lone pair of Cu. In both complexes, n^* Cu has *s* character, with a population of 0.123e and 0.117 in C3OH and C5OH, respectively.

4 Conclusions

This work has shown the effect of the coordination of Cu^{2+} with kaempferol on the molecular and electronic structures

of the latter. B3LYP, M06-2X and ωB97X-D functionals with the 6-311++G(2*d*,2*p*) basis set predict similar trends in the variation of the geometrical parameters if we compare neutral kaempferol with its anion and its coordination complexes. With respect to kaempferol, only B3LYP gives a coplanar structure and all of them predict coplanar ones for its anions. In general, coordination compounds are nonplanar but one, which is predicted to show a coplanar structure, at all theory levels.

In contrast, different coordination numbers and geometries have been predicted for the coordination compounds. Only ωB97X-D functional gives in all the cases coordination numbers and geometries in agreement with experimental works dealing with copper compounds, and these structures were chosen to carry out NBO and QTAIM studies.

QTAIM analysis has revealed hydrogen bonding interactions that are preserved from kaempferol to its metal complexes. At the same time, new electrostatic interactions have been found in one anion (a O···O interactions) and in one coordination compound (a C···C interaction). These interactions are found even at MP2 level, and thus an effect of the B3LYP functional used in the study should be discarded.

In addition, QTAIM describes Cu···O bonds with an intermediate character between ionic and covalent.

NBO analysis has shown that the systems under study are delocalised ones, and that electron delocalisation is similar in kaempferol and in its anions and metal complexes, although the net charge on atoms varies. On the other hand, kaempferol–copper dative bond in the metal complexes has been found where a proton is lost in the process of coordination, and changes in the single–double character of some bonds after coordination, and a flow of charge mainly from flavonoid moiety to metal cation in all the complexes. The charge of the central ion is predicted to be in the range of 1.300–1.400e.

Finally, there is no back donation from metal to ligands in any case.

Acknowledgments Authors are grateful to *University of Jaén (UJA)* and *Andalusian Government (Junta de Andalucía)* for financial support. Authors also are grateful to *Centro de Servicios de Informática y Redes de Comunicaciones (CSIRC),* belonging to the *University of Granada (UGR),* for computational time and facilities.

References

1. Andersen ØM, Markham KR (eds) (2006) Flavonoids: chemistry, biochemistry and applications. Taylor and Francis, Boca Raton
2. Jovanovic SV, Steenken S, Tosic M, Marjanovic B, Simic MG (1994) J Am Chem Soc 116:4846–4851
3. Pietta P-G (2000) J Nat Prod 63:1035–1042
4. Marfak A, Trouillas P, Allais D-P, Champavier Y, Calliste C-A, Duroux J-L (2003) J Agric Food Chem 51:1270–1277
5. Walle T (2004) Free Rad Biol Med 36:829–837
6. Williams RJ, Spencer JPE, Rice-Evans C (2004) Free Rad Biol Med 36:838–849
7. Fraga CG, Galleano M, Verstraeten SV, Oteiza PI (2010) Mol Asp Med 31:435–445
8. Procházková D, Boušová I, Wilhelmová N (2011) Fitoterapia 82:513–523
9. Han R-M, Zhang J-P, Skibsted LH (2012) Molecules 17:2140–2160
10. Pal D, Verma P (2013) Int J Pharm Pharm Sci 5:95–98
11. Aparicio S (2010) Int J Mol Sci 11:2017–2038
12. Rong YZ, Wang ZW, Zhao B (2013) Food Biophys 8:90–94
13. Leopoldini M, Marino T, Russo N, Toscano M (2004) Theor Chem Acc 111:210–216
14. Marković ZS, Mentus SV, Dimitrić Marković JM (2009) J Phys Chem A 113:14170–14179
15. van Acker SABE, de Groot MJ, van den Berg D-J, Tromp MNJL, Donné-op den Kelder G, van der Vijgh WJF, Bast A (1996) Chem Res Toxicol 9:1305–1312
16. Trouillas P, Marsal P, Siri D, Lazzaroni R, Duroux J-L (2006) Food Chem 97:679–688
17. Antonczak S (2008) J Mol Struct Theochem 856:38–45
18. Sarkar A, Middya TR, Jana AD (2012) J Mol Model 18:2621–2631
19. Kumar KS, Kumaresan R (2012) Comput Theor Chem 985:14–22
20. Grazul M, Budzisz E (2009) Coord Chem Rev 253:2588–2598
21. Selvaraj S, Krishnaswamy S, Devashya V, Sethuraman S, Krishnan UM (2013) Med Res Rev 4:677–702
22. Sanna D, Ugone V, Lubinu G, Micera G, Garribba E (2014) J Inorg Biochem 140:173–184
23. Rajendran P, Rengarajan T, Nandakumar N, Palaniswami R, Nishigaki Y, Nishigaki I (2014) Eur J Med Chem 86:103–112
24. Kepp KP (2012) Chem Rev 112:5193–5239
25. Migliorini C, Porciatti E, Luczkowski M, Valensin D (2012) Coord Chem Rev 256:352–368
26. Jomova K, Valko M (2011) Toxicology 283:65–87
27. Halliwell B, Gutteridge JMC (2013) Free radicals in biology and medicine, 4th edn. Oxford University Press, Oxford
28. Crichton RR (2008) Biological inorganic chemistry: an introduction. Elsevier, Amsterdam
29. Bader RFW (1990) Atoms in molecules: a quantum theory. Oxford University Press, Oxford
30. Popelier PLA (2000) Atoms in molecules: an introduction. Prentice Hall, London
31. Matta CF, Boyd RJ (eds) (2007) The quantum theory of atoms in molecules. Wiley-VCH, Weinheim
32. Weinhold F, Landis CR (2005) Valency and bonding: a natural bond orbital donor–acceptor perspective. Cambridge University Press, Cambridge
33. Glendening ED, Landis CR, Weinhold F (2012) WIREs Comput Mol Sci 2:1–42
34. Frisch MJ, Trucks GW, Schlegel HB, Scuseria GE, Robb MA, Cheeseman JR, Scalmani G, Barone V, Mennucci B, Petersson GA, Nakatsuji H, Caricato M, Li X, Hratchian HP, Izmaylov AF, Bloino J, Zheng G, Sonnenberg JL, Hada M, Ehara M, Toyota K, Fukuda R, Hasegawa J, Ishida M, Nakajima T, Honda Y, Kitao O, Nakai H, Vreven T, Montgomery JA Jr, Peralta JE, Ogliaro F, Bearpark M, Heyd JJ, Brothers E, Kudin KN, Staroverov VN, Keith T, Kobayashi R, Normand J, Raghavachari K, Rendell A, Burant JC, Iyengar SS, Tomasi J, Cossi M, Rega N, Millam JM, Klene M, Knox JE, Cross JB, Bakken V, Adamo C, Jaramillo J, Gomperts R, Stratmann RE, Yazyev O, Austin AJ, Cammi R, Pomelli C, Ochterski JW, Martin RL, Morokuma K, Zakrzewski VG, Voth GA, Salvador P, Dannenberg JJ, Dapprich S, Daniels AD, Farkas O, Foresman JB, Ortiz JV, Cioslowski J, Fox DJ,

Gaussian 09, Revision D.01, Gaussian, Inc., Wallingford CT (2013)
35. Cramer CJ, Truhlar DG (2009) Phys Chem Chem Phys 11(46):10757–10816
36. Neese F (2009) Coord Chem Rev 253:526–563
37. Tsipis AC (2014) Coord Chem Rev 272:1–29
38. Zhang W, Truhlar DG, Tang M (2013) J Chem Theory Comput 9:2965–397739
39. Scuseria GE, Staroverov VN (2005) Progress in the development of exchange-correlation functionals in theory and applications of computational chemistry. In: Dykstra CE et al (eds) The first forty years. Elsevier, AmsterdamThe Netherlands
40. Zhao Y, Truhlar DG (2008) Theor Chem Acc 120:215–241
41. Shil S, Bhattacharya D, Sarkar S, Misra A (2013) J Phys Chem A 117:4945–4955
42. Chai J-D, Head-Gordon M (2008) Phys Chem Chem Phys 10:6615–6620
43. Rulíšek L, Vondrášek J (1998) J Inorg Biochem 71:115–117
44. Dudev M, Wang J, Dudev T, Lim C (2006) J Phys Chem B 110:1889–1895
45. Lapouge C, Dangleterre L, Cornard J-P (2006) J Phys Chem A 110:12494–12500
46. Ren J, Meng S, Lekka ChE, Kaxiras E (2008) J Phys Chem B 112:1845–1850
47. Lekka ChE, Ren J, Meng S, Kaxiras E (2009) J Phys Chem B 113:6478–6483
48. Symonowicz M, Kolavek M (2012) Biotechnol Food Sci 76:35–45
49. Tarahovsky YS, Kim YA, Yagulnik A, Muzafarov EN (2014) Biochim Biophys Acta 1838:1235–1246
50. Agieienko VN, Kolesnik YN, Kalugiu ON (2014) J Chem Phys 140:194501
51. AIM200 (2002) A program to analyze and visualize atoms in molecules. SBK-Software
52. Macchi P, Sironi A (2003) Coord Chem Rev 238–239:383–412
53. Cortés-Guzmán F, Bader RFW (2005) Coord Chem Rev 249:633–662
54. Nakanishi W, Hayashi S, Narahara K (2009) J Phys Chem A 113:10050–10057
55. Stalke D (2011) Chem Eur J 17:9264–9278
56. Bagchi S, Mandal D, Ghosh D, Das AK (2013) J Phys Chem A 117:1601–1613
57. Cukrowski I, de Lange JH, Mitoraj M (2014) J Phys Chem A 118:623–637
58. International Union of Pure and Applied Chemistry (2005) Nomenclature of inorganic chemistry: IUPAC recommendations. RSC Publishing, Cambridge

Theor Chem Acc (2015) 134:48
DOI 10.1007/s00214-015-1649-z

REGULAR ARTICLE

Scavenger mechanism of methylglyoxal by metformin. A DFT study

Christian Solís-Calero[1] · Joaquín Ortega-Castro[1] · Juan Frau[1] · Francisco Muñoz[1]

Received: 14 November 2014 / Accepted: 18 March 2015 / Published online: 4 April 2015

Abstract We have studied the mechanism of the reaction between the most stable and the most represented in literature tautomers of metformin and methylglyoxal by density functional theory calculations. Designed models included 16 explicit water solvent, which forms hydrogen bond networks around the reactants and intermediates molecules, facilitating intramolecular proton transfer in some steps of the reaction mechanism. The reaction takes place in five steps, namely: (1) formation of a dimethylguanide–guanylhydrazone–acetylcarbinol adduct, (2) formation of a zwitterionic triazepine derivative by ring closure, (3) dehydration of this intermediate, (4) an imine–enamine tautomerism, (5) an enol–keto tautomerism. The first step was found as the rate-determining step for the reaction, having the reaction an overall activation energy value of 9.7 kcal mol^{-1}.

Keywords α-Dicarbonyl compound · Methylglyoxal · Metformin · Triazepine derivatives · Non-enzymatic glycation · AGEs · DFT calculations

Published as part of the special collection of articles derived from the 9th Congress on Electronic Structure: Principles and Applications (ESPA 2014).

Electronic supplementary material The online version of this article (doi:10.1007/s00214-015-1649-z) contains supplementary material, which is available to authorized users.

✉ Francisco Muñoz
paco.munoz@uib.es

[1] Departament de Química, Institut d'Investigació en Ciències de la Salut (IUNICS), Universitat de les Illes Balears, 07122 Palma de Mallorca, Spain

1 Introduction

Non-enzymatic glycation is a complex group of reactions that starts by nucleophilic attack on free reducing sugars by free amino groups of proteins, DNA and lipids. A highly unstable Schiff bases are produced and transformed into early glycation product also known as Amadori product. This intermediate undergoes a series of complex reactions and generates advanced glycation end-products (AGEs).

Non-enzymatic glycation is particularly important during hyperglycaemia where α-dicarbonyl compounds are generated. These compounds react with several biomolecules to generate α-dicarbonyl-derived glycation products, which are correlated with diabetic complications such as nephropathy, retinopathy, and neuropathy, among others, being also implicated in pathology of a wide range of other human diseases and ageing, such as Alzheimer's disease, Parkinson's disease, amyotrophic lateral sclerosis, and age-related erectile dysfunction [38, 48, 73]. One of these α-dicarbonyl compounds is methylglyoxal, which is extremely reactive, being a physiological metabolite formed by lipid peroxidation, ascorbate autoxidation, oxidative degradation of glucose and degradation of glycated proteins. Methylglyoxal is capable of stimulating several mechanisms of cellular signal transduction and gene expression as useful role in living organisms [63]. However, it could induce cellular damage through giving rise to a multitude of adducts and cross-links by its reactions with several kind of biomolecules, accelerating the rate of glycation leading to the formation of AGEs [27].

Several pharmacological reagents, such as aminoguanidine, tenilsetam, carnosine, metformin, and pyridoxamine, have been investigated experimentally for inhibiting the formation of AGEs by trapping reactive dicarbonyl species

[8, 46]. Previous experimental and theoretical studies of our group on the reactivity of AGEs inhibitors were refereed to pyridoxamine and analogues and their reactions with sugars and other glycating compounds [3, 4, 50]. Our group also has theoretical works about Cu^{2+}, Fe^{3+} and Zn^{2+} complexes of some AGEs inhibitors including aminoguanidine, pyridoxamine and LR-74, taking insights about their stability and potential ability for chelating metal ions as a mechanism for inhibiting the formation of AGEs [5, 49, 51, 52]. Then, it would be of great interest to obtain mechanisms of reactions describing at atomic level the reaction of these drugs with dicarbonyl compounds as a mechanism for preventing the formation of AGEs and its consequences [46].

Metformin (ME), or *N*,*N*-dimethylbiguanide, is a widely prescribed drug for the treatment of non-insulin-dependent diabetes mellitus and other metabolic syndromes. In addition, it exhibits antioxidant properties, either directly or indirectly [31], and it has been shown to increase neurogenesis, spatial memory formation and reduce the risk of Parkinson's disease [1]. There are also studies suggesting metformin as a possible anticancer agent, preventing the formation and progression of cancer [7, 12, 40]. Earlier, it has been proposed that metformin scavenges α-dicarbonyl compounds, preventing the subsequent production of AGEs from them [15, 62]. The results obtained under physiological conditions, pH 7.4 and 37 °C by these works, showed that metformin strongly reacted with methylglyoxal and glyoxal, forming triazepinone derivatives. One of the advantages of metformin as drug is its relatively safe toxicity profile [40].

In the past, the structure of metformin had been erroneously represented, which does not represent the most stable conformer, being only corrected by Bharatam in 2005 [14]. The biochemical and therapeutic properties of ME can be attributed to its electron distribution. As an example, it has been shown compounds with structural similarity to metformin, but lacking of π-electron delocalization are not antihyperglycemic [33], suggesting that this property and its high-affinity with metals are essential for its therapeutic properties [60]. In the present paper, we developed two theoretical mechanisms at atomic level for the reaction of ME and MG, having as starting structures the most represented in literature and the most stable tautomers, respectively, and having as a final product a triazepinone derivative in both cases. The reactivity is discussed by means of the description of the energy, and the geometry of the intermediate and transition state structures involved in such reaction.

2 Methodology

All of the calculations were performed in the frame of DFT with program package DMol3 of Accelrys, Inc [24–26],

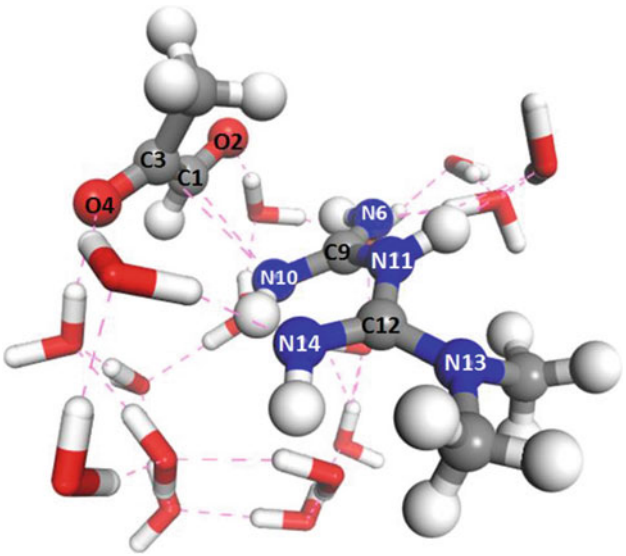

Fig. 1 Modelled molecular systems. Section of the initial model ($S1^B$) for ME, MG and the 16 water hydrogen bond network. Some atoms of the system are labelled, and *dotted lines* represent hydrogen bonds

using double numerical with polarization (DNP) basis sets [24] and Perdew–Burke–Ernzerhof (PBE) generalized gradient approximation (GGA) exchange–correlation functional [55, 56] with long-range dispersion correction via Grimme's scheme [34]. The DNP numerical basis set is comparable to Gaussian 6-31G (d,p) [42], minimizes the basis set superposition error [45], and its accuracy for describing hydrogen bond strengths showed a good agreement with experimental values [9]. PBE functional has been widely used in the study of great variety of molecular and extended systems, having accuracy for molecular systems, in the prediction of properties such as ionization potentials, electron affinities, and bond distances [22, 30, 32, 75]. The maximum number of numerical integration mesh points available in DMol3 was chosen for our computations, and the threshold of density matrix convergence was set to 10^{-6}. A Fermi smearing of 0.005 Hartree and a real-space cut-off of 4.5 Å were also used to improve the computational performance.

A model for a system with ME and MG was designed including 16 water molecules as explicit solvent, this number was sufficient for solvating all polar and charge groups of reagents, and keeping a hydrogen bond network in the molecular system (Fig. 1, $S1^B$ in Scheme 1), useful for modelling proton transfers involved in some steps of the reaction. A first optimization of metformine, methylglyoxal and 16 waters cluster was performed. Later, an additional solvent environment was modelled via the conductor-like screening model (COSMO) [10, 23, 37] and a second reoptimization was realized. Metformin can in principle adopt

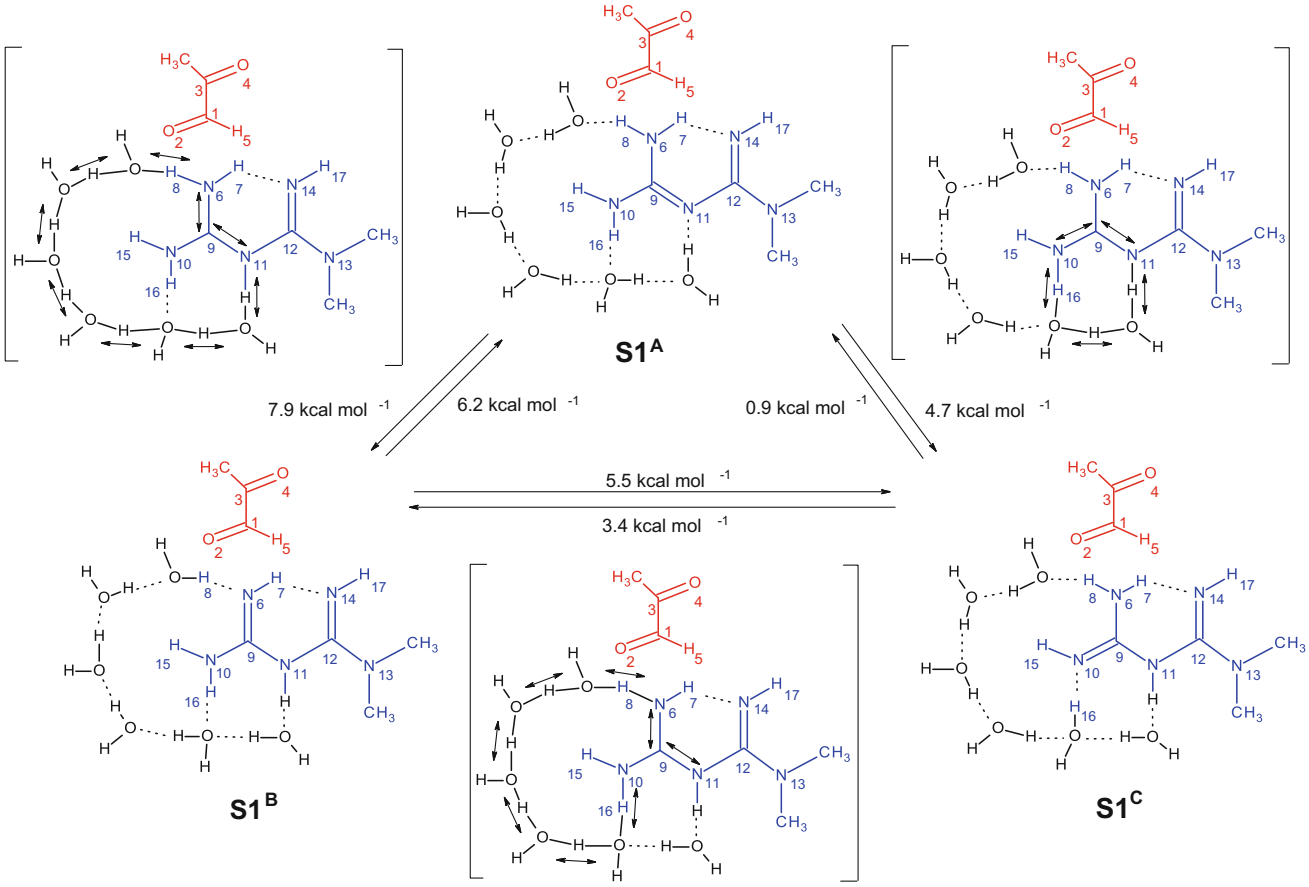

Scheme 1 Mechanism of the equilibrium reactions between the most stable ($S1^A$) and other metformin tautomers ($S1^B$, $S1^C$). *Dotted lines* represent hydrogen bonds and *arrows* represent the direction of the free energy barriers related to these equilibriums. Only 6 of the 16 water molecules are represented for clarity purposes (ME: *blue*, MG: *red*, H_2O: *black*)

several tautomeric forms, and some of them are characterized by delocalization of lone pair of electrons from the NH_2 groups in addition to conjugative delocalization as in biguanide [69]. Three tautomeric forms of ME were modelled and included in different starting structures, named them as $S1^A$, $S1^B$ and $S1^C$ (Scheme 1). The $S1^A$ tautomer was structurally equivalent to the most stable conformer of the mono-non-protonated biguanide determined by other theoretical study at the MP2/6-31+G* level [14]. This conformer is characterized by the absence of hydrogen atom at the bridging nitrogen N11. The $S1^B$ structure corresponded to the ME tautomeric form represented for several years in literature, with hydrogen at the bridging nitrogen N11 and a double bound between C9 and N6 atoms (Fig. 1). The third ME tautomer ($S1^C$) presents a hydrogen at the bridging nitrogen N11 as $S1^B$, but with a double bound between C9 and N10 atoms.

The initial models as reactants and the next models for stationary points of different steps of reaction between ME and MG in all the cases were optimized using the conjugated gradient algorithm. Transition state (TS) searches were performed with the complete LST/QST method [35]. The obtained TS was optimized via eigenvector following, searching for an energy maximum along one previous selected normal mode and a minimum along all other nodes, using Newton–Raphson method. After this procedure, one transition state was found for each reaction step. Each TS structure was characterized by a vibrational analysis with exactly one imaginary frequency, and their free energies (ΔG) values were obtained from the standard thermochemistry output of frequency calculations. The isomer of MG considered in these calculi was the trans-form, because experimental and theoretical studies have shown that this is the most estable isomer [11]. Although the formation of the final product of the reaction between ME and MG, a triazepinone derivative (a seven-membered unsaturated heterocycle), requires the availability of the two carbonyl groups of them to be cycled in their condensation with ME amine groups, the reaction could also be influenced by the equilibrium between MG and its hydrated form. Due to that, we also consider to evaluate the hydration of MG like a separated step, modelling the

structure for the monohydrated form of MG and calculating the TS for its conversion in conventional non-hydrated MG.

3 Results and discussion

In all the studied systems, Schemes 1, 2, 3, and 4 are included 16 water molecules forming hydrogen bond networks with hydrogen bond donors or acceptors groups of reagents and intermediates of reactions. These networks play a prominent role in all proton transfers, water molecules act in some steps as a proton-transfer carrier, in a hydrogen bond bridge between donor and acceptor groups. Additionally, water molecules influence on the free energy barriers in the reactions steps, through electrostatic stabilization of ionic intermediates and transition states structures. The chemical equilibrium between ME tautomers belonged to $S1^A$, $S1^B$, and $S1^C$ structures is represented in Scheme 1, including the free energy barriers related to them.

The most stable ME tautomer ($S1^A$) is characterized by the absence of a hydrogen joined covalently to the bridging nitrogen N11 and a strong conjugation between C9–N11 and C12–N14 double bonds, being the π bonding distributed over a set of atoms, (structure $S1^A$, Schemes 1, 2). The tautomerization of $S1^B$ to $S1^A$ had a free energy barrier of 6.2 kcal mol^{-1}, and the proton transfer from N6 to N11, inherent to this tautomerization, was realized through a hydrogen bond wire of six water molecules (Schemes 1, 3). The molecular system in $S1^B$ structure had a free energy value 1.7 kcal mol^{-1} higher than $S1^A$ (Table 1). This difference is increased in 5.7 kcal mol^{-1} when the pre-reactive complex of the ME structures are optimized. When the comparison was between pre-reactives $S1^A$ and $S1^C$ tautomers, this difference had a value of 6.1 kcal mol^{-1}. These values are close to the relative free energies obtained for biguanide tautomers through MP2/6-31+G* calculations [14], where biguanide tautomers equivalent to ME tautomers included in $S1^B$ and $S1^C$.

The reaction between ME and MG involves five steps (mechanism A, Scheme 2, and mechanism B, Scheme 3): (1) formation of a dimethylguanide–guanylhydrazone–acetylcarbinol adduct by condensation of ME and MG (structures 1–3), (2) formation of a zwitterionic triazepine derivative by ring closure (structures 3–5), (3) dehydration of this intermediate (structures 5–9), (4) an imine–enamine tautomerism (structures 9-11), (5) an enol–keto tautomerism (structures 11–13), with the formation of 2-amino-4-(dimethylamino)-7-methyl-5,7-dihydro-6*H*-[1,3,5]triazepine-6-one as final product. The pathway started from the more represented ME tautomer shares the same steps, adding an additional step, an imine–amine tautomerism with the formation of the same triazepinone derivative as final product (Scheme 3). The conversion of MG monohydrate form to conventional non-hydrated form of MG is shown in Scheme 4. The free energy (ΔG) values for each structure involved in the reaction between both tautomers of ME and MG are listed in Table 1, the comparative ΔG profiles are shown in Fig. 2. There are structurally data (atoms distances) and Mulliken charge analysis for each intermediate and transition state of the mechanism obtained for the reaction between the most stable ME tautomer and MG (Support Information Table S1 and S2).

3.1 Condensation of ME and MG

$S1^A$ tautomer is the starting point in the mechanism A (Scheme 2). In this initial structure, the amine group of ME (N6) and the carbonyl group (C1) of MG is located at a distance of 2.61 Å and with a N6–C1–C3 angle of 77.2°. An intramolecular hydrogen bond (1.95 Å) was established between H21 of an auxiliary water molecule and the carbonyl oxygen O2. Besides, a second water molecule was double-bridged to the incoming amine and the oxygen of the first auxiliary water molecule trough the formation of two hydrogen bonds, H8–O18 (1.76 Å) and H19–O20 (1.69 Å), connecting in a hydrogen bond wire N6 and O2 atoms, proton donor and acceptor, respectively. The mechanism A started with a nucleophilic attack of the basic amine group from ME at the aldehyde carbon from MG, concerted with a protonation of the O2 oxygen atom realized through the described hydrogen bond wire ($S1^A$ to $S3^A$ through $TS2^A$ in Scheme 2; Fig. 3).

The determined free energy barrier for this step has a value of 9.7 kcal mol^{-1}. This part of the reaction mechanism has been determined in other molecular systems, for analogous step in the reaction between 4-pyridinaldehyde and methylamine had a free energy barrier of 7.9 kcal mol^{-1} using B3LYP/6-31+G* level of calculus in gas phase [64]. In the reactions between 3-hydroxy-4-aminomethylpyridine and acetaldehyde and glycolaldehyde, analogous steps had free energy barriers of 9.4 and 6.0 kcal mol^{-1}, respectively, using a B3LYP/6-31+G(d) level of calculus with CPCM approach in order to mimic the water solvent effect, and 9.7 and 10.1 kcal mol^{-1}, respectively, using the same level of calculus in gas phase [50]. In our study, the inclusion of COSMO solvation model could have modified the free energy barriers, reducing it, in the same way it was described in the case of the glycoaldehyde reaction.

There is an alternative mechanism occurring in other systems where carbon–nitrogen bond formation and protonation of the oxygen atom do not occur in a concerted manner, existing a zwitterionic intermediate between both steps [53, 59, 67, 68]. There is experimental evidence that

Scheme 2 Mechanism of the reaction of metformin with methylglyoxal (mechanism A). *Dotted lines* represent hydrogen bonds and *arrows* represent changes in the electronic density and proton transfers. Only 6 of the 16 water molecules are represented for clarity purposes (ME: *blue*, MG: *red*, H_2O: *black*)

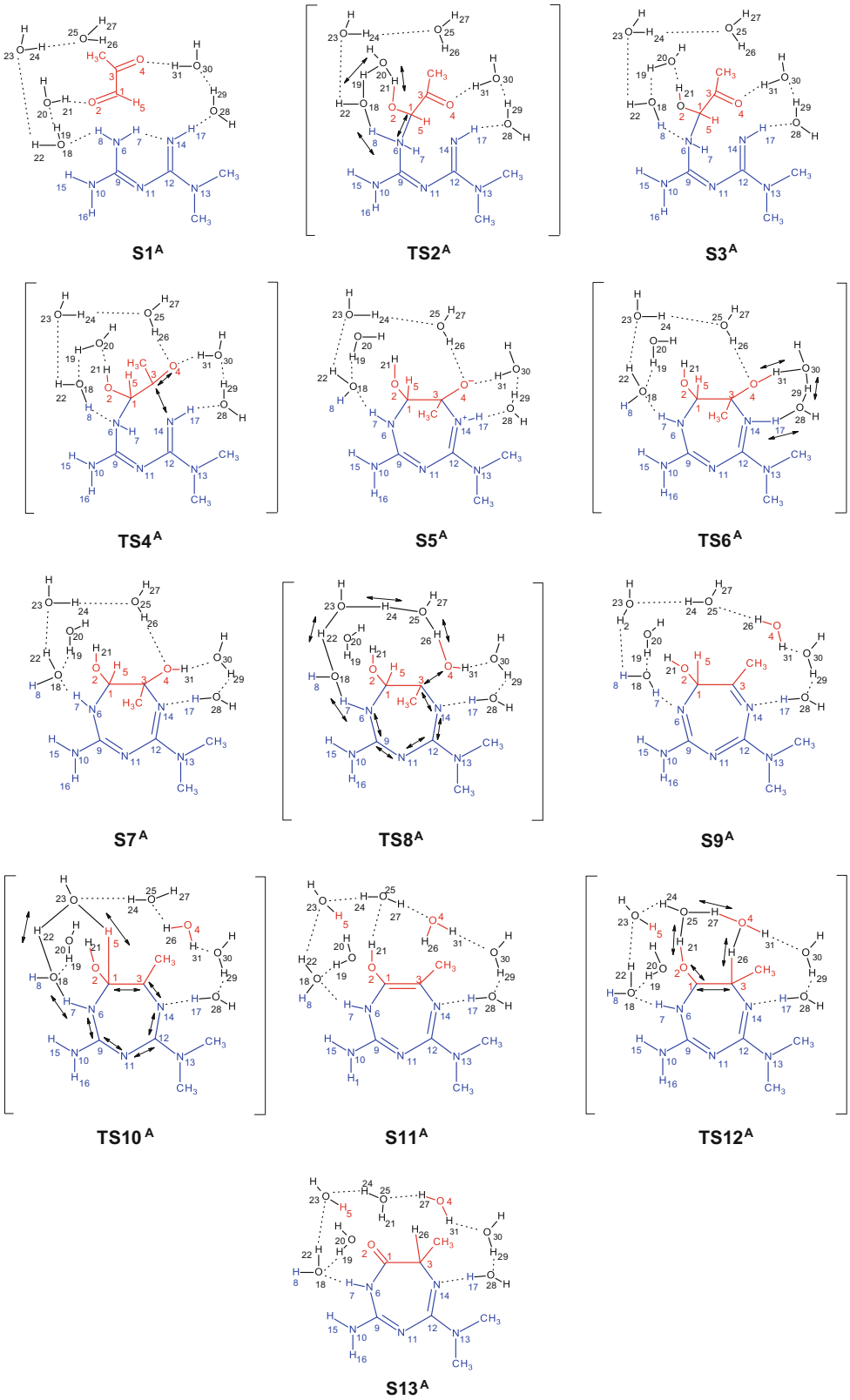

concerted and step-wise pathways may occur concomitantly in acid-catalysed *O*-methyloxime formation [61] and that the prevalence of one above the other is dictated by the stability of the zwitterionic form relative to the transition state for the "concerted" pathway. A zwitterionic intermediate was not found during calculus for the mechanism of

Scheme 3 Mechanism for the second evaluated for the reaction between metformin and methylglyoxal (mechanism B). *Dotted lines* represent hydrogen bonds and *arrows* represent changes in the electronic density and proton transfers. Only 6 of the 16 water molecules are represented for clarity purposes (ME: *blue*, MG: *red*, H_2O: *black*)

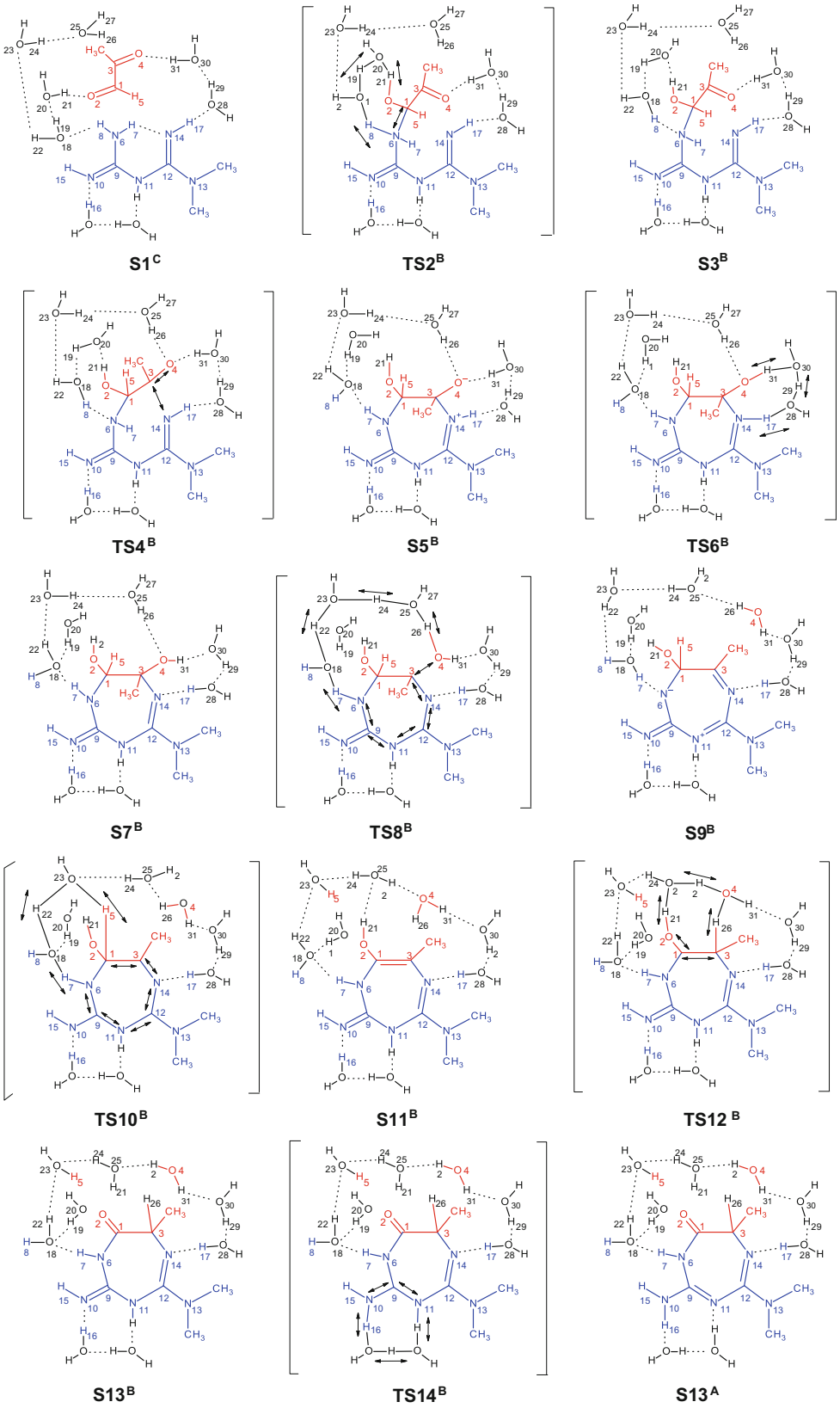

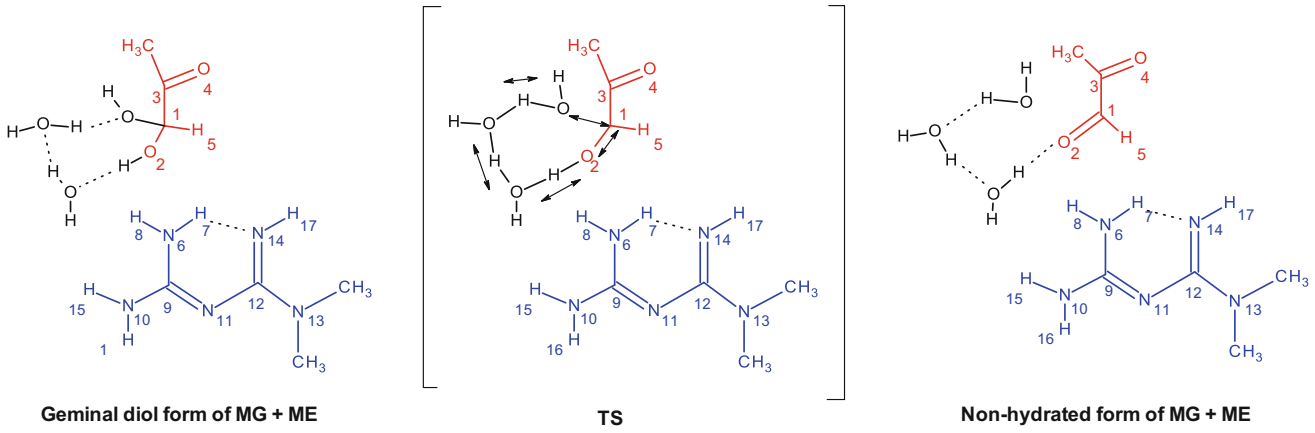

Scheme 4 Mechanism for the hydration of methylglyoxal. *Dotted lines* represent hydrogen bonds and *arrows* represent changes in the electronic density and proton transfers. Only 3 of the 16 water molecules are represented for clarity purposes (ME: *blue*, MG: *red*, H_2O: *black*)

Table 1 Relative free energies (ΔG) for each of the structures of the reaction paths from the standard thermochemistry output of a frequency calculation

Most stable tautomer		Alternative tautomer	
Structure	ΔG (kcal mol^{-1})	Structure	ΔG (kcal mol^{-1})
		$S1^B$	1.7
		$TS1^C$	7.2
$S1^A$	0.0	$S1^C$	3.7
$TS2^A$	9.7	$TS2^B$	16.9
$S3^A$	−1.5	$S3^B$	3.9
$TS4^A$	9.6	$TS4^B$	9.5
$S5^A$	−18.6	$S5^B$	−7.0
$TS6^A$	−13.0	$TS6^B$	2.9
$S7^A$	−14.7	$S7^B$	−2.5
$TS8^A$	3.0	$TS8^B$	15.7
$S9^A$	−10.5	$S9^B$	3.8
$TS10^A$	8.2	$TS10^B$	15.0
$S11^A$	−14.0	$S11^B$	−11.6
$TS12^A$	−0.9	$TS12^B$	−2.0
$S13^A$	−32.8	$S13^B$	−26.6
		$TS14^B$	−20.7
		$S13^A$	−32.8

reaction between ME and MG. The proximity of imine (N4–H17) and amine (H15–N10–H16) groups make less favourable the stability of a positive charged N6 atom in the zwitterionic intermediate.

The most represented conformer of ME ($S1^B$ structure) is taken as initial structure in the mechanism B. At first, a tautomerization of $S1^B$ to $S1^C$ was realized with a proton shift, moving the double bond from N6=C9 to C9=N10 (Scheme 1) with a free energy barrier value of 5.5 kcal mol^{-1} (Table 1). This $S1^C$ ME tautomer has a conformation with an amine group (H7–N6–H7) oriented to the MG aldehyde group for the nucleophilic attack. From $S1^C$ structure, the condensation of ME and MG was realized properly in the same way to the described pathway in the mechanism A ($TS2^B$ in Scheme 3). The free energy barrier for this step was 13.2 kcal mol^{-1}, a value higher than the obtained for the same step in mechanism A. This difference is found also in the next intermediates and transition states (free energy profile in Fig. 2) of both mechanisms, and it could be ascribed to the different electronic delocalization on their atomic frames.

The susceptibility of MG aldehyde group to a nucleophilic attack by thiols and amines has been detailed by other authors [36, 46]. Analogous condensation steps are known with amides like formamide, acetamide and benzamide when condensed with aromatic 1,2-diketones [58]. Products of this reactions need a posterior treatment with hydrazine hydrate to be cyclized to stable 1,2,4-substituted triazines. Pre-incubation of methylglyoxal with a variety of carbonyl scavengers such as aminoguanidine or tenilsetam and the thiol antioxidant lipoic acid significantly reduced its toxicity, offering a promising therapeutic strategy to reduce the toxicity of reactive carbonyl compounds [71, 74]. It has been also shown that biguanides react with α-diketones in strongly alkaline ethanolic media [70], and the reaction of ME with MG and glyoxal has been demonstrated under physiological conditions [62].

3.2 Formation of a zwitterionic triazepine derivative by ring closure

In the mechanism A, this step started from dimethylguanide–guanylhydrazone–acetylcarbinol adduct ($S3^A$ structure) formed in the before step. This cyclization step proceeds when the nearby nucleophilic nitrogen N14

attacks the electrophilic C3 atom, forming a zwitterionic triazepine derivative ($S5^A$ in Scheme 2). Atoms O4 and N14 were stabilized in $S5^A$ structure via intramolecular hydrogen bond with solvent molecules around. According Baldwin rules for general stereoelectronic constraints on cyclization reactions [13], this ring closure would be energetically favourable and could be classified as 7-exo-trig. This kind of heterocyclization has been reported by other studies [44, 54].

The ring closure of $S3^A$ structure proceeded with a value of 11.1 kcal mol^{-1} for its free energy barrier (Fig. 2; Table 1). In the mechanism B, this barrier has a value of 5.7 kcal mol^{-1}. It has been demonstrated by experimental studies that triazepine ring systems are difficult to synthesize, being cyclization to seven-membered rings, in general, much less common [44]. In the case of mechanism B, this step was only possible having $S1^C$ structure as one of previous intermediates because the cyclization depends upon the nitrogen atom involved in the nucleophilic attack.

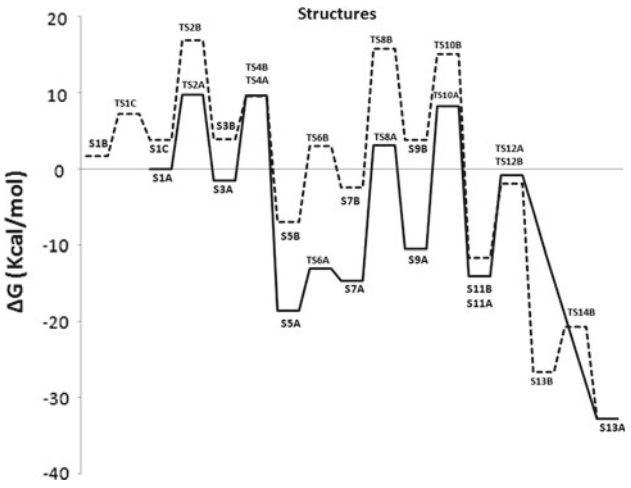

Fig. 2 Free energy (ΔG) profile for the reaction between ME and MG. Mechanism A (*continued line*) started with the most stable ME tautomer $S1^A$, mechanism B started with the most representative ME tautomer $S1^B$ (*dotted line*)

3.3 Dehydration

This step of reaction was considered in two parts, in the first the zwitterionic triazepine derivative is converted to the neutral form of this triazepine derivative though a proton transfer from N14 to O4 through an hydrogen bond chains of two water molecules ($S5^A$ to $S7^A$ through $TS6^A$ in Scheme 2). The free energy barrier of this part has a value of 5.6 kcal mol^{-1}, in the mechanism B this value had a value of 9.9 kcal mol^{-1} (Fig. 2). The second part of the considered step was the dehydration properly, with a concerted break of the bond C3–O4 with the proton transfer from N6 to O4 through a hydrogen bond chain of three water molecules and an electronic rearrangement in the nitrogen–carbon frame of ME ($S7^A$ to $S9^A$ through $TS8^A$ in Scheme 2; Fig. 4). This electronic rearrangement was showed with geometric parameters (tables S1), converting for example, the imine double bond between C12 and N14 into a single, and in fact, the distance between these two atoms increased from 1.32 Å in $S7^A$ structure to 1.40 Å in $S9^A$ structure. This rearrangement was also extended to the hydrogen bond network of water molecules connecting polar groups of the resulting $S9^A$ structure (Fig. 5).

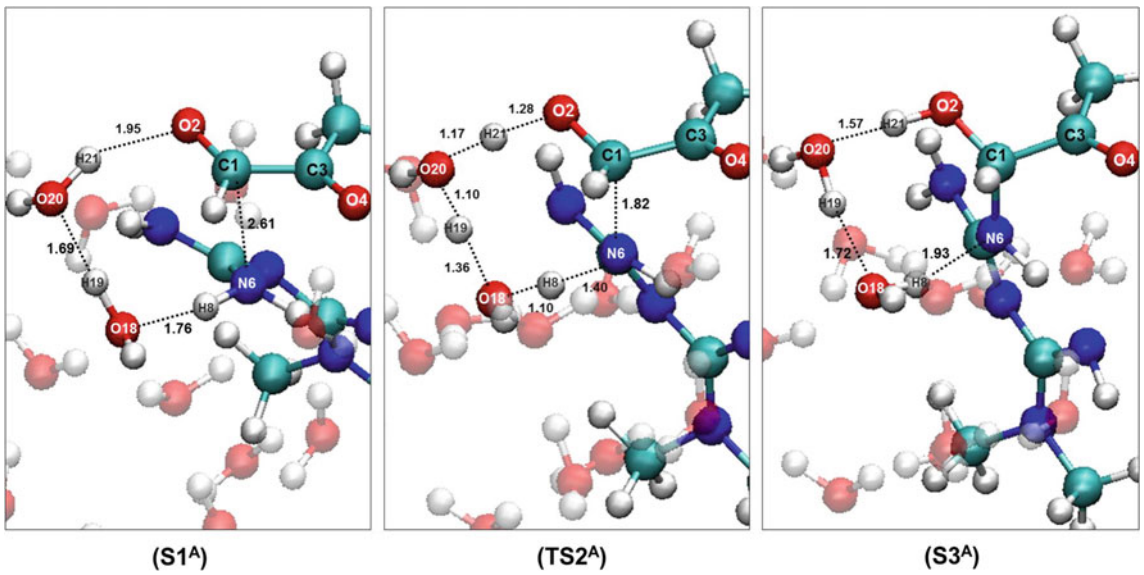

Fig. 3 The pathway for the formation of a dimethylguanide–guanylhydrazone–acetylcarbinol adduct in the reaction between ME and MG. ($S1^A$) Starting structures; ($TS2^A$) transition state; ($S3^A$) dimethylguanide–guanylhydrazone–acetylcarbinol adduct

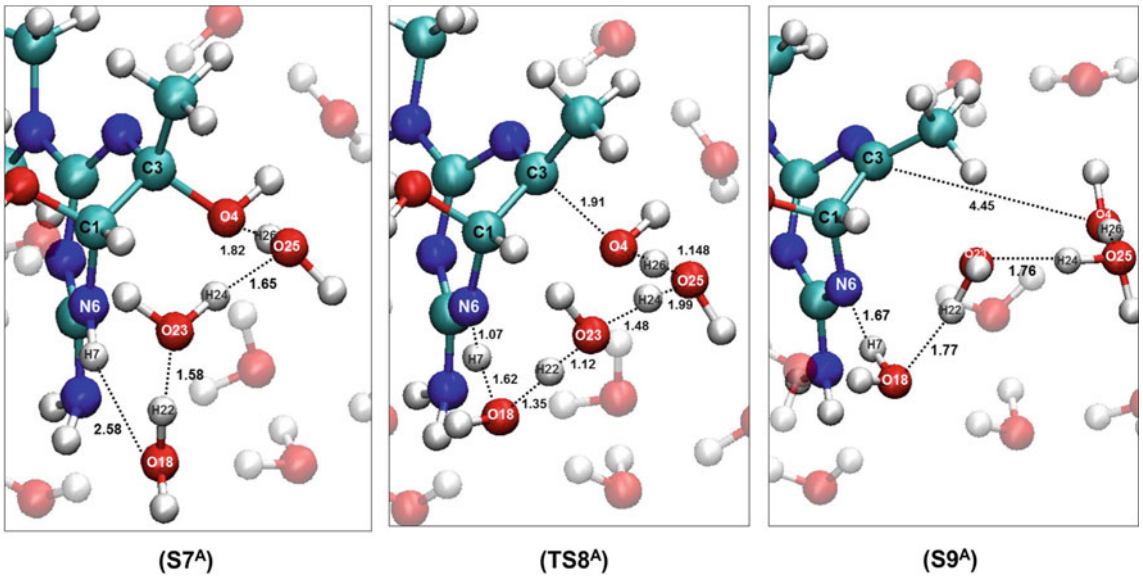

Fig. 4 The pathway for the dehydration of zwitterionic triazepine derivative in the reaction between ME and MG. ($S7^A$) Zwitterionic triazepine derivative; ($TS8^A$) transition state; ($S9^A$) triazepine intermediate

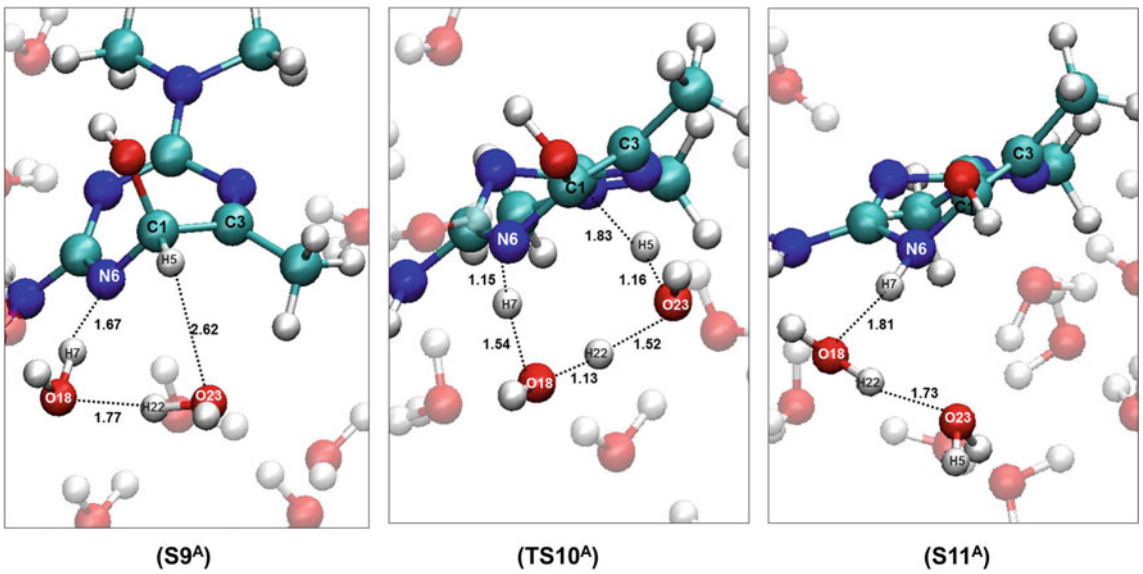

Fig. 5 The pathway for an imine–enamine tautomerism in the reaction between ME and MG. ($S9^A$) Triazepine intermediate; ($TS10^A$) transition state; ($S11^A$) triazepine enaminol intermediate

The obtained free energy barrier for this dehydration was 17.7 kcal mol^{-1}, a close value to 18.3 kcal mol^{-1} obtained in the alternative pathway for analogous dehydration (Table 1). These values represented one of the higher free energy barriers found in both pathways, and a feature also found in reactions with similar step in other molecular systems [41, 50, 64, 66]. The driving force for this dehydration could come from the generated conjugated system in $S9^A$ structure, stabilized by resonance in the triazepine ring, and changes in the Mulliken partial charges of ring atoms since $S7^A$ to $S9^A$ structures (table S2) give clues of this kind of influence. In the case of mechanism B, the $S9^B$ structure had a less stability, having a free energy value 14.3 kcal mol^{-1} higher than $S9^A$ (Table 1). This difference may be attributed to the presence of a hydrogen joined covalently to nitrogen N11, making difficult a regular π bonding distribution over the set of atoms of triazepine ring. Then, the intermediate, $S9^B$, is represented for

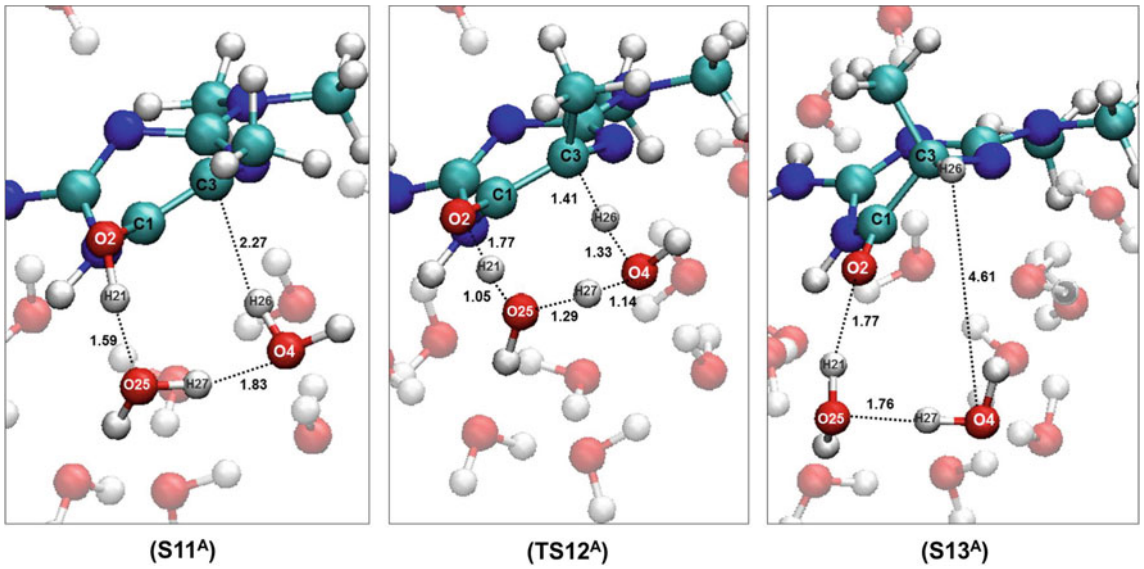

Fig. 6 The pathway for an enol–keto tautomerism in the reaction between ME and MG. ($S11^A$) Triazepine enaminol intermediate; ($TS12^A$) transition state; ($S13^A$) 2-amino-4-(dimethylamino)-7-methyl-5,7-dihydro-6*H*-[1,3,5]triazepine-6-one

didactic purposes in Scheme 3 with charges on N6 and N11 atoms ($S9^B$ structure in Scheme 3).

3.4 Imine–enamine tautomerism

In this step starting from $S9^A$ structure, N6 nitrogen atom as a Bronsted base does a nucleophilic attack on a proton joined to a carbon atom (C1) attached to the hydroxyl group (O2–H21), realizing a proton transfer from C1 to N6 atom through a chain of two water molecules ($S9^A$ to $S11^A$ through $TS10^A$ in Scheme 2; Fig. 5). When a proton (H5) is released from C1, a new π bond is formed between C3 and C1 carbon atoms what is evidenced by the reduction of the bond distance between these atoms from 1.52 Å in $S9^A$ structure to 1.36 Å in $S11^A$ structure. The effects of this intramolecular rearrangement are extended also to the bond distance between C3 and N14 which is increased from 1.30 Å in $S9^A$ structure to 1.42 Å in $S11^A$ structure.

According to the free energy profile (Fig. 2), this imine–enamine tautomerism had a free energy barrier value of 18.7 kcal mol^{-1} in the first pathway. This barrier had a value of 11.2 kcal mol^{-1} in the mechanism B, difference attributed to the less stability of $S9^B$ intermediate structure in comparison with $S9^A$. According to other theoretical works [18, 19, 43, 57], the rate of converting the imine to enamine depends on how easy it is for an α carbon in the imine to deprotonate and that is influenced directly by its substituents, which could contributed to lower the basicity of the α carbon during the reaction. In this triazepine ring system, this α carbon corresponds to C1 labelled atom (Scheme 2; Fig. 5). This atom has an electronegative hydroxyl group (O2–H21), which could render inductively electron-withdrawing during the deprotonation of the adjacent carbon atom, dispersing its negative charge, facilitating the proton release ($TS10^A$ in Scheme 2; Fig. 5). During this tautomerism, the hydroxyl group adjacent to C1 atom has a conversion from weak electron-withdrawing when it is attached to an sp3 carbon ($S9^A$ structure) to electron-releasing group due to the resonance effect when it is attached to an sp2 carbon ($S11^A$ structure).

3.5 Enol–keto tautomerism

As other molecules with an enamine group, the triazepine enaminol intermediate generated in the previous step yields a triazepinone compound due to an enol–keto tautomerism. The tautomerization proceeds in both cases through a concerted proton transfer from O2 atom donor to C3 atom acceptor, having two water molecules as a bridge ($S11^A$ to $S13^A$ through $TS12^A$ in Scheme 2; Fig. 6). The catalytic effect of explicit water molecules on keto–enol tautomerism has been shown theoretically in other molecular systems, such as the ketonization of vinyl alcohol in gas phase [72], keto–enol tautomerism in pyruvate, and acetylacetone [6, 76], acetone enolization [21], and Amadori product formation [65]. The evolution of this tautomerism could be appreciated through changes of the distance between atoms involved in it (Fig. 6), what is exemplified by the increase of the bond distances C1–C3 and C1–O2 from 1.36 and 1.37 Å in $S11^A$ structure to 1.52 and 1.24 Å in $S13^A$ structure, respectively.

The free energy barrier for this tautomerism was 13.1 kcal mol^{-1}. In the case of mechanism B, this value was 9.6 kcal mol^{-1} (Fig. 2; Table 1). The final products in both mechanisms S13^{A} and S13^{B} are very stable in comparison with their intermediates S11^{A} and S11^{B}, having free energy values 18.8 and 15.0 kcal mol^{-1} lower than them, respectively. The resulting product of this step in the first mechanism is a 2-amino-4-(dimethylamino)-7-methyl-5,7-dihydro-6*H*-[1,3,5]triazepine-6-one, a compound described experimentally as the final product of the reaction between ME and MG previously [62]. In order to get this product through the mechanism B, an imine–amine tautomerism step was added in this mechanism trough the proton transfer from N11 to N10 atoms, having as a bridge two water molecules (S13^{B} to S13^{A} through TS14^{B} Scheme 3). This additional step had as free energy barrier a value of 5.9 kcal mol^{-1} (Table 1).

3.6 Hydration of MG

One of the important properties of carbonyl compounds, mostly aldehydes, is the formation of hydrates in aqueous solutions by nucleophilic addition of water to their carbonyl groups. In solution, MG is present primarily as monohydrated form with the aldehydic group forming a geminal diol [39, 47]. This geminal diol form has not available in the necessary two carbonyl groups to generate the triazepinone final product of the reaction, but its equilibrium with its non-hydrated form influences in the development of the reaction. We found the conversion mechanism between of the monohydrated and non-hydrated forms of the MG with a free energy change of −7.0 kcal mol^{-1}, which agrees with bibliographic results [11, 39] (Scheme 4). The proposed mechanism involved the hydration over aldehydic group of MG (Scheme 4), taking in account that in solution the aldehyde group is hydrated more favourably than the ketone group [11, 39]. The free energy barrier for the direct reaction from the hydrated to non-hydrated MG forms was 8.6 kcal mol^{-1}, and in the inverse direction was 15.6 kcal mol^{-1}. These values could explain the slow speed of this conversion, shown by experimental works under physiological conditions, pH 7.4 and 37 °C [71]. Although the chemical equilibrium is shifted towards the formation of the hydrated compound, a small amount of non-hydrated species remain in the environment, being this specie preferentially attacked.

In the steps of the studied mechanisms, water had a significant catalytic effect because it can act both as a proton donor and as a proton acceptor and thus mediates concertedly the intramolecular proton transfer that leads to the formation of triazepinone final product, supplying furthermore a bridge for proton relay. Previous theoretical studies on tautomerism for other molecular systems in aqueous medium employed simplified models to describe the interconversion process, usually a few water molecules were included to mimic the water environment [17, 77]. However, the aqueous medium and its unique hydrogen-bonded structure provide numerous possibilities for participation of water. The modelled molecular systems included 16 water molecules, a reasonably number of water molecules which made possible the modelling of a hydrogen bond network connecting the polar groups of reactive molecules, and at the same time, the catalytic participation of different wire of water molecules in steps which involved proton transfers between atoms placed in a long distance for a direct transfer.

The presence of a guanidine group in the ME structure confers a potential use of this compound for the inhibition of non-enzymatic glycation reaction, by scavenging of carbonyl groups of reducing sugars and dicarbonyl compounds, decreasing carbonyl stress and inhibiting AGEs formation. However, it has been reported contradictory results about the efficiency of ME effect on diabetic complications through its ability to reduce toxic dicarbonyls and AGEs. There are studies that based on in vitro and in vivo assays, and clinical data support this hypothesis [15, 16, 20, 28, 62]. However, other studies reported ME to reduce α-dicarbonyls by an improvement in glycemic control than direct quenching of α-dicarbonyls [2, 29].

We have found as rate-limiting step the first step of condensation of ME and MG, giving to the reaction an apparent activation energy of 9.7 kcal mol^{-1} in the case of mechanism A. However, one of the steps with a higher free energy barrier was the dehydration step, having values of 17.7 and 18.3 kcal mol^{-1} in mechanisms A and B, respectively. It has been also shown in other reactions [41, 50, 64, 66] which share several steps in their mechanisms with the studied mechanisms of reaction between ME and MG. Higher values for free energy barriers were also obtained for imine–enamine tautomerism (18.7 kcal mol^{-1}), and they could explain in part the less efficiency of ME as dicarbonyl scavenger than aminoguanidine or pyridoxamine shown by some experimental works [2, 62].

4 Concluding remarks

We have studied the mechanism for the reaction between ME and MG in an aqueous medium by calculating intermediates, transition states structures and free energy profiles for all the elementary steps of the reaction. The pathway of the reaction between MG and the most stable tautomer of ME takes place in five steps: (1) formation of an acetylcarbinol adduct by condensation of ME and MG, (2) formation of a zwitterionic triazepine derivative by ring closure, (3) dehydration of this intermediate, (4) an imine–enamine

tautomerism, and (5) an enol–keto tautomerism, with the formation of 2-amino-4-(dimethylamino)-7-methyl-5,7-dihydro-6*H*-[1,3,5]triazepine-6-one as final product. We have found as rate-limiting step the first step of condensation of ME and MG, giving to the reaction an activation energy of 9.7 kcal mol^{-1}. However, the step with a higher free energy barrier was the dehydration step, what it has been also shown in other reactions that share several similarities in their mechanisms with the obtained mechanism. These features for the mechanism of reaction starting from the most stable tautomer of ME are shared for the mechanism started from the most represented tautomer of ME in literature. Intermediates and transition states structures of this alternative pathway are characterized for presenting higher values of their relative free energies than the equivalent structures of the first pathway. It seems to be that to the presence of a hydrogen joined covalently to nitrogen N11 in all the intermediates and transition states structures of the alternative pathway, making difficult a regular π bonding distribution over the set of atoms of ME frame and triazepine rings. The absence of hydrogen atom at the bridging nitrogen N11 makes possible a strong conjugation on extended atomic regions of different intermediates and transition states structures of the first pathway, stabilizing them.

Acknowledgments The financial support of Govern de les Illes Balears (AAEE27/2014) is gratefully acknowledged. C.S.-C. is grateful to the Spanish Ministry of Foreign Affairs and Cooperation for the award of a MAE-AECI fellowship. We are grateful to Centro de cálculo de Computación de Galicia (CESGA) and the Centro de cálculo de Computación de Cataluña (CESCA) for allowing the use of their computational facilities.

References

1. Adeyemi OO, Ishola IO, Adedeji HA (2013) Novel action of metformin in the prevention of haloperidol-induced catalepsy in mice: potential in the treatment of Parkinson's disease? Prog Neuropsychopharmacol Biol Psychiatry 48:245–251
2. Ahmad S, Shahab U, Baig MH, Khan MS, Khan MS, Srivastava AK, Saeed M (2013) Inhibitory effect of metformin and pyridoxamine in the formation of early, intermediate and advanced glycation end-products. PLoS ONE 8:e72128
3. Adrover M, Vilanova B, Muñoz F, Donoso J (2005) Inhibition of glycosylation processes: the reaction between pyridoxamine and glucose. Chem Biodivers 2:964–975
4. Adrover M, Vilanova B, Muñoz F, Donoso J (2007) Pyridoxamine, a scavenger agent of carbohydrates. Int J Chem Kinet 39:154–167
5. Adrover M, Vilanova B, Frau J, Muñoz F, Donoso J (2008) The pyridoxamine action on Amadori compounds: a reexamination of its scavenging capacity and chelating effect. Bioorg Med Chem 16:5557–5569
6. Alagona G, Ghio C, Nagy PI (2010) The catalytic effect of water on the keto–enol tautomerism. Pyruvate and acetylacetone: a computational challenge. Phys Chem Chem Phys 12:10173–10188
7. Aldea M, Craciun L, Tomuleasa C, Berindan-Neagoe I, Kacso G, Florian IS, Crivii C (2014) Repositioning metformin in cancer: genetics, drug targets, and new ways of delivery. Tumour Biol 35:5101–5110
8. Aldini G, Vistoli G, Stefek M, Chondrogianni N, Grune T, Sereikaite J, Sadowska-Bartosz I, Bartosz G (2013) Molecular strategies to prevent, inhibit, and degrade advanced glycoxidation and advanced lipoxidation end products. Free Radic Res 47:93–137
9. Andzelm J, Govind N, Fitzgerald G, Maiti A (2003) A DFT study of methanol conversion to hydrocarbons in a zeolite catalyst. Int J Quantum Chem 91:467–473
10. Andzelm J, Kölmel C, Klamt A (1995) Incorporation of solvation effects into density functional calculations of molecular energies and geometries. J Chem Phys 103:9312–9320
11. Axson JL, Takahashi K, De Haan DO, Vaida V (2010) Gas-phase water-mediated equilibrium between methylglyoxal and its geminal diol. Proc Natl Acad Sci USA 107:6687–6692
12. Azvolinsky A (2014) Repurposing to fight cancer: the metformin–prostate cancer connection. J Natl Cancer Inst 106:dju030
13. Baldwin JE (1976) Rules for ring closure. J Chem Soc Chem Commun 18:734–736
14. Bharatam PV, Patel DS, Iqbal P (2005) Pharmacophoric features of biguanide derivatives: an electronic and structural analysis. J Med Chem 48:7615–7622
15. Beisswenger P, Ruggiero-Lopez D (2003) Metformin inhibition of glycation processes. Diabetes Metab 29:6S95–6S103
16. Beisswenger PJ, Howell SK, Touchette AD, Lal S, Szwergold BS (1999) Metformin reduces systemic methylglyoxal levels in type 2 diabetes. Diabetes 48:198–202
17. Boekfa B, Pantu P, Probst M, Limtrakul J (2010) Adsorption and tautomerization reaction of acetone on acidic zeolites: the confinement effect in different types of zeolites. J Phys Chem C 114:15061–15067
18. Casasnovas R, Adrover M, Ortega-Castro J, Frau J, Donoso J, Muñoz F (2012) C–H activation in pyridoxal-5′-phosphate Schiff bases: the role of the imine nitrogen. A combined experimental and computational study. J Phys Chem B 116:10665–10675
19. Casasnovas R, Frau J, Ortega-Castro J, Donoso J, Muñoz F (2013) C–H activation in pyridoxal-5′-phosphate and pyridoxamine-5′-phosphate Schiff bases: effect of metal chelation. A computational study. J Phys Chem B 117:2339–2347
20. Chan NN (2001) Improved endothelial function with metformin in type 2 diabetes mellitus. J Am Coll Cardiol 38:2131
21. Cucinotta CS, Ruini A, Catellani A, Stirling A (2006) Ab initio molecular dynamics study of the keto–enol tautomerism of acetone in solution. Chem Phys Chem 7:1229–1234
22. Del Campo JM, Gázquez JL, Trickey SB, Vela A (2012) Non-empirical improvement of PBE and its hybrid PBE0 for general description of molecular properties. J Chem Phys 136:104108
23. Delley B (2006) The conductor-like screening model for polymers and surfaces. Mol Simul 32:117–123
24. Delley B (2000) From molecules to solids with the DMol3 approach. J Chem Phys 113:7756–7764
25. Delley B (1996) Fast calculation of electrostatics in crystals and large molecules. J Phys Chem 100:6107–6110
26. Delley B (1990) An all electron numerical method for solving the local density functional for polyatomic molecules. J Chem Phys 92:508–517
27. Desai K, Wu L (2007) Methylglyoxal and advanced glycation endproducts: new therapeutic horizons. Recent Pat Cardiovasc Drug Discov 2:89–99
28. Dhar I, Dhar A, Wu L, Desai KM (2013) Increased methylglyoxal formation with upregulation of renin angiotensin system in fructose fed Sprague Dawley rats. PLoS ONE 10:e74212

29. Engelen L, Lund SS, Ferreira I, Tarnow L, Parving HH, Gram J, Winther K, Pedersen O, Teerlink T, Barto R, Stehouwer CD, Vaag AA, Schalkwijk CG (2011) Improved glycemic control induced by both metformin and repaglinide is associated with a reduction in blood levels of 3-deoxyglucosone in nonobese patients with type 2 diabetes. Eur J Endocrinol 164:371–379
30. Ermzerhof M, Scuseria GE (1999) Assessment of the Perdew–Burke–Ernzerhof exchange-correlation functional. J Chem Phys 110:5029–5035
31. Esteghamati A, Eskandari D, Mirmiranpour H, Noshad S, Mousavizadeh M, Hedayati M, Nakhjavani M (2013) Effects of metformin on markers of oxidative stress and antioxidant reserve in patients with newly diagnosed type 2 diabetes: a randomized clinical trial. Clin Nutr 32:179–185
32. Fabiano E, Constantin LA, Della Sala F (2010) Generalized gradient approximation bridging the rapidly and slowly varying density regimes: a PBE-like functional for hybrid interfaces. Phys Rev B 82:113104
33. Fanshawe WJ, Bauer VJ, Ullman EF, Safir SR (1964) Synthesis of unsymmetrically substituted malonamides. J Org Chem 29:308–311
34. Grimme S (2006) Semiempirical GGA-type density functional constructed with a long-range dispersion correction. J Comput Chem 27:1787–1799
35. Halgren TA, Lipscomb WN (1977) The synchronous-transit method for determining reaction pathways and locating molecular transition states. Chem Phys Lett 49:225–232
36. Kalapos MP (1999) Methylglyoxal in living organisms: chemistry, biochemistry, toxicology and biological implications. Toxicol Lett 110:145–175
37. Klamt A, Schüürmann G (1993) COSMO: a new approach to dielectric screening in solvents with explicit expressions for the screening energy and its gradient. J Chem Soc Perkin Trans 2:799–805
38. Kovacic P, Somanathan R (2011) Cell signaling and receptors in toxicity of advanced glycation end products (AGEs): α-dicarbonyls, radicals, oxidative stress and antioxidants. J Recept Signal Transduct Res 31:332–339
39. Krizner HE, De Haan DO, Kua J (2009) Thermodynamics and kinetics of methylglyoxal dimer formation: a computational study. J Phys Chem A 113:6994–7001
40. Lettieri Barbato D, Vegliante R, Desideri E, Ciriolo MR (2014) Managing lipid metabolism in proliferating cells: new perspective for metformin usage in cancer therapy. Biochim Biophys Acta 1845:317–324
41. Liao R-Z, Ding W-J, Yu J-G, Fang W-H, Liu R-Z (2008) Theoretical studies on pyridoxal 5′-phosphate-dependent transamination of a-amino acids. J Comput Chem 29:1919–1929
42. Lin T, Zhang WD, Huang J, He C (2005) A DFT study of the amination of fullerenes and carbon nanotubes: reactivity and curvature. J Phys Chem B 109:13755–13760
43. Lin JF, Wu CC, Lien MH (1995) Ab-initio study on the imine–enamine tautomerism of the alpha-substituted imines (XH(2) CCH=NH, X=H, BH2, CH3, NH2, OH, F, CL, CN, NO). J Phys Chem 99:16903–16908
44. Martin N, Quinteiro M, Seoane C, Soto JL (1989) A novel example of a 7-exo-trig heterocyclization. Liebigs Ann Chem 10:1051–1053
45. Matsuzawa N, Seto J, Dixon DA (1997) Density functional theory predictions of second-order hyperpolarizabilities of metallocenes. J Phys Chem A 101:9391–9398
46. Monnier VM (2003) Intervention against the Maillard reaction in vivo. Arch Biochem Biophys 419:1–15
47. Nemet I, Vikic-Topic D, Varga-Defterdarovic L (2004) Spectroscopic studies of methylglyoxal in water and dimethylsulfoxide. Bioorg Chem 32:560–570
48. Neves D (2013) Advanced glycation end-products: a common pathway in diabetes and age-related erectile dysfunction. Free Radic Res 47:49–69
49. Ortega-Castro J, Frau J, Casasnovas R, Fernández D, Donoso J, Muñoz F (2012) High- and low-spin Fe(III) complexes of various AGE inhibitors. J Phys Chem A 116:2961–2971
50. Ortega-Castro J, Adrover M, Frau J, Salvà A, Donoso J, Muñoz F (2010) DFT studies on Schiff base formation of vitamin B6 analogues. Reaction between a pyridoxamine-analogue and carbonyl compounds. J Phys Chem A 114:4634–4640
51. Ortega-Castro J, Adrover M, Frau J, Donoso J, Muñoz F (2009) Cu^{2+} complexes of some AGEs inhibitors. Chem Phys Lett 475:277–284
52. Ortega-Castro J, Adrover M, Frau J, Donoso J, Muñoz F (2008) Chelating power of LR-74, a new AGE-inhibitor. Chem Phys Lett 465:120–125
53. Patil MP, Sunoj RB (2007) Insights on co-catalyst-promoted enamine formation between dimethylamine and propanal through ab initio and density functional theory study. J Org Chem 72:8202–8215
54. Pflästerer D, Dolbundalchok P, Rafique S, Rudolph M, Rominger F, Hashmi ASK (2013) On the gold-catalyzed intramolecular 7-exo-trig hydroamination of allenes. Adv Synth Catal 355:1383–1393
55. Perdew JP, Burke K, Ernzerhof M (1996) Generalized gradient approximation made simple. Phys Rev Lett 77:3865–3868
56. Perdew JP, Chevary JA, Vosko SH, Jackson KA, Pederson MR, Singh DJ, Fiolhais C (1992) Atoms, molecules, solids, and surfaces: applications of the generalized gradient approximation for exchange and correlation. Phys Rev B 46:6671–6687
57. Pérez P, Toro-Labbé A (2001) Theoretical analysis of some substituted imine–enamine tautomerism. Theor Chem Acc 105:422–430
58. Phucho T, Nongpiur A, Tumtin S, Nongrum R, Myrboh B, Nonghlaw RL (2008) Novel one pot synthesis of substituted 1,2,4-triazines. Arkivoc XV:79–87
59. Rankin KN, Gauld JW, Boyd RJ (2002) Density functional study of the proline-catalyzed direct aldol reaction. J Phys Chem A 106:5155–5159
60. Ray RK, Kauffman GB (1999) Metal and non-metal biguanide complexes. New Age International Publishers, New Delhi
61. Rosenberg S, Silver SM, Sayer JM, Jencks WP (1974) Evidence for two concurrent mechanisms and a kinetically significant proton transfer process in acid-catalyzed *O*-methyloxime formation. J Am Chem Soc 96:7986–7998
62. Ruggiero-Lopez D, Lecomte M, Moinet G, Patereau G, Lagarde M, Wiernsperger N (1999) Reaction of metformin with dicarbonyl compounds. Possible implication in the inhibition of advanced glycation end product formation. Biochem Pharmacol 58:1765–1773
63. Semchyshyn HM (2014) Reactive carbonyl species in vivo: generation and dual biological effects. Sci World J. doi:10.1155/2014/417842
64. Salvà A, Donoso J, Frau J, Muñoz F (2003) DFT studies on Schiff base formation of vitamin B6 analogues. J Phys Chem A 107:9409–9414
65. Solís-Calero C, Ortega-Castro J, Hernández-Laguna A, Muñoz F (2013) A DFT study of the Amadori rearrangement above a phosphatidylethanolamine surface: comparison to reactions in aqueous environment. J Phys Chem C 117:8299–8309
66. Solis-Calero C, Ortega-Castro J, Hernández-Laguna A, Muñoz F (2012) A comparative DFT study of the Schiff base formation from acetaldehyde and butylamine, glycine and phosphatidylethanolamine. Theor Chem Acc 131:1263–1275
67. Solís-Calero C, Ortega-Castro J, Muñoz F (2011) DFT study on amino-phospholipids surface-mediated decomposition of hydrogen peroxide. J Phys Chem C 115:22945–22953

68. Solís-Calero C, Ortega-Castro J, Muñoz F (2010) Reactivity of a phospholipid monolayer model under periodic boundary conditions: a density functional theory study of the Schiff base formation between phosphatidylethanolamine and acetaldehyde. J Phys Chem B 114:15879–15885
69. Sundriyal S, Khanna S, Saha R, Bharatam PV (2008) Metformin and glitazones: Does similarity in biomolecular mechanism originate from tautomerism in these drugs? J Phys Org Chem 21:30–33
70. Tanabe S, Sakaguchi T (1978) Reaction of guanidines with a-diketones. VL. Structures of fluorescent products of biguanides with 9,10-phenanthraquinone. Chem Pharm Bull 26:423–428
71. Thornalley PJ, Yurek-George A, Argirov OK (2000) Kinetics and mechanism of the reaction of aminoguanidine with the alpha-oxoaldehydes glyoxal, methylglyoxal, and 3-deoxyglucosone under physiological conditions. Biochem Pharmacol 60:55–65
72. Ventura ON, Lledos A, Bonaccorsi R, Bermin J, Tomasi J (1987) Theoretical study of reaction mechanisms for the ketonization of vinyl alcohol in gas phase and aqueous solution. Theor Chim Acta 72:175–195
73. Miranda HV, Outeiro TF (2010) The sour side of neurodegenerative disorders: the effects of protein glycation. J Pathol 221:13–25
74. Webster J, Urban C, Berbaum K, Loske C, Alpar A, Gärtner U, de Arriba SG, Arendt T, Münch G (2005) The carbonyl scavengers aminoguanidine and tenilsetam protect against the neurotoxic effects of methylglyoxal. Neurotox Res 7:95–101
75. Xu X, Goddard WA (2004) The extended Perdew–Burke–Ernzerhof functional with improved accuracy for thermodynamic and electronic properties of molecular systems. J Chem Phys 121:4068–4082
76. Yamabe S, Tsuchida N, Miyajima K (2004) Reaction paths of keto–enol tautomerization of ß-diketones. J Phys Chem A 108:2750–2757
77. Zakharov M, Masunov AE, Dreuw A (2008) Catalytic role of calix[4]hydroquinone in acetone–water proton exchange: a quantum chemical study of proton transfer via keto–enol tautomerism. J Phys Chem A 112:10405–10412

Theor Chem Acc (2015) 134:84
DOI 10.1007/s00214-015-1686-7

REGULAR ARTICLE

Effects of monohydration on an adenine–thymine base pair

Sara Watanabe[1] · Yudai Ogata[1] · Tsutomu Kawatsu[1,2] · Yukio Kawashima[3] · Masanori Tachikawa[1]

Received: 6 December 2014 / Accepted: 11 June 2015 / Published online: 4 July 2015

Abstract We analyzed the monohydration effect on the hydrogen-bonded structure between the adenine–thymine base pair using path integral molecular dynamics simulations including the nuclear quantum and thermal effects. We focused on two monohydration models for an adenine–thymine base pair with a water molecule bound to each adenine and thymine site. The adenine–thymine base pair without a water molecule was also discussed to reveal the role of a water molecule in monohydrated models. We found that the monohydration effect varies depending on the location of the water molecule. The monohydration effect on the inter-molecular motions is also investigated using the principle component analysis. The monohydration alters the inter-molecular motions of adenine–thymine base pair. We found that the nuclear quantum effect on the motion depends on the positions of the bound water molecule. The nuclear quantum effect on the hydrogen-bonded structure of adenine, thymine and water molecules is rather small, but we found significantly large nuclear quantum effect on the inter-molecular motions of the monohydrated base pair systems.

Keywords Adenine–thymine base pair · Microhydration · Monohydration · Nuclear quantum effect · Path integral molecular dynamics · Hydrogen bond · Principal component analysis

1 Introduction

Deoxyribonucleic acid (DNA) is an important molecule in biological systems since it plays a crucial role to store and transfer the genetic information. DNA is known by its double-helical structure composed of base pairs, phosphate groups and sugars, and the structure is mainly maintained by hydrogen bonds between each base pair [1]. For understanding the DNA structure, it is indispensable to study the hydrogen-bonded structure of the base pairs in both experimental and theoretical aspects [2–25].

Vibrational spectroscopy technique has been applied to obtain the information of the hydrogen-bonded structure of base pairs in gas phase [2–7]. Plützer et al. [2] have reported a vibrational spectrum of the adenine–thymine base pair using one-color resonant two-photon ionization spectroscopy and its theoretical investigation using the normal mode analysis with ab initio calculations. They found that the Watson–Crick isomer is not the most stable in gas phase. Krishnan and Kühn [3] assigned theoretical vibrational modes in these isomers to experimental spectrum using the anharmonic analysis. Guerra et al. [8] reported that a significant difference on hydrogen-bond lengths in

Published as part of the special collection of articles derived from the 9th Congress on Electronic Structure: Principles and Applications (ESPA 2014).

Electronic supplementary material The online version of this article (doi:10.1007/s00214-015-1686-7) contains supplementary material, which is available to authorized users.

✉ Masanori Tachikawa
tachi@yokohama-cu.ac.jp

[1] Graduate School of Nanobioscience, Yokohama City University, 22-2 Seto, Kanazawa-ku, Yokohama-City, Kanagawa 236-0027, Japan

[2] Graduate School of Arts and Sciences, The University of Tokyo, 4-6-1 Komaba, Meguroku, Tokyo 153-8902, Japan

[3] Computational Chemistry Research Unit, RIKEN Advanced Institute for Computational Science (RIKEN AICS), Minatojima-minami-machi, Chuo-ku, Kobe, Hyogo 650-0047, Japan

Watson–Crick base pairs is found among computational results at BP86/TZ2P level in gas phase and experiment measurements in X-ray crystal structures. They found that the difference arises from the molecular environment (water, sugar, hydroxyl groups, counterions) surrounding base pairs. After incorporating major elements of the environment, computational geometries were in agreement with the X-ray crystal structures. Furthermore, it was proposed that water is essentially important for the stability of DNA [5, 8–11]. In addition, Cerón-Carrasco et al. [9] suggested that the microhydration plays a crucial role for double proton transfer reaction on the hydrogen bonds of the adenine–thymine base pair at BP86 level. These studies show that treatment of environment is essential to study the structure of the base pairs in DNA.

Recently, various studies reported that both thermal and nuclear quantum effects are important to determine the hydrogen-bonded structures accurately [12–22]. Daido et al. [12, 13] studied the structure of Watson–Crick type isolated adenine–thymine and guanine–cytosine base pairs using the path integral hybrid Monte Carlo simulation. They found that the contributions of the nuclear quantum effect on hydrogen-bonded structures and the dynamics of the base pairs are significant, not only at low temperature, but also at temperature higher than room temperature. Most of the previous theoretical studies for base pairs, however, have been performed using static calculation or molecular dynamics simulation based on conventional electronic structure calculation without nuclear quantum effect of hydrogen atoms. It is well known that hydrogen-bonded structures are strongly influenced by the nuclear quantum fluctuation of the proton.

Summarizing above, the thermal, nuclear quantum and environmental effects are all important for the structure of the base pairs in DNA. However, to our knowledge, theoretical study including all of these effects has not been reported so far. In the present study, thus, we investigate a monohydration effect on the structure of an adenine–thymine base pair, as the first step, to clarify the surrounding environmental effects on the base pairs considering both thermal and nuclear quantum fluctuations. We carried out path integral molecular dynamics (PIMD) simulations, which treat nucleus of atoms as a quantum–mechanical particle expanded by classical beads, to include both thermal and nuclear quantum effects for two monohydrated model systems of the adenine–thymine base pair; we call these AT-WA and AT-WB associated with the position of the water molecule later in this article (see Fig. 1). Details of the monohydration effects are discussed by comparison with the computational results of the isolated adenine–thymine base pair without the water molecule, so-called AT-I. We then discuss the nuclear quantum effect on the hydrogen-bonded structure of AT-I, AT-WA and AT-WB

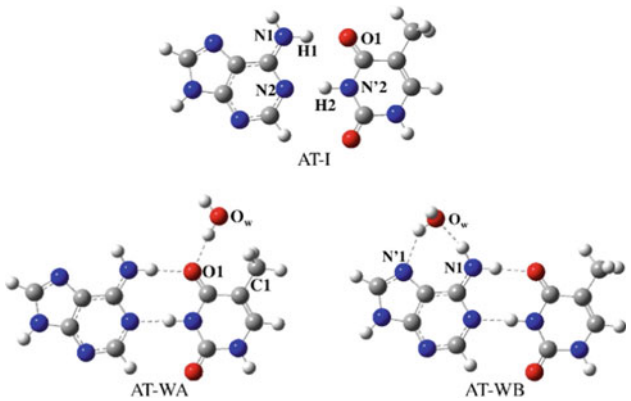

Fig. 1 Schematic illustration of an isolated and two monohydrated adenine–thymine base pairs (AT-I, AT-WA and AT-WB)

by comparing results of the PIMD simulation with conventional molecular dynamics (MD) simulation where nuclei are treated as classical point charges. We also discuss the nuclear quantum effects on the inter-molecular motion of the adenine–thymine base pair using principle component analysis (PCA) [26, 27].

In Sect. 2, we briefly describe our methods and computational details. We show results of preliminary calculations for choosing the level of quantum chemical calculation for potential calculations and the results of the static conventional electronic structure calculation for the adenine–thymine base pair in Sect. 3.1. We discuss the monohydration effects on the hydrogen-bonded structure of the adenine–thymine base pair in Sect. 3.2. The inter-molecular modes between the adenine and thymine are investigated using PCA in Sect. 3.3. The conclusion of this article is given in the final section.

2 Methods and computational details

We carried out PIMD and conventional MD simulations with massive Nosé–Hoover chain thermostats [28] to achieve a canonical ensemble in similar manner as in previous works, using our house codes [16–21]. The PIMD simulation (later denoted as "quantum simulation" or "Qm.") takes account of both thermal and nuclear quantum effects. Here, nuclei of all atoms are treated as quantum–mechanical particles by the expansion of classical beads based on the path integral procedure. The conventional MD simulation (later denoted as "classical simulation" or "Cla.") is based on conventional electronic structure calculation, which treats nuclei as point charges. The classical simulation only treats thermal fluctuation.

Simulations for AT-I, AT-WA and AT-WB were executed at 150 K to sample the structure of the hydrogen-bonded

molecular complex. We note that we chose a low temperature for comparisons between various simulations in present study, because the hydrogen bond in isolated adenine–thymine base pair easily dissociated in a simulation at 300 K in gas phase. The quantum simulations were performed for 500,000 steps after a thermal equilibration of 5000 steps with 32 beads using a time step size of 0.1 fs. The classical simulations were carried out for 2,000,000 steps after a thermal equilibration of 10,000 steps using a time step size of 0.1 fs. All electronic structure calculations to obtain atomic forces during the simulations were performed by semi-empirical PM6-DH+ [29] methods using MOPAC 2009 program package [30].

We applied principle component analysis (PCA) to the displacements of coordinates in the quantum and classical simulations for AT-I, AT-WA and AT-WB for studying the inter-molecular modes. PCA is a commonly used technique for analyzing statistical data. The variables of principle component (PC) represent dominant modes of the displacement from the reference coordinates [31]. The PCs are obtained as eigenvectors of the covariance matrix of displacements. The covariance matrix is calculated using all coordinates in the trajectories obtained from the simulations, in which relative positions of the adenine–thymine base pair are fitted with the minimum root-mean-square deviation. The reference coordinates are the average position of these structures in the trajectory. The diagonalization of the matrix is carried out using the LAPACK package.

Schematic illustrations of AT-I, AT-WA and AT-WB and atomic labeling of base pairs and water molecule are shown in Fig. 1. Guerra et al. [8] proposed a stable microhydration model with two water molecules, which strengthens the hydrogen bonds between the adenine–thymine base pair. In their model, a water molecule binds to an amino group of the adenine and another water molecule binds to a carbonyl group of the thymine. In the present study, we investigate the monohydration, thermal fluctuation and nuclear quantum effect of these two water molecules one by one. We consider two monohydration models including one of these water molecules, which we denote as AT-WA and AT-WB, shown in Fig. 1, to clarify the effect from each water molecule.

3 Results and discussion

3.1 Static molecular orbital calculation

In our simulation schemes, we need to obtain both energy and force from quantum chemical calculations. We have previously carried out PIMD simulation with ab initio molecular orbital method and density functional theory for several small molecular systems [16, 19]. However, very high computational cost is required to perform PIMD simulation for an adenine–thymine base pair consisted of 30 atoms using ab initio molecular orbital methods. On the other hand, semi-empirical molecular orbital methods can calculate both energy and force with low computational cost in the reasonable accuracy. The performance of some semi-empirical methods has been reported [14, 15]. Jiří et al. have investigated the performance of PM7, comparing with various PM6, for non-covalent interactions. Their results show that PM6 methods with dispersion and hydrogen-bonded interactions (PM6-DH+, PM6-DH2 and PM6-D3H4X) give similar or better performance than PM7 with respect to non-covalent complexes and biomolecules [14]. These various PM6 derivatives could be reliable on the electronic structure calculations for hydrogen-bonded system. Daido et al. [13] reported that PM6-DH+ method performed well for the electronic structure calculation in the molecular dynamics of a single adenine–thymine and guanine–cytosine pair. We found that PM6-DH+ method is a good candidate for our simulation.

We additionally checked the performance of the PM6-DH+ method for our models, comparing the structures of the hydrogen bonds and the vibrational frequencies of the normal mode analysis on AT-I, AT-WA, and AT-WB using Gaussian09 program package [32] at various levels of the quantum chemical method as listed in Table 1. The normal mode analysis is a method to probe motions around the equilibrium structure of molecules under the harmonic approximation [33]. The comparison is made by choosing second-order Møller–Plesset perturbation (MP2) [34–38] method with 6-31++G** basis set as the reference value, with other semi-empirical methods, i.e., AM1 [39], PM3 [40–43], PM6 [44], PM6-DH+. The MP2 method performs well for stable molecular structures; thus, it can be used to obtain the reference value to assess the semi-empirical methods for such structures. We here define ε_A as the normalized error of A ($A = R_{N1O1}$, $R_{N2N'2}$, R_{N1H1}, $R_{H2N'2}$, $R_{H1\cdots O1}$, $R_{N2\cdots H2}$, R_{O1O_w}, R_{N1O_w}) from MP2 results and list in Table 1 with the root-mean-square error (RMSE). The ε and RMSE values are obtained as follows:

$$\varepsilon_A = \frac{V_c - V_r}{V_r} \times 100(\%), \tag{1}$$

and

$$\mathrm{RMSE} = \sqrt{\frac{\left(\varepsilon_{R_{N1O1}}\right)^2 + \left(\varepsilon_{R_{N2N'2}}\right)^2 + \left(\varepsilon_{R_{N1H1}}\right)^2 + \left(\varepsilon_{R_{H2N'2}}\right)^2 + \left(\varepsilon_{R_{H1\cdots O1}}\right)^2 + \left(\varepsilon_{R_{N2\cdots H2}}\right)^2}{6}}, \tag{2}$$

Table 1 Structural parameters (Å) of the hydrogen-bonded moiety on AT-I, AT-WA and AT-WB and vibrational mode frequencies (cm^{-1}) from normal mode analysis and root-mean-square of error rates (RMSE)

	Equilibrium structure (Å)									Vibrational mode (cm^{-1})		
	R_{N1O1}	$R_{N2N'2}$	R_{N1H1}	$R_{H2N'2}$	$R_{H1\cdots O1}$	$R_{N2\cdots H2}$	R_{O1O_w}	R_{N1O_w}	RMSE	Buckle	Propeller	Opening
AT-I												
AM1	3.095 (+4.2 %)	3.469 (+21.7 %)	0.994 (−2.5 %)	1.001 (−4.1 %)	2.101 (+7.5 %)	2.479 (+37.2 %)	–	–	18.0 %	3.4	15.5	25.2
PM3	2.828 (−4.8 %)	2.814 (−1.3 %)	1.008 (−1.1 %)	1.035 (−0.8 %)	1.821 (−6.9 %)	1.780 (−1.5 %)	–	–	3.5 %	21.7	26.9	86.3
PM6	2.942 (−0.9 %)	3.013 (+5.7 %)	1.027 (+0.8 %)	1.061 (+1.7 %)	1.916 (−2.0 %)	1.952 (+8.0 %)	–	–	4.2 %	14.8	24.4	41.5
PM6-DH+	2.884 (−2.9 %)	2.883 (+1.2 %)	1.031 (+1.1 %)	1.070 (+2.5 %)	1.854 (−5.2 %)	1.813 (+0.3 %)	–	–	2.7 %	24.5	33.8	51.6
MP2/6-31++G**	2.969	2.850	1.019	1.044	1.955	1.807	–	–	–	20.5	30.7	58.8
AT-WA												
AM1	3.108 (+4.7 %)	3.416 (+20.3 %)	0.994 (−2.4 %)	1.002 (−4.2 %)	2.115 (+8.1 %)	2.422 (+34.8 %)	2.672 (−6.8 %)	–	15.9 %	19.5	28.4	21.6
PM3	2.832 (−4.6 %)	2.810 (−1.1 %)	1.008 (−1.0 %)	1.037 (−0.9 %)	1.826 (−6.6 %)	1.775 (−1.2 %)	2.747 (−4.2 %)	–	3.5 %	31.3	34.7	49.8
PM6	2.975 (+0.2 %)	2.978 (+4.8 %)	1.024 (+0.6 %)	1.066 (+1.9 %)	1.953 (−0.2 %)	1.912 (+6.4 %)	2.496 (−12.9 %)	–	5.8 %	12.6	26.5	36.0
PM6-DH+	2.907 (−2.1 %)	2.861 (+0.7 %)	1.028 (+1.0 %)	1.074 (+2.6 %)	1.879 (−3.9 %)	1.788 (−0.5 %)	2.803 (−2.3 %)	–	2.2 %	28.5	40.1	45.7
MP2/6-31++G**	2.970	2.840	1.018	1.046	1.956	1.797	2.867	–	–	22.2	30.4	47.7
AT-WB												
AM1	3.108 (+4.1 %)	3.452 (+21.1 %)	0.995 (−2.3 %)	1.001 (−4.1 %)	2.114 (+7.3 %)	2.466 (+36.5 %)	–	3.077 (+3.6 %)	16.4 %	23.9	20.3	27.0
PM3	3.397 (+13.7 %)	2.836 (−0.5 %)	0.993 (−2.5 %)	1.034 (−0.9 %)	2.420 (+22.8 %)	1.804 (−0.2 %)	–	2.833 (−4.7 %)	10.3 %	28.6	20.6	44.5
PM6	2.963 (−0.8 %)	3.013 (+5.7 %)	1.028 (+0.9 %)	1.061 (+1.6 %)	1.936 (−1.8 %)	1.953 (+8.1 %)	–	2.842 (−4.4 %)	4.2 %	15.1	19.6	39.2
PM6-DH+	2.904 (−2.8 %)	2.879 (+1.0 %)	1.030 (+1.1 %)	1.070 (+2.5 %)	1.875 (−4.9 %)	1.809 (+0.1 %)	–	2.820 (−5.1 %)	3.1 %	33.1	29.6	49.7
MP2/6-31++G**	2.986	2.850	1.019	1.044	1.971	1.807	–	2.971	–	25.1	50.0	57.0

Values in parentheses represent error rates from MP2/6-31++G**

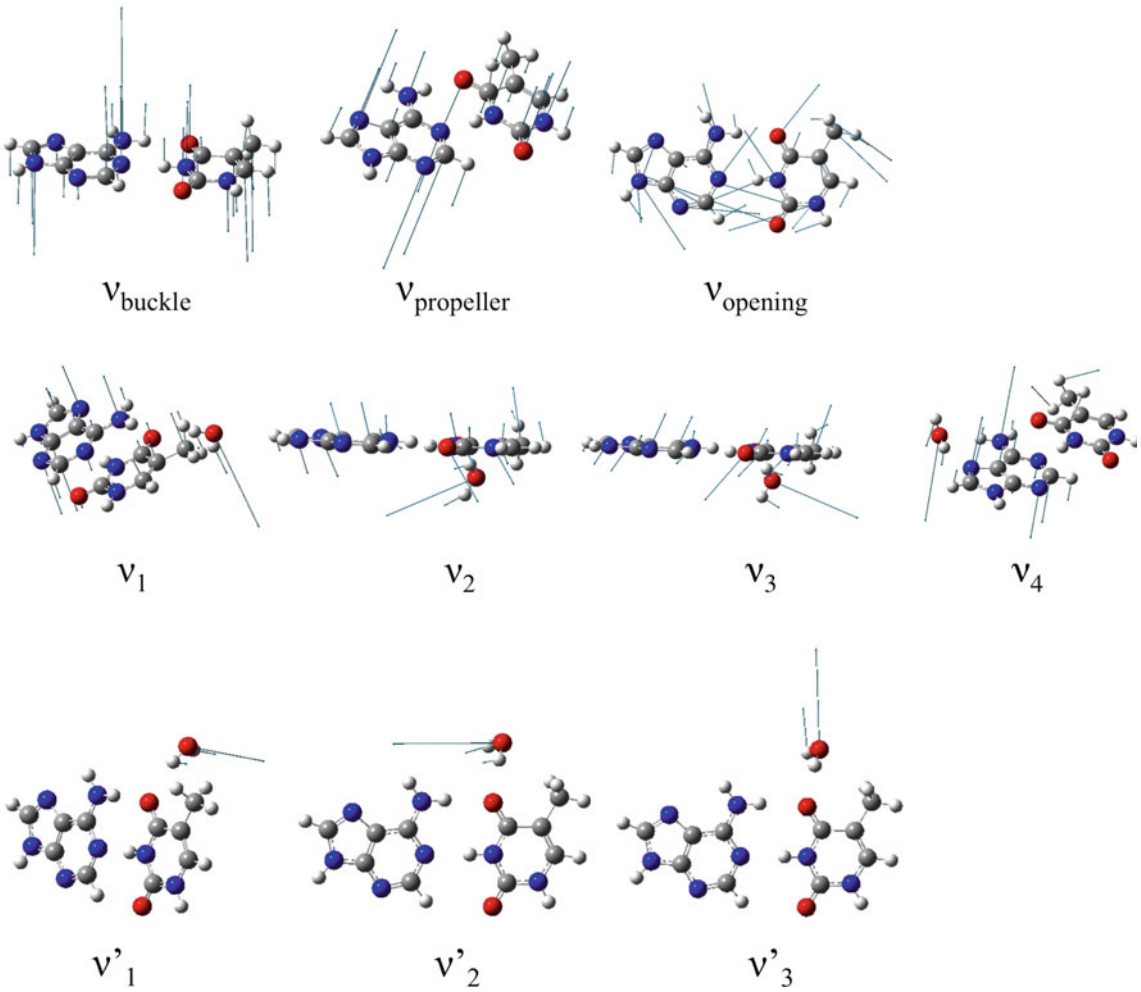

Fig. 2 Simplified schematic illustration of vibrational modes in AT-I, AT-WA and AT-WB

where V_c is the calculated value and V_r is the reference value obtained by the MP2 method. Here, we define R_{N1O1} as the hydrogen-bond length between the hydrogen donor N1 and acceptor O1 and $R_{N2N'2}$ between N2 and N′2 atoms; see Fig. 1 for atomic labels. Similarly, we define the covalent bond lengths of hydrogen bond between N1 and H1 atoms as R_{N1H1} and between H2 and N′2 atoms as $R_{H2N'2}$, respectively. The non-covalent bond lengths are defined as $R_{H1\cdots O1}$ and $R_{N2\cdots H2}$ in the same manner. In this study, we focus on the monohydration effect; thus, the hydrogen bonds between adenine–thymine base pair and the water molecule are investigated as well, which are defined as R_{O1O_w} and R_{N1O_w}.

We first assessed the hydrogen-bonded structure obtained from semi-empirical calculations. Overall, AM1 results had the largest RMSE, while PM6-DH+ methods had the smallest value. The largest error for AM1 and PM6 methods is found in $R_{N2\cdots H2}$ value and for PM3 and PM6-DH+ methods in $R_{H1\cdots O1}$. The PM6-DH+ method showed the best performance among these semi-empirical methods for all of the AT-I, AT-WA and AT-WB models.

We next compared the hydrogen-bonded structures of the studied model systems, AT-I, AT-WA and AT-WB. The calculated results by MP2 method show that the monohydration elongates R_{N1O1}, $R_{H2N'2}$ and $R_{H1\cdots O1}$ in AT-WA and shortens $R_{N2N'2}$, R_{N1H1} and $R_{N2\cdots H2}$. Among the assessed semi-empirical methods, PM6 and PM6-DH+ methods showed the same tendency with MP2 methods. The hydrogen-bonded structure for AT-WB obtained by MP2 method shows that the addition of the water molecule elongates R_{N1O1} and $R_{H1\cdots O1}$, while the other bonds are not influenced. All semi-empirical methods assessed did not show the completely same tendency with MP2; however, PM6 and PM6-DH+ methods showed a similar tendency. The monohydration effect on the hydrogen-bond length between the base pair was rather small. This is consistent with the past study of Guerra et al. [8], which suggest that the monohydration effect on the hydrogen-bonded structure

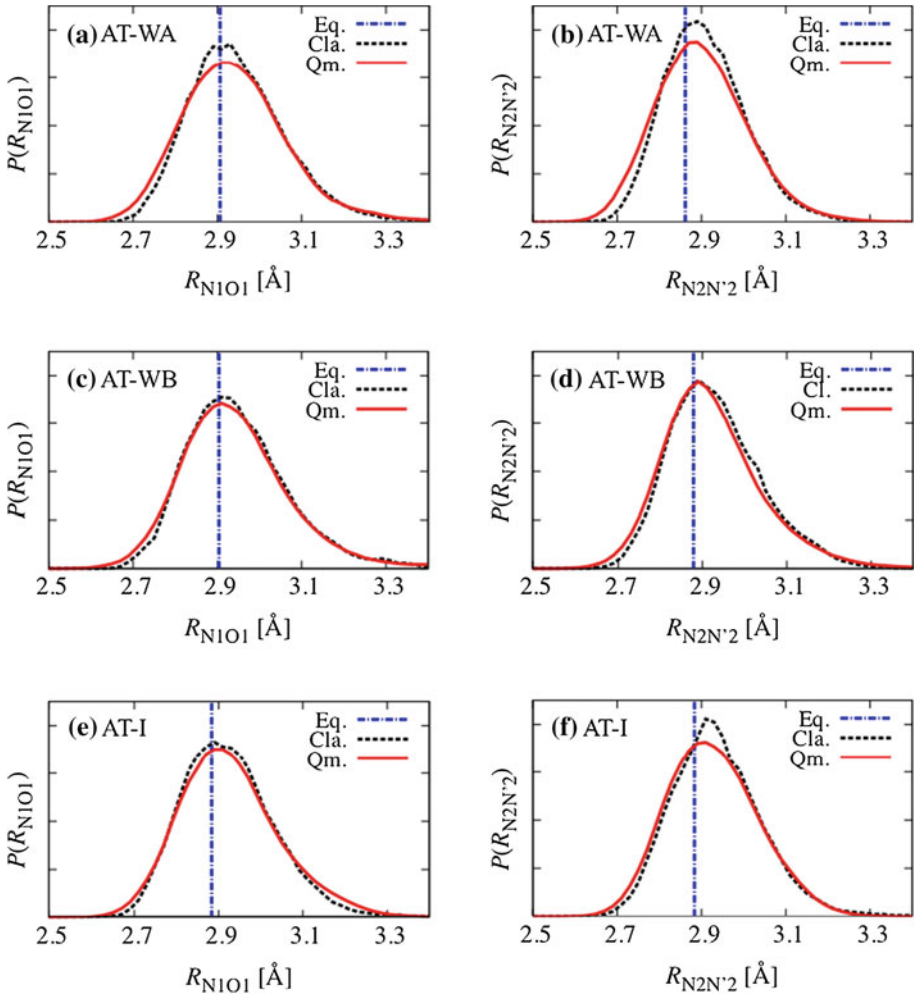

Fig. 3 Distributions of R_{N1O1} and $R_{N2N'2}$ for AT-WA, AT-WB and AT-I with the classical and quantum simulations. The *black dashed* and *red solid curves* represent the classical and quantum simulations, respectively. The *vertical blue dashed-dotted line* represents the equilibrium bond length obtained by the PM6-DH+ method

is relatively small compared to the microhydration effect with two water molecules, simultaneously.

We then evaluated the hydrogen-bond lengths between the adenine–thymine base pair and water molecule, R_{O1O_w} and R_{N1O_w}. The bond length R_{O1O_w} obtained by PM6-DH+ method agreed the best among the semi-empirical methods to that of MP2 method. The bond length R_{N1O_w} calculated by semi-empirical methods did not agree well with that of MP2 method. All semi-empirical methods performed similarly for R_{N1O_w}. We conclude that PM6-DH+ method showed the best agreement with MP2 method among the assessed semi-empirical methods.

We have so far compared the optimized geometries of the monohydrated systems. For further assessment, we compared the vibrational modes obtained from normal mode analysis, which can be used to assess the curvature or shape of the potential energy surface, not just the minimum of the surface. The three lowest vibrational modes obtained from the normal mode analysis for AT-I, AT-WA and AT-WB are listed in Table 1. These three modes are identified as corresponding inter-molecular vibrations between the adenine and thymine. We illustrate these inter-molecular three modes, so-called buckle, propeller and opening modes [31], in Fig. 2. The first two modes are out-of-plane modes, where the buckle and propeller modes are a bending mode of the adenine–thymine plane between the base pairs and a twisting one of the adenine–thymine base pair around the N2N′2 axis, respectively. The opening mode is an in-plane mode, which makes the N1O1 side of the base pair plane open and close, while N′2N2 side closes and opens. For the vibrational frequencies of AT-I, we found the value obtained from PM6-DH+ shows the best agreement with reference MP2 values. For AT-WA, the values obtained from PM3, PM6 and PM6-DH+ are in qualitatively good agreement with the MP2 values. For AT-WB, although all semi-empirical values underestimate the MP2 values, the buckle value of PM6-DH+ is not far from MP2, and the propeller and opening values of PM6-DH+ level are relatively close to the values of MP2, compared to other semi-empirical values.

Accurate description of the potential around the equilibrium becomes more important, because the monohydrated

Table 2 Peak positions of distributions with respect to α ($\alpha = R_{N1O1}$, $R_{N2N'2}$, R_{N1H1}, $R_{H2N'2}$, $R_{H1\cdots O1}$, $R_{N2\cdots H2}$, $\theta_{N1-H1\cdots O1}$, $\theta_{N2\cdots H2-N'2}$, R_{O1O_w}, R_{N1O_w}) for AT-I, AT-WA and AT-WB with the equilibrium (Eq.), classical (Cla.) and quantum (Qm.) simulations

	Peak positions									
	R_{N1O1}	$R_{N2N'2}$	R_{N1H1}	$R_{H2N'2}$	$R_{H1\cdots O1}$	$R_{N2\cdots H2}$	$\theta_{N1-H1\cdots O1}$	$\theta_{N2\cdots H2-N'2}$	R_{O1O_w}	R_{N1O_w}
AT-I										
Eq.	2.884	2.883	1.031	1.070	1.854	1.813	177.4	178.8	–	–
Cla.	2.890	2.910	1.029	1.065	1.885	1.885	172.3	172.3	–	–
Qm.	2.890	2.910	1.039	1.071	1.895	1.895	166.9	167.5	–	–
AT-WA										
Eq.	2.907	2.861	1.028	1.074	1.879	1.788	176.9	177.3	2.803	–
Cla.	2.930	2.890	1.027	1.065	1.895	1.825	171.9	172.7	2.810	–
Qm.	2.910	2.890	1.037	1.077	1.935	1.845	166.9	166.7	2.810	–
AT-WB										
Eq.	2.904	2.879	1.030	1.070	1.875	1.809	177.2	178.4	–	2.820
Cla.	2.910	2.890	1.029	1.065	1.895	1.825	172.1	172.5	–	2.830
Qm.	2.910	2.885	1.037	1.065	1.915	1.875	166.5	167.7	–	2.850

adenine–thymine pair is stable and proton transfer never occurs. Thus, we conclude that PM6-DH+ is a suitable choice for our purpose to describe the structure and dynamics of AT-I, AT-WA and AT-WB in our *on-the-fly* PIMD simulations.

3.2 Monohydration effect on the hydrogen-bonded structure of adenine–thymine base pair

Daido et al. [13] have discussed the relative position of protons along the hydrogen bonds of the adenine–thymine base pair. We investigated the structures of these hydrogen bonds in detail to understand the adenine–thymine base pair as well. As already stated in Sect. 3.1, the monohydration affects the geometry of the adenine–thymine base pair in static calculations. In this section, we investigate the thermal and nuclear quantum effects on AT-I, AT-WA and AT-WB models comparing the PIMD simulation with the static structures and MD simulations.

3.2.1 Hydrogen bond between the base pair

First, we focus on the lengths of two hydrogen bonds between adenine and thymine, defined as distances between the hydrogen donor and acceptor. Figure 3a and b shows the distributions of hydrogen-bond lengths, R_{N1O1} and $R_{N2N'2}$, for the classical and quantum simulations. The hydrogen-bond length of the equilibrium geometry obtained from static PM6-DH+ calculation is also shown as the vertical blue dashed-dotted line. The dashed and solid curves represent the distributions of the hydrogen-bond length for the classical and quantum simulations, respectively. Both distributions for the quantum simulations slightly broaden due to nuclear quantum effects comparing with the distributions for associated classical simulations. The same tendency also appears in the simulations for AT-I and AT-WB. The broadening of the distribution arises mainly from the zero-point motion.

The peak positions of the distributions shown in Fig. 3 for AT-WA are listed with AT-I and AT-WB results and the corresponding equilibrium values in Table 2. We note that the standard deviations of these distributions are shown in supplementary material for reference. The bond lengths of AT-I among the simulations have the following relations: $R^{\mathrm{Eq.}}_{N1O1} < R^{\mathrm{Cla.}}_{N1O1} = R^{\mathrm{Qm.}}_{N1O1}$ and $R^{\mathrm{Eq.}}_{N2N'2} < R^{\mathrm{Cla.}}_{N2N'2} = R^{\mathrm{Qm.}}_{N2N'2}$. The superscripts Eq., Cla. and Qm. represent equilibrium structure, classical simulation and quantum simulation, respectively. Thermal effect elongates the hydrogen-bond length, i.e., $R^{\mathrm{Eq.}}_{N1O1} < R^{\mathrm{Cla.}}_{N1O1}$ and $R^{\mathrm{Eq.}}_{N2N'2} < R^{\mathrm{Cla.}}_{N2N'2}$, whereas the nuclear quantum effect is small, i.e., $R^{\mathrm{Cla.}}_{N1O1} = R^{\mathrm{Qm.}}_{N1O1}$ and $R^{\mathrm{Cla.}}_{N2N'2} = R^{\mathrm{Qm.}}_{N2N'2}$. In contrast to AT-I, the AT-WA and AT-WB models have different trends. For AT-WA, R_{N1O1} in the classical simulation is longer than that in the quantum simulation, and $R_{N2N'2}$ is equivalent between the classical and quantum simulations. For AT-WB, R_{N1O1} is equivalent between the two simulations and $R_{N2N'2}$ in the classical simulation is slightly longer than that in the quantum simulation. The nuclear quantum effect appears in AT-WA, unlike the other models. Although the difference is relatively small, the location of the water molecule leads to difference in the nuclear quantum effect on the hydrogen bonds.

We investigate the hydrogen-bonded structure further by analyzing the hydrogen position within the hydrogen bond. The peak positions of the distributions for bond lengths R_{N1H1}, $R_{H2N'2}$, $R_{H1\cdots O1}$ and $R_{N2\cdots H2}$ in AT-WA and AT-WB are given in Table 2. We defined

Table 3 The ratios of the contribution of vibrational modes (ν_{buckle}, $\nu_{propeller}$, $\nu_{opening}$, ν_1, ν_2, ν_3, ν_4) in AT-I, AT-WA and AT-WB obtained by principle component analysis with the classical (Cla.) and quantum (Qm.) simulations and frequencies (cm^{-1}) of vibrational modes from normal mode analysis

Vibrational mode	Principle component analysis (%)		Normal mode analysis (cm^{-1})
	Cla.	Qm.	
AT-I			
ν_{buckle}	35	16	24.5
$\nu_{propeller}$	28	29	33.8
$\nu_{opening}$	8	8	51.6
AT-WA			
ν_{buckle}	25	36	28.5
ν_1	23	22	36.0
$\nu_{propeller}$	11	–	40.1
ν_2	10	8	–
ν_3	–	6	–
$\nu_{opening}$	4	3	45.7
AT-WB			
ν_{buckle}	19	19	33.1
$\nu_{propeller}$	34	34	29.6
$\nu_{opening}$	9	9	49.7
ν_4	6	–	–

angles N1–H1···O1 and $N2\cdots H2-N'2$ as $\theta_{N1-H1\cdots O1}$ and $\theta_{N2\cdots H2-N'2}$, which are also listed in Table 2. The distributions of these values obtained by each simulation are shown in supplementary material. Although these bond lengths slightly alter due to the monohydration effect in the classical and quantum simulations as shown in Table 2, the monohydration effect is similar to the tendency seen in equilibrium structures as discussed in Sect. 3.1. However, comparing the results of the quantum simulation with the classical simulation, the nuclear quantum effect enhances the monohydration effect.

All of the bond lengths R_{N1H1}, $R_{H2N'2}$, $R_{H1\cdots O1}$ and $R_{N2\cdots H2}$ for both simulations have the following relations: $R_X^{Cla.} < R_X^{Qm.}$ where X indicates each bond, that is, the nuclear quantum effect contributes to the anharmonicity of the bonds. For the angles, $\theta_{N1-H1\cdots O1}$ and $\theta_{N2\cdots H2-N'2}$, we found the following relations: $\theta^{Cla.}_{N1-H1\ldots O1} > \theta^{Qm.}_{N1-H1\cdots O1}$ and $\theta^{Cla.}_{N2\cdots H2-N'2} > \theta^{Qm.}_{N2\cdots H2-N'2}$. This relation indicates that the nuclear quantum effect enhances the fluctuation of H1 and H2 atoms perpendicular to axes along N1···O1 and $N2\cdots N'2$ bonds, respectively. We note that no significant difference is found between the models AT-WA and AT-WB for tendencies of these bonds and angles.

Table 4 The ratios of the contribution of vibrational modes (ν_{buckle}, $\nu_{propeller}$, $\nu_{opening}$) in adenine–thymine base pair fragment in AT-WA and AT-WB with classical (Cla.) and quantum (Qm.) simulations

Vibrational mode	Principle component analysis (%)	
	Cla.	Qm.
AT-WA		
ν_{buckle}	37	51
$\nu_{propeller}$	19	14
$\nu_{opening}$	9	6
AT-WB		
ν_{buckle}	36	32
$\nu_{propeller}$	21	21
$\nu_{opening}$	10	10

3.2.2 *Hydrogen bond between base pair and water molecule*

We next focus on the hydrogen-bonded structure between the base pair and the water molecule in models AT-WA and AT-WB. We analyzed the hydrogen-bond lengths of the hydrogen bonds between base pair and water molecule, R_{O1O_w} and R_{N1O_w}, for AT-WA and AT-WB, respectively. These bond lengths are given in Table 2. The hydrogen-bond length R_{O1O_w} in AT-WA has the relation of $R^{Cla.}_{O1O_w} = R^{Qm.}_{O1O_w}$, while the hydrogen-bond length R_{N1O_w} in AT-WB has the relation of $R^{Cla.}_{N1O_w} = R^{Qm.}_{N1O_w}$. Although the difference is small, the nuclear quantum effect in the hydrogen bond between base pair and water appears only in AT-WB model.

We investigated the hydrogen-bonded structure of the monohydrated adenine–thymine base pair and found that the monohydration effect varies depending on the location of the water molecule. We found different behaviors of the nuclear quantum effect among the monohydration models although such effect is comparatively small. We next explore how these small effects influence the large molecular motion of the base pairs.

3.3 Principle component analysis

We discussed the static properties of the hydrogen bonds above. In this subsection, we would like to analyze the monohydration effect on the inter-molecular motions in the adenine–thymine base pair using principle component analysis (PCA). We applied the PCA to displacements in sampled trajectories of AT-I, AT-WA and AT-WB models obtained by each simulation. Some of the lowest PCs and vibrational normal modes for AT-I, AT-WA and AT-WB models are listed in Table 3. The ratios of the contributions of PCs to the entire molecular motions and the

Table 5 The ratios of the contribution of vibrational modes (ν_1', ν_2', ν_3') of a water molecule fragment in AT-WA and AT-WB with classical (Cla.) and quantum (Qm.) simulations

Vibrational mode	Principle component analysis (%)	
	Cla.	Qm.
AT-WA		
ν_1'	70	75
ν_2'	18	13
ν_3'	4	4
AT-WB		
ν_1'	74	77
ν_2'	9	–
ν_3'	–	4

vibrational frequencies of the corresponding normal modes are also given in Table 3. The dominant three PCs for the AT-I model are characterized as inter-molecular motions between the adenine and thymine, ν_{buckle}, $\nu_{\text{propeller}}$ and ν_{opening}, as shown in the normal mode analysis in Sect. 3.1. Each of the PC corresponds to one of the lowest vibrational normal modes [31].

The ratio of ν_{buckle} PC in the quantum simulation is significantly smaller than that in the classical simulation, while the ratio of the $\nu_{\text{propeller}}$ mode in the quantum simulation is slightly larger than that in the classical simulation in AT-I. The ratio of ν_{opening} mode in the quantum simulation is the same as in the classical simulation in this case. These tendencies, arising from nuclear quantum effect, have also been found in the study by Daido et al. [13] using the path integral hybrid Monte Carlo simulation. The ratio of the three PCs in the classical simulation is in the order of the ν_{buckle}, $\nu_{\text{propeller}}$ and ν_{opening} modes, which order is the same as the opposite order of the frequency of the vibrational normal modes. In contrast, the order of the three PCs in the quantum simulation is the $\nu_{\text{propeller}}$, ν_{buckle} and ν_{opening} modes. Here, the nuclear quantum effect leads to a significant difference in the inter-molecular motions though the difference in hydrogen-bonded structure is relatively small, comparing with the non-quantum simulation.

In the case of AT-WA, six dominant PCs for AT-WA are ν_{buckle}, ν_1, $\nu_{\text{propeller}}$, ν_2, ν_3 and ν_{opening} as shown in Fig. 2, where the ν_1 is an inter-molecular motion between the adenine–thymine base pair and water molecule, and ν_2 and ν_3 modes are inter-molecular motions among all three molecules. The existence of water molecule results to emergence of these three modes, ν_1, ν_2 and ν_3. We found that the dominant PCs have a slight difference in the modes among the simulations. Meanwhile, $\nu_{\text{propeller}}$ and ν_3 modes were not found in the classical and quantum simulations, respectively. The normal mode analysis gives different order of low-frequency modes unlike the cases of both classical and quantum simulations, and ν_2 and ν_3 modes were not found in the low-frequency region.

For AT-WB model, there are four dominant PCs, ν_{buckle}, $\nu_{\text{propeller}}$, ν_{opening} and ν_4. The first three modes (ν_{buckle}, $\nu_{\text{propeller}}$ and ν_{opening}) are similar to the AT-I model. The ratios of ν_{buckle}, $\nu_{\text{propeller}}$ and ν_{opening} modes obtained from classical and quantum simulations are almost equivalent. The ν_4 mode corresponding to water molecular motion appears only in the classical simulation of AT-WB. We found that the inter-molecular PCA modes of AT-WB are similar to those of AT-I, which was not the case for AT-WA model. The monohydration effect and its nuclear quantum effect on the molecular fluctuation strongly depend on the position of the bound water molecule.

To focus on the inter-molecular modes between the adenine and thymine in AT-WA and AT-WB, we decomposed the motions of the entire system into two fragments, an adenine–thymine base pair and a water molecule. We then applied PCA to the displacement of each fragment separately.

The results for the adenine–thymine base pair fragment are given in Table 4. For AT-WA, the ratio of ν_{buckle} mode in the quantum simulation is much larger than that in the classical simulation, whereas the ratio of the $\nu_{\text{propeller}}$ and ν_{opening} modes in the quantum simulation is slightly smaller than that in the classical simulation. In this model, the ratio of ν_{buckle} mode significantly increases due to the monohydration, when the nuclear quantum effect is considered comparing with the AT-I model in Table 3, while the monohydration effect is not so large in the classical simulations. Similar to AT-I, the nuclear quantum effect for AT-WA model is large in these inter-molecular motions of the base pairs. In the case of AT-WB, the ratio of ν_{buckle} mode in the classical simulation is just slightly larger than that in the quantum simulation. There is no significant difference in inter-molecular motions of the base pairs for AT-WB model due to the nuclear effect, unlike the case of AT-WA.

The results of the water fragment for PCA are given in Table 5. These three PCA modes ν_1', ν_2' and ν_3' are translational motions of the water molecule. In the case of AT-WA, inclusion of the nuclear quantum effect leads to increase in the ratio for ν_1' mode and decrease for ν_2' mode; however, the order of these ratios is similar. In the case of AT-WB, we found significant differences between the classical and quantum simulations. The ν_2' mode found in classical simulation cannot be seen in the quantum simulation, and vice versa for ν_3' mode. In Sect. 3.2, we discussed that the nuclear quantum effect between the base pair and water molecule was found only in AT-WB, and the result is actually consistent with the above result of PCA.

We found relatively small nuclear quantum effect in the hydrogen-bonded structures between the base pair and between the base pair and water molecule. However, we found large nuclear quantum effect in the inter-molecular motions of the monohydrated base pair systems. For AT-WA model, nuclear quantum effect was enhanced in the hydrogen bond between the base pair, which influenced the inter-molecular motion between the adenine and thymine. For AT-WB model, the nuclear quantum effect was enhanced in the hydrogen bond between the base pair and water molecule, which influenced the translational motions of the water molecule. These results indicate that the nuclear quantum effect varies depending on the model of the monohydration and the small nuclear quantum effect on the molecular geometry influences the large effect on the inter-molecular motions.

We analyzed the inter-molecular motions of adenine–thymine base pair from the point of view: could a small local difference in the hydrogen-bond structure lead to a large difference in inter-molecular motion? We investigated the difference in the contribution of buckle and propeller modes enhanced by small difference in the hydrogen-bond angle introducing a simple model. The details of our analysis are shown in the "Appendix". The results indicate that large difference in the motions can be enhanced by small difference in the hydrogen-bond angle.

We also considered the origin of the large difference in the molecular motion from the nuclear quantum effect. One of the important features of the nuclear quantum effects is the vibrational zero-point motion, which is included in the quantum simulation. This can be one of the main contributions from the nuclear quantum effect, which leads to large differences in the inter-molecular motions of the base pairs. We consider that the second lowest vibrational mode may be enhanced in the quantum simulation due to zero-point effect, while the lowest mode mostly contributes to the motion in the classical simulation. This explains the origin of the large difference in molecular motion, though the nuclear quantum effect on the hydrogen-bond structure is small.

4 Conclusions

We elucidated the monohydration effect on the hydrogen-bonded structure in the adenine–thymine base pair using path integral molecular dynamics simulations The simulations are performed on semi-empirical PM6-DH+ potential energy surface at 150 K. We employed two monohydration models of the adenine–thymine pair, named AT-WA and AT-WB models, and compared with an isolated adenine–thymine base pair, named AT-I model.

We first analyzed the hydrogen-bonded structures of monohydrated adenine–thymine base pairs. Comparing the results of the path integral molecular dynamics simulation with the conventional molecular dynamics, we estimated the nuclear quantum effect. The nuclear quantum effect appears only in a hydrogen-bonded structure between a nitrogen atom of the adenine and an oxygen atom of the thymine in the AT-WA model. On the other hand, in the AT-WB model, the nuclear quantum effect appears in the hydrogen-bonded structure between the nitrogen of thymine and water molecule unlike the AT-WA. The position of the water molecule differs where the nuclear quantum effect appears. We then investigated the monohydration effect on the inter-molecular motions among the adenine, thymine and the water molecule, applying the principle component analysis to the path integral molecular dynamics trajectories. We found that the motions depend on the position of the bound water molecule. The inter-molecular motions between the adenine and thymine changed by the monohydration in the AT-WA model, however, not in the AT-WB model. The nuclear quantum effect in the AT-WA model mainly appears on the inter-molecular motions between the adenine and thymine, and the effect appears on inter-molecular ones between the base pair and water molecule in the AT-WB model. Such result is consistent with that nuclear quantum effect appears on a hydrogen-bonded structure between the adenine and thymine in the AT-WA model and between the base pair and the water molecule in the AT-WB model.

We found small nuclear quantum effect in the hydrogen-bonded structure between the adenine and thymine and between the base pair and water molecule. However, we found large nuclear quantum effect in the inter-molecular motions of the monohydrated base pair systems. Our results suggest that the nuclear quantum effect may play an important role in the inter-molecular floppy motions of DNA. We will insist on the importance of the nuclear quantum effect in near-future theoretical studies on DNA.

Acknowledgments This study was partly supported by a JSPS/MEXT KAKENHI Grant-in-Aid for Scientific Research.

Appendix

We analyzed the inter-molecular motions of buckle and propeller modes of adenine–thymine pair introducing a simple geometric model as shown in Fig. 4. The model is constructed with two plates $h_1h_2r_1r_2$ and $h_1h_2r_3r_4$ connected by two hinges h_1 and h_2. We assign 2a to both hydrogen-bond lengths and z_0 to the distance between two

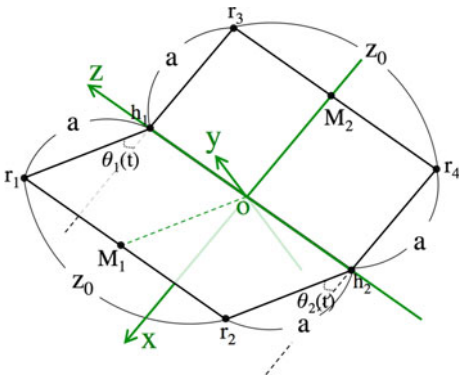

Fig. 4 A simple geometric model for the buckle and propeller modes of the adenine–thymine pair

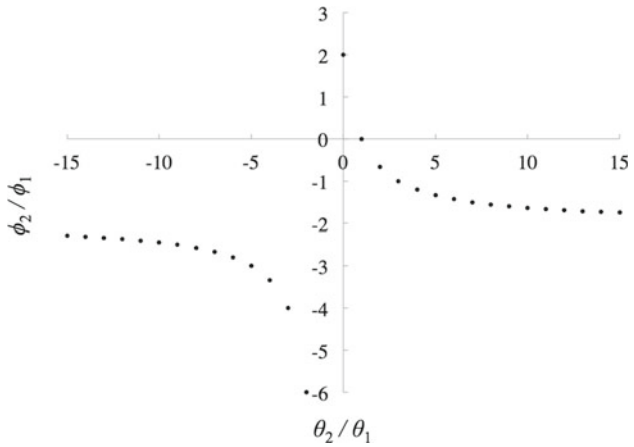

Fig. 5 The relation between ϕ_2/ϕ_1 and θ_2/θ_1 in Eq. (7)

hydrogen bonds in this model. We fix the plate $h_1h_2r_3r_4$ on the z–x plane. The angles θ_1 and θ_2 are defined as angles between vector $\overrightarrow{r_1h_1}$ and the z–x plane and vector $\overrightarrow{r_2h_2}$ and the z–x plane, respectively. The angle between $\overrightarrow{OM_1}$ and $\overrightarrow{M_2O}$ is ϕ_1, and the angle between $r_1 - r_2$ and $r_3 - r_4$ is ϕ_2. The displacement of ϕ_1 and ϕ_2 corresponds to the buckle and propeller modes, respectively. These angles ϕ_1 and ϕ_2 are expressed as follows using θ_1 and θ_2.

$$\phi_1 = \frac{\cos\theta_1 + \cos\theta_2}{\sqrt{2\cos(\theta_1 - \theta_2) + 2}}, \tag{3}$$

and

$$\phi_2 = \frac{z_0}{\sqrt{2a^2\cos(\theta_1 - \theta_2) + 2a^2 + z_0^2}}. \tag{4}$$

When θ_1 and θ_2 are small, Eqs. (3) and (4) can be approximated as

$$\phi_1 = \frac{\theta_1 + \theta_2}{2}, \tag{5}$$

and

$$\phi_2 = \frac{a(\theta_1 - \theta_2)}{z_0}. \tag{6}$$

The displacement ratio of buckle and propeller modes corresponds to the ratio of ϕ_1 and ϕ_2. The relation can be written as

$$\frac{\phi_2}{\phi_1} = \frac{2a}{z_0} \times \frac{1 - \theta_2/\theta_1}{1 + \theta_2/\theta_1}. \tag{7}$$

Figure 5 shows the relation between ϕ_2/ϕ_1 and θ_2/θ_1 in Eq. (7). We set the parameter a to be $a/z_0 = 1$. Only the buckle mode exists when $\theta_1 = \theta_2$ and $\phi_2/\phi_1 = 0$, while only the propeller mode exists when $\theta_1 = -\theta_2$ and $\phi_2/\phi_1 = \infty$. In other areas, both buckle and propeller modes exist. The figure shows that the ratio of buckle and propeller modes may alter if the vibrational frequencies of the hydrogen-bond angle shift. The ratio depends on the difference between θ_1 and θ_2 and can rapidly change from buckle dominant motion (region around $\theta_1 = \theta_2$) to propeller dominant motion (region around $\theta_1 = -\theta_2$). Our finding indicates that the small difference in the hydrogen-bond structure may lead to large difference in molecular motion.

References

1. Watson JD, Crick FHC (1953) Nature 171:737–738
2. Plützer C, Hünig I, Kleinermanns K, Nir E, Vries DSM (2003) Chem Phy Chem 4:838–842
3. Krishnan GM, Kühn O (2007) Chem Phys Lett 435:132–135
4. Plützer C, Hünig I, Kleinermanns K (2003) Phys Chem Chem Phys 5:1158–1163
5. Urashima S, Asami H, Ohba M, Saigusa H (2010) J Phys Cham A 114:11231–11237
6. Abo-Riziq A, Crews B, Grace L, Vries SM (2005) J Am Chem Soc 127:2374–2375
7. Bakker JM, Compagnon I, Meijer G, Helden G, Kabelác M, Hobza P, Vries MS (2004) Phys Chem Chem Phys 6:2810–2815
8. Guerra CF, Bickelhaupt FM, Sniders JG, Baerends EJ (2000) J Am Chem Soc 122:4117–4128
9. Cerón-Carrasco JP, Requena A, Michaux C, Perpete EA, Jacquemin D (2009) J Phys Chem A 113:7892–7898
10. Belau L, Wilson KR, Leone AR, Ahmed M (2007) J Phys Chem A 111:7562–7568
11. Rueda M, Kalko SG, Luque FJ, Orozco M (2003) J Am Chem Soc 125:8007–8014
12. Daido M, Koizumi A, Shiga M, Tachikawa M (2011) Theor Chem Acc 130:385–391
13. Daido M, Kawashima Y, Tachikawa M (2013) J Comp Chem 34:2403–2411
14. Jiří H, Jan R, Pavel H (2013) Chem Phys Lett 568–569:161–166
15. Antone M, Gerald M, Manuel FR (2014) J Chem Phys 141:034106

16. Tachikawa M, Shiga M (2005) J Am Chem Soc 127:11908–11909
17. Suzuki K, Shiga M, Tachikawa M (2008) J Chem Phys 129:144310
18. Suzuki K, Tachikawa M, Shiga M (2010) J Chem Phys 132:144108
19. Koizumi A, Suzuki K, Shiga M, Tachikawa M (2011) J Chem Phys 134:031101
20. Kawashima Y, Tachikawa M (2013) Chem Phys Lett 571:23–27
21. Ogata Y, Daido M, Kawashima Y, Tachikawa M (2013) RSC Adv 3:25252–25257
22. Sugioka Y, Yoshikawa T, Takayanagi T (2014) J Phys Chem A 117:11403–11410
23. Villani G (2005) Chem Phys 316:1–8
24. Villani G (2006) Chem Phys 324:438–446
25. Villani G (2008) J Chem Phys 128:114306
26. Kitao A, Go N (1999) Curr Opin Struct Biol 9:164
27. Potoyan DA, Papoian GA (2011) J Am Chem Soc 133:7405
28. Martyna GJ, Klein ML, Tuckerman M (1992) J Chem Phys 97:2635
29. Korth M (2010) J Chem Theory Comput 6:3808–3816
30. MOPAC2009, James JPS (2008) Stewart computational chemistry, Colorado Springs, CO, USA. http://OpenMOPAC.net
31. Srinivasan AR, Sauers RR, Fenley MO, Boschitsch AH, Matsumoto A, Colasanti AV, Olson WK (2009) Biophys Rev 1:13–20
32. Frisch MJ, Trucks GW, Schlegel HB, Scuseria GE, Robb MA, Cheeseman JR, Scalmani G, Barone V, Mennucci B, Petersson GA, Nakatsuji H, Caricato M, Li X, Hratchian HP, Izmaylov AF, Bloino J, Zheng G, Sonnenberg JL, Hada M, Ehara M, Toyota K, Fukuda R, Hasegawa J, Ishida M, Nakajima T, Honda Y, Kitao O, Nakai H, Vreven T, Montgomery JA, Jr, Peralta JE, Ogliaro F, Bearpark M, Heyd JJ, Brothers E, Kudin KN, Staroverov VN, Kobayashi R, Normand J, Raghavachari K, Rendell A, Burant JC, Iyengar SS, Tomasi J, Cossi M, Rega N, Millam MJ, Klene M, Knox JE, Cross JB, Bakken V, Adamo C, Jaramillo J, Gomperts R, Stratmann RE, Yazyev O, Austin AJ, Cammi R, Pomelli C, Ochterski JW, Martin RL, Morokuma K, Zakrzewski VG, Voth GA, Salvador P, Dannenberg JJ, Dapprich S, Daniels AD, Farkas Ö, Foresman JB, Ortiz JV, Cioslowski J, Fox DJ (2009) Gaussian 09, revision D.01. Gaussian, Inc., Wallingford CT
33. Brooks B, Karplus M (1983) Proc Natl Acad Sci USA 80:6571–6575
34. Head-Gordon M, Pople JA, Frisch MJ (1988) Chem Phys Lett 153:503–506
35. Saebø S, Almlöf J (1989) Chem Phys Lett 154:83–89
36. Frisch MJ, Head-Gordon M, Pople JA (1990) Chem Phys Lett 166:275–280
37. Frisch MJ, Head-Gordon M, Pople JA (1990) Chem Phys Lett 166:281–289
38. Head-Gordon M, Head-Gordon T (1994) Chem Phys Lett 166:122–128
39. Dewar MJS, Zoebisch EG, Healy EF, Stewart JJP (1985) J Am Chem Soc 107:3902–3909
40. Stewart JJP (1989) J Comp Chem 10:209–220
41. Stewart JJP (1989) J Comp Chem 10:221–264
42. Stewart JJP (1991) J Comp Chem 12:320–341
43. Anders E, Koch R, Freunscht P (1993) J Comp Chem 14:1301–1312
44. Stewart JJP (2007) J Mol Model 13:1173–1213

Theor Chem Acc (2015) 134:26
DOI 10.1007/s00214-015-1631-9

REGULAR ARTICLE

DFT investigation of the formation of linear aminols as the first step toward the induction of oxidatively generated interstrand cross-link DNA lesions

Raymond Grüber · Élise Dumont

Received: 15 November 2014 / Accepted: 29 January 2015 / Published online: 11 February 2015

Abstract Apyrimidinic/apurinic sites feature among the most prevalent DNA lesions. If not repaired, it has been recently evidenced that they are prone to react *in situ* with vicinal nucleobases, evolving toward more complex and highly mutagenic interstrand cross-links. Information concerning the structure and the multi-step reactivity leading to such clustered defects is scarce due to their low formation yield. This study reports a DFT exploration of the condensation reaction between a ketoaldehyde (derived from an oxidized C4' abasic site) and three nucleobases featuring an amino group. They are found to present a very similar intrinsic reactivity, indicating in turn that differences of reactivity arise more from the relative positioning of the two reactive fragments within a flexible B-DNA. We also probe the role of a vicinal water molecule for the formation of the aminol and the requirements to reach an adequate estimate of this strongly exothermic reaction, which drives the DNA damage process.

Keywords DNA interstrand cross-link · Oxidized abasic site · Density functional theory · Reactivity · Dispersion

Published as part of the special collection of articles derived from the 9th Congress on Electronic Structure: Principles and Applications (ESPA 2014).

Electronic supplementary material The online version of this article (doi:10.1007/s00214-015-1631-9) contains supplementary material, which is available for authorized users.

R. Grüber · É. Dumont (✉)
Institut de Chimie de Lyon, CNRS, Ecole Normale Supérieure de Lyon, Université de Lyon, 46 allée d'Italie, 69364 Lyon, Cedex 07, France
e-mail: elise.dumont@ens-lyon.fr

1 Introduction

Oxidatively generated tandem DNA lesions constitute a threat for genome integrity, whose importance has been firmly established over the last decade [1]. They correspond to the formation of a covalent bridge between two vicinal nucleobases, either in intrastrand or in interstrand. Experimental groups tackle successfully the detection and structural elucidation of these very rare adducts (0.050 lesions per 10^9 nucleosides per Gray for the prototype intrastrand guanine–thymine adduct [2]), relying on sophisticated tandem mass spectrometry, but their formation pathway within B-DNA is often postulated yet not established on a firm basis.

A detailed knowledge of these mechanisms is required if one wants to rationalize the preferential formation of some adducts, whereas other ones are not evidenced but may still exist, lying above the detection threshold of analytical techniques. The task is all the more complicated since oxidative DNA lesions are usually formed along multi-step, radical or ionic, pathways where the role of the B-DNA environment can be decisive. One of the most recent examples of such a reactivity is the formation of an interstrand cross-link (ICL) lesion named dCyd341 [3] (Fig. 1). This lesion is singled out by a peak at a high molecular mass (341) on the HPLC tandem mass spectrometry measurements. The mutagenicity of this interstrand oxidatively generated cross-link, probed in cellular DNA, urges to unravel its formation mechanism. The dCyd341 lesion is initiated by a hydrogen abstraction from the position C4' on the deoxyribose ring. It is then surmised that dCyd341 is formed from an C4'-abasic (AP) site that condensates *in situ* with cytosine, as represented in Fig. 1. Analog ICLs arising from non-oxidized abasic site reactions with adenine or guanine have been reported [4–6]. It remains to be elucidated if purines

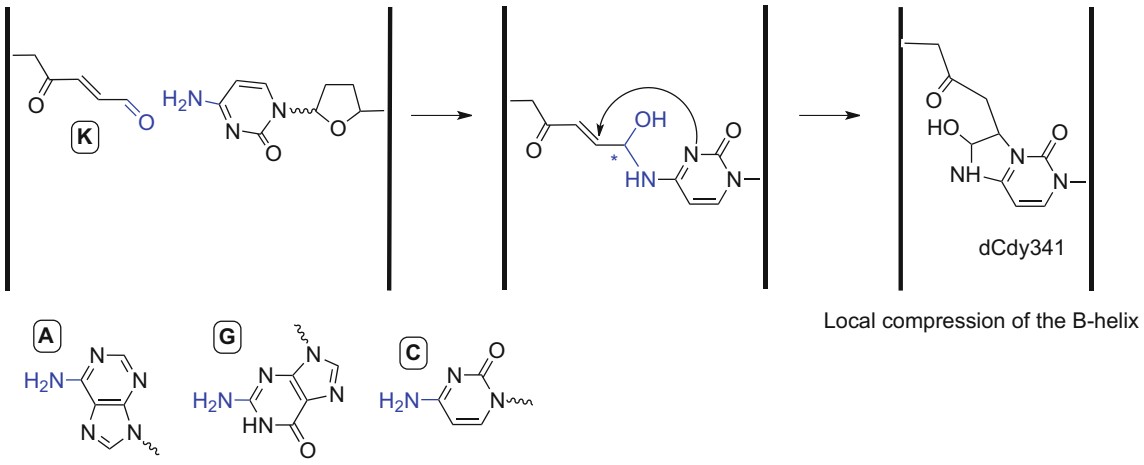

Fig. 1 Schematic view of the formation of an interstrand cross-link (ICL) by attack of an exocyclic amine (here cytosine) on a ketoaldehyde (oxidized C4'-abasic site). We investigate the first step, namely the condensation toward a linear aminol. The second step, involving an ionic intermediate and another proton transfer, is not studied here. Atoms treated in our study are displayed with fine lines: methyl groups were used to cap structures along the N-glycosidic bond

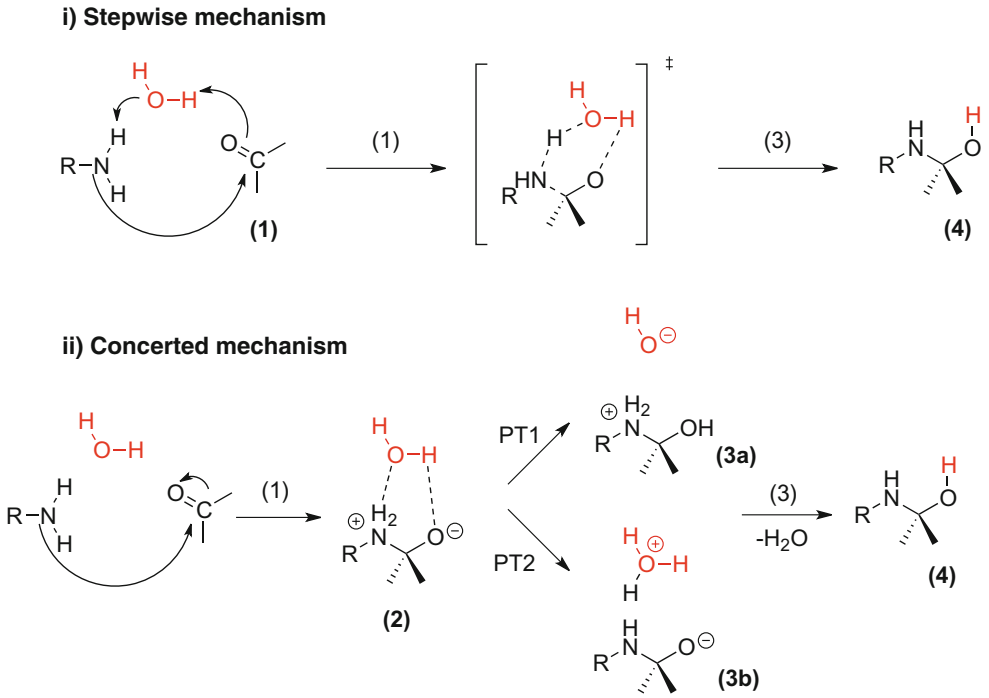

Fig. 2 Scheme for the formation of a linear aminol by condensation between a generic primary amine and an aldehyde. The inclusion of a water molecule in the high layer is represented in *red*. Two competitive pathways can be proposed: stepwise versus concerted

may also react with *oxidized* abasic sites to form analog ICLs, a possible occurence since they feature the same—N=C(–NH_2)—motif. Indeed, the latter lesions may occur without being yet detected experimentally. A first rationale comes from the analysis of the preferential affinity of the C4'-AP site for cytosine that we have recently inferred resorting to explicit solvent classical molecular dynamics [7]. Hence, the two reactive patterns remain close, with a locked conformation, which is expected to favor the reactivity of cytosine over purines. But the three nucleobases may present contrasted reactivities.

We report a computational study of the first step of this condensation between a C4'-AP site and the three nucleobases cytosine, adenine and guanine. Figure 2 details the

three-step mechanism leading to the formation of the aminol, which is known to be a transient intermediate. It constitutes an intermediate leading to the lesion detected by tandem mass spectrometry, which involves a subsequent 1,4-addition.

The condensation reaction between an aldehyde and a secondary amine to form an aminol is ubiquitous in organic, green and bioorganic chemistry. Yet this textbook reaction has been scarcely studied by quantum calculations. It is known to proceed at ambient temperature, with release of one water molecule. The mechanism can be written down as either stepwise or concerted as shown in Fig. 2. In this work we, set out to explore the formation of the aminol, in the absence of other environment than an implicit aqueous solvation, relying on a static approach. We aim at comparing the reactivity of cytosine, guanine and adenine toward the C4'-oxidized abasic site.

2 Methodology

Static calculations were performed within the framework of density functional theory (DFT), on model fragments: The α,β-unsaturated ketoaldehyde was modeled by replacing the phosphate group by methoxy group, resulting in 5-methoxy-4-oxopent-2-enal. The three nucleobases X=C, A and G were capped using a methyl group, thus resulting in the 9-methyl-substituted adenosine and guanine and 1-methyl-substituted cytosine and 5-methyl cytosine. In order to guarantee that the model fragments have orientations of the abasic site and the opposite nucleobase that are representative of the one within a B-DNA environment, the starting structures were extracted from snapshots along 100ns classical molecular dynamics trajectories of a 13-bp poly(dG-dC) ds-sequence featuring K:X as the central base pair. We refer the reader to a previous reference by one of us [8] for the details of these simulations. All stationary points were characterized as a minima or transition state on the potential energy surface through frequency calculations. Transition states imply a unique imaginary frequency pertaining to the relevant reaction coordinate. All DFT calculations are performed using Gaussian 09 Revision D.01 suite of programs [9]. The 6-31+G(d,p) basis set was used throughout, to account for a partial charge transfer in the transition state region. To situate the basis set dependence with the second-order Møller-Plesset perturbation theory (MP2), which is more sensitive than density functionals, single-point calculations using the higher-quality DZP++ basis set (see Reference [10]) were performed and lead to difference in energy that are trifling.

Since ionic intermediates are implied, an implicit model accounting for solvation in water (polarizable continuum model (PCM), ϵ_r=78.3) was used. We first perform a first series of DFT calculations to provide a comparison point with the previous study [11] for adenine, for which we confirm a concerted mechanism, although with a high activation energy ($\sim$40 kcal/mol). We extend the study to cytosine and guanine since our first motivation is to compare their reactivity toward K. To improve the description of non-isotropic environment effects, we included one water molecule. It is placed such that an hydrogen bond is formed in the vicinity of the amino group, which is found a slightly more favorable position for HB than the carbonyl group since a second nitrogen can participate in the H bonding.

First, the hybrid *meta* GGA M06-2X functional was used, in order to provide comparison with the previous study by Gorb and coworkers [11] and because this density functional has been pointed out as a performant one for DNA non-covalent interactions [12] as well as for DNA structure and chemistry [13, 14], probably due to its high percentage of exact exchange. It also includes dispersion in a parametrized manner. To probe the intramolecular interactions stabilizing the transition state (TS) structures, a non-covalent interaction (NCI) analysis [15] is conducted at the same level of theory. We remind that this method is based on the electronic density gradient and hessian principal values, and allows to pictorially identify dispersive interactions and π-stacking (green), hydrogen bonds (blue core) or steric clash (red). We also performed calculations with the GGA BLYP and hybrid GGA B3LYP functionals to assess the density functional dependence in section III.C. They are as popular when investigating ground-state reactivity of DNA [16–19]. They will be benchmarked against the MP2 approach. In the case of BLYP and B3LYP, the impact of including dispersion correction was also tested using a Grimme's style London dispersion correction (D3BJ) [20].

3 Results and discussion

3.1 Assistance by a water molecule

Nucleophilic addition of primary amines to carbonyl compounds generally leads to formation of imines via tetrahedral hemiaminal intermediates [21, 22]. This step occurs via a mechanism that can *a priori* be either stepwise or concerted (Fig. 2). We consider the conjugated aldehyde K and one of the three nucleobases C, A or G (see Fig. 1). It should be noted here that this condensation can result in two stereochemical outcomes; however, as both of the participating molecules are symmetric, this step is not expected to be enantio-selective. We thus report only the lowest energy as the static scheme does introduce small spurious difference between two enantiomers.

Cartoon representation of the corresponding TS structures are given alongside with their barrier heights

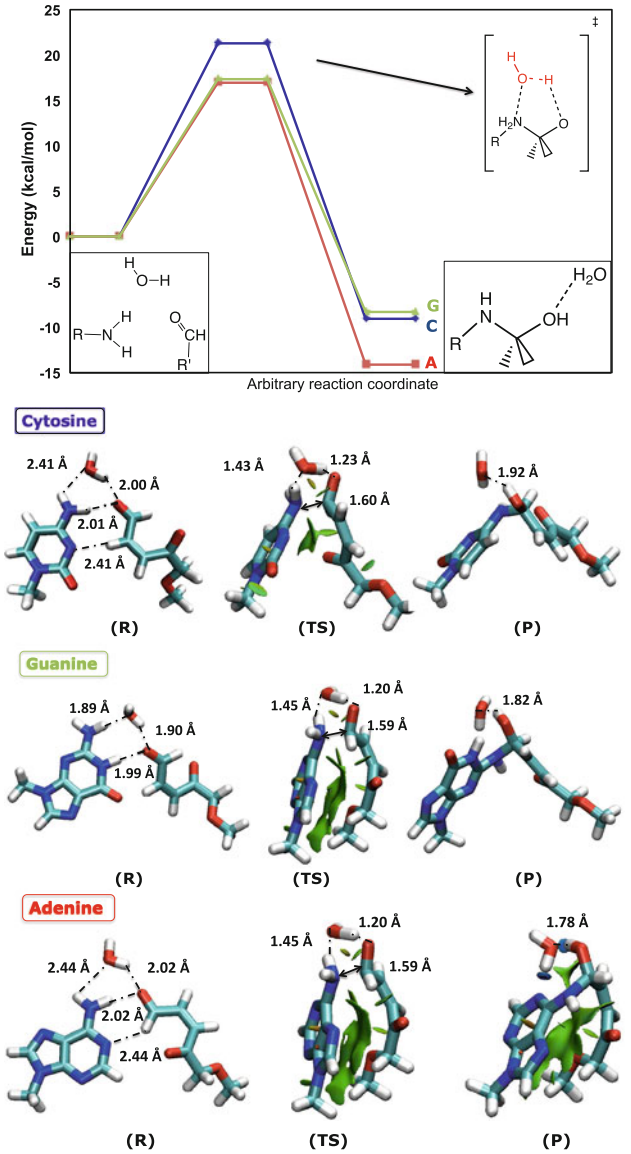

Fig. 3 Energy profile for the 1,2-addition between K and C, A or G. Cartoon representations are given for each stationary points. The *blue* and *green* NCI isodensities (the isovalue is 0.5 au, for a density cutoff of 0.1 au) reflect the presence of non-covalent interactions. Distances are given in Å

in Fig. 3. In agreement with Gorb and coworkers [11], who recently reported a computational study of adenine interacting with K, we found the concerted mechanism to be lower, yet with an activation energy as high as 40 kcal/mol. These values somewhat suffer from a systematic overshooting, given that aminol formation is known as a facile reaction in organic chemistry. Such a high-barrier would also contradict the fact that the lesion dCyd341 was unambiguously assigned.[1] This reflects the mechanical constraint for the four-centered transition state (TS) structure. In order to improve the description of the 1,2-addition—and hence to be able to compare cytosine, adenine and guanine—the participation of one water molecule, as displayed in red in Fig. 2, should be explicited. In the rest of the study, one water molecule was hence systematically included and we first re-examine this reaction for adenine, but also for cytosine and guanine. The profile obtained for adenine and the aldehyde model presents a similar profile to the one obtained by Gorb and coworkers, yet with a twofold reduction in the barrier heights (ca 20 kcal/mol).

We stress out that this decrease would correspond to several orders of magnitude once injected in a kinetic model. The presence of the water molecule will also lead to more flexibility and relax the constrained four-membered TSs by assisting the proton transfer process. This probes the catalytic role of the water molecule; all the more since along the 100 ns classical MD exploration, the radial distribution functions $g(r)$ witness two peaks, the first one clearly corresponding to one water molecule situated in direct hydrogen bonding interaction with the oxygen of the aldehyde of K group or the nitrogen atom of the amino group of X (see Fig. 4c, d).

3.2 Assessment of the nucleobases reactivity toward K

Based on this first series of calculations, the three nucleobases present rather similar energy profiles, both for barriers and for endergonicities. Hence, the formation of the transient aminol may not differ dramatically between C, A and G. Indeed this reactivity implies a chemical moiety, the amino group, exterior to the aromatic ring. A closer inspection reveals that the nucleophilicity is noticeably higher for purines, with respective values of 16.9 and 17.3 versus 21.3 kcal/mol for activation energies along the series $A \sim G < C$. This is in line with the documented nucleophilicity of the N6 amino group of adenine [23, 24]. Also adenine leads to the most stable product from the thermodynamical point of view, which is found to be exergonic by -14.1 kcal/mol (i.e., favored over G or C by $\Delta\Delta E_r = -5.0$ and -5.8, respectively). This difference can be explained by a special conformation of the aminol formed by condensation of adenine with K, where the two fragments are nearly parallel to maximize π-stacking interactions, as can be seen on the NCI plot given in Fig. 3 for the aminol formed by adenine.

We stress out that structural difference arises more in the TS region, since structures are more malleable, and weak interactions become strong enough to induce significant geometrical changes. It is important to note that the geometry of the TS with purines is stabilized by larger-extent dispersive interactions that are revealed in a pictorial manner on the NCI plots (green isodensities). This provides a

[1] One cannot isolate any transition states for ionic intermediates to assess the barriers, but product is ca. 20 kcal/mol higher.

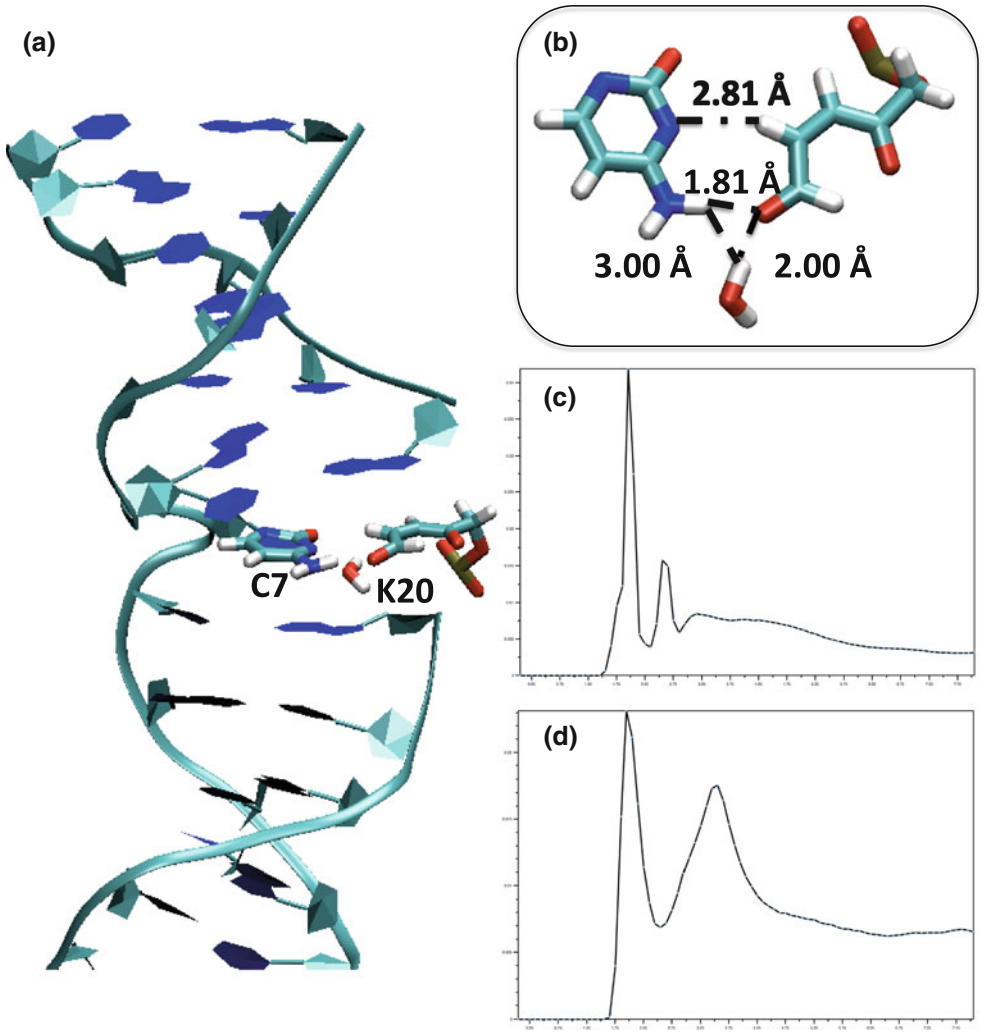

Fig. 4 Representative snapshot for an alternate poly(dG-dC) obtained after 100 ns of classical explicit solvent molecular dynamics [8] showing **a** the conserved B-helix owing to **b** the stable non-Watson–Crick C:K pairing with two hydrogen bonds and a proximal water (*inset*). Two radial distribution functions $g(r)$ are given in **c** for the oxygen of the aldehyde moiety and in **d** for the nitrogen of the amino group

straightforward interpretation for the decrease of 4.4 and 4.0 kcal/mol, which can be safely attributed to additional dispersive interactions as purines TS structures adopt a hairpin conformation. However, the occurence of such a folded TS conformation will imply a tremendously large B-DNA distortion to position A and K, or G and K in a near parallel way. Most likely, this geometry will differ from the one within B-DNA. Also for guanine, it is noteworthy that going from the reactant to the TS induces the disruption of the "central" HB, the sole nucleobase for which the amino group and the terminal -COH electrophilic moiety do not face. This implies an important reorganization that is probably not directly representative from the situation once the reactive partners are embedded in an oligonucleotide, even with a proximal single-strand break.

It becomes clear at this stage that the dispersion, but also the percentage of exact exchange, plays a critical role for an unbiased description of this (DNA) reactivity. Whereas it is imperative for studying *intra*strand cross-link to use a dispersion correction [25], it is possible here that the unconstrained geometry of a too simple model system combined with dispersion leads to a spurious interaction between purines and K, favoring stacked fragments around the TS region. The importance of dispersive component is corroborated by DFT-D3BJ calculations performed on the geometries of the stationary points, whose values are given in parenthesis in the penultimate column of Table 1. In the next section, we assess the performance of other functionals, popular for DNA systems, that do not include a dispersion correction. This examination is focussed on $\Delta_r E$,

Table 1 Estimate of the reaction energy $\Delta_r E$ defined between the reactant $X + K$ and the corresponding aminol (one water molecule is included)

$\Delta E_{R\rightarrow P}$ (kcal/mol)	BLYP	BLYP-D3BJ	B3LYP	B3LYP-D3BJ	M06-2X	MP2
A	−0.8	−7.1	4.4	−9.3	−14.1 (−14.8)	−14.6
C	3.1	−1.4	−0.7	−4.7	−9.1 (−5.9)	−2.7
G	3.3	-0.3	-0.2	-3.1	−8.3 (−4.9)	−11.2

The 6-31+G(d,p) basis set is used uniformly. For the M06-2X functional, we report the dispersive component estimated through single-point calculations and employing the D3BJ scheme. Cartoon representations are given in Figure S3

given that relatively low barriers are found for the reaction, and can be expected to be even lower in a dynamic scheme. For instance, the profile of G and K reaction obtained using the GGA BLYP functional is characterized by an energy barrier of 25.0 kcal/mol (versus 17.3 kcal/mol for M06-2X which triggers a high percentage of exact exchange), to form a transition state structure that does not longer present a hairpin conformation.

3.3 The exothermicity as a driving force

Cytosine and guanine do not present such long-range dispersion interactions yet are also stable, which is expected for this reaction, with respective $\Delta_r E$ of −9.1 and −8.3 kcal/mol. This contrasts with the inclusion of implicit solvent effects only, where hemiaminals are found to be destabilized [11]. The dependence of $\Delta_r E$ according to the level of theory is a legitimate question to be asked and can be commented from the values collected in Table 1. The very marked difference between M06-2X and BLYP and B3LYP as two other functionals, both of which being commonly used to tackle DNA chemistry [26–28], is intriguing and calls for comparison with a post-Hartree–Fock method. Values computed with the post-Hartree–Fock MP2 approach are reported in the last column of Table 1.

A marked exothermicity is also predicted using the post-Hartree–Fock MP2 approach, in perfect agreement with the M06-2X values for purines but not for cytosine. It is in line with the fact the formation of aminol is known as a facile reaction, even in B-DNA.

It is interesting to note that the BLYP functional, also a very popular choice for DFT study of reactivity of DNA when combined with *ab initio* molecular dynamics [8, 29], is qualitatively wrong in systematically predicting an endergonic reaction (by ca. 2.4 kcal/mol in average for the three nucleobases). Including 20 % of exact exchange through the three-parameter hybrid GGA B3LYP only slightly improves the results with respect to the MP2 estimates. The geometries of the products obtained at the M06-2X, BLYP and B3LYP levels of theory obtained after full geometry reoptimization are very similar, with the exception of adenine.

The exothermicity of the condensation reaction here acts as a driving force triggering the damage process and shall be strong enough to trigger the B-helix distortion. It should hence be reproduced with enough accuracy, especially since this quantity ("free" energy of destabilization) is central to understand the severity of ICLs [2].

This static study exemplifies a case where BLYP provides a *qualitatively* wrong picture. However, because of error cancellation due to the absence of dispersion, the BLYP or near-equivalently B3LYP description probably provides a more representative for two entities embedded in an oligonucleotide. From Fig. 4a, one can see that the positioning within B-DNA is dictated by adjacent nucleobases that are expected to enforce a linear approach between the C4' abasic site and the initially paired nucleobase.

4 Conclusions

The aminol formation is a versatile reaction in chemistry, yet it is still a challenge from the computational point of view. It involves a proton transfer, and our results confirm that the participation of one explicit water molecule is crucial. The inclusion of a dispersion correction on isolated fragments leads in one case (the adenine cross-link adduct) to a spurious description, with a folded structure not representative of B-DNA. This static exploration, independently of the density functional used (see ESI), reveals a slightly higher barrier for the 1,2-addition of cytosine. Yet the oxidatively generated formation of interstrand cross-link B-DNA also depends on the following 1,4 Michael addition and on eventual further dehydration and can be dramatically impacted as the reactive fragments are considered within a duplex B-DNA environment.

Acknowledgments This work was performed within the framework of the LABEX PRIMES (ANR-11-LABX-0063) of Université de Lyon, within the program "Investissements d'Avenir" (ANR-11-IDEX-0007) operated by the French National Research Agency (ANR). Calculations were performed using the local HPC resources of PSMN (Pôle Scientifique de Modélisation Numérique) at ENS-Lyon.

References

1. Cadet J, Ravanat JL, Taverna-Porro M, Menoni H, Angelov D (2012) Cancer Lett. 327:5
2. Hong H, Cao H, Wang Y (2007) Nucleic Acids Res. 35:7118
3. Regulus P, Duroux B, Bayle PA, Favier A, Cadet J, Ravanat JL (2007) Proc. Nat. Acad. Sc. USA 104:14032
4. Dutta S, Chowdhury G, Gates KS (2007) Journal of the American Chemical Society 129(7):1852. doi:10.1021/ja067294u
5. Johnson KM, Price NE, Wang J, Fekry MI, Dutta S, Seiner DR, Wang Y, Gates KS (2013) Journal of the American Chemical Society 135(3):1015. doi:10.1021/ja308119q
6. Price NE, Johnson KM, Wang J, Fekry MI, Wang Y, Gates KS (2014) Journal of the American Chemical Society 136(9):3483. doi:10.1021/ja410969x
7. Patel C, Drsata T, Lankas F, Dumont E (2013) Biochemistry 52(45):8115. doi:10.1021/bi401268q
8. Patel C, Garrec J, Dupont C, Dumont E (2013) Biochemistry 52(2):425. doi:10.1021/bi301198h
9. F MJ et al. (2009) Gaussian 09 Revision A.02. Gaussian Inc., Wallingford CT
10. Bera PP, S HF III (2005) Proc. Nat. Acad. Sc. USA 102:6698
11. Sviatenko L, Gorb L, Hovorun D, Leszczynski J (2012) The Journal of Physical Chemistry A 116(9):2333. doi:10.1021/jp211911u
12. Hohenstein EG, Chill ST, Sherrill CD (2008) Journal of Chemical Theory and Computation 4(12):1996. doi:10.1021/ct800308k
13. Zubatiuk TA, Shishkin OV, Gorb L, Hovorun DM, Leszczynski J (2013) Phys. Chem. Chem. Phys. 15:18155. doi:10.1039/C3CP51584B
14. Cerón-Carrasco JP, Requena A, Jacquemin D (2012) Theoretical Chemistry Accounts 131(3):1188. doi:10.1007/s00214-012-1188-9
15. Johnson ER, Keinan S, Mori-Sanchez P, Contreras-Garcia J, Cohen AJ, Yang W (2010) Journal of the American Chemical Society 132(18):6498. doi:10.1021/ja100936w
16. Jena NR, Mishra PC (2005) The Journal of Physical Chemistry B 109(29):14205. doi:10.1021/jp050646j
17. Loos PF, Dumont E, Laurent AD, Assfeld X (2009) Chemical Physics Letters 475(1–3):120
18. Garrec J, Patel C, Rothlisberger U, Dumont E (2012) Journal of the American Chemical Society 134(4):2111. doi:10.1021/ja2084042
19. Anil AK, Sevilla MD, Suhai S (2008) J. Phys. Chem. B 112:5189
20. Grimme S (2011) Wiley Interdisciplinary Reviews: Computational Molecular Science 1(2):211. doi:10.1002/wcms.30
21. Hooley RJ, Restorp P, Iwasawa T, Rebek J (2007) Journal of the American Chemical Society 129(50):15639. doi:10.1021/ja0756366
22. Kawamichi T, Haneda T, Kawano M, Fujita M (2009) Nature 461(7264):633
23. Goedecke K, Pignot M, Goody RS, Scheidig AJ, Weinhold E (2001) Nat. Struct. Mol. Biol. 8:121
24. Vijayalakshmi KP, Mohan N, Ajitha MJ, Suresh CH (2011) Org. Biomol. Chem. 9:5115. doi:10.1039/C1OB05093A
25. Dupont C, Patel C, Dumont E (2011) The Journal of Physical Chemistry B 115(50):15138. doi:10.1021/jp209074q
26. Chatgilialoglu C, Guerra M, Mulazzani QG (2003) Journal of the American Chemical Society 125(13):3839. doi:10.1021/ja029374d
27. Mantel C, Chandor A, Gasparutto D, Douki T, Atta M, Fontecave M, Bayle PA, Mouesca JM, Bardet M (2008) J. Am. Chem. Soc. 130:16978
28. Labet V, Morell C, Grand A, Cadet J, Cimino P, Barone V (2008) Org. Biomol. Chem. 6:3300
29. Abolfath RM, Biswas PK, Rajnarayanam R, Brabec T, Kodym R, Papiez L (2012) The Journal of Physical Chemistry A 116(15):3940. doi:10.1021/jp300258n

Theor Chem Acc (2015) 134:36
DOI 10.1007/s00214-015-1640-8

REGULAR ARTICLE

Modeling DNA electronic circular dichroism by QM/MM methods and Frenkel Hamiltonian

Hugo Gattuso · Xavier Assfeld · Antonio Monari

Received: 26 November 2014 / Accepted: 16 February 2015 / Published online: 26 February 2015

Abstract We report the modeling of the electronic circular dichroism spectra of different double helix B-DNA sequences. The circular dichroism spectra have been obtained in the framework of the Frenkel excitation theory, while DNA conformational space has been explored using molecular dynamics. Excited states are obtained using hybrid quantum mechanics/molecular mechanics theory at time-dependent density functional theory level. The validity of the effective Frenkel Hamiltonian approach is assessed by comparison with full quantum mechanics treatment of many interacting chromophores. The convergence of the simulated spectra with the number of interacting chromophores is assessed as well as their behavior with respect to experimental results.

Keywords Electronic circular dichroism · DNA structure and dynamic · Supramolecular dichroism · QM/MM methods · Frenkel exciton

Published as part of the special collection of articles derived from the 9th Congress on Electronic Structure: Principles and Applications (ESPA 2014).

Electronic supplementary material The online version of this article (doi:10.1007/s00214-015-1640-8) contains supplementary material, which is available to authorized users.

H. Gattuso · X. Assfeld · A. Monari (✉)
Theory-Modeling-Simulation SRSMC, Université de Lorraine - Nancy, Vandoeuvre-lès-Nancy, France
e-mail: antonio.monari@univ-lorraine.fr

H. Gattuso · X. Assfeld · A. Monari
Theory-Modeling-Simulation SRSMC, CNRS, Vandoeuvre-lès-Nancy, France

1 Introduction

DNA importance in biological processes cannot be underestimated, because of its role in storing, duplicating and coding the genetic information of almost all living individuals [1]. Also for this reason, it has attracted a considerable amount of interest in the scientific community [2–4], especially after the celebrated discovery of its double-helical arrangement [5]. Nevertheless, its structure and dynamic is still the subject of an intense research activity covering fields as diverse as molecular biology, chemistry and biophysics [6–9]. This is certainly due to the complexity of its behavior, characterized for instance by polymorphism with the presence of different competitive structures [10], but also by the combination of a flexible backbone with a rigid core that makes its dynamics rather peculiar [11]. Furthermore, it is important to precisely unravel the distortions induced in the DNA structure by the presence of lesions [12]. Indeed, the influence of large structural modifications can be related to the rate of repair of specific lesions and hence to their toxicity. At the same time, it is still important to achieve a good comprehension of the aggregates formed by the interaction between DNA and relatively small endogenous or exogenous compounds that may subsequently induce lesions for instance through photosensitization [13–20]. Indeed, especially in the case of non-covalent sensitization, the interactors may present different competitive interaction modes that are usually hard to access, for instance by using X-ray crystallographic techniques [21, 22]. The former subject should not be underestimated since it is not only related to the study of the induction of DNA lesions, but may also be exploited in the efficient design of selective chemotherapeutic agents, in particular for photodynamic therapy treatments [23–26]. Even in the case of non-sensitized DNA, it is indeed suitable to characterize

the different structural and dynamical characteristics as a function of the DNA sequence, since the former may have quite strong influences on the biological activity. In particular, one may want to access non-conventional DNA structures, i.e., DNA sequences that present a structure quite different from the conventional double helix. On that respect, we may cite the so-called G-quadruplexes [27], common for guanine-rich sequences and present in telomeres, where they exert an important biological role, regulating cell apoptosis [28], as well as in important noncoding regions of the genomes such as the ones regulating gene expression [29]. For those reasons, G-quadruplexes are emerging as a privileged target for the design of novel promising chemotherapeutics with enhanced selectivity and hence reduced side effects [30].

DNA being an inherent dynamic macromolecule, it is also crucial to follow the influence of environmental conditions, such as salt concentration or ionic strength, on the structure and the dynamics. Obviously, such an objective cannot be pursued by crystallographic techniques.

A method of choice to study the structure and dynamic of DNA large fragments, as well as stacked materials [31] such as liquid crystals, is the electronic circular dichroism (ECD) [32–36]. Indeed, because of their regular arrangements, for instance double helix, the non-chiral DNA components (nucleobases) are embedded in a chiral environment that induces a supramolecular dichroism signal [19, 20, 35–37]. The advantage of such a technique is due to the fact that supramolecular dichroism is extremely sensitive to the difference in the geometrical arrangements of the individual chromophores and hence to the DNA structural properties. Furthermore and despite its simplicity, induced circular dichroism signals can be efficiently used to differentiate the different binding modes of DNA sensitizers.

On the other hand, because of the extreme sensibility of ECD and the rich density of information embedded, the fine interpretation of the experimental spectra, and in particular drawing connections with the precise structure, is somehow quite complicated, or even impossible. Most often, indeed, one relies on rather empirical "rules of the thumb" to connect ECD signals to structural patterns.

Such a situation is precisely the one for which molecular modeling and simulation can be of extreme help. Indeed, by opportunely using molecular dynamics (MD), one may have access to the different DNA conformations. It can then be possible to model the spectroscopic signals using quantum mechanics (QM) on selected MD snapshots. As an example, one of us has recently proposed a specific ECD signature for a novel DNA/benzophenone interaction mode [19, 20]. Also a combined experimental and theoretical study on a very small model has been recently reported [36].

Although attractive, in the case of supramolecular dichroism, and in particular DNA ECD modeling, particular care should be taken in the treatment of the environmental effects. Indeed, DNA chromophores being embedded in a complex inhomogeneous environment, a multiscale treatment based on hybrid quantum mechanics/molecular mechanics (QM/MM) is compulsory to correctly reproduce the excited state energies and the spectroscopic properties, as shown by some of us for similar systems [13–17, 38]. Furthermore, the case of supramolecular-induced dichroism is even more complex since the experimental signal results from the coupling and interaction of many different chromophores. Therefore, without using appropriate effective Hamiltonian description of the problem, such as the one proposed by Frenkel, the size of the QM partition would grow so much to make the problem untreatable.

In the present contribution, we propose to use the Frenkel exciton theory [39–41], coupled with a QM/MM description of the excited states to recover the ECD spectra of different DNA sequences. The conformational space of the original sequences has been explored by classical MD techniques. By comparing effective Hamiltonian results with the ones obtained by an extended QM partition, we show how the simple Frenkel techniques proves effective in such respect and may be efficiently used to study ECD signals of complex DNA/sensitizers aggregates.

1.1 Theory

The easiest way to study the excited states of non-covalently interacting chromophores (π–π stacking) is to consider the exciton model [39, 40]. If we consider for simplicity a dimer composed of the monomers ϕ_A and ϕ_B, the global excited states may be constructed as the linear combination of individual monomer's excitations:

$$|\psi_{\pm}\rangle = c_{\pm}^{a}\left|\phi_A^{\dagger}\phi_B^{0}\right\rangle \pm c_{\pm}^{B}\left|\phi_A^{0}\phi_B^{\dagger}\right\rangle \tag{1}$$

where $\left|\phi_A^{\dagger}\phi_B^{0}\right\rangle$ represent an excitation on the monomer A. In order to obtain the global excitation energies as well as the eigenstates defining the exciton wavefunction, one may write a secular equation and diagonalize an effective Hamiltonian matrix $\boldsymbol{H}$ whose elements will be:

$$H_{ii} = \varepsilon_i,\ H_{ij} = \left\langle \phi_i^{\dagger}\middle|\hat{H}\middle|\phi_j^{\dagger}\right\rangle \tag{2}$$

where the diagonal elements ε_i are the excitation energies on the monomer i, while the off-diagonal elements represent the coupling between the different excited states. In practice, the coupling between the monomers will break the degeneracy between the excited states giving rise to two transitions. Nevertheless, since the coupling is usually

quite weak, the two transitions will normally be embedded in the vibronic band of the absorption spectra. However, in the case of chiral aggregates, such as helical arrangements, the two transitions may have different signs of the rotatory strengths and therefore they can be easily differentiated in the spectrum. Obviously, the extension to the case of a multichromophoric system is trivial. Although some more complicated schemes using the coupling between the monomers' excited state density matrices exist [42–44], the simplest formalism consists in simply considering the coupling between the monomeric transition dipoles as well as their distances and orientations. In this case, the Hamiltonian matrix elements simply become:

$$H_{ij} = \frac{\mu_i \cdot \mu_j}{|R_{ij}|^3} - 3\frac{(\mu_i \cdot R_{ij})(\mu_j \cdot R_{ij})}{|R_{ij}|^5} \tag{3}$$

In Eq. 3, μ_i is the transition dipole moment of the monomer i, R_{ij} is the distance vector relying the center of charges of the two chromophores i and j, and $|R_{ij}|$ is its module. Upon diagonalization of the H matrix, one gets the eigenvalues ε, i.e., the excitation energies and the matrix $\boldsymbol{U}$ whose columns store the different eigenvectors. The absorption oscillator strengths for an exciton state k will therefore be proportional to:

$$f_k = \sum_{i,j} (\mu_i \cdot \mu_j) U_{ik} U_{jk} \tag{4}$$

while the rotatory strength vector to:

$$r_k = \sum_{i,j} \varepsilon_k \left[R_{ij} \left(\mu_i \cdot \mu_j \right) \right] U_{ik} U_{jk} \tag{5}$$

For ECD in the case of homogeneous solution, the final spectroscopic observable intensity will simply be the average over the three components of the r_k vector.

1.2 Computational details

Two Watson- and Crick-paired double-helical B-DNA strands (poly[d(AT)] and poly[d(CG)] of 15 pairs each) were created in silico using the nucleic utility code implemented in Amber facilities [45]. The strands were then solvated in a 10.0 Å water solvation boxes (truncated octahedron). Water molecules were modeled using TIP3P model while Na^+ cations have been added to ensure the neutrality of the systems. The molecular dynamics simulations were performed using the AMBER99 force field with the bsc0 correction, developed for DNA [46]. Periodic boundary conditions and the particle mesh Ewald summation have been used throughout. Global simulations were divided into five steps. A first step consisted in the relaxation of the water box conformation over 8000 steps (4000 using the steepest descent algorithm and 4000 with the conjugated gradient), followed by the relaxation of DNA and solvent. The system was then heated up from 0 to 300 K in the NVT ensemble and equilibrated in the NPT ensemble to reach a pressure of 1 atm during 20 ps. Finally, 10-ns production runs were carried out again in the NPT ensemble. From the previous trajectories, 40 snapshots were extracted in order to compute the vertical electronic excitations of each DNA base using our QM/MM method [47, 48]. The QM/MM frontier was placed at the junction between the sugar and the nucleobase, and the dangling bond was treated with the link-atom scheme [47]. The quantum parts of the computations were conducted at the time-dependent density functional theory (TDDFT) level using the M06-2X [49] density functional and the 6-311+G(d) basis set [50]. In the case of poly[d(AT)], the energies of the four first excited states of each base were determined as well as their electronic transition dipole moments, while the six first excited states were calculated for the poly[d(CG)]. Excitation energies and transition dipole moments were used to build the Frenkel Hamiltonian and simulate the ECD of the DNA.

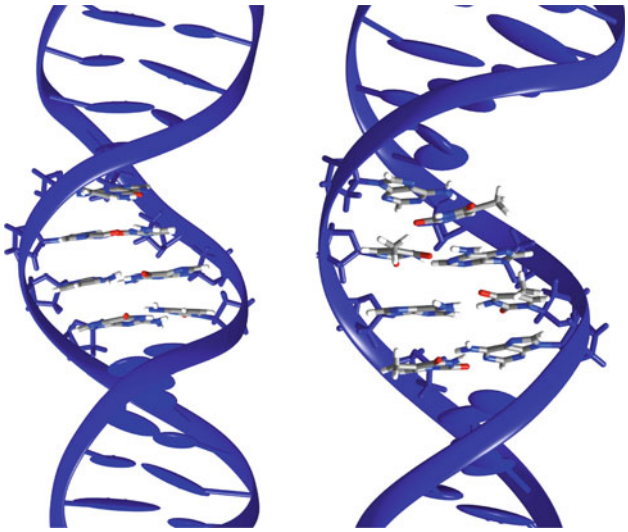

Fig. 1 Representative snapshots of the DNA structures of the two double strands poly[d(GC)] on the *right* and poly[d(AT)] on the *left*. The central base pairs included in the Frenkel Hamiltonian are evidenced in licorice representation

To assess the validity of the model, ECD spectra obtained with the Frenkel model have been compared to the ones obtained from the ab initio QM/MM calculations of a total of four DNA nucleobases constituting two nearby base pairs. Representative structures obtained from the molecular dynamic trajectories are reported in Fig. 1 with the bases put in the QM partition evidenced in licorice representation. Excited states have been calculated on top of ten snapshots extracted from the corresponding molecular dynamic trajectories. TDDFT level was used with the 6-311+G(d) basis set and the M06-2X functional.

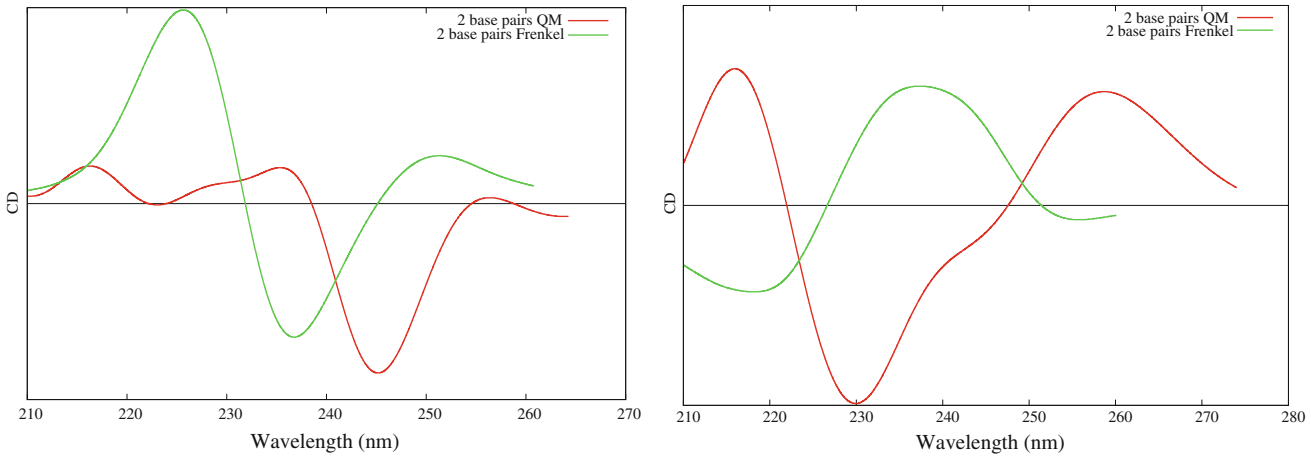

Fig. 2 ECD spectra for a poly[d(AT)] (*left panel*) and poly[d(CG)] (*right panel*) obtained with the Frenkel Hamiltonian or a full QM/MM approach on the two central base pairs. Wavelengths in nm, intensities in arbitrary units

Thirty-two excited states were calculated for poly[d(AT)] and 48 states for poly[d(CG)], this correspond to highest excitation energies of about 6.5 and 6.6 eV, respectively.

It is important to underline that for both the ab initio protocol and the Frenkel semiempirical Hamiltonian, the excited states of each individual monomer have been calculated using a QM/MM approach. More particularly, and thanks to the original electrostatic response of the environment (ERS) technique [47] mechanical, electrostatic and polarizable embeddings are accounted for.

All the QM/MM computations were performed using a local modified version of Gaussian 09, Revision B0.1 [51], coupled with Tinker [52]. Spectra band shapes have been obtained convoluting each vertical transition of each snapshot with a Gaussian function of full width at half-length of 0.2 eV. Frenkel Hamiltonian ECD spectra have been obtained using a code developed in our laboratory to post-process Gaussian 09 outputs and publicly available under GPL license. DNA global deformation parameters have been calculated using the Curves+ code developed in Lavery group [53], and the reader may refer to ref. 53 for the description of the collective deformation modes.

2 Results and discussion

In order to assess the performance of the simple Frenkel Hamiltonian approach in Fig. 2, we report the comparison of the ECD spectra obtained considering a subsystem composed of the two central base pairs, treated with the Frenkel effective Hamiltonian or calculating at ab initio QM/MM level (QM approach) the excited states for the four bases supersystem. For both double strands, one may notice that the QM approach leads to systematically red-shifted maxima compared to the effective Hamiltonian. Indeed, it appears that the maxima are systematically shifted by about 10–15 nm in a consistent way among different bands and different strands.

On the other hand, the band shapes for both systems appear to be quite correctly reproduced, as it is confirmed by the figure presented in Supplementary Information where we have applied a shift of 8 nm (0.17 eV) for poly[d(AT)] and 15 nm (0.35 eV) for poly[d(CG)] to the Frenkel Hamiltonian wavelengths. Indeed, after the shift, almost all the bands appear quite well superimposed. In the case of poly[d(AT)] strand, one can see the low-intensity positive maxima at longer wavelengths followed by a strongly negative band (at about 245 nm). Note, however, that the low-energy positive maximum is much more intense when considering the Frenkel approach. Poly[d(GC)] presents a more complex structure with a large positive band at lower energy (260–240 nm) followed by a negative band at about 230 nm; note, however, that the relative intensity of the negative band when using the Frenkel Hamiltonian appears reduced compared to the full QM/MM one. It is, however, evident, and despite some discrepancies, that even the crude Frenkel approximation used here is able to correctly recover the main features of DNA ECD provided the energy shift is taken into account. Note also that all the transitions are mainly of valence π–π^* nature, charge-transfer transitions appearing only at higher transition energies; this fact also justifies the use of the Frenkel Hamiltonian that does not take into account charge-transfer.

In Fig. 3, we report the analysis of the convergence with the number of monomers, i.e., the DNA nucleobases included in the Frenkel model Hamiltonian for the two representative DNA fragments. To facilitate comparison, the intensities have been renormalized per number of base pairs. From the spectra reported there, we may evidence a relatively fast convergence of the Frenkel ECD spectra.

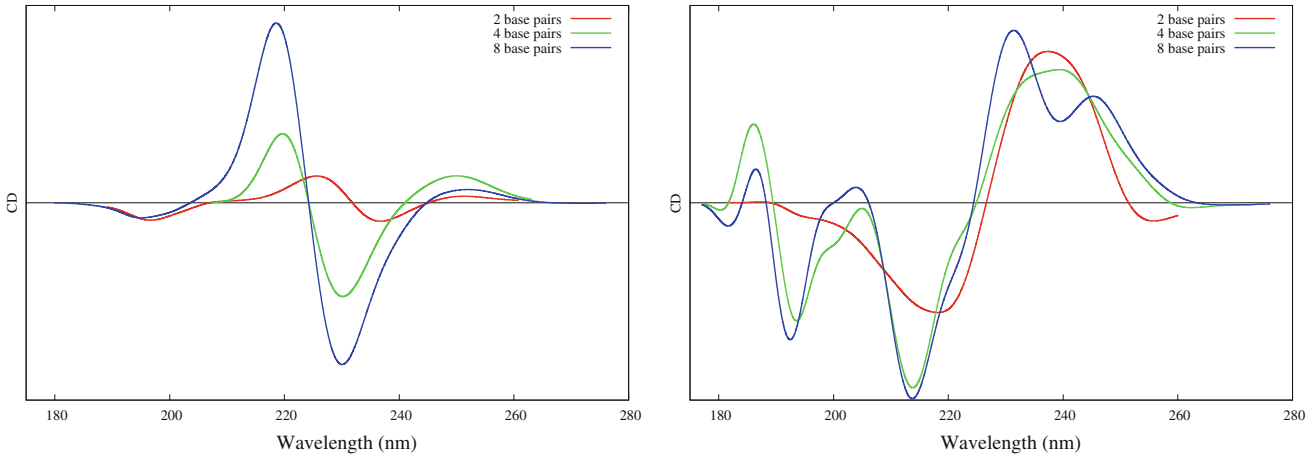

Fig. 3 Simulated ECD spectra using the Frenkel Hamiltonian for poly[d(AT)] (*left panel*) and poly[d(CG)] (*right panel*). An increasing number of bases were included in the model Hamiltonian to check the convergence. Wavelengths in nm, intensities in arbitrary units

Indeed, if the simplest model (i.e., the two base pairs) only gives a very approximated picture of the spectrum, the differences between the four and eight base pairs model are much smaller. More in detail in the case of the poly[d(AT)] spectrum, we may evidence the presence of a very low-intensity positive band at around 250–260 nm followed by a negative band at about 230 nm. The differences in the excitation wavelengths given by the four or eight base pair models are extremely negligible.

The spectrum of the poly[d(CG)] double strand appears again much more complicated, in particular in this case the low-energy band is much larger, extending from 260 to 230 nm, and presents an almost double maxima structure. The first band is followed by a negative band peaking at about 218 nm. Once again, the differences between the eight and four bases model are quite negligible, even if it has to be noted that the eight bases model seems much more suited to capture the complex structure of the first band. Nonetheless, we may quite safely conclude that the four and eight bases models appear as converged and are able to catch the main features of the DNA ECD spectra.

Indeed, even if a direct experimental comparison appears difficult since ECD spectra are extremely sensible for instance to salt concentration, we may note that our simulated spectra reproduce quite nicely experimental data as the ones reported by Kypr et al. [32], in particular concerning the presence of the low-intensity positive band followed by the important negative one for poly[d(AT)] strands as well as the large and complex positive band shown by the poly[d(CG)] strand. It has, however, to be cited that the intensity of the lower-energy positive band evidenced in the experimental poly[d(AT)] spectrum is strongly reduced in our model.

In all the previous calculations, we have reported results only for bases embedded in the central regions of the double strand, i.e., far from the borders. However, since we are using a finite strand, we may wonder whether the influence of border effects can induce important modification in the calculated ECD spectra.

In Fig. 4, we report the ECD spectra obtained including all the 15 base pairs constituting our two model strands in the Frenkel Hamiltonian. We can immediately see two very different situations, indeed the poly[d(AT)] strand present a spectrum that is absolutely coherent with the features evidenced by the eight base pairs model. On the other hand, the poly[d(CG)] strand gives now a spectrum that looks almost specular compared to the one obtained with the eight base pairs that satisfactorily reproduced the experimental measurements.

Indeed, the reason for such discrepancy should not be found in a bad convergence of the model, and on the contrary, the 15 base pairs spectrum is indeed plagued by border effects due to the terminal bases. This fact is rationalized in Fig. 5 in which we see that the general features of the 15 base pairs spectrum are strongly dominated by the edge bases. Indeed, the external bases at the 3′ and 5′ extremities have a total different spectroscopic signature compared to the central ones and are characterized by a negative band at higher wavelengths and a positive one at lower ones. Since incidentally the border bases ECD spectrum happens to have absolute values of the intensity that is almost double compared to the one calculated from the internal bases, the 15 bases spectrum will not be representative of a general and longer poly[d(CG)] B-DNA fragment.

Although no real ejection from the stacked structure of the terminal bases is observed all along the dynamic trajectory, we may observe a larger deviation from the ideal

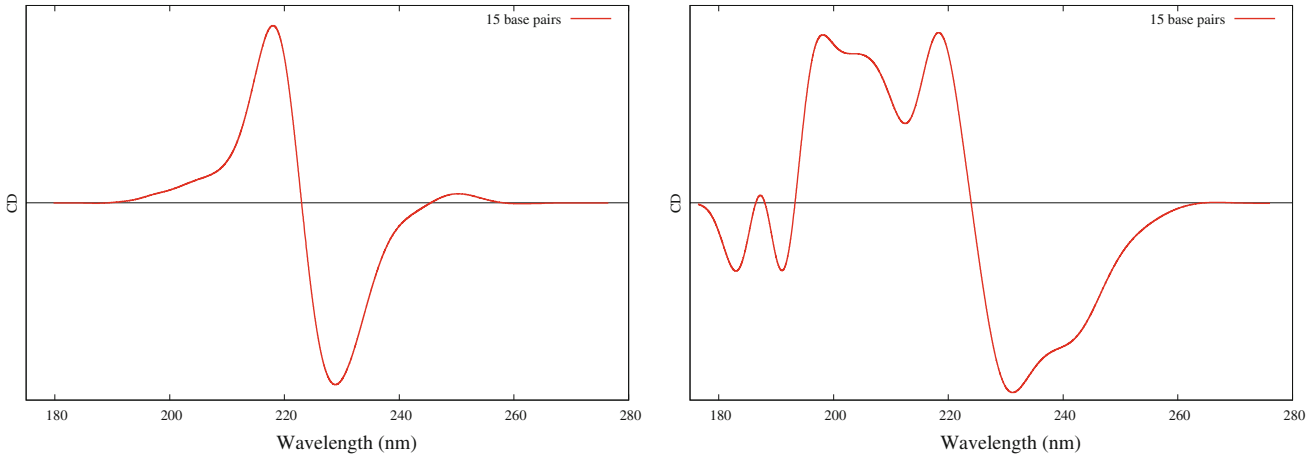

Fig. 4 Simulated ECD spectra calculated including all the 15 base pairs in the Frenkel Hamiltonian. Poly[d(AT)] in the *left panel* and poly[d(CG)] in the *right panel*, respectively. Wavelengths in nm, intensities in arbitrary units

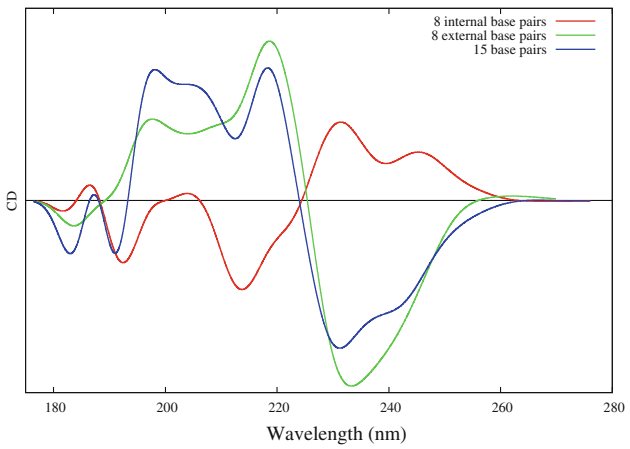

Fig. 5 Calculated ECD spectra for the poly[d(CG)] strand considering the 15 base pairs, only the eight central base pairs and the eight base pairs at the extremities. In the last case, we took four base pairs at the 3′ end and the four others at the 5′ border. Wavelengths in nm, intensities in arbitrary units

helical structure in the case of the poly[d(CG)] strand than in the case of the poly[d(AT)].

This aspect can be also be quantified using the global intra- and inter-base DNA deformation parameters [53]. Indeed, the terminal base of poly[d(CG)] strands experiences an average deviation from an ideal B-strand of about 20° for the "buckle" and "propel" angle and of about 14° for the "opening," and in contrast, central bases are not exceeding 10° deviations. The same behavior is found for the inter-base parameters with about 20° deviations for "tilt" and "roll" and 15° for the twist angles in the case of the poly[d(CG)] border bases. On the other hand, all the poly[d(AT)] parameters experience very limited deviations from the ideal B-DNA structure (smaller than 10°). Anyway, one would need longer molecular dynamics, with timescale approaching the μs, as well as longer DNA strands to extract all the structural information related to the border and sequence effect.

Anyway from that last analysis, it is evident that extreme care should be taken to avoid border effects using sufficiently long enough DNA fragments. Luckily enough due to the fast convergence of the Frenkel Hamiltonian ECD with the number of bases pairs, this aspect should not impose too heavy constraints in the calculation of circular dichroism spectra.

3 Conclusions

We have reported the simulation of ECD spectra for two different representative DNA double strands. Our proposed protocol consisted in the combination of molecular dynamic to obtain a reasonable sampling of the configuration space explored by the DNA fragments with QM/MM to obtain the properties of excited states of single chromophores. By comparison with larger QM treatment of multichromophoric ensemble of DNA nucleobases, we have validated the extremely simple Frenkel Hamiltonian approach to obtain a good simulation of ECD spectra. We have also evidenced the necessity to take extreme care to avoid unphysical border effects that could give unreliable spectra. However, we have shown that the convergence with the number of base pairs included in the effective Frenkel Hamiltonian is relatively fast, and hence, it allows an easy and efficient calculation of those properties.

The validation of our protocol gives us a general strategy to study and interpret ECD spectra of complex DNA aggregates, for instance, it will allow us to model the differences induced in DNA spectrum upon interactions with sensitizers, as well as to efficiently study induced circular

dichroism. Another possible extension of the protocol will be the study of non-canonical DNA structures such as G-quadruplex also in interaction with potential anti-tumoral drugs.

Acknowledgments The COST in Chemistry Action CM1201 "Biomimetic Radical Chemistry" and the French ANR BalanceSupra and QMC=Chem are acknowledged. AM thanks CNRS for the funding of the "Chaire d'excellence" program.

References

1. Stratmann SA, van Oijen AM (2014) DNA replication at the single molecular level. Chem Soc Rev 43:1201–1220
2. Zhao J, Bacolla A, Wang G, Vasquez KM (2010) Non-B DNA structure-induced genetic instability and evolution. Cell Mol Life Sci 67:43–62
3. Pérez A, Lucque FJ, Orozco M (2012) Frontiers in molecular dynamic simulations of DNA. Acc Chem Res 45:196–205
4. Garrec J, Patel C, Röthlisberger U, Dumont E (2012) Insights into intrastrand cross-link lesions of DNA from QM/MM molecular dynamics simulations. J Am Chem Soc 134:2111–2119
5. Watson JD, Crick FHC (1953) A structure for deoxyribose nucleic acid. Nature 171:737–738
6. Lyubchenko YL (2004) DNA structure and dynamics. Cell Biochem Biophys 41:75–98
7. Galindo-Murillo R, Cheatham TE III (2014) DNA binding dynamics and energetics of cobalt, nickel and copper metallopeptides. Chem Med Chem 9:1252–1259
8. Heddi B, Pahn AT (2011) Structure of human telomeric DNA in crowded solutions. J Am Chem Soc 133:9824–9833
9. Lavery R, Zakrzewska K, Beveridge D, Bishop TC, Case DA, Cheatham TC III, Dixit S, Jayaram B, Lankas F, Laughton C, Maddocks JH, Michon A, Osman R, Orozco M, Perez A, Singh T, Spackova N, Sponer J (2010) A systematic molecular dynamics study of nearest-neighbor effects on base pair and base pair step conformations and fluctuations in DNA. Nucleic Acids Res 38:299–313
10. Pahn AT, Mergny J-L (2002) Human telomeric DNA: G-quadruplex, i-motifs and Watson and Crick double-helix. Nucleic Acids Res 30:4618–4625
11. Pérez A, Lankas F, Luque FJ, Orozco M (2008) Towards a molecular dynamics consensus view of B-DNA flexibility. Nucleic Acids Res 36:2379–2394
12. Patel C, Drsata T, Lankas F, Dumont E (2013) Structure, dynamics and interactions of a C4'-oxidized abasic site in DNA: a concomitant strand scission reverse affinity. Biochemistry 52:8115–8125
13. Very T, Despax S, Hébraud P, Monari A, Assfeld X (2012) Spectral properties of polypyridyl Ruthenium complex intercalated in DNA: theoretical insights on the surrounding effects for $[Ru(dppz)(bpy)_2]^{2+}$. Phys Chem Chem Phys 14:12496–12504
14. Very T, Ambrosek D, Otsuka M, Gourlauen C, Assfeld X, Monari A, Daniel C (2014) Photophysical properties of Ru (II) polypyridyl DNA intercalators: effects of the molecular surroundings investigated by theory. Chem Eur J 20:12901–12909
15. Etienne T, Very T, Perpète EA, Monari A, Assfeld X (2013) A QM/MM study of the absorption spectrum of Harmane in water solution and interacting with DNA: the crucial role of dynamic effects. J Phys Chem B 117:4973–4980
16. Dumont E, Monari A (2015) Interaction of palmatine with DNA: an environmentally controlled drug. J Phys Chem B 119:410–419
17. Huix-Rottlant M, Dumont E, Ferré N, Monari A (2015) Photophysics of acetophenone interacting with DNA: why the road to photosensitization is open. Photchem Photobiol. doi:10.1111/php.12395
18. Cuquerella MC, Lhiaubet-Vallet V, Cadet J, Miranda MA (2012) Benzophenone photosensitized DNA damages. Acc Chem Res 45:1558–1570
19. Dumont E, Monari A (2013) Benzophenone and DNA: evidence for a double insertion mode and its spectral signature. J Phys Chem Lett 4:4119–4124
20. Dumont E, Wibowo M, Roca-Sanjuan D, Garavelli M, Assfeld X, MMonari A (2015) Resolving the benzophenone DNA-photosensitization mechanism at QM/MM level. J Phys Chem Lett 6:576–580
21. Zeglis BM, Pierre VC, Barton JK (2007) Metallo-intercalators and metallo-insertors. Chem Comm 44:4565–4579
22. Song H, Kaiser JT, Barton JK (2012) Crystal structure of Δ-[Ru(bipy)2d ppz]2+ bound to mismatched DNA reveals side-by-side metalloinsertion and intercalation. Nat Chem 4:615–620
23. Hirakawa K, Hirano T, Nishimura Y, Arai T, Nosaka Y (2012) Dynamics of singlet oxygen generation by DNA-binding photosensitizers. J Phys Chem B 116:3037–3044
24. Zhao J, Wu W, Sun J, Guo S (2013) Triplet photosensitizers: from molecular design to applications. Chem Soc Rev 42:5323–5351
25. Dougherty TJ, Gomer CJ, Henderson BW, Jori G, Kessel D, Korbelik M, Moan J, Peng Q (1998) Photodynamic therapy. J Natl Cancer Inst 90:889–905
26. Agostinis P, Berg K, Cengel KA, Foster TH, Girotti AW, Gollnick SO, Hahn SM, Hamblin MR, Juzeniene A, Kessel D (2011) Photodynamic therapy of cancer: an update cancer. J Clin 61:250–281
27. Biffi G, Tannahill D, Mc Cafferty J, Balasubramaniam S (2013) Quantitative visualization of DNA G-quadruplexes structure in human cells. Nat Chem 5:182–186
28. Shammas MA, Shmookler Reis RJ, Akiyama M, Koley H, Chauhan D, Hideshima T, Goyal RK, Hurley LH, Anderson KC, Munshi NC (2003) Telomerase inhibition and cell growth arrest by G-quadruplex interactive agent in multiple myeloma Mol. Cancer Ther 2:825–833
29. Lam EY, Beraldi D, Tannahil D, Balasubramaniam S (2013) G-quadruplex structures are stable and detectable in human genomic DNA. Nat Comm 4:1796
30. Terenzi A, Bonsignore R, Spinello A, Gentile C, Martorana A, Ducani C, Högberg B, Almerico AM, Lauria A, Barone G (2014) Selective G-quadruplex stabilizers: Schiff-base metal complexes with anticancer activity. RSC Adv 4:33245–33256
31. Norman P, Linares M (2014) On the interplay between chirality and exciton coupling: a DFT calculation of the circular dichroism in π -stacked ethylene. Chirality 26:483–489
32. Kypr J, Keinovska I, Renciuk D, Vorlickova M (2009) Circular dichroism and conformational polymorphism of DNA. Nucleic Acids Res 37:1713–1725
33. Gray DM, Morgan AR, Ratliff RL (1978) A comparison of the circular dichroism spectra of synthetic DNA sequences of the homopurine. homopyrimidine and mixed purine- pyrimidine types. Nucleic Acids Res 5:3679–3695
34. Nielsen LM, Hoffman SV, Nielsen SB (2013) Electronic coupling between photo-excited stacked bases in DNA and RNA strands with emphasis on the bright states initially populated. Photochem Photobiol Sci 12:1273–1285
35. Vorlickova M, Kejnovska I, Bednarova K, Renciuck D, Kypr J (2012) Circular dichroism spectra of DNA: from duplex to quadruplexes. Chirality 24:691–698
36. Di Meo F, Pdersen MN, Rubio-Magnieto J, Surin M, Linares M, Norman P (2015) DNA electronic circular dichroism on the

inter-base pair scale: an experimental-theoretical case study at the A-T homo-oligonucleotide. J Phys Chem Lett 6:355–359
37. Kubista M, Aakerman B, Norden B (1988) Induced circular dichroism in non-intercalative DNA-drug complexes: sector rules for structural applications. J Phys Chem 92:2352–2356
38. Chantzis A, Very T, Monari A, Assfeld X (2012) Improved treatment of surrounding effects: UV/vis absorption properties of a solvated Ru(II) complex. J Chem Theory Comput 8:1536–1541
39. Prokhorenko VI, Steensgaard DB, Holzwarth AR (2003) Exciton theory for supramolecular chlorosomal aggregates: 1. aggregate size dependence of the linear spectra. Biophys J 85:3173–3186
40. Spano FC, Meskers SCJ, Hennebicq E, Beljonne D (2007) Probing excitation delocalization in supramolecular chiral stacks by means of circular polarized light: experiment and modeling. J Am Chem Soc 129:7044–7054
41. Nieto-Ortega B, Ramirez FJ, Amabilino DB, Linares M, Beljonne D, Lopéz Navarete JT, Casado J (2012) Electronic and vibrational circular dichroism spectroscopies for the understanding of chiral organization in porphyrin aggregates. Chem Commun 48:9147–9149
42. Jurinovich S, Pescitelli G, Di Bari L, Mennucci B (2014) A TDDFT/MMPol/PCM model for the simulation of exciton-coupled circular dichroism spectra. Phys Chem Chem Phys 16:16407–16418
43. Viani L, Corbella M, Curutchet C, O'Reilly EJ, Olaya-Castro A, Mennucci B (2014) Molecular basis of the exciton-phonon interactions in PE545 light-harvesting complex. Phys Chem Chem Phys 16:16302–16311
44. Munoz-Losa A, Curutchet C, Krueger BP, Hartsell LR, Mennucci B (2009) Fretting about FRET: failure of the ideal dipole approximation. Biophys J 96:4779–4788
45. Case D, Babin V, Berryman J, Betz R, Cai Q, Cerutti D, Cheatham T III, Darden T, Duke R et al (2014) AMBER 14. University of California, San Francisco
46. Pérez A, Marchan I, Svozil D, Sponer J, Cheatham TE, Laughtonand CA, Orozco M (2007) Refinement of the AMBER force field for nucleic acids: improving the description of $\alpha\gamma$ conformers. Biophys J 92:3817–3829
47. Monari A, Rivail J-L, Assfeld X (2013) Theoretical modeling of large molecular systems. Advances in the local self consistent field method for mixed quantum mechanics, molecular mechanics calculations. Acc Chem Res 46:596–603
48. Ferré N, Assfeld X, Rivail JL (2002) Application of the local self-consistent-field method to core-ionized and core-excited molecules, polymers, and proteins: true orthogonality between ground and excited states. J Chem Phys 117:4119–4125
49. Zhao Y, Truhlar DG (2008) The M06 suite of density functionals for main group thermochemistry, thermochemical kinetics, noncovalent interactions, excited states, and transition elements: two new functionals and systematic testing of four M06-class functionals and 12 other functionals. Theor Chem Acc 120:215–241
50. Krishan R, Binkley JS, Seeger R, Pople JA (1980) Self-consistent molecular orbital methods. XX. A basis set for correlated wavefunctions. J Chem Phys 72:650–654
51. Frisch MJ, Trucks GW, Schlegel HB, Scuseria GE, Robb MA, Cheeseman JR, Scalmani G, Barone V, Mennucci B, Petersson GA et al. (2009) Gaussian09 revision D.01. Gaussian Inc., Wallingford, CT
52. http://dasher.wustl.edu/tinker/
53. Lavery R, Moakher M, Maddocks JH, Pekteviciute D, Zakrzewska K (2009) Conformational analysis of nucleic acids revisited: curves+. Nucleic Acids Res 37:5917–5929